Cumhuriyet Science Journal
Faculty of Science, Cumhuriyet University
58140 - Sivas - Türkiye
Phone: +90(346) 487 13 72
Fax: +90(346) 219 11 86
e-mail: csj@cumhuriyet.edu.tr
http://csj.cumhuriyet.edu.tr/en
http://dergipark.org.tr/en/pub/csj

Cumhuriyet Science Journal Vol: 44 No: 3 Year 2023

Sivas Cumhuriyet University

ISSN : 2680-2587
e-ISSN : 246-2587X
dergipark.org.tr/tr/pub/csj
e-mail: csj@cumhuriyet.edu.tr

Cumhuriyet Science Journal

Cumhuriyet Science Journal (CSJ) is an official publication of Sivas Cumhuriyet University, Science Faculty. The high quality research papers related to the natural sciences are published as online four times a year. CSJ is an open access, free of charge journal and all articles in CSJ have undergone peer review and upon acceptance are immediately and permanently free for everyone to read and download.

Volume: 44 Number: 3 Year: 2023

ISSN: 2587-2680
e-ISSN: 2587-246X
Period: Quarterly
Founded: 2002
Publisher: Sivas Cumhuriyet University

Cumhuriyet Science Journal (CSJ)

Journal Previous Name: Cumhuriyet Üniversitesi Fen-Edebiyat Fakültesi Fen Bilimleri Dergisi

Old ISSN: 1300-1949

Abstracted&Indexeding

ULAKBİM TR-Dizin

Index Copernicus (ICI Journals Master List)

Clarivate Analytics Zoological Record

Crossref

WorldCat

Akademik Dizin

Arastirmax Bilimsel Yayın İndeksi

Bielefeld Academic Search Engine (BASE)

Directory of Research Journal Indexing (DRJI)

Google Scholar

Research Gate

Idealonline

Publication Type: Peer Reviewed Journal

Cite Type: Cumhuriyet Sci. J.

Contact Information

Faculty of Science Cumhuriyet University
58140 Sivas- TURKEY
Phone: +90 (346) 487 13 72
Fax: +90 (346) 219 11 86
e-mail: csj@cumhuriyet.edu.tr
http://dergipark.gov.tr/csj

	CONTENTS		PAGES
1	Investigation of Antimicrobial and Antioxidant Activities of some Lichens **Dilek US Ayşe KARA Elif ÜNAL Hülya AKINCIOĞLU Ali ASLAN Mesut TAŞKIN**	*Research Article*	418 - 429
2	Electrochemical Study of Clopidogrel and its Determination in Pharmaceutical Preparations Using Square Wave Voltammetry **Bilal YILMAZ Semih YILMAZ**	*Research Article*	430 - 435
3	Melatonin as a Potential Therapeutic Tool in Allergic Rhinitis Induced by House-Dust Mite **Ayşe Sezim ŞAFAK Pakize Neslihan TAŞLI Ezgi AVŞAR ABDİK Hüseyin ABDİK Fikrettin ŞAHİN**	*Research Article*	436 - 443
4	Comparative Skull and Mandible Geometric Morphometrics of Two Species of Mice, Mus domesticus and Mus macedonicus (Muridae, Rodentia) in Turkey **Sadık DEMİRTAŞ Medine ÖZMEN Metin SİLSÜPÜR Damla KIRAL**	*Research Article*	444-449
5	A New Nickel(II) Complex Derived From Bisthiocarbohydrazone: Synthesis, Characterization, Crystal Structure and Antioxidant Activity **Yeliz KAYA**	*Research Article*	450 - 455
6	Determination of Progesterone in Pharmaceutical Preparations by UV, First-order Derivative Spectrophotometry and Gas Chromatography **Bilal YILMAZ Mevlüt ALBAYRAK Yücel KADIOĞLU**	*Research Article*	456 - 463
7	Effect of Knitting Pattern of PP Mesh on the Flexural Properties of Heat-cured PMMA Denture Base Resin **Kaan YERLİYURT Sinan EĞRİ**	*Research Article*	464 - 469
8	Antioxidant Capacity of Essential Oils Obtained from Myrtus communis L. and Citrus sinensis (L.) Osbeck Plants Widely Consumed in Adana Region **Merve NENNİ Seçil KARAHÜSEYİN**	*Research Article*	470 - 473
9	The Role of COVID-19 Vaccine Literacy in The Effect of e-Health Literacy on Vaccine Attitude **Rukiye ASLAN Ebrar ILIMAN YALTAGİL Aysel ARSLAN Ahmet ALİM**	*Research Article*	474 - 484
10	Determination of Caffeine in Human Plasma by Using Liquid Chromatography-Tandem Mass Spectrometry **Fırat YERLİKAYA Onursal SAĞLAM**	*Research Article*	485 - 490
11	A Density Functional Theory (DFT) based Analysis on the Inhibition Performances of Some Triazole Derivatives for Iron Corrosion **Nihat KARAKUŞ Savaş KAYA**	*Research Article*	491 - 496
12	The Effects of Heavy Metals and Molasses on Enzyme Activity of Candida Yeast **Gülşah BAŞKAN Unsal AÇIKEL**	*Research Article*	497 - 503
13	Effect of Synthesizing Process on the Formation of Fe3O4 Magnetic Nanoparticles **Cemal AKA Mustafa AKYOL**	*Research Article*	504 - 509
14	Investigation of Adsorption Isotherm Models for Interaction of P(AAm-ClAETA) and Carminic Acid, and Theoretical Approaches **Yasemin IŞIKVER Ali IŞIKVER**	*Research Article*	510 - 515
15	Determination Of Some Trace Elements In Some Lipstick Products By Inductive Coupled Plasma-Mass Spectrometry **Gözde Gülin DALTABAN İNAN Gülay ŞEREN**	*Research Article*	516 - 521
16	Construction of New Ostrowski's Type Inequalities By Using Multistep Linear Kernel **Yasır QAYYUM Haider ALİ Faiz RASOOL Ather QAYYUM**	*Research Article*	522 - 530

17	Relations Among Minimal Elements of a Family of Sets with Respect to Various Set Order Relations **İlknur ATASEVER GÜVENÇ**	*Research Article*	531 - 537
18	An Analytical Approach to Contaminant Transport with Spatially and Temporally Dependent Dispersion in a Heterogeneous Porous Medium **Sujata KUSHWAHA Raja Ram YADAV Lav Kush KUMAR Joy ROY**	*Research Article*	538 - 546
19	3D Stabilized FEM Solution of the MHD Equations in an External Medium and Around a Solid **Selçuk Han AYDIN Mahir Ceylan ERDOĞAN**	*Research Article*	547 - 560
20	Legendre Computational Algorithm for Linear Integro-Differential Equations **Taiye OYEDEPO Abayomi AYOADE Ganiyu AJİLEYE Nneoma Joyce IKECHUKWU**	*Research Article*	561 - 566
21	Exploration of Seasonal Metal Pollution in Karacaören II Dam Lake Sediment Samples using X-ray Fluorescence Method **Gökhan APAYDIN Oğuz Kağan KÖKSAL Erhan CENGİZ Murat ŞİRİN Hasan BALTAS Engin TIRASOĞLU**	*Research Article*	567 - 582
22	Cross-Section Calculations of Medical Radioisotope 64Cu via some Proton, Neutron and Deuteron Reactions **Tuğçe GÜLÜMSER Abdullah KAPLAN**	*Research Article*	583 - 589
23	Comparison of Proton and Photon Radiotheraphy for Left-sided Breast Cancer via Dosimetric Calculations **İnci YEŞİLDERE Sinan KUDAY**	*Research Article*	590 - 594
24	Synthesis and Characterization of Tb–Er Co–Doped Bi2O3 Solid Electrolyte Systems **Murat BALCI**	*Research Article*	595 - 601
25	Bayesian Analysis for the Modified Frechet–Exponential Distribution with Covid-19 Application **Neriman AKDAM**	*Research Article*	602 – 609
26	Estimation of the Density and Cumulative Distribution Functions of the Topp-Leone Distribution **Lazhar BENKHELIFA**	*Research Article*	610 -616

Cumhuriyet Sci. J., 44(3) (2023) 418-429
DOI: https://doi.org/10.17776/csj.1317923

Cumhuriyet Science Journal

| csj.cumhuriyet.edu.tr | Founded: 2002 ISSN: 2587-2680 e-ISSN: 2587-246X Publisher: Sivas Cumhuriyet University

Investigation of Antimicrobial and Antioxidant Activities of some Lichens

Dilek Us[1,a], Ayşe Aydan Kara[1,b,*], Elif Ünal Bülbül[1,c], Hülya Akıncıoğlu[2,d], Ali Aslan[3,e], Mesut Taşkın[4,f]

[1]*Department of Biology, Faculty of Science, Ataturk University, Erzurum,Türkiye*
[2]*Department of chemistry, Faculty of Science, Ağrı İbrahim Çeçen University, Ağrı, Türkiye*
[3]*Department of Pharmaceutical Botany, Faculty of Pharmacy, Van Yüzüncü Yıl University, Van.*
[4]*Department of Molecular Biology and Genetics, Faculty of Science, Ataturk University, Erzurum, Türkiye*
**Corresponding author*

Research Article

History
Received: 21/06/2022
Accepted: 18/09/2023

ABSTRACT

This study investigated the antimicrobial and antioxidant properties of methanol extracts from five lichen species: *Polycauliona candelaria* (Syn. *Xanthoria candelaria*), *Nephromopsis chlorophylla* (Syn. *Cetraria chlorophylla*), *Circinaria calcarea* (Syn. *Aspicilia calcarea*), *Bryoria capillaris* (Syn. *Alectoria cana*), and *Peltigera canina* (Syn. *Dermatodea canina*). Antimicrobial activities were determined using the agar disc diffusion method, while minimal inhibitory concentration (MIC) values were determined using the micro-well dilution method. Among the lichen species, methanol extract of *Circinaria calcarea* exhibited the highest antimicrobial activity, with a 15 mm zone of inhibition against *Escherichia coli* and *Bacillus cereus*. It also demonstrated the lowest MIC value (31.25 µg/mL) against *Bacillus cereus*, *Bacillus subtilis*, *Clostridium perfringens* and *Escherichia coli* were the most sensitive microorganisms to lichens. Various antioxidant determination methods were employed to assess the antioxidant activities of the lichens, including ferric ion (Fe^{+3}) reduction capacity, cupric ion (Cu^{+2}) reduction capacity, ferric ion reducing antioxidant power (FRAP), DPPH radical scavenging activity, DMPD radical scavenging activity and metal chelating activity using the bipyridyl reagent. All lichens exhibited excellent antioxidant activity, particularly in metal chelating activity using the bipyridyl reagent. *Peltigera canina* demonstrated the highest antioxidant activity among the studied lichen species across most of the applied method.

Keywords: Antimicrobial activity, Antioxidant activity, Lichen.

[a] dilekk.aktas@hotmail.com https://orcid.org/0009-0007-2374-2276
[b] aydan@atauni.edu.tr https://orcid.org/0000-0002-1889-3498
[c] elifunal25@gmail.com https://orcid.org/0009-0004-5228-7223
[d] hgakincioglu@agri.edu.tr https://orcid.org/0000-0001-5453-0953
[e] aliaslan@yyu.edu.tr https://orcid.org/0000-0002-5122-6646
[f] mesut.taskin@atauni.edu.tr https://orcid.org/0000-0002-9350-9628

Introduction

Lichens are symbiotic organisms of fungi and algae. These organisms that constitute the lichen form a new association with morphological and physiological features that are unlike themselves. These rootless, stemless, leafless organisms can live in the most difficult environmental conditions where algae and fungi cannot survive. They are common in almost every region of the world, from the Poles to the Equator, from the sea coast to the highest places in the mountains [1-5].

It is estimated that lichen symbiosis developed 400-600 million years ago [6]. It is stated that there are approximately 300 genera and 25,000 species of lichens in the world and more than 1800 of them are found in the flora of Turkey [4,7]. Various studies have stated that lichens were used for the treatment of diseases in ancient times [4,8]. Many types of lichens were believed to be effective against external burns, wounds, asthma, colds, tuberculosis, gastritis and other diseases [3,9]. Although lichens are occasionally used as food by humans, most lichen species are known to produce toxic substances. For this reason, it is recommended not to use lichens unconsciously [9].

Scientists studying lichen chemistry have found over 1050 compounds in lichens that are thought to be secondary metabolites. There are polyketide-derived aromatic compounds such as depsids, depsidons, dibenzofurans, xanthones and some other compounds such as pulvinic acid, esters, terpenes, steroids, among these compounds [2,3,5,10,11]. Lichens are evaluated as an important material in the fields of food, medicine and industry with these substances which they form as a result of their metabolic activities [3,5].

It has been documented in the literature that lichens and their metabolites have antibacterial, antifungal, antiviral, antiprotozoal, antitumor, anti-inflammatory, antipyretic, analgesic, antiallergic, antibiotic, cytotoxic effects [3,5,10,12,13].

Lichens contain phenolic compounds such as depsids, depsidones and dibenzofurans [5,10]. It has been stated in different studies that the antimicrobial activity of lichens comes from these compounds and their derivatives, lichen metabolites with acid character. As a matter of fact, it has been determined that lichen metabolites such as evernic acid (from the Depsid group), physodic acid, lobaric acid, fumarprotocetraric acid (from the Depsidon group), usnic acid (from the Dibenzofuran derivatives), protolicesterinic acid, pulvinic acid (from the Aliphatic acids) have high antimicrobial effects [3,9].

Numerous studies have highlighted the relationship between the antioxidant activities of lichens and the presence of phenolic compounds within their structures [12]. Literature has consistently reported that lichens harbor diverse secondary lichen substances known for their potent antioxidant properties, primarily attributed to their phenolic groups [2]. Specifically, certain depsides like atranorin (isolated from *Placopsis sp.*) and divaricatic acid (isolated from *Protousnea malacea*), as well as depsidones like pannarin (isolated from *Psoroma pallidum*) and 1'-chloropannarin (isolated from *Erioderma chilense*), have demonstrated notable antioxidant activity Furthermore, the extract of *Umbilicaria antarctica* has emerged as the most effective antioxidant in scavenging free radicals and superoxide anions, with lecanoric acid identified as the primary active compound [2]. These findings substantiate the notion that the remarkable antioxidant potential of lichens can be attributed to the presence of various phenolic compounds, which enable effective scavenging of harmful free radicals [3].

On the other hand, although synthetic antioxidants have been used instead of natural antioxidants in recent years, their use has been restricted or prohibited based on research results showing that they have been toxic and cancer-causing [2,3,8]. Reasons such as high side effects and multi-drug resistance of pathogenic microorganisms due to excessive use of antibiotics limit the use of synthetic drugs. This situation increases the interest in herbal-derived natural medicines with antimicrobial and antioxidant properties day by day. At the same time, researches in this direction on plants are constantly on the agenda. The use of plants for medicinal purposes is in demand all over the world as well as in our country. Among the reasons for this are that, unlike synthetic drugs, herbal medicines have much fewer side effects and are more easily obtainable and have several beneficial effects [5,8,14-16].

In this study, our aim to determine the in vitro antimicrobial and antioxidant activities of some lichens (*Polycauliona candelaria*, *Nephromopsis chlorophylla*, *Circinaria calcarea, Bryoria capillaris, Peltigera canina*) .

Materials and Methods

Collection and Identification of Lichens

In this study, we examined five lichen species. Lichen samples were collected by Prof. Dr. Ali ASLAN from the Oltu district of Erzurum province on 15 August 2011 and identified by using various flora books [17-20]. The lichen species investigated were as follows: Circinaria calcarea (L.) A. Nordin, Savić & Tibell (Syn. Aspicilia calcarea (L.) Körb), ATA-KKEF-772; Bryoria capillaris (Ach.) Brodo & D. Hawksw (Syn. Alectoria cana (Ach.) Leight), ATA-KKEF-771; Nephromopsis chlorophylla (Willd.) Divakar, A. Crespo & Lumbsch (Syn. Cetraria chlorophylla (Willd.) Poetsch;), ATA-KKEF-773; Peltigera canina (L.) Willd (Syn. Dermatodea canina (L.) A. St.-Hil.), ATA-KKEF-774; Polycauliona candelaria (L.) Frödén, Arup & Søchting (Syn. Xanthoria candelaria (L.) Th. Fr.), ATA-KKEF-775. Identified lichen samples were kept in herbarium of The Faculty of Pharmacy, Van Yüzüncü Yıl University.

Microorganisms

Microorganisms were obtained from Erzurum Provincial Health Directorate Public Health Laboratory and Atatürk University, Science Faculty, Biology Department. A total of 12 microorganisms (11 bacterial species and 1 fungus species) including, *Bacillus cereus* (ATCC 10876),*Clostridium perfringens* (Etlik Vet.5-10-7), *Escherichia coli* (ATCC 11229), *Enterococcus feacalis* (ATCC 29212),), *Klebsiella oxytoca* (ATCC 43086), *Listeria monocytogenes* (ATCC 7677), *Proteus mirabilis* (ATCC 15146), *Staphylococcus aureus* (ATCC 25923-12), *Streptococcus pyogenes* (ATCC 19615), *Bacillus subtilis* (ATCC 6633), *Salmonella enteritidis* (Clinical), *Candida albicans* (ATCC 60193)were used.

Preparation of Lichen Extracts

Lichens were dried and ground into powder. 10 g of each lichen was taken and extracted with 250 mL of methanol in a Soxhlet device (Soxhlet extractor (Isopad, Heidelberg, Germany)) for 72 hours. The mixture was filtered (with Whatman filter paper no: 1) and the solvent was removed in a rotary evaporator (Rotary evaporator, Buchi Labortechnic AG, Flawil, Switzerland) at 40°C. The obtained lichen extracts were stored at +4°C until use [12,21,22].

Antimicrobial Activity

Disc-diffusion method

The Agar disc diffusion method was applied to determine antimicrobial activity. 10 mg/mL solutions were prepared by dissolving 10 mg of each lichen extract in 1 mL of dimethyl sulfoxide (10% DMSO). Amounts of 30 µl (300µg/disc) taken from this solution were absorbed into each (6 mm diameter blank discs, Oxoid). The antibiotics [OFX: Ofloxacin (10 µg/disc), SCF: Sulbactam (30 µg) + Cefoperazona (75 µg) = (105µg/disc), NOV: Novobiocin (30 µg/disc) for bacteria, NYS: Nystatin (30µg/disc) for fungi] were used as a positive controls. Only discs impregnated with solvent (10% DMSO) were used as negative controls. Colonies taken with an inoculating loop from 18-24 hour pure cultures of microorganisms grown on the solid media plates were suspended in phosphate-buffered saline (PBS). The dilutions were prepared to be 10^8 CFU/mL according to McFarland turbidity standard (No.0.5). The samples taken from these dilutions using sterile cotton swab sticks were spread over the surface of proper agar plates (Nutrient Agar (NA,, Oxoid) for bacteria and Potato Dextrose Agar (PDA, Oxoid) for fungi) Then the absorbed discs were placed on the inoculated agar plates. Bacteria were incubated at 37°C for 24 -48 hours and fungi at 30°C for 48 hours. The antimicrobial activities of the lichens were evaluated according to the diameters of the inhibition zone that they were formed against the test microorganisms. The diameters of the inhibition zones

formed as a result of incubation were measured in a millimeter ruler. All the assays were performed in duplicate. [15,22,23]

Minimum Inhibitory Concentration (MIC)

MIC values of methanol extracts of 3 lichen species (*Nephromopsis chlorophylla*, *Circinaria calcarea*, *Bryoria capillaris*) which were found to be effective in terms of antimicrobial activity values were determined by modifying the microwell dilution method [30,31]. 100 µl of medium (Nutrient Broth, Oxoid) was poured into each well of 96-well ELISA microplates for this purpose.

On the other hand, 500 µg/mL dilutions of lichen extracts with dimethyl sulfoxide (10% DMSO) were prepared and 100 µl volume taken from here was transferred to the first well. Then, it was transferred volume of 100 µl from one well to the other. Thus it was prepared serial dilutions that the first well was 250 µg/mL and the other wells were at concentrations of 125 µg/mL, 62.5 µg/mL, 31.25 µg/mL, 15.625 µg/mL, 7.8125 µg/mL, respectively.

The same procedures were applied for Maxipine (µg/mL) antibiotic used as a positive control. DMSO solution was used as a negative control. Colonies taken with an inoculating loop from 18-24 hour pure cultures of microorganisms grown on the solid media plates were suspended in phosphate-buffered saline (PBS). The dilutions were prepared to be 10^8 CFU/mL according to McFarland turbidity standard (No.0.5). 5 µl was inoculated into each well with a micropipette from these dilutions. Then the plates were incubated for 24 hours at 37 °C in a shaker incubator. The lowest essential oil concentration without growth of test microorganisms was evaluated as MIC [15, 22-24]

Antioxidant Activity

Fe^{3+} reducing power activity

The Fe^{3+} reducing power activity of the lichen extracts was determined following the method described by Oyaizu [25]. Firstly, stock solutions of lichen extracts and standard antioxidant compounds (BHA, BHT, α-Tocopherol, and Trolox) were prepared at a concentration of 1 mg/mL. From these stock solutions, different concentrations (10, 20, and 30 µg/mL) were prepared by transferring the appropriate volume (1 mL) to test tubes and diluting with distilled water.

To each tube, 2.5 mL of phosphate buffer (0.2 M, pH 6.6) and 1% $K_3Fe(CN)_6$ were added sequentially, followed by incubation at 50°C for 20 minutes. Subsequently, 2.5 mL of 10% trichloroacetic acid (TCA) was added to the reaction mixture. From the upper phase of the solution, 2.5 mL was taken and mixed with 2.5 mL of distilled water and 0.5 mL of 0.1% $FeCl_3$. The absorbance of the resulting solution was measured at 700 nm against the blank sample. The blank sample consisted of distilled water.

In the control tube, no sample (lichen extracts or standard antioxidant compounds) was added, and the volume was made up with distilled water. Standard antioxidant compounds such as BHA, BHT, α-tocopherol, and trolox were used as positive controls. In this bioanalytical method commonly used in antioxidant studies, the yellow color of the test solution changes to various shades of green due to the reducing activities of the antioxidant substances present in the environment [25]. An increase in absorbance of the reaction mixture indicates an enhancement in the reduction capability.

Fe^{3+} reducing power activities of methanol extracts of the lichens used in the study was determined by measuring the absorbance of solutions of 10,20,30 µg/mL concentrations of the lichens at 700nm. Ferric ions (Fe^{3+}) reducing powers activities of the lichens and standard antioxidant compounds were compared with each other at this concentrations (10,20,30 µg/mL).

Cu^{2+} reducing power-CUPRAC assay

In this method, equal volumes (0.25 mL) of $CuCl_2$ solution (0.01 M), ethanolic neocuproine solution (7.5x10-3 M), and CH_3COONH_4 buffer solution (1 M) were added to test tubes containing lichen extracts at concentrations of 10, 20, and 30 µg/mL, respectively. The reaction mixtures were allowed to incubate for 30 minutes, after which the absorbance values were measured at 450 nm [26].

FRAP Assay

Solutions of lichen extracts and standard antioxidant compounds at concentrations of 10, 20 and 30 µg/ml were placed in test tubes. The volumes were made up to 0.5 mL with buffer solution. Afterward, the same volume (2250 µl) of $FeCl_3$ solution (20 mM) and FRAP reagent were added to the test tubes, respectively and the volume was completed to 5 mL. The mixture in the test tubes was homogenized using a vortex (tube mix). After about 10 minutes, absorbance values were measured at 593 nm wavelength [27].

Bipyridyl ferrous ions (Fe^{2+}) chelating activity

In this antioxidant activity determination method, firstly, $FeSO_4$ solution (0.25 mL, 2 mM) was placed in test tubes. 0.12 mL of lichen extracts or standard antioxidant compounds were added to the solution. Then, 1.5 mL of bipyridyl solution (0.2%) dissolved in 1 mL of Tris-HCl buffer (pH: 7.4) and HCl (0.2 M) were added, respectively. The absorbance of the solution was then measured spectrophotometrically at 562 nm [27].

DPPH· radical scavenging activity

In the method employed to determine antioxidant activity, a solution of 10^{-3}M 2,2-diphenyl-1-picrylhydrazyl (DPPH•) was used as the free radical. Test tubes were prepared with solutions of lichen extracts and standard antioxidant compounds at concentrations of 10, 20, and 30 µg/mL, with the total volume adjusted to 3 mL using ethanol. Subsequently, 1 mL of the stock DPPH• solution was added to each sample tube. The tubes were then incubated at room temperature, shielded from light, for 30 minutes. After the incubation period, the absorbance values were measured at a

wavelength of 517 nm. The decrease in absorbance indicates the amount of DPPH• solution remaining, thereby reflecting the scavenging activity of the samples against the free radical [28].

DMPD radical scavenging activity

In this antioxidant activity determination method, colored radical cation (DMPD•+) was obtained in the first step. 105 mg of DMPD was dissolved in 5 mL of distilled water to prepare 100 mM DMPD solution. Then, 1 mL of the prepared DMPD solution was added to 100 mL of phosphate buffer (0.1 M and pH 5.3). Finally, 0.2 mL of 0.05 M $FeCl_3$ was added. Measurements were made at 505 nm for 1 mL of this solution. Before using the DMPD radical solution, the absorbance value of the control solution was adjusted to 0.900±0.100 nm at 505 nm wavelength with phosphate buffer (0.1 M and pH 5.3). Then, solutions (10, 20, 30 µg/mL) prepared from lichen extracts and standard antioxidant compounds were placed in test tubes and the volume was made up to 0.5 ml with distilled water. Thereupon, DMPD (1ml) solution was added. After waiting for 50 minutes, absorbance values were measured at 505 nm wavelength [29].

Results

Antimicrobial Activities of Lichens

Disc- diffusion method

Metanol extracts of 5 lichen species used in our research were determined antimicrobial activities against 11 bacteria and 1 fungus species and the results are shown in Table 1. Methanol extracts of *C. calcarea*, *N. chlorophylla*, *B. capillaris* lichen species were determined that they showed antimicrobial activity against *B. cereus*, *B. subtilis, C. perfringens* ve *E. coli* with diameter of inhibition zone varying between 9-15 mm. it was determined that *C. calcarea* lichen species among these lichen species showed maximum antimicrobial with diameter of inhibition zone 15 mm against *E. coli* and *B. cereus* bacteria.

Table 1. Antimicrobial activities of methanol extracts of lichens against test microorganisms (Disc Diffusion Method)

Lichens	Diameter of inhibition zone (mm)											
	Proteus mirabilis (ATCC 15146)	*Staphylococcus aureus* (ATTC 25923-12)	*Escherichia coli* (ATCC 11229)	*Bacillus cereus* (ATCC 10876)	*Bacillus subtilis* ATCC 6633	*Clostridium perfringens* (Etlik Vet.5-10-7)	*Enterococcus fecalis* (ATCC 29212)	*Salmonella enteritidis* (Klinik)	*Streptococcus pyogenes* (ATCC 19615)	*Klebsiella oxytoca* (ATCC 43086)	*Listeria monocytogenes* (ATCC 7677)	*Candida albicans* (ATCC 60193)
Polycauliona candelaria	-	-	-	-	-	-	-	-	-	-	-	-
Nephromopsis chlorophylla	-	-	13	10	12	10	-	-	-	-	-	-
Circinaria calcarea	-	-	15	15	10	13	-	-	-	-	-	-
Bryoria capillaris	-	-	13	9	10	9	-	-	-	-	-	-
Peltigera canina	-	-	7	-	-	-	-	-	-	-	-	-
Negative control	-	-	-	-	-	-	-	-	-	-	-	-
Positive control (Antibiotics)	34 (OFX)	21 (SCF)	32 (OFX)	25 (NOV)	28 (OFX)	24 (OFX)	28 (NOV)	25 (OFX)	28 (OFX)	23 (OFX)	25 (SCF)	18 (NYS)

Antibiotics: OFX=Oflaxacin (10 µg/disc), SCF=Sulbactam (30 µg) + Cefoperazona (75 µg)= (105 µg/disc), NYS= Nystatin (30µg/disc) ve NOV= Novobiocin (30 µg/disc)
(-):No inhibition.

It was observed that the extract of the *P. canina* lichen species was effective only against *E. coli* bacteria with a 7 mm diameter of inhibition zone, while the extract obtained from the *P. candelaria* species did not show antimicrobial activity against any of the microorganisms studied.

E. coli, *B. subtilis*, *B. cereus*, *C. perfringens* was understood to be the most sensitive microorganism species against methanol extracts of lichen species in our study. It was determined that none of the methanol extracts of lichens showed antimicrobial activity against *E. feacalis*, *K. oxytoca*, *L. monocytogenes*, *S. pyogenes, S. enteritidis*, *P. mirabilis*, *S. aureus, C. albicans* microorganism species. Negative control discs prepared by impregnation with DMSO alone showed no antimicrobial effect on any of the test microorganisms.

Minimum Inhibitory Concentration (MIC)

MIC values of methanol extracts of *N. chlorophylla, C. calcarea, B. capillaris* lichen species which were effective in terms of antimicrobial activity among the 5 lichen species in our study were determined and the results were shown in Tables 2,3,4.

Among these 3 lichen species, methanol extract of *C. calcarea* lichen species showed the best (lowest) MIC value (31.25 µg/mL) against *E. coli* bacteria species.

Table 2. Antimicrobial activities and MIC values of *Nephromopsis chlorophylla* against test microorganisms

Microorganisms	*N. chlorophylla*		Antibiotics	
	[l]DD	[l]MIC	[a]DD	[a]MIC (Maxipime)
Enterococus fecalis	-	NT	28 (NOV)	125
Proteus mirabilis	-	NT	34(OFX)	125
Streptecoccus pyogenes	-	NT	28(OFX)	62.5
Klebsiella oxytoca	-	NT	23 (OFX)	125
Staphylococcus aureus	-	NT	21(SCF)	62.5
Escherichia coli	13	62.5	32(OFX)	31.25
Bacillus cereus	10	125	25(NOV)	125
Bacillus subtilis	12	250	28 (OFX)	125
Salmonella enteritidis	-	NT	25(OFX)	125
Clostridium perfringens	10	125	24(OFX)	125
Listeria monocytogenes	-	NT	25(SCF)	62.5
Candida albicans	-	NT	18 (NYS)	NT

[a]DD: Agar disc diffüsion method, OFX=Oflaxacin (10 µg/disc), SCF=Sulbactam (30 µg) + Cefoperazona (75 µg) = (105 µg/disc), NYS= Nystatin (30 µg/disc) ve NOV= Novobiocin (30 µg/disc) standard antibiotic discs were used (Oxoid).

[l]DD:, Disc diffusion method, diameters of inhibition zone (mm) formed against test microorganisms by methanol extracts of lichens (300g/disc)

[a]MIC: Minimum inhibitory concentration, standard antibiotic, Maxipime (µg/mL).

[l]MIC: Minimum inhibitory concentration formed against test microorganisms by methanol extracts of lichens (µg/mL)

(-): Inhibition zone not formed.

NT: Not Tested.

Table 3. Antimicrobial activities and MIC values of *Bryoria capillaris* against test microorganisms.

Microorganisms	*B. capillaris*		Antibiotics	
	[l]DD	[l]MIC	[a]DD	[a]MIC (Maxipime)
Enterococus fecalis	-	NT	28 (NOV)	125
Proteus mirabilis	-	NT	34(OFX)	125
Streptecoccus pyogenes	-	NT	28(OFX)	62.5
Klebsiella oxytoca	-	NT	23 (OFX)	125
Staphylococcus aureus	-	NT	21(SCF)	62.5
Escherichia coli	13	62.5	32(OFX)	31.25
Bacillus cereus	9	125	25(NOV)	125
Bacillus subtilis	10	125	28 (OFX)	125
Salmonella enteritidis	-	NT	25(OFX)	125
Clostridium perfringens	9	250	24(OFX)	125
Listeria monocytogenes	-	NT	25(SCF)	62.5
Candida albicans	-	NT	18 (NYS)	NT

[a]DD: Agar disc diffüsion method, OFX=Oflaxacin (10 µg/disc), SCF=Sulbactam (30 µg) + Cefoperazona (75 µg) = (105 µg/disc), NYS= Nystatin (30 µg/disc) ve NOV= Novobiocin (30 µg/disc) standard antibiotic discs were used (Oxoid).

[l]DD:, Disc diffusion method, diameters of inhibition zone (mm) formed against test microorganisms by methanol extracts of lichens (300g/disc)

[a]MIC: Minimum inhibitory concentration, standard antibiotic, Maxipime (µg/mL).

[l]MIC: Minimum inhibitory concentration formed against test microorganisms by methanol extracts of lichens (µg/mL)

(-): Inhibition zone not formed.

NT: Not Tested.

Table 4. Antimicrobial activities and MIC values of *Circinaria calcarea* against test microorganisms.

Microorganisms	*C.calcarea*		Antibiotics	
	[l]DD	[l]MIC	[a]DD	[a]MIC (Maxipime)
Enterococus fecalis	-	NT	28 (NOV)	125
Proteus mirabilis	-	NT	34 (OFX)	125
Streptecoccus pyogenes	-	NT	28(OFX)	62.5
Klebsiella oxytoca	-	NT	23 (OFX)	125
Staphylococcus aureus	-	NT	21(SCF)	62.5
Escherichia coli	15	31.25	32(OFX)	31.25
Bacillus cereus	15	62.5	25(NOV)	125
Bacillus subtilis	10	125	28 (OFX)	125
Salmonella enteritidis	-	NT	25(OFX)	125
Clostridium perfringens	13	250	24(OFX)	125
Listeria monocytogenes	-	NT	25(SCF)	62.5
Candida albicans	-	NT	18 (NYS)	NT

[a]DD: Agar disc diffüsion method, OFX=Oflaxacin (10 µg/disc), SCF=Sulbactam (30 µg) + Cefoperazona (75 µg) = (105 µg/disc), NYS= Nystatin (30 µg/disc) ve NOV= Novobiocin (30 µg/disc) standard antibiotic discs were used (Oxoid).

[l]DD:, Disc diffusion method, diameters of inhibition zone (mm) formed against test microorganisms by methanol extracts of lichens (300g/disc)

[a]MIC: Minimum inhibitory concentration, standard antibiotic, Maxipime (µg/mL).

[l]MIC: Minimum inhibitory concentration formed against test microorganisms by methanol extracts of lichens (µg/mL)

(-): Inhibition zone not formed.

NT: Not Tested.

Antioxidant activities of lichens

Fe^{3+} reducing power activity

As a result of the application of this antioxidant activity determination method, the yellow color of the test solution changes to green in different shades in the presence of antioxidant compounds. This is due to the reducing activities of antioxidant compounds. The reducing capacity of lichen extracts increases in direct proportion to the increasing concentration values. The reducing potential of lichen extracts was determined by measuring the absorbance of sample solutions at different concentrations (10, 20, 30 µg/mL) at 700 nm wavelength.

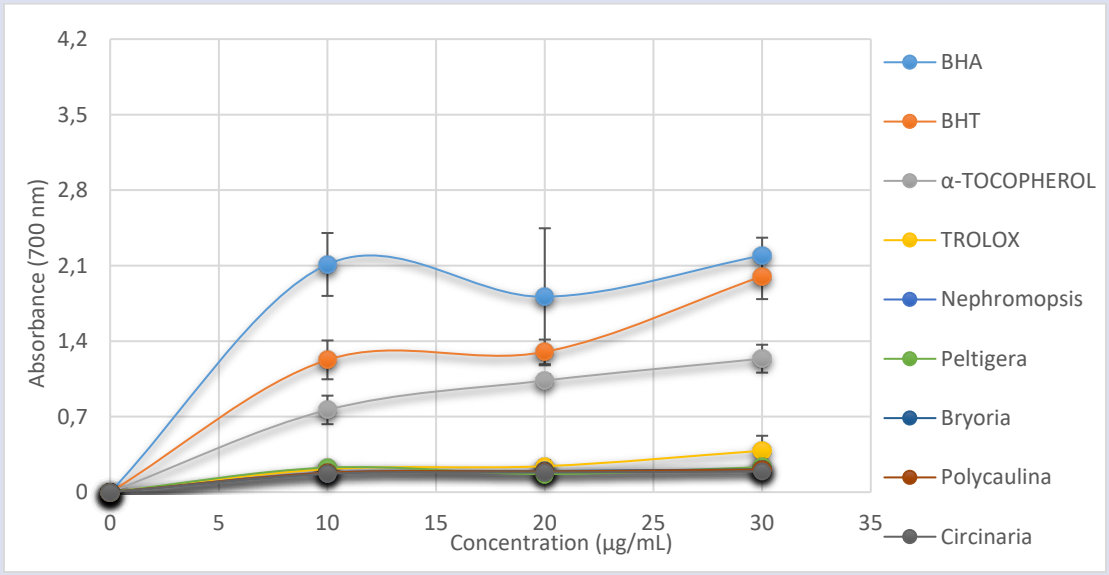

Figure 1. Fe^{3+} reducing activities of lichens (10-30 µg/mL)

The graph showing the reducing capacity of ferric ions (Fe^{3+}) to ferrous ions (Fe^{2+}) of lichen extracts is given in Figure 1. The absorbance values corresponding to 30 µg/mL for standard antioxidant compounds and lichen extracts were shown in Table 5. High absorbance values shown in Table 5 indicate high reducing capacity. For this antioxidant activity determination method, lichen extracts and standard antioxidants were compared with each other at a concentration of 30µg/mL.

As a result, lichens and the standard antioxidant compounds showed Fe^{3+} reducing power activity respectively to be BHA > BHT > -Tokoferol > Troloks > *P. canina*> *B. capillaris* > *P. candelaria* > *N. chlorophylla* > *C. calcarea.*

Cu^{2+} reducing power-CUPRAC assay

This assay is based on the measurement of the absorbance of a complex that results from the reaction of antioxidant with Cu^{2+}-neocuproine reagent. It was found that the reducing capacity of cupric ions (Cu^{2+}) to cuprous ions (Cu^{+}) of lichen extracts increased in direct proportion to the concentration. This reducing capacity of lichen extracts was determined by measuring the absorbance values of solutions of lichen extracts at different concentrations (10, 20, 30 µg/mL) at a wavelength of 450 nm. The graphs showing the cupric ions (Cu^{2+}) reduction results of lichen extracts and standard antioxidant compounds were shown in Figure 2, and the absorbance values corresponding to 30µg/ml for standard antioxidant compounds and lichen extracts were shown in Table 5.

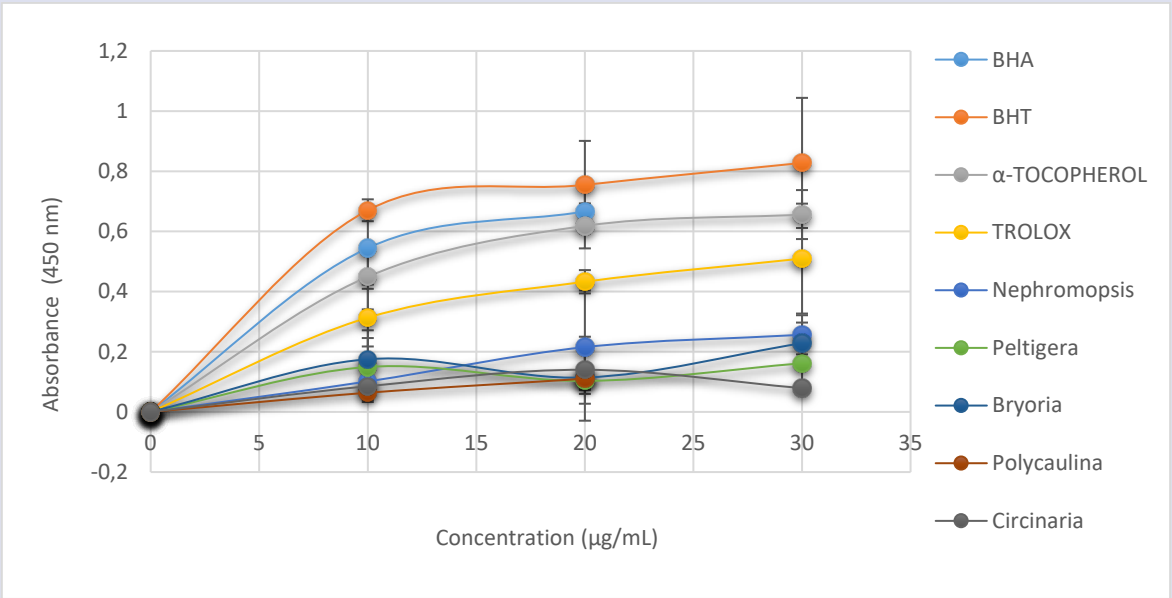

Figure 2. Cu^{2+} reducing activities of lichens (10-30 µg/mL)

The order of antioxidant activity of lichen extracts and standard antioxidants at a concentration of 30µg/ml as a result of this method was as follows; BHT> BHA> α-Tokoferol > Trolox > *N. chlorophylla* > *B. capillaris* > *P. candelaria* > *P. canina*> *C. calcarea*.

FRAP Assay

In the FRAP method, ferric ions (Fe^{3+}) are reduced to ferrous ions (Fe^{2+}). The ferrous (Fe^{2+}) ions formed form a blue complex with Tripyridyl triazine (TPTZ). This blue complex gives the maximum absorbance value at 593 nm wavelength. It was determined that the reducing capacity of lichen extracts, according to the FRAP method, increased in direct proportion to the concentration. The graphs of lichen extracts and standard antioxidant compounds showing the results of the FRAP method were shown in Figure 3 and the absorbance values corresponding to 30µg/mL for standard antioxidant compounds and lichen extracts were shown in Table 5. For this antioxidant activity determination method, when lichen extracts were compared with standard antioxidant compounds at a concentration of 30µg/mL; It was determined that there was a sequence as BHA>α-Tokoferol>BHT> *P. canina* > *B. capillaris* > *N. chlorophylla* > *P.candelaria* > *C.calcarea* > Troloks

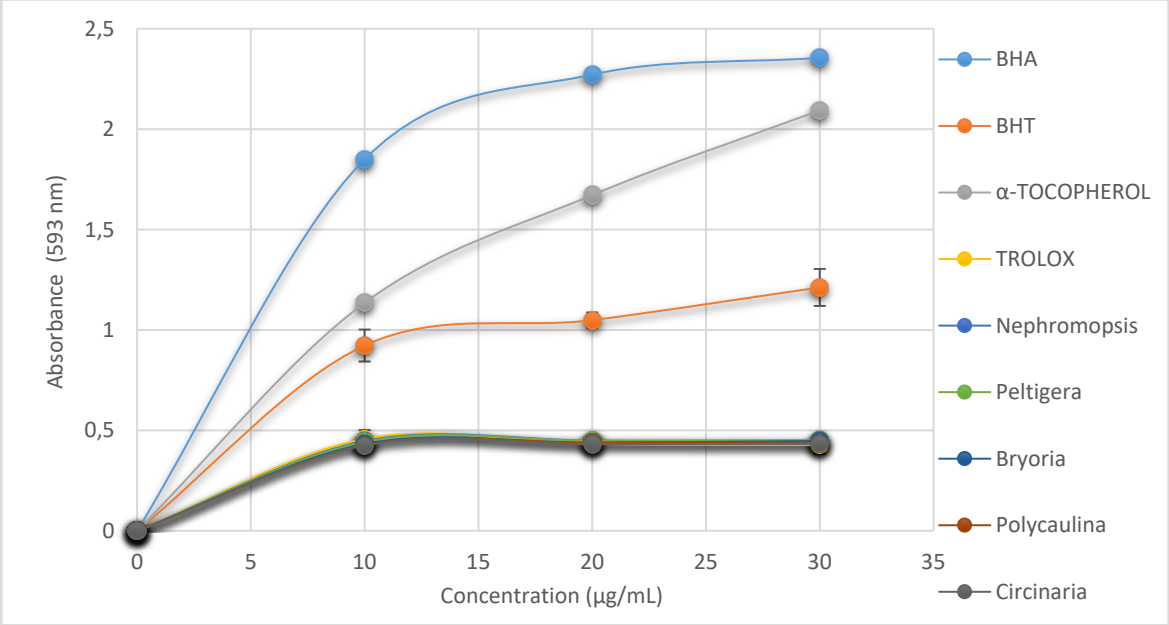

Figure 3. Ferric reducing activities (FRAP) of lichens (10-30 µg/mL)

Table 5. Absorbance values of lichens (30µg/mL) obtained from different antioxidant activity determination methods (Reducing capacity). Standard antioxidant compounds (BHA,BHT, α-Tocopherol, Trolox)

Antioxidants	Fe^{3+}reducing power activity (700nm)	Cu^{2+} reducing power (450nm)	FRAP Assay (593nm)
Control	0	0	0
BHA	2,194	0,691	2,355
BHT	2,001	0,828	1,212
α-Tokoferol	1,237	0,656	2,094
Troloks	0,384	0,510	0,428
Nephromopsis chlorophylla	0,210	0,256	0,440
Peltigera canina	0,232	0,162	0,452
Bryoria capillaris	0,212	0,228	0,447
Polycauliona candelaria	0,211	0,179	0,435
Circinaria calcarea	0,191	0,079	0,433

DPPH radical scavenging activity

Calculations related to the DPPH free radical scavenging activity were made according to the following equation

$$\text{DPPH}\cdot \text{ scavenging effect } (\%) = \left(\frac{\text{Acontrol} - \text{Asample}}{\text{Acontrol}}\right) \times 100$$

A sample is the absorbance value found after the addition of DPPH· solution to lichen extracts or standart antioxidants. A control is the absorbance value of the control value containing only DPPH solution.

The graphs showing the DPPH radical scavenging activity results of lichen extracts and standard antioxidant compounds were shown in Figure 4.

DPPH radical scavenging activities of lichen extracts increase in direct proportion to the concentration, as can be seen in Figure 4. Absorbance values of lichen extracts and standard antioxidant compounds at 30 µg/mL concentrations were shown in Table 6.

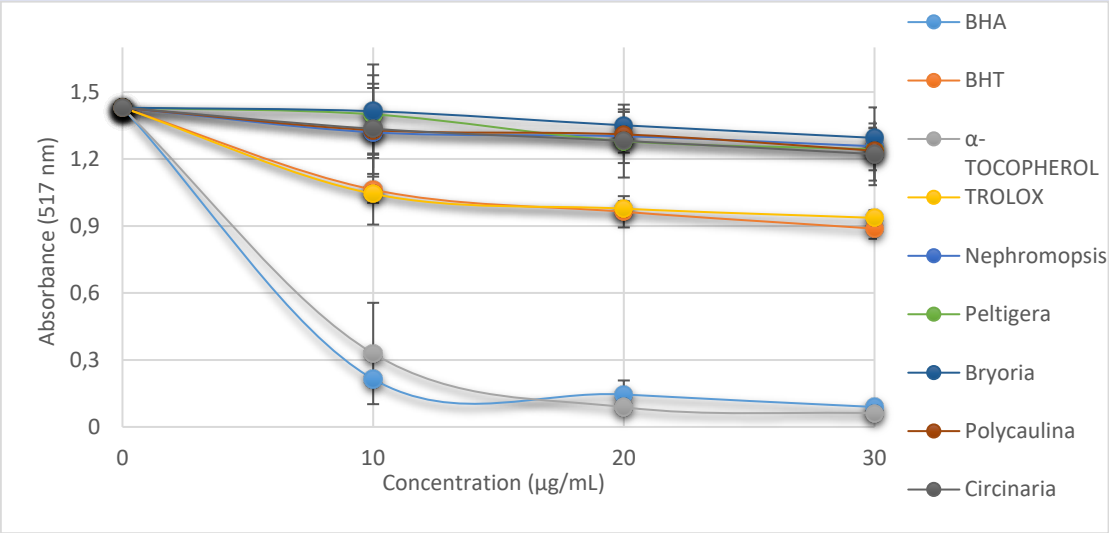

Figure 4. DPPH radical scavenging activities of lichens (10-30 µg/mL).

Lichen extracts and standard antioxidant compounds showed DPPH radical scavenging activity, respectively, as to be α-Tocopherol > BHA > BHT > Trolox > *C. calcarea* > *P. candelaria* > *P. canina* > *N.chlorophylla* > *B. capillaris* at 30µg/mL concentration.

DMPD Scavenging Activity

Calculations related to the DMPD free radical scavenging activity were made according to the following equation

$$\text{DPMD} \cdot \text{ scavenging effect } (\%) = \left(\frac{Acontrol - Asample}{Acontrol}\right) \times 100$$

A sample is the absorbance value found after the addition of DMPD solution to lichen extracts or standart antioxidant. A control is the absorbance value of the control value containing only DMPD solution.

Some standard antioxidant compounds (BHA and Trolox) were used as a positive control. As a matter of fact, BHT and α-Tocopherol, which are among the standard antioxidant compounds, do not show activity in DMPD radical scavenging activity. The graphs showing the results of this antioxidant activity determination method of lichen extracts and standard antioxidant compounds were shown in Figure 5, and the absorbance values of lichen extracts and standard antioxidant compounds at 30 µg/mL concentrations were shown in Table 6.

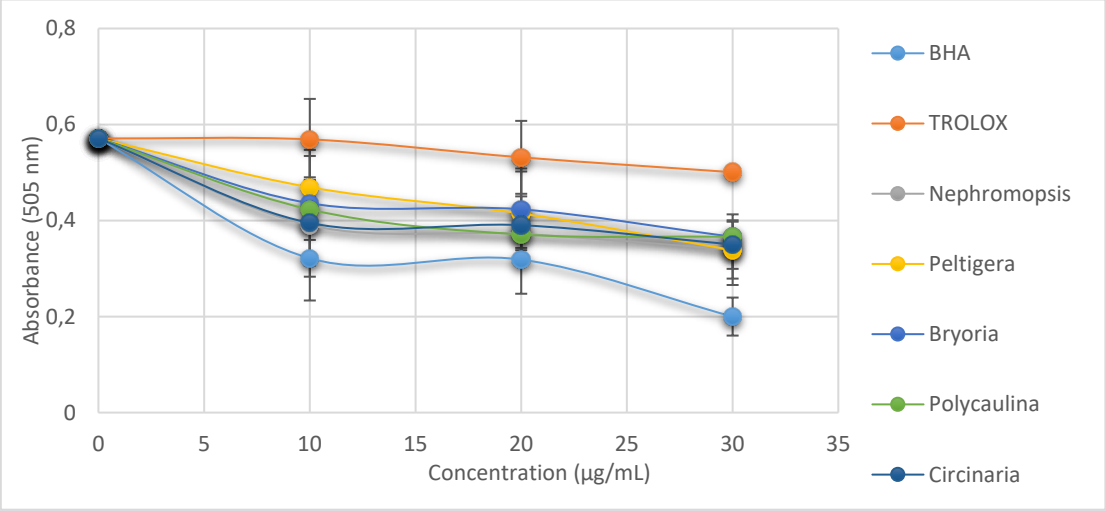

Figure 5. DMPD free radical scavenging activities of lichens (10-30 µg/mL).

Lichen extracts and standard antioxidant compounds showed DMPD radical scavenging activity, respectively, as to be; BHA> *P. canina* > *N. chlorophylla* > *C. calcarea* > *B. capillaris* =*P. candelaria* > Troloks at 30µg/mL concentration.

Bipyridyl Ferrous Ions (Fe^{2+}) Chelating Activity

Metal chelating activities of lichen extracts and standard antioxidant compounds were determined using bipyridyl. The graphs showing the results of this antioxidant activity determination method for lichen extracts and standard antioxidant compounds are given

in Figure 6, and the absorbance values of lichen extracts and standard antioxidant compounds at 30 µg/mL concentrations are given in Table 6. Lichen extracts and standard antioxidant compounds showed metal chelating activities,respectively, as to be Troloks> *P. candelaria* =*P. canina* > *C. calcarea* > *B. capillaris* > *N. chlorophylla* > BHT> BHA> α-Tokoferol at 30µg/mL concentration.

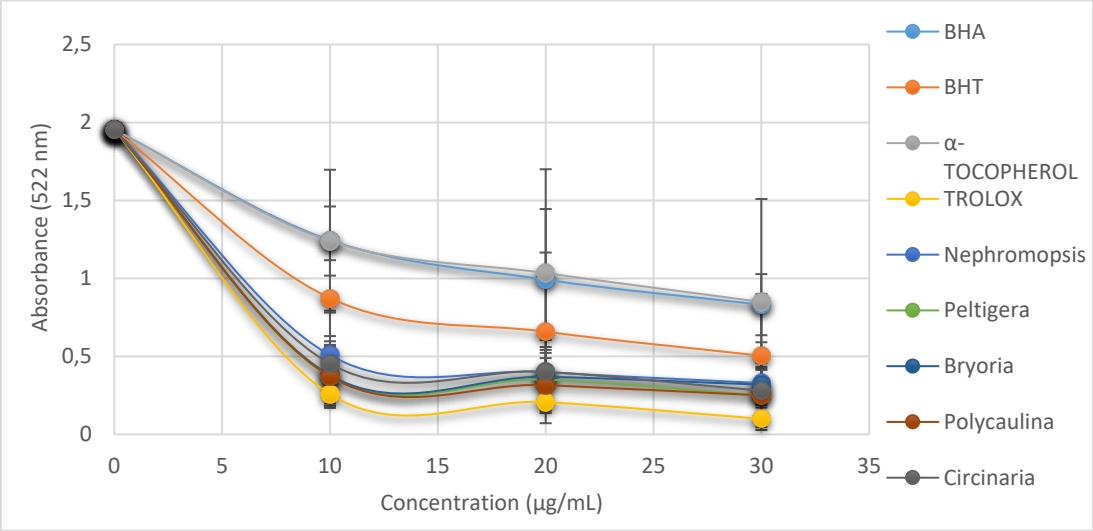

Figure 6. Bipyridyl metal chelating activities of lichens (10-30 µg/mL).

Table 6. Absorbance values of lichen extracts (30µg/mL) obtained from different antioxidant activity determination methods (radical removal). Standard antioxidant compounds (BHA, BHT, αTocopherol, Trolox).

Antioxidants	DPPH•scavenging activity (517 nm)	DMPD• scavenging activity (505 nm)	Bipyridyl metal chelating activity (522nm)
Kontrol	1,43	0,571	1,954
BHA	0,089	0,200	0,832
BHT	0,888	-	0,504
αTokoferol	0,061	-	0,849
Troloks	0,936	0,501	0,100
Nephromopsis chlorophylla	1,257	0,339	0,329
Peltigera canina	1,243	0,338	0,250
Bryoria capillaris	1,295	0,366	0,319
Polycauliona candelaria	1,237	0,366	0,250
Circinaria calcarea	1,222	0,350	0,280

Discussions

Preparation of Lichen Extracts

It is known that various solvents can be used for the preparation of lichen extracts, and each solvent enables the extraction of different lichen components. Therefore, the biological activities of the prepared lichen extracts can differ depending on the solvent used. In this case, it does not seem possible to determine exactly which solvent is more suitable for the preparation of a lichen extract with high biological activity. However, we preferred to use methanol as a solvent for the extraction processes of lichens evaluating some literature studies investigating the antimicrobial and antioxidant activities of lichens [10,12,13,30].

We suggest that extracts of lichens should be prepared using different solvents such as water, ethanol, acetone, as well as methanol, and the antimicrobial and antioxidant activities of these extracts should be determined.

Antimicrobial Activities of Lichens

Disc diffusion methods

The antimicrobial activity results of methanol extracts of lichens were shown in Table 1.

It was determined that a diameters of the inhibition zone forming against test microorganisms of methanol extracts of *N. chlorophylla, C. calcarea, B. capillaris* lichen species varied between 10-13mm;10-15mm;9-13mm, respectively. It was observed that methanol extract of *C. calcarea* among methanol extracts of lichens formed diameter of maximum inhibition zone (15 mm) against *E. coli* and *B. cereus* bacteria species.

It was understood that the most sensitive species to lichen extracts among test microorganisms were *B. cereus*, *B. subtilis*, *C. perfringens*, *E. coli. Escherichia coli* are Gram negative bacteria, *B. cereus, B. subtilis, C. perfringens* are Gram positive bacteria. When these results were examined, it was understood that the lichen extracts in our study were more effective on Gram-positive bacteria.

It was determined that lichen extracts showed a stronger antimicrobial activity against Gram positive bacteria compared to Gram negative bacteria in some

studies on the antimicrobial activities of lichens in the same as line with our results [11, 13, 15, 21,31].

Such a result is due to the differences in the cell wall structure of Gram-positive and Gram-negative bacteria according to various sources. Both Gram-positive and Gram-negative bacteria have a peptidoglycan layer in their cell wall structure. However, unlike Gram-positive bacteria, Gram-negative bacteria have an outer membrane over the peptidoglycan layer. This outer membrane has a lipopolysaccharide (LPS) layer. This layer is thought to slow down or prevent the entry of some compounds into the cell. Therefore, Gram-negative bacteria are less affected by antimicrobial compounds than Gram-positive bacteria [11, 22, 32].

The lichen species used in our study showed antimicrobial activity against test microorganisms with diameter of the inhibition zone varying between 7-15 mm. There have been many studies examining the antimicrobial activities of lichens 4,8,12,15,21,31]. When all these literature informations are evaluated, inhibition zone diameter sizes in our findings are comparable with other studies.

None of the lichen species in our study were effective on *Candida albicans*, which is the only fungus species among the test microorganisms. Some studies examining the antimicrobial activity of various lichen species have similar results to ours [12, 15, 34,35,]. According to a literature report due to differences in cell wall composition and permeability, bacteria are more sensitive to antimicrobial activity than fungi. In the same study, it has been stated that the cell wall of the fungus contains polysaccharides such as chitin and glucan and its permeability is weak [10]. In another a literature, it has been reported that the antibacterial properties of plants are more than their antifungal properties, and this is related to the structural differences between prokaryotic bacteria and eukaryotic fungal cells. As a matter of fact, it has been emphasized that while antimicrobial agents must bind to sterols in eukaryotic membranes to be effective, such binding is not necessary for bacterial cells [32]. When the antimicrobial activities of lichens in our study have been compared with other studies on this subject as considering the size of diameters of the inhibition zone and spectrum of antimicrobial activity formed against the test microorganisms, it has seen that the antimicrobial activities of methanol extracts of our lichens have been at an average level.

However, when all these research results are evaluated, it does not seem possible to determine exactly which lichen extract is stronger in terms of antimicrobial activity. As a matter of fact, there are many factors that affect the antimicrobial activities of lichens. Among these can be counted factors as differences in the methods of obtaining lichen extracts, the type of solvent used for lichen extraction, the contents of lichen species, the amount of lichen extracts absorbed into the discs, and which microorganism species are used [10,11,31,36,37].

MIC Values of Lichens

It was determined that the extracts of the lichens in our study formed MIC values ranging between 31.25-250 µg/mL against the test microorganisms. Among the lichens, the extract of *Circinaria calcarea* lichen species showed the best (lowest) MIC value (31.25 µg/mL) against *E. coli* bacteria.

When the MIC values obtained in some studies examining the antimicrobial properties of various lichen species are compared, it is understood that our results are at an average level.(8,23,38).

Antioxidant Activities of Lichens

Different antioxidant activity determination methods including (Fe^{3+}) reducing capacity, (Cu^{2+}) reducing capacity, Ferric reducing capacity (FRAP), DPPH radical scavenging activity, DMPD radical scavenging activity, Bipyridyl metal chelating activities were used to determine the antioxidant activities of *Polycauliona candelaria, Nephromopsis chlorophylla*, *Circinaria calcarea*, *Bryoria capillaris*, *Peltigera canina* lichen species in our study.

The absorbance values of methanol extracts of lichen species and standard antioxidant compounds (BHA, BHT, α-Tocopherol and Trolox) at 10, 20 and 30 µg/mL concentrations were measured for each antioxidant activity determination method applied to determine the antioxidant activities of lichens. Graphs showing the antioxidant activities of lichen extracts and standard antioxidant compounds were drawn considering these absorbance values. Graphs were shown in Figures 1-6. Absorbance values of lichen extracts and standard antioxidant compounds at concentrations of only 30 µg/mL were shown in Tables 5,6.

In order to determine the antioxidant properties of compounds or natural products, antioxidant activity determination methods such as reduction, radical scavenging and metal chelation must be applied. If positive results are obtained from at least three of these methods with separate principles, the studied compound can be evaluated as having potential antioxidant properties.

Bipyridyl metal chelation antioxidant activity determination method was used for the metal chelation test. It is necessary heavy metals such as Zn, Fe and Cu for the functioning of enzymes in metabolism. However, if the same metals are above the required level, they accumulate and can become toxic and cause harmful effects on biomolecules. In this case, it causes peroxidation of biological molecules such as lipids in the plasma membrane by inducing the formation of ROS and nitrogen species (RNS). If the substances or sources, whose antioxidant properties have been investigated, show the ability to chelate heavy metals, the formation of the above-mentioned radicals is prevented. Once metals are chelated with appropriate chelating agents, their damage in metabolism can be prevented and effectively removed from the body.

Antioxidant activity determination methods such as (Fe^{3+}) reducing, (Cu^{2+}) reducing Ferric reducing (FRAP) were used for the reduction test. Redox reactions in metabolism are the main reaction of biological oxidation. This is a chain of chemical reactions in which we use oxygen in the air to oxidize chemicals obtained from the breakdown of food to provide energy to the living system. If the metal ions present in metabolism are more than necessary, it negatively affects the metabolism as it increases the formation of free radicals. For example, Fe^{2+} is a reactive metal ion and its presence in free form is dangerous for metabolism. Therefore, its harmful potential is reduced by reducing it to Fe^{3+}. Otherwise, extremely dangerous free radicals and their precursors such as hydroxyl radicals are formed.

DPPH radical scavenging and DMPD radical scavenging antioxidant activity determination methods were used for the radical scavenging test. Determining the radical scavenging activities and antioxidant potentials of antioxidant compounds is important for biological systems, but also for the pharmaceutical industry. Free radicals may occur during normal biological processes in metabolism, and antioxidant systems and substances are needed to eliminate them. Otherwise, damage will occur in the biological system. In this respect, determining radical scavenging capacities is important to talk about antioxidant capacity (39,40).

As a result of the antioxidant activity determination methods that we applied, it was determined that the lichen species in our study showed an average antioxidant activity. *Peligera canina* lichen species among the lichens in our study showed the highest antioxidant activity in most of the antioxidant activity determination methods that we applied. It was determined that all lichens produced the best antioxidant activity in the bipyridyl metal chelating activity determination method.

Based on our antioxidant activity results, it does not seem possible to say which lichen species has the highest antioxidant activity among lichen species. As a matter of fact, there are many factors that affect the antioxidant properties of lichens. These include the climatic conditions in which lichens live, the contents of lichen species, the differences in the methods of obtaining lichen extracts, the type of solvent used in extraction processes and the determination of antioxidant activity applied [10,39].

On the other hand, it is known that the determination of lichen compounds that cause antimicrobial and antioxidant activity in lichens is also important in such studies. As a matter of fact, there have been many sources stating that the antimicrobial and antioxidant activities of lichens may be related to the phenolic compounds in their structures [12,40].

It is necessary also to purify the main components and then investigate their antagonistic or synergistic interactions with their each other and other components in order to fully understand the reason of biological activities of lichens [4,10,11].

Conclusions

Among the lichen species in our study, *Circinaria calcarea* showed the highest antimicrobial activity and *Peltigera canina* lichen species showed the highest antioxidant activity. These lichens can be evaluated for use in fields such as pharmacology, by conducting much more comprehensive studies on the antimicrobial and antioxidant properties.

Conflicts of interest

The authors declare that they have no conflict of interest.

References

[1] Negi H.R., Lichens: A valuable bioresource for environmental monitoring and sustainable development, *Resonance*, 8(1) (2003) 51-58.

[2] Molnár K., Farkas E., Current results on biological activities of lichen secondary metabolites: a review, *Z. Naturforsch. C.*, 65 (2010)157-173.

[3] Bhattacharyya S., Deep P.R., Singh S., Nayak B., Lichen secondary metabolites and ıts biological activity, *Am. J. Pharmtech. Res.*, 6(6) (2016) 29-44.

[4] Murugesan P., Phytochemical analysis and antimicrobial activity of edible lichen, *J. Drug Deliv. Ther.*, 10 (2020) 102-104.

[5] Kocovic A., Jeremic J., Bradic J., Sovrlic M., Tomovic J., Vasiljevic P., Andjic M., Draginic N., Grujovic M., Mladenovic K., Baskic D., Popovic S., Matic S., Zivkovic V., Jeremic N., Jakovljevic V. Manojlovic N., Phytochemical analysis, antioxidant, antimicrobial and cytotoxic Activity of different extracts of *Xanthoparmelia stenophylla* lichen from Stara Planina, Serbia, *Plants*, 11(1624) (2022) 1-26.

[6] Oksanen I. Ecological and biotechnological aspects of lichens, *Appl. Microbiol. Biotechnol.*, 73 (2006) 723-734.

[7] Çobanoğlu G., Geçmişten bugüne İstanbul liken çalışmaları üzerine bir derleme, *Bağbahçe Bilim Dergisi, Marmara Üniversitesi, Fen Edebiyat Fakültesi, Biyoloji Bölümü,* 8(1) (2021) 259-266.

[8] Pradhan S., Dash S., Parida S., Sahoo B. and Rath B., Antioxidant and antimicrobial activities and GC/MSbased phytochemical analysis of two traditional Lichen species *Trypethellium virens* and *Phaeographis dendritica*, *J. Genet. Eng. Biotechnol.* , 21(41) (2023) 1-18.

[9] Odabaşoğlu F., Likenler. Pharma Şark, *Eczacı Odası Yayınları,* 3 (2001) 16-19.

[10] Kosanıć M., Šeklıć D., Markovıć S.and Ranković, B. Evaluatıon of antıoxıdant, antımıcrobıal and antıcancer propertıes of selected lıchens from Serbia**,** *Dig. J. Nanomater. Biostructures*, 9(1) (2014) 273 – 287.

[11] Aoussar N., Laasri F.E., Bourhia M., Manoljovic N., Mhand R.A., Rhallabi N., UllahR., Shahat A.A., Noman O.M., Nasr F.A., Almarfadi O.M., El Mzibri M., Vasiljevi´c P., Benbacer L. And Mellouki. F., Phytochemical analysis, cytotoxic, antioxidant, and antibacterial activities of lichens**,** *Evid.-based Complement. Altern. Med.*, (2020) 1-11.

[12] Aslan A., Güllüce M., Sökmen M., Adıgüzel A., Şahin F. and Özkan H., Antioxsidant and antimicrobial properties of the lichens *Cladonia Foliacea, Dermatocarpon Miniatum,*

Everinia Divaricata, Evernia Prunastri and *Neofuscella pulla*, Pharm. Biol., 44 (4) (2006) 247-252.

[13] Paudel B., Bhattarai H. D, Lee J.S., Hong S.G., Shin H. W. and Yim, J.H., Antibacterial potential of Antarctic lichens against human pathogenic gram-positive bacteria, *Phytother. Res.*, 22 (2008) 1269-1271.

[14] Zeybek U., John V., Likenler (Lichens), Kimyasal Bileşikleri ve Tıbbi Kullanımları, *Pharmacia-JTPA*, (1992) 37-48.

[15] Dülger B., Gücin F.and Aslan A., *Cetraria İslandica* (L.) Ach. Likeninin antimikrobiyal aktivitesi, *Turk. J. Biol.*, 22 (1998) 111-118.

[16] Baytop T., Türkiye'de Bitkiler ile Tedavi, Nobel Tıp Kitapevleri, (1999) 480 , İstanbul.

[17] Clauzade G., Roux C, Likenoj De Okcidenta Europo. Ilustrita Determinlibro. Bulletin De La Societe Botanique Du Centre-Ouest, *Nouvelle Serie, Numero Special,* 7 (1985) 893.

[18] Purvis O.W., Coppins B.J., Hawksworth D. L., James P.W., Moore D.M, The Lichen Flora of Great Britain and Ireland. Natural History Museum Publications in association with The British Lichen Society, London, England, (1992) 710.

[19] Dobson F., Lichens: An Illustrated Guide To The British And Irish Species 4th Edition. Richmond Publishing Company, Slough, (2000) 431.

[20] Brodo I.M., Sharnoff S.D. and Sharnoff S., Lichens of North America. Yale University Press, xxiii, New Haven, (2001) 795.

[21] Gücin F., Dülger B. and Aslan, A., 1997a. *Pseudevernia Furfuracea* (L.) Zopf Likeninin antimikrobiyal aktivitesi, *Ekoloji Çevre Dergisi*, 25 (1997) 22-24.

[22] Rankovic´ B., Mišic´ M.and Sukdolak S., Antimicrobial activity of extracts of the lichens *Cladonia furcata*, *Parmelia caperata*, *Parmelia pertusa*, *Hypogymnia physodes* and *Umbilicaria polyphylla*, *Biologia*, 64(1) (2009) 53-58.

[23] Gulluce M., Aslan A., Sokmen M., Sahin F., Adiguzel A., Agar G., Sokmen, A., Screening the antioxidant and antimicrobial properties of the lichens *Parmelia saxatilis*, *Platismatia glauca*, *Ramalina pollinaria*, *Ramalina polymorpha* and *Umbilicaria nylanderiana*, *Phytomedicine*, 13 (2006) 515–521.

[24] Altundağ Ş., Karahan A., Aksu P., Kılınç A.O., İnvitro koşullarda *Satureja cuneifolia* Ten. uçucu yağının bazı buğday patojeni bakteriler üzerine antibakteriyel etkisinin araştırılması, *Bitki Koruma Bülteni*, 50 (2010) 25-33.

[25] Oyaizu, M., Studies on product of browning reaction prepared from glucose amine, *Jpn J. Nut.*, 44 (1986)307-315.

[26] Apak R., Güçlü K., Özyürek M., Karademir S.E., Erça E., The Cupric ion reducing antioxidant capacity and polyphenolic content of some herbal teas*, Int. J. Food Sci. Nutr.*,57 (2006) 292–304.

[27] Re R., Pellegrini N., Proteggente A., Pannala A., Yang M. and Rice-Evans, C. 1999. Antioxidant activity applying an ımproved abts radical cation decolorization assay, *Free Radic. Biol. Med.*, 26 (1999) 1231-1237.

[28] Blois M.S. Antioxidant deteminations by the use of a stable free radical, *Nature,* 26(1958) 1199-1200*.*

[29] Fogliano V., Verde V., Randazzo G.and Ritiene, A., Method for measuring antioxidant activity and its application to monitoring the antioxidant capacity of wines, *J. Agric. Food Chem.*, 47 (1999) 1035-1040.

[30] Odabaşoğlu F., Aslan A., Çakır A., Süleyman H., Karagöz Y., Halıcı M.and Bayir, Y., Comparison of antioxidant activity and phenolic content of three lichens species, *Phytother. Res.*, 18 (2004) 938-941.

[31] KaragözA., DoğruözN., Zeybek Z.and Aslan, A. Antibacterial activity of some lichen extracts, *J. Med. Plant Res.*, 3(12) (2009) 1034-1039.

[32] Ali-Shtayeh M.S., Yaghmour M.R., Faidi Y.R., Salem, K. and Al-Nuri, M.A., Antimicrobial activity of 20 plants used in folkloric medicine in the Palestinian area, *J. Ethnopharmacol.*, 60(3) (1998), 265-271.

[33] Nikaido H, Molecular basis of bacterial outer membrane permeability revisited, Microbiology & Molecular Biology Review, 67 (2003) 593-656.

[34] Rankovic, B., Misic, M., Sukdolak, S., Evaluation of Antimicrobial Activity Of The Lichens *Lasalia Pustulata, Parmelia Sulcata*, *Umbilicaria Crustulosa* and *Umblicaria Cylindrica*, *Microbiology*, 76(6) (2007) 723-727.

[35] Gücin F., Öztürk Ş., Dülger B.and Güvenç, Ş. *Umbilicaria Crustulosa* (Ach.) Frey'nin Antimikrobiyal aktivitesi üzerine bir araştırma, *Ekoloji Çevre Dergisi,* 24 (1997) 21-24.

[36] Negi P.S., Jayaprakasha G.K., Jagan Mohan Rao L., Sakariah K.K., Antibacterial activity of turmeric oil: a byproduct from curcumin manufacture, *J. Agric. Food Chem.*, 47(1999) 4297-4300.

[37] Uçarkuş E., Gökalsın B., Yıldırım N., Açıkgöz B., Özyiğitoğlu G.and Sesal, N.C., Balıkesir bölgesinden toplanan liken örneklerine ait özütlerin *Escherichia coli* ATCC 25922 Üzerindeki antibakteriyal etkinlikleri, *Türk Mikrobiyoloji Cemiyeti Dergisi*, 47(1) (2017) 26-32.

[38] Manojlovic N.T., Vasiljevic P.J., Maskovic P.Z., Juskovic, M., Bogdanovic-Dusanovic, G., Chemical composition, antioxidant and antimicrobial activities of lichen *Umbilicaria cylindrica* (L.) Delise (Umbilicariaceae). *Evid.-based Complement. Altern. Med.*, (2012) 1-8.

[39] Güneş Yücel D., Özyiğitoğlu **G.,** Antibacterial and Antioxidant Activities of the Lichen Species *Ramalina calicaris* (L.) Fr**,** *Marmara Fen Bilimleri Dergisi*, 3 (2018) 269-275

[40] Gülçin İ., Oktay M., Küfrevioğlu Ö.İ. and Aslan A. Determination of Antioxidant Activity Of Lichen *Cetraria İslandica* (L) Ach., *J Ethnopharmacol*., 79(3) (2002) 325-329.

Cumhuriyet Sci. J., 44(3) (2023) 430-435
DOI: https://doi.org/10.17776/csj.1282586

Cumhuriyet Science Journal

| csj.cumhuriyet.edu.tr | Founded: 2002 ISSN: 2587-2680 e-ISSN: 2587-246X Publisher: Sivas Cumhuriyet University

Electrochemical Study of Clopidogrel and its Determination in Pharmaceutical Preparations Using Square Wave Voltammetry

Bilal Yılmaz [1,a,*], Semih Yılmaz [2,b]

[1] *Department of Analytical Chemistry, Faculty of Pharmacy, Ataturk University, Erzurum, Türkiye*
[2] *Faculty of Medicine, Ankara University, 06050, Ankara, Türkiye*
**Corresponding author*

Research Article

History
Received: 13/04/2023
Accepted: 01/09/2023

ABSTRACT

In the present study, the electroanalytical behaviour of clopidogrel was investigated by cyclic voltammetry method. The procedure was based on clopidogrel being electrochemically oxidized at a platinum electrode in nonaqueous solutions. At 1.93 V, the oxidation peak was noted. It was discovered that clopidogrel's oxidation was diffusion-controlled. Additionally, a quick and easy SWV approach was developed and validated in this work to determine clopidogrel in pharmaceutical preparations. At concentrations between 5 and 50 µg/mL, the calibration curve was linear. The precision was given by relative standard deviation and was less than 2.73%. Accuracy was given with relative error and did not exceed 3.89%. In pharmaceutical preparations, clopidogrel had an average recovery of 100.1%. Under the chosen experimental conditions, no interference was found. The suggested method is extremely accurate and precise. Therefore, the method is applicable to the measurement of clopidogrel in pharmaceutical formulations.

Keywords: Clopidogrel, Voltammetry, Validation, Analysis.

[a] *yilmazb@atauni.edu.tr* *https://orcid.org/0000-0002-8574-7570* [b] *semihyilmaz.0720@gmail.com* *https://orcid.org/0009-0000-9629-8849*

Introduction

Antithrombotic medications are prescribed to stop thrombosis. Thrombosis, which is the development of blood clots in veins, can be lethal for individuals. These medications lessen the chance of blood clotting. Due to their preventive qualities against cardiovascular disorders, antithrombotic medicines are one of the pharmacological classes that have recently been investigated [1–7].

Drugs that contain "clopidogrel" as a medication ingredient are used therapeutically to lower myocardial infarction risk, atherothrombotic disorders, and cardiovascular diseases [8,9]. The molecular name of clopidogrel is 4,5,6,7-tetrahydrothieno[3,2-c] pyridine (Figure 1). After examining its effects in more than 30000 patients worldwide, the clinical advantage of long-term clopidogrel treatment in reducing atherothrombotic disorders is demonstrated [10,11].

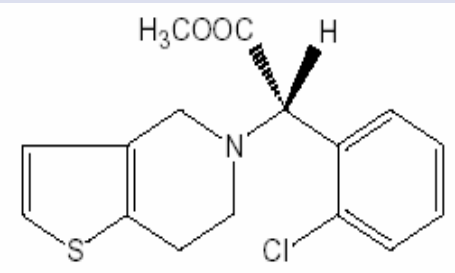

Figure 1. Structure of clopidogrel.

Reviews of the literature indicate that UV spectrophotometry [12], high-performance liquid chromatography with ultraviolet detection [13], gas chromatography with mass spectrometry [14], and high-performance liquid chromatography with mass spectrometry [15,16] are used to quantitatively analyze clopidogrel in pharmaceutical preparations or biological liquids.

There are many chromatographic methods for determining the presence of clopidogrel in human plasma, according to a thorough literature review. Endogenous interference, possible drug loss during re-extraction, arduous and time-consuming plasma sample preparation and extraction processes, and the necessity for sophisticated and expensive equipment all had an impact on the reported techniques.

It is crucial to develope a new technique for figuring out how much medication is in pharmaceutical dosage forms. Numerous pharmaceutical substances have been identified utilizing electroanalytical techniques, which have the benefits of not typically requiring derivatization and being less susceptible to matrix effects than other analytical techniques. The identification of electrode mechanism is another electrochemistry application. Drugs' redox characteristics can provide information about their pharmacological efficacy, in vivo redox activities, or metabolic destiny.

Although the electrochemical behavior and oxidation mechanism of clopidogrel have analytical significance, no

research on the voltammetric oxidation of clopidogrel in nonaqueous fluids has been published. It is widely known that the electrochemical process and voltammetric response of pharmaceuticals are directly influenced by the experimental and operational parameters. So, it would be interesting to look at how clopidogrel oxidizes in aprotic environments. However, the voltammetry method has not yet been used to quantitatively assess clopidogrel using a platinum electrode. The major goal of this work was the development of a novel SWV technique for the rapid and precise evaluation of clopidogrel in pharmaceutical preparations without the necessity for laborious extraction or evaporation procedures prior to drug testing.

This study describes SWV methods using a platinum disc electrode to determine clopidogrel using simple, quick, and selective processes that have been completely verified. Also, the technique was effectively used to evaluate the consistency of the formulation content and to quantitate a commercially available clopidogrel medication for QC.

Materials and Methods

Chemicals

Clopidogrel bisulfate standard (98≥ purity), *lithium perchlorate* ($LiClO_4$) and acetonitrile were purchased from Sigma (Germany). Plavix and Karum tablets that included 75 mg clopidogrel were purchased from a pharmacy (Erzurum, Turkey).

Electrochemical Instrumentation

Using the software PHE 200 and PV 220, electrochemical experiments were carried out on a Gamry Potentiostat Interface 1000. The single-compartment electrochemical cell used for all tests has a conventional three-electrode setup. Platinum wire served as the counter electrode and a platinum disk served as the working electrode. On microcloth pads, 1.0, 0.3, and 0.05 µm alumina slurries were used to incrementally polish the working electrode. The reference electrode for each potential was made of Ag/AgCl/KCl (3.0 M). The potential was cycled between 1.7 and 2.1 V at a sweep rate of 0.1 V/s. The SWV was operated at pulse amplitudes of 25 mV, 10 Hz, 4 mV potential step and 0.1 V/s scan rate.

Preparation of Standard Solutions

In 0.1 M $LiClO_4$/acetonitrile, the stock standard solution of clopidogrel (100 µg/mL) was prepared. This stock solution was used to prepare working standard solutions. The concentrations of the standard solutions were 5, 10, 15, 20, 25, 30, 40, and 50 µg/mL. The QC solutions were created at concentrations of 7.5, 27.5, and 45 µg/mL.

Results and Discussion

Development and Optimization of the Method

The electrochemical behavior of clopidogrel was investigated at the Pt disc electrode. An acetonitrile solution containing 0.1 M $LiClO_4$ was used as the supporting electrolyte in cyclic voltammetry. Figure 2 depicts a typical cyclic voltammogram for 100 µg/mL clopidogrel at 0.1 V/s scan rate. The oxidation peak was seen in the anodic sweep at 1.93 V.

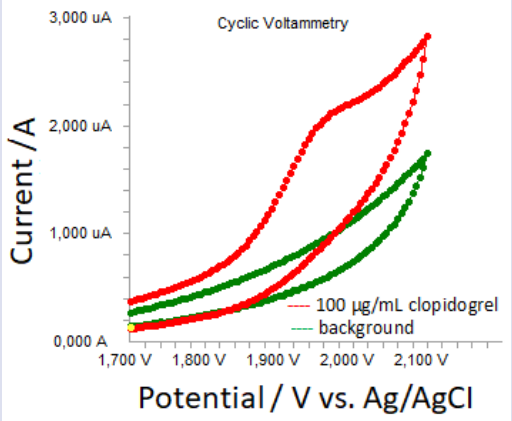

Figure 2. Cyclic voltammogram of clopidogrel (100 µg/mL)

The influence of scan rate on the anodic peak currents and peak potentials was investigated in the range of 0.01-1 V/s of the potential scan rates in 0.1 M $LiClO_4$/acetonitrile solution containing clopidogrel in order to better comprehend the voltammetric waves (Figure 3).

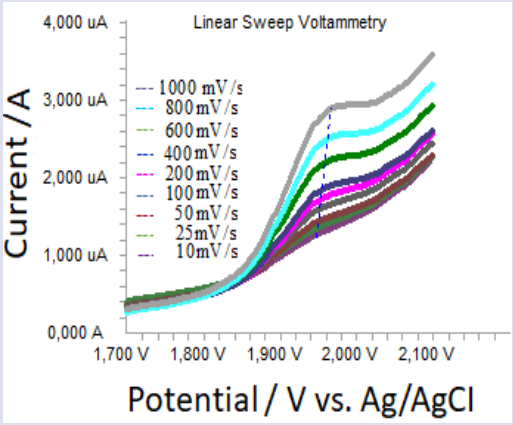

Figure 3. Linear sweep voltammograms for the oxidation of 30 µg/mL clopidogrel as a function of scan rate (10, 25, 50, 100, 200, 400, 600, 800 and 1000 mV/s)

Figure 4a,b shows the linear sweep voltammograms for clopidogrel as a function of scan rate. However, at clopidogrel concentrations of 30 µg/mL, the logarithm of peak currents against logarithm of scan rates graphs display straight lines with a slope of 0.36 (Figure 4c), which is close to the predicted value of 0.5 anticipated for an ideal diffusion-controlled electrode process [17].

In order to accomplish this, the *log I-log v* curve is more suitable, therefore a diffusional process for the peak should be taken into account. These findings show that the redox species are readily diffusing from the solution as opposed to precipitating onto the electrode surface. This phenomenon can be brought on by either a

lack of product adhesion to the electrode surface or the solubility of the intermediate species in acetonitrile.

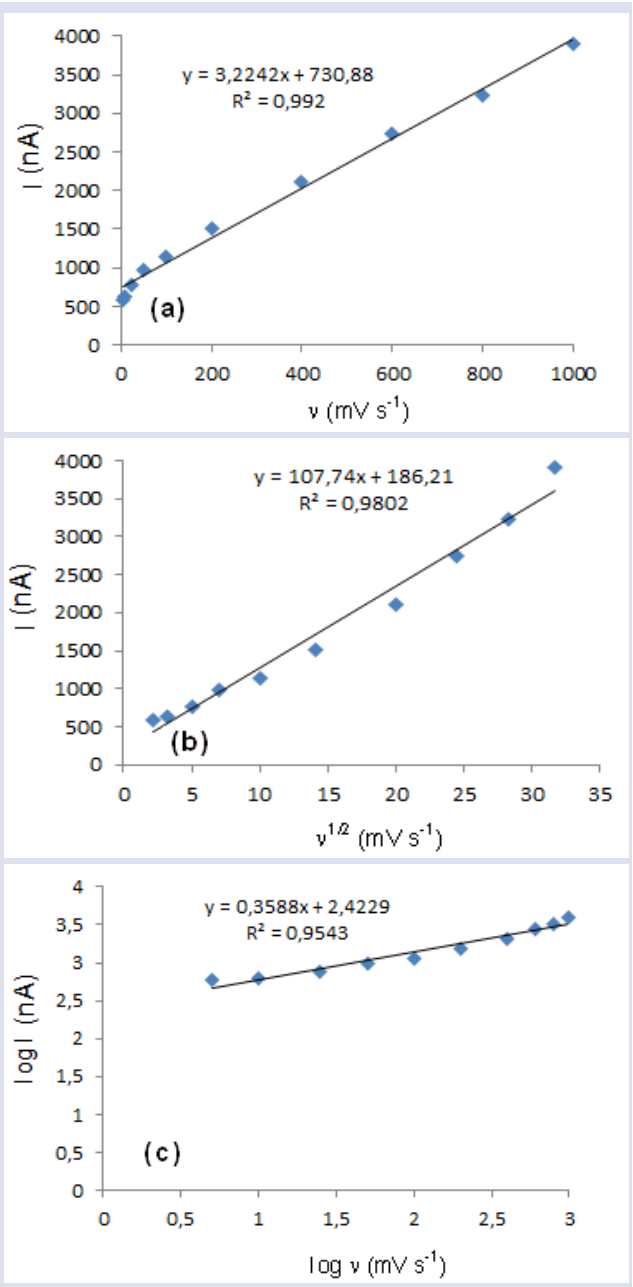

Figure 4(a-c). Peak current dependence on scan rate (30 µg/mL).

Figure 3 shows the movement of the oxidation peak potential *(E_{pa})* for peaks toward higher positive values as the scan rate is increased. The equation below [18] describes the relationship between the peak potential and scan rate,

$$E_{pa} = E^{0'} + RT/\left[(1-\alpha)n_a F\right]\left[0.78 + \ln\left(D^{1/2}k_s^{-1}\right) - 0.5\ln RT/\left[(1-\alpha)n_a F\right]\right] + RT/\left[(1-\alpha)n_a F\right]/2\ln v$$

and from the variation of peak potential with scan rate αn_a can be determined, where α is the transfer coefficient and n_a is the number of electrons transferred in the rate determining step. The plots of the oxidation peak potentials against *ln v* demonstrate a linear connection in accordance with this equation (Figure 5).

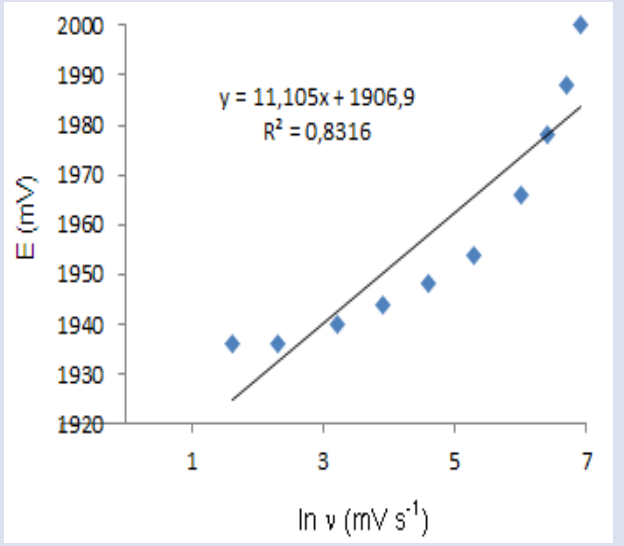

Figure 5. Dependence of the clopidogrel anodic peak potentials on the scan rate.

The slope indicates that the highest value of αn is 11.105. Additionally, this value shows that the processes of electron transfer are completely irreversible. This outcome demonstrates that the chemical step is a charge transfer and a quick following reaction.

Validation of the Method

ICH Q2B guidelines were followed while determining the validation parameters [19]. These criteria include specificity, linearity, precision, accuracy, recovery, limit of detection (LOD), limit of quantification (LOQ), robustness and stability.

Specificity

In this study, it was investigated the potential interferences of common excipients and additives. The control samples were prepared and examined. At the concentrations present in dosage forms, there is no evidence of any interference from these chemicals. The excipient employed in this formulation was one that the pharmaceutical industry employs most frequently. The method's specificity was examined by keeping an eye out for any interference from common tablet ingredients like talc, lactose, sodium chloride, titanium dioxide, and magnesium stearate. These exceptions had no negative effects on the suggested method. The procedure might be specific in accordance with the findings of the analysis.

Linearity

Standard solutions at concentration of 5, 10, 15, 20, 25, 30, 40 and 50 µg/mL were prepared for SWV (Figures 6). Plotting the clopidogrel concentration versus peak current responses allowed for the construction of the calibration curve for the clopidogrel (Fiure 7).

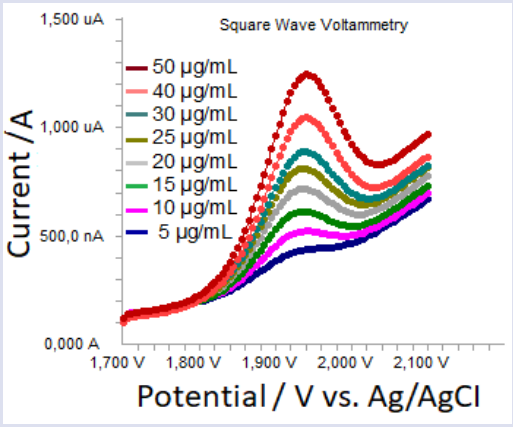

Figure 6. SWV voltammograms of clopidogrel

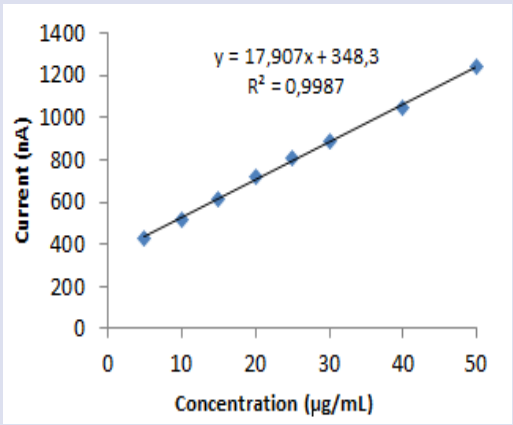

Figure 7. Calibration curve of clopidogrel (5, 10, 15, 20, 25, 30, 40 and 50 µg/mL).

All of the calibration curves' correlation coefficients (r) were consistently higher than 0.99. Using the least squares method and the Microsoft Excel® application, the linear regression equations were derived and described in Table 1.

Table 1. Linearity of clopidogrel

Parameters	Clopidogrel
Linearity range (µg/mL)	5-50
Slope	17.907
Intercept	348.3
Correlation coefficient	0.9987
LOD (µg/mL)	1.50
LOQ (µg/mL)	4.50

Precision and accuracy

Using the QC samples, the SWV method's precision and accuracy were assessed for intra-day and inter-day. The same-day analysis of the QC samples served to assess intra-day precision and accuracy. It was able to assess the precision and accuracy between days by contrasting the assays performed on two distinct days. The intra-day accuracy ranged from 1.11% to 2.54%, while the precision ranged from 0.95% to 3.06% (Table 2). It is evident from the results that this process has good accuracy and precision.

Table 2. Precision and accuracy of clopidogrel

Added (µg/mL)	Intra-day Found ± SD[a]	Intra-day Precision % RSD[b]	Intra-day Accuracy[c]	Inter-day Found ± SD[a]	Inter-day Precision % RSD[b]	Inter-day Accuracy[c]
7.5	7.4 ± 0.142	1.92	-1.33	7.6 ± 0.205	2.70	1.33
27.5	26.8 ± 0.821	3.06	-2.54	27.2 ± 0.914	3.36	-1.09
45	44.5 ± 0.424	0.95	-1.11	45.9 ± 0.532	1.16	2.00

Recovery

At three different concentrations, the recovery was examined to investigate the impacts of formulation interference. The recoveries were carried out by mixing pre-analyzed samples of clopidogrel tablets with a known quantity of pure medicines. The recoveries were calculated by comparing the amounts extracted from the spiked samples with the actual added concentrations. The results are listed in Table 3.

Table 3. Recovery of clopidogrel in tablets (n=6)

Tablet	Added (µg/mL)	Found ± SD	%Recovery	%RSD
Plavix (20 µg/mL)	5	4.9 ± 0.131	98.0	2.67
	15	14.9 ± 0.312	99.3	2.09
	25	25.3 ± 0.684	101.2	2.70
Karum (20 µg/mL)	5	4.9 ± 0.107	98.0	2.18
	15	14.7 ± 0.362	98.0	2.46
	25	25.2 ± 0.439	100.8	1.74

LOD and LOQ

The suggested technique's LOD and LOQ values were calculated using calibration standards. LOD and LOQ values were calculated as 3.3 /S and 10 /S, respectively. In this equation, S is the calibration curve's slope and is the y-intercept's standard deviation (n=6). The results are summarized in Table 1.

Ruggedness

The same instrument and standard standard solution were used in this study by a separate analyst to assess the concentration of clopidogrel (Table 4). No statistically significant discrepancies between the operators were found in the results, indicating the ruggedness of the developed approach.

Table 4. Results of another analyst's studies of clopidogrel

Method	Added (µg/mL)	Found (µg/mL) (Mean±SD)	% Recovery	% RSD[a]
SWV	5	5.1 ± 0.19	102.0	3.72
	15	14.9 ± 0.24	99.3	1.61
	35	35.1 ± 1.67	100.2	4.76

[a]Six replicate measurements' mean values

Stability

The stability of clopidogrel stock solution was examined over a period of at least 72 hours. Furthermore, clopidogrel standard solutions were stable for 72 hours at 4 and -20 °C refrigeration temperatures as well as ambient temperature. The clopidogrel accuracy is within the acceptable range of 90 to 110% (Table 5). There are no major clopidogrel breakdown products under these circumstances.

Table 5. Clopidogrel's stability at various temperatures (n=6)

Added (µg/mL)	Room temperature 24 h (Mean ± SD)	Room temperature 72 h (Mean ± SD)	Refrigeratory +4 °C, 72 h (Mean ± SD)	Frozen -20 °C, 72 h (Mean ± SD)
15	100.2 ± 1.76	98.3 ± 3.71	101.8 ± 1.37	98.9 ± 2.42
30	98.7 ± 3.14	101.8 ± 3.42	98.7 ± 2.47	100.6 ± 1.49
45	99.5 ± 2.11	101.3 ± 3.52	98.8 ± 1.67	98.4 ± 2.53

Procedure for Pharmaceutical Preparations

Each Plavix and Karum tablet, which contains 75 milligrams of clopidogrel, was precisely weighed and finely powdered. A suitable amount of powder was dissolved in 50 mL of 0.1 M $LiClO_4$/acetonitrile. Then, the final volume was made up to 100 mL in a balloon flask. Whatman filter (paper no 42) was used to filter the tablet solutions after they had been properly diluted in order to provide a final concentration that was within the linearity constraints of the SWV method (Figure 8). The calibration curve was used to determine the drug concentration for clopidogrel (Table 6).

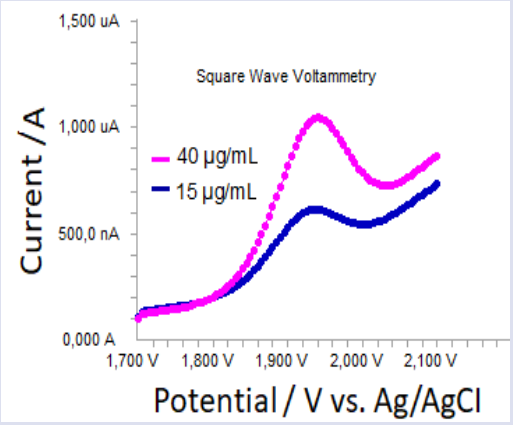

Figure 8. The voltammograms of Plavix tablet containing clopidogrel.

Table 6. The comparison of the presence of clopidogrel in two commercial drugs

Tablet	N	Mean	Standard Deviation	%RSD
Plavix	10	75.1	1.147	1.53
Karum	10	74.6	1.370	1.84

N: The number of analysis (n=6)

Additionally, the official method [20] and the new SWV voltammetric approach were statistically evaluated using the t-test. The computed t-values don't go over the theoretical values at a 95% confidence level (Table 7).

Table 7. Comparison of the methods

Parameters		Official Method
Mean (75 mg per tablet mg)[a]	75.1	74.88
% RSD (Calculated t-value)	0.21[b]	
T theoretical value (p=0.05)		

[a]Each value is the mean of six experiments, [b]NS: not significant

The analytical findings in this investigation showed that the level of active ingredient in the medicine is within the pharmacopoeia's recommended range. The approach can be used as a substitute for the spectrophotometric approach. The developed method was demonstrated to be practical, accurate, and adaptable to drug dose forms. Therefore, developed SWV method can be advised for the routine QC analyses of clopidogrel in pharmaceutical preparations.

Conclusions

In the current work, CV method has been used to examine the electrochemical behavior of clopidogrel in nonaqueous media. Additionally, a quick, accurate, specific, and precise SWV method was developed and validated in the study for the detection of clopidogrel in pharmaceutical formulations. Voltammetry runs for one minute. The method enables the speedy analysis of a large number of samples. As a result, the method can be used to regularly examine clopidogrel in both its formulations and pure form.

Conflicts of interest

The author states that did not has conflict of interests

References

[1] Nurden A.T., Nurden P., Sanchez M., Andia I., Anitua E., Platelets and Wound Healing, *Front Biosci.,* 13(9) (2008) 3532-3548.

[2] Hernandez Hernandez R., Carvajal A.R., Guerrero Pajuelo J., Armas de Hernandez M.J., Armas Padilla M.C., Barragan O., Boada J.J., Roa E., The Effect of Doxazosin on Platelet Aggregation in Normotensive Subjects and Patients with Hypertension: An in Vitro Study, *Am. Heart J.,* 121(1) (1991) 389-394.

[3] Davi G., Patrono C., Platelet Activation and Atherothrombosis, *N. Engl. J. Med*., 357(24) (2007) 2482-2494.

[4] Watson S.P., Auger J.M., McCarty O.J., Pearce A.C., GPVI and Integrin Alphaiib Beta3 Signaling in Platelets, *J. Thromb Haemost.,* 3(8) (2005) 1752-1762.

[5] Namrata K., Prashant P., Sunil A., Role of micronutrients in Heart Diseases, *Int. J. Curr. Pharm. Res.,* 13(5) (2021) 1-5.

[6] Epstein F.H., Fuster V., Badimon L., Badimon J.J., Chesebro J.H., The pathogenesis of Coronary Artery Disease and the Acute Coronary Syndromes, *N. Engl. J. Med.,* 326(4) (1992) 242-250.

[7] El Haouari M., Rosado J.A., Medicinal Plants with Antiplatelet Activity. *Phytother. Res.,* 30(7) (2016) 1059-1071.

[8] Rada F.H., Antiplatelet Adequacy of Cyclopentyl Triazolopyrimidine versus Clopidogrel in-Patients with Coronary Heart Disease, *Asian J. Pharm. Clin. Res.,* 11(12) (2018) 536-539.

[9] Mazyed E.A., Zakaria S., Enhancement of Dissolution Characteristics of Clopidogrel Bisulphate by Proniosomes, *Int. J. Appl. Pharm.,* 11(2) (2019) 77-85.

[10] Deshkar S.S., Pawara A.S., Shirolkar S.V., Formulation and Optimization of Floating Tablets of Clopidogrel Bisulfate using Design of Experiments, *Int. J. Appl. Pharm.,* 10(6) (2018) 94-102.

[11] Shifrin M.M., Widmar S.B., Platelet Inhibitors, *Nurs. Clin. North Am.,* 51(1) (2016) 29-43.

[12] Suhas G., Venkatamahesh R., Development and Validation of a Derivative UV-Spectrophotometric Method for Quantitative Estimation of Clopidogrel Bisulfate in Bulk and Pharmaceutical Dosage Form, *Int. J. Chem. Res.,* 4 (2012) 497-501.

[13] Jain H.K., Deore D.D., Bioanalytical Method Development and Validation for Estimation of Clopidogrel Bisulfate in Human Plasma by RP-HPLC, *Int. J. Appl. Pharm.,* 8(4) (2018) 18-21.

[14] Lagorce P., Perez Y., Ortiz J., Necciari J., Bressole F., Assay Method for the Carboxylic Acid Metabolite of Clopidogrel in Human Plasma by Gas Chromatography Mass-Spectrometry, *J. Chromatogr B: Biomed. Sci. Appl.,* 720 (1998) 107-117.

[15] Venkanna B., Shreedhara C., Ajitha M., Rapid and Rugged Bioanalytical Method Development and Validation Clopidogrel in Human Plasma using Liquid Chromatography/Tandem Mass Spectroscopy, *Am. J. PharmTech. Res.,* 1(2) (2011) 66-80.

[16] Harahap Y., Maysyarah I., Analytical Validation of Clopidogrel in Human Plasma through Ultrahigh Performance Liquid Chromatography-Tandem Mass Spectrometry, *Int. J. Appl. Pharm.,*9(1) (2017) 163-167.

[17] Laviron E., Roullier L., Degrand C., A Multilayer Model for the Study of Space Distributed Redox Modified Electrodes: Part II. Theory and Application of Linear Potential Sweep Voltammetry for a Simple Reaction, *J. Electroanal. Chem.*, 112 (1980) 11-23.

[18] Yilmaz B., Ekinci D., Voltammetric Behavior of Carvedilol in Non-Aqueous Media and its Analytical Determination in Pharmaceutical Preparations, *Rev. Anal. Chem.,* 30 (2011) 187-193.

[19] The European Agency for the Evaluation of Medicinal Products. ICH Topic Q2B Note for Guideline on Validation of Analytical Procedures: Methodology GPMP/ICH/281/95 (1996).

[20] The United States Pharmacopoeia, Thirtieth Revision, and The National Formulary, 25th ed., Rockville, USA, (2007) 1802-1805.

Cumhuriyet Sci. J., 44(3) (2023) 436-443
DOI: https://doi.org/10.17776/csj.1202272

Cumhuriyet Science Journal

| csj.cumhuriyet.edu.tr | Founded: 2002 ISSN: 2587-2680 e-ISSN: 2587-246X Publisher: Sivas Cumhuriyet University

Melatonin as a Potential Therapeutic Tool in Allergic Rhinitis Induced by House-Dust Mite

Ayşe Sezim Şafak [1,2,a], Pakize Neslihan Taşlı[1,b], Ezgi Avşar Abdik[3,c], Hüseyin Abdik[4,d], Fikrettin Şahin[1,e,*]

[1]*Department of Genetics and Bioengineering, Faculty of Engineering and Architecture, Yeditepe University, İstanbul, Türkiye.*
[2]*Department of Odiometry, Faculty of Medicine, Istanbul YeniYüzyıl University, İstanbul, Türkiye.*
[3] *Department of Genomics, Faculty of Aquatic Sciences, Istanbul University, Istanbul, Türkiye.*
[4]*Department of Molecular Biology and Genetics, Faculty of Engineering and Natural Sciences, Istanbul Sabahattin Zaim University, İstanbul, Türkiye.*
**Corresponding author*

Research Article

History
Received: 03/01/2023
Accepted: 13/09/2023

ABSTRACT

Melatonin is known as an important regulator of circadian rhythm in humans. In the literature, there are no studies evaluating the efficacy of melatonin in the management of allergic rhinitis (AR) or nasal polyps (Np). Np tissue was taken from nasal cavity and mucosal tissue (Mu) was taken from the nasal septal area. Melatonin (25-200nM) and Mite Allergen (2.5-12.5%) were prepared in complete media. Cell viability, apoptosis, intracellular reactive oxygen species production and gene expression levels were determined. Our results showed that there is no toxic effect of Melatonin, Mite and their combination which was given to Np-MSCs and Mu-MSCs. Melatonin significantly reduced reactive oxygen species levels in both mite-treated Np-MSCs and Mu-MSCs. Indoleamine 2,3-dioxygenase level was significantly decreased in melatonin-treated cells. Cyclooxygenase-1 level was significantly decreased in melatonin-treated healthy and allergic Np-MSCs while there was no significant difference in 100 and 150nM Melatonin-treated Mu-MSCs. Interestingly, 50nM Melatonin significantly increased Cyclooxygenase-1 level in Mu-MSCs. 50, 100 and 150nm Melatonin significantly decreased Interleukin-6 level in Mite-treated Np-MSCs. In addition, 100 and 150nM Melatonin significantly decreased Interleukin-6 level in Mite-treated Mu-MSCs. Melatonin has well-established anti-oxidant and anti-neoplastic activity, could be a promising therapeutic agent in the treatment of AR and nasal polyposis.

Keywords: Melatonin mite allergen, Allergic rhinitis, Nasal polyp tissue, Mucosal tissue, Mesenchymal stem cell.

[a] *sezim25@hotmail.com* *https://orcid.org/0000-0001-8514-7172*
[b] *neslush@gmail.com* *https://orcid.org/0000-0002-0455-9894*
[c] *e.avsarabdik@istanbul.edu.tr* *https://orcid.org/0000-0003-0132-3234*
[d] *huseyin.abdik@izu.edu.tr* *https://orcid.org/0000-0003-3756-0645*
[e] *fsahin@yeditepe.edu.tr* *https://orcid.org/0000-0002-7208-8967*

Introduction

Allergic rhinitis (AR), an inflammatory disease affecting nasal mucosa tissues, is seen in 10–30% of the population, with the highest prevalence in young adults and children [1]. Nasal obstruction is one of the most typical symptoms of AR, often has a circadian rhythm in terms of severity; the worst is at night and the early morning. Other typical symptoms of AR such as runny nose and sneezing, are more severe in the early morning; possibly in conjuncture with the high levels of inflammatory cells and mediators during this time period [2]. The reason for the circadian rhythm in AR is not yet fully understood.

It is also known that atopic diseases, such as asthma, nasal polyposis (NP) and AR generally coexist in the same patient [3]. Also, the patients with NP are often affected by the same problems, and considering that nasal polyps develop due to the presence of chronic inflammation, it is quite possible that their pathophysiology is influenced by similar mechanisms. This has been suggested to be associated with factors such as oxidative stress, genetic predisposition and environmental stimuli that trigger the underlying inflammatory reactions [4]. In addition, the measurement of Cyclooxygenase 1 (*COX1*), indoleamine 2,3-dioxygenase (*IDO*) and Interleukin-6 (*IL-6*) amounts, which are detected in high amounts in AR, can be used as an indicator in AR and asthma models [5,6]. One of the major problems described in clinical guidelines for AR is sleep disturbance and patients often have a dysfunctional circadian rhythm that affects cortisol and melatonin secretion [7].

Melatonin (N-acetyl-5 methoxideriptamine) is an indolamine which is synthesized mainly in the pineal gland [8], but extrapineal melatonin synthesis has been described in many other sites of the body including the brain, retina, harderian gland, ciliary body, lens, thymus, airway epithelium, bone marrow, immune cells, gonads, placenta, gastrointestinal tract

and skin [9]. Melatonin is known to be an important regulator of circadian rhythm in humans, and is a direct radical scavenger in addition to its indirect antioxidant effects on the cell membrane. In both in vivo and in vitro studies, melatonin has been shown to be a potent endogenous free radical scavenger that acts as an anti-inflammatory agent [9]. Melatonin stimulates several antioxidative enzymes such as superoxide dismutase, glutathione peroxidase and glutathione reductase, and thereby protecting cell membranes from lipid peroxidation by neutralizing toxic radicals [10]. In addition, previous study has shown that melatonin has neuro-immunological effects and may affects immunomodulatory activity in allergic diseases [11]. However, the potential use of melatonin in atopic diseases is rarely considered. On the other hand, melatonin has also been reported to play an important role in the pathogenesis of AR [12]. Melatonin and its precursor, 1-tryptophan, have been shown to decrease serum total IgE and IL-4 levels [13]; therefore, chronic inflammatory activity seen in patients with AR and NP may be compensated by the effects of melatonin. This effect can be explained as, by increasing the amount of melatonin, the suppression of indoleamine 2,3-dioxygenase (IDO), a tryptophan dehydrogenase enzyme, may increase the amount of melatonin precursor 1-tryptophan [6]. Melatonin causes partial inhibition of nuclear factor-kappa B (NF-κB) expression which is a trigger of pro-inflammatory activity and down-regulation of inducible nitric oxide synthase (iNOS) activity in lung tissue in an experimental model of asthma [14]. Plasma melatonin levels are reportedly reduced in patients with AR [15], atopic dermatitis (AD) [3] and in the exacerbation period of patients with bronchial asthma (BA).

There are no studies evaluating the efficacy of melatonin in the management of AR or nasal polyps, which have no definitive treatment. In the present study, we aimed to investigate the effect of melatonin in the treatment of Nasal-polyp Mesenchymal Stem Cells (Np-MSCs) and Mucosal Mesenchymal Stem Cells (Mu-MSCs).

Materials and Methods

Tissue Collection and Ethical Consideration

Nasal polyp tissue was taken from the nasal cavity in functional endoscopic sinus surgery of allergic rhinitis patient and mucosal tissue was taken from the nasal septal area of the non-allergic patient during septorinoplasty surgery while reconstructing the nasal cavity. Written consent was obtained from 2 patients; nasal polyp with allergic rhinitis was 35 years old, white man, had grade 3 nasal polyps in both nasal cavities originated from osteomeatal complex, had house dust mite allergy, non-allergic patient was 38 years old, white woman, had minimal septal deviation and had negative prick test. We did prick test (intradermal allergy test) for both patients. Institutional Ethical approval was obtained from Istanbul Yeniyüzyıl University Medical Faculty Ethical Committee (Ethic no :09.11.2018/032). All phases of the work were carried out in accordance with the Helsinki Declaration and Good Clinical Practice Guide.

Isolation, Cell Culture Conditions and Characterization

Cells were cultured in complete media that consists of Dulbecco's modified essential medium (DMEM, Gibco, Carlsbad, CA) supplemented with 10 % fetal bovine serum (FBS, Gibco, Carlsbad, CA) and 1 % of penicillin, streptomycin, and amphotericin (PSA, Gibco, Paisley, UK) and incubated at 37°C and 5 % CO2 in a humidified incubator. When cells had enough confluency, they were trypsinized and incubated with primary antibodies diluted in phosphate-buffered saline (PBS, Gibco, Paisley, UK) for 1 h. Conjugated antibodies against CD14, CD29, CD31, CD34, CD44, CD45, CD73, CD90, CD105 and CD117 (Abcam, Bristol, UK) were used to determine their mesenchymal stem cell surface profile according to criteria of International Mesenchymal Stem Cell Committee. Cells were washed with PBS. The flow cytometry analysis of cells was performed using a Becton Dickinson FACSCalibur (Becton Dickinson, San Jose, CA) flow cytometry system.

Cell Viability Assay

Cell viability was measured by the 3-(4,5-dimethyl-thiazol-2-yl)-5-(3-carboxymethoxy-phenyl)-2-(4-sulfo-phenyl)-2H-tetrazolium (MTS) assay (CellTiter96 Aqueous One Solution; Promega, Southampton, UK) according to the manufacturer's instructions. Five different concentrations of melatonin between 25 and 200 nM (25, 50 100, 150 and 200nM) and Mite Allergen (Allutard, 10000U) between 2.5 and 12.5 % (2.5, 5, 7.5, 10 and 12.5 %) from 10.000U stock solutions were prepared in complete media. Np-MSCs and Mu-MSCs (passage number 2-4) were seeded onto 96-well plates (Corning Plasticware, Corning, NY) at a concentration of 5,000 cells/well and cells were treated with melatonin and mite allergen alone and in combination for 24, 48 and 72 hours. MTS solution was prepared according to the manufacturer's instructions and the cells were incubated for 2 hours in the dark. Cell viability was measured by ELISA Plate Reader (Biotech, USA) at 490nm absorbance.

Annexin-V and Propidium Iodide Staining

Determining the apoptotic effect of melatonin and mite allergen alone and in combination on Np-MSCs and Mu-MSCs, cells were stained with fluorescent annexin V (annexin V- FITC) and propidium iodide (PI) using FITC Annexin V Apoptosis Detection Kit I (BD Biosciences Pharmingen, San Diego, CA, USA), according to the manufacturer's instructions. The cells were seeded onto 6-well-plates (2x105 cells/well) and incubated for 24 hours. After the incubation period, cells were treated with melatonin and mite allergen alone and in combination. After 24 hours, cells were harvested and resuspended in Annexin V binding buffer. Then, Annexin V-FITC and Propidium Iodide (PI) staining solution were added to each experimental group and incubated at RT for 20 minutes in the dark. Samples were analyzed using BD FACS Calibur Cell Sorting System (BD Biosciences Pharmingen; San Diego, CA, USA).

Determination of Intracellular Reactive Oxygen Species (ROS) Production

In order to measure the ROS levels on Np-MSCs and Mu-MSCs and investigate the effects of melatonin and mite allergen alone and in combination dichlorodihydrofluorescein diacetate (DCFH-DA) (Abcam, Cambridge, UK) was used as an intracellular ROS probe according to manufacturer's instructions. Cells were seeded onto black 96 well plates with a clear bottom (Greiner F-bottom chimney 96-well plate) at 10,000 cells/well. Then, the cells were treated with melatonin and mite allergen alone and in combination at different concentrations for 16 hours. After washing with PBS, cells stained with DCF-DA and CellTracker™ Red CMTPX Dye in serum free media and incubated at 37ºC for 30 min in the dark. Fluorescence intensities (Ex/Em; 495/529 nm, 577/602 nm) were measured with Varioskan LUX fluorescence microplate reader (Thermo Fisher Scientific, NY, USA).

Reverse Transcription and Quantitative Polymerase Chain Reaction (qPCR)

Total RNAs were isolated from melatonin and mite allergen alone and in combination treated groups by using High Pure RNA-isolation kit (Roche, Mannheim, Germany) according to the manufacturer's instructions. cDNA was synthesized from isolated Total RNAs by using High Fidelity cDNA Synthesis Kit (Roche, Mannheim, Germany). RT-PCR using SYBR Green PCR Master Mix (Applied Biosystems, Thermo Fisher Scientific, NY, USA) staining method was used to determine mRNA levels of the COX1, IDO, IL-6 and 18S RNA genes. cDNAs were mixed with primers and SYBR Green Master Mix. The primer sequences for qPCR were: for COX1 5'-GAGTTTGTCAATGCCACCT-3'(forward) and 5'-CAACTGCTTCTTCCCTTTG-3'(reverse); IDO 5'-CGCTGTTGGAAATAGCTTC-3'(forward) and 5'-CAGGACGTCAAAGCACTGAA-3'(reverse); IL-6 5'-GACAACTTTGGCATTGTGG-3'(forward) and 5'-ATGCAGGGATGATGTTCTG-3'(reverse); 18SRNA 5'-CGGCTACCACATCCAAGGAA-3' (forward) and 5'-GCTGGAATTACCGCGGCT-3'(reverse). The 18S RNA housekeeping gene was used for normalization of data. All RT-PCR experiments were performed using iCycler RT-PCR system (Bio-Rad, Hercules, CA). Additionally, PCR conditions were performed as initial denaturation at 95 for 3min, 39 cycle of following steps; denaturation at 95 for 30sec, annealing at 58 for 45 sec, extension at 72 for 30 sec and lastly final extension at 72 for 3 min.

Statistical Analysis

The data were statistically analyzed using one-way analysis of variance (ANOVA) with Tukey post-hoc test. The values of $p<0.05$ were considered statistically significant.

Results

Isolation and Characterization of Mesenchymal Stem Cell-Derived from Nasal Polyp and Mucosal Tissues

Np-MSCs and Mu-MSCs, which were successfully isolated and expanded from nasal polyp and mucosal tissue samples (Figure 1a, d), showed fibroblast-like cell morphology (Figure 1b, e). Isolated and cultured cells at passage 3 to 6 were characterized for their MSC surface markers using flow cytometry. Nasal polyp and Mucosal tissue derivative cells were characterized for the surface markers including CD29, CD14, CD31, CD44, CD34, CD45, CD73, CD90, CD105, and CD117 by flow cytometry. Cells were positive for CD29, CD44, CD73, CD90, and CD105, MSC surface markers, whereas they were negative for CD14, CD34, CD45, and CD117 hematopoietic stem cell (HSC), surface markers, and for CD31, endothelial cell marker (Figure 1c, f).

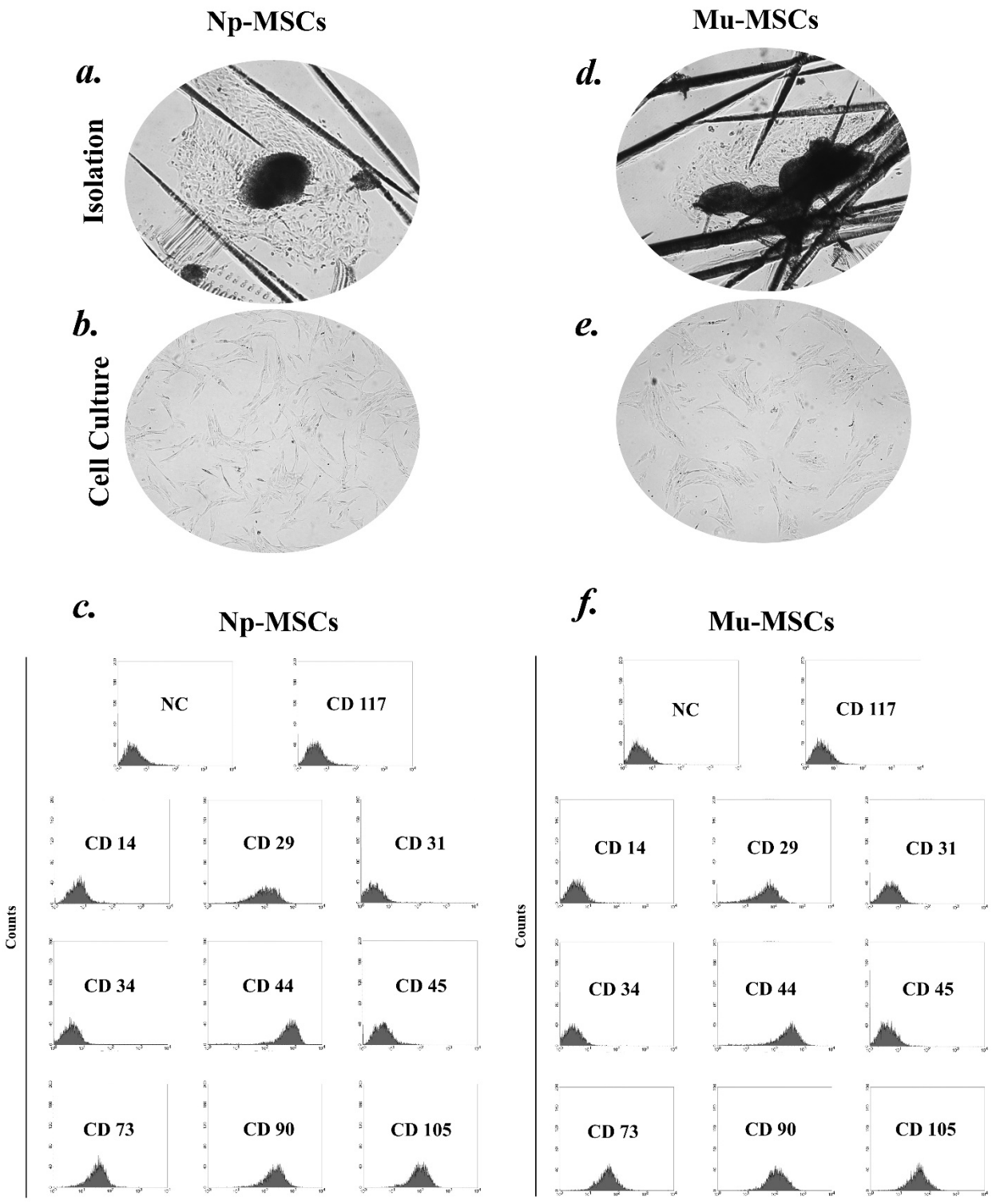

Figure 1. Cell images from isolation and culture process of the Np-MSCs (a, b and c) and Mu- MSCs cells (d, e and f). Characterization of MSCs Nasal polyp and Mucosal tissues.

Cytotoxicity of Melatonin and Mite Allergen W/O Combination

The cytotoxic effect of different Melatonin (25, 50, 100, 150 and 200 nM) and Mite Allergen (25, 50, 75, 100, 125 µg/mL) concentrations on Np-MSCs and Mu-MSCs viability were tested for 2 days at 24 and 48-h time points using the MTS assay. The results showed that there is no toxic effect of Melatonin (Figure 2a and d), Mite Allergen (Figure 2b and e) and their combination (Figure 2c and f), which was given to Np-MSCs and Mu-MSCs cells at different doses. On the contrary at some doses, they were increased the survival of cells significantly when compared to only growth media treated group.

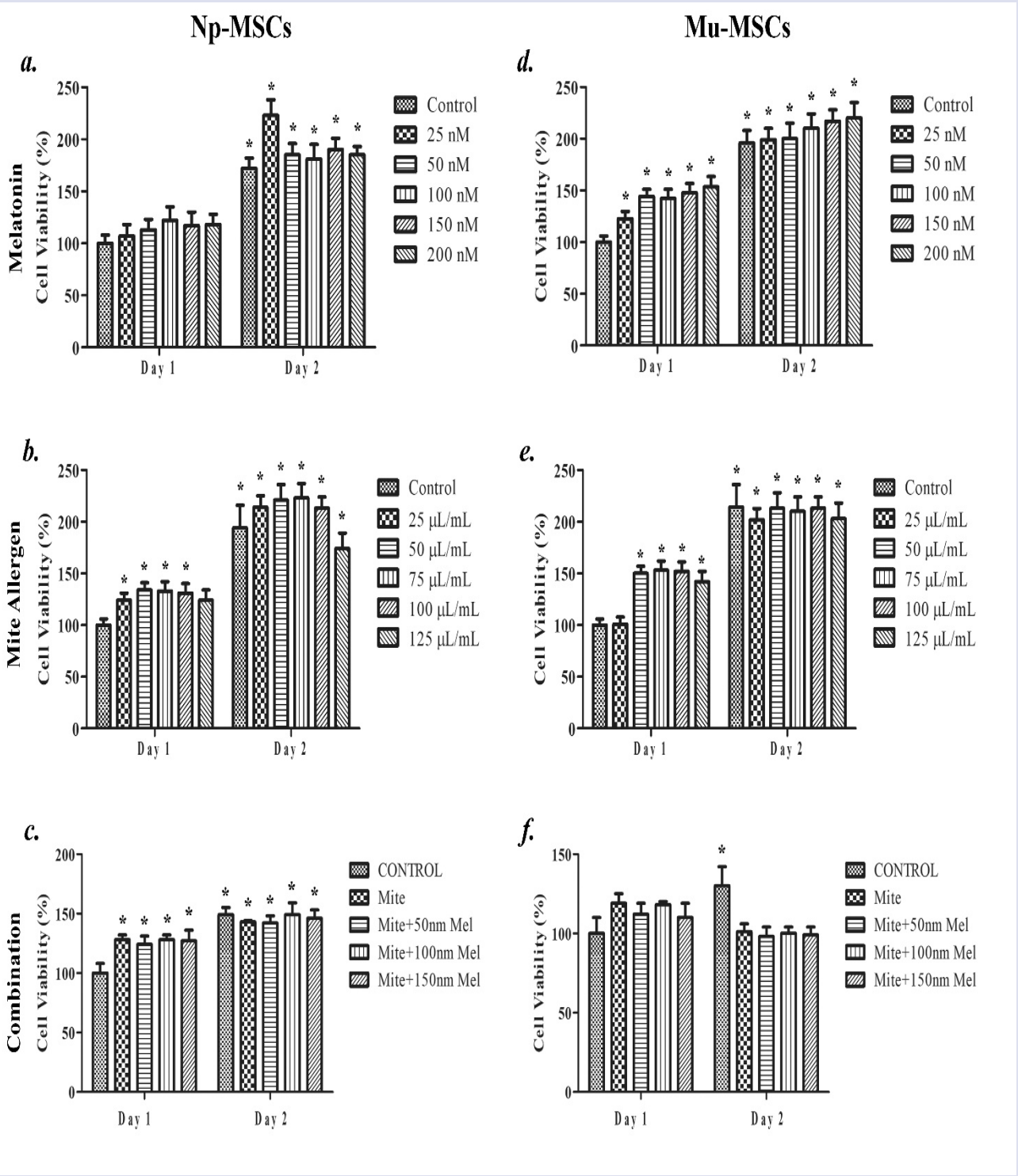

Figure 2. Cell images from isolation and culture process of the Np-MSCs (a, b and c) and Mu- MSCs cells (d, e and f). Characterization of MSCs Nasal polyp and Mucosal tissues.

Evaluation of Reactive Oxygen Species Levels in Melatonin-Treated Allergic Cells

In order to determine the indirect inflammation response, the ROS levels of NP-MSCs and Mu-MSCs were measured by the treatment of melatonin and mite allergen alone and in combination. Intracellular ROS levels were detected by using DCFH-DA fluorescence dye. Three different dose of melatonin (50, 100 and 150 nM) treatment of the allergic cell models reduced the ROS levels significantly in both mite allergen treated Np-MSCs and Mu-MSCs for all doses (Figure 3) compared to mite allergen treatment alone.

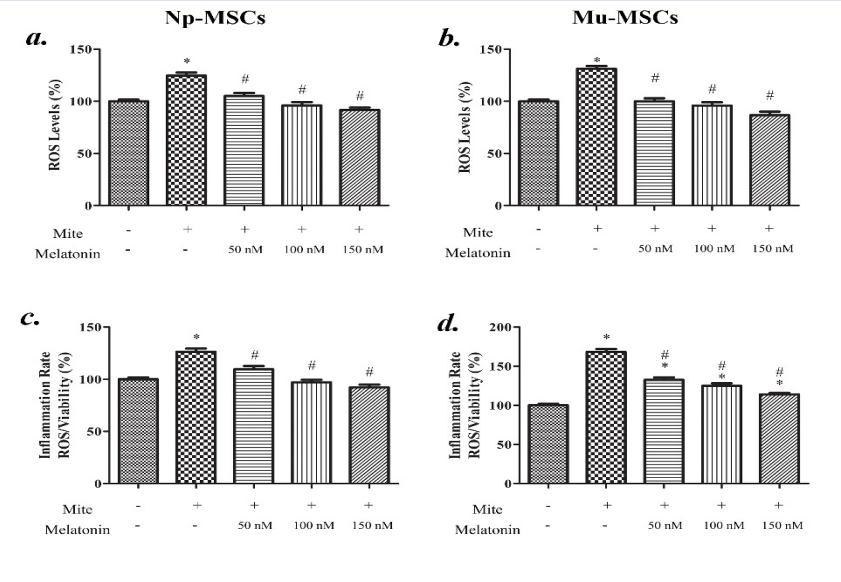

Figure 3. Cell images from isolation and culture process of the Np-MSCs (a, b and c) and Mu- MSCs cells (d, e and f). Characterization of MSCs Nasal polyp and Mucosal tissues.

Melatonin Treatment can Reduce Inflammation and Allergic Response to Allergic Cells in a Gene Level Manner

To determine the suppressive effects of Melatonin treatment on the allergic cell models, inflammation and allergic response related *IDO*, *COX1* and *IL-6* mRNA levels were evaluated by relative RT-PCR. Levels of *IDO* mRNA was decreased significantly in all 3-melatonin treated allergic cells (Figure 4a, d) when compared to Mite allergen treated Np-MSCs and Mu-MSCs. *IDO* level was significantly decreased when Np-MSCs were treated with 150nM Melatonin and Mu-MSCs were treated with 100 and 150 nM compared to only growth media treated group (Figure 4a, d). *COX1* gene expression were significantly decreased in melatonin treated healthy and allergic Np-MSCs groups (Figure 4b) while there was no significant difference in 100 and 150 nM Melatonin treated Mu-MSCs cells (Figure 4e). Interestingly, 50 nM Melatonin significantly increased *COX1* level in Mu-MSCs (Figure 4e). 50, 100 and 150 nm Melatonin treatment significantly decreased *IL-6* gene level in Mite-exposed Np-MSCs (Figure 4c). In addition, 100 and 150 nM Melatonin significantly decreased *IL-6* gene level in Mite-exposed Mu-MSCs compared to 50 nM Melatonin (Figure 4f).

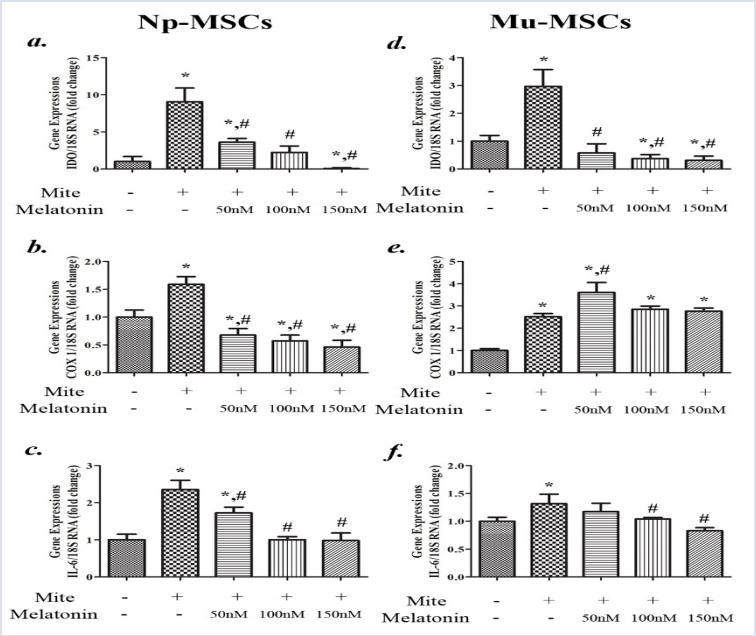

Figure 4. Cell images from isolation and culture process of the Np-MSCs (a, b and c) and Mu- MSCs cells (d, e and f). Characterization of MSCs Nasal polyp and Mucosal tissues.

Discussion

Atopic rhinitis is one of the most common chronic inflammatory diseases in all age groups (16). The pathophysiology of AR is based on IgE-mediated hypersensitivity reactions and the release of Th2-mediated cytokines, similar to other atopic diseases. However, since there is no permanent curative treatment, research has remained active on this topic, especially in terms of the elucidation of pathophysiology and treatment options. In the current literature, there are promising findings with new substances which directly affect development of disease or reduce AR severity (17,18). In our study, the effectiveness of melatonin in AR treatment was evaluated (as well as its possible cytotoxicity) by *IL-6*, *COX-1*, *IDO* and ROS levels. Our findings revealed that melatonin significantly reduced *COX-1* gene expression in Np-MSCs groups and also ROS intensity, *IDO* and *IL-6* gene levels in both Np-MSCs and Mu-MSCs groups –without any toxic effects. Thus, our results show that melatonin has significant anti-inflammatory and anti-oxidant activity in the presence of chronic inflammatory conditions of the respiratory tract, including AR and nasal polyps.

For nearly four decades, several studies have been conducted on the role of melatonin in the development and treatment of many diseases, including AD, BA and AR which are atopic diseases with similar pathophysiology. In previous studies with murine models, melatonin was reported to reduce IgE, IL-4 and IFN-γ levels and severity of AD symptoms through its reduction of activated CD4+ T cells (13). Furthermore, it was shown to contribute to the control of asthma symptoms by reducing MMP-9 (19), TLR-9 (20) and MUC5AC (21). In addition, melatonin levels have been shown to decrease in AD (3), BA (22) and AR in clinical studies (23,24). Chang et al. demonstrated that 3 mg / day oral melatonin treatment was more effective than placebo in the control of AD symptoms in children (25). In a study evaluating the effectiveness of oral melatonin in lung inflammation and airway hyperactivity, it was determined that it shows anti-inflammatory activity by reducing eosinophil and neutrophil and TNFα level in Broncho-alveolar Lavage (BAL). Moreover, melatonin was reported to decrease NO and hydroxyl radical concentrations and iNOS, TNF-α, nitrotyrosine and myeloperoxidase (MPO) activity in lung tissue (26). Our findings indicated that melatonin treatment causes anti-oxidant and immunomodulatory activity by reducing COX-1, ROS, IDO mRNA levels and IL-6 expression for the first time. These findings indicate that melatonin may be a new therapeutic approach for the treatment of AR.

Nasal polyps are benign inflammatory masses that are considered as a subset of chronic rhinosinusitis, originating from the nasal mucosa and paranasal sinuses, and their frequency increases with age (27). In the pathophysiology of nasal polyps, similar to AR, there are type 2 inflammation patterns characterized by eosinophilia and high IL-4, IL-5 and IL-13 cytokine levels (28). Mainly intranasal glucocorticoids are used on the basis of nasal polyp treatment and prevention. In patients whose symptoms cannot be controlled by medical treatment, polypectomy is performed with endoscopic sinus surgery (29). However, relief of attacks of their symptoms after surgery may not be curative because the nasal polyps show high recurrence rates; therefore, indicating that the treatment of underlying mechanisms is crucial. In a prospective multicenter cohort study was evaluated that relapse rates of 363 adult patients who underwent endoscopic sinus surgery for polyposis, within 18 months were found to be around 40% (30). In our study, melatonin has been shown to have more prominent anti-inflammatory and anti-oxidant activity in the nasal polyp tissue. According to our results, Np-MSC's has higher response to melatonin treatment, thus we believe that the effects of melatonin on nasal polyp treatment should be assessed in future studies.

Considering the results of the study, it is predicted that some limitations may be encountered. The effects of melatonin on the serum levels of various cells, mediators and cytokines (which could influence inflammatory response) could not be evaluated. Therefore, additional animal and clinical studies are required to reveal the effectiveness of melatonin in AR and nasal polyposis.

In conclusion, for the first time, our study demonstrated that the effectiveness of melatonin treatment in AR and nasal polyposis. Our findings indicated that the anti-oxidant and anti-inflammatory activity of melatonin in experimental AR and NP cell culture models could be an important source of data for future in vivo and clinical studies. On the basis of these data, melatonin could be a promising agent for the treatment of AR and nasal polyposis.

Aknowledgement

This study was supported by Yeditepe University.

Conflicts of interest

No conflict of interest was declared by the authors.

References

[1] Meltzer E.O., Allergic Rhinitis: Burden of Illness, Quality of Life, Comorbidities, and Control, *Immunol. Allergy Clin. North Am.,* 36 (2016) 235–48.

[2] Craig T.J., Ferguson B.J., Krouse J.H, Sleep impairment in allergic rhinitis, rhinosinusitis, and nasal polyposis, *Am. J. Otolaryngol.,* 29 (2008) 209–17.

[3] Marseglia L., D'Angelo G., Manti S., et al., Melatonin and atopy: role in atopic dermatitis and asthma, *Int. J. Mol. Sci.,* 15 (2014) 13482–93.

[4] Ciprandi G., Caimmi D., Del Giudice M.M., La Rosa M., Salpietro C., Marseglia G.L.,: Recent developments in united airways disease, *Allergy Asthma Immunol. Res.,* 4 (2012) 171–7.

[5] Vorsprach M., Arens C., Knipping S., et al., Expression of COX-1, COX-2, 5-LOX and CysLT2 CysLT2 in nasal polyps and bronchial tissue of patients with aspirin exacerbated airway disease, *Allergy Asthma Clin. Immunol.,* 15 (2019) 1–14.

[6] Refaat M.M., Abdel Rehim A.S.M., El-Sayed H.M., Mohamed N.A., Khafagy A.G., Serum indolamine 2, 3 dioxygenase as a marker in the evaluation of allergic rhinitis, *Am. J. Rhinol Allergy,* 29 *(*2015) 329–33.

[7] D'Elia C., Gozal D., Bruni O., Goudouris E., e Cruz MM: Allergic rhinitis and sleep disorders in children--coexistence and reciprocal interactions, *J Pediatr* (Rio J) 98(5) (2021) 444-454.

[8] Reiter R.J., Pineal melatonin: cell biology of its synthesis and of its physiological interactions, *Endocr. Rev.,* 12 (1991) 151–80.

[9] Mauriz J.L., Collado P.S., Veneroso C., Reiter R.J., González-Gallego J., A review of the molecular aspects of melatonin's anti-inflammatory actions: recent insights and new perspectives, *J. Pineal Res.,* 54 (2013) 1–14.

[10] Hacısevki A., Baba B., An overview of melatonin as an antioxidant molecule: a biochemical approach, *Melatonin Mol. Bio.l Clin. Pharm. Approaches, (*2018) 59–85.

[11] Li Y., Li S., Zhou Y., et al., Melatonin for the prevention and treatment of cancer, *Oncotarget,* 8 (2017) 39896.

[12] Lu T., Galijasevic S., Abdulhamid I., Abu-Soud H.M., Analysis of the mechanism by which melatonin inhibits human eosinophil peroxidase, Br. *J. Pharmacol.,* 154 (2008) 1308–17.

[13] Kim T.H., Jung J.A., Kim G.D., et al., Melatonin inhibits the development of 2, 4-dinitrofluorobenzene-induced atopic dermatitis-like skin lesions in NC/Nga mice, *J. Pinea.l Res.,* 47 (2009) 324–9.

[14] Wang Y.T., Chen S.L., Xu S.Y., Effect of melatonin on the expression of nuclear factor-kappa B and airway inflammation in asthmatic rats, *Chinese J. Pediatr.,* 42 (2004) 94–7.

[15] Fidan V., Alp H.H., Gozeler M., Karaaslan O., Binay O., Cingi C., Variance of melatonin and cortisol rhythm in patients with allergic rhinitis, *Am. J. Otolaryngol.,* 34 (2013) 416–9.

[16] Pawankar R., Canonica G.W., Holgate S.T., Lockey R.F., Blaiss M.S., WAO White Book on Allergy: Updates 2013, *World Allergy Organization*, (2013).

[17] Hosoki K., Gandhe R., Boldogh I., Sur S., Reactive oxygen species and allergic responses. In: Systems biology of free radicals and antioxidants. Berlin: Springer-Verlag Heidelberg, (2012) 3239–3266.

[18] Gostner J.M., Becker K., Kofler H., Strasser B., Fuchs D., Tryptophan metabolism in allergic disorders, *Int. Arch. Allergy Immuno.,l* 169 (2016) 203–15.

[19] Shin I.S., Park J.W., Shin N.R., et al., Melatonin reduces airway inflammation in ovalbumin-induced asthma, *Immunobiology,* 219(2014) 901–8.

[20] Wu H.M., Shen Q.Y., Fang L., et al., JNK--TLR9 signal pathway mediates allergic airway inflammation through suppressing melatonin biosynthesis, *J. Pineal. Res.,* 60 (2016) 415–23.

[21] Shin I.S., Park J.W., Shin N.R., et al., Melatonin inhibits MUC 5 AC production via suppression of MAPK signaling in human airway epithelial cells, *J. Pineal Res.,* 56 (2014) 398–407.

[22] Gumral N., Naziroglu M., Ongel K., et al., Antioxidant enzymes and melatonin levels in patients with bronchial asthma and chronic obstructive pulmonary disease during stable and exacerbation periods, *Cell Biochem. Funct. 27(5)* (2009) 276–83.

[23] Bayrak Degirmenci P., Aksun S., Altin Z., et al.: Allergic rhinitis and its relationship with IL-10, IL-17, TGF-$β$, IFN-$γ$, IL 22, and IL-35, *Dis. Markers,* (2018) 9131432.

[24] Sarnowski C., Laprise C., Malerba G., et al., DNA methylation within melatonin receptor 1A (MTNR1A) mediates paternally transmitted genetic variant effect on asthma plus rhinitis, *J. Allergy Clin. Immunol.,* 138 (2016) 748–53.

[25] Chang Y.S., Lin M.H., Lee J.H., et al., Melatonin supplementation for children with atopic dermatitis and sleep disturbance: a randomized clinical trial, *JAMA Pediatr,* 170 (2016) 35–42.

[26] Chen C.F., Wang D., Reiter R.J., Yeh D.Y., Oral melatonin attenuates lung inflammation and airway hyperreactivity induced by inhalation of aerosolized pancreatic fluid in rats, *J. Pineal Res.,* 50 *(2011)* 46–53.

[27] Hopkins C., Chronic rhinosinusitis with nasal polyps, *N. Engl. J. Med.,* 381 (2019) 55–63.

[28] Tomassen P., Vandeplas G., Van Zele T., et al., Inflammatory endotypes of chronic rhinosinusitis based on cluster analysis of biomarkers, *J. Allergy Clin. Immunol.,* 137 *(*2016) 1449–56.

[29] Newton J.R., Ah-See K.W., A review of nasal polyposis, *Ther. Clin. Risk. Manag.,* 4 (2008) 507.

[30] DeConde A.S., Mace J.C., Levy J.M., Rudmik L., Alt J.A., Smith T.L., Prevalence of polyp recurrence after endoscopic sinus surgery for chronic rhinosinusitis with nasal polyposis, *Laryngoscope,* 127 (2017) 550–555.

Cumhuriyet Sci. J., 44(3) (2023) 444-449
DOI: https://doi.org/10.17776/csj.1250269

Cumhuriyet Science Journal

| csj.cumhuriyet.edu.tr | Founded: 2002 ISSN: 2587-2680 e-ISSN: 2587-246X Publisher: Sivas Cumhuriyet University

Comparative Skull and Mandible Geometric Morphometrics of Two Species of Mice, *Mus domesticus* and *Mus macedonicus* (Muridae, Rodentia) in Turkey

Sadık Demirtaş[1,a], Medine Özmen[1,b,*], Metin Silsüpür[1,c], Damla Kıral[1,d]

[1] *Department of Biology, Faculty of Science, Ondokuz Mayıs University, Samsun, Turkey.*
**Corresponding author*

Research Article

History
Received: 13/02/2023
Accepted: 25/07/2023

ABSTRACT

Using a geometric morphometrics approach, we examined shape and size variations of skull and mandible bone of two evolutionarily distantly related mice from Turkey: *Mus domesticus* and *Mus macedonicus*. PCA analyses revealed overlap in dorsal cranium and mandible shapes of both species, consistent with previous traditional morphological methods. The skull of *M. macedonicus* seems to be larger in size than *M. domesticus* according to box-plot analyses of centroid size values, however there is no obvious difference for the mandible. No difference was observed between sexes in either of the characters. We suggest that future studies focus on dental characteristics and also consider the variation among local populations and ecological variables.

Keywords: House mouse, Macedonian mouse, Geometric morphometrics, Systematics, *Mus* sp.

[a] *sadikd@omu.edu.tr* *https://orcid.org/0000-0003-0859-7887*
[b] *mmedineozmenn@gmail.com* *https://orcid.org/0000-0002-8913-1175*
[c] *metins.ms@gmail.com* *https://orcid.org/0000-0001-5209-4019*
[d] *damla.kiral@gmail.com* *https://orcid.org/0000-0001-7610-0102*

Introduction

The genus *Mus* (Clerck, 1757) includes numerous subgenera, species and subspecies, and is one of the most well-known and widely distributed murid genera in the mammalian world [1,2]. The genus is represented by two species in Turkey: *Mus domesticus* (Rutty, 1772), commonly known as the western European house mouse, and *Mus macedonicus* (Petrov & Ruzíc, 1983), which is commonly known as the eastern Mediterranean short-tailed mouse or Macedonian mouse [3]. These species are widespread in both the European part (Thrace) and Asian part of Turkey (Anatolia) [2,4]. The house mice usually occupy areas that are in close association with humans, such as houses, barns, granaries, fencerows and cultivated fields. The short-tailed mouse, on the other hand, prefers cultivated fields, grasses, bushes and mixed forests away from human settlements [5]. Traditional morphological studies have often used ZI (zygomatic index) and H+B/T (the index of head plus body length/tail length) as well as external body, tooth and baculum measurements to distinguish between two species of mice in Turkey [4,6,7]. However, despite the apparent success of this method in distinguishing between the two species, the usability of the index is limited due to the range of ZI values for each species being large and slightly overlapping when the species are compared. In addition, these studies do not provide detailed statistical data in terms of shape and size analyses related to the morphometry of the skull and the entire mandible of the species.

The use of geometric morphometrics technique has increased rapidly in the field of zoological data analysis over the past two decades. The geometric morphometrics approach is useful for investigating shape variation and morphological transformation when species are difficult to differentiate using traditional methods [8]. Digitized geometric data are compared and differences are calculated by using various mathematical and statistical tests. The technique based on a landmark method is widely used and accepted in studies of animals, especially muroid rodents, that are hard to identify and differentiate with standard morphometric approaches [9,10]. Landmark coordinates describe specific, evolutionarily homologous points located on body parts of the specimens subjected to morphometric analysis, such as the skull and the teeth [11].

In the present study, the geometric morphometrics approach was used to evaluate the shape and size differences of the mandible and the dorsal side of the cranium between *M. macedonicus* and *M. domesticus* specimens from Thrace and Anatolia regions of Turkey, which were previously subject to molecular species identification using the control region of mitochondrial DNA [12-15]. In addition, shape and size variations between males and females of two species were compared to clarify ambiguous reports on sexual dimorphism proposed based on traditional morphometrics.

Materials and Methods

Study Specimens

We assessed skull and mandible shape, and size variation in two species of mice, *Mus domesticus* (33 males, 30 females) and *Mus macedonicus* (95 males, 52 females), using two-dimensional geometric morphometrics [11, 16] (Figure 1 and Table 1). Sample sizes for the skull and the mandible data set were: *M. domesticus* skull = 54, mandible = 51; *M. macedonicus* skull = 137, mandible = 102). All specimens used in this study were obtained from museum collections of İslam Gündüz and Sadık Demirtaş (subcollection IG/SD, Department of Biology, Faculty of Sciences, Ondokuz Mayıs University, Samsun, Turkey).

Table 1. Number of samples per collection locality of *Mus domesticus* and *Mus macedonicus* specimens used in this study. Location numbers correspond to map locations shown in Figure 1.

Species	Table of Localities		
	Locality Number	***Locality***	***Number of Samples***
Mus domesticus	1	Edirne	3
	4	Bursa	4
	7	Sinop	3
	8	Samsun	6
	11	Trabzon	1
	12	Rize	1
	13	Balıkesir	16
	16	Sivas	3
	18	Iğdır	1
	20	Manisa	1
	23	Kayseri	5
	24	Elazığ	2
	25	Van	2
	28	Muğla	1
	27	Denizli	8
	34	Adana	1
	37	Adıyaman	1
	38	Şanlıurfa	4
			63
Mus macedonicus	2	Tekirdağ	1
	3	Çanakkale	8
	4	Bursa	13
	5	Bilecik	2
	6	Kastamonu	1
	8	Samsun	4
	9	Tokat	10
	10	Ordu	2
	13	Balıkesir	1
	14	Eskişehir	2
	15	Ankara	4
	16	Sivas	7
	17	Erzincan	2
	19	İzmir	5
	20	Manisa	23
	21	Afyonkarahisar	2
	22	Konya	12
	23	Kayseri	2
	25	Van	1
	26	Aydın	11
	28	Muğla	1
	29	Burdur	5
	30	Isparta	2
	31	Antalya	6
	32	Karaman	3
	33	Mersin	3
	34	Adana	1
	35	Kahramanmaraş	4
	36	Gaziantep	2
	38	Şanlıurfa	3
	39	Hatay	4
			147
		Total	210

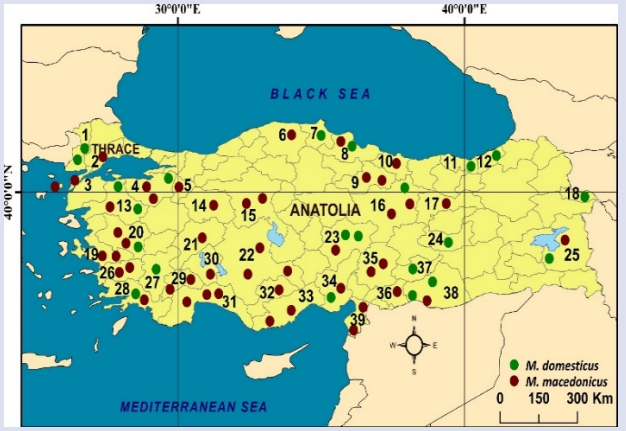

Figure 1. Capture locations of specimens used in this study. Location names (indicated by numbers) have been listed in Table 1.

Imaging and Landmarks

High resolution digital images of the dorsal cranium and the right mandible of each specimen were obtained using a Nikon D5000 (18-55 mm) camera with skull roof and mandible positioned in parallel with to the photographic plane. The images were scaled, edited, and digitized using TPS (Thin-Plate Spin) software series [17,18] for subsequent analyses. In order to emphasize the local impact of possible shape deformation on different parts of the skull and the mandible, we selected to describe 12 landmarks and 5 semilandmarks for the dorsal cranium and 10 landmarks and 22 semilandmarks for the mandible (Figure 2). The landmarks and semilandmarks were placed in accordance with previous studies [19-21].

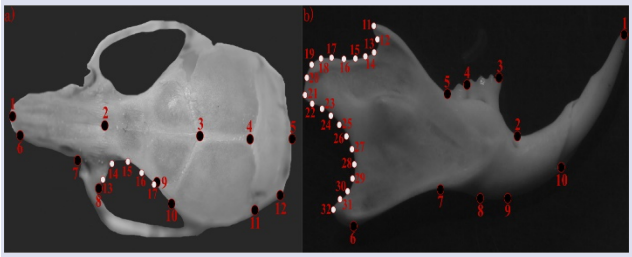

Figure 2. Landmarks (black points) and semilandmarks (white points) used in this study. (specimen: Mus macedonicus, Manisa vicinity, W. Turkey). Landmark locations on dorsal cranium (a): (1) the most rostral point of the nasal bone, (2) intersection of interfrontal and fronto-nasal suture, (3) intersection of the coronal and sagittal sutures, (4) intersection of the sagittal and parietal-interparietal sutures, (5) caudal end of the occipital curve, (6) intersection of the rostral curvature of the nasal process of the incisive bone (Processus nasalis ossis incisivi) and the nasal bone in the dorsal projection, (7) anterior notch on frontal process lateral to infraorbital fissure (8) anterior part of the orbit, (9) the most rostral point of the parietal bone, (10) intersection point of the squamosal and parietal bone, (11) exterior tip of the occipital crest, (12) caudolateral end of the occipital bone in the dorsal projection. The semi landmarks (13-17) surround the frontal bone. Landmark locations on mandible (b): (1) tip of the incisor, (2) mental foramen, (3) distal tip of the first molar, (4) the proximal end point of the first molar, (5) the proximal end point of the second molar, (6) The curve of angular process, (7) superior-most point on inferior border of mandibular ramus, (8) inferior-most point on border of ramus inferior to incisor alveolar, (9) The most inferior point of mental protuberance, (10) inferior-most point on incisor alveolar rim. The semilandmarks (11-32) are placed between coronoid and angular processes of the mandible.

Geometric Morphometric Analysis

After digitalization configuration of landmark and semilandmark coordinates, Generalized Procrustes Analysis (GPA) was applied to superimpose the shape information from each specimen to eliminate the effects of location, orientation, and scaling from the raw data coordinates [22,23]. The resulting projections were displayed on a series of axes and the patterns of inter- and intra-specific shape variation were analysed by using Principal Component Analysis (PCA) and Procrustes ANOVA. Wireframe graphs were used to illustrate the differentiation in shape between two species based on the utilized landmark and semilandmark points.

To account for the effect of size on shape, a centroid size (CS) analysis was implemented, which was calculated as the square root of the summed squared distances of each landmark from the center of the landmark configuration. The centroid size values generated for the dorsal cranium and the mandible bone were analysed using a Mann-Whitney U test to determine whether there is a significant difference between two species. The CS variation for each species has been visualized with a box-plot graphic.

GPA, PCA, Procrustes ANOVA and wireframe analyses were performed using MorphoJ version 1.07 [24]; Mann-Whitney U test analyses were performed using SPSS version 22.0 [25]; centroid size and box-plot analyses were obtained using PAST version 4.01 [26]. Program outputs were edited and visualized using Inkscape version 0.92 [27].

Results and Discussion

Shape Variation

PCA and comparative wireframe graphs were visualized for the skull and mandible shapes based on PC1 and PC2 values (Figure 3 and Figure 4). The variance was calculated based on the scatter plot along PC1 (explains 23.58% of the variance) and PC2 (explains 16.15% of the variance) for the skull. *M. domesticus* skulls predominantly included positive values in PC1 and negative values in PC2, whereas *M. macedonicus* skulls predominantly contained negative values in PC1 and positive values in PC2, however, the two species were not distinctly separated from each other. According to the wireframe graphs obtained from *Mus domesticus* PC1 and PC2, the variation in shape is mostly explained by the landmarks 3, and 7-10. This indicates that the skull is flattened from the top and narrowed from the orbital area. Similarly, the wireframe analysis for *Mus macedonicus* based on PC1 and PC2 revealed that the points with the most influence on skull shape were landmark numbers 3 and 7-10, resulting in an arched skull shape with a narrow eye socket. Procrustes ANOVA shows significant shape differences between species ($F = 16.90$, $P<0.05$), while differences between sexes were insignificant ($F=1.21$ and $P=0.2009$ for *M. domesticus*; $F=1.0$ and $P=0.4618$ for *M. macedonicus*).

Wireframe graphs revealed morphological differences in the orbital socket and the central part of the skull between the species, which were not clearly supported by the PCA graphs. This discrepancy is probably due to the large variation in breadth of the zygomatic arch within both species [4,6,7]. A wide variety of zygomatic index values have also been previously reported from various European *Mus* populations [28-30]. Recent studies with Quantitative Trait Loci (QTL) mapping methods have shown that many QTLs provide the basis for the genetic architecture of shape variation in *Mus* skulls [31-33]. For these reasons, the use of zygomatic index to distinguish between these species, as well as other *Mus* species, should be approached carefully [34,35].

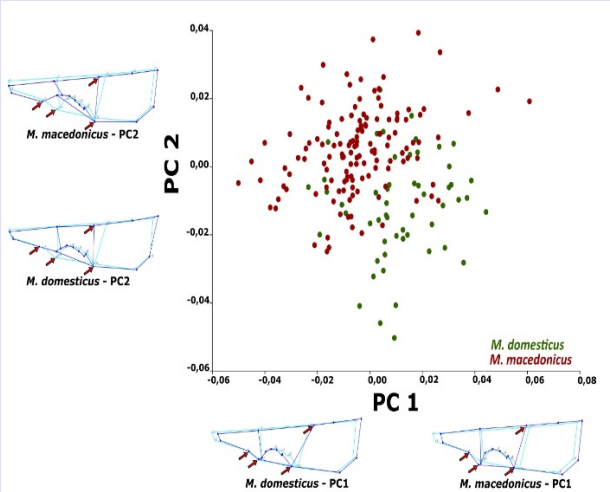

Figure 3. Inter-species principal component and wireframe analyses of skull shapes of *M. domesticus* and *M. macedonicus*. Wireframe diagrams compare the variation in shape with light blue showing the mean shape and dark blue showing the most extreme shape variation explained by each principal component.

Similarly, the variance was calculated along with PC1 (explains 34.68% of the variance) and PC2 (explains 18.57% of the variance) based on the scatter plot graphic for the mandible. *M. domesticus* showed intensity on the negative side of the graph for both PC1 and PC2 (Figure 4). In contrast, *M. macedonicus* showed an intensely positive distribution for PC1 and showed both positive and negative distribution for PC2. Both species showed the greatest amount of shape variation in the ramus region between the coronoid process and the angular process illustrated by the wireframe analyses, however, this difference was not reflected in the PCA graphs. Therefore, our results failed to provide support for the use of jaw morphometry for the differentiation of these two species of *Mus*. The main reasons for this discrepancy can be explained by the attachment styles of the temporalis and masseter muscle groups, as well as the mandible being a malleable bone. While masseter muscles help molar mastication activity, temporal muscles serve a role in gnawing [36]. Therefore, the development of these muscles is related to both nutrient content and ecological environment of the species [37]. Another factor that may have a role in the observed lack of differentiation can be due to the pleiotropic

effects of QTLs, which also function in the modular organization of both the skull and the mandible [38]. Procrustes ANOVA shows significant shape differences between species (F = 31.32, P<0.05), while differences between sexes were insignificant (F=1.15 and P=0.1974 for *M. domesticus*; F=0.63 and P=0.9879 for *M. macedonicus*).

Our results demonstrate that skull and jaw morphometry fail to provide a clear distinction between two species, and support that dental morphometry has the potential to provide more superior data for distinguishing between these species, as previously proposed by Macholán (2006) for various species of *Mus*.

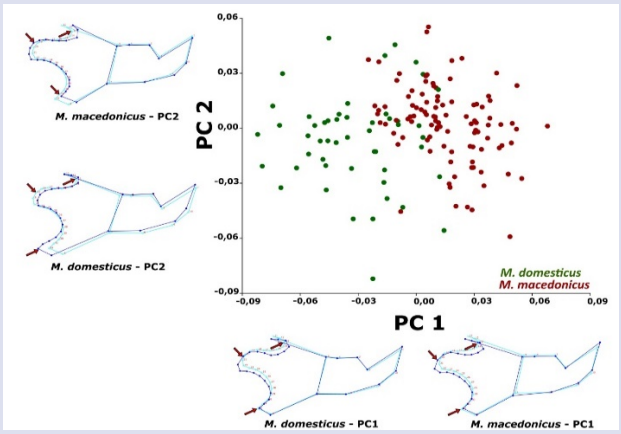

Figure 4. Inter-species principal component and wireframe analyses of mandible of *M. domesticus* and *M. macedonicus*. Wireframe diagrams compare the variation in shape with light blue showing the mean shape and dark blue showing the most extreme the shape variation explained by each principal component.

Finally, there was no difference between sexes in the amount of variation explained by PC1 or PC2 for skull or mandible shape in either of the species (Figure 5 and Figure 6). Principal component values were distributed uniformly among sexes in terms of both species and characters.

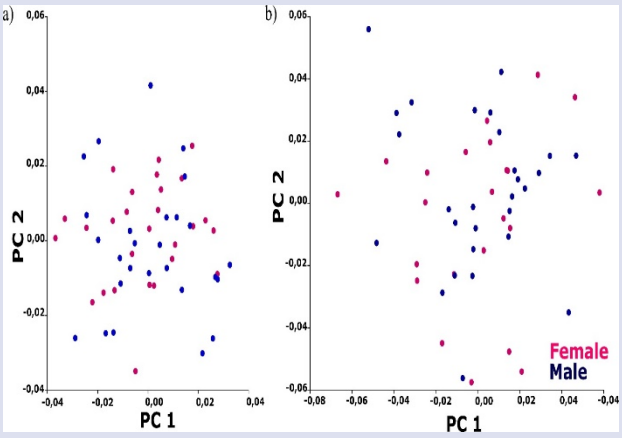

Figure 5. Intra-specific sex-linked principal component analysis of the skull shape (a) and mandible shape (b) of *M. domesticus*.

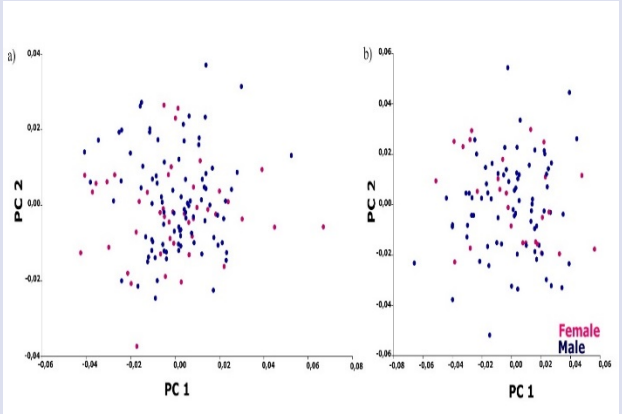

Figure 6. Intra-specific sex-linked principal component analysis of the skull shape (a) and mandible shape (b) of *M. macedonicus*.

Size Variation

The results of the Mann-Whitney U test indicate that the two species significantly differed in dorsal cranium centroid size (U=2181, P=0.05) but there was no significant difference for the mandible (U=2546, P=0.696). Also, we failed to reject the null hypothesis and therefore we inferred that there was no significant difference between sexes of both species for the two characters (P>0.05).

In parallel with the Mann-Whitney U test, the boxplot analysis indicates that *M. macedonicus* is larger in size than *M. domesticus* by log-centroid size values of the dorsal cranium, but, there is no obvious difference for the mandible (Figure 7). Previous morphometric studies revealed that there could be slight variations in size among local populations within both species [20, 39]. Moreover, Macholán (1996) showed that size variation can fluctuate within populations due to different age structure of populations and due to ecological variables. In this study, we did not consider local populations, age structures and ecological variables; we focused solely on the variation of shape and size between two species found in Turkey. Therefore, the number of specimens and localities in our study may not be satisfactory for centroid size analysis. For this reason, future studies should consider repeating the centroid size analysis on a large number of specimens from different local populations, also takes ecological variables into consideration. In other words, further studies are needed to clarify this observed difference in size between two species.

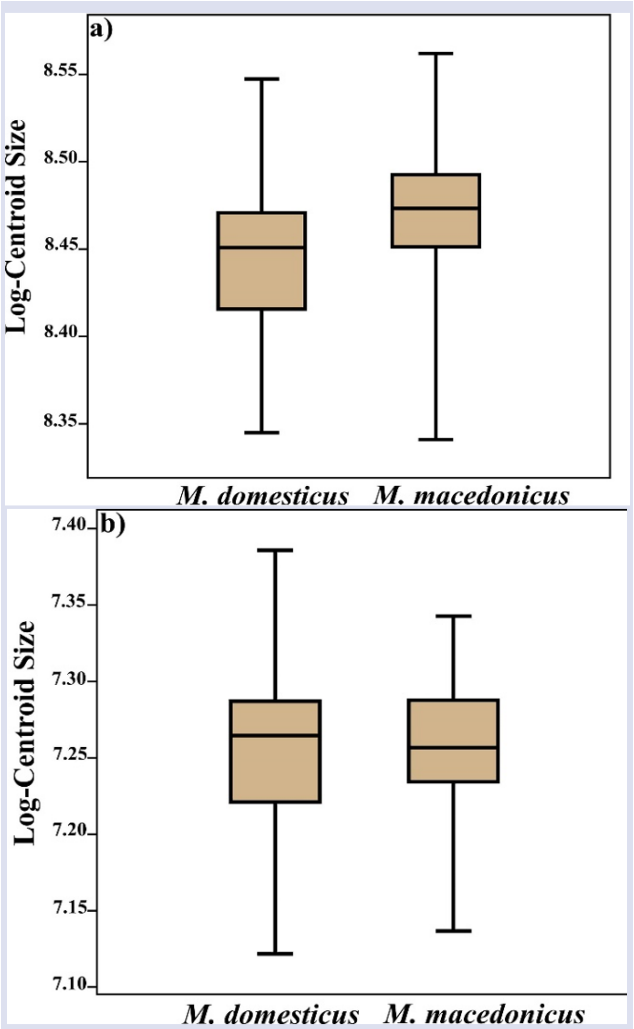

Figure 7. Boxplot graphics showing maximum, minimum and median values of log-centroid size for dorsal cranium (a) and mandible (b) between Turkish mice.

Conclusions

The current study enabled us to obtain morphometric data regarding the analysis of shape and size between two evolutionarily distantly related species, namely *Mus macedonicus* and *M. domesticus*. The results revealed that there was no significant difference in shape of the dorsal side of the skull and the mandible between the two species despite a statistically significant difference in centroid size values for the dorsal cranium. The centroid size values indicate that the dorsal side of the cranium is larger in *M. macedonicus* compared to *M. domesticus* in Turkey. Moreover, there were no morphometric differences between males and females for either of the studied features. Future studies using dental characters, which are frequently used in *Mus* species-subspecies studies, and gene expression analyses such as QTL mapping can identify morphological variations at inter- and intra-specific level in mice of Turkey.

Acknowledgment

We are very grateful to Dr. İ. GÜNDÜZ for providing access to the study material.

Conflicts of interest

There are no conflicts of interest in this work.

References

[1] Berry R.J., Town Mouse, Country Mouse: adaptation and adaptability in *Mus domesticus* (*M. musculus domesticus*), *Mammal Review*, 11 (1981) 91-136.

[2] Wilson D.E., Reeder D.M., Mammal species of the world: a taxonomic and geographic reference (Vol. 1). Johns Hopkins University Press, Bucknell University, Baltimore, Maryland, (2005).

[3] Kryštufek B., Vohralík V., Mammals of Turkey and Cyprus Rodentia II: Cricetinae, Muridae, Spalacidae, Calomyscidae, Capromyidae, Hystricidae, Castoridae. University of Primorska, Science and Research Centre, Koper, Slovenia, (2009) 146-169.

[4] Yavuz G., Examination of some cranial characteristics of *Mus domesticus* Linnaeus 1758 and *Mus macedonicus* Petrov & Ruzic 1983 (Mammalia: Rodentia) distributed in Turkey, *Kırşehir Ahi Evran Üniversitesi Ziraat Fakültesi Dergisi*, 2 (1) (2022) 43-55.

[5] Abi-Said M.R., Karam S.S., Morphological Cranial Study and Habitat Preference of *Mus macedonicus* (Petrov & Ruzic, 1983) (Mammalia: Rodentia) in Lebanon, *Jordan Journal of Biological Sciences (JJBS)*, 10 (4) (2017) 235-237.

[6] Gözcelioğlu B., Çolak R., Çolak E., Yiğit N., A study on *Mus domesticus* Rutty, 1772 and *Mus macedonicus* Petrov and Ruzic, 1983 (Mammalia: Rodentia) Distrubuted along the Line of Ankara, Bolu and Zonguldak, *Turkish Journal of Zoology*, 29 (2) (2005) 133-140.

[7] Çolak E., Yiğit E., Sözen M., Çolak R., Özkurt Ş., Kankılıç T., Kankılıç T., The morphological analysis of *Mus domesticus* and *Mus macedonicus* (Mammalia: Rodentia) in Turkey, *Turkish Journal of Zoology*, 30 (3) (2006) 309-317.

[8] Adams D.C., Rohlf F.J., Slice D.E., Geometric morphometrics: ten years of progress following the 'revolution', *Italian Journal of Zoology*, 71 (2004) 5-16.

[9] Barčiová L., Advances in insectivore and rodent systematics due to geometric morphometrics, *Mammal Review*, 39(2) (2009) 80-91.

[10] Miele V., Dussert G., Cucchi T., Renaud S., Deep learning for species identification of modern and fossil rodent molars, *bioRxiv*, (2020).

[11] Bookstein F.L., Morphometric Tools for Landmark Data. Cambridge University Press, New York, (1991).

[12] Gündüz İ., Tez C., Malikov V., Vaziri A., Polyakov A.V., Searle J.B., Mitochondrial DNA and chromosomal studies of wild mice *Mus* from Turkey and Iran, *Heredity*, 84(4) (2000) 458-467.

[13] Gündüz İ., Rambau R.V., Tez C., Searle J.B., Mitochondrial DNA variation in the western house mouse (*Mus musculus domesticus*) close to its site of origin: studies in Turkey, *Biological Journal of the Linnean Society*, 84(3) (2005) 473-485.

[14] Demirtaş S., Genetic variations in genus of *Mus* L., 1758 (Mammalia: Rodentia) distributed in Turkey, Master Thesis, Ondokuz Mayıs University, Graduate School of Education, 2006.

[15] Özçam P., Molecular phylogeography of the mouse *Mus macedonicus* Petrov&Ruzic, (1983) (Rodentia: Mammalia) in Turkey, Master Thesis, Ondokuz Mayıs University, Graduate School of Education, 2010.

[16] Dryden I.L., Mardia K.V., Statistical Analysis of Shape. John Wiley, New York, (1998).
[17] Rohlf F.J., tpsDig2 Software, Version 2.31. Ecology and Evolution, Stony Brook University, New York, (2017).
[18] Rohlf F.J., tpsUtil Software, Version 1.78. Ecology and Evolution, Stony Brook University, New York, (2019).
[19] Richtsmeier J.T., Baxter L.L., Reeves R., Parallels of Craniofacial Maldevelopment in Down Syndrome and Ts65Dn Mice, *Developmental Dynamics*, 217 (2000) 137-145.
[20] Macholán M., Mikula O., Vohralik V., Geographic phenetic variation of two eastern-Mediterranean non-commensal mouse species, *Mus macedonicus* and *M. cypriacus* (Rodentia: Muridae) based on traditional and geometric approaches to morphometrics, *Zoologischer Anzeiger-A Journal of Comparative Zoology*, 247(1) (2008) 67-80.
[21] Anderson P.S., Renaud S., Rayfield E.J., Adaptive plasticity in the mouse mandible, *BMC Evolutionary Biology*, 14 (2014) 85.
[22] Rohlf F.J., Slice D.E. Extensions of the Procrustes method for the optimal superimposition of landmarks, *Systematic Zoology*, 39 (1990) 40-59.
[23] Zelditch M.L., Swiderski D.L., Sheets H.D., Fink W.L., Geometric Morphometrics for Biologists. Academic Press, (2004) 1-20.
[24] Klingenberg C.P., MorphoJ: an integrated software package for geometric morphometrics, *Molecular Ecology Resources*, 11 (2011) 353-357.
[25] SPSS: IBM SPSS Statistics 22.0 for Windows. Armonk, New York, (2013).
[26] Hammer Ø., Harper D.A.T., Ryan P.D., PAST: Paleontological Statistics software package for education and data analysis, *Paleontologia Electronica*, 4 (1) (2001) 1-9.
[27] Inkscape (Version:0.92). Available at: https://inkscape.org/
[28] Lyalyukhina S., Kotenkova E., Walkova W., Adamczyk K., Comparison of craniological parameters in *Mus musculus musculus* Linnaeus, 1758 and *Mus musculus hortulanus* Nordmann, 1840, *Acta Theriologica*, 36 (1991) 95-107.
[29] Cserkész T., Gubányi A., Farkas J., Distinguishing *Mus spicilegus* from *Mus musculus* (Rodentia, Muridae) by using cranial measurements, *Acta Zoologica Academiae Scientiarum Hungaricae*, 54 (2008) 305-318.
[30] Csanády A., Mošanský L., Skull morphometry and sexual size dimorphism in *Mus musculus* from Slovakia, *North-Western Journal of Zoology*, 14 (2018) 102-106.
[31] Klingenberg C.P., Leamy L.J., Cheverud J.M., Integration and modularity of quantitative trait locus effects on geometric shape in the mouse mandible, *Genetics*, 166 (2004) 1909-1921.
[32] Burgio G., Baylac M., Heyer E., Montagutelli X., Genetic analysis of skull shape variation and morphological integration in the mouse using interspecific recombinant congenic strains between C57BL/6 and mice of the *Mus spretus* species, *Evolution*, 63 (10) (2009) 2668-2686.
[33] Ishikawa A., A Strategy for Identifying Quantitative Trait Genes Using Gene Expression Analysis and Causal Analysis, *Genes (Basel)*, 8 (12) (2017) 347.
[34] Macholán M., Morphometric analysis of European house mice, *Acta Theriologica*, 41 (1996) 255-275.
[35] Macholán M., A geometric morphometric analysis of the shape of the first upper molar in mice of the genus *Mus* (Muridae, Rodentia), *Journal of Zoology*, 270 (2006) 672-681.
[36] Klingenberg C.P., Navarro N., Development of the mouse mandible: a model system for complex morphological structures. In: Macholán M., Baird S.J.E., Munclinger P., Pialek J., (Eds). Evolution of the house mouse. Cambridge: Cambridge University Press, (2012) 135-149.
[37] Boell L., Tautz D., Micro-evolutionary divergence patterns of mandible shapes in wild house mouse (*Mus musculus*) populations, *BMC Evolutionary Biology*, 11 (2011) 306.
[38] Ehrich T., Vaughn T.T., Koreishi S.F., Linsey R.B., Pletscher L.S., Cheverud J.M., Pleiotropic effects on mandibular morphology I. Developmental morphological integration and differential dominance, *Journal of Experimental Zoology Part B: Molecular and Developmental Evolution*, 296 (2003) 58-79.
[39] Babiker H., Tautz D., Molecular and phenotypic distinction of the very recently evolved insular subspecies *Mus musculus helgolandicus* Zimmermann, 1953, *BMC Evolutionary Biology*, 15 (2015) 160.

Cumhuriyet Sci. J., 44(3) (2023) 450-455
DOI: https://doi.org/10.17776/csj.1248428

Cumhuriyet Science Journal

| csj.cumhuriyet.edu.tr | Founded: 2002 ISSN: 2587-2680 e-ISSN: 2587-246X Publisher: Sivas Cumhuriyet University

A New Nickel(II) Complex Derived From Bisthiocarbohydrazone: Synthesis, Characterization, Crystal Structure and Antioxidant Activity

Yeliz Kaya[1,a,*]

[1]*Department of Chemistry, Faculty of Engineering, Istanbul University-Cerrahpaşa, Istanbul, Turkey.*
**Corresponding author*

Research Article

History
Received: 06/02/2023
Accepted: 22/08/2023

ABSTRACT

A new complex with composition [Ni(L)(PPh_3)] (PPh_3 = triphenylphosphine) was obtained from the reaction of 1,5-bis(salicylidene)thiocarbohydrazone (L) with an equimolar amount of [$NiCl_2(PPh_3)_2$]. The complex was identified by FT-IR, ^{1}H NMR and UV-Vis spectroscopic methods and elemental analysis. The solid state structure of [Ni(L)(PPh_3)] was established by X-ray diffraction analysis. It was determined that the complex, whose nickel center has a distorted square planar configuration, crystallizes in the monoclinic space group I2/c. Bisthiocarbohydrazone (L) binds to the nickel center through its phenolate O, azomethine N and thioenolate S atoms in a dianionic tridentate mode. The antioxidant capacity of L and Ni(II) complex was examined using the CUPRAC (cupric reducing antioxidant capacity) method. Also, the DPPH (1,1-Diphenyl-2-picrylhydrazyl) method was used to test free radical scavenging activity of the compounds. Antioxidant activity results showed that L exhibited better activity than Ni(II) complex.

Keywords: Thiocarbohydrazone, Nickel(II) complex, Triphenylphosphine, Crystal structure, Antioxidant activity.

[a]*yeliz.kaya@iuc.edu.tr* *https://orcid.org/0000-0001-5606-8088*

Introduction

Compounds with C=S and C-SH groups are substantial organic compounds as they are potential donor ligands for transition metal ions [1, 2]. Thiocarbohydrazide is a compound with two hydrazine and one thione group. Thiocarbohydrazide is a precursor compound in the formation of macrocyclic ligands for the binding of a wide variety of metals [3, 4]. The hydrazine groups of thiocarbohydrazide can react with aldehydes or ketones to form bis- or monothiocarbohydrazones [5, 6]. Thiocarbohydrazones have the ability to form chelates with various metal ions through donor groups originating from both thiocarbohydrazide and aldehyde or ketone molecules [7]. Thiocarbohydrazones and their metal complexes have some activities or features such as antitumor, antioxidant, antimicrobial, antiviral, antitubercular, physicochemical, carbonic anhydrase and acetylcholinesterase inhibitors, electrochemical and corrosion inhibitors [8, 9]. Thiocarbohydrazones can also be used for the extraction and sensing of heavy metal ions [10, 11].

Nickel(II) complexes containing S and N donor ligands are of great interest because some enzymes such as hydrogenases and carbon monoxide dehydrogenases have nickel complexes in their active sites [12].

Phosphine-based ligands are among the important compounds as they exhibit significant efficiency in transition metal-catalyzed reactions. The development of suitable new phosphine ligands to make a reaction more efficient is an important aspect in catalyst development [13, 14]. These compounds also have important bioactivities such as antitumor, antiviral, antifungal, antibacterial and antioxidant [15, 16].

Reactive oxygen species (ROS) produced in high concentrations cause adverse changes in lipids, proteins and DNA components. The disruption of the balance between the detoxification of ROS and the production and accumulation of these reagents is called "oxidative stress". Oxidative stress causes some diseases such as cancer, hypertension, neurological disorders and diabetes. Antioxidants, which are effective in eliminating the detrimental effects of ROS, can protect cells from the formation of diseases caused by oxidative stress [17, 18]. So, in this study, a new Ni(II) complex was synthesized from 1,5-bis(salicylidene)thiocarbohydrazone (L) and [$NiCl_2(PPh_3)_2$] in order to test its potential antioxidant activity. L and Ni(II) complex were characterized using FT-IR, ^{1}H NMR, UV-Vis spectroscopies and elemental analysis. The antioxidant activities of the compounds were also examined using DPPH and CUPRAC methods.

Materials and Methods

Thiocarbohydrazide was gained as described in the previously published procedure [19]. All other chemicals and solvents were purchased and used as received. IR and ^{1}H NMR spectra, UV-Vis data (in 4 x 10^{-5} M DMSO), elemental analysis and magnetic moment measurements were obtained using an Agilent Cary 630 FTIR, a Varian UNITY INOVA 500

MHz NMR device, a Shimadzu 2600 UV-Vis spectrophotometer, a Thermo Finnigan Flash EA 1112 elemental analyzer and a Sherwood Scientific MK I model device, respectively.

Single crystals of [Ni(L)(PPh_3)] were obtained by slow evaporation of a methanol+dichloromethane+DMSO solution of the solid complex. A Bruker APEX II CCD diffractometer was used for data collection at room temperature. Structure solution and refinement were performed with the SHELXT [20] and SHELXL [21] programs. Indexing, data reduction and integration were performed using APEX2 [22] and SAINT [23]. The crystallographic data of [Ni(L)(PPh_3)] are given in Table 1. The selected bond angles and distances are listed in Table 2.

Synthesis of 1,5-bis(salicylidene)thiocarbohydrazone (L)

1,5-bis(salicylidene)thiocarbohydrazone (L) was obtained according to our published procedure (Figure 1) [24].

Color: Light yellow. Yield: 85%. M.p.: 190-191 °C. Calc. for $C_{15}H_{14}N_4O_2S$ (314.36 g mol^{-1}): C: 57.31, H: 4.49, N: 17.82, S: 10.20%; found: C: 57.50, H: 4.46, N: 17.84, S: 10.28%. IR (cm^{-1}): ν(OH) 3195, ν(NH) 3133, ν(C=N) 1613, ν(C=S) 1240. ^{1}H NMR (500 Mhz, DMSO-d_6, ppm): 11.70 (s, 2H, -OH), 11.62 (s, 1H, -NH), 10.62 (s, 1H, -NH), 8.67 (s, 2H, -CH=N-), 7.35-6.89 (m, 8H, aromatic H). UV-Vis [λ_{max} (log ε), nm (dm^3 cm^{-1} mol^{-1})]: 251 (3.90) π→π*, 302 (4.19) π→π*, 351 (4.53) n→π*, 367 (4.43) n→π*.

Synthesis of 1,5-bis(salicylidene)thiocarbohydrazone-triphenylphosphine-nickel(II) [Ni(L)(PPh_3)]

A solution of [$NiCl_2(PPh_3)_2$] (0.654 g, 1 mmol) in ethanol (10 mL) was added to a stirring solution of L (0.314 g, 1 mmol) in ethanol (10 mL) and dichloromethane (5 mL). 2 drops of triethylamine were added to the mixture and the mixture was stirred under reflux for 5 h to give a red solution. Red colored product was obtained by slow evaporation. The product was filtered and washed with ethanol and dried under vacuum (Figure 1).

Color: Dark red. Yield: 54%. M.p.: 242-244 °C. Calc. for $C_{33}H_{27}N_4NiO_2PS$ (633.32 g mol^{-1}): C: 62.58, H: 4.30, N: 8.85, S: 5.06%; found: C: 62.33, H: 4.12, N: 8.64, S: 4.91%. IR (cm^{-1}): ν(OH) 3185, ν(NH) 3116, ν(C=N) 1617 and 1598, ν(PPh_3) 1433, 1096, 737, 690. ^{1}H NMR (500 Mhz, DMSO-d_6, ppm): 11.53 (s, 1H, -OH), 10.71 (s, 1H, -NH), 8.50 (s, 1H, -CH=N-), 8.09 (s, 1H, -CH=N-), 7.76-5.75 (m, 23H, aromatic H). UV-Vis [λ_{max} (log ε), nm (dm^3 cm^{-1} mol^{-1})]: 257 (4.47) π→π*, 287 (4.34) π→π*, 339 (4.29) n→π*, 387 (4.36) n→π* and 435 (4.22) LMCT.

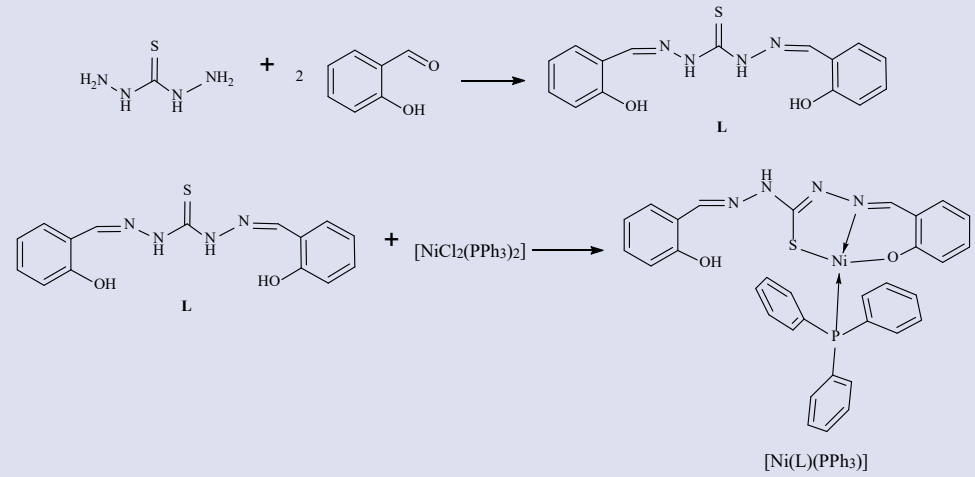

Figure 1. The general synthesis of L and Ni(II) complex.

Determination of Antioxidant Activity by DPPH and CUPRAC Assays

The DPPH radical scavenging activities of L and Ni(II) complex were determined by the method of Brand-Williams et al. with minor changes [25]. 2 mL of 10^{-4} M DPPH in ethanol, 1 mL of 10^{-4} M of the sample in ethanol (containing 1% DMSO) and (1-x) mL of ethanol were added to a glass test tube. The mixture was incubated for 30 min at 25 °C. Then, the absorbance values of the solutions in test tubes were measured against ethanol at 515 nm. The control solution consisted of a mixture of DPPH solution (2 mL) and ethanol (2 mL). Trolox was used as the reference compound. The radical scavenging activity was computed from this equation: % DPPH radical scavenging activity = [$A_{control}$ – A_{sample} / $A_{control}$] x 100, where $A_{control}$ is the absorbance of the control solution and A_{sample} is the absorbance of the sample-radical mixture solution.

Antioxidant capacities of L and Ni(II) complex were determined by CUPRAC method [26]. 1 mL of 10^{-2} M $CuCl_2.2H_2O$ in water, 1 mL of 7.5 x 10^{-3} M neocuproine in ethanol, 1 mL of 1 M NH_4Ac in water, x mL of 10^{-4} M sample in ethanol (containing 1% DMSO) and (1.1 - x) mL of water were added to a glass test tube. The mixture was incubated for 30 min at 25 °C. Then, the absorbance values of the solutions in test tubes were recorded at 450

nm. The results were given as TEAC (trolox equivalent antioxidant capacity) coefficient. TEAC values were calculated by dividing the molar absorptivity (Ɛ) of the compounds by that of Trolox ($Ɛ_{trolox}$ = 1.67 x 10^4 L mol^{-1} cm^{-1}).

Results and Discussion

Synthesis and Spectral Features

1,5-bis(salicylidene)thiocarbohydrazone (L) was obtained by the reaction of thiocarbohydrazide with salicylaldehyde in a mole ratio of 1:2. The reaction of L (1 mmol) with [$NiCl_2(PPh_3)_2$] (1 mmol) resulted in the formation of the Ni(II) complex {[Ni(L)(PPh_3)]}. [Ni(L)(PPh_3)] is soluble in DMF, DCM and DMSO solvents. The μ_{eff} measurement showed that the complex is diamagnetic. The elemental analysis and spectroscopic data agree with the proposed molecular formula of L and Ni(II) complex.

The characteristic bands of OH and NH groups were seen at 3195 and 3133 cm^{-1} in the IR spectrum of L. These bands, whose intensity decreased after complex formation, were observed at 3185 and 3116 cm^{-1} in the spectrum of [Ni(L)(PPh_3)]. The appearance of these bands in the spectrum of the complex supports that one of the OH and NH groups of L did not participate in the formation of the complex. The fact that the band seen in the spectrum of L and attributed to ν(C=S) did not appear in the spectrum of [Ni(L)(PPh_3)] can be explained as one NH group and the C=S group form C-SH by tautomerism. The shift of one of the bands of the azomethine groups in the spectrum of L to a lower wave number (1598 cm^{-1}) in the spectrum of [Ni(L)(PPh_3)] indicates the coordination of one of the azomethine nitrogen atoms with the metal atom. In the spectrum of [Ni(L)(PPh_3)], characteristic peaks of triphenylphosphine were also observed at 1433, 1096, 737, 690 cm^{-1}, respectively [24, 27, 28]. IR spectrum of [Ni(L)(PPh_3)] is given in Figure S1.

In the ^{1}H NMR spectrum of L, one of the peaks corresponding to two $OH_{phenolic}$ protons at 11.70 ppm was observed at 11.53 ppm, corresponding to a single OH phenolic proton in the NMR spectrum of [Ni(L)(PPh_3)]. This indicates that one of the OH groups of L is bonded to the nickel(II) ion by deprotonation. The spectrum of L exhibited two NH signals at 11.62 and 10.62 ppm. In the spectrum of [Ni(L)(PPh_3)], only one NH signal was found at 10.71 ppm. The disappearance of one of the H atoms of the two NH groups indicates the deprotonation of the H atom in the NH group through the sulfur atom by tautomerism. One of the signals belonging to the two azomethine protons at 8.67 ppm in the spectrum of L shifted to 8.09 ppm after the formation of the complex. This indicates the coordination of one of the azomethine groups of L to the nickel(II) ion [24, 29, 30]. ^{1}H NMR spectrum of [Ni(L)(PPh_3)] is given in Figure S2.

The UV-Vis spectrum of L exhibited two absorptions at 251 and 302 nm corresponding to π→π* transitions of aromatic rings. These bands were seen at 257 and 287 nm in the spectrum of [Ni(L)(PPh_3)]. Other bands at 351 and 367 nm in the spectrum of L are assigned to n→π* transitions of the C=N and C=S groups. These bands appear at 339 and 387 nm in the spectrum of [Ni(L)(PPh_3)]. This can be interpreted that the metal atom is coordinated to the ligand via the azomethine nitrogen and sulfur atoms. In addition, the band attributed to the charge transfer transition (LMCT) was observed at 435 nm in the spectrum of [Ni(L)(PPh_3)] [27, 31, 32]. UV-Vis spectrum of [Ni(L)(PPh_3)] is given in Figure S3.

Crystal Structure Interpretation

Crystallographic analysis results showed that [Ni(L)(PPh_3)] crystallizes in the I2/c space group and as a monoclinic crystal system. The molecular structure of [Ni(L)(PPh_3)] is shown in Figure 2. The asymmetric unit of the complex contains two crystallographically independent [Ni(L)(PPh_3)] molecules with almost similar parameters. In the complex, bisthiocarbohydrazone (L) is coordinated to nickel(II) ion by using its phenolic O, azomethine N and thiolate S atoms and acted as a dibasic tridentate donor by forming six and five-membered rings with O2-Ni1-N4, O4-Ni2-N8 and N4-Ni1-S1, N8-Ni2-S2 angles of 95.3(2)°, 94.8(2)° and 87.59(17)°, 87.81(17)°. These angles are similar to those observed in related Ni(II) complexes [30, 33, 34]. Fourth coordination site is completed by the phosphorus atom of PPh_3 molecule and the variation in the bonding parameters indicates that there is a distorted square planar geometry around the nickel(II) ion. Ni1-S1 [2.139(3) Å], Ni2-S2 [2.135(3) Å], Ni1-O2 [1.843(4) Å], Ni2-O4 [1.844(4) Å], Ni1-N4 [1.892(5) Å], Ni2-N8 [1.888(5) Å], Ni1-P1 [2.210(2) Å] and Ni2-P2 [2.228(2) Å] bond distances are within normal ranges and are in good agreement with those found in four-coordinate Ni(II) complexes containing triphenylphosphine [15, 35, 36]. C-S bond distances are 1.737(6) Å and 1.748(6) Å, indicating that free bisthiocarbohydrazone (L) is bound to metal in the thiolate form [37]. Finally, the crystal structure of [Ni(L)(PPh_3)] is stabilized by weak and moderately bound intramolecular and intermolecular hydrogen bonds (Table 3).

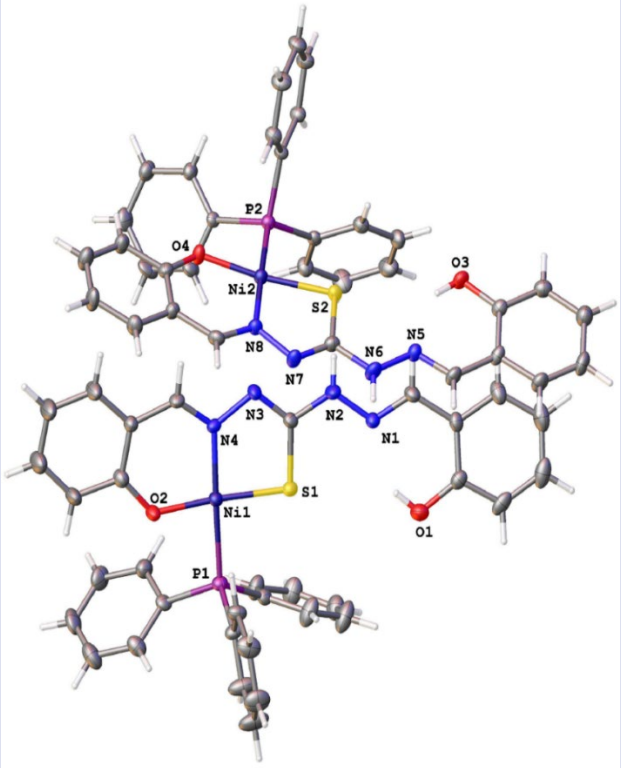

Figure 2. The molecular structure of [Ni(L)(PPh_3)] with hetero atom numbering scheme.

Table 1. Crystal data and structure refinement parameters for [Ni(L)(PPh_3)].

CCDC	2196021
Empirical formula	$C_{33}H_{27}N_4NiO_2PS$
Formula weight	633.31
Temperature (K)	298
Crystal system	Monoclinic
Space group	I2/c
a (Å)	27.95(3)
b (Å)	7.852(10)
c (Å)	57.84(7)
α (°)	90
β (°)	102.08(5)
γ (°)	90
Volume ($Å^3$)	12413(26)
Z	16
Crystal size (mm^3)	0.707 × 0.14 × 0.062
Wavelength (Å)	0.71073
D_{calc} ($g.cm^{-3}$)	1.356
μ (mm^{-1})	0.780
F(000)	5248.0
θ range for data collection (°)	2.88 to 49.998
Index ranges	-32≤h≤32, -9≤k≤9, -68≤l≤68
Reflections collected	36995
Independent reflections	10908
Data/restraints/parameters	10908/0/759
Goodness-of-fit on F^2 (S)	0.909
Final R indexes [I ≥ 2σ(I)]	R_1 = 0.0693, wR_2 = 0.1255
Final R indexes [all data]	R_1 = 0.1862, wR_2 = 0.1539
Largest diff. peak/hole ($e.Å^{-3}$)	0.51/-0.53

Table 2. The selected bond lengths (Å) and angles (°) of [Ni(L)(PPh_3)].

Bond lengths (Å)		Bond angles (°)	
Ni1—S1	2.139(3)	S1—Ni1—O2	175.14(14)
Ni2—S2	2.135(3)	S2—Ni2—O4	173.26(13)
Ni1—O2	1.843(4)	N4—Ni1—P1	177.48(16)
Ni2—O4	1.844(4)	N8—Ni2—P2	176.25(15)
Ni1—N4	1.892(5)	O2—Ni1—P1	86.50(15)
Ni2—N8	1.888(5)	O4—Ni2—P2	86.72(14)
Ni1—P1	2.210(2)	O2—Ni1—N4	95.3(2)
Ni2—P2	2.228(2)	O4—Ni2—N8	94.8(2)
N4—N3	1.415(6)	S1—Ni1—P1	90.69(9)
N8—N7	1.410(6)	S2—Ni2—P2	91.03(10)
N2—N1	1.351(6)	S1—Ni1—N4	87.59(17)
N6—N5	1.380(6)	S2—Ni2—N8	87.81(17)
C8—S1	1.737(6)		
C41-S2	1.748(6)		

Table 3. Geometric values for hydrogen bonds for [Ni(L)(PPh_3)].

D-H···A	D-H [Å]	H···A [Å]	D···A [Å]	D-H···A [°]
O1-H1···N1	0.820(4)	1.918(5)	2.634(7)	145.3(4)
O3-H3A···N5	0.820(4)	1.924(5)	2.636(7)	144.6(3)
N2-H2···S2	0.860(6)	2.700(3)	3.335(6)	131.8(4)
N6-H6A···S1^{i}	0.860(6)	2.784(3)	3.446(7)	135.0(4)
O3-H3A···S2	0.820(4)	2.911(3)	3.616(5)	145.5(3)
C35-H35···O3^{ii}	0.931(7)	2.608(5)	3.507(9)	162.4(4)
C53-H53···S2^{iii}	0.930(8)	3.002(3)	3.820(9)	147.7(5)
O1-H1···S1	0.820(4)	3.015(3)	3.723(6)	146.0(4)

Symmetry codes: (i) +x, -1+y, +z; (ii) 1-x, +y, ½-z; (iii) +x, 1+y, +z.

Antioxidant Properties

The total antioxidant capacity of L and Ni(II) complex was determined using the CUPRAC method. When the TEAC values (Table 4) are examined, it is seen that the total antioxidant capacity of both L and Ni(II) complex is better than Trolox ($TEAC_{trolox}$ = 1). Also, L (TEAC = 3.54 ± 0.719) exhibits higher activity than [Ni(L)(PPh_3)] (TEAC = 2.58 ± 0.107). The free radical scavenging activity (Table 5) of [Ni(L)(PPh_3)] is also lower than that of L, which is parallel with the antioxidant capacity results. The position and number of OH groups and the contribution of NH groups are factors that affect the antioxidant activity of thiocarbohydrazone [38, 39]. Therefore, we can say that the decrease in the number of OH and NH groups in L by complexation is the reason why the antioxidant activity of [Ni(L)(PPh_3)] is lower than that of L.

Table 4. The TEAC values of the compounds.

Compounds	TEAC	Correlation coeff. (r)
L	3.54 ± 0.719	0.9939
[Ni(L)(PPh_3)]	2.58 ± 0.107	0.9997

$TEAC_{Trolox}$ = 1.00.

Table 5. % free radical scavenging activities of the compounds.

Compounds	Free Radical Scavenging Activity (%)
L	77.84 ± 0.19
[Ni(L)(PPh_3)]	63.65 ± 3.28
Trolox	82.33 ± 2.95

Conclusion

A new Ni(II) complex was synthesized from 1,5-bis(salicylidene)thiocarbohydrazone (L) and [$NiCl_2(PPh_3)_2$] and its structure was characterized by various spectroscopic methods and elemental analysis. The distorted square planar geometry around the nickel center with surrounding ONSP atoms was confirmed by single crystal crystallographic results. The X-ray diffraction analysis showed that L binds with nickel(II) ion in a tridentate mode through N atom of the azomethine, O atom of the hydroxyl group and S atom in [Ni(L)(PPh_3)]. The fourth coordination was completed with a phosphorus atom of triphenylphosphine co-ligand. The examination of the antioxidant activities of L and its Ni(II) complex by various antioxidant assays (CUPRAC and DPPH methods) disclosed that L exhibited higher antioxidant capacity and free radical scavenging abilities compared to the Ni(II) complex. The antioxidant potential of phenolic compounds depends on the number and arrangement of the hydroxyl groups in the molecules of interest. Also, the presence of NH and SH groups contributes to antioxidant properties. So, we can say that the excess of OH and NH groups in L is the reason why L has higher antioxidant activity compared to Ni(II) complex. In conclusion, L and Ni(II) complex with

good antioxidant activity can be used for therapeutic purposes to eliminate radical oxygen species formed as a result of some metabolic diseases.

Acknowledgments

I dedicate this paper to Prof. Dr. Ayşe ERÇAĞ, the mentor of my research career.

Conflicts of Interest

There are no conflicts of interest in this work.

References

[1] Reddy B.N., Avaji P.G., Badami P.S., Patil S.A., Synthesis, spectral and biological studies of cobalt(II), nickel(II) and copper(II) complexes with 1,5-bis (thiophenylidene) thiocarbohydrazone, *J. Saudi Chem. Soc.*, 11 (2) (2007) 253-268.

[2] Sathisha M.P., Shetti U.N., Revankar V.K., Pai K.S.R., Synthesis and antitumor studies on novel Co(II), Ni(II) and Cu(II) metal complexes of bis(3-acetylcoumarin) thiocarbohydrazone, *Eur. J. Med. Chem.*, 43 (11) (2008) 2338-2346.

[3] Chee D.N.A., Affan M.A., Ahmad F.B., Asaruddin M.R., Sam N., Salam M.A., Ismail A., Tan S.H., Synthesis, characterization, and antibacterial activity of organotin(IV) complexes with 2-hydroxyacetophenone thiocarbohydrazone, *J. Coord. Chem.*, 64 (23) (2011) 4191-4200.

[4] Metwally M.A., Khalifa M.E., Koketsu M., Thiocarbohydrazides: Synthesis and reactions, *Am. J. Chem.*, 2 (2) (2012) 38-51.

[5] Kaya Y., Erçağ A., Koca A., Synthesis, structures, electrochemical studies and antioxidant activities of *cis*-dioxomolybdenum(VI) complexes of the new bisthiocarbohydrazones, *J. Mol. Struct.*, 1102 (2015) 117-126.

[6] Mrđan G.S., Vastag G.G., Škorić D.Đ., Radanović M.M., Verbić T.Ž., Milčić M.K., Stojiljković I.N., Marković O.S., Matijević B.M., Synthesis, physicochemical characterization, and TD–DFT calculations of monothiocarbohydrazone derivatives, *Struct. Chem.*, 32 (2021) 1231-1245.

[7] Kadam S.S., Gotarne R.P., Shinde M.N., Mane V.S., Khan A.A., Kumbhar A.A., Fe(III), Co(II), Ni(II), Cu(II) and Zn(II) complexes of fluorophore-anchored asymmetric thiocarbohydrazone: Synthesis, characterization and biological studies, *Inorg. Chim. Acta*, 536 (2022) 120887.

[8] Kaya Y., Erçağ A., Zorlu Y., Demir Y., Gülçin İ., New Pd(II) complexes of the bisthiocarbohydrazones derived from isatin and disubstituted salicylaldehydes: Synthesis, characterization, crystal structures and inhibitory properties against some metabolic enzymes, *J. Biol. Inorg. Chem.*, 27 (2) (2022) 271-281.

[9] Çavuş M.S., Yakan H., Özorak C., Muğlu H., Bakır T.K., New *N*,*N*′-bis (thioamido) thiocarbohydrazones and carbohydrazones: synthesis, structure characterization, antioxidant activity, corrosion inhibitors and DFT studies, *Res. Chem. Intermed.*, 48 (4) (2022) 1593-1613.

[10] Manoj E., Kurup M.R.P., Suresh E., Synthesis and spectral studies of bisthiocarbohydrazone and biscarbohydrazone of quinoline-2-carbaldehyde: crystal structure of bis (quinoline-2-aldehyde) thiocarbohydrazone, *J. Chem. Crystallogr.*, 38 (2008) 157-161.

[11] Kaya Y., Investigation of spectroscopic, crystallographic, thermal and antioxidant properties of mononuclear dioxomolybdenum(VI) complexes derived from a new symmetric bisthiocarbohydrazone, *Polyhedron*, 227 (2022) 116151.

[12] Paison F., Su B., Pan D., Yan T., Wu J., The study of biological activities of various mixed ligand complexes of Nickel(II), *Austin Biochem.*, 5 (1) (2020) 1-12.

[13] Ma Y.-N., Li S.-X., Yang S.-D., New approaches for biaryl-based phosphine ligand synthesis via P=O directed C–H functionalizations, *Acc. Chem. Res.*, 50 (6) (2017) 1480-1492.

[14] Güveli Ş., Agopcan Çınar S., Karahan Ö., Aviyente V., Ülküseven B., Nickel(II)–PPh_3 complexes of *S,N*-substituted thiosemicarbazones–structure, DFT study, and catalytic efficiency, *Eur. J. Inorg. Chem.*, 2016 (4) (2016) 538-544.

[15] Kaya Y., Erçağ A., Koca A., New square-planar nickel(II)-triphenylphosphine complexes containing ONS donor ligands: Synthesis, characterization, electrochemical and antioxidant properties, *J. Mol. Struct.*, 1206 (2020) 127653.

[16] Shabbir M., Akhter Z., Ashraf A.R., Ismail H., Habib A., Mirza B., Nickel(II) and palladium(II) triphenylphosphine complexes incorporating tridentate Schiff base ligands: Synthesis, characterization and biocidal activities, *J. Mol. Struct.*, 1149 (2017) 720-726.

[17] Birben E., Sahiner U.M., Sackesen C., Erzurum S., Kalayci O., Oxidative stress and antioxidant defense, *World Allergy Organ. J.*, 5 (2012) 9-19.

[18] Bentz E.N., Pomilio A.B., Lobayan R.M., Donor-acceptor interactions as descriptors of the free radical scavenging ability of flavans and catechin, *Comput. Theor. Chem.*, 1110 (2017) 14-24.

[19] Burns G.R., Metal complexes of thiocarbohydrazide, *Inorg. Chem.*, 7 (2) (1968) 277-283.

[20] Sheldrick G.M., SHELXT–Integrated space-group and crystal-structure determination, *Acta Crystallogr. Sect. A: Found. Adv.*, 71 (1) (2015) 3-8.

[21] Sheldrick G.M., Crystal structure refinement with SHELXL, *Acta Crystallogr. Sect. C: Struct. Chem.*, 71 (1) (2015) 3-8.

[22] APEX2, version 2014.11-0, Bruker (2014), Bruker AXS Inc., Madison, WI.

[23] SAINT, version 8.34 A, Bruker (2013), Bruker AXS Inc., Madison, WI.

[24] Kaya İ., Temizkan K., Kaya Y., Erçağ A., The monomers and polymers of azomethine-based thiocarbohydrazones: Fluorescent activities, fluorescence quantum yields of polymers in water and DMF solutions, *Mater. Sci. Eng., B*, 282 (2022) 115782.

[25] Brand-Williams W., Cuvelier M.-E., Berset C., Use of a free radical method to evaluate antioxidant activity, *LWT-Food Sci. Technol.*, 28 (1) (1995) 25-30.

[26] Apak R., Güçlü K., Özyürek M., Karademir S.E., Novel total antioxidant capacity index for dietary polyphenols and vitamins C and E, using their cupric ion reducing capability in the presence of neocuproine: CUPRAC method, *J. Agric. Food Chem.*, 52 (26) (2004) 7970-7981.

[27] Kaya Y., Erçağ A., Uğuz Ö., Koca A., Zorlu Y., Hacıoğlu M., Birteksöz Tan A.S., New asymmetric bisthiocarbohydrazones and their mixed ligand nickel(II) complexes: Synthesis, characterization, crystal structure, electrochemical-spectroelectrochemical property,

antimicrobial and antioxidant activity, *Polyhedron*, 207 (2021) 115372.

[28] Rana A., Dinda R., Sengupta P., Ghosh S., Falvello L.R., Synthesis, characterisation and crystal structure of *cis*-dioxomolybdenum(VI) complexes of some potentially pentadentate but functionally tridentate (ONS) donor ligands, *Polyhedron*, 21 (9-10) (2002) 1023-1030.

[29] Deng Y., Yang Y., Zhang Y., Yan Q., Liu J., Formation of an asymmetrical ligand (H_3L_{cyclic}) *via* a metal-induced cyclization of symmetrical thiocarbohydrazone (H_4L) in synthesizing an oxovanadium(IV) complex $VO(HL_{cyclic})(EtOH)_2$, *J. Coord. Chem.*, 65 (8) (2012) 1409-1416.

[30] Priyarega S., Kalaivani P., Prabhakaran R., Hashimoto T., Endo A., Natarajan K., Nickel(II) complexes containing thiosemicarbazone and triphenylphosphine: Synthesis, spectroscopy, crystallography and catalytic activity, *J. Mol. Struct.*, 1002 (1-3) (2011) 58-62.

[31] Kundu S., Pramanik A.K., Mondal A.S., Mondal T.K., Ni(II) and Pd(II) complexes with new N,O donor thiophene appended Schiff base ligand: Synthesis, electrochemistry, X-ray structure and DFT calculation, *J. Mol. Struct.*, 1116 (2016) 1-8.

[32] Tamizh M.M., Mereiter K., Kirchner K., Bhat B.R., Karvembu R., Synthesis, crystal structures and spectral studies of square planar nickel(II) complexes containing an ONS donor Schiff base and triphenylphosphine, *Polyhedron*, 28 (11) (2009) 2157-2164.

[33] Prabhakaran R., Kalaivani P., Huang R., Poornima P., Vijaya Padma V., Dallemer F., Natarajan K., DNA binding, antioxidant, cytotoxicity (MTT, lactate dehydrogenase, NO), and cellular uptake studies of structurally different nickel(II) thiosemicarbazone complexes: Synthesis, spectroscopy, electrochemistry, and X-ray crystallography, *J. Biol. Inorg. Chem.*, 18 (2013) 233-247.

[34] Kumar S.M., Dhahagani K., Rajesh J., Nehru K., Annaraj J., Chakkaravarthi G., Rajagopal G., Synthesis, characterization, structural analysis and DNA binding studies of nickel(II)–triphenylphosphine complex of ONS donor ligand–Multisubstituted thiosemicarbazone as highly selective sensor for fluoride ion, *Polyhedron*, 59 (2013) 58-68.

[35] Güveli Ş., Koca A., Özdemir N., Bal-Demirci T., Ülküseven B., Electrochemistry and structural properties of new mixed ligand nickel(II) complexes based on thiosemicarbazone, *New J. Chem.*, 38 (11) (2014) 5582-5589.

[36] Elsayed S.A., Badr H.E., di Biase A., El-Hendawy A.M., Synthesis, characterization of ruthenium(II), nickel(II), palladium(II), and platinum(II) triphenylphosphine-based complexes bearing an ONS-donor chelating agent: Interaction with biomolecules, antioxidant, in vitro cytotoxic, apoptotic activity and cell cycle analysis, *J. Inorg. Biochem.*, 223 (2021) 111549.

[37] Kılıç-Cıkla I., Güveli Ş., Bal-Demirci T., Aygün M., Ülküseven B., Yavuz M., X-ray diffraction, spectroscopic and DFT studies on nickel(II)-triphenylphosphine complexes of 2-hydroxyacetophenone thiosemicarbazones, *Polyhedron*, 130 (2017) 1-12.

[38] Apak R., Güçlü K., Özyürek M., Çelik S.E., Mechanism of antioxidant capacity assays and the CUPRAC (cupric ion reducing antioxidant capacity) assay, *Microchim. Acta*, 160 (4) (2008) 413-419.

[39] Asha T.M., Prathapachandra Kurup M.R., An insight into the potent antioxidant activity of a dithiocarbohydrazone appended cis-dioxidomolybdenum(VI) complexes, *Appl. Organomet. Chem.*, 34 (9) (2020) e5762.

Cumhuriyet Sci. J., 44(3) (2023) 456-464
DOI: https://doi.org/10.17776/csj.1303270

Cumhuriyet Science Journal

| csj.cumhuriyet.edu.tr | Founded: 2002 ISSN: 2587-2680 e-ISSN: 2587-246X Publisher: Sivas Cumhuriyet University

Determination of Progesterone in Pharmaceutical Preparations by UV, First-order Derivative Spectrophotometry and Gas Chromatography

Bilal Yılmaz[1,a], Mevlut Albayrak[2,b], Yucel Kadioglu[1,c,*]

[1] *Department of Analytical Chemistry, Faculty of Pharmacy, Ataturk University, Erzurum,Türkiye*
[2] *Department of Medical Laboratory Techniques, Health Services Vocational Training School, Ataturk University, Erzurum, Türkiye*
**Corresponding author*

Research Article

History
Received: 26/05/2023
Accepted: 13/09/2023

ABSTRACT

The determination of progesterone in pure and capsule form was accomplished in this work using new, simple and quick procedures by UV spectrophotometry, first-order derivative spectrophotometry and gas chromatography. To increase the sensitivity of the suggested methods, it was necessary to optimize the solvent system, the detection wavelength, and the chromatographic conditions. The linear regression equations for the UV spectrophotometry, first-order derivative spectrophotometry and gas chromatography were y=0.0536x+0.0002, y=0.1362x+0.0014, and y=1.8217x-1.239, respectively, as determined by the least square regression approach. Under the chosen experimental conditions, no interference was found. The suggested methods are extremely accurate and precise. When the suggested methods' findings were compared to those of two published reference methods, there was statistically no discernible difference. Therefore, the methods are applicable to the measurement of progesterone in pharmaceutical formulations.

Keywords: Progesterone, Spectrophotometry, Gas chromatography, Validation.

[a] *yilmazb@atauni.edu.tr* *https://orcid.org/0000-0002-8574-7570*
[b] *mevlutalbayrak@atauni.edu.tr* *https://orcid.org/0000-0001-8673-6577*
[c] *yucel@atauni.edu.tr* *https://orcid.org/0000-0001-6590-7306*

Introduction

Steroid hormones, which are produced naturally in the gonads, placenta, and adrenal glands from cholesterol, are crucial for the regulation of many bodily processes. Low levels of them are found in the body, and alterations in them have been linked to conditions like diabetes, cancer, and even diabetes [1]. According to World Anti-Doping Agency standards [2-4], steroids are a crucial component of an athlete's biological passport. Therefore, it is thought that determining steroids accurately is a crucial task in order to avoid inaccurate results and investigate the mechanisms of diseases linked to steroid hormones.

Progesterone (Fig. 1) is a steroid hormone that is produced from cholesterol [5]. Progestagens or gestagens are the collective names for progesterone and other progestational substances. Progestagens are medically prescribed for use as male and female contraceptives, indicating a risk to fertility when exposure is unintended or used for other purposes. Progesterone is produced during the synthesis of steroid hormones in both males and females, as well as serving as an early intermediate. Exogenous progesterone exposure results from medicinal usage (contraception, prevention of premature labor, menstrual problems), use of cosmetics and supplements, and exposure through environmental media. Progesterone is most frequently used therapeutically for dysfunctional uterine bleeding or amenorrhea, for contraception (either alone or in combination with other hormones, such as estradiol or mestranol in oral contraceptives), and for hormone replacement therapy in post-menopausal women [6,7].

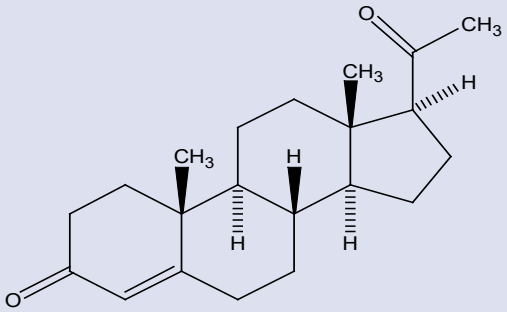

Figure 1. Structure of progesterone

Progesterone is widely used in hormone therapy, hence a quick and accurate way to identify and measure it in pharmaceutical formulations is needed. GC-MS [8-12] and HPLC [13-17] methods have all been described for progesterone in the literature. The analysis of progesterone in pharmaceutical formulations using UV spectrophotometry [18, 19] and derivative spectrophotometry [20] methods has been covered in a number of studies in the literature.

The first-order derivative spectrophotometry (^{1}D) method has not yet been covered in any articles in the literature. Spectrophotometric techniques are known for being quick, easy to use, and accessible, making them excellent for use in regular preparation analysis.

The use of flame ionization detection (FID) for progesterone determination together with simple, affordable, and reasonable analysis time were attempted to be demonstrated using the GC method.

Therefore, the goal of this study was to ascertain whether sample pre-treatment was required for the UV, 1D spectrophotometry and GC-FID methods to detect progesterone in pharmaceutical preparations. According to the International Conference on Harmonization's criteria, the developed methods were validated [21]. Statistics were used to compare the outcomes of developed and validated methods with two reference methods [18,19].

Materials and Methods

Chemicals

A progesterone reference standard with a purity of 99.9% was generously given by Riedel De Haen. Methanol of the analytical grade was bought from Merck (Germany). Local Turkish suppliers provided the Progestan® soft capsule (Kocak Pharm. Ind., Turkey). It was said that each Progestan® soft capsule contained 100 mg of progesterone and titanium dioxide as an excipient.

Equipments

It was carried out using a Thermospectronic double-beam UV-Visible spectrophotometer (HEλIOSβ). Standard and sample solutions' UV and ^{1}D spectra (N=6. Δλ=4.0 nm) between wavelength ranges of 200-300 nm.

An Agilent 6890 N Network GC with a flame ionization detector, an Agilent 7683 series autosampler, an Agilent chemstation, and an HP-5 column with a 0.25 µm film thickness (30 m x 0.320 mm I.D.) was used to execute the GC-FID system. Temperatures for the injection and detector are 250 and 300 °C, respectively. A split injection of 2 µL was performed. Throughout the experiment, the flow rate of the carrier gas (N_2) was held constant at 2 mL/min.

Preparation of Standard Solutions

For UV and ^{1}D methods, a stock solution (100 µg/mL) of progesterone was made by dissolving 10 mg of it in 100 mL of methanol. Daily working solutions (WS) containing 2, 4, 6, 8, 10 and 12 µg/mL of progesterone were prepared by methanol dilution of the stock solution. The WS was prepared each day through analysis. To conduct the study, solutions were moved to quartz cells. Before use, the stock solution was warmed to room temperature from its -20 °C storage location in a glass flask. Aliquots of progesterone standard solution were added to QC samples to develope final concentrations of 3, 7 and 11 µg/mL.

For GC-FID method, progesterone stock standard solution was made in methanol at a concentration of 100 µg/mL and kept at -20 °C for storage. Working standard solutions were developed from the stock solutions. For progesterone (n=6), a calibration graph was drawn in the range of 0.25, 0.5, 0.75, 1.25, 2.5, 5, 7.5, 10, 15, 20 and 30 µg/mL. The stock solution was diluted with methanol for QC samples containing progesterone at concentrations of 1, 12.5 and 25 µg/mL.

Data Analysis

The Statistical Product and Service Solutions (SPSS) for Windows, version 15.0, was used for all statistical computations. Calculated P values of 0.05 or less were used to determine whether a correlation was statistically significant.

Results and Discussion

Development and Optimization of the Method

Optimization of spectrophotometric conditions

The experimental parameters, such as the solvent, the level of derivation, the wavelength range, and smoothing, were improved in order to construct sensitive UV and ^{1}D spectrophotometric methods. UV and ^{1}D spectrophotometry were used to evaluate the 200-300 nm wavelength region, and this produced the best findings. Different solvent systems, including methanol, ethanol, water and acetonitrile were tested in this assay either singly or in varied ratios.

The final choice was made because of methanol's sensitivity, interference, simplicity of fabrication, suitability for pharmaceuticals, content estimate, and cost, in that order. Due of its lack of toxicity, methanol was used in this study. In methanol at a concentration of 2-12 µg/mL, progesterone's UV and ^{1}D spectra are shown in Figs. 2 and 3, respectively. Any spectrum may be used to identify this substance. The greatest peak of progesterone's UV spectra was found to be at 240 nm. The ^{1}D spectra of progesterone showed a high peak at 231 nm and a low peak at 252 nm (Fig. 3).

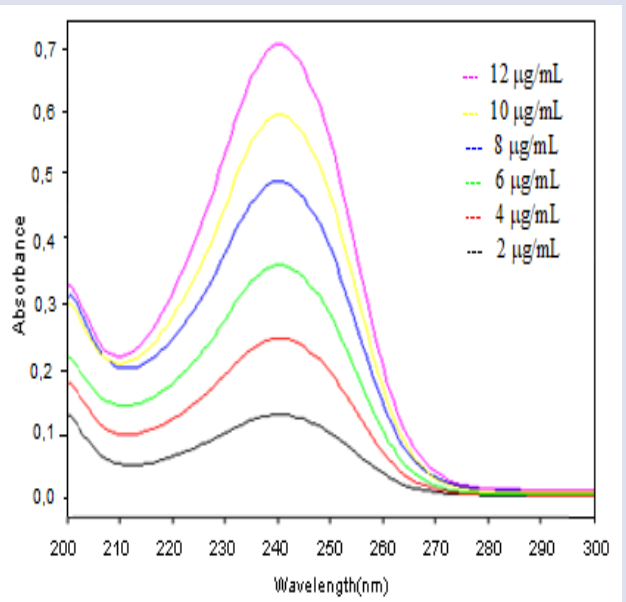

Figure 2. Spectra obtained from UV method

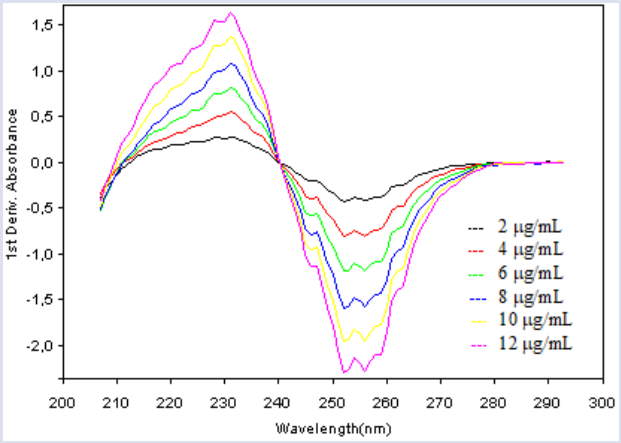

Figure 3. Spectra obtained from ^{1}D method

Optimization of chromatographic conditions

Based on the chemical characteristics of progesterone, a method for measuring it was developed. Methanol was utilized as the diluent since progesterone is a polar molecule and methanol is a polar solvent. For the separation of this analyte, HP-5 capillary column used in the study.

The boiling point served as the foundation for the GC-FID parameters employed in the method development. The temperature of the detector and injection port were set at 250 and 300 °C, respectively. For the GC oven, various temperature regimens were examined. The optimal temperature program was chosen for a decent resolution at the conclusion of this experiment. The GC oven's temperature programs, which had a 12-minute run length, were as follows: beginning temperature 150 °C, hold for 1.5 min; medium temperature 260 °C, hold for 5 min; ramp rate 50 °C/min; final temperature 270 °C, hold for 3.3 min; ramp rate 10 °C/min.

A 44 mL per minute hydrogen flow was ensured by setting the head pressure. Split mode (20:1) was selected. Progesterone had a retention duration of almost 9.7 min and a well-defined peak. No additional method optimization was necessary. Fig. 4 displays a typical chromatogram produced using standard progesterone.

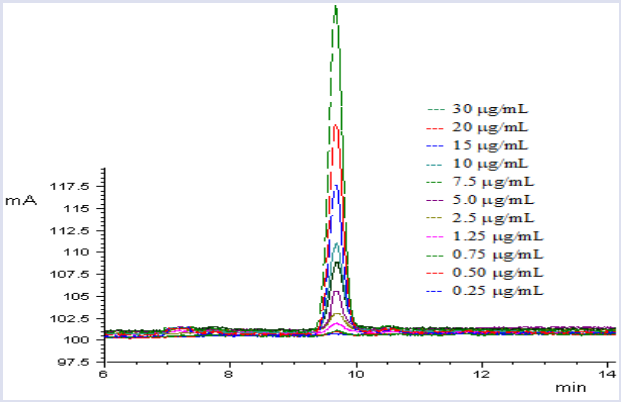

Figure 4. GC-FID chromatograms of progesterone

Validation of the Method

ICH Q2B guidelines were followed while determining the validation parameters [21]. These criteria include specificity, linearity, precision, accuracy, recovery, limit of detection (LOD), limit of quantification (LOQ), ruggedness and stability.

Specificity

In this study, it was investigated the potential interferences of common excipients and additives. The control samples were prepared and examined. At the concentrations present in dosage forms, there is no evidence of any interference from these chemicals. The excipient employed in this formulation was one that the pharmaceutical industry employs most frequently. Arachite oil, lecithin, gelatin, glycerin, and titanium oxide are common tablet additives that may interfere with the method's specificity. These exceptions had no negative effects on the suggested methods. The procedure might be specific in accordance with the findings of the analysis.

Linearity

The working solutions were scanned at 200-300 nm against a similarly prepared blank in the UV and ^{1}D spectrophotometry methods. Calibration curves were drawn using the 240 nm wavelength for UV and the 231 and 252 nm wavelengths for the ^{1}D method. Six analyses were performed at each concentration level in a six-level calibration series. The absorbance values were plotted vs progesterone concentrations for UV and ^{1}D spectrophotometry method.

For all calibration curves, UV and ^{1}D methods demonstrated satisfactory linearity in the concentration range of 2-12 µg/mL. The least-square regression technique was used to obtain the regression equations (Table 1).

Progesterone concentrations between 0.25 and 30 µg/mL were tested for the GC-FID method to determine the linearity of peak area response vs concentration. The calibration curve's accuracy was evaluated using the correlation coefficient. The method's linearity was shown by the calibration equation which was derived from six repeat trials. All of the calibration curves' correlation coefficients were consistently higher than 0.99.

Table 1. Results of regression analysis of proposed methods

Methods	Range (µg/mL)	λ (nm)	LR[a]	R	LOD (µg/mL)	LOQ (µg/mL)
UV	2-12	240	y=0.0536x+0.0002	0.9998	0.15	0.50
^{1}D	2-12	231	y=0.1362x+0.0014	0.9998	0.15	0.50
	2-12	252	y=0.1880x+0.0597	0.9996	0.15	0.50
GC-FID	0.25-30	-	y=1.8217x -1.239	0.9997	0.08	0.25

λ: Wavelength, [a] Based on six calibration curves LR: Linear regressionequation, R: Coefficient of correlation

Precision and accuracy

Precision and accuracy both within and between days are used to describe repeatability. It was assessed using an examination of three different progesterone concentrations on three separate days. To assess the accuracy of these methods, six replicate determinations at three distinct concentrations (3, 7 and 11 µg/mL) were made using the UV method at 240 nm and the ^{1}D spectrophotometry method at 231 and 252 nm. All samples were made from scratch. The acceptable RSD% values for the UV and ^{1}D spectrophotometry methods were 2.98% and 3.76% (n=6), respectively, for the within-day precision, and 3.13% and 4.27% (n=6), respectively, for the between-day precision (intermediate precision) (Table 2). According to Table 2, the accuracy of UV and ^{1}D spectrophotometry procedures yielded acceptable relative error (RE%) levels of 2.71 and 2.67 (n=6), respectively.

The repeatability (within-day) and intermediate precision (between-day) of the GC-FID method were used to assess its level of precision. Three separate concentrations which served as QC samples were examined six times. The concentrations were 1.0, 12.5 and 25.0 µg/mL. Within-day precision's RSD value was 1.56%, and between-day precision's value was 1.81%. Within-day and between-day accuracy biases (relative error-RE%) were 2.00% and 3.00%, respectively. Table 2 provides a summary of these figures. The data gathered using the suggested methods showed that each method devised had a reasonable level of precision and accuracy.

Table 2. Precision and accuracy of proposed methods (n=6)

Method	λ (nm)	Added (µg/mL)	Within-day			Between-day		
			Found±SD (µg/mL)	Accuracy RE%	Precision RSD%	Found±SD (µg/mL)	Accuracy RE%	Precision RSD%
UV Method	$A_{240\ nm}$	3.0	2.95±0.06	-1.67	1.93	3.04±0.07	1.33	2.14
		7.0	7.14±0.21	2.00	2.98	7.19±0.23	2.71	3.13
		11.0	10.88±0.17	-1.09	1.57	10.84±0.23	-1.45	2.10
^{1}D Method	$^1D_{231\ nm}$	3.0	3.06±0.01	2.00	0.23	3.08±0.09	2.67	3.18
		7.0	7.10±0.14	1.43	1.93	7.13±0.21	1.86	2.93
		11.0	11.24±0.42	2.18	3.76	11.28±0.48	2.55	4.27
	$^1D_{252\ nm}$	3.0	3.06±0.05	2.00	1.57	3.07±0.09	2.33	2.77
		7.0	7.17±0.16	2.43	2.27	7.18±0.25	2.57	3.45
		11.0	11.20±0.22	1.82	1.97	11.23±0.34	2.09	3.04
GC-FID		1.0	1.02±0.01	2.00	1.28	1.03±0.02	3.00	1.65
		12.5	12.40±0.19	-0.80	1.56	12.30±0.22	-1.60	1.81
		25.0	24.90±0.22	-0.40	0.87	25.10±0.29	0.40	1.14

Recovery

The common addition methodology was used to verify the proposed spectrophotometry methods' accuracy. The 5.0 µg/mL concentration of capsule solution was mixed with the three different concentrations of pure sample solution (2.5, 7.5 and 12.5 µg/mL) before being analyzed. The following equation was used to compute the analytical recovery of the assay samples with the added standard.

Recovery % = $[(C_t-C_u) / C_a] \times 100$

Where C_t is the total amount of the analyte that was measured, C_u is the amount of the analyte in the formulation, and C_a is the amount of the pure analyte that was added to the formulation. Table 3 contains the findings of the commercial capsule analysis and the recovery investigation. The average percent recoveries were quantified as 100.3% for the UV method and 99.8% for the ^{1}D method, confirming the methodologies' high degree of accuracy. There was no evidence of any interference from common excipients.

Analytical recovery investigations were carried out by adding pre-analyzed samples of commercial dosage form to predetermined concentrations of pure medicines. The recovery was studied at three different concentration levels (4.0, 9.0 and 20.0 µg/mL). The accuracy of the GC-FID method was evaluated, and the interference of formulation additives was investigated. By comparing the concentrations obtained from the spiked samples with the actual added concentrations, the percent analytical recovery values were computed. The results are listed in Table 3.

Table 3. Results of recovery studies by standard addition method (n=6)

Method	Amount taken (µg/mL)	Amount added (µg/mL)	Total amount found (µg/mL) (mean ±SD)	Recovery±RSD (%)
UV	5.0	2.5	7.55±0.10	100.60±1.33
		7.5	12.49±0.15	99.90±1.22
		12.5	17.25±0.28	98.60±1.64
$^1D_{231\ nm}$	5.0	2.5	7.49±0.11	99.90±1.51
		7.5	12.51±0.35	100.10±2.81
		12.5	17.48±0.13	99.90±0.75
GC-FID	1.0	4.0	5.08±0.12	101.60±2.38
		9.0	9.92±0.19	99.20±1.94
		20.0	20.90±0.41	99.50±1.97

LOD and LOQ

The calibration standards were used to get the LOD and LOQ values for the indicated technique [22]. Table 1 provides a summary of the findings. For both techniques of preparing standard progesterone solutions, the LOQ and LOD values were discovered to be 0.50 µg/mL and 0.15 µg/mL, respectively. All RSD values were discovered to be less than 5%.

Serial progesterone stock solution dilutions were used to analyze the LOD and LOQ values in the GC-FID method in order to achieve signal to noise ratios of 3:1 for LOD and 10:1 for LOQ. The LOD and LOQ values for the analyte were determined to be, respectively, 0.075 and 0.25 µg/mL (Table 1).

Ruggedness

The same instruments and standard standard solutions were used in this study by a separate analyst to assess the concentration of progesterone (Table 4).

Table 4. The results of analyses of progesterone by a different analyst (n=3)

Method	Added (µg/mL)	Found (µg/mL) (Mean±SD)	% Recovery	% RSD
UV	4.0	4.10±0.09	102.50	2.21
	8.0	7.92±0.17	99.20	2.17
	12	11.93±0.13	99.40	1.09
$^1D_{231\ nm}$	4.0	4.09±0.09	102.00	2.15
	8.0	8.01±0.12	100.10	1.53
	12.0	12.19±0.17	101.60	1.37
GC-FID	1.25	1.26±0.02	100.80	1.83
	5.0	4.97±0.14	99.40	2.86
	15.0	14.93±0.13	99.50	0.89

No statistically significant discrepancies between the operators were found in the results, indicating the ruggedness of the developed methods.

Stability

Progesterone solutions of 2.0, 4.0 and 10.0 µg/mL concentrations as well as stock solution were maintained in the refrigerator and at ambient temperature for four days to test the stability of progesterone standard solutions spectrophotometrically. The stability measurements were then performed. By comparing these measures to those of standards and expressing the results as a percentage deviation, the results were assessed. Progesterone solutions were stored for three days in the refrigerator and two days at room temperature to test their stability. Under either circumstance, a significant change in concentration was not discovered. Additionally, it was discovered that the stock solution remained stable for a week in the refrigerator.

Stability experiments using the GC-FID method showed that the samples were stable at room temperature, 4 and -20 °C for 24 hours (short-term refrigeration) and for 72 hours (long-term refrigeration). These stability studies' findings fall within the 90-110% acceptable range (Table 5).

Table 5. Stability of progesterone in solution (n=3)

Stability (%)		Room temperature stability (Recovery %±RSD)		Refrigeratory stability +4 °C (Recovery %±RSD)		Frozen stability - 20 °C (Recovery %±RSD)	
Method	Added (µg/mL)	24 h	72 h	24 h	72 h	24 h	72 h
UV	2.0	99.5±3.1	101.3±4.0	99.4±3.1	101.2±4.0	97.4±4.2	101.2±3.9
	4.0	101.4±3.0	99.2±3.5	98.2±4.2	98.2±3.2	101.2±2.9	98.6±4.1
	10.0	98.4±3.0	98.6±2.1	101.3±2.6	99.6±3.8	102.3±1.7	101.4±2.1
$^1D_{231\ nm}$	2.0	99.8±2.9	101.2±3.0	99.6±3.4	100.4±3.0	98.2±3.5	100.3±3.3
	4.0	100.1±2.8	99.6±3.1	99.2±3.9	98.9±2.3	99.4±3.4	99.4±1.6
	10.0	101.3±1.8	102.3±2.1	101.4±2.7	99.8±2.6	99.5±2.4	99.6±2.4
GC-FID	5.0	99.9±1.4	101.3±1.2	99.8±2.2	100.3±2.1	99.4±2.2	99.3±2.2
	10.0	99.1±1.4	98.9±2.6	99.4±2.4	99.7±1.2	99.7±2.4	99.6±1.1
	20.0	99.8±2.0	99.6±2.4	101.3±2.8	101.2±1.9	101.2±3.1	99.7±2.2

Procedure for Pharmaceutical Preparations

Ten progesterone-containing capsules from Progestan were accurately weighed and finely ground. The precise weight of a powdered tablet containing 100 mg of progesterone was combined with methanol, and the mixture was ultrasonically dissolved for 15 minutes at room temperature. The resulting solution was then diluted with methanol to attain the proper concentration before being filtered through a 0.45 µm nylon 25 mm filter (Figs. 5-7).

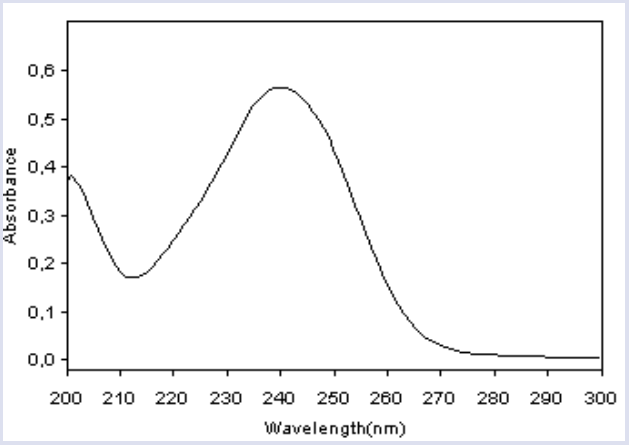

Figure 5. UV spectrum of Progestan® soft capsule solution (10 µg/mL)

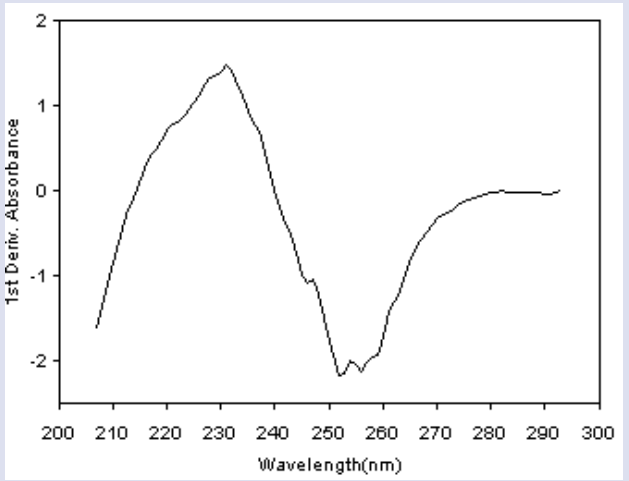

Figure 6. ^{1}D spectrum of Progestan® soft capsule solution (10 µg/mL).

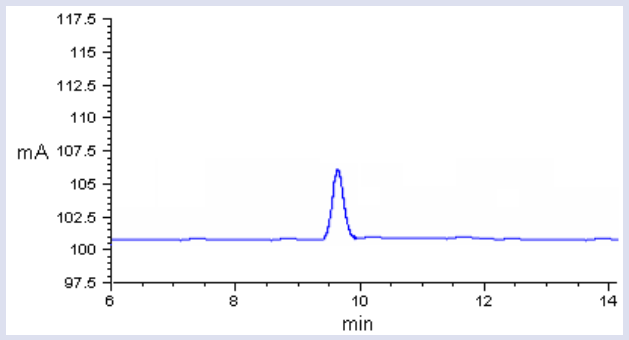

Figure 7. GC-FID chromatogram of progestan capsule solution (10 µg/mL).

Comparison of the Methods

Due to their speed and simplicity, UV and ^{1}D spectrophotometry methods have been widely used in the QC analyses of pharmaceutical preparations. These methods don't call for the pricey equipment needed for chromatographic methods or the time-consuming sample preparation steps like filtration and degassing required for HPLC operations. Derivative spectrophotometry methods can also be used to analyze a wide range of completed goods, with the benefit of resolving complex issues thanks to precise slope differentiation and producing a clean spectrum.

The spectrophotometry method in the visible range used in pharmacopoeias for the quantitative determination of norgestrel and norethisterone tablets [22] and hydroxyprogesterone in injection solutions [13,22] is based on the creation of derivatives, typically through a reaction with isonicotinic acid hydrazide. As a result, the quantitative measurement of progestogen hormones in substances and pharmaceutical preparations is frequently carried out using spectrophotometric methods. One major flaw in this method is that it can only be used to establish the general composition of the main component and a few admixtures. With visible-range spectrophotometry, progesterone and hydroxyprogesterone capronate in oil solutions are especially simple to assess for progestogen hormones in various pharmaceutical preparations.

This study uses UV and ^{1}D spectrophotometry to quantify progesterone in capsules and in pure forms with minimal sample preparation. In this study, UV and ^{1}D spectrophotometry methods were used to quickly, accurately and simply assess progesterone in pharmaceutical preparations. Progesterone's absorptivity in methanol was tested between 200 and 300 nm, and the UV method's "max value" (location of peak's maximum absorbance) was noted at 240 nm. A maximum peak and a low peak for the ^{1}D technique were measured at 231 and 252 nm, respectively. Progesterone in capsules was determined using the developed spectrophotometric methods (Table 6).

Table 6. Determination of progesterone in capsule (100 mg progesterone/capsule)

Commercial Preparations	Method	λ (nm)	Found±SD (mg)	Recovery (%)	RSD (%)	Confidence Interval
Progestan® soft capsule	UV	240	101.1±0.1	101.1	0.09	101.0-101.2
	^{1}D	231	99.7±0.5	99.7	0.53	99.6-100.1
	GC-FID	-	99.3±0.2	99.3	0.24	98.2-102.1

In Figs. 5 and 6, respectively, the UV and ^{1}D spectra obtained from Progestan® soft capsules are displayed. It was clear that the drug solution's maximum and

minimum wavelengths were identical to those of conventional solutions. Additionally, two reference methods from the literature [18,19] were statistically compared with the suggested UV and ^{1}D spectrophotometry methods.

Progesterone in capsules is analyzed using UV spectrophotometry and HPLC methods as one of the reference methods, and progesterone in commercial formulations is determined using HPLC and derivative spectrophotometry methods as the second reference method.

Progesterone's absorptivity in methanol: water (80:20) was tested in the first reference method [18], and the max value (position of maximum absorbance of a peak) was noted at 254 nm. These groups also operated in the HPLC system C_{18} (250x 4.0 mm, I.D. 5 µm) column with methanol as the mobile phase.

Progesterone had been measured using liquid chromatography and derivative spectrophotometry methods in both experimental micellar systems and commercial pharmaceutical formulations [19]. The spectrophotometric experiments had been carried out at 240 nm employing direct UV spectra.

The derivative values that were employed for quantitative calculations were determined as the difference between the heights of the first derivative spectra's maximum at 253.6 nm and minimum at 227.2 nm. In addition, Pucci et al. [19] conducted liquid chromatography using the C_8 (Res Elut, 150x/4.6 mm, I.D. 5 µm) column, a mobile phase made up of 2-propanol and a pH 2.5, 30 mM phosphate buffer, flow rate of 1.5 mL/min, and UV detection carried out at 254 nm.

The proposed UV and ^{1}D spectrophotometry methods were linear over the concentration range of 2-12 µg/mL. The LOD and LOQ for both methods were found to be 0.15 and 0.50 µg/mL, respectively. For both of the suggested procedures, the RSD% values obtained from within-day and between-day testing of quality control samples ranged from 0.25% to 3.50%, suggesting high accuracy and precision. The average recovery value for progesterone in 100 mg capsule composites ranged from 91.7 to 101.1%.

The new UV and ^{1}D spectrophotometry methods were used to analyze a pharmaceutical formulation that didn't need its samples to be separated or treated beforehand. Over the concentration ranges of 5-30 µg/mL and 2-50 µg/mL, respectively, the first and second reference techniques had been confirmed to be linear. The average recovery values in the first and second reference methods were 98.6-100.8% (for capsules) and 98.4-101.7% (for oily injection, capsules, and alcoholic intramuscular solution), respectively. The RSD% values ranged from 0.1-0.4% and from 0.3-1.1%, respectively. The second reference method's LOQ and LOD values were discovered to be 2.0 µg/mL and 1.5 µg/mL, respectively.

With a 95% confidence level and five degrees of freedom, the findings were statistically compared using the Student's t-test (for accuracy) and variance F-test (for precision) with reference methodology [18,19]. The outcomes demonstrated that there was no appreciable difference between the suggested and reference methods for P-values greater than P=0.05 (Table 7).

Table 7. Statistical comparison (Student *t*-test and *F*-test) of two reference methods with proposed methods

	Method	n	X	RSD (%)	Std. Error Mean	*t*-values	P-Values
First comparison	Proposed UV method	10	101.1	0.09	1.29	2.15	0.098
	First reference method	10	97.9	1.66	0.96		
Second comparison	Proposed UV method	10	101.1	0.09	1.29	0.02	0.988
	Second reference method	10	101.3	1.71	0.99		
First comparison	Proposed ^{1}D method	10	99.7	0.53	1.39	2.17	0.098
	First reference method	10	101.9	1.67	0.99		
Second comparison	Proposed ^{1}D method	10	99.7	0.53	1.39	0.02	0.998
	Second reference method	10	101.7	1.81	0.99		
Third comparison	Proposed UV method	10	101.1	0.09	1.29	F_c=1.43	
	Proposed ^{1}D method	10	99.7	0.53	1.39		
	Proposed GC-FID method	10	99.3	0.24	0.08	F_t=3.29	

n:Number of determination, X: Mean, RSD: Relative standard deviation, t_c: Calculated t values, H_o: Hypothesis: No statically significant difference exists between two methods $t_t > t_c$; H_o hypothesis in accepted (α=0.05), F_c: Calculated F values, F_t: Tabulated F values, H_o: Hypothesis: no statitically significant difference exists between methods $F_t > F_c$; H_o hypothesis in accepted (α=0.05)

Additionally, the recently proposed methods for measuring progesterone in capsules were contrasted with existing spectrophotometric methods. Methods were discovered to have benefits like great performance (RSD <2% for pure samples and dose form) and quick

reaction. As a result, it can be used in place of the current procedures.

Additionally, to our knowledge, there isn't a published GC-FID method for determining progesterone levels in pharmaceutical preparations. In order to determine progesterone in pharmaceutical preparations without the need for sample pre-treatment, we needed to design a new GC-FID method. The suggested techniques are also extremely efficient for measuring progesterone in pharmaceutical preparations. Recovery studies utilizing the conventional addition method were presented to demonstrate the viability of the suggested procedures. To do this, designed tablets were spiked with a known quantity of a reference medication, and the nominal value of the drug was calculated using the suggested approach.

Conclusions

Using newly developed and validated UV, ^{1}D spectrophotometry and GC-FID methods that were simple, rapid, dependable, specific, accurate, and precise, progesterone in pharmaceutical formulations was found in the current investigation. Progesterone in its pure form and in its formulation can be routinely analysed using the suggested procedures without separation or interference. They can be used for dissolution or related research as well. The use of UV and ^{1}D spectrophotometry techniques, on the other hand, can be advantageous for routine examination of formulations and raw materials as well as sample analysis during accelerated stability tests.

Conflicts of interest

The author states that did not has conflict of interests

References

[1] Yuan T.F., Le J., Wang S.T., Li Y., An LC/MS/MS Method for Analyzing the Steroid Metabolome with High Accuracy and from Small Serum Samples, *J. Lipid Res.,* 61 (2020) 580-586.

[2] De Wilde L., Roels K., Van Renterghem P., Van Eenoo P., Deventer K., Steroid Profiling in Urine of Intact Glucuronidated and Sulfated Steroids Using Liquid Chromatography-Mass Spectrometry, *J. Chromatogr. A.,* 1624 (2020) 461231.

[3] Van Renterghem P., Viaene W., Van Gansbeke W., Barrabin J., Iannone M., Polet M., T'Sjoen G., Deventer K., Van Eenoo P., Validation of an Ultra-Sensitive Detection Method for Steroid Esters in Plasma for Doping Analysis Using Positive Chemical Ionization GC-MS/MS., *J. Chromatogr. B.,* 1141 (2020) 122026.

[4] Gomez-Gomez A., Miranda J., Feixas G., Arranz Betegon A., Crispi F., Gratacós E., Pozo O.J., Determination of the Steroid Profile in Alternative Matrices by Liquid Chromatography Tandem Mass Spectrometry, *J. Steroid Biochem. Mol. Biol.,* 197 (2020) 105520.

[5] Sayeed I., Wali B., Guthrie D.B., Saindane M.T., Natchus M.G., Liotta D.C., Stein D.G., Development of a Novel Progesterone Analog in the Treatment of Traumatic Brain Injury, *Neuropharmacology,* 145 (2019) 292-298.

[6] Struk W.R., Progestogens in Hormonal Replacement Therapy: New Molecules, Risks, and Benefits, *Menopause* 9 (2002) 6-15.

[7] Belchetz PE., Hormonal Treatment of Postmenopausal Women, *N. Engl. J. Med*., 330 (1994) 1062-1071.

[8] Kawaguchi M., Takatsu A., Miniaturized Hollow Fiber Assisted Liquid-Phase Microextraction and Gas Chromatography-Mass Spectrometry for the Measurement of Progesterone in Human Serum, *J. Chromatogr. B.,* 877 (2009) 343-346.

[9] Ishibashi M., Takayama H., Nakagawa Y., Harima N., Diethylhydrogensilyl-Cyclic Diethylsilylene Derivatives in Gas Chromatography/Mass Spectrometry of Hydroxylated Steroids. Analysis of Cortisol and 6 Beta-Hydroxycortisol in Human Urine, *Chem. Pharm. Bull.,* 36 (1988) 845-848.

[10] Ichimiya H., Egestad B., Nazer H., Baginski E.S., Clayton P.T., Sjövall J., Bile Acids and Bile Alcohols in a Child with Hepatic 3 Beta-Hydroxy-Delta 5-C27-Steroid Dehydrogenase Deficiency: Effects of Chenodeoxycholic Acid Treatment, *J. Lipid Research,* 32 (1991) 829-841.

[11] Setchell K.D., Suchy F.J., Welsh M.B., Zimmer-Nechemias L., Heubi J., Balistreri W.F., Delta 4-3-Oxosteroid 5 Beta-Reductase Deficiency Described in Identical Twins with Neonatal Hepatitis. A New Inborn Error in Bile Acid Synthesis, *The J. Clin. Invest.,* 82 (1988) 2148-2157.

[12] Meng L.J., Sjövall J., Method for Combined Analysis of Profiles of Conjugated Progesterone Metabolites and Bile Acids in Serum and Urine of Pregnant Women, *J. Chromatogr. B.,* 688 (1997) 11-26.

[13] British Pharmacopoeia, British Pharmacopeia Commission, London, (2000) 2197.

[14] Shi Y., Yao J., Liu F., Hu C., Yuan J., Zhang Q., Jin S., Establishment of an HPLC Identification System for Detection of Counterfeit Steroidal Drugs, *J. Pharm. Biomed. Anal.,* 46 (2008) 663-669.

[15] De Orsi D., Pellegrini M., Pichini S., Mattioli D., Marchei E., Gagliardi L., High-Performance Liquid Chromatography-Diode Array and Electrospray-Mass Spectrometry Analysis of Non-Allowed Substances in Cosmetic Products for Preventing Hair Loss and Other Hormone-Dependent Skin Diseases, *J. Pharm. Biomed. Anal.,* (2008) 48641-648.

[16] Alambiaga-Caravaca A.M., Domenech-Monsell I.M., Sebastián-Morelló M., Miranda M., Balaguer-Fernández C., Calatayud-Pascual A., Rodilla V., López-Castellano A., HPLC-UV Analytical Validation of a Method for Quantification of Progesterone in Ex Vivo Trans-Corneal and Trans-Scleral Diffusion Studies, *J. Pharm. Biomed. Anal.,* 193 (2021) 113749.

[17] Sun L., Zhang B., Sun J., The Solubility-Permeability Trade-Off of Progesterone with Cyclodextrins under Physiological Conditions: Experimental Observations and Computer Simulations, *J. Pharm. Sci.,* 107 (2018) 488-494.

[18] Maliwal D., Jain P., Jain A., Patidar V., Determination of Progesterone in Capsules by High-Performance Liquid Chromatography and UV-Spectrophotometry, *J. Young Pharmacist.,* (2009) 1371-374.

[19] Pucci V., Bugamelli F., Mandrioli R., Luppi B., Raggi M.A., Determination of Progesterone in Commercial Formulations and in Non Conventional Micellar Systems, *J. Pharm. Biomed. Anal.,* 30 (2003) 1549-1559.

[20] El-Yazbi F.A., Korany M.A., Abdel-Razzak O., Elsayed M.A., Derivative Spectrophotometric Analysis of Oestradiol Esters, Testosterone and Progesterone in Oily Injections, *Anal. Lett.,* 18 (1985) 2127-2142.

[21] The European Agency for the Evaluation of Medicinal Products. ICH Topic Q2B Note for Guideline on Validation of Analytical Procedures: Methodology GPMP/ICH/281/95 (1996).

[22] United States Pharmacopeia, 23th ed., Rockville United States: Pharmacopeial Convention, Inc., (1995).

Cumhuriyet Sci. J., 44(3) (2023) 464-469
DOI: https://doi.org/10.17776/csj.1184249

Cumhuriyet Science Journal

| csj.cumhuriyet.edu.tr | Founded: 2002 ISSN: 2587-2680 e-ISSN: 2587-246X Publisher: Sivas Cumhuriyet University

Effect of Knitting Pattern of PP Mesh on the Flexural Properties of Heat-cured PMMA Denture Base Resin

Kaan Yerliyurt [1,a], Sinan Eğri [2,3,b,*]

[1] *Department of Prosthodontics, Faculty of Dentistry, Tokat Gaziosmanpaşa University, Tokat, Türkiye*
[2] *Department of Chemistry, Faculty of Science and Letters, Tokat Gaziosmanpaşa University, Tokat, Türkiye*
[3] *Bioengineering Division, Institute of Graduate Studies, Tokat Gaziosmanpaşa University, Tokat, Türkiye*
**Corresponding author*

Research Article

History
Received: 04/10/2022
Accepted: 19/06/2023

ABSTRACT

Heat-cured polymethyl methacrylate is (PMMA) is the most common denture base material and some mechanical properties such as flexural strength and impact resistance etc. may lead to fail, besides its excellent properties. Polypropylene (PP) hernia mesh is a commercially available medical textile used in surgical repair of different types of hernia. It was aimed to investigate the effect of two different knitting patterns of PP meshes on the flexural properties of the PMMA denture base resin when they are used as reinforcement and compare with glass fiber mesh reinforced and no mesh used resins. Knitting patterns of the PP mesh structures were hexagonal honeycomb pattern and square pattern and these were used as single or double layer as reinforcement. 6 groups were established in the study: control group with no mesh and 5 reinforced groups with meshes (glass fiber mesh, single layer honeycomb patterned PP mesh, double layer honeycomb patterned PP mesh, single layer square patterned PP mesh, double layer square patterned PP mesh). A total of 60 samples with the dimensions of 65x10x3 mm, n=10 in each group were fabricated. The flexural strength, maximum deformation, and flexural modulus were determined by three-point bending test. Fracture surfaces were evaluated by scanning electron microscopy. The obtained data were statistically analyzed by two-way ANOVA test with Bonferroni corrections. The single layer square patterned PP mesh group exhibited the highest (76.67 ± 7.64 MPa), and the control group showed the lowest (63.49 ± 7.18 MPa) flexural strength values. The single layer glass fiber mesh group showed the highest (7.13 ± 0.55 mm) and the control group showed the lowest (4.72 ± 0.81 mm) maximum deformation values. The single layer glass fiber mesh group exhibited the highest (2131.87 ± 205.76 MPa), and the control group exhibited the lowest (1582.26 ± 98.63 MPa) flexural modulus values. Significant increase in flexural strength was observed in all polypropylene mesh-reinforced groups compared to the control group except double layer honeycomb patterned PP mesh group ($p < 0.05$). Using PP fiber mesh for reinforcement provide a very favorable aesthetic view and PP fiber mesh is concluded to be a promising material for reinforcement of heat-cured PMMA denture base resins.

Keywords: PMMA denture base resin, Glass fiber mesh, Polypropylene hernia mesh, Reinforcement, Flexural strength

[a] *kaanyerliyurt@hotmail.com* *https://orcid.org/0000-0002-9236-2732* [b] *sinan.egri@gop.edu.tr* *https://orcid.org/0000-0002-0120-385X*

Introduction

The most commonly used denture base material for production of removable dentures is heat cured polymethyl methacrylate (PMMA) acrylic resin [1]. Due to its favorable properties such as biocompatibility, superior aesthetic view, low water sorption, ease of modification, capability of being repaired, and ease and simplicity in processing achieved a great success in clinical dentistry [2]. Despite these favorable properties, the weakness of PMMA in mechanical properties like low flexural strength (FS), low impact strength (IS) and low surface hardness reduces the clinical longevity of the prosthesis which may end up with patient dissatisfaction [3]. Although the reasons of failure with fracture are well known, acrylic resin fracture is still an unavoidable problem in removable prosthodontics. Reinforcement with additives, copolymerization, improved cross-linking, and plasticization of acrylic resin are some of the strategies applied to overcome this challenge [4].

However, resin substrates with low mechanical strength are susceptible to deformation and impact during the chewing process [5,6]. Therefore, reinforcing materials enhancing the mechanical properties of complete dentures are required. Currently, metal frameworks are primarily used in clinical practice as reinforcements to improve the fracture resistance, volume stability, and precision of complete dentures [5]. However, metal frameworks are comparably heavier because of their high densities and also they are less favorable due to more complicated fabrication processes than resins. Beyond these, metal frameworks are made of alloys which may cause hypersensitivity [7]. Using metal wires or plates as reinforcement within the denture base resin is the most common method for enhancing the mechanical strength. However, adhesion of the resin to the metal framework is low due weak bonding and also exhibit poor aesthetic properties. Nanoparticles or various fiber reinforcements, such as

carbon and glass fibers, plyometric polyamide, and ultra-high molecular- weight polyethylene were reported to be used in reinforcing PMMA based denture bases [8-11].

Glass fiber is one of the materials used as reinforcement in dentistry. Because of its ductility that allows the material to be bent without fracture, researchers have focused on using glass fiber instead of metal frame to enhance the fracture resistance of dentures [10,12-16]. A complete denture fabricated using glass fiber frame has a shorter fabrication time, lighter in weight and exhibit better aesthetic properties compared to using a metal frame. However, only a few experimental and clinical studies have focused on enhancing the mechanical properties of complete dentures reinforced with glass fiber mesh. In particular, the fatigue resistance and long-term prognosis of glass fiber mesh reinforced complete dentures have been rarely studied [5]. Orthopedic casting tape (OCT) which is basically formed by a mesh made from glass fibers and a self curing resin surrounding the mesh, has been used for fracture management of long bones and provides excellent outcomes of immobilization and rigid support in the field of orthopedics. However, their potential in denture reinforcement still needs to be investigated [1]. From the available indexed literature, it was observed that inadequate data is available about the mechanical properties of complete dentures reinforced using glass-fiber mesh. Also, the using OCT as reinforcement of PMMA acrylic resin denture bases is a novel approach to enhance the mechanical strength of complete dentures. Therefore, it is hypothesized that PMMA acrylic resin denture bases reinforced with glass-fiber mesh and OCT can exhibit better fracture loads when compared with the PMMA dentures bases without reinforcement [1].

Poly propylene (PP) fiber is an important member of family of synthetic fibers. It possesses good mechanical and chemical properties such as high-level resilience, elasticity, and tensile strength, durable in acid and similar medium, low density (0.91 g/cm3) and low cost. Due to all of these advantageous features, polypropylene fiber is a suitable candidate for PMMA-based resin reinforcement [17-19]. Polypropylene fibers are available in various forms in the medical market. PP mesh is one of these products; it is a surgical mesh commonly used to repair different types of hernia [19,20].

The aim of this study is to evaluate the effect of addition of single- or double-layer polypropylene hernia meshes with two different patterns on the flexural properties of the heat-cured acrylic resin. Since the meshes used in this study were readily available medical textiles, they were not subjected to any surface treatment in order to compare the solely effect of the PP mesh on flexural properties.

Materials and Methods

Heat-cured PMMA denture base resin (Meliodent, Kulzer GmbH, Frankfurt, Germany) was used. Two different PP meshes; one of the mesh PP-4A (4A Medical, Ankara, Turkey) which was honeycomb patterned (Figure 1A), and the other one PP-Supro (Supro Mesh, Klas Medical, Istanbul, Turkey) which was square patterned (Figure 1B), were used. The PP meshes were obtained in sterile package that is produced for surgical operations. Delta Plus orthopedic cast (Delta Lite Plus, BSN Medical GmbH, Frankfurt, Germany) was obtained in sealed package and washed with ethanol to get rid of the curing resin initiated by air contact. Cleansing with alcohol procedure is as follows, material was cut in dimensions suitable to fit in the mold, immersed in excess amount of ethanol (96% v/v), swung with gentle movements periodically within first two hours and kept in for 24 hours, washed with fresh ethanol and dried prior to use.

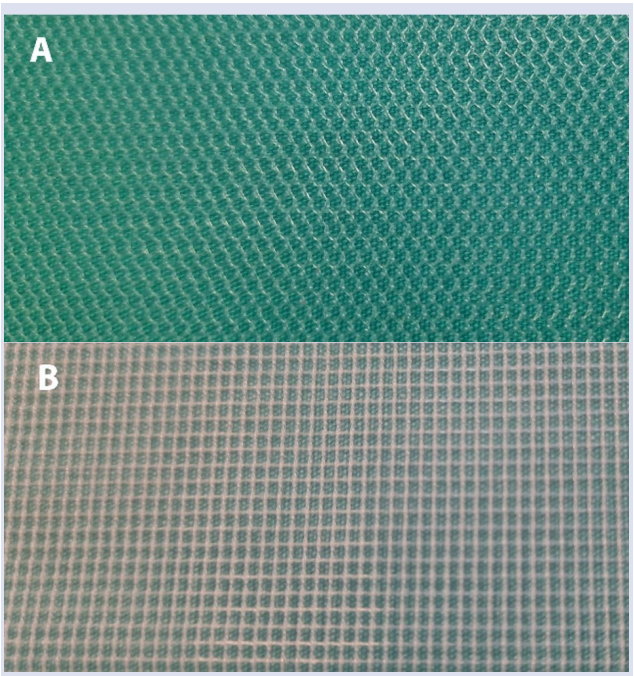

Figure 1. Two different patterned hernia meshes; (A) Honeycomb patterned PP-4A; (B) Square patterned PP-Supro

A total of 6 groups were established in the study: control group and 5 reinforced groups with different meshes. Mesh reinforced groups were, single layer PP-4A group (4A1), two layers PP-4A group (4A2), single layer PP-Supro group (SP1), two layers PP-Supro group (SP2) and single layer Delta - Lite Plus glass fiber mesh washed with ethanol (DPA).

PMMA resin was fabricated as reported before [19]. Briefly, ideal powder-liquid mixing ratio was used as 25 g powder and 10 ml liquid and complete wetting was observed. Acrylic paste was cast using a mold made of chromium designed with the dimensions of 65x150x3 mm. Then, the mold was pressed in the hydraulic press device (GLS, Gulersan Lubrication Equipment Industry and Trade Co. Ltd., İstanbul, Turkey) for 5 minutes and the excess acrylic was removed. Then, the polymerization was completed by making temperature and time adjustments in accordance with the manufacturer's instructions. Three point bending test specimens were cut in 65x10x3 mm dimensions using a laser

cutting machine (LazerFix Laser Technology, Konya, Turkey) in order to match dimensions described in ISO 178 standard. All specimens were stored in distilled water for 24 hours. In this way, residual monomers were removed.

Flexural properties of the control and mesh reinforced groups were determined by three point bending test in accordance with ISO 178 standard. A representative image of the test specimens before and after three-point bending test and tensile test was shown in Figure 2. Three point bending tests were performed on a total of 60 samples in 6 groups and n=10 samples for each group using a universal testing machine (Autograph AGS-X, Shimadzu, Japan) at a compression rate of 3 mm/min cross head speed. Samples placed between the shoulders having a gap of 50 mm. All tests were carried out at room temperature.

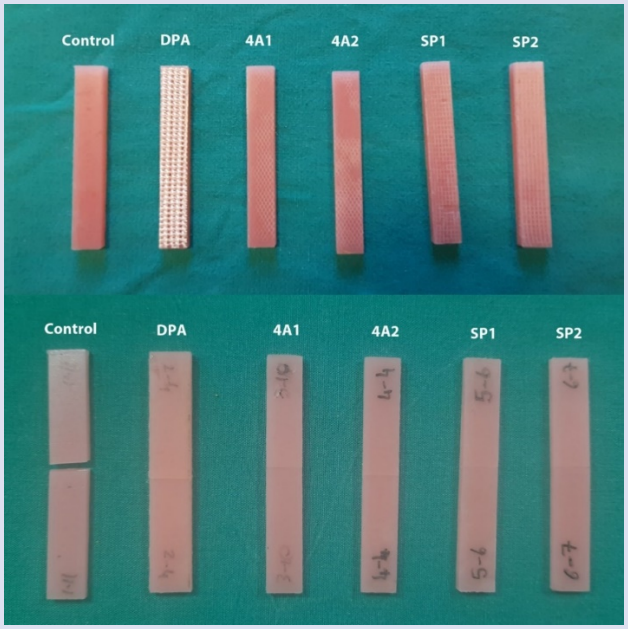

Figure 2. Representative image of the test specimens before and after three point bending test

Results and Discussion

The basis of using PP fiber mesh for reinforcement of the PMMA resin was the unique properties of PP such as low density, resistance to corrosion, high mechanical stability, moisture repellence, resilience and elasticity [21,22]. In this study, three different mesh reinforcements were set in five groups: woven glass fiber mesh group, two PP mesh groups based on mesh pattern and number of layers used, and two PP mesh groups based on another mesh pattern and number of layers used, within the heat polymerized PMMA resin. A control group, PMMA resin with no fiber mesh additive was used for the comparisons with each mesh-reinforced group. Flexural loading is an important parameter for dental prosthetic materials as it mimics the conditions they are exposed to in the oral environment [17,23]. Three-point bending test was used to measure the flexural properties of the prepared acrylic samples. For this purpose, specimens were cut into 65x10x3 mm dimensions and kept in distilled water from fabrication to testing period in order to avoid potential reduction in flexural strength that is previously reported [13,24].

Three Point Bending Test

Test results for between subject effects obtained by one-way ANOVA analysis of three point bending test results for three flexural properties as flexural strength (MPa), maximum deformation (mm) and flexural modulus (MPa) are summarized on Table 1. Mean with standard deviations and scoring on significance of the tested variables obtained by comparisons of three point bending test results are presented as Table 1 (in group comparison). Test results obtained by three-point testing were plotted and presented in Figure 3. According to the test results, any type of mesh use for reinforcement exhibited a significant change in all flexural properties of the ($p<0.001$).

Table 1. Mean and standard deviations for three flexural properties and their significance obtained by three point bending test

Groups	Flexural strength (MPa) Mean ± SD	Maximum deformation (mm) Mean ± SD	Flexural Modulus (MPa) Mean ± SD
Control	63.49 ± 7.18^{c}	4.72 ± 0.81^{y}	$1582.26\pm98.63^{\beta}$
DPA	67.71 ± 2.93^{bc}	7.13 ± 0.55^{x}	$2131.87\pm205.76^{\alpha}$
4A1	72.48 ± 6.57^{ab}	6.57 ± 0.65^{x}	$2054.50\pm97.07^{\alpha}$
4A2	70.72 ± 7.71^{abc}	6.36 ± 1.25^{x}	$2045.72\pm76.70^{\alpha}$
SP1	76.67 ± 7.64^{a}	7.04 ± 1.12^{x}	$2051.59\pm91.29^{\alpha}$
SP2	74.64 ± 4.57^{ab}	6.62 ± 0.68^{x}	$2105.56\pm62.21^{\alpha}$

a,b,c: Comparison of flexural strength values between groups; x,y: Comparison of maximum deformation values between groups; α,β: Comparison of flexural modulus values between groups. Values with different superscript letters indicate significant differences.

It is evident by the results presented on Table 1 that a significant increase in flexural strength was achieved for single-layer polypropylene-Supro group (SP1) which exhibited the highest (76.67 ± 7.64 MPa) flexural strength, while the control group exhibited the lowest (63.49 ± 7.18 MPa). Compared to the control group, significantly higher flexural strength was observed in all polypropylene mesh reinforced groups except the 4A2 group ($p < 0.05$). Although, a slight decrease in average flexural strength values was observed for double layer PP mesh usage, it did not reveal significance ($p > 0.05$). DPA glass fiber mesh group did not show a significant difference in flexural strength compared to control. The reason for this behavior was concluded to be the poor adhesion of PMMA matrix on to glass fibers together with the void spaces between the fibers forming the bundle.

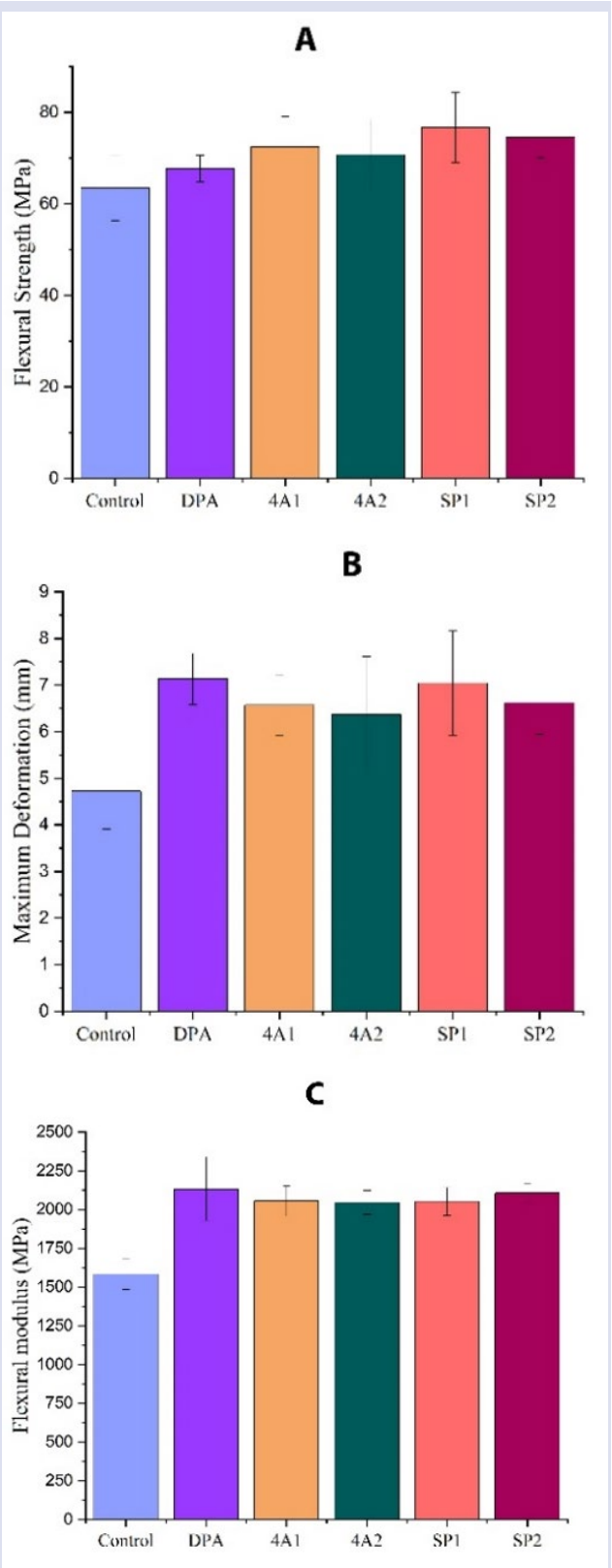

Figure 3. Flexural properties of samples obtained by three point bending test

As a result, this void space may lead the PMMA matrix to form a weak point where fracture starts and propagate from. The knitting pattern of the PP mesh did not exhibit significant difference on flexural strength where the average values of the square patterned SP1 and SP2 PP mesh groups were greater than 4A1 and 4A2 PP mesh groups.

All of the mesh reinforcements resulted with a significant increase in maximum deformation of the test specimens ($p < 0.05$). The single-layer DPA glass fiber mesh group showed the highest (7.13 ± 0.55 mm) maximum deformation, while the control group showed the lowest (4.72 ± 0.81 mm) maximum deformation. All of the mesh-reinforced groups did not exhibit a significant difference comparing their maximum deformation values in between ($p > 0.05$). PMMA resin showed a brittle fracture character, and a more ductile fracture was observed by using any type of mesh reinforcement.

Using any type of fiber mesh for reinforcement resulted with a significant increase in flexural modulus values ($p < 0.05$), but these mesh reinforcements did not exhibit a significant difference comparing each other. The single-layer DPA glass fiber mesh group exhibited the highest (2131.87 ± 205.76 MPa) flexural modulus values, while the control group exhibited the lowest (1582.26 ± 98.63 MPa) flexural modulus values. Significantly higher flexural modulus values were obtained in all mesh reinforced groups than the control group.

SEM Analysis

SEM images of the fracture surfaces were obtained from test specimens that were used for thee point bending tests, and presented in Figure 4 with two different magnifications (100X and 1000X). A brittle fracture was observed for the control group and fracture patterns in the form of a river lines were formed in the direction almost parallel to the force applied (Figure 4A1 and 4A2). The length of these lines was in the range of 10 µm to 40 µm long and these river line patterns were mainly located close to the surface where the force applied and lying along the mid part of the specimen. Fisheye patterns which were formed as a result of the tensile forces occurred perpendicular to the direction of the force applied, were observed to be distributed around mid to bottom part of the specimens. Brittle fracture created a rough fracture surface.

The SEM image of the DPA glass fiber mesh confirmed that alcohol washing was successful in removing the self-curing resin surmounting the glass fiber mesh, and clear and separate glass fiber bundles can easily be recognized (Figure 4B1). Although a brittle fracture was also exhibited by these samples, the fiber mesh structure provided a more ductile fracture to the PMMA resin. The void space between the glass fibers, which form the knitted mesh and could not be filled with PMMA during pack and press process, may be the reason for comparatively lower flexural strength exhibited by DPA mesh reinforcement compared to PP mesh reinforced groups.

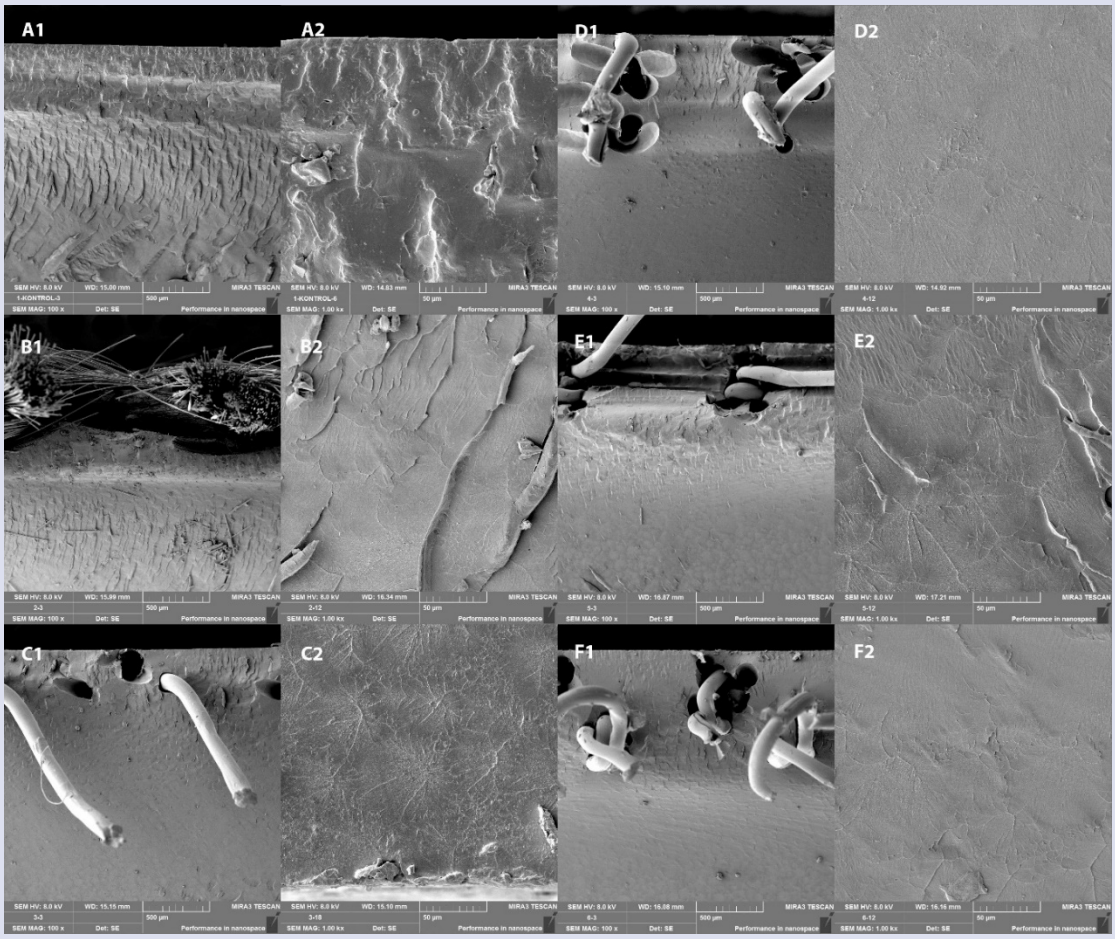

Figure 4. SEM images of the samples from test groups: (A) Control, (B) DPA, (C) 4A1, (D) 4A2, (E) SP1, (F) SP2 - with different magnifications: (1) 100×, (2) 1000×

The SEM images of the 4A1 group revealed that the PMMA matrix tightly fit with the PP fibers, and the minimal void spaces observed around the fibers were formed by the plastic deformation of the PP fibers during the mechanical test or during the separation of the fractured fragments for SEM sample preparation. Fisheye patterns were observed in the middle and lower parts of the fracture. Smooth and clean stripping of the fibers that belong to the mesh structure demonstrated the poor adhesion of the PMMA matrix on to the fibers (Figure C1).

Although double layer PP mesh was used in both 4A2 and SP2 groups, it was observed that the PMMA matrix filled the gaps between PP fibers tightly (Figure D1 and F1). These images also demonstrated that hills and plateaus formed along the borders of the fiber layers during fracture. This behavior was observed only with the double PP mesh layered PMMA resins, that can be associated with the weaker spots formed during filling of the voids by PMMA during pack and press process. Both of these double PP mesh layered samples were fractured from the borders of the knots of the fibers and these knots forms the weak spots for fracture. It was concluded that using multiple PP mesh layers are better be used with a suitable distance between them to avoid the formation of weak spots.

Conclusions

In this study, it was aimed to investigate the potential use of single or double layered PP hernia meshes with two different knitting patterns as reinforcement for heat-cured PMMA denture base resins by comparing them with glass fiber mesh reinforcement and no-mesh used control. Single layer square knitting patterned PP mesh reinforced resin exhibited the highest flexural strength, while DPA glass fiber mesh reinforced resin exhibited the highest maximum deformation and flexural modulus. Using any type of PP mesh except double layer honeycomb knitting patterned PP mesh reinforced group provided a significant increase in flexural strength of the PMMA resin. In this study, each kind of reinforcement was used without any surface treatment for enhancement of fiber-matrix adhesion, since surface treatment is an another parameter that is also dependent to multiple variables. Further enhancement in fiber-matrix adhesion can be achieved by using the methods for surface modification of the fibers. From the aesthetic point of view, it was evident that using PP fibers for reinforcement provide a very favorable view even for double layer usage, PP fiber mesh is a promising material for reinforcement of heat-cured PMMA denture base resins.

Conflicts of interest

All authors declare that they have no conflict of interest.

References

[1] Abduljabbar T., Influence of dental glass fibers and orthopedic mesh on the failure loads of polymethyl methacrylate denture base resin, *Polymers*, 13 (2021) 2793.

[2] Rahal J.S., Mesquita M.F., Henriques G.E.P., Nóbilo M.A.A., Surface roughness of acrylic resins submitted to mechanical and chemical polishing, *J. Oral Rehabil*., 31 (2004) 1075-1079.

[3] Phoenix, R.D. Denture base materials, *Dent. Clin. N Am.*, 40 (1996) 113-120.

[4] Calamote C., Coelho I.C., Silva A.S., Esteves J.L, Moreira L., Pinto A.C., Manzanares-Céspedes M.C., Escuín T., Comparison of the masticatory force (with 3D models) of complete denture base acrylic resins with reline and reinforcing materials, *Materials*, 14 (12) (2021) 3308.

[5] Im S.M., Huh Y.H., Cho L.R., Park C.J., Comparison of the fracture resistances of glass fiber mesh- and metal mesh-reinforced maxillary complete denture under dynamic fatigue loading, *J. Adv. Prosthodont*., 9 (2017) 22-30.

[6] Jagger D.C., Harrison A., Jandt K.D., The reinforcement of dentures, *J. Oral Rehabil.*, 26 (1999) 185-194.

[7] Geurtsen W., Biocompatibility of dental casting alloys, Crit. Rev. *Oral Biol. Med.*, 13 (2002) 71-84.

[8] Jagger D., Harrison A., Vowles R., Jagger R., The effect of the addition of surface treated chopped and continuous poly (methyl methacrylate) fibres on some properties of acrylic resins, *J. Oral Rehabil.*, 28 (2001) 865-872.

[9] Tsue F., Takahashi Y., Shimizu H., Reinforcing effect of glass-fiber-reinforced composite on flexural strength at the proportional limit of denture base resin, *Acta Odontol. Scand.,* 65 (2007) 141-148.

[10] Yu S.H., Cho H.W., Oh S., Bae J.M., Effects of glass fiber mesh with different fiber content and structures on the compressive properties of complete dentures, *J. Prosthet Dent.,* 113 (2015) 636-644.

[11] Alla R.K., Sajjan S., Alluri V.R., Ginjupalli K., Upadhya N., Influence of fiber reinforcement on the properties of denture base resins, *J. Biomater.* Nanobiotechnol., 4 (2013) 91-97.

[12] Hedzelek W., Gajdus P., Mechanical strength of an acrylic resin palatal denture base reinforced with a mesh or bundle of glass fibers, Int. *J. Prosthodont.,* 20 (3) (2007) 311-312.

[13] Takahashi Y., Yoshida K., Shimizu H., Effect of location of glass fiber-reinforced composite reinforcement on the flexural properties of a maxillary complete denture in vitro, *Acta Odontol. Scand*., 69 (2011) 215-221.

[14] Vallittu P.K., A review of fiber-reinforced denture base resins, *J. Prosthodont*., 5 (1996) 270-276.

[15] Kim S.H., Watts D.C., The effect of reinforcement with woven E-glass fibers on the impact strength of complete dentures fabricated with high-impact acrylic resin, *J. Prosthet. Dent.*, 91 (2004) 274-280.

[16] Vallittu P.K., Flexural properties of acrylic resin polymers reinforced with unidirectional and woven glass fibers, *J. Prosthet. Dent*., 81 (1999) 318-326.

[17] Mathew M., Shenoy K., Ravishankar K.S., Flexural strength of hydrogen plasma-treated polypropylene fiber-reinforced polymethyl methacrylate denture base material, *J. Indian Prosthodont. Soc*., 18 (2018) 257-262.

[18] Mathew M., Shenoy K., Ravishankar K.S., Impact strength of poly propylene fiber reinforced PMMA, *Int. J. Sci. Eng.* Res., 5 (2014) 951-955.

[19] Yerliyurt K., Eğri S., Investigation on the potential use of polypropylene mesh for the reinforcement of heat-polymerized PMMA denture base resin, *Polymers*, 14 (2022) 3300.

[20] Cobb W.S., Kercher K.W., Heniford B.T., The argument for lightweight polypropylene mesh in hernia repair, *Surg. Innov*., 12 (2005) 63-69.

[21] Mowade T.K., Dange S.P., Thakre M.B., Kamble V.D., Effect of fiber reinforcement on impact strength of heat polymerized polymethyl methacrylate denture base resin: In vitro study and SEM analysis, *J. Adv. Prosthodont*., 4 (2012) 30-36.

[22] Silva E.P.E., Rosa E.L., Barbosa S.V., Tissue reactions to polypropylene mesh used in maxillofacial trauma, *Braz. Dent. J.*, 12 (2001) 121-125.

[23] Qasim S.B., Al Kheraif A.A., Ramakrishaniah R., An investigation into the impact and flexural strength of light cure denture resin reinforced with carbon nanotubes, *World Appl. Sci. J*., 18 (2012) 808 812.

[24] Vojvodic D., Komar D., Schauperl Z., Celebic A., Mehulic K., Zabarovic D., Influence of different glass fiber reinforcements on denture base polymer strength (Fiber reinforcements of dental polymer), *Med. Glas*., 6 (2009) 227-234.

Cumhuriyet Sci. J., 44(3) (2023) 470-473
DOI: https://doi.org/10.17776/csj.1195938

Cumhuriyet Science Journal

| csj.cumhuriyet.edu.tr | Founded: 2002 ISSN: 2587-2680 e-ISSN: 2587-246X Publisher: Sivas Cumhuriyet University

Antioxidant Capacity of Essential Oils Obtained from *Myrtus communis* L. and *Citrus sinensis* (L.) Osbeck Plants Widely Consumed in Adana Region

Merve Nenni [1,a], Seçil Karahüseyin [2,b,*]

[1] *Department of Analytical Chemistry, Faculty of Pharmacy, Cukurova University, Adana, Türkiye.*
[2] *Department of Pharmacognosy, Faculty of Pharmacy, Cukurova University, Adana, Türkiye*
**Corresponding author*

Research Article

History
Received: 28/10/2022
Accepted: 13/07/2023

ABSTRACT

Vitamin C, an antioxidant, is abundant in oranges (*Citrus sinensis* (L.) Osbeck), which are consumed worldwide. It has treated constipation, diarrhea, upper respiratory illnesses, obesity, menstruation issues, hypertension, and stress. Traditional medicine worldwide uses myrtle (*Myrtus communis* L.). Clinical and experimental studies show that the plant has a wide range of pharmacological and therapeutic activities, including antioxidant, anticancer, antidiabetic, antibacterial, antifungal, antiviral, pulmonary and skin diseases, dysentery, vomiting, rheumatism, sinusitis, leucorrhoea, and hair loss control. These plants contain flavonoids, terpenes, steroids, fatty acids, carbohydrates, volatile chemicals, carotenoids, and nutritional components. Plant antioxidants have gained popularity due to their health benefits. Many studies focused on medicinal organic antioxidants. The main goal of this research was to investigate the volatile components and antioxidant capacities of the essential oils of myrtle and orange, both of which are commonly utilized for medicinal purposes in the Adana region. Myrtle and orange extracts demonstrated substantial antioxidant properties when tested with the 2,2-diphenyl-1-picrylhydrazyl (DPPH) assay, a test based on the scavenging of the DPPH radical. It has been revealed that myrtle essential oil has a higher capacity in terms of antioxidant activity than orange essential oil.

Keywords: *Myrtus communis, Citrus sinensis*, Essential oils, Antioxidant activity, DPPH.

[a] *mnenni@cu.edu.tr* *https://orcid.org/0000-0003-3165-1060* [b] *skarahuseyin@cu.edu.tr* *https://orcid.org/0000-0002-3515-2974*

Introduction

Plants have traditionally been a valuable source of sustenance and medicinal value in treating a wide range of human diseases. Recent investigations on the phytochemistry of medicinal plants have shown the efficacy of traditional remedies. Plants have long been used to treat a variety of illnesses and infections [1]. Natural products are a great source of molecules for medication development since they contain a wider range of size structures than synthetic ones. The discovery of new medicines will continue to rely heavily on natural products, which have historically been important sources of bioactive chemicals [2].

Only 10% of the plant kingdom has essential oils, which are pungent volatile chemicals. Because of their general safety, widespread consumer acceptability, and potential for several uses, essential oils, and their constituent parts can be very promising biological agents. Brittle secretory structures in plants, such as glands, secretory hairs, secretory ducts, secretory cavities, or resin ducts, are stored. Essential oils are intricate concoctions made up of numerous different components. They come from terpenes and their oxygenated compounds chemically. Essential oils are found in many families such as Lamiaceae, Rutaceae, and Myrtaceae [3, 4].

The family Rutaceae includes the genus *Citrus*, with an output of over 123 million tons per year in 2010, this genus is the most significant fruit tree crop in the entire planet. Asia is the original home of *C. sinensis*, which is now found across the Pacific and warm regions of the globe. *C. sinensis* is a flowering evergreen tree. Orange trees often reach a height of 9 to 10 m, and their branches have thick spines. *Citrus limon* (lemon), *C. medica* L. (citron), *C. x aurantium* L. (sour orange), *C. paradisi* Macfad. (grapefruit), *C. reticulata* Blanco (mandarin, tangerine), *C. clementina* (clementine), and *C. sinensis* (sweet orange) are useful plants in the genus. *C. sinensis* is widely consumed across the world as a top source of vitamin C, a potent natural antioxidant that strengthens the immune system. Traditional treatments for ailments such as colic, constipation, cramps, diarrhea, tuberculosis, bronchitis, cough, cold, menstrual disorders, obesity, angina, hypertension, anxiety, depression, and stress all involve the use of Citrus species. The secondary metabolites found in abundance in *C. sinensis* contribute to the pharmacological effects attributed to this plant. Flavonoids, steroids, alkanes, hydroxy amides and fatty acids, peptides, coumarins, carbohydrates, carbamates and alkylamines, volatile compounds, carotenoids, and nutritional components like potassium, calcium, magnesium, and sodium have all

been found in fruits, peel, leaves, juice, and roots of *C. sinensis* [2, 5, 6].

The evergreen plant known as myrtle (*Myrtus communis*) is a member of the Myrtaceae family. This family of naturally occurring, up to 5 m tall, evergreen shrubs or small trees includes the genus, *Myrtus*. It naturally grows throughout the Mediterranean region and has been used for centuries as a spice, food, and medicine. Although clinical and experimental studies suggest it has a wider range of pharmacological and therapeutic effects, including antioxidative, anticancer, anti-diabetic, antiviral, antibacterial, antifungal, hepatoprotective, and neuroprotective activity, the herb is traditionally used to treat disorders like peptic ulcer, diarrhea, inflammation, hemorrhoid, pulmonary and skin diseases, vomiting, dysentery, rheumatism, sinusitis, leucorrhoea and cosmetic purposes like hair loss control. Among the substances thought to be the primary biologically active components are myrtucommulone, semimyrtucommulone, polyphenols, α-pinene, 1,8-cineole, myrtenyl acetate, linalool, limonene, and α-terpinolene [4, 7-9].

In this study, it was aimed to evaluate the volatile components and antioxidant capacities of essential oils of myrtle and orange that are frequently used therapeutically in Adana region. Terpene and essential oil content of *C. sinensis* and *M. communis* essential oils were analyzed qualitatively by their phytochemical reactions, and their antioxidant activity capacities were analyzed and compared with the 2,2-diphenyl-1-picrylhydrazine (DPPH) method.

Materials and Methods

Chemicals

2,2-diphenyl-1-picrylhydrazine (DPPH), ascorbic acid (AA, as a positive control), and ferric chloride were purchased from Sigma-Aldrich (USA). We used methanol (MeOH, as a solvent and negative control), chloroform, ferric chloride, and sulfuric acid from Merck (Germany). Every chemical was analytic reagent grade.

Essential Oil Samples

Orange essential oil (*C. sinensis*) and myrtle essential oil (*M. communis*) were acquired from Adana, Türkiye, a local market for use in this study. All samples of essential oils were verified and stored in the Analytical Chemistry Laboratory of the Faculty of Pharmacy, Cukurova University in Türkiye.

Extract Screening for Bioactive Agent

Following are some key constituents of the plants' essential oil samples that were subjected to phytochemical screening utilizing their respective qualitative methods descriptions [10, 11].

Test for Terpenoids

To dissolve the 2 mL of the plants' essential oil samples, 2 mL of chloroform was employed, and the mixture was then allowed to dry. After heating for approximately 2 minutes, another 2 mL of concentrated sulfuric acid was added. After adding, the sulfuric acid was heated for about 2 minutes. Terpenoids were evident because of the development of a greenish color [10].

Test for Essential Oils

A little amount of the extracts was dissolved in 90% alcohol, and two drops of $FeCl_3$ were added. There was a greenish color that also suggested the presence of essential oils [11].

DPPH Assay

An assay for free radical scavenging activity uses 1,1-diphenyl-2-picrylhydrazine (DPPH radical). The decrease in the stable free radical DPPH's absorbance at 517 nm can be used to assess the scavenging capacity of natural compounds. Scavenger combines with the purple free radical to produce the colorless product DPPH. A 0.1 M stock solution of DPPH in methanol was prepared. To prevent deterioration, this solution is stored in the refrigerator wrapped in foil. By adapting the methods of Brand-Williams et al. (1995) [12], and Blois (1958) [13], the DPPH test of the essential oil samples was investigated (2019). The essential oil samples were diluted with MeOH in twelve stages. A 96-well plate was loaded with 120 µL of the diluted essential oil samples and AA. To start the reaction, 40 µL of 0.1 M DPPH in MeOH was added. A UV spectrophotometer was used to test the reaction mixture's absorbance at 517 nm after it had stood at room temperature for 45 minutes (Thermo Scientific, Multiskan Sky Microplate Spectrophotometer, Waltham, MA, USA). The mean expression was calculated using three observations of the data. From the drop in absorbance, the % DPPH radical scavenging activity of samples and standards was determined. It was determined what percentage of DPPH was removed (($A_{Control}$ A_{Sample})/$A_{Control}$) x 100). The value of the half-maximal inhibitory concentration (IC_{50}) is then determined. The values of effective concentration (EC_{50}), antiradical power (ARP), and ascorbic acid equivalent antioxidant capacity (AEAC) were determined using the IC_{50}, respectively [14-18].

Statistical Analysis

The mean and standard deviation (mean ± SD) of the IC_{50} was used to express all data. The data were compared using a one-way ANOVA analysis, and all tests were deemed statistically significant at $p < 0.05$.

Results

Test for Phytochemical Screening

This test was carried out to determine the volatile compounds found in essential oils of myrtle and orange and whether they contain terpenes. Results of phytochemical screening tests on *Citrus sinensis* and *Myrtus communis* samples showed in Table 1. The results

show that the essential oils tested contain terpene and volatile substances.

Table 1. Phytochemical study of samples.

	Terpenoids	Essential oil
Citrus sinensis	+	+
Myrtus communis	+	+

Essential Oils Antioxidant Activities

The antioxidant capacity of the samples of essential oils rose as the IC_{50} value declined. The IC_{50} value displays the antioxidant activity when it is lower. If an antioxidant has low IC_{50}-EC_{50} and high ARP-AEAC values, it is known to be more potent. The essential oils (EO) were ranked in terms of antioxidant potency based on antioxidant criteria: AA (IC_{50}: 0.0111 ± 0.001 mg/mL)> *Myrtus communis* EO (IC_{50}: 2.810 ± 0.558 mg/mL)> *Citrus sinensis* EO (IC_{50}: 5.787 ± 0.994 mg/mL). AA has a stronger antioxidant potential when compared to the antioxidant characteristics of essential oils. These outcomes are those of nature. The antioxidant ascorbic acid is particularly effective. AA has the highest action as a result. However, it was discovered that myrtle and orange also showed antioxidant activity after statistical analysis. Results are given in Table 2.

Table 2. Antioxidant properties of the samples of essential oils.

	IC_{50} (mg/mL)	EC_{50} (mg/mL)	ARP (mL/mg)	AEAC
Ascorbic acid	0.0111 ± 0.001	0.289	345.260	-
***Citrus sinensis* EO**	5.787 ± 0.994[a]	140.089	0.7138	192.329
***Myrtus communis* EO**	2.810 ± 0.558[b]	70.831	1.411	396.080

EC_{50}: Effective concentration, ARP: Antiradical power, AEAC: Ascorbic acid equivalent antioxidant capacity. IC_{50} values expressed are means ± standard deviation of three measurements. The values of the superscript-containing essential oil samples differed considerably ($p \leq 0.05$).

Overview

Turkey has a remarkable variety of plants, which differ by area. There are over 10,000 vascular plants in its flora, and nearly one-third (34.4%) of them are native to the nation. The utilization of ethnobotanical data gathered from studies on therapeutic plants has recently attracted interest on a global scale. For this reason, a great deal has been written about medicinal plants in our nation and recently, numerous ethnobotanical studies have been published. The public has utilized these medicinal plants for folk medicine for a long time, thus knowledge on how to use them to heal illnesses has been passed down the centuries [1].

Turkish people have used herbal medicine to cure various common illnesses for generations. A core of the Mediterranean region with a wide variety of plants is the Taurus Mountains in Adana. As a result, traditional herbal remedies are essential for maintaining human life [19].

Antioxidants are substances that interact with free radicals to neutralize them and avert or lessen the harmful effects they have on the body. Antioxidants, whether synthetic or natural, are frequently added to lipids, fatty foods, and cosmetics in order to stop oxidation. Due to their carcinogenicity, synthetic antioxidants are no longer allowed to be utilized in products for human consumption, which has greatly increased interest in antioxidants of natural origin [4].

The cause of many diseases is reactive stress. A lot of work has been done to find natural antioxidants that could be used as medicines. Antioxidative activity has been measured in many different ways [20]. Because secondary metabolites like phenylpropanoids and essential oils are active, aromatic, and medicinal plants like myrtle and orange are a good source of natural antioxidants. Since ancient times, these plant essential oils and extracts have been employed in medications, alternative remedies, and food preservation [4, 6]. In this study, different results were found compared to the literature data. Numerous studies have shown a substantial correlation between phenolic content and the ability of plant extracts to serve as antioxidants. Anthocyanins, flavonoids, and phenolic acids appear to be particularly important for the antioxidant capacity. However, since essential oils contain terpenes (Table 1) as the main compounds, the results in our study are very natural as in Table 2. Myrtle essential oil is found to have more antioxidant activity than orange essential oil, according to this research. This shows that the substances in myrtle essential oil are more active than the substances in orange essential oil. However, both essential oils do not have as strong antioxidant properties as the standard ascorbic acid. Future research will focus on what drug or substance family this characteristic comes from.

Conclusion

Even though essential oils are known to have antioxidant properties, their use may be constrained due to changes in their chemical composition. The fluctuations in their chemical makeup can be attributed to a variety of factors, including the aromatic plant's harvest time, climatic and agronomic circumstances, the plant's vegetative development, the portion of the plant employed, and the method of extraction. Due to its potential as a preservative, cosmetic, or nutraceutical, essential oils have been the subject of research in the food and cosmetic industries. Studies have also demonstrated that the essential oil's constituent parts work in concert because, when used as a benchmark, the active compounds had lower levels than the essential oil. Studies on synergism and antagonism should be created as a result.

Conflicts of interest

All authors declare that they have no conflict of interest.

References

[1] Karahüseyin S., Aynur S., Plants used in traditional treatment against diarrhea in Turkey, *Istanbul J Pharm*, 49(1) (2019) 33-44.

[2] Favela-Hernández J.M.J., González-Santiago O., Ramírez-Cabrera M.A., Esquivel-Ferriño P.C., Camacho-Corona M. d. R., Chemistry and Pharmacology of Citrus sinensis, *Molecules*, 21(2) (2016) 247.

[3] Bouayed J., Bohn T., Nutrition, well-being and health. 2012: BoD–Books on Demand.

[4] Aleksic V., Knezevic P., Antimicrobial and antioxidative activity of extracts and essential oils of Myrtus communis L, *Microbiol Res.*, 169(4) (2014) 240-254.

[5] Abbate L., Tusa N., Del Bosco S. F., Strano T., Renda A., Ruberto G., Genetic improvement of Citrus fruits: New somatic hybrids from Citrus sinensis (L.) Osb. and Citrus limon (L.) Burm. F, *Food Res. Int.*, 48(1) (2012) 284-290.

[6] Etebu E., Nwauzoma A., A review on sweet orange (Citrus sinensis L Osbeck): health, diseases and management*, Am. J. Res. Commun.*, 2(2) (2014) 33-70.

[7] Bouzabata A., Cabral C., Gonçalves M.J., Cruz M.T., Bighelli A., Cavaleiro C., Casanova J., Tomi F., Salgueiro L., Myrtus communis L. as source of a bioactive and safe essential oil*, Food Chem. Toxicol.*, 75 (2015) 166-172.

[8] Hennia A., Miguel M.G., Nemmiche S., Antioxidant activity of myrtus communis l. and myrtus nivellei batt. & trab. extracts: a brief review*, Medicines*, 5(3) (2018) 89.

[9] Mimica-Dukić N., Bugarin D., Grbović S., Mitić-Ćulafić D., Vuković-Gačić B., Orčić D., Jovin E., Couladis M., Essential oil of Myrtus communis L. as a potential antioxidant and antimutagenic agents*, Molecules*, 15(4) (2010) 2759-2770.

[10] Richardson P.M., Phytochemical methods: a guide to modern techniques of plant analysis*, Brittonia*, 2(42) (1990) 115-115.

[11] Runde M., Kubmarawa D., Maina H., Compositional Analysis and Anti-Oxidant Assesment of Essential Oil of some Aromatic Plants Obtained from North-Eastern Nigeria*, Res J Chem Sci.* ISSN, 2231 (2015) 606X.

[12] Brand-Williams W., Cuvelier M.E., Berset C., Use of a free radical method to evaluate antioxidant activity, L*WT-Food Sci Technol*, 28(1) (1995) 25-30.

[13] Blois M. S., Antioxidant determinations by the use of a stable free radical*, Nature*, 181(4617) (1958) 1199-1200.

[14] Yamali C., Gul H.I., Sakarya M.T., Saglik B.N., Ece A., Demirel G., Nenni M., Levent S., Oner A.C., Quinazolinone-based benzenesulfonamides with low toxicity and high affinity as monoamine oxidase-A inhibitors: Synthesis, biological evaluation and induced-fit docking studies*, Bioorg. Chem.*, 124 (2022) 105822.

[15] Kayiran S.D., Özkan E.E., Kara E.M., Bekraş N.Y., Tari Ö., Nenni M., Determination of the chemical composition, antioxidant potential of Sambucus ebulus L.(dwarf elder) fruit extracts and investigation of antimicrobial activity on Trichophyton rubrum (Castell.) Sabour and some microorganisms*, Istanbul J Pharm*, 52(2) (2022) 148-155.

[16] Güven U.M., K. Serpil Demirci, Aygül A., Nenni M., Kirici S., Design of microemulsion formulations loaded Scutellaria salviifolia Benth, Sideritis libanotica Labill. subsp. linearis (Bentham) Bornm, and Ziziphora clinopodioides Lam. extracts from Turkey and in vitro evaluation of their biological activities*, Turk J. Bot*., 45(8) (2021) 789-799.

[17] Aynur S., Özsoy N., Karahüseyin S., Taraxacum farinosum Hausskn. & Bornm. bitkisinin antioksidan aktivite yönünden incelenmesi*, SABİAD*, 3(1) (2020) 13-19.

[18] Karahüseyin S., Aynur S., Ozsoy N., Antioxidant activity and three phenolic compounds from the roots of Taraxacum gracilens Dahlst, *Istanbul J Pharm*, 52(1) (2022) 69-72.

[19] Everest A., Ozturk E., Focusing on the ethnobotanical uses of plants in Mersin and Adana provinces (Turkey)*, J Ethnobiol. Ethnomed.*, 1(1) (2005) 1-6.

[20] Alipour G., Dashti S., Hosseinzadeh H., Review of pharmacological effects of Myrtus communis L. and its active constituents*, Phytother. Res.*, 28(8) (2014) 1125-1136.

Cumhuriyet Sci. J., 44(3) (2023) 474-484
DOI: https://doi.org/10.17776/csj.1310731

Cumhuriyet Science Journal

| csj.cumhuriyet.edu.tr | Founded: 2002 ISSN: 2587-2680 e-ISSN: 2587-246X Publisher: Sivas Cumhuriyet University

The Role of COVID-19 Vaccine Literacy in The Effect of e-Health Literacy on Vaccine Attitude

Rukiye Aslan [1,4,a,*], Ebrar Ilıman Yaltagil [2,b], Aysel Arslan[3,c], Ahmet Alim[4,d]

[1] *Department of Medical Services and Techniques, Vocational School of Health Services, Sivas Cumhuriyet University, 58140, Sivas, Türkiye*
[2] *Department of Health Tourism, Vocational School of Social Sciences, Sivas Cumhuriyet University, 58140, Sivas, Türkiye*
[3] *Department of Educational Sciences, Faculty of Education, Sivas Cumhuriyet University, 58140, Sivas, Türkiye*
[4] *Department of Medical Microbiology, Faculty of Medicine, Sivas Cumhuriyet University, 58140, Sivas, Türkiye*
**Corresponding author*

Research Article

History
Received: 07/06/2023
Accepted: 07/09/2023

ABSTRACT

Immunization is one of the most successful practices for the maintenance of public health. With the emergence pandemic, distant health services, in other words the e-Health concept, has gained importance. It was aimed to develop the COVID-19 vaccine attitude scale and to determine the effect of e-Health literacy on the impact of people's COVID-19 vaccine literacy levels on their vaccine attitudes, in this study. The COVID-19 vaccine attitude scale was developed by the researchers. The scale development process of the research started with the literature review. This process continued with creating an item pool, receiving expert opinions, piloting, and finalizing the scale. As a result of the research, the Cα value of the COVID-19 vaccine attitude scale was found to be 0.745. The total variance explanatory power of the scale was determined as 56,972. Confirmatory factor analysis was determined as χ2/sd = 4.902. In this context, the construct validity of the scale was confirmed. As a result of the research, it was determined that 90,4% of the participants had been vaccinated. It was concluded that the e-Health literacy of the participants was at a medium level (37.38±7.90), while their COVID-19 vaccine literacy was at a low level (30.88±7.34). It was concluded that the participants' attitudes towards vaccination were positive. It has been determined that the increase in the e-Health and COVID-19 vaccine literacy levels of the participants caused a positive increase in their attitudes toward the vaccine.

Keywords: COVID-19, Vaccine, Vaccine Literacy, e-Health, e-Health Literacy.

[a] raslan@cumhuriyet.edu.tr https://orcid.org/0000-0001-5843-626X
[b] ebrar@cumhuriyet.edu.tr https://orcid.org/0000-0002-5255-8482
[c] ayselarslan@cumhuriyet.edu. https://orcid.org/0000-0002-8775-1119
[d] ahmetalim@cumhuriyet.edu.tr https://orcid.org/0000-0001-9577-5965

Introduction

The discovery of the vaccine has been one of the turning points in the history of medicine. The first studies on vaccination were developed against smallpox in the 16th century. For this purpose, scabs were ground and snuffed into the nose in smallpox. This method has started to be used for vaccination purposes. This practice was discovered to generate protective immunization in humans. Modern vaccine studies were developed by Edward Jenner in 1976 against smallpox [1].

Immunization is one of the most successful practices for the maintenance of public health. The preventive immunization process is carried out with the vaccine. Vaccines are biological preparations that provide humoral or cellular immunity, which, when given to the organism in the right way, form specific antibodies against the disease-causing antigen by stimulating the immune system cells [2]. Due to the vaccine and vaccination, the mortality and morbidity rates of many infectious diseases have been reduced, and the continuation of public health throughout the world has been ensured. In this context, many diseases such as Smallpox, Measles, Rubella, Tetanus, Diphtheria, Poliomyelitis, Malaria, and Tuberculosis have been controlled by immunization. According to the World Health Organization (WHO), it is stated that an average of the 3 million people survive each year using vaccination. In addition to protection from infectious diseases, vaccination also contributes to public health and the country's economy, such as preventing antibiotic resistance, reducing the incidence of some cancer diseases, protecting against bioterrorism, and reducing health care costs [3].

Literacy is people's understanding of the meanings of certain symbols and their interpretation in life [4]. Health literacy is defined by WHO as the ability of people to access accurate and reliable health information sources and services to understand basic health information, protect and improve their well-being, and make correct health decisions by understanding this information [5]. Vaccine literacy is the period of accessing and processing basic health information and services, which are necessary for people to get the correct information about vaccines and make the right decisions about vaccination. It is the understanding and transfer of accurate information about vaccines to other people [6]. e-Health is the use of information and communication technologies with all its functions to improve the medical condition of people and increase openness to medical

services to provide efficient health services to all people in the health sector [7].

People advocated that the internet is the easiest and fastest way to access information, and it has a significant influence on understanding health-related topics. There are many studies in the literature that express the people researching and understanding the internet of health-related topics [8,9]. Insufficient levels of health literacy and vaccine literacy; cause the limitation of accessing and using the health services, irrational drug use, increase in incidence, morbidity, and mortality rates of diseases, spreading of infectious diseases, and disruption of public health order [10].

According to WHO data, 1.5 million people die every year from diseases that can be prevented by vaccination [11]. Negative attitudes towards vaccines occur in people due to many reasons, such as concerns about the content of vaccines, possible side effects of vaccines, religious beliefs, and information pollution on social media and the internet [11]. For the protection of public health, it is very important for people to have a sufficient vaccination literacy level. It is difficult for people who do not have sufficient health literacy and e-Health literacy levels to reach accurate and reliable information about vaccines due to reasons such as confusion of information about vaccines, unlimited sources of vaccine information on the internet and websites, and information pollution about vaccines in social media. The attitudes of these people towards vaccination are changing.

Although the vaccine provides the continuation of public health in terms of individual and social aspects, serious public health problems occur with the decrease in the rate of vaccination in the community as a result of vaccine hesitancy which is commonly encountered during the Coronavirus disease-19 (COVID-19) pandemic too. Today, the importance of e-Health literacy is a stubborn fact to easily access, understand, process, and evaluate correct and reliable information from today's electronic/digital sources for both COVID-19 vaccines and all vaccines.

When the literature in this context was examined, "*vaccine, attitude towards vaccines, anti-vaccination, vaccine acceptance, and health literacy*" studies had been conducted in the world and Türkiye, and no study had been found on attitudes toward e-Health literacy, and COVID-19-vaccines.

The COVID-19 pandemic, which started to be seen in 2019 and is thought to decrease in the middle of 2022, has affected the whole world and continues to affect it. On the other hand, not only this contagious disease but also the vaccines developed for the disease have become very important all over the world, and these issues have not been clarified. With the emergence of this pandemic, distant health services, in other words, the e-Health concept, has gained importance. In this context, it is important for people to be conscious.

The aim of this study is developing the COVID-19 vaccine attitude scale. Also, measuring people's e-Health and vaccine literacy levels and evaluate the impact of these concepts on people's attitudes toward vaccines and determine the effect of e-Health literacy on the impact of people's COVID-19 vaccine literacy levels on their vaccine attitudes. The research model and hypotheses developed in this direction are as follows:

H_1: The level of e-Health literacy has a positive effect on vaccination attitude.

H_2: The level of e-Health literacy has a positive effect on the COVID-19 vaccine literacy level.

H_3: The COVID-19 vaccine literacy level has a positive effect on the vaccine attitude.

H_4: The COVID-19 vaccine literacy level has an effect on the effect of e-Health literacy level on vaccination attitude.

Parallel to the purpose of the research, the research model that was developed is given in Figure 1.

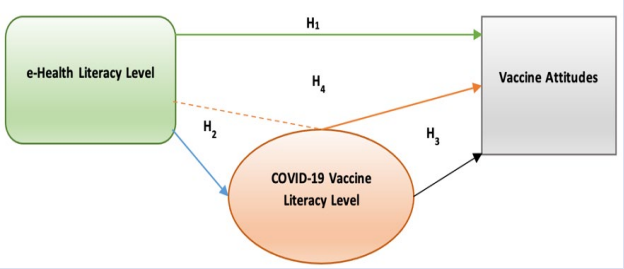

Figure 1. Research Model

Material and Methods

In this study, which was conducted with a quantitative research method, a valid and reliable scale was developed to determine the attitudes of patients towards medical practice errors. The scale development process started with a theoretical literature search. Studies on this subject have been examined in the literature. Finally, it has been determined that there is a gap in the literature on this subject. A research pattern was created in line with the studies and theoretical frameworks. In the second stage of scale development, İn order to create an item pool, all studies in the related literature were tried to be examined. After a comprehensive review of the entire literature, a 20-item pool was created to develop a scale measuring COVID-19 vaccine attitude. While creating the item pool, the items were prepared in such a way as to provide variety in the answers of the participants. While creating the item pool, it was decided to use a 5-point Likert scale (*strongly agree, agree, undecided, disagree, strongly disagree*) for the answers of the participants. Expert opinions were taken according to Davis technique for the content validity of the scale. Four-point ratings were requested as "*appropriate*", "*item should be slightly revised*", "*item should be seriously reviewed*" and "*item not appropriate*". In addition, whether there was any item they deemed necessary to be added to experts. In this context, the opinions of 15 people from different fields of expertise, including biostatisticians, health care workers, academics, and doctors, were taken. In the

fourth step of the scale development process, the items shaped in line with expert opinions were converted into a draft survey. After the formal structure of the scale in the draft survey was completed, the items were revised. A pilot study was conducted with a draft questionnaire on 50 people. At the end of the pilot study, the Cronbach's alpha value for the total reliability of the scale was checked, and it was decided to exclude two items from the form as they lowered the reliability coefficient value. Finally, the Cronbach's alpha value of 18 items was measured as 0.75, and this value gave a preliminary idea that the scale was reliable. After the pilot study, there was no problem with the form detected. Only two items were eliminated. Using this form, it was decided to start the actual data collection process.

In this study, face-to-face and online survey methods were preferred as data collection method. In this context, 1000 people were reached from many different parts of the world by using the convenience sampling method. In the study, three different scales were used. Inspired by Norman and Skinner (2006) [8], the "*e-Health Literacy Scale*" consists of 10 items and one sub-dimension. The Turkish validity and reliability of the scale were conducted by Coşkun and Bebiş in 2015 [12] and by Tamer-Gencer in 2017 [13]. The "*COVID-19 Vaccine Literacy scale*", developed by Ishikawa et al. [14] and adapted into Turkish by Durmuş et al. [15], consists of 12 items and two sub-dimensions. The scale was adapted as COVID-19 vaccine literacy by Biasio et.al. (2021) [16]. The first factor is called "*functional skills*" (FS) and consists of 4 items. The second factor is called "*critical skills*" (CS). The vaccine attitude scale, which was compiled from the studies of Kwok et al. 2020 [17]; Betsch et al. 2018 [18]; Nath et al. 2021 [19] and finalized by the researchers after taking specialist opinions, consists of 18 items and three sub-dimensions. The first dimension of the scale, which is 'belief in the usefulness of the vaccine', consists of seven judgment statements. The second dimension of the scale, which is 'vaccination rejection' and includes negative attitude, consists of seven judgment statements. The third dimension of the scale, which is the 'vaccine preference criteria', consists of four judgment statements. Ethical committee approval for this study; received from Sivas Cumhuriyet University Scientific Research and Publication Ethics Social and Human Sciences ethics committee on 29.04.2022 with the number 159562.

Results

In this part of the study, the findings obtained for the purpose of the study are presented. Approximately 2/3 of the people participating in the research are women, and more than half are single. The age range of the participants is between 16-37. It has been determined that the participants mostly work in the health and education sector, and the other participants are mostly students. Half of the people who responded to the survey stated that they had a low-income level. 45.7% of the participants are from different countries such as Netherlands, Germany, France, Qatar, Syria, and Afghanistan. Internet usage time of the participants mostly exceeds 2 hours a day, but the rate of participants doing health-related research on the internet is low. The demographic data of participants are given in Table 1.

Table 1. Demographic Data

Gender	**f**	**%**	**Age**	**f**	**%**
Women	654	65.4	16-26	525	52.5
Men	346	34.6	27-37	255	25.5
Marriage status			38-48	165	16.5
Single	582	58.2	49-59	55	5.5
Married	418	41.8	**Occupation**		
Country			Health Sector	153	15.3
Türkiye	543	54.3	Education Sector	240	24.0
Other	457	45.7	Student	354	35.4
Level of income			Housewife	51	5.1
Low	511	51.1	Retired	16	1.6
Middle	165	16.5	Self-employment	96	9.6
High	324	32.4	Unemployed	53	5.3
Internet usage time			Other	37	3.7
More than 2 hours a day	716	71.6	**Testing the health status in the last week**		
Average 1-2 hours a day	195	19.5	Yes	349	34.9
Every 2-3 days	68	6.8	No	651	65.1
Average 1-2 hours per week	21	2.1	**Total**	**1000**	**100.0**

According to the data obtained from the research, it was determined that 90.4% of the participants had been vaccinated. It was determined that the reasons for getting vaccinated by the participants were mostly because they thought it necessary to be vaccinated. The fact that vaccination is a state policy is the second reason why the participants are vaccinated. Table 2 shows vaccination status and reasons of the participants.

It was determined that the reliability levels of the scales used in the study were high and they came from a normal distribution. When the scale averages were examined; the mean score of the COVID-19 Vaccine Literacy Scale was determined to be low level, with a

score of 30.00; e-Health Literacy scale was determined to be moderate level with a score of 37.38; and the mean score of the Vaccine Attitude Scale was determined to be positive with a score of 58.

Table 2. Vaccination Status and Reasons

Reason for vaccination	f	%
Obligation (Government policy)	288	28.8
Social pressure	76	7.6
Because I thought it necessary	540	54.0
Total	**904**	**90.4**

Reason for not getting vaccinated	f	%
I'm afraid of the side effects of the vaccine	26	2.6
I don't trust the vaccine	50	5.0
I am against vaccination	6	0.6
I don't believe in vaccine protection	14	1.4
Total	**96**	**9.6**

Since the vaccine attitude scale was rearranged by the researchers, the EFA (Exploratory Factor Analysis) and CFA (Confirmatory Factor Analysis) analyzes were separately performed and reported. In addition, confirmatory factor analyzes of all the scales used in the study were performed again. It was seen that all scales were also confirmed for the valid sample. Table 3 shows the results related to the scales used in the study.

After this step firstly, a path analysis was conducted that measures the relationship between e-Health literacy and vaccination attitude. Subsequently, the COVID-19 vaccine literacy scale was added to the model as a mediator variable. The analysis results related to the models are presented in order.

Table 3. Results Related to the Scales Used in the Study

	n	Min	Max	Mean	Std. D.	Ca	Skewness		Kurtosis	
EHL Total	1000	10.00	50.00	37.38	7.90	.90	-.340	.077	-.351	.155
VL Total	1000	12.00	60.00	30.88	7.34	.86	-.314	.077	.518	.155
FC	1000	4.00	16.00	9.38	2.95	.78	.090	.077	-.405	.155
CS	1000	8.00	32.00	21.49	5.54	.86	-.331	.077	-.013	.155
VA Total	1000	18.00	90.00	58.47	9.63	.75	.012	.077	.743	.155
VBB	1000	7.00	35.00	23.62	6.95	.89	-.402	.077	-.308	.155
VR	1000	6.00	30.00	17.38	5.27	.80	-.184	.077	-.331	.155
VPC	1000	4.00	20.00	14.54	3.34	.70	-.244	.077	-.307	.155

Vaccination Attitude EFA

The factor loads of the expression's result of the factor analysis of 18 variables in the scale are between 0.54 and 0.83. It was determined that the scale consists of three dimensions with the TVA 56.972% ratio.

Table 4. EFA Results of the COVID-19 Vaccine Attitude Scale

Question Expression	The codes	Factors: Belief in Vaccine Benefit	Vaccine Rejection	Vaccine Preference Criteria	Factor Explanatory	Reliability
1	VA-1	.743			30.350	.893
2	VA-2	.769				
3	VA-3	.820				
4	VA-4	.830				
15	VA-15	.538				
16	VA-16	.614				
17	VA-17	.808				
5	VA-5		.748		18.698	.801
6	VA-6		.818			
7	VA-7		.764			
8	VA-8		.658			
9	VA-9		.699			
14	VA-14		.475			
18	VA-18		.590			
10	VA-10			.667	7.914	.703
11	VA-11			.745		
12	VA-12			.629		
13	VA-13			.702		

* TVA: 56.972; KMO Test: 0.849; Bartlett Test (χ2: 7234.970; sd: 136; p: 0.000). (Cα: 0.745)

* * TVA (Total Variance Explanation), KMO (Kaiser-Meyer-Olkin), df (degree of freedom)

Therefore, the overall reliability of the scale was determined as 0.745. These results probably indicate that the data were analyzed correctly (Table 4).

Vaccination Attitude CFA

After testing the structural validity with exploratory factor analysis, the first-level multi-factor CFA model was used to test the suitability of the scale used for the sample. The Vaccine Attitude Scale's model fit values are given in Table 5, the regression coefficients are given in Table 6, and the model fit diagram is given in Figure 2.

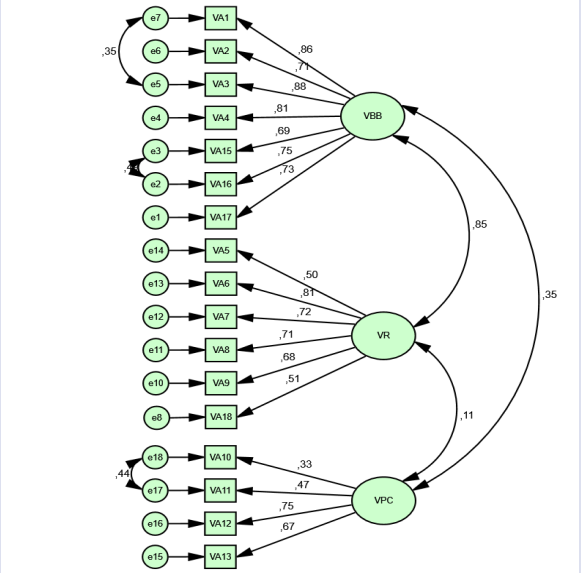

Figure 2. DFA Diagram of the Vaccine Attitude Scale

Table 5. Measuring Model Fit Indexes of Vaccine Attitude Scale

Measuring Model	p	χ2/sd	GFI	AGFI	NFI	IFI	TLI	RMSEA
Reference Values		≤ 5	≥ 0.850	≥ 0.850	≥ 0.900	≥ 0.900	≥ 0.900	≥0.080
Vaccine Attitude Scale Values (With modification)	0.000	4.902	0.906	0.863	0.901	0.920	0.912	0.084

When the vaccine attitude scale values goodness-of-fit indexes are examined, it can be said that after the modified DFA, the model is an acceptably fit since all values are at reference values. Table 5 shows measuring model fit indexes of vaccine attitude scale.

Table 6 shows parameter values of the measurement model of vaccination attitude. When Table 6 containing the parameter values of the measurement model is examined, it is seen that the SRA values vary between 0.332 and 0.883, and therefore, there is no SRA value below 0.30. In this context, no variables were removed from the model. In addition, it was determined that the paths representing the relationships among all latent variables were significant ($p<0.05$).

Table 6. Parameter Values of the Measurement Model of Vaccination Attitude

			Prediction	SRA	SH	T	p
VA17	<---	VBB	1.000	.728			0.000
VA16	<---	VBB	.999	.752	.056	17.811	0.000
VA15	<---	VBB	.904	.686	.053	16.924	0.000
VA4	<---	VBB	1.063	.811	.057	18.783	0.000
VA3	<---	VBB	1.374	.883	.066	20.958	0.000
VA2	<---	VBB	1.114	.714	.067	16.698	0.000
VA1	<---	VBB	1.312	.856	.070	18.615	0.000
VA18	<---	VR	1.000	.512			0.000
VA14	<---	VR	.946	.365	.102	11.870	0.000
VA9	<---	VR	1.395	.678	.123	11.345	0.000
VA8	<---	VR	1.447	.708	.128	11.266	0.000
VA7	<---	VR	1.251	.724	.107	11.665	0.000
VA6	<---	VR	1.522	.813	.128	11.918	0.000
VA5	<---	VR	.865	.503	.094	9.160	0.000
VA13	<---	VPC	1.000	.670			0.000
VA12	<---	VPC	1.187	.754	.134	8.860	0.000
VA11	<---	VPC	.932	.473	.177	5.259	0.000
VA10	<---	VPC	.771	.332	.173	4.456	0.000

In the 18-item vaccine attitude precursors within the scope of the research model, the latent variables "Belief in Vaccine Benefit" (VBB) with 7 items, "Vaccine Rejection" (VR) with 7 items, and "Vaccine Preference Criteria" (VPC) with 4 items were handled and examined as the first level multifactor model in the CFA process. When the factor loads of the variables in the vaccination attitude scale were examined, it was determined that the factor loads of all items varied between 0.33 and 0.88. It was determined that there were no problematic items in any of the sub-dimensions of the scale. When the results obtained from the study were evaluated together, it was found that the scale was reliable and valid (Table 5,6; Figure 2).

Testing the Structural Equation Models

In our research for model building, two types of statistical models were designed: measurement model (CFA) and structural model that tests the relationship between variables (SEM). The CFA models were statistically validated for the sake of compatibility with the data. Statistical Validation Tests of the developed SEM model are given in this section.

SEM Model of the Relationship between e-Health Literacy and Vaccination Attitude

The SEM results that were developed to test the H1 hypothesis are presented below. Model fit values are given in Table 7. Regression coefficients are given in Table 8. The model fit diagram is shown in Figure 3.

Table 7. Fit Indexes of the Effect of e-Health Literacy on Vaccination Attitude

Measuring Model	p	χ2/sd	GFI	AGFI	NFI	IFI	TLI	CFI	RMSEA
Reference Values		≤ 5	≥ .850	≥ 0.850	≥ 0.900	≥ 0.900	≥ 0.900	≥ 0.950	≥ 0.080
Model 1 Values (With modification)	0.000	4.441	0.853	0.851	0.917	0.936	0.912	0.952	0.079

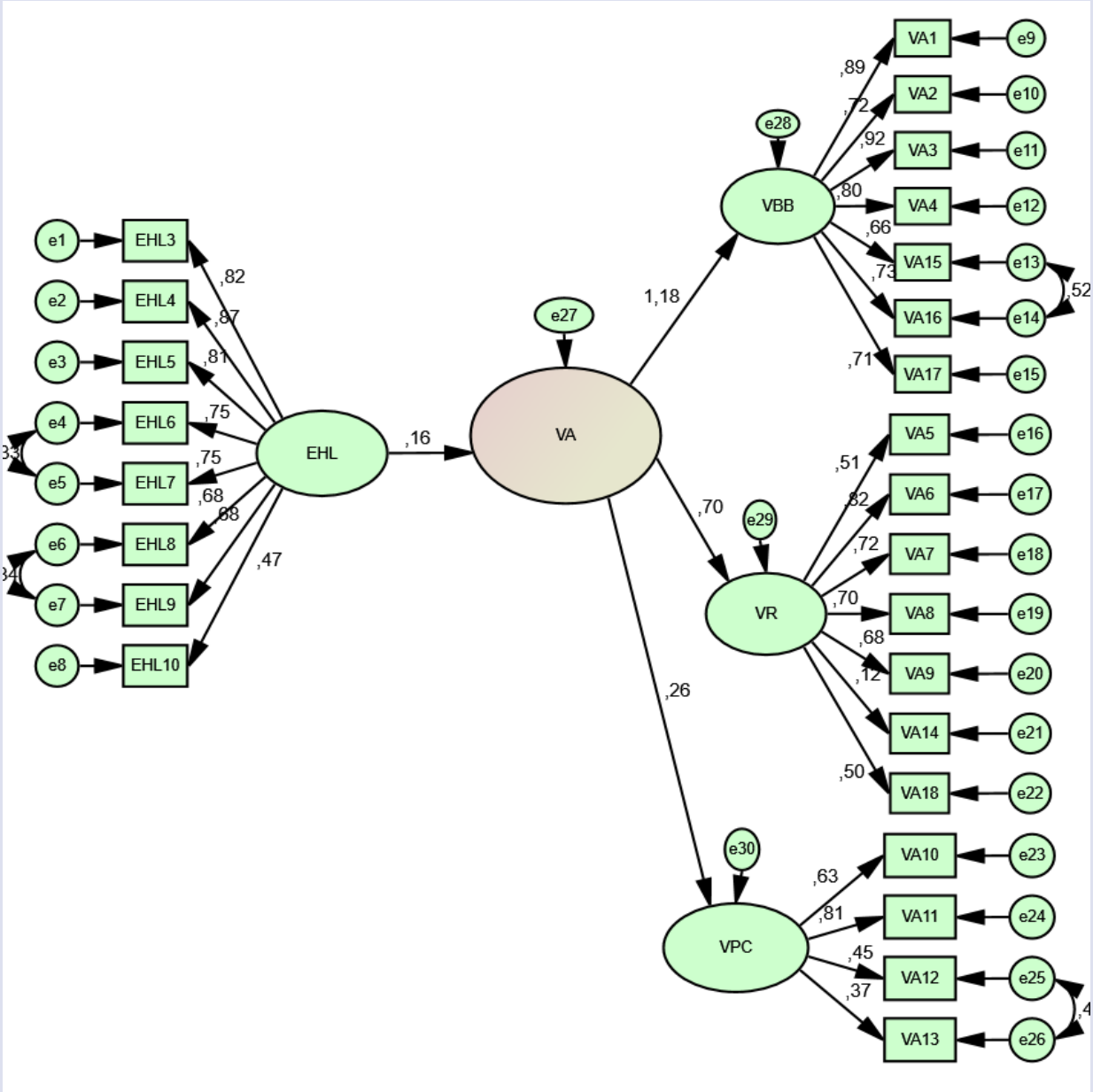

Figure 3. The Effect of e-Health Literacy on Vaccination Attitude Diagram

It was determined that the variables in the model were in acceptable threshold values after the modification. Therefore, the Model adjusts well to the data. Model parameter values are given in Table 8.

When the data in Table 8 are analyzed, it is seen that the relationships between factor loadings and latent variables are significant since the *p* values are less than *0.01* in all relationships.

In order to test the H1 (*The level of e-Health literacy has a positive effect on vaccination attitudes*) hypothesis, the implicit variable structural model in which e-Health literacy is an exogenous variable and vaccine attitude is an endogenous variable was tested. When the data in Figure 3 and Table 8 are analyzed, it was determined that e-Health literacy predicted vaccination attitude (ß=.16; *p<.01*) as a result of the path coefficient (ß) showing the total effect without the mediating variables. Therefore, the H1 hypothesis was accepted.

Table 8. Model 1 Parameter Values

			Prediction	SRA	SH	T	p
VA	<---	EHL	.296	.164	.069	4.317	0.000
VBB	<---	VA	1.000	1.183			0.000
VR	<---	VA	.283	.702	.053	5.362	0.000
VPC	<---	VA	.139	.256	.037	3.764	0.000
EHL3	<---	EHL	1.000	.816			0.000
EHL4	<---	EHL	1.118	.871	.047	23.780	0.000
EHL5	<---	EHL	.974	.808	.045	21.468	0.000
EHL6	<---	EHL	.959	.753	.049	19.422	0.000
EHL7	<---	EHL	.858	.751	.044	19.351	0.000
EHL8	<---	EHL	.816	.684	.047	17.197	0.000
EHL9	<---	EHL	.838	.678	.049	17.006	0.000
EHL10	<---	EHL	.619	.472	.056	11.140	0.000
VA1	<---	VBB	1.000	.889			0.000
VA2	<---	VBB	.839	.719	.041	20.494	0.000
VA3	<---	VBB	1.061	.918	.033	32.481	0.000
VA4	<---	VBB	.797	.802	.032	24.675	0.000
VA15	<---	VBB	.661	.663	.036	18.131	0.000
VA16	<---	VBB	.721	.726	.035	20.842	0.000
VA17	<---	VBB	0.725	0.714	0.036	20.298	0.000
VA5	<---	VR	1.000	0.505			0.000
VA6	<---	VR	1.751	0.819	0.149	11.741	0.000
VA7	<---	VR	1.345	0.722	0.121	11.108	0.000
VA8	<---	VR	1.643	0.704	0.150	10.973	0.000
VA9	<---	VR	1.514	0.681	0.140	10.794	0.000
VA14	<---	VR	0.259	0.123	0.097	2.673	0.000
VA18	<---	VR	1.102	0.503	0.122	9.022	0.000
VA10	<---	VPC	1.000	0.632			0.000
VA11	<---	VPC	1.100	0.814	0.124	8.847	0.000
VA12	<---	VPC	0.637	0.448	0.077	8.247	0.000
VA13	<---	VPC	0.502	0.366	0.073	6.909	0.000

Mediated Structural Model

The SEM results developed to test the $H_{2\text{-}3\text{-}4}$ hypotheses are presented below.

Model fit values are given in Table 9. Regression coefficients are given in Table 10. The model fit diagram is shown in Figure 4. It was determined that the variables in the model were in acceptable threshold values after the modification. Therefore, the Model adjusts well to the data. Mediated structural model parameter values are given in Table 10.

When the data in Table 10 are analyzed, it is seen that the relationships between factor loadings and latent variables are significant since the *p* values are less than *0.01* in all relationships. The path analysis test based on the bootstrap method was conducted to test whether COVID-19 vaccine literacy has a mediating role in the effect of e-Health literacy on vaccine attitude through mediated structural model analysis. According to the bootstrap results, it can be said that the indirect effect of e-Health literacy on vaccine attitude is significant (ß=.16) even after adding the COVID-19 vaccine literacy mediator variable. Therefore, it can be stated that the H4 hypothesis is accepted (ß=.16, 95% CI [.016, 1.05]).

Table 9. Mediated Structural Model Fit Index

Measuring Model	p	χ2/sd	GFI	AGFI	NFI	IFI	TLI	CFI	RMSEA
Reference Values		≤ 5	≥ 0.850	≥ 0.850	≥ 0.900	≥ 0.900	≥ 0.900	≥ 0.950	≥ 0.080
Model 2 Values (With modification)	0.000	4.389	0.874	0.862	0.917	0.912	0.916	0.952	0.079

Table 10. Parameter Values of the Mediated Structural Model

			Prediction	SRA	SH	T	p
Vaccination Literacy	<---	e-Health Literacy	.124	.326	.032	3.864	0.000
Vaccine Attitude	<---	e-Health Literacy	.381	.394	.043	8.927	0.000
Vaccine Attitude	<---	Vaccination Literacy	.413	.162	.081	5.108	0.000
VBB	<---	Vaccine Attitude	.810	.663	.078	10.382	0.000
VR	<---	Vaccine Attitude	-.372	-.383	.048	-7.797	0.000
VPC	<---	Vaccine Attitude	1.000	1.023			0.000
FB	<---	Vaccination Literacy	1.000	.403			0.000
EB	<---	Vaccination Literacy	2.740	1.302	.648	4.226	0.000
EHL3	<---	e-Health Literacy	1.000	.713			0.000
EHL4	<---	e-Health Literacy	1.124	.793	.047	23.723	0.000
EHL5	<---	e-Health Literacy	1.057	.777	.045	23.276	0.000
EHL6	<---	e-Health Literacy	1.112	.805	.046	24.073	0.000
EHL7	<---	e-Health Literacy	1.065	.793	.045	23.723	0.000
EHL8	<---	e-Health Literacy	.925	.700	.044	20.962	0.000
EHL9	<---	e-Health Literacy	.862	.637	.045	19.077	0.000
EHL10	<---	e-Health Literacy	.789	.542	.048	16.300	0.000
VA1	<---	VBB	1.000	.687			0.000
VA2	<---	VBB	1.002	.682	.045	22.391	0.000
VA3	<---	VBB	1.133	.771	.041	27.312	0.000
VA4	<---	VBB	1.026	.759	.049	21.010	0.000
VA15	<---	VBB	.877	.691	.046	19.199	0.000
VA16	<---	VBB	.947	.747	.046	20.615	0.000
VA17	<---	VBB	.973	.744	.047	20.670	0.000
VA5	<---	VR	1.000	.591			0.000
VA6	<---	VR	1.259	.726	.075	16.683	0.000
VA7	<---	VR	1.175	.714	.071	16.522	0.000
VA8	<---	VR	1.078	.620	.072	15.067	0.000
VA9	<---	VR	1.120	.660	.071	15.715	0.000
VA14	<---	VR	.850	.487	.068	12.554	0.000
VA18	<---	VR	.788	.497	.062	12.769	0.000
VA10	<---	VPC	1.000	.607			0.000
VA11	<---	VPC	.899	.596	.063	14.225	0.000
VA12	<---	VPC	1.081	.695	.069	15.667	0.000
VA13	<---	VPC	.800	.542	.060	13.280	0.000
VL4	<---	FB	1.000	.734			0.000
VL3	<---	FB	.779	.614	.046	16.907	0.000
VL2	<---	FB	1.006	.778	.050	20.064	0.000
VL1	<---	FB	.773	.621	.045	17.083	0.000
VL12	<---	EB	1.000	.663			0.000
VL11	<---	EB	1.043	.658	.058	17.929	0.000
VL10	<---	EB	1.058	.663	.059	18.042	0.000
VL9	<---	EB	1.145	.735	.058	19.639	0.000
VL8	<---	EB	1.124	.663	.062	18.034	0.000
VL7	<---	EB	1.049	.690	.056	18.611	0.000
VL6	<---	EB	.832	.552	.055	15.264	0.000
VL5	<---	EB	.913	.579	.057	16.055	0.000

Likewise, the direct effect of COVID-19 vaccine literacy on vaccine attitude appears to be significant in this model. (ß=.198; *p<.05*). In addition, according to the results of mediated structural model analysis, to which all variables were added, it was determined that the overall effect of e-Health literacy level on vaccination attitude was significant and 0.39 (ß=.394; *p<.01*). Also, the overall effect on the mediating variable COVID-19 vaccine literacy was found to be significant and 0.33 (ß=.326; *p<.01*). Hence, the $H_{2\text{-}3}$ hypotheses were accepted.

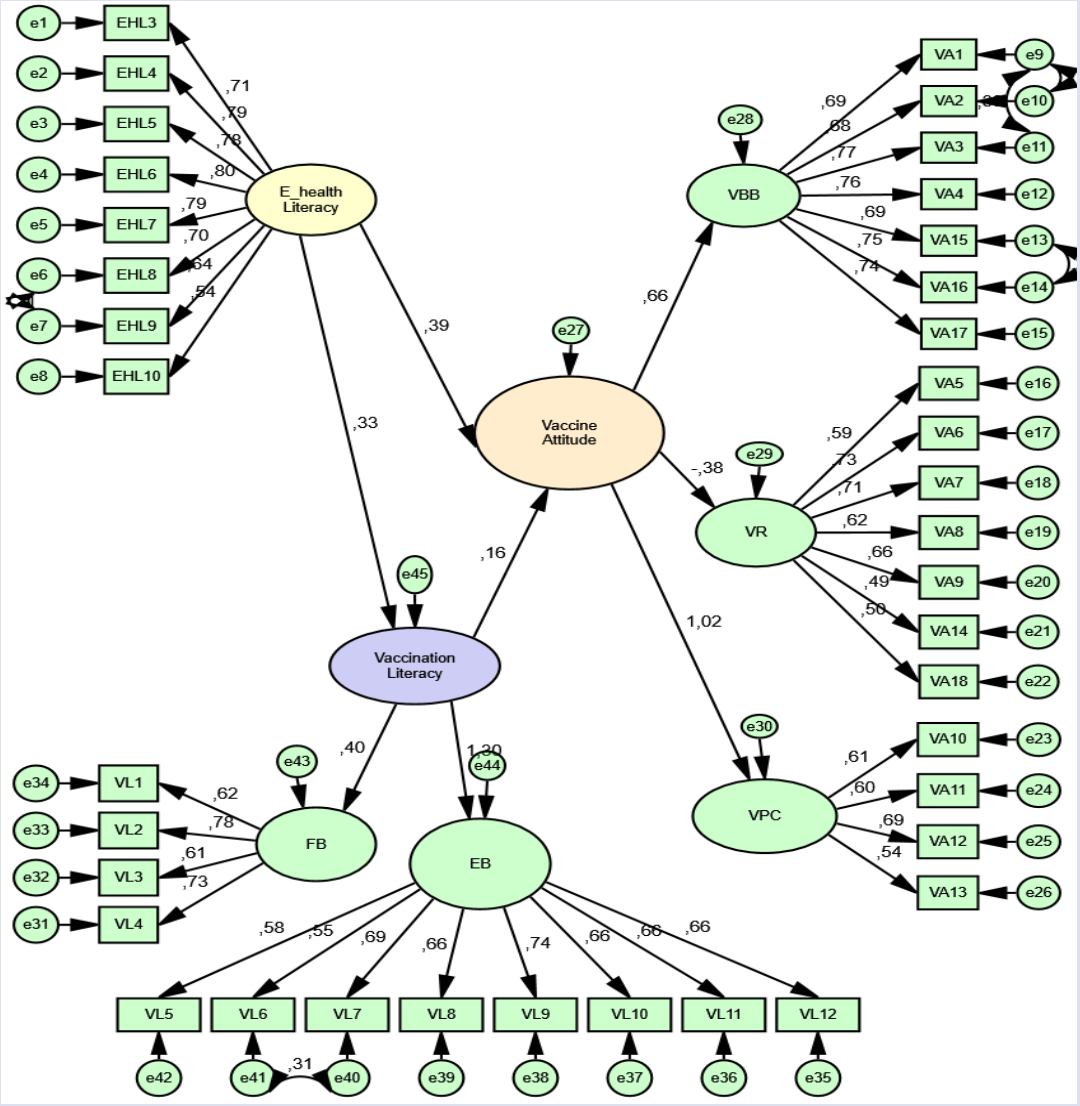

Figure 4. Mediated Structural Model Diagram

Discussion

In this study, which was conducted to develop the COVID-19 vaccine attitude scale, a scale consisting of 18 items and 3 factors was developed. As a result of the statistical analyzes, it was determined that the scale was valid and safe. As a result of this research, which was conducted to determine the COVID-19 vaccine literacy has a role in the effect of e-Health literacy on vaccine attitude, it was defined that almost all of the participants were vaccinated. It was determined that the e-Health literacy of the participants was at a moderate level, and their COVID-19 vaccine literacy was at a low level. It was concluded that the participants' attitudes towards the vaccine were positive. It was determined that the increase in e-Health and COVID-19 vaccine literacy levels of the participants caused their attitudes towards vaccines to increase positively. Also, it was determined the role of COVID-19 vaccine literacy level in the effect of e-Health literacy level against vaccine attitude.

When the literature is examined, it has been noticed that in societies with low health literacy levels, the reason for this situation is related to the lack of knowledge and inadequacy in hygiene. As a result, it has been determined that there is an increase in the rate of people being affected by infectious diseases and a decrease in the response to the treatment applied. In addition, due to chronic diseases, it has been determined that the high economic burden on health institutions, due to the increase in hospitalization rates and morbidity and mortality rates [20].

Vaccine rejection has become one of the notable issues today. Many parameters were effective among the reasons for the hesitations about the vaccine experienced in the COVID-19 pandemic, such as inadequacy of individual health literacy, the inadequacy of prophylaxis, doubts about the vaccines developed due to time constraints, and the inadequate information of vaccines' side effects. The importance of these factors should not be overlooked in the decisions affecting the vaccination attitude. It is very momentous to examine the relationship between these factors and health

literacy. The increase in health literacy should not be accepted as an increase in the positive attitude toward vaccines. This should be understood as people knowing to protect their health interests. However, the correct determination of the reasons for vaccine hesitancy will pave the way for the formation of the right strategies while making new vaccination plans [21]. In the study conducted by Nath, Imtiaz, Nath, and Hasan (2021) [19], they examined the impact of young adults' vaccine hesitancy, e-health literacy, and vaccine literacy levels on getting a COVID-19 vaccine. It was determined that the most effective predictor of the participants being vaccinated is vaccination hesitancy, in the results. In addition, a positive association between e-Health literacy and vaccine acceptance was determined. It has been stated that the announcing the current developments regarding vaccine safety through official and secure channels is effective in eliminating the hesitations of young adults about vaccination.

People's attitudes toward the COVID-19 vaccine affect their decisions about whether or not to get vaccinated [22]. Wilson and Wiysonge (2020) [23] detected that social media posts highly affect vaccination attitudes. Since COVID-19 vaccines are still being developed, the lack of a clear balance of benefit and harm can be a determining factor, especially for autoimmune patients.

Gendler and Ofri (2021) [24] investigated the thinking of parents' to vaccinate their children" in their study in Israel. It was determined in the study that the vaccination literacy of the parents was at a moderate level. Also, it was found that as the vaccination literacy level of the parents increased, they experienced less hesitance about vaccination. Vaccine hesitancy for the COVID-19 vaccine can be overcome by scientific evidence, consistent and clearly presented information, healthy communication, and raising the health literacy of those who provide and demand information. Despite the efforts of scientists and medical experts regarding the COVID-19 pandemic, the low level of health literacy and negative vaccination attitudes in the general population present a serious obstacle to the campaigns carried out all over the world on this regard. In the study conducted by Gusar et al. (2021) [25], it was determined that the vaccine literacy of the participants was at a moderate level.

Another study conducted to understand vaccine hesitancy and determine the level of health literacy was carried on in the United States by Willis et al. (2021). It was determined that approximately one-fifth of the participants had hesitations about vaccination. There is no trust in vaccines in general, university graduates have more hesitations about vaccination, fear of infection, and the belief that vaccination will increase existing health inequalities were among the other findings.

In the study conducted by Costantini (2021) [26], the vaccination status and vaccination literacy levels of elderly people in Japan were examined. It has been determined that the people who care for their elderly-parents have a lower level of vaccination literacy than their health literacy.

While vaccination is an effective way to combat COVID-19, vaccine hesitation is also seen to be a hindering factor in the fight against the disease. The findings obtained in the studies conducted indicate that behavior that reveals vaccine rejection is not a simple decision that can be expressed as acceptance or rejection; there are many different factors, such as lack of information, negative perception about vaccines, conspiracy theories, and religious reservations. In the study conducted by Harada and Watanabe (2022) [27], it was concluded that the psychological and emotional states of people, such as anxiety and risk perception affect the vaccination attitude.

In the study conducted by Turhan et al. (2021) [28], it was determined that not relying on vaccination affects vaccination hesitancy. It was concluded that people with a low level of health literacy and low trust in the health system experience a higher level of vaccination hesitancy. In a study conducted by students by Çetin et al. (2021) [29], it was determined that students' hesitations about vaccination are high. It is noteworthy that hesitancy about vaccination is high, especially among students studying in the branches of health. Because it is the health workers who need to raise awareness of the public about vaccination. In this context, it is substantial to revise the course contents of health education departments in universities and to raise awareness among students about vaccines.

Conclusion

WHO defined vaccine hesitancy as a major threat to global health due to the resurgence of vaccine-preventable diseases, although there have been great advances in vaccines in the last century. Vaccine hesitancy should not be perceived only as a concept related to the COVID-19 vaccine; it should not be overlooked that it has become widespread concerning many vaccines. Social media posts about anti-vaccination increase vaccine hesitancy. Globally, access to technology and social media platforms is increasing. Social media users not only have easy access to information but also create content themselves. Public confidence in the future development of vaccines for new pathogens such as SARS-CoV-2 is being shaken, due to significant public health concerns, which are fueled by anti-vaccine messages on social media [30]. The emergence of vaccine rejection in the COVID-19 pandemic has led to an increase in deaths related to this disease. It is necessary to develop different and innovative strategies to overcome vaccine hesitation. In the prevention of anti-vaccine movements, the development of vaccines with proven safety, strict implementation of vaccine control, and inclusion of compensations for the victims who suffered as a result of vaccination are important. Many different solutions need to be developed for those who fully accept the vaccine,

the responses for those who hesitate, and those who reject all vaccines completely [2].

Conflict of Interest

The authors stated that did not have conflict of interests.

References

[1] Riedel S., Edward Jenner and the History of Smallpox and vaccination. Baylor University Medical Center Proceedings Taylor & Francis, (2005).

[2] Dube E., Vivion M., Mac Donald N.E., Vaccine hesitancy, vaccine refusal and the anti-vaccine movement: influence, impact and implications, *Expert Review of Vaccines,* 14(1) (2014) 99-117.

[3] Andre F.E., Booy R., Bock H.L., Clemens J, Datta S.K., John T.J. et al., Vaccination greatly reduces disease, disability, death and inequity worldwide, *Bulletin of the World Health Organization,* 121 (2008) 28-35.

[4] Young S., Macrae C., Cairns G., Pia A., Adult literacy and numeracy in Scotland, Scotland: The Scottish Government Publications, (2001).

[5] Nutbeam D., Health literacy as a public health goal: a challenge for contemporary health and communication strategies into the 21st century. *Health Promotion International,* 15 (3) (2000) 259-267.

[6] Biasio L.R., Vaccine literacy and undervalued. *Hum. Vaccin. Immunother,* 15 (2552) (2014) 3.

[7] Özer Ö., Şantaş B., Budak F., Examining the usage levels of health websites: a sample application, *E-Journal of Faculty of Communication,* 4(1) (2014) 128-40.

[8] Norman C.D., Skinner H.A., eHEALS: The ehealth literacy scale, *Journal of Medical Internet Research*, 8 (4) (2006) 1-7.

[9] Birru M.S., Monaco V.M., Charles L., Drew H., Njie V., Bierria T. et all., Internet usage by low-literacy adults seeking health information: an observational analysis, *Journal of Medical Internet Research*, 6(3) (2004) 25-29.

[10] Kalaça S., Sağlık okuryazarlığı ve internet. *15. Ulusal Halk Sağlığı Kongresi Bursa*, (2012) 126-30.

[11] World Health Organization. Vaccines and immunization. (2004). https://www.who.int/health-topics/vaccines-and-immunization.

[12] Coşkun S., Bebiş H., Adolesanlarda e-sağlık okuryazarlığı ölçeği: Türkçe geçerlik ve güvenirlik çalışması, *Gülhane Tıp Dergisi,* 57 (4) (2015) 378-384.

[13] Tamer-Gencer Z., Norman ve Skinner'in e-sağlık okuryazarlığı ölçeğinin kültürel uyarlaması için geçerlilik ve güvenilirlik çalışması, *İstanbul Üniversitesi İletişim Fakültesi Dergisi* ,1 (2017) 131-145.

[14] Ishikawa H., Takeuchi T., Yano E., Measuring functional, communicative, and critical health literacy among diabetic patients, *Diabetes Care,* 31 (5) (2008) 874-879.

[15] Durmuş A., Akbolat M., Amarat M., COVID-19 aşı okuryazarlığı ölçeğinin Türkçe geçerlilik ve güvenirliliği, *Cukurova Medical Journal,* 46 (2) (2021) 732-741.

[16] Biasio L.R., Bonaccorsi G., Lorini C., Pecorelli S., Assessing COVID-19 vaccine literacy: a preliminary online survey, *Human vaccines & Immunotherapeutics,* 17 (5) (2021) 1304-1312.

[17] Kwok K.O., Li K.K., Wei W.I., Tang A., Wong S.Y.S., Lee S.S., Influenza vaccine uptake, COVID-19 vaccination intention and vaccine hesitancy among nurses: a survey, *International Journal of Nursing Studies*, 114 (2021) 103854.

[18] Betsch C., Schmid P., Heinemeier D., Korn L., Holtmann C., Bohm R., Beyond confidence: development of a measure assessing the 5C psychological antecedents of vaccination, *PLoS ONE*, 13 (12) (2008) 12-25.

[19] Nath R., Imtiaz A., Nath S.D., Hasan E., Role of vaccine hesitancy, eHealth literacy, and vaccine literacy in young adults' COVID-19 vaccine uptake intention in a lower-middle-income country, *Vaccines,* 9(12) (2021) 1405.

[20] Akbal E., Gökler M.E., COVID-19 salgını sürecinde eksikliği ortaya çıkan bir gerçek: sağlık okuryazarlığı, *STÜDAM Halk Sağlığı Dergisi,* 5 (2020) 148-155.

[21] Biasio L.R., Vaccine hesitancy and health literacy, *Human Vaccines & Immunotherapeutics,* 13 (3) (2017) 701-702.

[22] Mir H.H., Parveen S., Mullick N.H., Nabi S., Using structural equation modeling to predict Indian people's attitudes and intentions towards COVID-19 vaccination, *Diabetes & Metabolic Syndrome: Clinical Research & Reviews,* 15(3) (2021) 1017-1022.

[23] Wilson S.L, Wiysonge C., Social media and vaccine hesitancy, *BMJ Global Health,*5 (10) (2020) e004206.

[24] Gendler Y., Ofri L., Investigating the influence of vaccine literacy, vaccine perception and vaccine hesitancy on Israeli parents' acceptance of the COVID-19 vaccine for their children: a cross-sectional study, *Vaccines,* 9 (12) (2021) 1391-1399.

[25] Gusar I., Konjevoda S., Babić G., Hnatešen D., Čebohin M., Orlandini R., Dželalija B., Pre-Vaccination COVID-19 vaccine literacy in a Croatian adult population: a cross-sectional study, *International Journal of Environmental Research and Public Health,* 18 (13) (2021) 7070-7075.

[26] Costantini H., COVID-19 vaccine literacy of family careers for their older parents in Japan, *In Healthcare,* 9 (8) (2021) 1038-1345.

[27] Harada T., Watanabe T., Changes in vaccine hesitancy in Japan across five months during the COVID-19 pandemic and its related factors, *Vaccines,* 10 (1) (2021) 13- 25.

[28] Turhan Z., Dilcen H.Y., Dolu İ., The mediating role of health literacy on the relationship between health care system distrust and vaccine hesitancy during COVID-19 pandemic, *Current Psychology,* 41(11) (2022) 8147-8156.

[29] Çetin A., Şaşmaz A., Kurtuluş D., Badur İ., Balkan İ.İ., Owiwi M. et all., Sağlık öğrencilerinde aşı tereddüdü, *Anatolian Clinic the Journal of Medical Sciences,* 26(3) (2021) 39-248.

[30] Puri N., Coomes E.A., Haghbayan H., Gunaratne K., Social media and vaccine hesitancy: new updates for the era of COVID-19 and globalized infectious diseases, *Human Vaccines & Immunotherapeutics,* 16 (11) (2020) 2586-2593.

Cumhuriyet Sci. J., 44(3) (2023) 485-490
DOI: https://doi.org/10.17776/csj.1319590

Cumhuriyet Science Journal

| csj.cumhuriyet.edu.tr | Founded: 2002 ISSN: 2587-2680 e-ISSN: 2587-246X Publisher: Sivas Cumhuriyet University

Determination of Caffeine in Human Plasma by Using Liquid Chromatography-Tandem Mass Spectrometry

Fırat Yerlikaya[1,2,3,a,*], Onursal Sağlam[4,b]

[1] Elixir İlaç Araştırma ve Geliştirme AŞ, Ankara, Türkiye
[2]Galventa AG, St. Gallen, Switzerland
[3]Department of Pharmaceutical Technology, Faculty of Pharmacy, Lokman Hekim University, Ankara, Türkiye
[4]Novagenix Biyoanalitik İlaç Ar-Ge Merkezi San. ve Tic. AŞ, Ankara, Türkiye
*Corresponding author

Research Article

History
Received: 24/06/2023
Accepted: 28/08/2023

ABSTRACT

A liquid chromatography-tandem mass spectrometry (LC-MS/MS) method was developed and validated to determine caffeine (CAF) in human plasma. The plasma samples were extracted by protein precipitation using CAF-D3 as an internal standard (IS). The chromatographic separation was performed on GL Sciences InertSustain C18 Column (4.6 x 50 mm, 5 µm) maintained at 40 °C with a mobile phase consisting of formic acid, water, and methanol at a 1 mL/min of flow rate using two separate lines. CAF was detected and identified by mass spectrometry with electrospray ionization (ESI) in positive ions and multiple-reaction monitoring (MRM) mode. The MRM transitions of m/z 195.10 > 138.00 for CAF and 198.10 > 141.10 for IS were used for quantification. The standard curve was linear in the range of 10 - 10000 ng/mL for CAF. The within-batch precision and accuracy were evaluated by analyzing QC samples at five different concentration levels with six replicates in a batch. The between-batch precision and accuracy were determined by analyzing three different batches. The within-batch accuracy and precision was -8.76% - 9.61% and 0.95% - 7.22%, respectively. The between-batch accuracy and precision was -7.47% -1.42% and 1.83% - 8.66%, respectively. The results of the intra- and inter-day precision and accuracy studies were within the limits. The validated method applied to a pharmacokinetic study and the test product containing 60 mg CAF administered to total of 12 subjects. The mean ± SD of maximum plasma concentration (Cmax) was found to be 147.94 ± 139.39 ng/mL and the mean ± SD of area under the plasma concentration-time curve from zero to last measurable concentration (AUC0-tlast) was found to be 1119.59 ± 1468.30 h.ng/mL for the fasting conditions. The median time to reach peak plasma concentration (Tmax) was found to be 12.00 (6.50 - 12.00). The developed and validated method can be used for bioavailability and bioequivalence studies in human plasma samples..

Keywords: Caffeine, Caffeine-D3, human plasma, LC-MS/MS

[a] *firat.yerlikaya@elixirlabs.com.tr* *https://orcid.org/0000-0003-4648-3258* [b] *osaglam@novagenix.com* *https://orcid.org/0000-0002-1421-6633*

Introduction

CAF is a naturally occurring stimulant found in coffee, tea, and various other plants. It is a central nervous system stimulant that can increase alertness and reduce fatigue. CAF works by blocking the action of adenosine, a neurotransmitter that normally slows down brain activity and causes drowsiness. By blocking adenosine, CAF allows other neurotransmitters like dopamine and norepinephrine to become more active, leading to increased alertness and a feeling of wakefulness. It is also found in some medications, such as pain relievers and cold and allergy medications. The amount of CAF in different products can vary widely, with coffee and tea generally containing higher amounts than soft drinks and energy drinks. While CAF can have some benefits, such as increasing alertness and improving cognitive performance, it can also have negative effects, such as interfering with sleep, causing anxiety or jitters, and leading to addiction or dependence. It is important to consume CAF in moderation and to be aware of its potential risks and benefits [1-2].

The chemical formula of CAF is 1,3,7-Trimethylpurine-2,6-dione. The empirical formula is $C_8H_{10}N_4O_2$ and its molecular weight is 194.19 [3]. Due to its high selectivity and sensitivity, a bioanalytical method based on liquid chromatography and tandem mass spectrometry (LC-MS/MS) was used to determine the amount of CAF in human plasma. In several published reports, CAF has been successfully separated using diode array detection HPLC combined with electrospray tandem mass spectrometry (HPLC-DAD/ESI-MS/MS) as well as HPLC and UFLC-Q-TOF-MS/MS [4-8]. However, HPLC techniques have certain limitations such as lower specificity, selectivity, and longer analysis times. Alvi et al. (2011) described a method for determining CAF levels in human plasma, but the chromatographic analysis time was quite long (10 min), making it unsuitable for high-throughput analysis. Thus, our aim was to develop a sensitive and specific LC-MS/MS method that employed simple protein precipitation and a short 3-min run time for the quantitative determination of CAF in human

plasma. The validated method was successfully applied to CAF pharmacokinetic studies.

Experimental

Chemicals and Materials

CAF (purity 99.8%) was supplied by Siegfried Pharma Chemikalien (Minden, Germany). CAF -D3, the internal standard (IS), was obtained from Clearsynth (Mumbai, India). Formic acid, methanol, and ethanol were purchased from Merck (Darmstadt, Germany). The ethylene diamine tetra acetic acid (K_2EDTA) blank human plasma was obtained from Bioivt Laboratories International Ltd. (UK). The ultrapure water was produced in-house using Millipore's (USA) Milli-Q water purification system.

Stock Solutions, Calibration Standards and QCs

Stock solutions of CAF (1 mg/mL) in methanol were diluted to make working solutions (0.2 - 200 µg/mL).The internal standard working solution was prepared at a concentration of 1 µg/mL. Stock solutions of CAF and IS were stored at -20 °C. Calibration standards (10 – 10000 ng/mL) and QC samples (10, 30, 300, 4000, and 8000 ng/mL) were prepared in human blank plasma. All calibration standards and QC samples were stored at -70 °C until analysis.

Instrument

The system of LC-MS/MS (Shimadzu, Japan) consists of LC-20AD XR solvent pumps, SIL-20AC XR autosampler, CTO-10AS VP column oven, and Shimadzu 8040 Tandem Mass Spectrometer. Lab Solutions Version 5.93 was used to acquire and evaluate chromatographic data. Separations were carried out on GL Sciences InertSustain C18 Column (50 x 4.6 mm, 5 µm) at 40 °C. The mobile phase consisted of methanol, water and formic acid (30:70:0.1 *v/v/v*) with a flow rate of 1 mL/min. The run time was 3.0 minutes. A 20 µL sample was injected into the LC-MS/MS system for analysis.

The multiple reaction monitoring (MRM) transitions were carried out at *m/z* 195.10 > 138.0 for CAF and *m/z* 198.10 → 141.10 for IS. Mass spectrometric detection was performed using an ESI ion source operating in the positive ionization mode. The nebulizing gas flow rate, drying gas flow rate, and ESI voltage were set to 2.5 L/min, 15 L/min, and 4500 V, respectively. The nebulizing and drying gases used were high-purity nitrogen generated by the Peak Scientific NL-60 system. MS data acquisition was conducted in the MRM mode in order to quantify and identify the target analytes. MS parameters are presented in Table 1.

Table 1. MS parameters for CAF and CAF-D3.

Compound	Precursor	Product	Dwell Time	Q1 pre-bias (V)	Collision energy (V)	Q3 pre-bias (V)
CAF	195.1	138.0	100.0	-13.0	-20.0	-22.0
IS	198.1	141.1	100.0	-13.0	-28.0	-21.0

Sample Preparation

Prior to analysis, the plasma sample was allowed to thaw to room temperature. Next, aliquots of 100 µL plasma samples and 50 µL of IS (1 µg/mL) was added into a 10 mL centrifuge tube and vortexed for 5 s. 300 µL of methanol was added to the tube to precipitate proteins and then vortex for 30 s. The samples were centrifuged at 5500 rpm for 10 min. After centrifugation, 20 µL of the supernatant was injected into the LC-MS/MS system.

Result and Discussion

Method Validation

The method was validated according to US-FDA Guidance for Industry: Bioanalytical Method Validation [9] with respect to selectivity, linearity, accuracy and precision, matrix effect, recovery, carry over, dilution integrity, batch size, and stabilities. Method validation was conducted using K_2EDTA human plasma as the sample matrix.

Selectivity

Eight different sources of human blank plasma (including haemolysed and hyperlipidaemic plasma) were subjected to a selectivity test. The selectivity assessment revealed that the presence of an interfering peak accounted for less than 20% of the response at the same retention time as the analyte's lower limit of quantification (LLOQ). Figure 1 shows chromatograms of (a) blank plasma spiked with IS and analytes at LLOQ, and (b) drug-free human plasma.

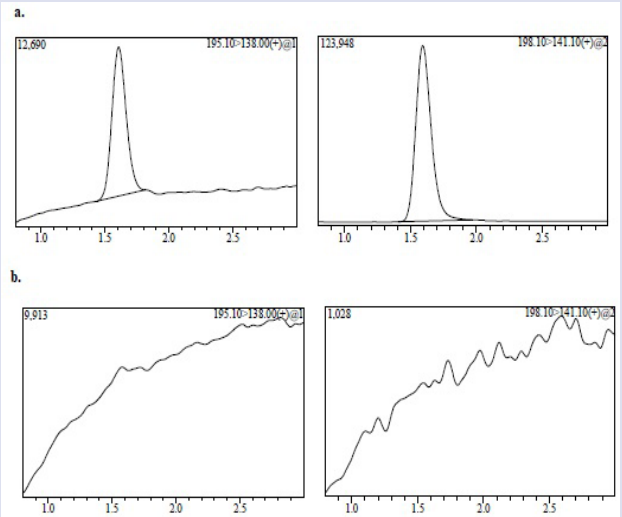

Figure 1. MRM chromatogram of 10 ng/mL (LLOQ) of CAF spiked with internal standard (a), blank human plasma (b).

Linearity

In the concentration range of 10 to 10000 ng / mL, including the LLOQ, the method's linearity was demonstrated for CAF. Eight freshly prepared calibration standards for CAF (10, 20, 100, 500, 2500, 5000, 9000, and 10000 ng/mL) were assayed in each of the three validation batches. The best fit based on accuracy was found using a linear equation with $1/C^2$ weighting. The analyte's average determination coefficients (r^2) were 0.9987 or higher (x = 0.00398556a + 0.000103298). The standard curves covered the quantitation range and were made up of eight non-zero samples, a blank sample, and an IS sample that had been spiked with zero. RE of calculated concentrations from the nominal values should be within ± 15% (LLOQ: ± 20%). At least 75% of the calculated concentrations of the calibration curve should fulfil the acceptance criteria (at least 6 non-zero samples, including the LLOQ and the ULOQ) [9, 10].

Accuracy and precision

The within-batch and between-batch precision and accuracy were assessed by analysing QC samples at five different concentration levels: 10 ng/mL (LLOQ), 30 ng/mL (QC Low), 300 ng/mL (QC Medium), 4000 ng/mL (QC High), 8000 ng/mL (ULLOQ), with six replicates in three consecutive validation runs. The acceptance criteria were defined for within batch and between batch precision as CV ≤ 15 % (20% for LLOQ), for within-batch accuracy as RE of calculated concentrations from the nominal values must be within ±15% (±20% for LLOQ), and two third of the QC samples at each concentration must fulfil the acceptance criteria. Additionally, RE of the mean concentration from the nominal value must be within the ±15% range (±20% for LLOQ). The within-batch and between-batch values did not exceed 15% for QC samples, as expected for LLOQ which did not exceed 20%. Table 2 and Table 3 provide a summary of the method's within- and between-batch precision and accuracy data. Based on the analyte to IS peak-area ratios, the regression algorithm was $1/C^2$ weighting linear regression. Shimadzu LabSolutions version 5.93 Software program was used for data acquisition and evaluation of chromatographic data. Results in detail are given in Table 2 - 3 and the results demonstrate that the acceptance criteria were met.

Table 2. Within-batch precision and accuracy of the method for determining CAF in plasma samples.

Nominal Concentration (ng/mL)	Batch No. 1 (n = 6)			Batch No. 2 (n=6)			Batch No. 3 (n=6)		
	Actual Concentration (mean ± SD; ng/mL)	RD (%)	CV (%)	Actual Concentration (mean ± SD; ng/mL)	RD (%)	CV (%)	Actual Concentration (mean ± SD; ng/mL)	RD (%)	CV (%)
10	9.65 ± 0.70	-3.45	7.22	9.81 ± 0.67	-1.89	6.84	10.96 ± 0.67	9.61	6.19
30	28.24 ± 0.37	-5.87	1.30	28.11 ± 0.70	-6.31	2.49	29.05 ± 0.28	-3.17	0.95
300	277.24 ± 6.05	-7.59	2.18	281.84 ± 6.17	-6.05	2.19	273.72 ± 4.69	-8.76	1.71
4000	3770.95 ± 59.66	-5.73	1.58	3932.88 ± 76.32	-1.68	1.94	3791.00 ± 77.59	-5.23	2.05
8000	7832.89 ± 186.67	-2.09	2.38	7960.40 ± 87.25	-0.50	1.10	7783.05 ± 86.20	-2.71	1.11

Table 3. Between-batch precision and accuracy of the method for determining CAF in plasma samples.

Nominal Concentration (ng/mL)	Batch No. 1-3 (n = 18)		
	Actual Concentration (mean ± SD; ng/mL)	RD (%)	CV (%)
10	10.14 ± 0.88	1.42	8.66
30	28.47 ± 0.62	-5.12	2.20
300	277.60 ± 6.34	-7.47	2.28
4000	3831.61 ± 100.16	-4.21	2.61
8000	7858.78 ± 143.45	-1.77	1.82

For between-batch accuracy, calculated mean concentration from three different runs must be in the ±15% range (±20% for LLOQ) of the nominal value.

Matrix Effect

For the matrix effect, blank plasma samples were taken from six different human plasma sources, including one lipemic and one haemolytic plasma. For both the analyte and the internal standard, the matrix factor (MF) in each matrix was calculated by determining the ratio of the peak area in the presence of the matrix (measured by analysis of the matrix blank spiked with the analyte at the concentration of QC low and QC high after extraction) to the peak area in absence of matrix (pure solution of the analyte). The normalized IS MF was calculated by dividing the analytes MF IS by the IS MF. The precision (CV%) of QC Low and QC High were 1.02% and 4.09% observed for CAF. The matrix effect result was summarized in Table 4. The accuracy should be within ±15% of the nominal concentration and the precision should not be greater than 15% in all individual matrix sources/lots [10]. Our findings show that, at both low and high concentrations of the analyte in all six lots of human plasma, there was no matrix effect. The matrix effect result was summarized in Table 4.

Table 4. Results of matrix effects for CAF (n = 6).

Sample	Plasma QC Low					Plasma QC High				
	Mean Peak Area (n = 6)	Matrix Factor	Mean Peak Area IS (n = 6)	IS Matrix Factor	IS Normalised MF	Mean Peak Area (n = 6)	Matrix Factor	Mean Peak Area IS (n = 6)	IS Matrix Factor	IS Normalised MF
Solution	99220.00	-	1081952.67	-	-	24168940.00	-	1081952.67	-	-
Matrix 1	108246.50	1.09	1180754.33	1.09	1.00	25915277.50	1.07	1180754.33	1.09	0.98
Matrix 2	105866.50	1.07	1188919.17	1.10	0.97	27440756.33	1.14	1188919.17	1.10	1.03
Matrix 3	106676.50	1.08	1179014.83	1.09	0.99	27974463.83	1.16	1179014.83	1.09	1.06
Matrix 4	103945.67	1.05	1152197.00	1.07	0.98	27981808.33	1.16	1152197.00	1.07	1.09
Matrix 5	103981.33	1.05	1149130.67	1.06	0.99	25555420.83	1.06	1149130.67	1.06	1.00
Matrix 6	100725.33	1.02	1102840.67	1.02	1.00	24540301.50	1.02	1102840.67	1.02	1.00

Recovery

The recovery of CAF was assessed by comparing the analyte responses of six extracted samples of low, medium, and high QC concentrations (30, 4,000, 8,000 ng/mL) with those of six appropriately diluted standard solutions. The mean total recovery of CAF was determined to be 93.99 %.

For IS, the mean responses of six internal diluted standard solutions and six extracted samples with medium QC concentrations (4000 ng/ mL) were compared. Internal standard recovery was found to be 99.44% on average.

Results are given in Table 5 and the results demonstrate that the acceptance criteria were met.

Acceptance criteria: The CV of the recovery results of the QC levels should be lower than ±15%.

Table 5. Recovery rates and calculated CV (3 concentrations: QC2, QC32, QC4) for precision (n = 6).

Concentration (ng/mL)	Mean (Ext/Unext) %	Recovery Rate (%)	SD	CV (%)
30.000	82.030332			
4000.000	100.373935	93.990340	10.365531	11.028294
8000.000	99.566754			
Internal Standard	99.440756			

Carryover

A high-quality control concentration sample (QC) and a blank sample after calibration at the upper limit of quantification (ULOQ) were used to evaluate carry-over in validation batches. Figure 2 shows that no carry-over was observed.

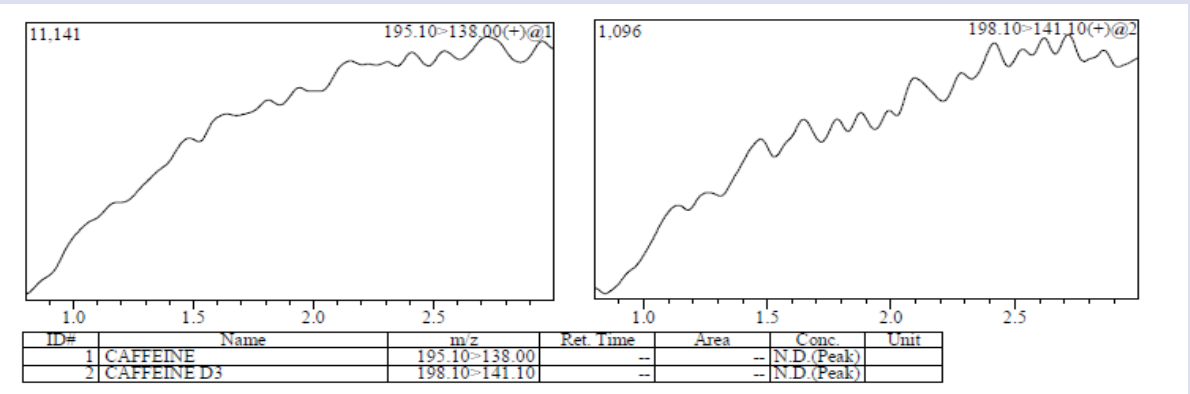

Figure 2. Visual presentation for the absence of carry-over effect for CAF.

Dilution integrity

The integrity of the dilution was confirmed by producing 1.7 times the ULOQ. This dilution sample was then diluted 1/2 and 1/20 with blank human plasma and tested with freshly spiked calibration standards. After accounting for dilution, the results were compared to the concentration. The mean values of diluted samples for the analyte CAF were within 15.0% of nominal value (0.758% for 1/2 dilution and -0.083% for 1/20 sample), and CV at each level was within ± 15.0% (1.464% for 1/2 and 1.320 % for 1/20 sample). Accordingly, the samples can be diluted 1/2 or 1/20 times to fit within the

calibration curve when their calculated concentration exceeds ULOQ.

Batch size

To determine the maximum batch size, the accuracy and precision of QC samples were tested over a run in a size equivalent to the expected analytical run. To mimic the actual size of a study run, blank samples were injected into the system between two validation batches. The QC samples were evaluated against the calibration curve obtained from the first validation batch. Based on this analysis, it was concluded that the maximum injection capacity of the instrument, which is 103, could be used as the batch size.

Stability

Stability evaluation in the matrix were made using freshly spiked calibration standards. The stability of QC samples at both low and high levels (n = 6, each) was evaluated by subjecting them to a freeze-thaw cycle. The samples were initially stored and frozen at -70 °C for 24 h, followed by unassisted thawing at room temperature. Once thawed, the samples were refrozen at -70 °C for a minimum of 12 h. This freeze-thaw cycle was repeated 4 times. After the 4th freeze-thaw cycle, the stability samples were processed with freshly prepared calibration standards and freshly prepared low and high QC samples. All samples were analysed in a single run. The results of the analysis indicated that CAF remains stable in human plasma for up to 4 freeze-thaw cycles when stored at -70 °C and thawed to room temperature.

The benchtop stability was assessed by maintaining CAF QC plasma samples at room temperature for 5 h at low and high QC values (n = 6 each). The QC samples were left on the bench at room temperature before extraction for 5 h. After 5 h, the stability samples were processed with freshly prepared calibration standards. All samples were analysed in a single run. Benchtop stability test results indicated that CAF in plasma remains stable for 5 hours at room temperature.

The processed sample stability was assessed by leaving sets of low and high QC samples in the autosampler for a longer period of time than required for processing a run of study samples. The samples were stored at autosampler conditions (10 °C) for 27 h and then injected with freshly prepared calibration standards and QC samples. CAF was stable in extracts.

During method validation, long-term plasma stabilities at both -20 °C and -70 °C was assessed for 7 days. The summarized stability results were presented in Table 6.

Table 6. Results of stability of CAF in human plasma under different storage conditions (n = 6).

Storage Condition	Nominal Concentration (ng/mL)	Actual Concentration (mean ± SD; ng/mL)	CV (%)	RD (%)
Autosampler stability a	30	29.40 ± 0.72	2.45	-1.98
	8000	7771.33 ± 94.20	1.21	-2.86
Short-term plasma stability b	30	29.04 ± 0.44	1.52	-3.19
	8000	7867.11 ± 130.81	1.66	-1.66
Validation long-term plasma stability c	30	27.53 ± 0.77	2.79	-8.23
	8000	7867.80 ± 109.22	1.38	-1.65
Validation long-term plasma stability d	30	29.09 ± 0.40	1.39	-3.05
	8000	7832.86 ± 58.23	0.74	-2.09
Freeze-thaw stability d	30	29.54 ± 0.82	2.76	-1.54
	8000	7765.21 ± 70.84	0.91	-2.94

RD: Relative Deviation (Accuracy), CV: Coefficient of Variation (Precision), SD: Standard Deviation

[a] Kept at autosampler temperature, 10 °C. [b] Stored at room temperature. [c] Stored at -20 °C. [d] Stored at -70 °C.

Application to a Pharmacokinetic Study

The successfully validated method was applied to a pharmacokinetic study. A total of 12 subjects completed the clinical phase of the study. Serial blood samples were collected throughout 16 h. The plasma samples obtained from 12 subjects following oral administration of a single dose of CAF 60 mg capsules under fasting conditions (the volunteers were fasted at least 2 hours) were analysed. The mean ± SD of maximum plasma concentration (C_{max}) for the fasting conditions was found to be 147.94 ± 139.39 ng/mL. The median (min-max) times to reach peak plasma concentration (T_{max}) for the fasting was found to be 12.00 (6.50 - 12.00). The mean ± SD of area under the plasma concentration-time curve from zero to last measurable concentration ($AUC_{0\text{-tlast}}$) for the fasting conditions was found to be 1119.59 ± 1468.30 h.ng/mL. When the clinical studies in the literature are evaluated, different results are striking both among other studies and with this study. The root cause of this is considered to be differences in study design, research products, and inter-subject variations [11].

Conclusion

We created and tested a positive ion mode LC-MS/MS method for simultaneously determining CAF in human plasma. Using deuterated internal standards ensured the success of the assay by eliminating the matrix effects. The parameters (selectivity, linearity,

lower limit of quantification, accuracy, precision, dilution integrity, carry-over, and recovery) were successfully validated. Further, the stability of the analyte was evaluated, as was the matrix effect. The developed method's adequate sensitivity, satisfactory selectivity, and good reproducibility were all confirmed. In order to achieve good extraction recovery without any obvious matrix effects, the protein precipitation method was developed. After an oral administration of CAF capsules, the validated method could be used to assess their pharmacokinetics and ascertain their bioavailability.

Conflicts of Interest

There are no conflicts of interest in this work.

References

[1] Nehlig A., Daval JL., Debry G., Caffeine and the central nervous system: mechanisms of action, biochemical, metabolic and psychostimulant effects, *Brain Research Reviews*, 17 (2) (1992) 139-170.

[2] Guest N.S., VanDusseldorp T.A., Nelson M.T., International society of sports nutrition position stand: caffeine and exercise performance, *J Int Soc Sports Nutr*., 18 (1) (2021).

[3] PubChem Compound Summary for CID 2519, Caffeine, *National Center for Biotechnology Information,* (2023). Available at: https://pubchem.ncbi.nlm.nih.gov/compound/caffeine. Retrieved June 24, 2023.

[4] De Maria C.A.B., Moreira R.F.A., Analytical methods for caffeine, *Química Nova,* 30 (1) (2007) 99-105.

[5] Alvi S.N., Hammami M.M., Validated HPLC method for determination of caffeine level in human plasma using synthetic plasma: application to bioavailability studies, *J Chromatogr Sci.,* 49 (4) (2011) 292-6.

[6] Wang Y.H., Mondal G., Butawan M., Bloomer R.J., Yates C.R., Development of a liquid chromatography-tandem mass spectrometry (LC–MS/MS) method for characterizing caffeine, methylliberine, and theacrine pharmacokinetics in humans, *Journal of Chromatography B*, 1155 (2020).

[7] Lu J.L., et al., Determination of purine alkaloids and catechins in different parts of Camellia assamica var. kucha by HPLC-DAD/ESI-MS/MS, *J. Sci. Food Agric.* 89 (2009) 2024–2029.

[8] Li Y.F., et al., A comparative analysis of chemical compositions in Camellia sinensis var. puanensis Kurihara, a novel Chinese tea, by HPLC and UFLC-Q-TOF-MS/MS, *Food Chemistry,* 216 (2017) 282–288.

[9] U.S. Department of Health and Human Services, Food and Drug Administration (FDA). *Guidance for Industry. Bioanalytical Method Validation*, (2018). Available at: https://www.fda.gov/media/70858/download. Retrieved June 24, (2023).

[10] European Medicines Agency (EMA), Committee for Medicinal Product for Human Use (CHMP), *Guideline on Bioanalytical Method Validation*, (2022). Available at: https://www.ema.europa.eu/en/ich-m10-bioanalytical-method-validation-scientific-guideline. Retrieved August 23, (2023).

[11] Grzegorzewski J., Bartsch F., Köller A. and König M., Pharmacokinetics of caffeine: A systematic analysis of reported data for application in metabolic phenotyping and liver function testing, *Frontiers in Pharmacology,* 12 (2022) 752826.

Cumhuriyet Sci. J., 44(3) (2023) 491-496
DOI: https://doi.org/10.17776/csj.1330590

Cumhuriyet Science Journal

| csj.cumhuriyet.edu.tr | Founded: 2002 ISSN: 2587-2680 e-ISSN: 2587-246X Publisher: Sivas Cumhuriyet University

A Density Functional Theory (DFT) based Analysis on the Inhibition Performances of Some Triazole Derivatives for Iron Corrosion

Nihat Karakuş[1,a], Savaş Kaya[1,b,*]

[1]*Sivas Cumhuriyet University, Faculty of Science, Department of Chemistry, 58140, Sivas, Türkiye*
**Corresponding author*

Research Article

History
Received: 20/07/2023
Accepted: 21/09/2023

ABSTRACT

Iron is one of the widely used metals in industry. For that reason, the prevention of the corrosion of such metals via new designed inhibitor systems is among the interest of corrosion scientists. In the present paper, we investigated the corrosion inhibition performance of 2-((1-(4-nitrophenyl)-1H-1,2,3-triazol-4-yl) methoxy) benzaldehyde (A), 4-((1-(4-nitrophenyl)-1H-1,2,3-triazol-4-yl) methoxy) benzaldehyde (B), 4-((4-nitrophenoxy) methyl)-1-(4-nitrophenyl)-1H-1,2,3-triazole (C), 4-methyl-7-((1-(4-nitrophenyl)-1H-1,2,3-triazol-4-yl) methoxy)-2H-chromen-2-one (D) against iron corrosion. For the mentioned inhibitor systems, important reactivity descriptors like frontier orbital energies, chemical potential, electronegativity, hardness, softness, polarizability, dipole moment, back-donation energy, electrophilicity, electroaccepting power and electrodonating power were calculated and discussed. Calculations were repeated using various methods and basis sets in different phases. The chemical reactivities of the inhibitors were predicted in the light of well-known electronic structure rules like Maximum Hardness and Minimum Polarizability Principles. The obtained data showed that the best corrosion inhibitor among them is molecule D while the most stable molecule is molecule C. The theoretical data support the experimental observations.

Keywords: DFT, Electronic Structure, Corrosion inhibitor, Thiazole derivatives.

[a] *nkarakus@cumhuriyet.edu.tr* *https://orcid.org/0000-0001-6223-7669* [b] *savaskaya@cumhuriyet.edu.tr* *https://orcid.org/0000-0002-0765-9751*

Introduction

Corrosion can be defined as natural process converting the metals to their sulfides, oxides and hydroxides [1,2]. Adding the inhibitor molecules to corrosive media, the prevention of the corrosion of metals is among the interests of corrosion scientists. The molecules acting as effective corrosion inhibitors are easily adsorbed on metal surfaces through an electron transfer between inhibitor and metal surface. Many theoretical and experimental corrosion scientists reported the high inhibition performance of π-systems and heterocyclic compounds including especially heteroatoms like nitrogen, sulfur and oxygen [3,4]. It is well-known that a triazole is a heterocyclic molecule including a five membered ring with two carbons and three nitrogens. Triazole's closed molecular formula is $C_2H_3N_3$. Some important papers about the high effectiveness of triazole derivatives against the corrosion of various metal and alloys are available in the literature. M. M. Abdelsalem and coworkers [5] synthesized three triazole derivatives, namely -((1H-1,2,4-triazol-3-ylimino) methyl)naphthalen-2-ol (TMN), N-(furan-2-ylmethylene)-1H-1,2,4-triazol-3-amine (FTA) and N-(thiophen-2-ylmethylene)-1H-1,2,4-triazol-3-amine (TTA) with the help of ultrasonic irradiation and investigated their corrosion inhibition performances. In the analysis made via some experimental and theoretical tools, corrosion inhibition effiency ranking obtained for steel was reported as: TMN> TTA>FTA. In another paper penned by Belghiti and coworkers [6] analyzed the corrosion inhibition performance of four triazole derivative in strong phosphoric acid medium for steel. This study was also a proof of which triazole derivatives are effective corrosion inhibitors against the corrosion of metals and alloys.

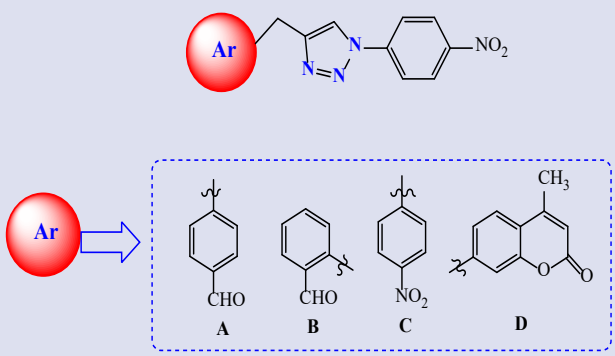

Figure 1. Molecular structures of the inhibitor systems considered in this study.

In a recent paper published by Jaber and coworkers [7], four new triazole derivatives were synthesized via regioselective click reaction and investigated their corrosion inhibition performances using only experimental procedures. The molecular structures of the mentioned triazole derivatives are presented in Fig.

1. The aim of this article is to theoretically analyze the corrosion inhibition performances of molecules A, B, C and D and is to predict their chemical reactivities through the some electronic structure rules. The obtained theoretical data will be helpful to experimental corrosion scientists in the design of new triazole derivatives.

Computational Details and Equations

Conceptual Density Functional Theory (CDFT) can be considered as the reactivity related branch of DFT. CDFT includes many simple formulae to compute the quantum chemical descriptors and well-known electronic structure rules based on these descriptors. In CDFT, the following mathematical relations for chemical potential (μ), electronegativity (χ), hardness (η) and softness (σ) are presented [8,9].

$$\mu = -\chi = \left[\frac{\partial E}{\partial N}\right]_{v(r)} \quad (1)$$

$$\eta = \left[\frac{\partial^2 E}{\partial N^2}\right]_{v(r)} \quad (2)$$

$$\sigma = 1/\eta \quad (3)$$

Here, E and N represents the total electronic energy and total number of the electrons of any chemical system, respectively. If one applies the finite differences approach to the mathematical relations given above, for the calculation of the aforementioned quantum chemical descriptors, the following simple formulae based on ground state ionization energy (I) and ground state electron affinity (A) of atoms, ions and molecules are obtained [10].

$$\mu = -\chi = -\left(\frac{I + A}{2}\right) \quad (4)$$

$$\eta = I - A \quad (5)$$

First electrophilicity index (ω_1) mathematically introduced by Parr, Szentpaly and Liu [11] is calculated based on absolute hardness and absolute electronegativities of the chemical systems via the equation given below

$$\omega_1 \equiv \chi^2 / 2\eta \quad (6)$$

Second electrophilicity index that its usefulness is emphasized by especially Szentpaly and Kaya [12] is calculated as:

$$\omega_2 = I.A / I - A \quad (7)$$

Electroaccepting power (ω^+) and electrodonating power (ω^-) parameters introduced by Gazquez and coworkers [13] in 2007 are calculated from the following equations. These parameters depending on ionization energy and electron affinity of atom, ions and molecules like other Conceptual DFT based descriptors are widely used in corrosion science.

$$\omega^+ = (I + 3A)^2 / (16(I - A)) \quad (8)$$

$$\omega^- = (3I + A)^2 / (16(I - A)) \quad (9)$$

Back-donation energy ($\Delta E_{b\text{-}d}$) is closely related to the absolute hardness of a chemical system and is calculated from the following equation

$$\Delta E_{b-d} = -\frac{\eta}{4} \quad (10)$$

In the corrosion science, to compute the fraction of the electrons transferred from inhibitor to metal surface and metal-inhibitor interaction energy, the following equations are used.

$$\Delta N = \frac{\phi_{Fe} - \chi_{inh}}{2(\eta_{Fe} + \eta_{inh})} \quad (11)$$

$$\Delta \psi = -\frac{(\phi_{Fe} - \chi_{inh})^2}{4(\eta_{Fe} + \eta_{inh})} \quad (12)$$

In these equations, φ_{Fe} is work function computed for Fe (110) surface and its numerical value is 4.82 eV. Chemical hardness of Fe surface is taken as ηFe=0 because I=A for a bulk. In the equations χ_{inh} and η_{inh} represent the electronegativity and chemical hardness of inhibitor molecule, respectively [15].

Gas phase calculations were performed using HF, B3LYP and M062X methods and considering 6-31++G(d,p), SDD, 6-311++G(d,p) basis sets. In the calculations in water phase, only B3LYP method was preferred. Since the corrosion process is generally carried out in aqueous environments, it is essential to make the calculations also in the aqueous phase. For this reason, we performed the PCM (polarisable continuum model) method to investigate the solvent effect of water. In the prediction of ionization energy and electron affinities of the studied inhibitor molecules, we considered Koopmans Theorem [16] giving the following relations based on HOMO and LUMO orbital energies.

$$I = -E_{HOMO} \quad (13)$$

$$A = -E_{LUMO} \quad (14)$$

Results and Discussion

In this paper, using Conceptual Density Functional Theory based chemical reactivity parameters and electronic structure rules, we investigated the corrosion inhibition performances of some triazole derivatives against the corrosion of the iron. For this goal, well-known parameters like hardness, electrophilicity, electronegativity, back-donation energy, polarizability, metal-inhibitor interaction energy, electrodonating/accepting powers were computed and their relation with electron donating ability of molecules were discussed in detail. In Table 1, computed quantum chemical parameters for studied inhibitor molecules in the gas phase while Table 2 reflects the results obtained in aqueous media. Fig. 2 visually presents optimized structures, HOMOs, LUMOs and ESP maps obtained at B3LYP/6-311++g (d p) calculation level of the studied molecular systems. The different values in the electrostatic potential maps (ESP) are presented through different colors. In these maps, red color presents the region of the most negative electrostatic potential, blue color stands for the region of the most positive electrostatic potential and green color stands for the region of the zero electrostatic potential. The reddest region is the region most suitable for protonation

Molecular Orbital Theory widely uses the HOMO and LUMO energies to explain the acidic and basic behaviour of the molecules. It should be noted that the molecules with high value of HOMO energy acts as effective corrosion inhibitors because they give the electrons easily to metals and alloys. Additionally, the molecular systems with low values of LUMO energy are good electron acceptors. According to computed HOMO and LUMO orbital energies, the corrosion inhibition efficiency order of the studied molecules can be given as: D>B>A>C. Chemical hardness [17] is a powerful tool to explain the stability of molecules as a good measure of the chemical reactivity because this quantity represents the resistance towards electron cloud polarization of atomic and molecular systems. According to Maximum Hardness Principle [18], it can be noted that hard chemical systems exhibits high stability and cannot show high efficiency against the corrosion of metal surfaces. Considering the inverse relation between hardness and polarizability, it can be said with ease that the molecular systems with high polarization are effective corrosion inhibitor [19]. As can be seen from the computational details section, back-donation energy is closely related to the chemical hardness of molecules.

Table 1. Calculated quantum chemical parameters for studied inhibitor molecules in the gas phase

Molecule	E_{HOMO}	E_{LUMO}	χ	η	ω_1	ω_2	$\Delta E_{b\text{-}d}$	ω^-	ω^+	α (au)
B3LYP/6-31++G (d, p)										
A	-7.046	-3.260	5.153	3.786	3.507	6.067	-0.947	9.827	4.674	245.542
B	-7.029	-3.302	5.166	3.727	3.580	6.227	-0.932	9.975	4.809	251.926
C	-7.423	-3.355	5.389	4.068	3.569	6.122	-1.017	10.088	4.699	253.456
D	-6.650	-3.260	4.955	3.39	3.621	6.395	-0.848	9.932	4.977	295.346
B3LYP/SDD										
A	-7.080	-3.535	5.308	3.545	3.973	7.060	-0.886	10.822	5.514	221.750
B	-7.042	-3.574	5.308	3.468	4.062	7.257	-0.867	10.995	5.687	228.346
C	-7.514	-3.638	5.576	3.876	4.011	7.053	-0.969	11.052	5.476	232.081
D	-6.734	-3.530	5.132	3.204	4.110	7.419	-0.801	10.986	5.854	270.050
B3LYP/6-311++G (d, p)										
A	-7.092	-3.255	5.174	3.837	3.488	6.016	-0.959	9.802	4.629	244.061
B	-7.076	-3.295	5.186	3.781	3.556	6.166	-0.945	9.941	4.755	250.424
C	-7.468	-3.348	5.408	4.12	3.549	6.069	-1.030	10.060	4.652	251.479
D	-6.693	-3.253	4.973	3.44	3.595	6.329	-0.860	9.891	4.918	294.058
HF/6-31++G (d, p)										
A	-9.302	0.685	4.309	9.987	0.929	-0.638	-2.497	4.637	0.329	214.386
B	-9.263	0.662	4.301	9.925	0.932	-0.618	-2.481	4.634	0.333	217.548
C	-9.842	0.599	4.622	10.441	1.023	-0.565	-2.610	5.009	0.387	217.744
D	-8.785	0.699	4.043	9.484	0.862	-0.647	-2.371	4.338	0.295	255.031
HF/SDD										
A	-9.577	0.204	4.687	9.781	1.123	-0.200	-2.445	5.200	0.514	194.892
B	-9.513	0.188	4.663	9.701	1.120	-0.184	-2.425	5.178	0.516	198.034
C	-10.200	0.111	5.045	10.311	1.234	-0.110	-2.578	5.635	0.590	200.356
D	-9.097	0.224	4.437	9.321	1.056	-0.219	-2.330	4.912	0.476	234.639
HF/6-311++G (d, p)										
A	-9.324	0.712	4.306	10.036	0.924	-0.661	-2.509	4.628	0.322	214.850
B	-9.287	0.635	4.326	9.922	0.943	-0.594	-2.481	4.669	0.343	274.138
C	-9.866	0.577	4.645	10.443	1.033	-0.545	-2.611	5.041	0.396	217.927
D	-8.800	0.709	4.046	9.509	0.861	-0.656	-2.377	4.338	0.293	255.792
M062X/6-31++G (d, p)										
A	-8.355	-2.098	5.227	6.257	2.183	2.801	-1.564	7.370	2.144	231.889
B	-8.313	-2.128	5.221	6.185	2.203	2.860	-1.546	7.403	2.183	236.737
C	-8.753	-2.185	5.469	6.568	2.277	2.912	-1.642	7.699	2.230	237.164
D	-7.898	-2.094	4.996	5.804	2.150	2.849	-1.451	7.161	2.165	278.454
M062X/SDD										
A	-8.519	-2.491	5.505	6.028	2.514	3.520	-1.507	8.157	2.652	209.602
B	-8.459	-2.517	5.488	5.942	2.534	3.583	-1.486	8.184	2.696	214.384
C	-8.998	-2.585	5.792	6.413	2.615	3.627	-1.603	8.527	2.735	217.044
D	-8.108	-2.480	5.294	5.628	2.490	3.573	-1.407	7.979	2.685	254.286
M062X/6-311++G (d, p)										
A	-8.413	-2.106	5.260	6.307	2.193	2.809	-1.577	7.410	2.150	230.562
B	-8.373	-2.136	5.255	6.237	2.213	2.868	-1.559	7.444	2.189	235.462
C	-8.821	-2.194	5.508	6.627	2.289	2.920	-1.657	7.745	2.238	235.753
D	-7.951	-2.101	5.026	5.85	2.159	2.856	-1.463	7.197	2.171	277.196

So, it is not difficult to predict that the molecules with more negative values of the back-donation energy are not effective corrosion inhibitors. In the light of computed hardness, polarizability and back-donation energy data, the corrosion inhibition efficiency order can be given as: D>B>A>C. Electronegativity [20,21] is among key parameters used to explain the nature of the chemical interactions and chemical bonding. Shortly, it can be defined as the electron withdrawal powers of atoms, ions and molecules. In the light of this definition, it is clear that effective corrosion inhibitors should not have high electronegativity values. Computed electronegativity values also imply the high efficiency of molecule D. According to Minimum Electrophilicity Principle, in stable states and conformers, electrophilicity is minimized. Normally, in corrosion inhibition studies that don't consider the Minimum Electrophilicity Principle, it is noted that the molecules with high value of electrophilicity index cannot act effective corrosion inhibitors. On the other hand, Minimum Electrophilicity Principle implies that the molecules with large value of electrophilicity index are more reactive than others. Our results support the Minimum Electrophilicity Principle and this principle predicts the best corrosion inhibitor as molecule D. Electrodonating power and electroaccepting power are among the parameters used in corrosion inhibition prediction. Good corrosion inhibitors have high value of electrodonating power and low value of electroaccepting power. The experimentally obtained corrosion inhibition efficiency ranking for the studied inhibitor systems is the same of the ranking obtained with the help of Conceptual Density Functional Theory based theoretical analyses. Chemical reactivity analysis made here will assist experimental chemists in the synthesis or design of more reactive or more stable Triazole derivatives.

Table 2. Calculated quantum chemical parameters for studied inhibitor molecules in the aqueous phase

Molecule	E_{HOMO}	E_{LUMO}	χ	η	ω_1	ω_2	ΔE_{b-d}	ω^-	ω^+	α (au)
B3LYP/6-311++G (d, p)										
A	-6.778	-3.279	5.0285	3.499	3.613	6.352	-0.8748	9.960	4.931	331.174
B	-6.853	-3.266	5.0595	3.587	3.568	6.240	-0.8968	9.890	4.831	335.582
C	-7.080	-3.284	5.182	3.796	3.537	6.125	-0.9490	9.902	4.720	343.462
D	-6.489	-3.278	4.8835	3.211	3.714	6.624	-0.8028	10.070	5.186	398.115
HF/6-311++G (d, p)										
A	-9.082	0.818	4.132	9.9	0.862	-0.750	-2.4750	4.409	0.277	283.113
B	-9.072	0.819	4.1265	9.891	0.861	-0.751	-2.4728	4.403	0.277	284.948
C	-9.507	0.817	4.345	10.324	0.914	-0.752	-2.5810	4.646	0.301	286.180
D	-8.640	0.822	3.909	9.462	0.807	-0.751	-2.3655	4.161	0.252	335.839
M062X/6-311++G (d, p)										
A	-8.193	-2.074	5.1335	6.119	2.153	2.777	-1.5298	7.256	2.122	307.319
B	-8.181	-2.074	5.1275	6.107	2.153	2.778	-1.5268	7.251	2.123	311.069
C	-8.494	-2.076	5.285	6.418	2.176	2.748	-1.6045	7.396	2.111	313.699
D	-7.814	-2.073	4.9435	5.741	2.128	2.822	-1.4353	7.087	2.144	368.684
B3LYP/6-311++G (d, p)										
A	-6.778	-3.279	5.0285	3.499	3.613	6.352	-0.8748	9.960	4.931	331.174
B	-6.853	-3.266	5.0595	3.587	3.568	6.240	-0.8968	9.890	4.831	335.582
C	-7.080	-3.284	5.182	3.796	3.537	6.125	-0.9490	9.902	4.720	343.462
D	-6.489	-3.278	4.8835	3.211	3.714	6.624	-0.8028	10.070	5.186	398.115
HF/6-311++G (d, p)										
A	-9.082	0.818	4.132	9.9	0.862	-0.750	-2.4750	4.409	0.277	283.113
B	-9.072	0.819	4.1265	9.891	0.861	-0.751	-2.4728	4.403	0.277	284.948
C	-9.507	0.817	4.345	10.324	0.914	-0.752	-2.5810	4.646	0.301	286.180
D	-8.640	0.822	3.909	9.462	0.807	-0.751	-2.3655	4.161	0.252	335.839
M062X/6-311++G (d, p)										
A	-8.193	-2.074	5.1335	6.119	2.153	2.777	-1.5298	7.256	2.122	307.319
B	-8.181	-2.074	5.1275	6.107	2.153	2.778	-1.5268	7.251	2.123	311.069
C	-8.494	-2.076	5.285	6.418	2.176	2.748	-1.6045	7.396	2.111	313.699
D	-7.814	-2.073	4.9435	5.741	2.128	2.822	-1.4353	7.087	2.144	368.684
B3LYP/6-311++G (d, p)										
A	-6.778	-3.279	5.0285	3.499	3.613	6.352	-0.8748	9.960	4.931	331.174
B	-6.853	-3.266	5.0595	3.587	3.568	6.240	-0.8968	9.890	4.831	335.582
C	-7.080	-3.284	5.182	3.796	3.537	6.125	-0.9490	9.902	4.720	343.462
D	-6.489	-3.278	4.8835	3.211	3.714	6.624	-0.8028	10.070	5.186	398.115
HF/6-311++G (d, p)										
A	-9.082	0.818	4.132	9.9	0.862	-0.750	-2.4750	4.409	0.277	283.113
B	-9.072	0.819	4.1265	9.891	0.861	-0.751	-2.4728	4.403	0.277	284.948
C	-9.507	0.817	4.345	10.324	0.914	-0.752	-2.5810	4.646	0.301	286.180
D	-8.640	0.822	3.909	9.462	0.807	-0.751	-2.3655	4.161	0.252	335.839
M062X/6-311++G (d, p)										
A	-8.193	-2.074	5.1335	6.119	2.153	2.777	-1.5298	7.256	2.122	307.319
B	-8.181	-2.074	5.1275	6.107	2.153	2.778	-1.5268	7.251	2.123	311.069
C	-8.494	-2.076	5.285	6.418	2.176	2.748	-1.6045	7.396	2.111	313.699
D	-7.814	-2.073	4.9435	5.741	2.128	2.822	-1.4353	7.087	2.144	368.684

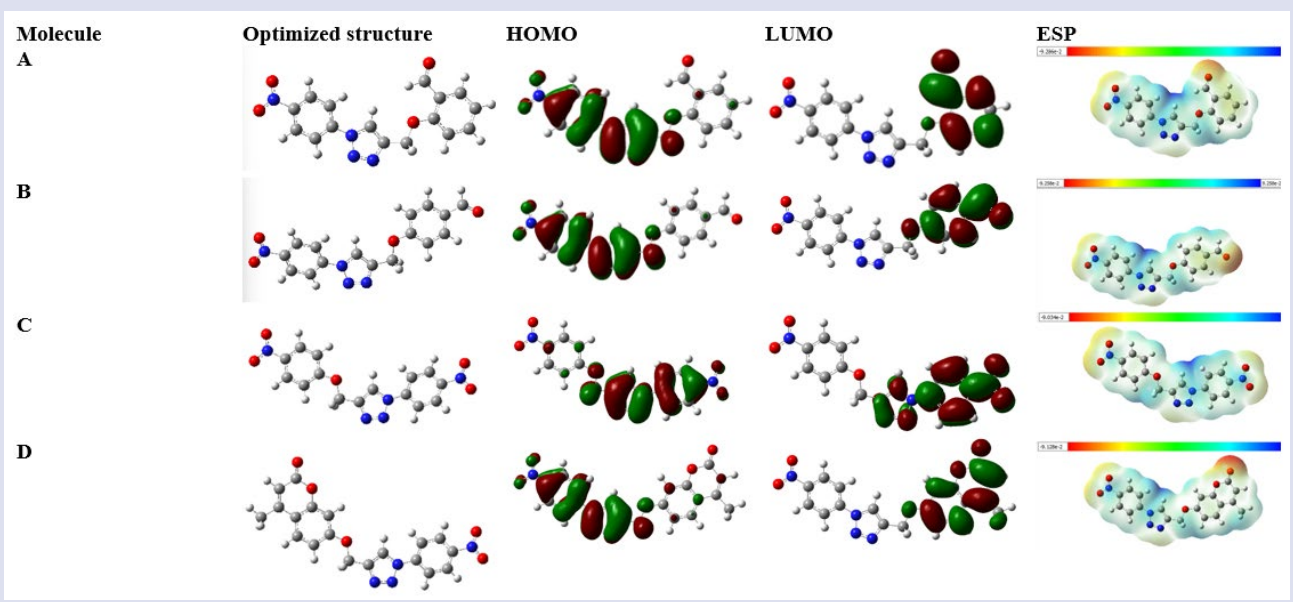

Figure 2. Optimized structures, HOMOs, LUMOs and ESP maps obtained at B3LYP/6-311++g (d p) calculation level of the studied molecular systems.

Conclusion

The present paper includes detailed Conceptual Density Functional Theory based computations to predict the corrosion inhibition performances of some triazole derivatives, namely, 2-((1-(4-nitrophenyl)-1H-1,2,3-triazol-4-yl) methoxy) benzaldehyde (A), 4-((1-(4-nitrophenyl)-1H-1,2,3-triazol-4-yl) methoxy) benzaldehyde (B), 4-((4-nitrophenoxy) methyl)-1-(4-nitrophenyl)-1H-1,2,3-triazole (C), 4-methyl-7-((1-(4-nitrophenyl)-1H-1,2,3-triazol-4-yl) methoxy)-2H-chromen-2-one (D). According to obtained data in both gas phase and aqueous phase, the best corrosion inhibitor among studied molecules is molecule D. Theoretical analyzes made are in good agreement with experimental observations and the predictions done in the light of popular electronic structure rules like Minimum Polarizability, Minimum Electrophilicity and Maximum Hardness Principles. The calculations and structural analyses made will be helpful for experimentalists in the design and synthesis of new triazole derivatives as corrosion inhibitor.

Conflicts of Interest

There are no conflicts of interest in this work.

References

[1] Erdoğan Ş., Safi Z.S., Kaya S., Işın D.Ö., Guo L., Kaya C., A Computational Study on Corrosion Inhibition Performances of Novel Quinoline Derivatives Against the Corrosion of Iron, *J. Mol. Struct*., 017 (1134) (2017) 751-761.

[2] Işın D.Ö., Karakuş N., Lgaz H., Kaya S., Chung I.M., Theoretical Insights About Inhibition Efficiencies of Some 8-Hydroxyquinoline Derivatives Against the Corrosion of Mild Steel, *Mol. Simul.,* 46(17) (2020) 1398-1404.

[3] Madkour L.H., Kaya S., Obot I.B., Computational, Monte Carlo Simulation and Experimental Studies of Some Arylazotriazoles (AATR) and Their Copper Complexes in Corrosion Inhibition Process, *J. Mol. Liquids*, 260 (2018) 351-374.

[4] Wazzan N.A., Obot I.B., Kaya S., Theoretical Modeling and Molecular Level Insights into the Corrosion Inhibition Activity of 2-Amino-1, 3, 4-Thiadiazole and its 5-Alkyl Derivatives, *J. Mol. Liquids*, 221 (2016) 579-602.

[5] Abdelsalam M.M., Bedair M.A., Hassan A.M., Heakal B.H., Younis A., Elbialy Z.I., et al., Green Synthesis, Electrochemical, and DFT Studies on the Corrosion Inhibition of Steel by Some Novel Triazole Schiff Base Derivatives in Hydrochloric Acid Solution, *Arabian J. Chem.,* 15(1) (2022) 103491.

[6] Belghiti M.E., Benhiba F., Benzbiria N., Lai C.H., Echihi S., Salah M., et al., Performance of Triazole Derivatives as Potential Corrosion Inhibitors for Mild Steel in a Strong Phosphoric Acid Medium: Combining Experimental and Computational (DFT, MDs & QSAR) Approaches, *J. Mol. Struct.*, 1256 (2022) 132515.

[7] Abdul-Rida N.A., Sayyah M.H., Jaber Q.A.H., Synthesis, Characterization, Efficiency Evaluation of Some Novel Triazole Derivatives as Acid Corrosion Inhibitors, *Int. J. Corros. Scale Inhib.,* 12(1) (2023) 101-125.

[8] Islam N., Kaya S., (Eds). Conceptual Density Functional Theory and Its Application in the Chemical Domain. *CRC Press*, (2018).

[9] Bolayır G., Soygun K., Avşar M.K., Boztuğ A., Kaya S., Katin K.P., Effect of Hemp Fiber Addition on Mechanical Properties of Acrylic Resin: Coupled Experimental and Theoretical Study, *Fibers Polym.*, 23(8) (2022) 2271-2278.

[10] Kaya Y., Erçağ A., Kaya S., Katin K.P., Atilla D., New Mixed-Ligand Iron (III) Complexes/Containing Thiocarbohydrazones: Preparation, Characterization, and Chemical Reactivity Analysis Through Theoretical Calculations, *Appl. Organomet. Chem.,* 36(7) (2022) e6762.

[11] Parr R.G., Szentpály L.V., Liu S., Electrophilicity Index, *J. Am. Chem. Soc.,* 121(9) (1999) 1922-1924.

[12] von Szentpály L., Kaya S., Karakuş N., Why and When is Electrophilicity Minimized? New Theorems and Guiding Rules*, J. Phys. Chem. A*, 124(51) (2020) 10897-10908.

[13] Gázquez J.L., Cedillo A., Vela A., Electrodonating and Electroaccepting Powers, J. Phys. Chem. A, 111 (10) (2007) 1966-1970.

[14] Gómez B., Likhanova N.V., Domínguez-Aguilar M.A., Martínez-Palou R., Vela A., Gázquez J.L., Quantum Chemical Study of the Inhibitive Properties of 2-Pyridyl-Azoles, *J. Phys. Chem. B.*, 110(18) (2006) 8928-8934.

[15] Mobin M., Aslam R., Salim R., Kaya S., An Investigation on the Synthesis, Characterization and Anti-Corrosion Properties of Choline Based Ionic Liquids as Novel and Environmentally Friendly Inhibitors for Mild Steel Corrosion in 5% HCl, *J. Colloid Interface Sci.,* 620 (2022) 293-312.

[16] Koopmans T., Über die Zuordnung von Wellenfunktionen und Eigenwerten zu den Einzelnen Elektronen eines Atoms, *Physica,* 1(1-6) (1934) 104-113.

[17] Kaya S., Kaya C., A New Equation for Calculation of Chemical Hardness of Groups and Molecules, *Mol. Phys.,* 113(11) (2015) 1311-1319.

[18] Kaya S., Kaya C., Islam N., Maximum Hardness and Minimum Polarizability Principles Through Lattice Energies of Ionic Compounds, *Physica B: Condens. Matter*, 485 (2016) 60-66.

[19] Kandemirli F., Sagdinc S., Theoretical Study of Corrosion Inhibition of Amides and Thiosemicarbazones, *Corros. Sci.*, 49(5) (2007) 2118-2130.

[20] Kaya S., Kaya C., A New Equation Based on Ionization Energies and Electron Affinities of Atoms for Calculating of Group Electronegativity, *Comput. Theor. Chem.,* 1052 (2015) 42-46.

[21] Kaya S., Banerjee P., Saha S.K., Tüzün B., Kaya C., Theoretical Evaluation of Some Benzotriazole and Phosphono Derivatives as Aluminum Corrosion Inhibitors: DFT and Molecular Dynamics Simulation Approaches, *RSC Adv.,* 6(78) (2016) 74550-74559.

Cumhuriyet Sci. J., 44(3) (2023) 497-503
DOI: https://doi.org/10.17776/csj.1127921

Cumhuriyet Science Journal

| csj.cumhuriyet.edu.tr | Founded: 2002 ISSN: 2587-2680 e-ISSN: 2587-246X Publisher: Sivas Cumhuriyet University

The Effects of Heavy Metals and Molasses on Enzyme Activity of *Candida* Yeast

Gülşah Başkan[1,a,*], Ünsal Açıkel[2,b]

[1]*Project Support Unit, Technology Transfer Office, Uşak University, Uşak, Türkiye*
[2]*Chemical Engineering Department, Faculty of Engineering, Sivas Cumhuriyet University, Sivas, Türkiye*
**Corresponding author*

Research Article

History
Received: 08/06/2022
Accepted: 22/08/2023

ABSTRACT

Lipases are mainly applied in the food, abluent and medicine industries. Through the high production costs of lipase enzymes for industrial applications, cheap and eco-friendly enzyme production has gained great importance in recent years. Yeasts can produce lipase enzyme and grow in acidic media. In the present study, the act of Cu^{2+}, Ni^{2+} and molasses concentrations on the enzyme activity of *Candida* yeasts were investigated in a batch system. The maximum enzyme activities of microorganisms were determined at pH:4. Lipase enzyme activity was investigated changing metal ion and molasses sucrose concentrations by 25-250 mg/L and 1-20 g/L respectively. When molasses sucrose concentration was increased, the enzyme activity of all yeasts increased to 10 g/L, and the lipase enzyme activity decreased at the higher molasses concentrations. Enzyme activity of yeasts decreased with increasing both metal ion concentrations at constant molasses sucrose concentrations. Ni^{2+} cations were more inhibited to enzyme activity of all yeasts than Cu^{2+}. Among the yeasts, *Candida membranefeciens* (936.96 U/L) showed the highest enzyme activity in media containing a constant molasses concentration of 10 g/L.

Keywords: *Candida*, Lipase, Cu^{2+}, Ni^{2}, Enzyme activity.

[a] *gulsah.mersin@usak.edu.tr* *https://orcid.org/0000-0002-2852-6114* [b] *uacikel@cumhuriyet.edu.tr* *https://orcid.org/0000-0003-4969-8502*

Introduction

Enzymes are known as biocatalysts with protein structure specific to a particular substrate naturally occur and can be synthesized artificially. The most common enzymes in nature are Amylase, cellulase, invertase, lactase, and lipase. Among these enzymes, lipases, which possess industrial and physiological importance are obtained from several herbs, bacteria, and yeasts. Hydrolysis of triglycerides to glycerol and free fatty acids through an oil-water interface is catalyzed by Lipases which are a member of hydrolase. Furthermore, they catalyze the hydrolysis and synthesis of other esters and play important role in transesterification [1,2]. Lipases exhibit a highly stable structure at high temperatures, pH, and organic solvents. Their enzymatic specificity regarding chemoselectivity, substrate selectivity, functional group selectivity, regional selectivity, stereoselectivity make it popular for the industry such as organic chemistry, detergent, milk, cosmetics, paper, and medicine [3,4]. Extracellular lipase is generally produced from various microorganisms and used in commercial applications [5]. Microbial lipases have some advantages such as high conversion efficiency of the substrate in comparison to other lipases that are produced from animal and plant cells [6]. One of the microorganisms that can produce lipase enzyme is yeasts. Among yeasts, *Candida* species can bind to metal ions in the environment as well as produce extracellular lipase with low nutritional requirements and high biomass production. Owing to active transport mechanisms, it transfers absorbed elements and accumulates them into cells as metal form [7]. The biomass of *Candida* yeast can be a source of mineral content by accumulating various substances that exceed the essential nutrients of the cells [8]. *Candida* yeasts are aerobic microorganisms and rapidly increase their biomass during aeration [9]. Optimum production conditions usually occur at 25-30 ^{o}C and pH 4.0-6.0 [2]. The enzyme activity of *Candida* yeasts is determined using appropriate carbon and nitrogen-based substrates in the nutrient medium and the presence of activating agents. Lipase activity may also change several parameters such as pH, temperature, substrate concentration, and inoculation level [10]. Lipid carbon sources, nitrogen sources, and micronutrients are required to obtain highly efficient lipase [11]. Furthermore, the synthesis and activation of lipase are affected by compounds that act as nitrogen source. Several nitrogen sources such as ammonium and sodium salts, yeast extracts, urea, peptone, etc. provide higher lipases activity for many microorganisms [12, 13]. Metal ions can stimulate or inhibit microbial enzyme production according to the genetic structure of the microorganism. Especially Ca^{2+}, effects structural and functional properties of enzymes, and plays a vital role in the production of some lipases with calcium-dependent metabolism. While Ca^{2+} ions increase enzyme activity, $Zn^{2+}$and ferric (Fe^{2+}, Fe^{3+}) ions strongly inhibit. Metal ions such as Co^{2+}, Zn^{2+}, Mg^{2+}, Mn^{2+}, Al^{3+} and Na^{+} have slightly inhibitory effects on microbial lipase production [14,15].

For yeasts and fungi, acidic pH increases lipase production, and these microorganisms can grow in an acidic medium. A good lipase production efficiency was determined using *Rhodotorula glutinis* HL25 at pH:6 [16]. It was reported that lipase production and activity of *Penicillium sp.* section Gracilenta increased at pH:4 [17]. Temperature plays an important role in microbial lipase production. Low temperatures can decrease lipase enzyme production whereas high temperatures may cause enzyme degradation [18]. Temperature affects the enzyme activity of microorganisms according to microorganism type. Incubation time affects the lipase activity produced by the yeast due to optimum conditions for yeast growth and lipase production [19]. According to most studies, *Candida* yeasts are the most efficient lipase producer. *Candida utilis* [20], *Candida* [21], *Candida tropicalis* [22], (*Candida* albicans [23], *Candida* rugosa [24], *Candida cylindracea* [25], *Candida lipolytica* [26], *Candida antarctica* [27] can be given as examples.

Lipases are largely used in wastewater treatment under both aerobic and anaerobic conditions and are effective in water treatment for food and textile industries. For this reason, enzymatic techniques in water treatment have gained more attention because of specific properties such as enantiomeric, regional selectivity and substrate specificity [28]. Due to the *Candida* biomass can bioaccumulate metal ions, produce lipase enzyme and growth in metal contained media, uptake of Cu^{2+} and Ni^{2+} ions were investigated with changing molasses sucrose and Cu^{2+} and Ni^{2+} ion concentrations in our previous study [29]. We observed that biomass concentrations and specific growth rates increased when initial molasses sucrose concentration were increased in a medium containing metal and metal-free media. Specific growth rates of the yeasts were inhibited with Cu^{2+} and Ni^{2+} and the inhibition effect of Ni^{2+} ions was higher than Cu^{2+}. In this study, we aimed to investigate the enzyme activity of candida species in different fermentation media. Enzyme activities of yeasts were determined by changing growth media contents such as molasses and heavy metal concentrations in a batch reactor.

Material and Method

Candida membranafiens (*C. membranafiens*), *Candida utilis* (*C. utilis*), *Candida tropicalis* (*C. tropicalis*) and *Candida lipolytica* (*C. lipolytica*) were provided by the Department of Biology in Ankara University (Turkey). $(NH_4)_2SO_4$ and K_2PO_4 were bought from Sigma-Aldrich Company. Sugar factory which is in main Ankara (Turkey) donated molasses sucrose. Molasses consisting of 47-48% sugar was applied as the one carbon source of the yeasts for microbial growth [29].

Microorganism Growth Media

Growth media of *Candida* yeasts were prepared with 1 g/L $(NH_4)_2SO_4$ and K_2PO_4. Molasses sucrose concentration was varied from 1 to 10 g/L. Fermentation media was sterilized in an autoclave operated at 121°C at 0.99 bar for 15 minutes. Subcultures of yeasts were growth in 4 days by agitating at 150 rpm. 1 g $Cu(NO_3)_2.3H_2O$ and $Ni(NO_3)_2.6H_2O$ dissolved in water by one by and 1 g/L stock solutions of were prepared for Cu^{2+} and Ni^{2+} solutions. All experiments were conducted at pH:4 and 25 °C. Details of the adaptation experiments of the yeasts were discussed in our previous study. Microorganism concentration, residual Cu^{2+} and Ni^{2+} concentrations were determined at 360, 460 nm and 340 nm, respectively [29].

Analytical Procedure

P-nitro-phenylpalmitate (pNPP) method was used to the prediction of lipase activity of *Candida* yeasts. Experimental studies were compared in terms of lipase activity (U/L). In this method, the amount of enzyme needs to hydrolyze 1 µmol of pNP per minute describes as the one enzyme unit (U) of lipase activity. For the determination of enzyme activity spectrophotometrically, solutions A solution B and p-nitro-phenylpalmitate (pNPP) were used. For solution A: pNPP was dissolved in propan-2-ol and solution B: gum arabic and Triton X-100 was dissolved in distilled water. Solutions pH were adjusted to 8. Solution A was added to solution B by dropwise and it was used as the substrate solution. Tris buffer was used to adjust of pH as 8.5 [30]. This mixture was incubated for 30 min. at 150 rpm and 37°C. Enzyme activity of *Candida* yeasts was determined at 420 nm using a UV-vis spectrophotometer.

Results and Discussion

In our previous study we investigated microorganism growth by changing metal ions and molasses sucrose concentrations at pH: 4 and 25°C. The results indicated that biomass concentration was related to the metal concentrations in the fermentation medium and the physiological properties of the yeasts. pH was varied from 2 to 5 for the determination of pH effect on specific growth rate and maximum microorganism concentrations of *Candida* yeasts in a medium containing 10 g/L molasses sucrose. Maximum specific growth rate and microorganism concentrations were obtained at pH: 4. The highest specific growth rate and microorganism concentration were obtained as 0.308 h^{-1} and 3.111 g/L respectively using *C. lipolytica* in metal free medium. Molasses sucrose concentrations were varied from 1.0 to 20.0 g/L for investigation of growth rates of yeasts at pH: 4 and 25°C in metal-free media. Saturation kinetics were used to determination of the relevance of specific growth rate-substrate concentration. Detail results were presented in our previous study [29].

Lipase Enzyme Activity of Yeasts at Different Ph Values

Enzyme reaction rate changes with different hydrogen ion concentrations. Microbial growth and enzyme activity also changes the pH value of culture media. Most of the studies showed that the enzyme activity of yeasts is significantly sensitive to pH changes

during microbial growth and enzyme reaction slows down at pH values just next to the optimum pH value. In this case, the enzyme may denature and becomes inactive. Buffer solutions are used in enzyme studies to work at a constant optimum pH [31]. Lipase enzyme activities of yeasts at different pH values were investigated at pH: 2-5 and 10 g/L constant molasses sucrose concentration. From Figure 1, it was seen that lipolytic activity of yeasts increased with increasing pH up to 4.0. The highest value of enzyme activity was found as 934.52 U/L using *C. membranafiens*. Among the yeasts *C.utilis* showed the lowest lipase activity at pH:4 as 470.92 U/L (Figure 1). Keklikçioğlu Çakmak and Açikel (2015) reported that the lipase activity of *Candida utilis* was 788.5 U/L in aqueous media containing soybean oil at pH: 4 and 25°C [32].

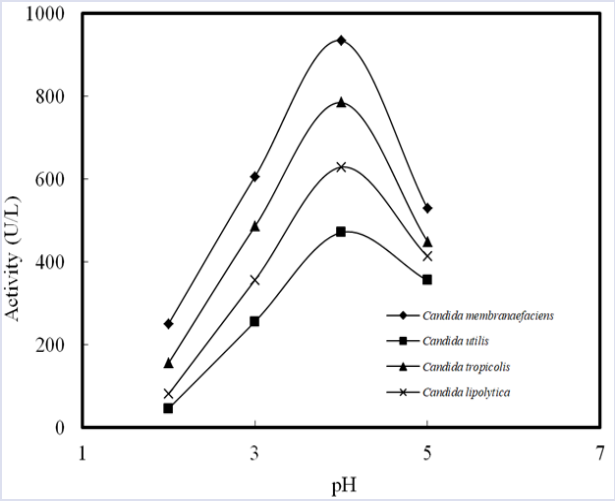

Figure 1. Lipase enzyme activity of yeasts at different pH values.

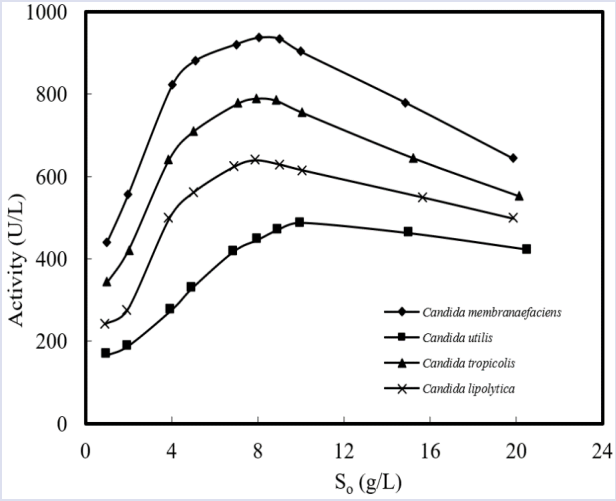

Figure 2. Lipase enzyme activity of yeasts at different molasses sucrose concentrations

Lipase Enzyme Activity of Yeasts at Different Molasses Sucrose Concentrations

Our results showed that initial molasses concentration influenced the enzyme activity of the yeasts. To investigate that, molasses sucrose concentrations were varied from 1.0 to 20.0 g/L, at pH 4.0 and at 25 ◦C. Enzyme activity of all yeasts increased with an increase in initial molasses sucrose concentration up to 10 g/L (Figure 2). It was attributed that higher molasses concentrations reduced the ethanol yield and efficiency of microorganisms. It also indicates catabolite or sugar inhibition that reduces enzyme activity in the fermentation medium. At high sugar concentrations, microorganisms produce ethanol rather than biomass under aerobic conditions. In this case, oxidative enzymes were less produced, and the cells shows fermentative metabolism [33]. Molasses contains trace elements such as K^+, Na^+, Ca^{2+}, Mg^{2+}, Fe^{2+}, Al^+, Cl^-, SO_4^-, PO_4^-, NO_3^- that did not show any significant influence on the lipid content in microorganisms [30]. Among the yeasts, *C. membranifaciens* showed the maximum activity at pH 4.0. It was determined as 903.41 U/L. Lipase activity of *C. membranifaciens* decreased from 903.41 U/L to 778.848 U/L with an increase in the initial molasses sucrose concentration from 10 to 15 g/L.

Açikel et al. (2011) used glucose and molasses sucrose as carbon sources for the determination of the lipase activity of *R. delemar*. They observed that the maximum lipase enzyme activity was obtained with 5 g/L of molasses sucrose [30]. Mihajlovski et al. (2016) examined the β-Amylase enzyme activity of *P. chitinolyticus* CKS1. Maximum β-amylase activity were stated as 2.237 U/ml under optimal conditions (inoculum concentration: 10%, incubation time: 83.07 h) [34]. Galvão de Morais et al. (2016) investigated lipase enzyme activity of *C. rugosa* at pH: 3.5 and 27 °C. They used 200 g/L of soybean molasses as a carbon nutrient. After 12 h, lipolytic activity was measured as 12.3 U/mL [35].

Lipase Enzyme Activity of Yeasts at Different Cu^{2+} and Ni^{2+} Ion Concentrations

The combined effect of single Cu^{2+} and Ni^{2+} ion and molasses concentrations on the lipase activities of *Candida* yeasts was studied. Initial Cu^{2+} and Ni^{2+} ion concentrations and molasses concentrations were varied from 25 to 250 mg/L and from 1 to 20 g/L respectively. Lipase activities of yeasts at different molasses and metal ion concentrations were presented in Table 1 and Table 2. The results showed lipase enzyme activity of yeasts increased with an increase in initial molasses sucrose concentration. But Cu^{2+} and Ni^{2+} ions showed adverse impact on the lipase production of *Candida* yeasts and lipase activity significantly decreased with an increase in Cu^{2+} and Ni^{2+} ion concentrations. It can be attributed that decreasing enzyme activity in metal-containing media may be related to the growth of microorganisms and was produced less enzyme as the microorganism growth decreases. This decrease might be due to a change in solubility of Cu^{2+} and Ni^{2+} ions, the catalytic properties of the enzyme and the properties of the ionized fatty acids at interfaces [14]. Lipase activities were determined as 701.04 U/L, 362.95 U/L, 578.52 U/L, 464.69 U/L for *C.*

membranaefaciens, *C. utilis*, *C. tropicalis*, *C. lipolytica*, respectively, at medium contained 10 g/L constant molasses and 200 mg Cu^{2+}/L (Figure 3 and Table 1). Under the same conditions, lipase activity decreased for all yeasts in a medium containing Ni^{2+} ions when compared to Cu^{2+} ions. For example, lipase activity was determined in a medium containing 200 mg Ni^{2+}/L and 10 g/L molasses as 634.19 U/L, 326.95 U/L, 525.65 U/L, 419.21 U/L for *C. membranaefaciens*, *C. utilis*, *C. tropicalis, C. lipolytica*, respectively (Figure 4 and Table 2).

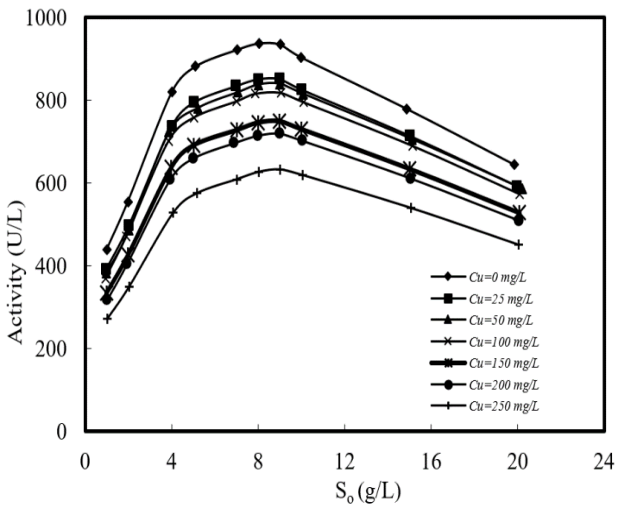

Figure 3. Lipase enzyme activity of *C. membrananaficiens* at different Cu^{2+} and molasses concentrations.

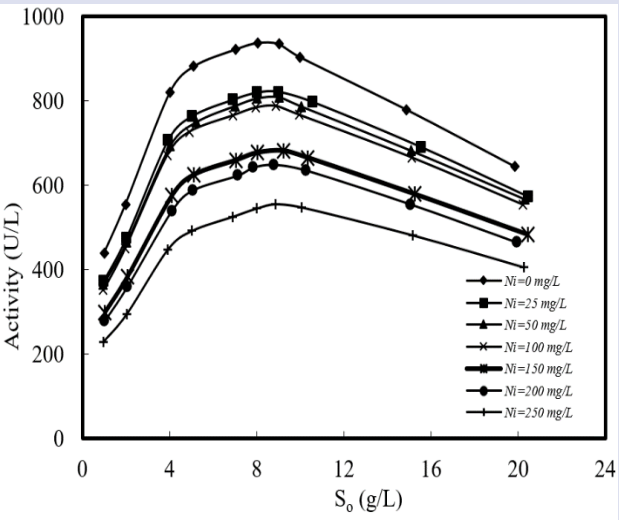

Figure 4. Lipase enzyme activity of *C. membrananaficiens* at different Ni^{2+} and molasses concentrations.

Lipase activities were determined as 903.4 U/L, 486.5 U/L, 755.2 U/L, 614.7 U/L respectively for *C.membranaefaciens*, *C. utilis*, *C. tropicalis*, *C. lipolytica* at 10 g/L molasses concentration in metal-free media (Table 3). For example, lipase activity decreased from 903.4 to 795.0 U/L with an increase in Cu^{2+} ion concentration 0.0 from to 100 mg/L at 10 g/L of constant molasses concentration using *C. membranaefaciens*. It was found that the inhibition effect of Ni^{2+} ions on lipase activity of all yeasts was higher than Cu^{2+} ions. Lipase activity decreased from 903.4 to 397.90 U/L with an increase in the initial Ni^{2+} concentration from 0 to 100 mg/L for *C. membranaefaciens* (Table 3). Lipase determination using living biomass, the chemical nature of metal ions plays an important role. Apart from essential trace metals for metabolic activities of microorganisms, higher concentrations of heavy metals might be deadly toxic and can be inhibited to enzyme activity [29, 36].

According to our results, molasses sucrose was efficient for lipase production by *Candida* species. In previous studies, it can be concluded that *Candida* species produced lipase and showed different enzyme activities in various fermentation mediums. Grbavcic et al. (2007) investigated the lipase activity of *Candida utilis* and they obtained the highest lipolytic activity of 284 U/dm^3 in a medium containing oleic acid and hydrolyzed casein as carbon and nitrogen sources, respectively, and supplemented with Tween 80 [37]. Andrade Silva et al. (2015) evaluated the use of cheese whey for lipase production by *Candida lipolytica*. The highest lipase activity was found as 118 U/mL at pH 5.0 -5.3 and 28 °C in the presence of cheese whey [26]. Rehman et al. (2014) investigated lipase activity of various yeast cultures including *Candida lipolytica* NRRL-Y-1095, *Candida utilis* NRRL-Y-900, *Candida tropicalis* NRRL-Y-1552 in a fermentation medium containing agro-industrial by-products. The maximum enzyme activity was determined as (1.12±0.09 U) with *C. utilis* NRRL-Y-900 when soybean meal was used in growth media [38].

Table 1. Lipase activities of yeasts at different initial molasses sucrose and Cu^{2+} ion concentrations

		U/L			
Yeast	**C_{oCu} (mg/L) S_o (g/L)**	**25**	**100**	**200**	**250**
C. memb.	2	496.29	470.81	404.35	348.95
	5	795.06	758.04	659.32	574.70
	10	825.71	795.00	701.04	617.93
	15	714.20	689.28	609.83	538.96
	20	592.08	572.78	508.42	450.50
C. uti.	2	162.32	154.06	132.07	113.66
	5	287.23	273.40	236.50	204.88
	10	430.09	413.55	362.95	318.19
	15	409.04	394.29	347.25	305.28
	20	374.91	362.28	320.15	282.24
C. tro.	2	373.23	353.85	304.56	263.28
	5	632.31	602.53	523.14	455.09
	10	682.74	657.07	578.52	509.04
	15	584.63	564.00	498.26	439.60
	20	502.70	486.13	430.89	381.17
C. lip.	2	242.18	229.45	197.34	170.22
	5	495.37	471.78	408.88	354.96
	10	549.52	528.63	464.69	408.15
	15	492.47	474.90	418.90	368.94
	20	447.75	432.82	383.07	338.30

Table 2. Lipase activities of yeasts at different initial molasses sucrose and Ni^{2+} ion concentration

Yeast	C_{oNi} (mg/L) S_o (g/L)	U/L 25	100	200	250
C. memb.	2	474.69	449.21	358.37	295.23
	5	763.33	726.31	587.04	491.84
	10	796.80	766.10	634.19	547.46
	15	690.05	665.13	553.76	481.32
	20	572.78	553.47	463.37	405.45
C. uti.	2	155.37	146.73	115.92	187.88
	5	275.37	261.54	209.49	329.40
	10	414.52	397.98	326.95	280.24
	15	394.75	379.99	314.05	461.16
	20	362.28	349.64	290.66	421.25
C. tro.	2	356.80	337.00	275.50	220.73
	5	606.79	577.01	473.52	388.46
	10	658.57	632.89	525.65	450.13
	15	564.65	544.02	453.14	391.90
	20	486.13	469.55	392.22	342.50
C. lip.	2	231.66	218.93	173.54	141.99
	5	475.15	451.56	362.82	302.16
	10	529.85	508.96	419.21	360.20
	15	475.45	457.88	379.37	328.31
	20	432.82	417.90	348.25	303.47

In recent years, green synthesis methods have gained importance in enzyme production. It is known as an environmentally friendly method that agricultural wastes are reused as a carbon source. Production of lipases using waste substrates such as molasses reduces the cost of obtaining valuable metabolites. *Candida* type yeasts are crucial, particularly for the food industry However, their specific properties enable *Candida* yeasts to be used in biotechnological processes such as lipase production and to be used in many commercial and industrial areas [39]. So, interest in the bioconversion of molasses sucrose into a value-added product such as lipase has increased. Molasses offers a wide range of potential uses in the manufacture of industrial enzymes like lipase and value-added bioproducts, according to recent studies and available data.

Lipase enzyme production using microorganism culture in a liquid medium is often preferred because of better control of growth and environmental conditions. This approach makes it possible to conduct essential optimization studies for maximum enzyme production. This study comparatively presents the inhibitory effect of heavy metals on the lipase production of *Candida* strains. Investigation of the survival of *Candida* type yeasts in a stressful environment has enabled the optimization of sustainable lipase production with wastes such as molasses.

Table 3. Decrease in lipase enzyme activities of yeasts in media contained 100 and 250 mg/L single Cu^{2+} and Ni^{2+} ions

Metal Ion (mg/L)		*C. membranefeciens*		*C. utilis*		*C. tropicalis*		*C. lipolytica*	
C_{oCu}	C_{oNi}	Activity U/L	Decrease %	Activity U/L	Decrease %	Activity U/L	Decrease %	Activity U/L	Decrease %
0.0	0.0	903.41	0.0	486.54	0.0	755.25	0.0	614.68	0.0
100.0	0.0	795.00	12.0	413.55	15.0	657.07	13.0	528.63	14.0
250.0	0.0	617.93	31.6	318.19	34.6	509.04	32.6	408.15	33.6
0.0	100.0	766.10	15.2	397.98	18.2	632.89	16.2	508.96	17.2
0.0	250.0	547.46	39.4	280.24	42.4	450.13	40.4	360.20	41.4

Conclusion

In this study, lipase enzyme activities of *Candida* species were investigated at pH:4 and 25 °C. Lipase activity of the *Candida* yeasts increased with an increase in initial molasses sucrose concentration to 10 g/L. In the experiments performed at a constant sucrose concentration of 10 g/L, maximum enzyme activity was obtained at pH 4.0 and *Candida membranaefaciens* showed the highest activity (934.52 U/L). It was found that the enzyme activities of all yeasts increased with the increasing initial sucrose concentration up to 10 g/L but it decreased above this value. We have found that molasses was a suitable carbon source for fermentation medium of *Candida* species. A significant decrease in enzyme activities of yeasts was observed when concentrations of Cu^{2+} and Ni^{2+} were increased. Enzyme activities of yeasts were inhibited with Cu^{2+} and Ni^{2+} ions and the contribution of Cu^{2+} ions in inhibition was lower than Ni^{2+}. The highest lipase activity was obtained using *Candida membranifaciens* in fermentation media not contained Cu^{2+} and Ni^{2+} ions singly.

Eco-friendly applications of lipase enzymes which were produced by *Candida* cells offer wastewater treatments that contain both lipid and heavy metal contaminations. Our studies showed that metal resistant *Candida* cells highly had lipase activity and they bioaccumulated Cu^{2+} and Ni^{2+} ions, simultaneously. We found that both microbial growth and lipase production depended upon initial pH, molasses and Cu^{2+} and Ni^{2+} ion concentrations of the growth medium. Compatible relevance was seen between lipase activity and biomass concentration. In our previous study, *Candida utilis* was sensitive to high concentrations of Cu^{2+} and Ni^{2+} with an

extension in lag phase duration, correlated with a decrease in lipase production. Although, we obtained the highest specific growth rate and microorganism concentration using *Candida lipolytica* in metal media, it did not show the highest lipase activity. So, there was an inverse relation between metal bioaccumulation and lipase activity. This difference may be due to the adaptation of yeasts to growth medium containing Cu^{2+} and Ni^{2+} ions, chemical properties of metals and differences in microorganism nature.

Our studies showed that *Candida* species can be innovative in lipase production and bioaccumulation of heavy metals from wastewaters. The study can also help other researchers in choosing an effective *Candida* strain for lipase production and metal bioaccumulation.

Conflicts of interest

There are no conflicts of interest in this work.

Acknowledge

This research was supported by Sivas Cumhuriyet University Scientific Research Projects Unit (Project Number: BAP- M-354).

References

[1] Geoffry K., Achur R.N., A Novel Halophilic Extracellular Lipase with Both Hydrolytic and Synthetic Activities, *Biocatal. Agric. Biotechnol.*, 12 (2017) 125–130.

[2] Kieliszek M., Kot A.M., Bzducha-Wróbel A., Błażejak S., Gientka I., Kurcz A., Biotechnological Use of *Candida* Yeasts in The Food Industry: A Review, *Fungal Biol. Rev*., 3(4) (2017) 185-198.

[3] Tan J.S., Abbasiliasi S., Ariff A.B., Ng H.S., Bakar M., Chow Y.H., Extractive Purification of Recombinant Thermostable Lipase from Fermentation Broth of *Escherichia coli* Using An Aqueous Polyethylene Glycol Impregnated Resin System, *3Biotech.*, 8(6) (2018) 288.

[4] Thapa S., Li H., OHair J., Bhatti S., Chen F.C., Nasr K.A., Johnson T., Zhou S., Biochemical Characteristics of Microbial Enzymes and Their Significance from Industrial Perspectives, *Mol. Biotechnol*., 61(8) (2019) 579–601.

[5] Gurung N., Ray S., Bose S., Rai V., A Broader View: Microbial Enzymes and Their Relevance in Industries, Medicine, and Beyond, *Biomed Res. Int.*, (2013) 329121.

[6] Seth S., Chakravorty D., Dubey V.K., Patra S., An Insight into Plant Lipase Research Challenges Encountered, *Protein Expr. Purif*., (95) (2014) 13-21.

[7] Santos C.A., Caldeira M.L., Lopes da Silva T., Novais J.M., Reis A., Enhanced Lipidic Algae Biomass Production Using Gas Transfer from A Fermentative *Rhodosporidium toruloides* Culture to An Autotrophic *Chlorella protothecoides* Culture, *Bioresour. Technol*., 138 (2013) 48-54.

[8] Kieliszek M., Błażejak S., Bzducha-Wróbel A., Influence of Selenium Content in The Culture Medium on Protein Profile of Yeast Cells *Candida utilis* ATCC 9950, *Oxid. Med. Cell. Longev.*, (2015a) 659750.

[9] Krüger W., Vielreicher S., Kapitan M., Jacobsen I.D., Niemiec M.J., Fungal-Bacterial Interactions in Health And Disease, *Pathogens.,* 8(2) (2019) 70.

[10] Rekha K.S.M., Lakshmi C.M.V., Sri Devi V., Kumar S.M., Production and Optimization of Lipase from *Candida rugosa* Using Groundnut Oilcake Under Solid State Fermentation, *Int. J. Eng. Res. Appl.*, 1(4) (2012) 571-577.

[11] Alishah Aratboni H., Rafiei N., Garcia-Granados R., Alemzadeh A., Morones-Ramirez J.R., Biomass and Lipid İnduction Strategies in Microalgae for Biofuel Production and Other Applications, *Microb. Cell Fact.*, 18 (2019) 178.

[12] Oliveira F., Moreira C., Salgado J.M., Abrunhosa L., Venancio A., Belo I., Olive Pomace Valorization by *Aspergillus* Species: Lipase Production Using Solid-State Fermentation, *J. Sci. Food Agric.*, 96(10) (2016) 3583–3589.

[13] Priyanka P., Kinsella G., Henehan G.T., Ryan B.J., Isolation, Purification and Characterization of A Novel Solvent Stable Lipase from *Pseudomonas reinekei*, *Protein Expr. Purif.* 153 (2019) 121–130.

[14] Rasmey A.M., Aboseidah A.A., Gaber S., Mahran F., Characterization and Optimization of Lipase Activity Produced by *Pseudomonas monteilli* 2403-KY120354 Isolated from Ground Beef, *Afr. J. Biotechnol.*, 16(2) (2017b) 96-105.

[15] Zheng X., Cheng W., Ji C., Zhang J., Yin M., Detection of Metal Ions in Biological Systems: A Review, *Rev. Anal. Chem.*, 39(1) (2020) 231-246.

[16] Taskin M., Ucar M.H., Unver Y., Kara A.A., Ozdemir M., Ortucu S., Lipase Production with Free and Immobilized Cells of Cold-Adapted Yeast *Rhodotorula glutinis* HL25, *Biocatal. Agric. Biotechnol*., 8 (2016) 97-103.

[17] Turati D.F.M., Almeida A.F., Terrone C.C., Nascimento J.M., Terrasan C.R., Fernandez-Lorente G., Carmona E.C., Thermotolerant Lipase from *Penicillium sp.* Section *Gracilenta* CBMAI 1583: Effect of Carbon Sources on Enzyme Production, Biochemical Properties of Crude and Purified Enzyme and Substrate Specificity, *Biocatal. Agric. Biotechnol*., 17 (2019) 15–24.

[18] Bharathi D., Rajalakshmi G., Komathi S., Optimization and Production of Lipase Enzyme from Bacterial Strains Isolated from Petrol Spilled Soil, *J. King Saud Univ. Sci*., 31(4) (2018) 898-901.

[19] Bharathi D. and Rajalakshmi G., Microbial Lipases: An Overview of Screening, Production and Purification, *Biocatal. Agric. Biotechnol*., 22 (2019) 101368.

[20] Moftah O.A., Grbavčić S., Zuža M., Luković N., Bezbradica D., Knežević-Jugović Z., Adding Value to The Oil Cake As A Waste from Oil Processing Industry: Production of Lipase and Protease by *Candida utilis* in Solid State Fermentation, *Appl. Biochem. Biotechnol.*, 166 (2) (2012) 348–364.

[21] Divya K. and Padma P.N., Psychrophilic Yeast Isolates for Cold-Active Lipase Production, *Int. J. Sci. Prog. Res*., 10 (2015) 93-97.

[22] Dias B., Lopes M., Ramôa R., Pereira A.S., Belo I., *Candida tropicalis* As A Promising Oleaginous Yeast for Olive Mill Wastewater Bioconversion, *Energies.*, 14 (3) (2021) 640.

[23] Jalal M., Ansari M.A., Alzohairy M.A., Ali S.G., Khan H.M., Almatroudi A., Siddiqui M.I., Anticandidal Activity of Biosynthesized Silver Nanoparticles: Effect on Growth, Cell Morphology, and Key Virulence Attributes of *Candida* species, *Int. J. Nanomedicine.*, 14 (2019) 4667-4679.

[24] Su F., Peng C., Li G.L., Xu L., Yan Y.J., Biodiesel Production from Woody Oil Catalyzed by *Candida rugosa* Lipase in Ionic Liquid, *Renew. Energy*., 90 (2016) 329–335.

[25] Salihu A., Alam M.Z., Abdulkarim M.I., Salleh H.M., Optimization of Lipase Production by *Candida cylindracea* in Palm Oil Mill Effluent Based Medium Using Statistical Experimental Design, *J. Mol. Catal. B.: Enzym.,* (69) (2011) 66–73.

[26] Andrade Silva M., Silva T., Amorim Salgueiro A., Campos Takaki G., Tambourgi E., Reuse of Whey Cheese for Lipase Production by *Candida lipolytica*, *Chem. Eng. Trans.,* 43 (2015) 331-336.

[27] Theron C.W., Vandermies M., Telek S., Steels S., Fickers P., Comprehensive Comparison of *Yarrowia lipolytica* and *Pichia pastoris* for Production of *Candida antarctica* Lipase B, *Sci. Rep*., 10 (2020) 1741.

[28] Zhong L., Feng Y., Wang G., Wang Z., Bilal M., Lv H., Jia S., Cui J., Production and Use of Immobilized Lipases in/on Nanomaterials: A Review from The Waste to Biodiesel Production, *Int. J. Biol. Macromol*., 152 (2020) 207–22.

[29] Mersin G. and Açıkel Ü., Production of *Candida* Biomasses for Heavy Metal Removal from Wastewaters, *Trakya Univ. J. Nat. Sci*., 22(1) (2021) 67-76.

[30] Açikel U., Erşan M., Sağ Açikel Y, The Effects of The Composition of Growth Medium and Fermentation Conditions on The Production of Lipase by *R. Delemar*, *Turk. J. Biol.*, 35 (2011) 35-44.

[31] Robinson P.K., Enzymes: Principles and Biotechnological Applications, *Essays Biochem*., 59 (2015) 1-41.

[32] Keklikçioğlu Çakmak N. and Açıkel Ü., *Candida utilis* Mayasıyla Lipaz Enzimi Aktivitesinin Farklı Ortam Koşullarında İncelenmesi, *J. Fac. Eng. Archit. Gazi Univ*., 30 (3) (2015) 475-485.

[33] Taherzadeh M. J. and Karimi K., Fermentation Inhibitors in Ethanol Processes and Different Strategies to Reduce Their Effects, *Biofuels.*, (2011) 287–311.

[34] Mihajlovski K.R., Radovanović N.R., Veljović N., Šiler-Marinković S.S, Dimitrijević-Branković S.I., Improved β-amylase Production on Molasses and Sugar Beet Pulp by A Novel Strain *Paenibacillus chitinolyticus* CKS1, *Ind. Crops Prod.*, 80 (2016) 115- 122.

[35] Galvão de Morais W., Kamimura E.S., Ribeiro E.J., Pessela B.C., Cardoso V.L., de Resende M.M., Optimization of The Production and Characterization of Lipase from *Candida rugosa* and *Geotrichum candidum* in Soybean Molasses by Submerged Fermentation, *Protein Expr. Purif*., 123 (2016) 26-34.

[36] Açikel U. and Alp T., A Study on the Inhibition Kinetics of Bioaccumulation of Cu(II) and Ni(II) Ions Using *Rhizopus delemar*, *J. Hazard. Mater*., 168 (2-3) (2009) 1449-1458.

[37] Grbavcic S., Dimitrijevic-Brankovic S., Bezbradica D., Siler-Marinkovic S., Knezevic Z., Effect of Fermentation Conditions on Lipase Production by *Candida utilis*, *J. Serb. Chem. Soc*., 72(8-9) (2007) 757–765.

[38] Rehman A.U., Rasool S., Mukhtar H., Haq I.U., Ikram U.H., Production of An Extracellular Lipase by *Candida utilis* NRRL-Y-900 Using Agro-Industrial By-Products, *Turk. J. Biochem.*, 39(2) (2014) 140–149.

[39] Zieniuk B., Mazurczak-Zieniuk P., Fabiszewska A., Exploring the Impact of Lipid-Rich Food İndustry Waste Carbon Sources on The Growth of *Candida cylindracea* DSM 2031, *Fermentation,* 6(4) (2020) 122.

Cumhuriyet Sci. J., 44(3) (2023) 504-509
DOI: https://doi.org/10.17776/csj.1284327

Cumhuriyet Science Journal

| csj.cumhuriyet.edu.tr | Founded: 2002 ISSN: 2587-2680 e-ISSN: 2587-246X Publisher: Sivas Cumhuriyet University

Effect of Synthesizing Process on the Formation of Fe_3O_4 Magnetic Nanoparticles

Cemal Aka [1,a], Mustafa Akyol [1,b,*]

[1] *Department of Materials Science and Engineering, Adana Alparslan Türkeş Science and Technology University, 01250 Adana, Türkiye*
**Corresponding author*

Research Article

History
Received: 17/04/2023
Accepted: 28/08/2023

ABSTRACT

In this work, the effect of synthesizing process on the morphology, structure, and magnetic properties of Fe_3O_4 magnetic nanoparticles have been studied by performing X-ray diffraction, scanning electronic microscopy, and vibrating sample magnetometer measurements. Fe_3O_4 nanoparticles were synthesized by hydrothermal and solvothermal methods. X-ray diffraction analysis revealed that both samples have cubic crystal phase. However, Fe_2O_3 impurity peaks were observed in the sample synthesized by hydrothermal method. The crystallite sizes of samples synthesized by hydrothermal and solvothermal methods were approximately 38 and 24 nm, respectively. The scanning electron microscope images show that spherical porous and cubic shape Fe_3O_4 nanoparticles were obtained by solvothermal and hydrothermal method, respectively. The average particle sizes of Fe_3O_4 samples synthesized by hydrothermal and solvothermal methods were determined as 220 and 450 nm, respectively. Both samples behave a soft ferromagnetic characteristic having almost zero coercive field. The magnetic saturation values of Fe_3O_4 nanoparticles synthesized by hydrothermal and solvothermal methods were determined as 28.78 and 77.31 emu/g, respectively. As a result of the characterizations, porous Fe_3O_4 nanoparticles synthesized by solvothermal method show better crystal structure, morphological and magnetic properties than Fe_3O_4 nanoparticles synthesized by hydrothermal method.

Keywords: Fe_3O_4, Magnetic nanoparticles, Hydrothermal, Solvothermal, Magnetic hysteresis.

[a] *cemalakaa@gmail.com* *https://orcid.org/0009-0009-3780-0822* [b] *makyol@atu.edu.tr* *https://orcid.org/0000-0001-8584-0620*

Introduction

Magnetic materials have an important place in modern technology. One of the most commonly used magnetic material is magnetite (Fe_3O_4) due to its low cost, low toxicity and good magnetic properties [1]. It is a ferrimagnetic material because its crystal lattice is composed of FeO and Fe_2O_3 that means its Fe (II) and Fe (III) ions are unequal in magnitude and aligned in antiparallel direction. In addition, Fe_3O_4 exhibits better conductivity at room temperature than some other metal oxides in the same category [2-4]. Generally, physical and chemical properties of magnetic nanomaterials depend on their morphology and size [5]. As a result of the tuning physical and chemical properties, many usage areas of Fe_3O_4 nanoparticles have emerged in technology. Fe_3O_4 nanoparticles can be used as catalysts [6], drug delivery systems [7], magnetic resonance imaging [8], antibacterial agents [9], heavy metal absorbers [10], and for solar thermal energy harvesting [11]. In addition, nanocomposite materials including Fe_3O_4 nanoparticles can be used as electrochemical sensors and radar absorbing materials [12-14]. Various synthesis methods have been developed to increase the magnetic properties and application areas of Fe_3O_4 nanoparticles. Some of synthesis methods of Fe_3O_4 nanoparticles can be listed as hydrothermal [15], co-precipitation [16], thermal decomposition [17] and sol-gel [18]. Co-precipitation method is a simple, inexpensive and easy way to synthesize Fe_3O_4 [19]. In the co-precipitation method, Fe_3O_4 can be obtained by precipitating Fe (II) and Fe (III) ions in an alkaline medium (1:2 ratio). As a result of the reaction, single and multicomponent Fe_3O_4 particles can be synthesized [20]. Thermal decomposition method is known as one of the best ways to synthesize nanomaterials with controllable size and morphology. However, the compounds used in the synthesis are toxic and additionally require relatively high temperatures [21, 22]. Hydrothermal and solvothermal methods are almost identical, but there is a fundamental difference. Hydrothermal synthesis is synthesis through chemical reactions in an aqueous solution above the boiling point of water. On the other hand, solvothermal synthesis is a synthesis that takes place in a non-aqueous solution at relatively high temperatures. Hydrothermal/solvothermal synthesis methods have more advantageous than other listed methods above. Although these methods are generally considered low-efficiency, this problem can be solved by adjusting the critical temperature and pressure value of almost all materials and solvent systems [23]. Nanomaterials can be synthesized under high vapor pressure with minimum material loss. Thus, high quality nanostructured materials can be synthesized by hydrothermal and/or solvothermal methods [23]. *Radoń et al.* investigated the structure and optical properties of Fe_3O_4 nanoparticles synthesized by co-precipitation with different organic modifiers [24]. They synthesized Fe_3O_4

nanoparticles with different crystal size in the range of 2.9-12.2 nm and band gap ranging from 2.6-3.01 eV by co-precipitation method. *Ahmadi et al.* synthesized Fe_3O_4 nanocrystals using the hydrothermal approach and studied some of their structural and physical properties [25]. They found that crystallite size, particle size and saturation magnetization increase with reaction temperature. *Lemine et al.* synthesized Fe_3O_4 nanoparticles by sol-gel method and studied their magnetic properties [26]. The synthesized Fe_3O_4 nanoparticles have a particle size of 8 nm. Since it is the lower than the critical size for superparamagnetic property, the Fe_3O_4 nanoparticles have a for hyperthermia applications.

In this study, Fe_3O_4 nanoparticles were synthesized by hydrothermal and solvothermal methods. The differences between these two very similar methods are revealed by examining their crystal structure, morphology, and magnetic properties. The results showed that the solvothermal method has better crystal structure, morphology, and magnetic properties than the hydrothermal method.

Experimental Procedure

Materials

Iron (III) chloride hexahydrate-$FeCl_3{\cdot}6H_2O$ (Sigma-Aldrich), Iron (II) chloride tetrahydrate-$FeCl_2{\cdot}4H_2O$ (Sigma-Aldrich), Sodium hydroxide-NaOH (Sigma-Aldrich) were used to hydrothermal synthesis method. Iron (III) chloride hexahydrate-$FeCl_3{\cdot}6H_2O$ (Sigma-Aldrich), Polyvinylpyrrolidone (PVP)- $(C_6H_9NO)_n$ (BioShop), Sodium acetate- NaAc, Ethylene glycol-$C_2H_6O_2$ (ISOLAB chemicals) were used to solvothermal synthesis method.

Synthesis of Fe_3O_4

Hydrothermal synthesis

The hydrothermal method was used to synthesize Fe_3O_4 nanoparticles. Figure 1 shows the schematically illustrated synthesizing procedure (blue arrows) of Fe_3O_4 nanoparticles. $FeCl_2{\cdot}4H_2O$ (0.288 g) and $FeCl_3{\cdot}6H_2O$ (0.799 g) were dissolved in 50 ml distilled water. Then, 0.8 g NaOH was dissolved in 10 ml of distilled water to obtain a 2M NaOH solution. 2M NaOH solution was slowly added dropwise to mixture [25]. The mixture was transferred into a 100 ml Teflon and then into the Teflon-lined stainless-steel autoclave and sealed for heating at 200 ºC for 8 h. As a result of the reaction, Fe_3O_4 nanoparticles were obtained and washed with ethanol several times. Finally, it was dried at 75 ºC for 24 h and brown color Fe_3O_4 nanoparticles were obtained. This sample is called as #1-Fe_3O_4.

Solvothermal synthesis

Here, the Fe_3O_4 nanoparticles were synthesized by the following procedure as green color arrows shown in Fig.1. $FeCl_36H_2O$ (1.5 g), PVP (1.0 g), and NaAc (2.0 g) were added into 30 mL of ethylene glycol [15]. To make sure all the ingredients completely dissolved, the liquid was rapidly mixed for 2 hours. Then, the mixture was transferred to a 100 ml Teflon-lined stainless-steel autoclave and sealed for heating at 200 ºC for 8 h. As a result of the reaction, Fe_3O_4 nanoparticles were obtained and washed with ethanol several times. Finally, it was dried at 75 ºC for 24 h and black color Fe_3O_4 nanoparticles were obtained. This sample is called as #2-Fe_3O_4.

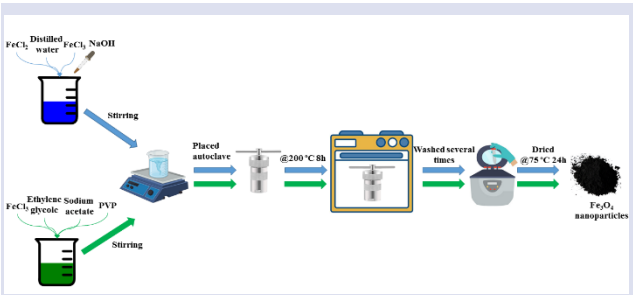

Figure 1. Schematically illustrated synthesizing process of Fe_3O_4 magnetic nanoparticles.

Characterization Techniques

X-ray diffractometer (XRD) with Cu-Kα radiation was used to analyze some structural properties of particles. Morphology and surface properties of samples were examined by scanning electron microscope (SEM). Vibrating sample magnetometer (VSM) was used to characterize the magnetic properties of magnetic particles at room temperature.

Results and Discussions

Structural Analysis

The structural properties of Fe_3O_4 nanoparticles synthesized by different methods were investigated by XRD. Figure 2 indicates the XRD patterns of Fe_3O_4 nanoparticles synthesized by different methods. The diffraction peaks in both samples are at 2ϑ = 18.38, 21.61 30.24, 35.58, 37.12, 42.96, 53.49, 56.92, 62.68, 71.28 and 74.05 angles which are corresponding to (111), (002), (311), (222), (400), (422), (511), (440), (620) and (553) planes, respectively. These peaks indicate the formation of cubic Fe_3O_4 crystals. In the hydrothermal method, in addition to main crystal peaks, two impurity peaks belonging to Fe_2O_3 phases which are indicated by * symbol, have been observed in sample #1-Fe_3O_4. These impurity peaks might be occurred due to insufficient reaction time. The lattice parameters of #1-Fe_3O_4 and #2-Fe_3O_4 samples are found as 8.376 Å and 8.395 Å, respectively. The crystallite sizes of the samples were calculated by using the basic Scherrer equation [27].

$$D = \frac{K\lambda}{\beta\, cos\theta} \quad (1)$$

where D is the crystallite size, λ is the x-ray wavelength (CuKα = 1.5406 Å), β is the width of the x-ray peak on the 2ϑ axis measured as full width at half

maximum (FWHM), ϑ is the Bragg angle, K is the so-called Scherrer constant. K depends on the crystallite shape and the size distribution, indices of the diffraction line, and the actual definition used for β whether FWHM or integral breadth [28]. K can have values anywhere from 0.62 and 2.08. In this paper, K = 0.9 was used. The calculated average crystallite sizes of #1-Fe_3O_4 and #2-Fe_3O_4 samples are found as 38 nm and 24 nm, respectively.

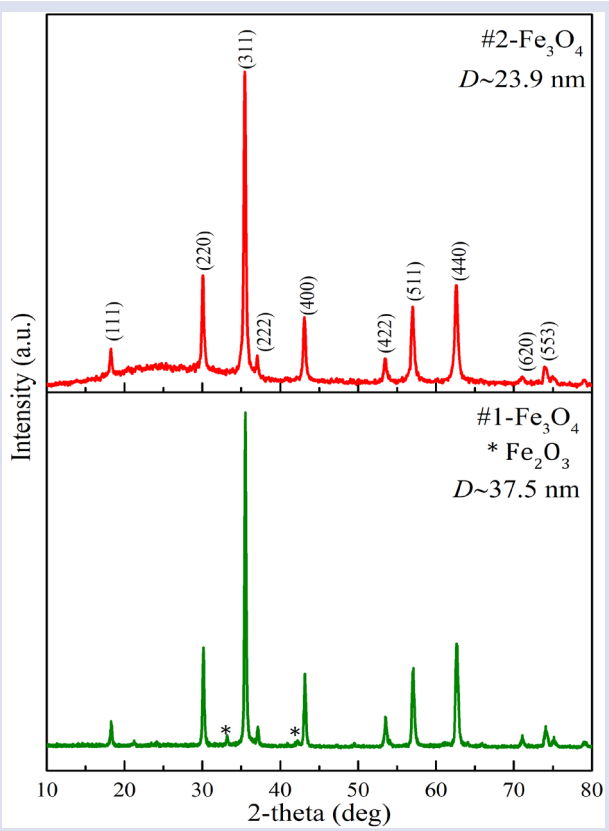

Figure 2. X-ray diffraction patterns of #1-Fe_3O_4 and #2-Fe_3O_4 samples.

Morphological Analysis

The morphologies of the synthesized samples were analyzed by using the SEM imaging technique. SEM images taken at various magnitudes and particle size distribution histogram of Fe_3O_4 nanoparticles produced by hydrothermal method are given in Figs.3a-d. In Figs. 3a-c, it is seen that Fe_3O_4 nanoparticles were successfully synthesized by hydrothermal method. The particles are formed as cubic shape and they are almost uniformly and homogenously distributed through the sample. The particle size distribution histogram of #1-Fe_3O_4 sample is given in Fig. 3d. The histogram was created by randomly selected 100 particles in the SEM images. The sizes of Fe_3O_4 nanoparticles are between 100 and 500 nm. The average particle size was found as 220 nm by taking lognormal fitting of experimental data as shown a red color curve in Fig.3d.

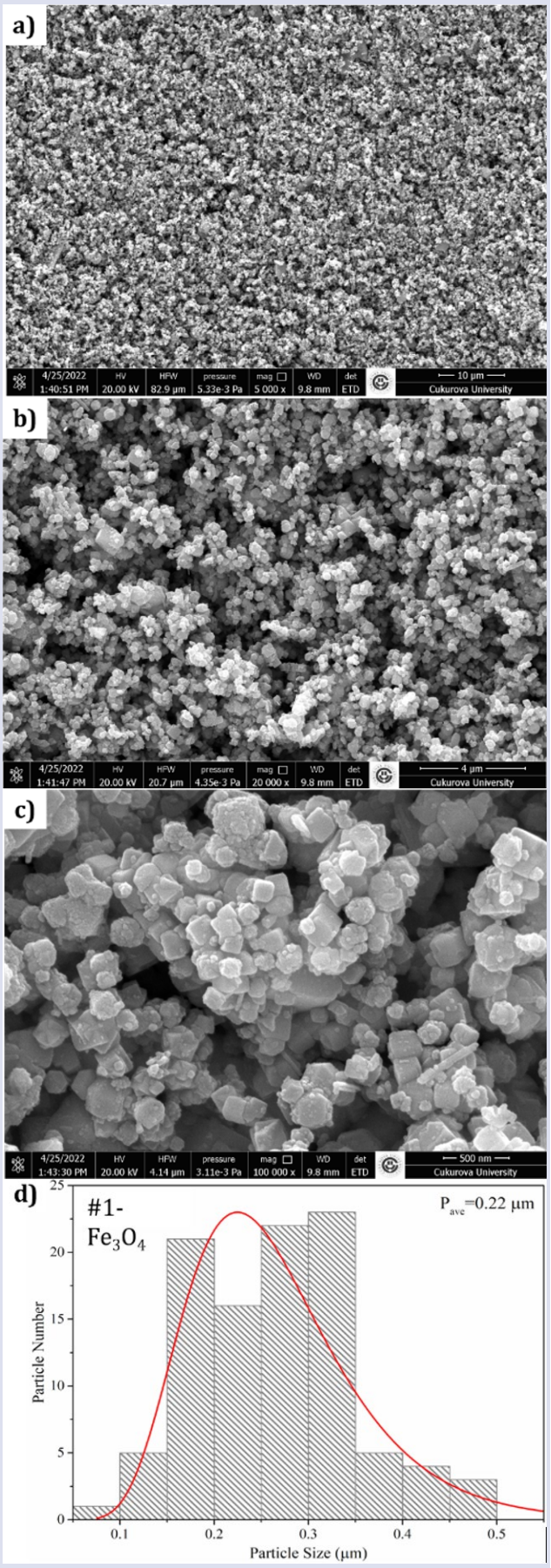

Figure 3. a-c) SEM images and d) particle size distribution histogram of #1-Fe_3O_4 sample.

The images in Fig.3 show that the nanocrystals synthesized by hydrothermal method form finite aggregate crystals due to its high surface energy. The particle size difference may be due to the variation of the dropping rate of NaOH. Because of fast dropping of NaOH solution, the Fe_3O_4 crystals form agglomerate and stick together having different sizes.

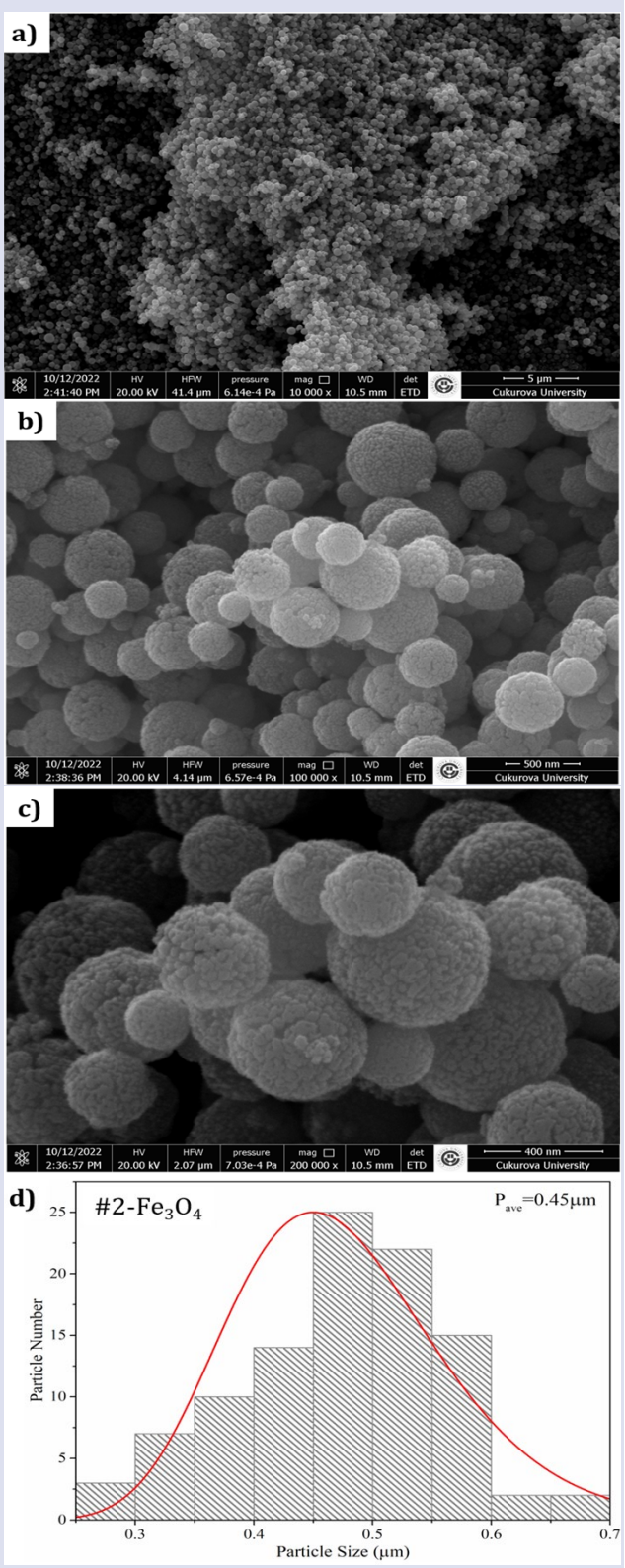

Figure 4.a-c) SEM images and d) particle size distribution histogram of #2-Fe_3O_4 sample.

SEM images taken at various magnitudes and particle size distribution histogram of #2-Fe_3O_4 sample produced by solvothermal method are given in Figs.4a-d. In Figs. 4a-c, in contrast to #1-Fe_3O_4 sample, spherical and porous shape Fe_3O_4 nanoparticles were successfully synthesized by solvothermal method. Similarly, the particle size distribution histogram of porous Fe_3O_4 nanoparticles were created by randomly selected 100 grains in the sample (see Fig.4d). The particle sizes of #2-Fe_3O_4 sample are between 200 and 700 nm. The average particle size was found as 450 nm by taking lognormal fitting of experimental data as shown a red color curve in Fig.4d. When the average particle size is compared between two samples, it is clearly seen that the #2-Fe_3O_4 sample's size is almost ×2 larger than #1-Fe_3O_4 sample. The increment in the particle size might be related to the lower atmosphere pressure in the solvothermal method than the hydrothermal method. *Zhu et al.* studied the reaction conditions such as precursor, capping agent, precipitation agent concentration, reaction temperature and reaction time to understand the formation mechanism of porous Fe_3O_4 nanospheres [15]. The regularity of morphology and particle size can be adjusted by changing the amount of $FeCl_3$, reaction temperature and time, amount of NaAc and amount of PVP [15].

Magnetic Analysis

Magnetic hysteresis (*M(H)*) measurements of the synthesized Fe_3O_4 nanoparticles were performed at room temperature under ∓2T magnetic field range. *M(H)* curves of #1-Fe_3O_4 and #2-Fe_3O_4 coded nanoparticles are given in Fig.5. It is understood from the hysteresis curves that the samples have no coercive field values and behaves like a ferrimagnetic characteristic. It can be said that the XRD and *M(H)* curves are consistent with each other, since both samples were found as inverse spinel structure. The saturation magnetization values were determined as 28.78 emu/g and 77.31 emu/g for the #1-Fe_3O_4 and #2-Fe_3O_4 coded samples, respectively. The increase in magnetization with the increase of particle size in the #2-Fe_3O_4 rather than #1-Fe_3O_4 sample is expected. In addition to size effect, since the magnetization of the Fe_2O_3 crystal which is observed in #1-Fe_3O_4 sample, is very small compared to Fe_3O_4, it is thought to reduce the total magnetization [29].

Further, we calculate the effective magnetic moment from the following equation,

$$\mu_{eff} = \frac{MM_S}{N_A\beta} \quad (2)$$

where M is the molecular weight, N_A is the Avogadro's number and β is the conversion factor (9.27×10^{-21} erg/Oe). The effective magnetic moment values are found as 1.19 μ_B and 3.21 μ_B for #1-Fe_3O_4 and #2-Fe_3O_4 coded samples, respectively. Since there is

a linear relation between particle size and moment, the reason of higher moment value of #2-Fe_3O_4 sample is related to the relatively its large particle size. But it is still lower than the theoretical value (4 μB)[30, 31]. The calculated effective magnetic moments of Fe_3O_4 magnetic nanoparticles are consistent with the previously reported studies[30-32].

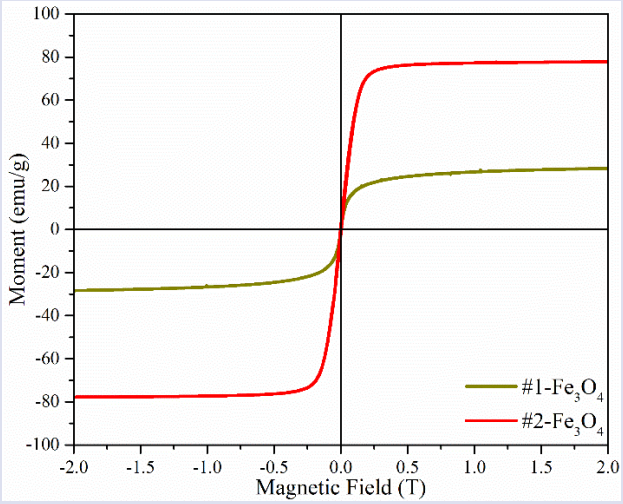

Figure 5. Magnetic hysteresis curves of #1-Fe_3O_4 and #2-Fe_3O_4 samples.

Table 1. Structural and magnetic parameters of #1-Fe_3O_4 and #2-Fe_3O_4 magnetic nanoparticles.

Sample Code	*D* (nm)	*P* (nm)	M_s (emu/g)	μ_{eff} (μ_B)
#1-Fe_3O_4	38	220	28.78	1.19
#2-Fe_3O_4	24	450	77.31	3.21

Conclusions

In summary, the effect of hydro-/solvothermal methods on the structure, morphology, and magnetic properties of Fe_3O_4 magnetic nanoparticles were studied in this work. It is found that the synthesizing procedure affects the morphology of the Fe_3O_4 particles that cubic and porous spherical shape Fe_3O_4 nanoparticles were determined when they are synthesized by hydrothermal and solvothermal methods, respectively. In addition, although both samples have similar magnetic characteristic, #2-Fe_3O_4 sample has almost ×2.5 higher magnetic saturation than #1-Fe_3O_4 sample. The difference in saturation magnetization might come from the particle size effect and/or Fe_2O_3 impurity phases which is observed in #1-Fe_3O_4 sample. It was determined that the solvothermal method showed much better crystal structure, morphology, and magnetic properties than the hydrothermal method.

Conflicts of interest

The authors stated that did not have conflict of interests.

Acknowledgement

This work is supported by the Adana Alparslan Türkeş Science and Technology University Scientific Research Council under Project Number: 22303006.

References

[1] Zhao T., Hierarchical Bi2O2CO3 microspheres with improved visible-light-driven photocatalytic activity, *Cryst. Eng. Comm.*, 13 (2011) 4010-4017.

[2] Miles P.A., Westphal W.B.,A. Von Hippel, Dielectric Spectroscopy of Ferromagnetic Semiconductors, *Reviews of Modern Physics*, 29 (1957) 279-307.

[3] Evans B.J., Experimental studies of the electrical conductivity and phase transition in Fe3O4. *AIP Conference Proceedings*, 24 (1975) 73-78.

[4] Vella L. D. Emerson, Electrical Properties of Magnetite- and Hematite-Rich Rocks and Ores, *ASEG Extended Abstracts*, 2012 (2012) 1-4.

[5] Qiao L., Standardizing Size- and Shape-Controlled Synthesis of Monodisperse Magnetite (Fe3O4) Nanocrystals by Identifying and Exploiting Effects of Organic Impurities, *ACS Nano*, 11 (2017) 6370-6381.

[6] Arefi M., Superparamagnetic Fe(OH)3@Fe3O4 Nanoparticles: An Efficient and Recoverable Catalyst for Tandem Oxidative Amidation of Alcohols with Amine Hydrochloride Salts, *ACS Combinatorial Science*, 17 (2015) 341-347.

[7] Li Q., Xuan Y., Wang J., Experimental investigations on transport properties of magnetic fluids, *Experimental Thermal and Fluid Science*, 30 (2005) 109-116.

[8] Jordan A., Endocytosis of dextran and silan-coated magnetite nanoparticles and the effect of intracellular hyperthermia on human mammary carcinoma cells in vitro, *Journal of Magnetism and Magnetic Materials*, 194 (1999) 185-196.

[9] Prabhu Y.T., Synthesis of Fe3O4 nanoparticles and its antibacterial application, *International Nano Letters*, 5 (2015) 85-92.

[10] Kalantari K., Rapid Adsorption of Heavy Metals by Fe3O4/Talc Nanocomposite and Optimization Study Using Response Surface Methodology, *International Journal of Molecular Sciences*, 15 (2014) 12913-12927.

[11] Chen Y., Stably dispersed high-temperature Fe3O4/silicone-oil nanofluids for direct solar thermal energy harvesting, *Journal of Materials Chemistry A*, 4 (2016) 17503-17511.

[12] Narang S. S. Bahel, Low loss dielectric ceramics for microwave applications: A review, *Journal of Ceramic Processing Research*, 11 (2010) 316-321.

[13] Sanaeifar N., A novel electrochemical biosensor based on Fe3O4 nanoparticles-polyvinyl alcohol composite for sensitive detection of glucose, *Analytical Biochemistry*, 519 (2017) 19-26.

[14] Jian X., Facile Synthesis of Fe3O4/GCs Composites and Their Enhanced Microwave Absorption Properties, *ACS Applied Materials & Interfaces*, 8 (2016) 6101-6109.

[15] Zhu M. G. Diao, Synthesis of Porous Fe3O4 Nanospheres and Its Application for the Catalytic Degradation of Xylenol Orange, *The Journal of Physical Chemistry C*, 115 (2011) 18923-18934.

[16] Hariani P., Synthesis and Properties of Fe3O4 Nanoparticles by Co-precipitation Method to Removal

Procion Dye, *International Journal of Environmental Science and Development*, 4 (2013) 336-340.

[17] Kimata M., Nakagawa D., Hasegawa M., Preparation of monodisperse magnetic particles by hydrolysis of iron alkoxide, *Powder Technology*, 132 (2003) 112-118.

[18] Albornoz C., Jacobo S.E., Preparation of a biocompatible magnetic film from an aqueous ferrofluid, *Journal of Magnetism and Magnetic Materials*, 305 (2006) 12-15.

[19] Wang X., Fabrication and characterization of magnetic Fe3O4–CNT composites, *Journal of Physics and Chemistry of Solids*, 71 (2010) 673-676.

[20] Kentish S.E., Stevens G.W., Innovations in separations technology for the recycling and re-use of liquid waste streams, *Chemical Engineering Journal*, 84 (2001) 149-159.

[21] Rockenberger, J., Scher E.C., Alivisatos A.P., A New Nonhydrolytic Single-Precursor Approach to Surfactant-Capped Nanocrystals of Transition Metal Oxides, *Journal of the American Chemical Society*, 121 (1999) 11595-11596.

[22] Deng Y., Magnetic nanoparticles prepared in natural deep eutectic solvent for enzyme immobilisation, *Biocatalysis and Biotransformation*, 40 (2022) 450-460.

[23] Wang S., Recyclable solar evaporator based on hollow glass microspheres for water purification and desalination, *Journal of Environmental Chemical Engineering*, 10 (2022) 108254.

[24] Radoń A., Structure and optical properties of Fe3O4 nanoparticles synthesized by co-precipitation method with different organic modifiers, *Materials Characterization*, 131 (2017) 148-156.

[25] Ahmadi S., Synthesis of Fe3O4 nanocrystals using hydrothermal approach, *Journal of Magnetism and Magnetic Materials*, 324 (2012) 4147-4150.

[26] Lemine O.M., Sol–gel synthesis of 8nm magnetite (Fe3O4) nanoparticles and their magnetic properties, *Superlattices and Microstructures*, 52 (2012) 793-799.

[27] Scherrer P., Bestimmung der inneren Struktur und der Größe von Kolloidteilchen mittels Röntgenstrahlen, in *Kolloidchemie Ein Lehrbuch*, R. Zsigmondy, Editor., Springer Berlin Heidelberg: Berlin, Heidelberg. (1912) 387-409.

[28] Langford J.I., Wilson A.J.C., Scherrer after sixty years: A survey and some new results in the determination of crystallite size, *Journal of Applied Crystallography*, 11 (1978) 102-113.

[29] Bahari A., Characteristics of Fe3O4, α -Fe2O3, and γ-Fe2O3 Nanoparticles as Suitable Candidates in the Field of Nanomedicine, *Journal of Superconductivity and Novel Magnetism*, 30 (2017) 2165-2174.

[30] Li Q., Correlation between particle size/domain structure and magnetic properties of highly crystalline Fe3O4 nanoparticles, *Scientific Reports*, 7 (2017) 9894.

[31] Hedayatnasab Z., Abnisa F., Daud W.M.A.W., Review on magnetic nanoparticles for magnetic nanofluid hyperthermia application, *Materials & Design*, 123 (2017) 174-196.

[32] Rajan A., Sharma M., Sahu N.K., Assessing magnetic and inductive thermal properties of various surfactants functionalised Fe3O4 nanoparticles for hyperthermia, *Scientific Reports*, 10 (2020) 15045.

Cumhuriyet Sci. J., 44(3) (2023) 510-515
DOI: https://doi.org/10.17776/csj.1268752

Cumhuriyet Science Journal

| csj.cumhuriyet.edu.tr | Founded: 2002 ISSN: 2587-2680 e-ISSN: 2587-246X Publisher: Sivas Cumhuriyet University

Investigation of Adsorption Isotherm Models for Interaction of P(AAm-ClAETA) and Carminic Acid, and Theoretical Approaches

Yasemin Işıkver[1,a,*], Ali Işıkver[2,b]

[1] *Department of Chemistry, Faculty of Science, Sivas Cumhuriyet University, Sivas, Türkiye.*
[2] *MEB Ulaş ÇPAL, Sivas, Türkiye.*
**Corresponding author*

Research Article

History
Received: 21/03/2023
Accepted: 22/08/2023

ABSTRACT

In this study, the adsorption isotherm models for the sorption of carminic acid on P(AAm-ClAETA) hydrogels are explained by experimental and theoretical studies. The crosslinked hydrogels with ethylene glycol dimethacrylate were prepared by radical addition reaction of acrylamide (AAm) and 2-(acryloyloxy)ethyl trimethylammonium chloride (ClAETA) monomers in an aqueous solution. The spectral and morphological analyses of P(AAm-ClAETA) hydrogels were performed by FTIR/ATR and SEM, respectively. The adsorbed amounts of carminic acid on P(AAm-ClAETA) hydrogels were evaluated by Giles, Langmuir, and Freundlich adsorption isotherm models. Langmuir parameters were calculated for the adsorption of the dye on the hydrogels according to the L-type Giles isotherm. In addition, it was determined that its adsorption was appropriate from the RL values calculated for 500 mg L^{-1} carminic acid concentration. In addition, molecular electrostatic potential (MEP) mapping was performed to predict the reactive sites of P(AAm-ClAETA) hydrogels and carminic acid. The results showed that the theoretical and experimental data of the hydrogels were in agreement with each other. As a result, it can be said that P(AAm-ClAETA) hydrogels are suitable for the removal of anionic dyes such as carminic acid from aqueous solutions.

Keywords: 2-(acryloyloxy)ethyl trimethylammonium chloride, Acrylamide, Hydrogel, Carminic acid, Molecular electrostatic potential (MEP).

[a] caldiran@cumhuriyet.edu.tr https://orcid.org/0000-0001-6481-188X [b] isikverali@gmail.com https://orcid.org/0000-0003-3871-9435

Introduction

Pollution from dyes has been and continues to be a major global problem due to their toxicity. Dyes, which are used in large quantities as colorants in paper, printing and textiles, plastics and paints, excessively pollute domestic and agricultural waters. A paramount variety of adsorbents have been used, manufactured and designed to remove these pollutants [1-10].

Although there are many studies on dye removal with these adsorbents, there are fewer studies on the removal of anionic dyes compared to cationic dyes.

Carminic acid (E120), which is widely used in textile, cosmetic, printing, food, medical, and pharmaceutical applications [4], is a red anionic natural dye derived from Dactylopius coccus species and the insect known as the cochineal beetle [2,3]. In addition, carminic acid is the dye that gives color to cola, which is consumed worldwide in thousands of tons per day. According to the World Health Organization (WHO), carminic acid is considered safe at concentrations as low as 0.005 mg L^{-1}. At higher intakes, it is a toxic and neurotoxic dye that can cause skin and eye diseases and cancer [5].

In the literature, some adsorbents such as 4.03 mg g^{-1} on glass powder [2], 33.44 mg g^{-1} on (CuAl-CLDH/CNT/PVDF400) composites [3], 10.10 mg g^{-1} on activated carbon [5], 48.5 mg g^{-1} on mesoporous carbon [6], 148 mg g^{-1} on Prunus mahaleb bark [7] have been reported to be used for removal of carminic acids.

The adsorbents used in environmental applications to remove various harmful pollutants such as dyes from the water system are desired to be environmentally friendly and cost-effective [8-10]. Functional hydrogels are the adsorbents that best meet this desire.

The aim of this study was to prepare synthetic acrylamide-based functional hydrogels, which are different from the natural and natural product-derived adsorbents such as glass powder, carbon-based, and plant shell-based reported in the literature, and to use them for anionic dye removal. 2-(Acryloyloxy) ethyl trimethylammonium chloride (ClAETA) containing functional groups such as a quaternary ammonium group desired for carminic acid removal, an anionic dye, and acrylamide (AAm) monomers that increase mechanical strength were copolymerized in the presence of a crosslinking agent. The removal of carminic acid from the prepared P(AAm-ClAETA) was determined to be L-type according to the Giles adsorption isotherm classification by Freundlich isotherm, and the removal performance was evaluated using the Langmuir adsorption isotherm model.

Materials and Methods

Materials

Acrylamide (AAm), ethylene glycol dimethacrylate (EGDMA), ammonium persulfate (APS) were purchased from Merck Company (Germany). 2-(Acryloyloxy)ethyl trimethylammonium chloride (ClAETA), N, N, N', N'-tetramethylethylenediamine (TEMED) were purchased from Sigma Aldrich (USA). Double-distilled water was used in all experiments.

Synthesis of Hydrogels

8.0 mol of AAm and 2.0 mol of ClAETA monomers and 0.5 mol of EGDMA were dissolved in water, 0.01 mol of APS as initiator and 0.01 mol of TEMED as accelerator were added and filled into plastic pipettes. The gelled samples were removed from the pipettes, cut into 3-4 mm pieces, washed with double-distilled water, dried and named P(AAm-ClAETA).

Characterization of Hydrogels

Bruker Tensor II and Tescan-Mira 3 were used to obtain FTIR/ATR spectra and SEM images of the hydrogels, respectively.

Adsorption Studies

The adsorption of carminic acid in the range of 10-500 mg L^{-1} on P(AAm-ClAETA) hydrogels was investigated by keeping it in a shaker at 25 °C for 24 hours. The equilibrium concentrations of carminic acid were determined by Shimadzu A160 model UV-VIS.

Results and Discussion

Synthesis of Hydrogels

The feed composition of copolymer hydrogels affects their performance in the field of application. In this study, P(AAm-ClATA) hydrogels were prepared by adding ClAETA comonomer containing ionizable groups to AAm monomer, which is inexpensive and has high mechanical strength but is neutral. As a result of preliminary experiments, the feed composition of P(AAm-ClATA) hydrogels was determined to be AAm:ClAETA = 8:2. The use of higher amounts of ClAETA caused the hydrogels to disintegrate.

P(AAm-ClAETA) hydrogels were prepared by a free radical addition reaction in the presence of EGDMA, and the plausible polymerization mechanism is shown in Figure 1.

In an aqueous medium, hydroxyl and/or sulfate radicals were formed from the initiator. These radicals then led to the copolymerization of AAm and ClAETA and their crosslinking with EGDMA [8-10].

The hydrogels prepared in a cylindrical structure were hard when dry and soft when swollen. The hydrogels maintained the cylindrical geometry in the dry and swollen states.

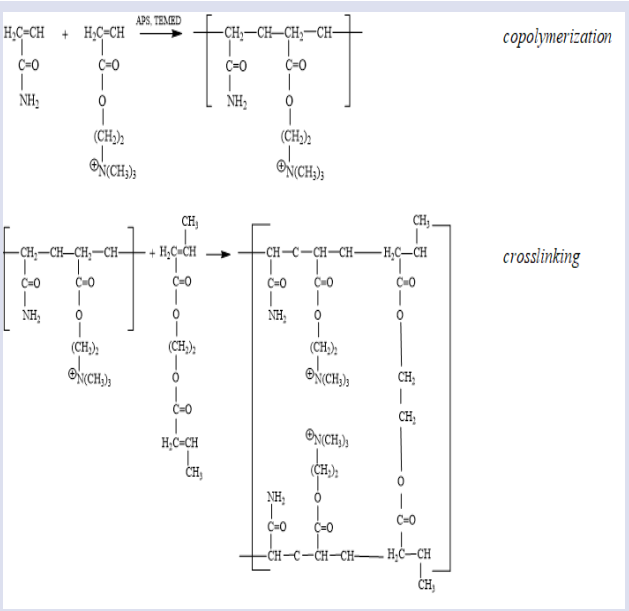

Figure 1. Plausible copolymerization/croslinking mechanism of P(AAm-ClAETA).

Characterization of hydrogels

The spectroscopic examinations necessary to elucidate the chemical structures of the P(AAm-ClAETA) hydrogels before and after adsorption was performed with FTIR/ATR spectrophotometer, and the FTIR/ATR spectra are presented in Figure 2.

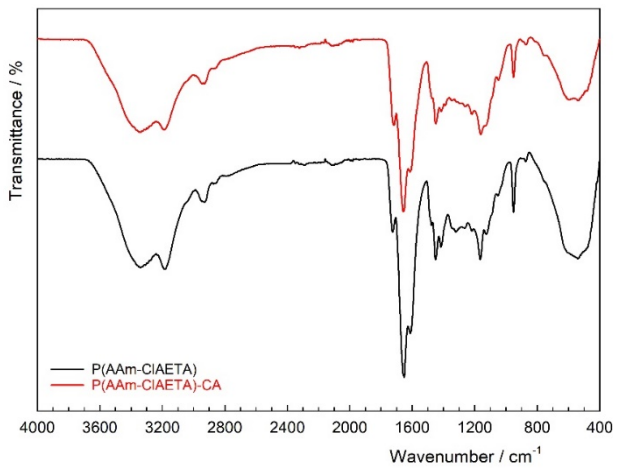

Figure 2. The FTIR/ATR spectrum before and after carminic acid adsorption onto the hydrogels

The bands at 3200-3600 cm^{-1} are the N-H stretching vibration of the amide group. The C-N stretch of the quaternary ammonium (N^+-$(CH_3)_3$) groups in the ClAETA monomer is observed at 1476 cm^{-1} and the -CH bending of the ammonium methyl groups is observed at 952 cm^{-1}. The bands at 1729 cm^{-1} and 1655 cm^{-1} are considered to belong to the carbonyl group (C=O) in the crosslinker with the ClAETA monomer. In addition, the bands at 1162 cm^{-1} and 1042 cm^{-1} belong to the asymmetric and symmetric stretching vibration of the ester bond C-OC- in the ClAETA monomer. The FTIR/ATR spectral results

show the interactions between the hydrogels and dye molecules due to the decrease in density in characteristic bands such as C=O, N^+-$(CH_3)_3$, and C-OC- of the hydrogels after adsorption [11-14].

The plausible mechanism of interaction between P(AAm-ClAETA) hydrogels and carminic acid is presented in Figure 3.

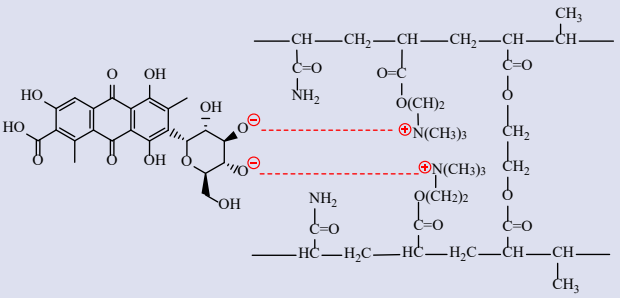

Figure 3. Plausible mechanism of interaction between the hydrogels and carminic acid.

The main interactions between the hydrogels and anionic dye may be electrostatic interactions, dipole-dipole interactions, hydrogen bonds, and hydrophobic interactions. Especially, electrostatic interactions will be expected between hydroxyl groups on the dye molecules and -$N^+(CH_3)_3$ on the hydrogels.

SEM images of P(AAm-ClAETA) hydrogels, photos of carminic acid solution before/after adsorption, and photos of P(AAm-ClAETA) hydrogels before/after adsorption are presented in Figure 4.

a b c

Figure 4. (a) SEM images of the hydrogels, (b) photos of carminic acid solution before/after adsorption, (c) photos of dried the hydrogels before/after adsorption.

SEM images show that the hydrogels have a smooth and regular surface morphology. It is also seen that the cavities on the surface of the hydrogels are homogeneous [8].

From Figure 4. b-c, it can be seen that the color of P(AAm-ClAETA) hydrogels kept in carminic acid solution changed to red. This indicates that P(AAm-ClAETA) hydrogels interact with carminic acid and can be used for removal from an aqueous solution.

Adsorption Studies

For the adsorption equilibrium, the total dye concentration (C, mg L^{-1}) is:

$$C = C_b + C_e \quad (1)$$

C_e and C_b are the equilibrium concentration of the dye in the solution and hydrogels (mg L^{-1}), respectively. The amount of adsorbed dye (q, mg g^{-1}) on 0.1 g hydrogel from 50 mL carminic acid solutions was calculated by Equation 1, 2.

$$q=(C_b.V)/m \quad (2)$$

The adsorption of carminic acid on the hydrogels was investigated with the Giles, Langmuir, and Freundlich adsorption isotherm models [8,15,16].

Adsorption isotherms were constructed by calculating the amount of dye adsorbed from carminic acid solutions onto the hydrogels in the concentration range of 10-500 mg L^{-1} and are shown in Figure 5 [8,9,15].

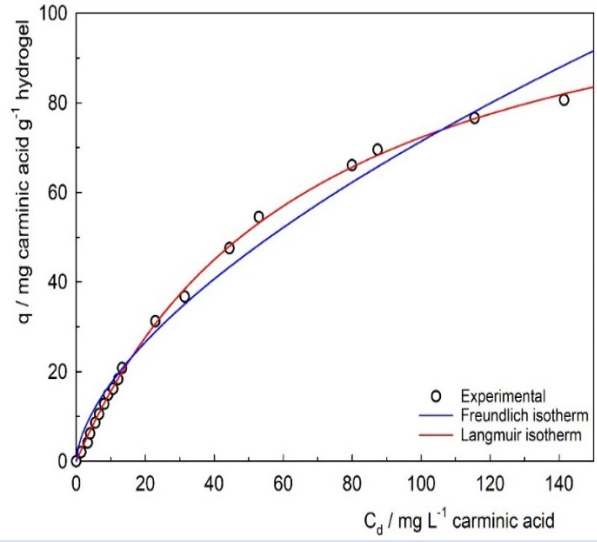

Figure 5. Carminic acid adsorption isotherms on the P(AAm-ClAETA) hydrogels.

According to the isotherms classified by Giles as S (sigmoidal), L (Langmuir), H (high affinity) and C (constant distribution), the adsorption isotherms of carminic acid on P(AAm-ClAETA) hydrogel resemble L-type curves [15].

The adsorption parameters calculated from the nonlinear equations of the graphs presented in Figure 5 are summarized in Table 1.

Table 1. Isotherm parameters of carminic acid adsorption on P(AAm-ClAETA) hydrogels

Models	Equations	Values
Freundlich	$q = X_F C_d^{1/n}$	
Freundlich constant, K_F [(mg g^{-1})(L mg^{-1})$^{1/n}$]		4.21
Heterogeneity factor, n		1.63
Correlation coefficient, r		0.991
Isotherm type		L-type
Langmuir	$q = \frac{X_L K_L C_d}{1 + K_L C_d}$	
Monolayer adsorption capacity, X_L (mg g^{-1})		120.9
Distribution coefficient, K_L (L mg^{-1})		0.015
Correlation coefficient, r		0.999
Adsorbent dose, AD_L (g L^{-1})	$AD_L = \frac{C - C_e}{q}$	4.45
Dimensionless dispersion factor, R_L	$R_L = \frac{1}{1 + K_L C}$	0.117

In addition, the type of isotherm can be determined from the n value found in the Freundlich isotherm model. At the same time, the n values are related to the Giles classification, S-, L-, and C-type isotherms. n < 1 corresponds to S-type, n = 1 to C-type, and n > 1 to L-type. The Freundlich constant for the P(AAm-ClAETA) hydrogel was n > 1, indicating that the isotherm type is L-type. The L-type isotherm curve indicates a strong intermolecular interaction between carminic acid and the P(AAm-ClAETA) hydrogel. On the other hand, higher values of K_F represent easy adsorbate uptake from the solution [16].

In order to determine the suitability of adsorption, the R_L value for removal from the dye solution with an initial concentration of 500 mgL^{-1} was calculated as 0.117. This R_L value shows that carminic acid adsorption on P(AAm-ClAETA) is in the range of suitability [8,10].

The adsorbent dose required for 50 % removal from 500 mg L^{-1} carminic acid solution was calculated as AD_L= 4.45 g L^{-1}. This result shows that P(AAm-ClAETA) hydrogels are effective in carminic acid removal and can be easily used.

The maximum adsorption capacities of previous studies on carminic acid adsorption on various adsorbents are presented in Table 2 and compared with the results of this study.

Table 2 shows that the amount of carminic acid adsorbed by P(AAm-ClAETA) hydrogels is 2.5 to 30 times higher compared to previously studied adsorbents (except Prunus mahaleb shell).

Table 2. The maximum adsorption capacities of some adsorbents for carminic acid adsorption

Adsorbent	Maximum adsorption capacities/mg g^{-1}	References
glass powder (GP)	4.03	[2]
carbon nanotubes/polyvinylidene fluoride (CuAl-CLDH/CNT/PVDF400) composite	33.44	[3]
activated carbon	10.10	[5]
mesoporous carbon	48.50	[6]
Prunus mahaleb shell	148.00	[7]
P(AAm-ClAETA) hydrogels	120.90	In this study

There are 667526 adsorption studies in the Web of Science (WOS) database since 1970. 38 of these studies are related to carminic acid adsorption on different natural and natural product-derived adsorbents [17]. As a result of the evaluations, this study can be recommended as a pioneering study for the use of polymeric structures, especially hydrogels, in the excellent removal of carminic acid.

Molecular Electrostatic Potential Map

The molecular electrostatic potential (MEP) is widely used in the qualitative evaluation of the chemical reactivity of surfaces with molecular electron density. The nucleophilic (electron-poor) and electrophilic (electron-rich) regions of the molecule are determined by MEP maps. In the MEP map, electrophilic regions are shown in red and nucleophilic regions in blue. In MEP maps, the electrostatic potential increases in the order of Red<Orange<Yellow<Green<Blue. Green-colored regions in MEP maps indicate neutral regions and blue-colored regions indicate nucleophilic regions. With the help of these colors, charge distributions on the molecular surface, plausible electrostatic interaction regions, and electrophilic and nucleophilic regions are determined [18-20].

In this study, it was aimed to determine the active sites in the molecular structure of P(AAm-ClAETA) hydrogels and carminic acid by using MEP maps and to evaluate plausible interaction sites with each other.

Molecular simulation calculations were done using Gaussian 16 AML64L-Revision-C.01 [21] and visualization of results using GaussView 6.0 [22]. The molecular structures of the repeating units of the hydrogels were optimized using density functional theory (DFT) with the Lee-Yang-Parr non-local correlation functional (B3LYP) using 6-31G (d,p) basis set [23-25].

Molecular electrostatic potential maps of P(AAm-ClAETA) hydrogels and carminic acid are presented in Figure 6.

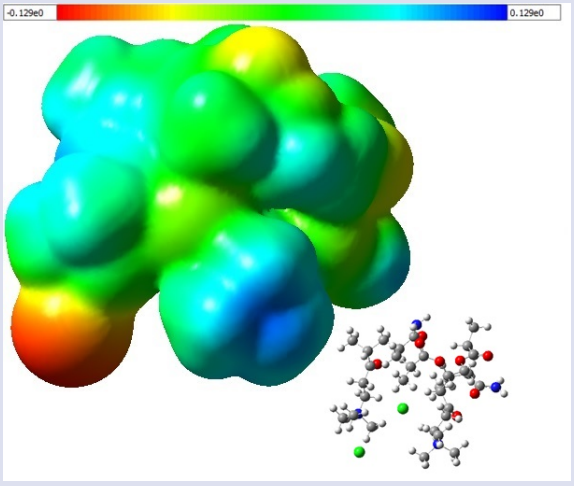

P(AAm-ClAETA) hydrogels

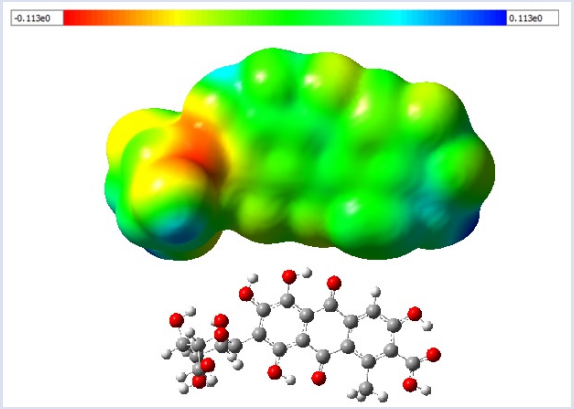

Carminic acid

Figure 6. Molecular electrostatic potential maps of P(AAm-ClAETA) hydrogels and carminic acid, H: white, C: gray, O: red, N: blue, Cl^-: green.

When MEP maps were examined, the following conclusions and evaluations were reached [18-20].

✓ In the MEP map of the P(AAm-ClAETA) hydrogels, the regions with the quaternary ammonium [N^+-$(CH_3)_3$] group are shown in blue, these regions are the nucleophilic attack regions.

✓ The regions of hydroxyl groups attached to the tetrahydropyran ring in the carminic acid molecules are shown in red, these regions are the electrophilic attack regions.

According to these results, it can be said that the electrostatic interactions between the quaternary ammonium groups of the P(AAm-ClAETA) hydrogels and the hydroxyl groups attached to the tetrahydropyran ring in the carminic acid molecules are stronger and more likely. This evaluation with MEP maps supports the proposed plausible interaction mechanism between P(AAm-ClAETA) hydrogels and carminic acid, presented in Figure 3.

Conclusions

The crosslinked P(AAm-ClAETA) hydrogels were prepared by free radical addition polymerization. The absence of any change in the FTIR spectra taken before and after adsorption indicated that the hydrogel-carminic acid interactions were physical. According to the MEP maps, electrostatic interactions between the quaternary ammonium groups of P(AAm-ClAETA) hydrogels and the hydroxyl groups attached to the tetrahydropyran ring in carminic acid molecules are stronger and more likely. The adsorption of carminic acid on P(AAm-ClAETA) hydrogels was determined to be L-type according to Giles adsorption isotherms classification. In addition, the heterogeneity factor n=1.63 calculated from the Freundlich isotherm model supported the L-type adsorption isotherm. The monolayer adsorption capacity was calculated as 120.9 mg g^{-1} from the Langmuir isotherm model. It was determined that carminic acid adsorption on P(AAm-ClAETA) hydrogels were favorable, and the adsorbent dose value was AD_L= 4.45 g L^{-1}.

According to these results, it can be said that P(AAm-ClAETA) hydrogels can be used in carminic acid removal.

Acknowledgments

We thank Assoc. Prof. Nihat Karakuş for his help in the calculation of MEP maps.

Conflicts of interest

There are no conflicts of interest in this work.

References

[1] El-Azazy M., Dimassi S., El-Shafie A., Issa A., Bio-Waste Aloe vera Leaves as an Efficient Adsorbent for Titan Yellow from Wastewater: Structuring of a Novel Adsorbent Using Plackett-Burman Factorial Design, *Appl. Sci.,* 9 (2019) 4856.

[2] Atun G., Hisarli G. Adsorption of carminic acid, a dye onto glass powder, *Chemical Engineering Journal*, 95(1-3) (2003) 241-249.

[3] Abbasi M., Sabzehmeidani M. M., Ghaedi M., Jannesar R., Shokrollahi A., Adsorption performance of calcined copper-aluminum layered double hydroxides/CNT/PVDF composite films toward removal of carminic acid, *Journal of Molecular Liquids*, 329 (2021) 115558.

[4] Dastgerdi Z. H., Abkhiz V., Meshkat S. S., Ghorbani N., Preparation of novel magnetic grafted raft agent nanocomposite: Application in carmine dye adsorptive removal from waste water, *Journal of Environmental Chemical Engineering*, 7(3) (2019) 103109.

[5] Mahnashi M. H., Abu-Alrub S. S., Amer M. W., Alqarni A. O., Kinetics and thermodynamics of enhanced adsorption of E120 dye using activated carbon, *Tropical Journal of Pharmaceutical Research*, 20(3) (2022) 585-592.

[6] Misriyani M., Setianingsih T., Darjito D., Effect of Carbonization Time of Mesoporous Carbon in the Dyes Adsorption: Rhodamine B, Methylene Blue and Carmine, *Indonesian Journal of Fundamental and Applied Chemistry*, 5(1) (2020) 1-6.

[7] Keskin Z. S., Şenol Z. M., Kaya S., Şimşek S., *Prunus mahaleb* shell as a sustainable bioresource for carminic acid removal from aqueous solution: Experimental and

theoretical studies, *Journal of Molecular Structure*, (2023) 134618.

[8] Işıkver Y., Işıkver A., Synthesis and Characterization of Cationic P(AAm-CLAETA) Hydrogels, and Their Uses in Adsorption of Titan Yellow, *Cumhuriyet Science Journal*, 43(1) (2022) 38-44.

[9] Işıkver Y., Synthesis of Anionic Hydrogels for Uranyl Ion Adsorption, *Cumhuriyet Science Journal*, 38(4) (2017a) 770-780.

[10] Işıkver Y., Removal of some cationic dyes from aqueous solution by acrylamide- or 2-hydroxyethyl methacrylate-based copolymeric hydrogels, *Fibers and Polymers*, 18(11) (2017b) 2070-2078.

[11] Roa K., Tapiero Y., Thotiyl M. O., Sánchez J., Hydrogels Based on Poly([2-(acryloxy)ethyl] Trimethylammonium Chloride) and Nanocellulose Applied to Remove Methyl Orange Dye from Water, *Polymers*, 13(14) (2021) 2265.

[12] Onder A., Ilgin P., Ozay H., Ozay O., Removal of dye from aqueous medium with pH-sensitive poly[(2-(acryloyloxy)ethyl]trimethylammonium chloride-co-1-vinyl-2-pyrrolidone] cationic hydrogel, *Journal of Environmental Chemical Engineering*, 8(5) (2020) 104436.

[13] Sánchez J., Mendoza N., Rivas B. L., Basáez L., Santiago-García J. L., Preparation and characterization of water-soluble polymers and their utilization in chromium sorption, *Journal of Applied Polymer Science*, 134(39) (2017) 45355.

[14] Tapiero Y., Sánchez J., Rivas B. L., Ion-selective interpenetrating polymer networks supported inside polypropylene microporous membranes for the removal of chromium ions from aqueous media, *Polymer Bulletin*, 73(4) (2015) 989-1013.

[15] Giles C. H., MacEwan T. H., Nakhwa S. N., Smith D., 786. Studies in adsorption. Part XI. A system of classification of solution adsorption isotherms, and its use in diagnosis of adsorption mechanisms and in measurement of specific surface areas of solids, *Journal of the Chemical Society* (Resumed), (1960) 3973.

[16] Saraydın D., Işıkver Y., Karadağ E., A Study on the Correlation Between Adsorption and Swelling for Poly(Hydroxamic Acid) Hydrogels-Triarylmethane Dyes Systems, *Journal of Polymers and the Environment*, 26(9) (2018) 3924-3936.

[17] WOS: https://www.webofscience.com/wos/woscc/summary/7b524d87-0438-4aea-b0ea-f935dc80c3b9-657d4d37/relevance/1.

[18] Politzer P., Truhlar D.G. (Eds.), Chemical Applications of Atomic and Molecular Electrostatic Potentials: Reactivity, Structure, Scattering and Energies of Organic, Inorganic and Biological Systems, Plenum, New York, 1981.

[19] Ehresmann B., Martin B., Horn A.H.C., Clark T., Local molecular properties and their use in predicting reactivity, *Journal of Molecular Modelin*g, 9(5) (2003) 342-347.

[20] Akman F., Spectroscopic investigation, HOMO-LUMO energies, natural bond orbital (NBO) analysis and thermodynamic properties of two-armed macroinitiator containing coumarin with DFT quantum chemical calculations, *Canadian Journal of Physics*, 94(6) (2016) 583-593.

[21] Gaussian 16, Revision C.01, Frisch M. J., Trucks G. W., Schlegel H. B., Scuseria G. E., Robb M. A., Cheeseman J. R., Scalmani G., Barone V., Petersson G. A., Nakatsuji H., Li X., Caricato M., Marenich A. V., Bloino J., Janesko B. G., Gomperts R., Mennucci B., Hratchian H. P., Ortiz J. V., Izmaylov A. F., Sonnenberg J. L., Williams-Young D., Ding F., Lipparini F., Egidi F., Goings J., Peng B., Petrone A., Henderson T., Ranasinghe D., Zakrzewski V. G., Gao J., Rega N., Zheng G., Liang W., Hada M., Ehara M., Toyota K., Fukuda R., Hasegawa J., Ishida M., Nakajima T., Honda Y., Kitao O., Nakai H., Vreven T., Throssell K., Montgomery Jr. J. A., Peralta J. E., Ogliaro F., Bearpark M. J., Heyd J. J., Brothers E. N., Kudin K. N., Staroverov V. N., Keith T. A., Kobayashi R., Normand J., Raghavachari K., Rendell A. P., Burant J. C., Iyengar S. S., Tomasi J., Cossi M., Millam J. M., Klene M., Adamo C., Cammi R., Ochterski J. W., Martin R. L., Morokuma K., Farkas O., Foresman J. B., Fox D. J., Gaussian, Inc., Wallingford CT, 2019.

[22] Dennington R., Keith T.A., Millam J.M., GaussView, Version 6, Semichem, Inc., Shawnee Mission, KS, 2016.

[23] Frisch M.J., Trucks G., Schlegel H., Scuseria G., Robb M., Cheeseman J., Scalmani G., Barone V., Mennucci B., Petersson G., Gaussian 09, Revision D. 01, Gaussian, Inc., Wallingford, CT, 2009.

[24] Stephens P.J., Devlin F., Chabalowski C., Frisch M.J., Ab initio calculation of vibrational absorption and circular dichroism spectra using density functional force fields, *Journal of Physical Chemistry*, 98(45) (1994) 11623-11627.

[25] Raghavachari K., Perspective on "Density functional thermochemistry. III. The role of exact exchange", *Theoretical Chemistry Accounts,* 103(3-4) (2000) 361-363.

Cumhuriyet Sci. J., 44(3) (2023) 516-521
DOI: https://doi.org/10.17776/csj.1263223

Cumhuriyet Science Journal

| csj.cumhuriyet.edu.tr | Founded: 2002 ISSN: 2587-2680 e-ISSN: 2587-246X Publisher: Sivas Cumhuriyet University

Determination Of Some Trace Elements In Some Lipstick Products By Inductive Coupled Plasma-Mass Spectrometry

Gözde Gülin İnan[1,3,a,*], Gülay Şeren[2,b]

[1] *Department of Analytical Chemistry, Faculty of Pharmacy, University of Health Sciences, İstanbul, Türkiye*
[2] *Department of Analytical Chemistry, Faculty of Pharmacy, Trakya University, Edirne, Türkiye*
[3] *Institute of Graduate Studies in Health Sciences, İstanbul University, İstanbul, Türkiye*
**Corresponding author*

Research Article

History
Received: 10/03/2022
Accepted: 15/08/2023

ABSTRACT

Cosmetics have been attracting the attention of humanity since it existed. Over the years, the reach of the cosmetics industry has increased exponentially. In recent years, cosmetic manufacturers have developed many formulations on cosmetic products that are brighter in color, more permanent and not easily affected by external factors. However, heavy metal powders are used while producing these formulations especially inside in dyestuffs and stabilizers. Cosmetic products can be absorbed through the skin and cause systemic toxicity. Hundreds of chemicals are used in many cosmetic products such as make-up products, shampoos, creams, aftershaves, and these chemicals may cause significant health problems. Thus, this study is designed to investigate the heavy metal content of lipstick samples which are used extensively by women. Determination of aluminum (Al), chromium (Cr), iron (Fe), nickel (Ni), copper (Cu), zinc (Zn), elements in 35 different lipstick samples (including 15 brands) were performed by Inductively Coupled Plasma-Mass Spectrophotometer (ICP-MS) device. Before the analysis, two different solubilization methods, wet solubilization and dry ashing, were applied to the samples in order to take the metals in the lipstick samples into inorganic environment.

Keywords: Heavy metals, ICP-MS, Lipstick products, Dry ashing, Wet solubilization.

[a] *gozdegulin.daltabaninan@sbu.edu.tr* *https://orcid.org/0000-0002-1997-410X* [b] *gulayseren@trakya.edu.tr* *https://orcid.org/0000-0003-1470-8889*

Introduction

In the Dictionary of the Turkish Language Association, cosmetics are defined as any substance that helps to beautify the skin and hair and keep them alive, and by the Cosmetic Council of the European Union Cosmetics Legislation 1223/2009, Article 2.1.a, "Cosmetic product; It is prepared to be applied to different external parts of the human body such as the epidermis, nails, hairs, hair, lips and external genitalia, teeth and oral mucosa, with the sole or main purpose of cleaning these parts, giving scent, changing their appearance and/or correcting body odors and/or defined as "all preparations or substances intended to preserve or keep in good condition" [1].

All cosmetic products authorized for use must be completely safe for users and the responsibility for ensuring the safety of these products is the manufacturer, distributor, and importer. In cosmetic products, it is estimated that approximately 10,000 chemicals are present, including parabens, phthalates, p-phenylenediamine, formaldehyde, dioxane, triclosan and numerous metals [2]. Moreover, preservatives, softeners, surfactants, or UV (ultra-violette) protectors may be added to cosmetic products depending on the ingredients in the composition and the purpose of use [3].

Lip products constitute a large proportion of all cosmetic products. The desire to color the lips has attracted the attention of humanity in the historical process. The first records of people using any product to beautify their lips appear in the Sumerians around 7000 BC. While the use of the first lip products started with mixing wax, oil and pigments and applying them to the lips, it took the form of sticks after the 1920s. When looking at the periods of Ancient Egypt, Greek and Roman Empire, it was seen that women applied some red minerals and herbs to their cheeks and lips in order to beautify. Therefore, lip cosmetics can be traced back thousands of years. Lip cosmetics, which moisturize the lips and increase their attractiveness, are one of the most used cosmetics by modern women [4,5]. Lip cosmetics usually consist of three main ingredients which are wax, oil and coloring agents. In addition to these three main ingredients, lip products contain some excipient substances such as antioxidants, preservatives and perfumes. On the other hand, studies are continuing on whether heavy metals are used as in these products and on safe usage intervals. Lip products can be classified as lip balm, lipstick, lip brilliant and lip gloss [6].

Lipsticks basically contain various oils, beeswax, pigments, antioxidants and preservatives. Compounds of some basic elements can also be added to the formulation to improve the quality of cosmetic products. The presence and amounts of metal components in cosmetic products require processes that must be followed continuously since there is direct contact with

the skin or mucous membranes. Despite exposure to very low amounts of heavy metals because of the use of lip products, significant chronic health risks may occur due to accumulation in long-term use. Lipsticks may contain heavy metals such as iron (Fe), cadmium (Cd), and copper (Cu) [7]. Serious problems due to excess heavy metals in cosmetics have been reported by the United States Food and Drug Administration (FDA) and the China National Drug Administration [8]. Considering the usage area, it is estimated that the products that cause the most toxic metal intake are lipsticks and lip glosses. There is risk that cosmetic products applied to the lips may be taken directly orally. When lipstick and other lip products are applied to the lips, it is easy to dissolve in the saliva and enter the bloodstream [9].

Microelements are defined as elements required in amounts less than 100 mg per day and present in tissues at mg/kg tissue levels. Iron, copper, zinc, cobalt, manganese, chromium, molybdenum, selenium, fluorine, and iodine are examples of microelements. Since the concentrations of microelements in the body are very low, they are also called trace elements [10]. Trace elements are found in the structure of the organism and play a role in many important functions. These vital elements must be taken in sufficient quantities to maintain a healthy life. Regulation of body functions, oxygen transport, and elimination of free radicals are the most important functions of trace elements. However, their excess amounts have a toxic effect on the body. Moreover, elements that have not been shown to be essential for the body's structure and function, are known as non-essential or toxic elements. All the trace elements, which are necessary for metabolism and listed above, also create a toxic effect if they are taken into the body more than a certain amount. [11].

In recent years, studies on the determination of trace elements in lip products have been increasing. Al-Saleh et al. investigated the levels of lead, cadmium, nickel, chromium, mercury, antimony, and arsenic in 14 brands of lipstick (28 samples) that are widely used in local Saudi markets. According to their results, the levels of all metals were generally lower than the rules of the US Food and Drug Administration for metallic impurities in color additives used in cosmetics. Only one brand of lipstick exceeded the specifications, containing levels of arsenic higher than 3 mg/kg [12]. In another study, lead values of 12 lipsticks, 13 lip glosses and 9 lip balms and the averages were determined by ICP-MS (Inductively Coupled Plasma-Mass Spectrophotometer) device which found as 0.05482 mg/kg, 0.04976 mg/kg and 0.07380 µg/g, respectively [8]. In another study, Cr, Mn, Co, Ni, Cu, Cd, Sb, Pb measurements were made in 32 lip sticks and their values were found as 6.72 mg/kg, 12.27 mg/kg, 0.48 mg/kg, 4.10 mg/kg, 93.93 mg/kg, 0.10 mg/kg, 1.13 mg/kg, 7.42 mg/kg respectively. The study also contained bioaccessibility which was the first study in this area. According to their results, only bioaccessible Pb in all samples significantly exceeded the FDA limit 0.1 mg/kg in candy [6].

In this context, the main goal of this study is to investigate the concentration of aluminum (Al), chromium (Cr), iron (Fe), nickel (Ni), copper (Cu), zinc (Zn) in 35 different lipstick samples (including 15 brands) in Turkey market by inductive coupled plasma-mass spectrometry.

Materials and Methods

Chemicals and Devices

All chemicals, used in the analysis were purchased from Sigma Chemical Co. (St. Louis, MO, USA). All chemicals were of analytical grade. HNO_3 %65, HF %40, $HClO_3$ %35 were used for solubilization methods. Quantitative filter paper, (FILTER-LAB® ref. 1238 125 mm diameter) was used for filtration process. Agilent 7700 Series ICP-MS was employed for analysis.

Sample Preparation

Before ICP-MS analysis, two different solubilization techniques were employed to prepare the samples for analysis. The first of these is the wet solubilization method with the acid mixture and the second one is the dry ashing method in the muffle furnace. At first, the microwave solubilization method was tried in order to solubilize the lipstick samples. However, as result of trials with many acid mixtures, explosions, burns, or melted lid boils were experienced in the vials due to high temperature and acid interaction. For this reason, it was decided to solubilize the lipstick samples with acid mixed wet solubilization and dry ashing method.

Wet Solubilization Method

The lipstick samples were numbered after they were categorized. Precise weights of 0.500 grams were taken from the numbered samples with using analytical balance. The weighed samples were placed in equally numbered vials. The elements were added to the inorganic medium by 5.00 mL nitric acid (HNO_3) and 1.00 mL hydrofluoric acid (HF) onto the weighed samples. After the solubilization process of the lipstick samples was carried out, they were diluted to 50.00 mL and stored in HDPE (High Density Polyethylene) storage containers until analysis. Trace element contents in the extracts were determined by ICP-MS device [13].

Dry Ashing Method

The lipstick samples were numbered after they were categorized. Precise weights of 0.500 grams were taken from the numbered samples with using analytical balance. The weighed samples were placed in equally numbered porcelain crucibles. The lids of the crucibles were closed and placed vertically in the muffle furnace. Lipstick samples were allowed to become ashes at 900 °C for 4 hours in the muffle furnace. By adding 5.00 mL of HNO_3 to 1.00 mL of chloric acid ($HClO_3$) to the crucibles, the ashes were taken to the liquid medium and filtered with the help of filter paper. After dissolving the lipstick

samples, they were diluted to 50.00 mL and stored in HDPE storage containers until analysis. Trace element contents in the extracts were determined by ICP-MS device [13].

ICP-MS Analysis

An Agilent 7700 Series (Agilent Technologies, Tokyo, Japan) was used for all measurements. All measurements were performed in triplicates from each vial. The instrument parameters are described in Table 1.

Table 1. Setting parameters for the ICP-MS method.

Plasma Parameters	*Lens Parameters*	*Cell Parameters*
Power: 1550 W	Omega Lens: 10V	OctP Slope: -8V
Matcher voltage: 1.80V	Cell Input: -30V	OctP RF: 180V
Sample depth: 8mm	Cell Output: -50V	Energy separator: 5V
Carrier gas velocity: 1.05 l/min	Deviation: 13V	Stabilization time: 50 seconds
Nebulizer pump: 0.1 rps	Layer training: -40V	Sampling time: 50 seconds
S/C temperature: 2°C		Calibration curve confidence interval : 0.95

Results and Discussion

In this study, the concentrations of the selected heavy metals; aluminum (Al), chromium (Cr), iron (Fe), nickel (Ni), copper (Cu), zinc (Zn) in 35 different lipstick samples were determined by using ICP-MS device. The values detected in lipsticks solubilized by the wet solubilization method (Table 2) and dry ashing method (Table 3). In this study, the standard addition method was used while working with the ICP-MS device to minimize the matrix effects and prevent interference. Although there is widespread suspicion about the toxicity of cosmetics, there have not been enough controlled studies and the reported studies are generally as uncontrolled and case reports. In our literature research, it was realized that there is a great deficiency in this area. Trace elements, which are of great importance especially for human health; aluminum (Al), chromium (Cr), iron (Fe), nickel (Ni), copper (Cu), zinc (Zn) concentrations in different lipstick samples was determined by ICP-MS instrument by using 2 different solubilization techniques.

According to the results of the analyze using the wet solubilization method; the values were found for the element aluminum vary between 0.23 mg/kg and 87.93 mg/kg. The results were determined by using the dry ashing method ranged from 0.25 mg/kg to 89.10 mg/kg. The values determined in the wet solubilization method for chromium vary between 0.02 mg/kg and 0.41 mg/kg. The values determined in the dry ashing method for chromium vary between 0.03 mg/kg and 0.14 mg/kg. The values determined in the wet solubilization method for iron vary in a wide range between 3.19 mg/kg and 605.00 mg/kg. The values determined in the iron element dry ashing method vary between 3.71 mg/kg and 54.16 mg/kg. In nickel element, the values determined in the wet solubilization method was very close to each other her but vary between 0.01 mg/kg and 0.25 mg/kg. The amount of nickel determined by the dry ashing method was found between 0.03 mg/kg and 0.13 mg/kg. In the wet solubilization method for copper element, it was ranged between 0.01 mg/kg and 0.22 mg/kg. The results of the dry ashing method of the same element were detected between 0.02 mg/kg and 0.10 mg/kg. The values found for the results obtained in the study are compatible with the studies in the literature in which determinations were made with different or the same device. As a result, the difference in the solubilization method caused the elements to be detected in different amounts. The acids used in the 2 methods are different and therefore the contribution of acidity to ionization in the mass detector is different. Therefore, different results were obtained in wet solubilization and dry ashing methods. According to the Medical Drug Device Agency, the maximum values that should be found in cosmetics are 20 mg/kg for lead, 5 mg/kg for arsenic, 5 mg/kg for cadmium, 1 mg/kg for mercury, and 10 mg/kg for antimony. However, there is no specified limit value for aluminum, chromium, copper, iron, nickel, and zinc determined by Medical Drug Device Agency. Moreover, FDA (US Food & Drug Administration) addresses the maximum values of some trace elements such as 3 mg/kg for arsenic, 20 mg/kg for lead, 1 mg/kg for mercury. However, there is no specified limit value for aluminum, chromium, copper, iron, nickel, and zinc determined by FDA. According to the various studies, chronic and long-term exposure to trace elements can lead to serious health problems [10].

While chromium, when consumed in small quantities, serves as a vital element that aids the body in utilizing sugar, protein, and fat, excessive inhalation of chromium can result in nasal irritation, leading to symptoms such as a runny nose, nosebleeds, and the formation of sores or perforations in the nasal septum. Ingesting large amounts of chromium can lead to gastrointestinal disturbances, ulcers, seizures, as well as damage to the kidneys and liver, potentially resulting in fatality. Contact with specific chromium compounds on the skin can give rise to the development of skin ulcers. Individuals highly sensitive to chromium may experience severe allergic reactions characterized by intense skin inflammation and swelling [14].

Prolonged contact with nickel can lead to allergic reactions of the skin, such as skin rashes and other related symptoms. Moreover, the International Agency for Research on Cancer (IARC) has categorized nickel compounds as belonging to Group 1, indicating they are known to cause cancer in humans, while metallic nickel is classified as Group 2B, suggesting it is possibly carcinogenic to humans. Nickel is a significant contributor to allergic contact dermatitis in people worldwide, affecting both children and adults, and it has a global occurrence rate of approximately 8.6% [15].

Copper is present in plants and animals as a natural component. It is a vital element required by all living organisms, including humans and other animals, in small quantities. However, when found in significantly higher concentrations, copper can have harmful effects that are considered toxic. Prolonged copper exposure may cause cancer, infertility, skin allergy and greenish discoloration of the skin, hair, and teeth. [16].

According to the literature, there are no known risks for healthy people from normal dietary intakes of aluminum. The risks are only harmful longer than the usual consumption of grams of aluminum antacids which is significantly increased in people with impaired renal function. Moreover, long-term intravenous administration always causes serious toxicity. Aluminium may cause gene instability, alter gene expression or enhance oxidative stress in the body [17].

While iron is an essential mineral necessary for various physiological processes, such as oxygen transport and energy production, an overload of iron can lead to toxicity. This can happen in individuals with hereditary disorders like hemochromatosis or through repeated excessive iron supplementation. Prolonged iron toxicity can cause damage to organs such as the liver, heart, and pancreas, leading to conditions like cirrhosis, cardiomyopathy, and diabetes. Symptoms may include fatigue, joint pain, abdominal pain, and skin discoloration. [18].

While zinc is an essential trace element necessary for various physiological functions, such as immune system regulation and enzymatic activity, an excessive intake or chronic exposure to high levels of zinc can lead to toxicity. Prolonged zinc toxicity can occur due to factors such as excessive zinc supplementation, occupational exposure, cosmetic produtcs or genetic disorders affecting zinc metabolism. The adverse effects of prolonged zinc toxicity may include gastrointestinal disturbances, such as nausea, vomiting, and abdominal pain. It can also interfere with copper absorption, leading to copper deficiency and associated neurological symptoms. Additionally, long-term zinc toxicity can impact immune function, disrupt hormonal balance, and affect the liver and kidneys. [19].

When the values of all the elements determined in our study are compared with the literature and the value in lipsticks does not pose any risk. However, long-term, and continuous use may cause adverse effects on health. In continuous use, the accumulation effect in the body should be considered. In addition, there is no limit value determined for these elements by the Medical Drug Device Agency and US Food and Drug Administration. As a result, the accumulation of heavy metals taken from cosmetic products poses a health risk and needs to be inspected with continuous measurements and controls.

Table 2. Amounts of aluminum, chromium, iron, nickel, copper, and zinc (mg/kg) detected in lipsticks using the wet solubilization method.

Samples	*Al*	*Cr*	*Fe*	*Ni*	*Cu*	*Zn*
1	38.55	0.07	191.05	0.05	0.04	8.01
2	28.52	0.09	338.59	0.04	0.05	8.36
3	74.52	0.08	53.62	0.13	0.16	3.98
4	0.23	0.02	3.19	0.01	0.01	0.00
5	11.49	0.04	64.44	0.04	0.03	6.24
6	77.42	0.06	23.55	0.07	0.11	11.79
7	48.73	0.12	176.75	0.13	0.05	10.07
8	20.17	0.05	338.38	0.17	0.06	10.72
9	40.34	0.04	128.03	0.04	0.03	8.15
10	86.93	0.06	14.80	0.07	0.04	8.06
11	50.86	0.06	4.57	0.25	0.03	6.83
12	6.18	0.05	419.68	0.09	0.22	12.00
13	2.32	0.05	239.10	0.24	0.08	11.20
14	33.28	0.08	247.49	0.06	0.13	10.76
15	32.18	0.11	172.99	0.10	0.03	12.70
16	31.50	0.07	56.09	0.06	0.04	10.54
17	20.71	0.06	171.30	0.17	0.03	15.42
18	72.28	0.17	33.76	0.20	0.09	11.73
19	59.40	0.41	29.99	0.20	0.11	11.47
20	20.87	0.05	312.43	0.08	0.13	10.44
21	60.82	0.05	4.09	0.10	0.04	7.29
22	87.93	0.18	23.28	0.18	0.05	10.18
23	80.55	0.04	146.37	0.08	0.04	5.47
24	50.95	0.12	326.64	0.08	0.04	9.22
25	39.04	0.06	200.96	0.05	0.08	8.28
26	12.24	0.03	5.97	0.18	0.03	3.37
27	8.28	0.06	605.00	0.06	0.03	6.33
28	22.03	0.13	11.23	0.10	0.04	6.43
29	12.23	0.04	211.26	0.05	0.03	5.08
30	27.24	0.03	3.26	0.02	0.03	4.37
31	14.79	0.05	66.12	0.05	0.02	2.61
32	23.59	0.22	469.58	0.14	0.15	8.21
33	4.14	0.04	5.16	0.02	0.02	5.65
34	27.65	0.08	360.68	0.04	0.02	11.73
35	12.33	0.06	117.55	0.06	0.08	4.05

Table 3. Amounts of aluminum, chromium, iron, nickel, copper, and zinc (mg/kg) detected in lipsticks using the dry ashing method.

Samples	Al	Cr	Fe	Ni	Cu	Zn
1	25.91	0.07	13.37	0.06	0.10	0.57
2	3.97	0.05	5.76	0.04	0.05	0.53
3	58.86	0.05	4.38	0.03	0.05	0.54
4	18.64	0.05	7.79	0.04	0.05	0.56
5	1.09	0.04	4.45	0.04	0.04	0.56
6	4.77	0.03	4.19	0.03	0.05	0.57
7	9.45	0.04	4.55	0.04	0.09	0.55
8	0.85	0.14	9.90	0.13	0.06	0.82
9	2.82	0.06	4.51	0.05	0.04	0.26
10	4.92	0.05	3.75	0.04	0.04	0.19
11	3.40	0.06	3.71	0.04	0.03	0.19
12	1.76	0.04	4.90	0.06	0.03	0.52
13	1.87	0.03	4.46	0.03	0.03	0.49
14	0.28	0.04	4.43	0.04	0.04	0.53
15	1.36	0.03	4.17	0.04	0.04	0.52
16	3.98	0.05	4.47	0.03	0.04	0.52
17	0.42	0.03	4.05	0.04	0.03	0.52
18	32.77	0.05	4.67	0.04	0.05	0.54
19	41.00	0.07	4.71	0.05	0.06	0.54
20	11.57	0.03	6.82	0.04	0.04	0.54
21	24.73	0.04	3.70	0.04	0.04	0.17
22	3.33	0.03	4.19	0.03	0.02	0.17
23	2.90	0.03	5.10	0.03	0.02	0.17
24	57.42	0.05	54.16	0.04	0.04	0.18
25	1.70	0.03	4.17	0.03	0.03	0.48
26	89.07	0.05	3.97	0.04	0.06	0.54
27	4.14	0.04	5.10	0.04	0.04	0.52
28	7.70	0.05	4.23	0.05	0.03	0.53
29	0.97	0.03	4.03	0.04	0.04	0.52
30	2.52	0.05	3.82	0.04	0.04	0.54
31	0.25	0.03	4.06	0.03	0.03	0.52
32	15.92	0.03	4.98	0.04	0.08	0.26
33	5.81	0.04	4.01	0.04	0.06	0.19
34	2.41	0.03	4.16	0.04	0.03	0.25
35	1.95	0.03	7.83	0.04	0.04	0.49

Conclusion

The results acquired from the study are essential to understanding the risks of trace element exposure and their occurrence in lipsticks. The contents of the trace elements were ordered in the following decreasing order according to the maximum concentrations Al > Fe > Zn > Cr, Ni, Cu and the levels of all investigated metals were generally lower than the limit values determined by literature . Turkey Drug and Medical Device Agency and FDA has set limit values only for lead, arsenic, cadmium, mercury, and antimony. Therefore, risk analysis regarding the concentrations of other trace elements cannot be performed. As a conclude, continuous analysis is essential for all cosmetic products since prolonged exposure of trace elements have significant negative effects on human health.

Acknowledgment

This study was funded by Trakya University Scientific Research Foundation (Project No: TUBAP-2017/136).

Conflicts of interest

There are no conflicts of interest in this work.

References

[1] de Paula C.E.R., Cruz G.F.B., Rezende C.M.S.P., Cassella R.J., Determination of Cr and Mn in moisturizing creams by graphite furnace atomic absorption spectrometry through direct introduction of the samples in the form of emulsions, *Microchemical Journal,* 127 (2016) 1-6.

[2] Ullah H., Noreen S., Fozia, Rehman A., Waseem A., Zubair S., Adnan M., Ahmad I., Comparative study of heavy metals content in cosmetic products of different countries marketed in Khyber Pakhtunkhwa, Pakistan, *Arabian Journal of Chemistry*, 10(1) (2017) 10-18.

[3] Borowska S., Brzóska M.M., Metals in cosmetics: Implications for human health, *Journal of Applied Toxicology*, 35(6) (2015) 551-572.

[4] Iwegbue C.M.A., Bassey F.I., Tesi G.O., Onyeloni S.O., Obi G., Martincigh B.S., Safety evaluation of metal exposure from commonly used moisturizing and skin-lightening creams in Nigeria, *Regulatory Toxicology and Pharmacology*, 71(3) (2015) 484-490.

[5] Parish L.C., Crissey J.T., Cosmetics: A historical review*, American Journal of Clinical Dermatology,* 6(3) (1988) 1-4.

[6] Gao P., Lei T., Jia L., Yury B., Zhang Z., Du Y., Feng Y., Xing B.İ., Bioaccessible trace metals in lip cosmetics and their health risks to female consumers, *Environmental Pollution*, 238 (2018) 554-561.

[7] Zakaria A., Ho Y., Heavy metals contamination in lipsticks and their associated health risks to lipstick consumers, *Regulatory Toxicology and Pharmacology*, 73(1) (2015) 191-195.

[8] Li Y., Fang Y., Liu Z., Zhang Y., Liu K., Jiang L., Yang B., Yang Y., Song Y., Liu C., Trace metal lead exposure in typical lip cosmetics from electronic commercial platform: Investigation, health risk assessment and blood lead level analysis, *Front Public Health*, 9(11) (2021) 1-13.

[9] Khazaal S., Al-Azawi K., Eessa H., AL-Gebori A., Obayes H., Khasraghi A., Levels of Lead and Chromium Ions in Different brands of lipstick sold at local markets in Iraq, *Engineering and Technology Journal,* 36(2B) (2018) 147-151.

[10] Saah S.A., Boadi N.O., Sakyi P.O., Darko G., Mensah M.B., Risk of exposure to trace elements through the application of facial makeup powders*, Journal of Chemistry*, 2022 (2022).

[11] Davoudi-Kiakalayeh A., Mohammadi R., Pourfathollah A.A., Siery Z, Davoudi-Kiakalayeh S., Alloimmunization in thalassemia patients: New insight for healthcare, *International Journal of Preventive Medicine*, 8(2) (2017) 1-17.

[12] Al-Saleh I., Al-Enazi S., Trace metals in lipsticks, *Toxicological & Environmental Chemistry*, 93(6) (2011) 1149-1165.

[13] Papadopoulos A., Assimomytis N., Varvaresou A., Sample Preparation of Cosmetic Products for the Determination of Heavy Metals, *Cosmetics*, 9(21) (2022) 1-12.

[14] Becker L.C., Boyer I., Bergfeld W.F, Belsito D.V., Hill R.A., Klaassen C.D., Liebler D.C., Marks J.G., Shank R.C., Slaga T.J., Snyder P.W., Andersen F.A., Safety assessment of alumina and aluminum hydroxide as used in cosmetics, *International Journal of Toxicology*, 35(3) (2016) 16-33.

[15] Gondal M.A., Seddigi Z.S., Nasr M.M., Gondal B., Spectroscopic detection of health hazardous contaminants in lipstick using Laser Induced Breakdown Spectroscopy, *Journal of Hazardous Materials,* 175(1-3) (2010) 726-732.

[16] Safavi S., Najarian R., Rasouli-Azad M., Masoumzadeh S., Ghaderi A., Eghtesadi R., A narrative review of heavy metals in cosmetics; health risks, *International Journal of Pharmaceutical Research,* 11 (4) (2019) 182-190.

[17] Nathan R.J., Sharma P., Nathan L.S., Determination of the toxic lead and copper levels in cosmetic hair-dye powders by flame atomic absorption spectrophotometry, *Medico-Legal Update*, 14(1) (2014) 35–40.

[18] Sanajou S., Şahin G., Baydar T., Aluminium in cosmetics and personal care products, *Journal of Applied Toxicology* 41 (11) (2021) 1704–1718.

[19] Lansdown A.B.G., Iron: A cosmetic constituent but an essential nutrient for healthy skin, *International Journal of Cosmetic Science*, 23(3) (2001) 129-137.

[20] Kim K.B., Kim Y.W., Lim S.K., Roh T.H., Bang D.Y., Choi S.M., Lim D.S., Kim Y.J., Baek S.H., Kim M.K., Seo H.S., Kim M.H., Kim H.S., Lee J.Y., Kacew S., Lee B.M., Risk assessment of zinc oxide, a cosmetic ingredient used as a UV filter of sunscreens, *Journal of Toxicology and Environmental Health*, 20(3) (2017) 155–182.

Cumhuriyet Sci. J., 44(3) (2023) 522-530
DOI: https://doi.org/10.17776/csj.1145020

Cumhuriyet Science Journal

| csj.cumhuriyet.edu.tr | Founded: 2002 ISSN: 2587-2680 e-ISSN: 2587-246X Publisher: Sivas Cumhuriyet University

Construction of New Ostrowski's Type Inequalities By Using Multistep Linear Kernel

Yasir Qayyum [1,a], Haider Ali [1,b], Faiz Rasool [1,c], Ather Qayyum [1,d,*]

[1] *Department of Mathematics, Institute of Southren punjab, Multan, Pakistan.*

**Corresponding author*

Research Article

History
Received: 19/07/2022
Accepted: 31/03/2023

ABSTRACT

In this paper, we construct a generalisation of Ostrowski's type inequalities with the help of new identity. By using this identity, we construct further results for $\acute{g}' \in L^1[\dot{c}, \breve{d}], \acute{g}' \in L^2[\dot{c}, \breve{d}], \acute{g}'' \in L^2[\dot{c}, \breve{d}]$. To prove our main and related results, we utilized some famous inequalities such as Gruss-inequality, Diaz-Mıtcaf's inequality and Cauchy's inequality. To prove our main results, we used a new multistep kernel (9-step linear kernel). Some related results are also discussed. In the end, we apply our results to numerical integration also.

Keywords: Ostrowski inequalities, Numerical integration, Linear Kernel.

[a] *m.yasir031300@gmail.com* *https://orcid.org/0000-0002-3084-9019*
[b] *haiderali031995@gmail.com* *https://orcid.org/0000-0002-9989-1629*
[c] *faizgujjar6@gmail.com* *https://orcid.org/0000-0001-7742-3683*
[d] *atherqayyum@isp.edu.pk* *https://orcid.org/0000-0003-4149-5305*

Introduction

In 1970, Mitrinovi'c [1-3] stressed the significance of inequalities. Ostrowski type integral inequalities for 2-times differentiable mappings. Barnett *et al.* [4] released research about Ostrowski type integral inequalities for $L_p(c,d)$ and $L_1(c,d)$. Qayyum and Husain[5] generalized Ostrowski type integral inequalities to present new estimates. Qayyum *et al.* [6-11] provided a generalized form of Ostrowski type Gruss-inequality for twice derivable mappings. Barnett *et al.* [4] stressed another new concept i.e. proved Ostrowski type integral inequalities by utilizing $\beta-$ function for 1st and 2nd differential mappings and they applied their all findings for numerical quadrature rules. Few people (for example [9, 10, 12]) worked on different type of inequalities.

Main Findings

Lemma 1 Let $\acute{g}: [\dot{c}, \breve{d}] \to \mathbb{R}$ be such that $\acute{g}'$ is absolutely continuous on $[\dot{c}, \breve{d}]$. Define the kernel $P(u, \hat{U})$ as:

$$P(u,\hat{U}) = \begin{cases} \hat{U} - \dot{c} & , \quad \hat{U} \in \left(\dot{c}, \frac{7\dot{c}+u}{8}\right] \\ \hat{U} - \frac{15\dot{c}+\breve{d}}{16} & , \quad \hat{U} \in \left(\frac{7\dot{c}+u}{8}, \frac{3\dot{c}+u}{4}\right] \\ \hat{U} - \frac{7\dot{c}+\breve{d}}{8} & , \quad \hat{U} \in \left(\frac{3\dot{c}+u}{4}, \frac{\dot{c}+u}{2}\right] \\ \hat{U} - \frac{3\dot{c}+\breve{d}}{4} & , \quad \hat{U} \in \left(\frac{\dot{c}+u}{2}, u\right] \\ \hat{U} - \frac{\dot{c}+\breve{d}}{2} & , \quad \hat{U} \in \left(u, \dot{c}+\breve{d}-u\right] \\ \hat{U} - \frac{\dot{c}+3\breve{d}}{4} & , \quad \hat{U} \in \left(\dot{c}+\breve{d}-u, \frac{\dot{c}+2\breve{d}-u}{2}\right] \\ \hat{U} - \frac{\dot{c}+7\breve{d}}{8} & , \quad \hat{U} \in \left(\frac{\dot{c}+2\breve{d}-u}{2}, \frac{\dot{c}+4\breve{d}-u}{4}\right] \\ \hat{U} - \frac{\dot{c}+15\breve{d}}{16} & , \quad \hat{U} \in \left(\frac{\dot{c}+4\breve{d}-u}{4}, \frac{\dot{c}+8\breve{d}-u}{8}\right] \\ \hat{U} - \breve{d} & , \quad \hat{U} \in \left(\frac{\dot{c}+8\breve{d}-u}{8}, \breve{d}\right] \end{cases} \tag{1}$$

for all ų$\in \left[\dot{c}, \frac{\dot{c}+\check{d}}{2}\right]$, the following identity holds:

$$\frac{1}{\check{d}-\dot{c}}\int_{\dot{c}}^{\check{d}} P(\mathrm{u},\widehat{U})\mathrm{g}'(\widehat{U})d\widehat{U}$$
$$= \frac{1}{16}\left[\mathrm{g}\left(\frac{7\dot{c}+\mathrm{u}}{8}\right)+\mathrm{g}\left(\frac{3\dot{c}+\mathrm{u}}{4}\right)+2\mathrm{g}\left(\frac{\dot{c}+\mathrm{u}}{2}\right)+4\mathrm{g}(\mathrm{u})+4\mathrm{g}(\dot{c}+\check{d}-\mathrm{u})+2\mathrm{g}\left(\frac{\dot{c}+2\check{d}-2\mathrm{u}}{2}\right)+\mathrm{g}\left(\frac{\dot{c}+4\check{d}-\mathrm{u}}{4}\right)\right.$$
$$\left.+\mathrm{g}\left(\frac{\dot{c}+8\check{d}-\mathrm{u}}{8}\right)\right]-\frac{1}{\check{d}-\dot{c}}\int_{\dot{c}}^{\check{d}} \mathrm{g}(\widehat{U})d\widehat{U}. \quad (2)$$

Proof. We obtain the desired identity (2) by applying integration by parts on (1);

$$\int_{\dot{c}}^{\check{d}} P(\mathrm{u},\widehat{U})\mathrm{g}'(\widehat{U})d\widehat{U} = \int_{\dot{c}}^{\frac{7\dot{c}+\mathrm{u}}{8}} (\widehat{U}-\dot{c})\mathrm{g}'(\widehat{U})d\widehat{U} + \int_{\frac{7\dot{c}+\mathrm{u}}{8}}^{\frac{3\dot{c}+\mathrm{u}}{4}} \left(\widehat{U}-\frac{15\dot{c}+\check{d}}{16}\right)\mathrm{g}'(\widehat{U})d\widehat{U} + \int_{\frac{3\dot{c}+\mathrm{u}}{4}}^{\frac{\dot{c}+\mathrm{u}}{2}} \left(\widehat{U}-\frac{7\dot{c}+\check{d}}{8}\right)\mathrm{g}'(\widehat{U})d\widehat{U}$$
$$+\int_{\frac{\dot{c}+\mathrm{u}}{2}}^{\mathrm{u}} \left(\widehat{U}-\frac{3\dot{c}+\check{d}}{4}\right)\mathrm{g}'(\widehat{U})d\widehat{U} + \int_{\mathrm{u}}^{\dot{c}+\check{d}-\mathrm{u}} \left(\widehat{U}-\frac{\dot{c}+\check{d}}{2}\right)\mathrm{g}'(\widehat{U})d\widehat{U} + \int_{\dot{c}+\check{d}-\mathrm{u}}^{\frac{\dot{c}+2\check{d}-\mathrm{u}}{2}} \left(\widehat{U}-\frac{\dot{c}+3\check{d}}{4}\right)\mathrm{g}'(\widehat{U})d\widehat{U}$$
$$+\int_{\frac{\dot{c}+2\check{d}-\mathrm{u}}{2}}^{\frac{\dot{c}+4\check{d}-\mathrm{u}}{4}} \left(\widehat{U}-\frac{\dot{c}+7\check{d}}{8}\right)\mathrm{g}'(\widehat{U})d\widehat{U} + \int_{\frac{\dot{c}+4\check{d}-\mathrm{u}}{4}}^{\frac{\dot{c}+8\check{d}-\mathrm{u}}{8}} \left(\widehat{U}-\frac{\dot{c}+15\check{d}}{16}\right)\mathrm{g}'(\widehat{U})d\widehat{U} + \int_{\frac{\dot{c}+8\check{d}-\mathrm{u}}{8}}^{\check{d}} (\widehat{U}-\check{d})\mathrm{g}'(\widehat{U})d\widehat{U}$$

After simplification, we get(2).

Now by using (2) , we construct five different cases:

Case. 1: $When\ \acute{g}' \in L^1[\dot{c},\check{d}]$

Theorem 1 Let ǵ: $[\dot{c},\check{d}] \to \mathbb{R}$ be differentiable on $(\dot{c},\check{d})$. If $\acute{g}' \in \mathrm{L}^1[\dot{c},\check{d}]$ and $\gamma \le \acute{g}'(\widehat{U}) \le \Gamma$, for all $\widehat{U} \in [\dot{c},\check{d}]$, then,

$$\left|\frac{1}{16}\left[\mathrm{g}\left(\frac{7\dot{c}+\mathrm{u}}{8}\right)+\mathrm{g}\left(\frac{3\dot{c}+\mathrm{u}}{4}\right)+2\mathrm{g}\left(\frac{\dot{c}+\mathrm{u}}{2}\right)+4\mathrm{g}(\mathrm{u})+4\mathrm{g}(\dot{c}+\check{d}-\mathrm{u})+2\mathrm{g}\left(\frac{\dot{c}+2\check{d}-2\mathrm{u}}{2}\right)+\mathrm{g}\left(\frac{\dot{c}+4\check{d}-\mathrm{u}}{4}\right)\right.\right.$$
$$\left.\left.+\mathrm{g}\left(\frac{\dot{c}+8\check{d}-\mathrm{u}}{8}\right)\right]-\frac{1}{\check{d}-\dot{c}}\int_{\dot{c}}^{\check{d}} g(\widehat{U})d\widehat{U}\right| \le \frac{1}{64}(\check{d}-\dot{c})(\Gamma-\gamma) \quad (3)$$

holds for all ų$\in \left[\dot{c}, \frac{\dot{c}+\check{d}}{2}\right]$.

Proof. As we know that for all $\widehat{U} \in [\dot{c},\check{d}]$ and ų$\in \left[\dot{c}, \frac{\dot{c}+\check{d}}{2}\right]$, we have

$$\mathrm{u}-\frac{15\dot{c}+\check{d}}{16} \le P(\mathrm{u},\widehat{U}) \le \mathrm{u}-\dot{c}.$$

Using Gruss-inequality [5] on the mappings $P(\mathrm{u},\widehat{U})$ and $\acute{g}'(\widehat{U})$,

$$\left|\frac{1}{\check{d}-\dot{c}}\int_{\dot{c}}^{\check{d}} P(\mathrm{u},\widehat{U})\mathrm{g}'(\widehat{U})d\widehat{U} - \frac{1}{\check{d}-\dot{c}}\int_{\dot{c}}^{\check{d}} P(\mathrm{u},\widehat{U})d\widehat{U}\,\frac{1}{\check{d}-\dot{c}}\int_{\dot{c}}^{\check{d}} \mathrm{g}'(\widehat{U})d\widehat{U}\right| \le \frac{1}{64}(\check{d}-\dot{c})(\Gamma-\gamma) \quad (4)$$

for all ų$\in \left[\dot{c}, \frac{\dot{c}+\check{d}}{2}\right]$.

It is straight forward exercise to show that

$$\frac{1}{\check{d}-\dot{c}}\int_{\dot{c}}^{\check{d}} P(\mathrm{u},\widehat{U})d\widehat{U} = \int_{\dot{c}}^{\frac{7\dot{c}+\mathrm{u}}{8}} (\widehat{U}-\dot{c})d\widehat{U} + \int_{\frac{7\dot{c}+\mathrm{u}}{8}}^{\frac{3\dot{c}+\mathrm{u}}{4}} \left(\widehat{U}-\frac{15\dot{c}+\check{d}}{16}\right)d\widehat{U} + \int_{\frac{3\dot{c}+\mathrm{u}}{4}}^{\frac{\dot{c}+\mathrm{u}}{2}} \left(\widehat{U}-\frac{7\dot{c}+\check{d}}{8}\right)d\widehat{U}$$
$$+\int_{\frac{\dot{c}+\mathrm{u}}{2}}^{\mathrm{u}} \left(\widehat{U}-\frac{3\dot{c}+\check{d}}{4}\right)d\widehat{U} + \int_{\mathrm{u}}^{\dot{c}+\check{d}-\mathrm{u}} \left(\widehat{U}-\frac{\dot{c}+\check{d}}{2}\right)d\widehat{U} + \int_{\dot{c}+\check{d}-\mathrm{u}}^{\frac{\dot{c}+2\check{d}-\mathrm{u}}{2}} \left(\widehat{U}-\frac{\dot{c}+3\check{d}}{4}\right)d\widehat{U}$$
$$+\int_{\frac{\dot{c}+2\check{d}-\mathrm{u}}{2}}^{\frac{\dot{c}+4\check{d}-\mathrm{u}}{4}} \left(\widehat{U}-\frac{\dot{c}+7\check{d}}{8}\right)d\widehat{U} + \int_{\frac{\dot{c}+4\check{d}-\mathrm{u}}{4}}^{\frac{\dot{c}+8\check{d}-\mathrm{u}}{8}} \left(\widehat{U}-\frac{\dot{c}+15\check{d}}{16}\right)d\widehat{U} + \int_{\frac{\dot{c}+8\check{d}-\mathrm{u}}{8}}^{\check{d}} (\widehat{U}-\check{d})d\widehat{U}.$$

Again after simplification, we have

$$\frac{1}{\check{d}-\dot{c}}\int_{\dot{c}}^{\check{d}} P(\mathrm{u},\widehat{U})d\widehat{U} = 0 \quad (5)$$

And

$$\frac{1}{\breve{d}-\dot{c}}\int_{\dot{c}}^{\breve{d}} g'(\hat{U})d\hat{U} = \frac{g(\breve{d})-g(\dot{c})}{\breve{d}-\dot{c}}. \tag{6}$$

Hence using $(4)-(6)$, we get our required result (3).

Now we will discuss some corollaries.

Corollary 1 By substituting ų$= \frac{\dot{c}+\breve{d}}{2}$ in (3), then

$$\left|\frac{1}{16}\left[g\left(\frac{15\dot{c}+\breve{d}}{16}\right)+g\left(\frac{7\dot{c}+\breve{d}}{8}\right)+2g\left(\frac{3\dot{c}+\breve{d}}{4}\right)+4g\left(\frac{\dot{c}+\breve{d}}{2}\right)+4g\left(\frac{\dot{c}+\breve{d}}{2}\right)+2g\left(\frac{\breve{d}}{2}\right)+g\left(\frac{\dot{c}+7\breve{d}}{8}\right)+g\left(\frac{\dot{c}+15\breve{d}}{16}\right)\right]-\frac{1}{\breve{d}-\dot{c}}\int_{\dot{c}}^{\breve{d}} g(\hat{U})d\hat{U}\right| \le \frac{1}{64}(\breve{d}-\dot{c})(\Gamma-\gamma).$$

Corollary 2 By substituting ų$= \frac{3\dot{c}+\breve{d}}{4}$ in (3), we get

$$\left|\frac{1}{16}\left[g\left(\frac{31\dot{c}+\breve{d}}{32}\right)+g\left(\frac{15\dot{c}+\breve{d}}{16}\right)+2g\left(\frac{7\dot{c}+\breve{d}}{8}\right)+4g\left(\frac{3\dot{c}+\breve{d}}{4}\right)+4g\left(\frac{\dot{c}+3\breve{d}}{4}\right)+2g\left(\frac{3\breve{d}-\dot{c}}{4}\right)+g\left(\frac{\dot{c}+15\breve{d}}{16}\right)+g\left(\frac{\dot{c}+31\breve{d}}{32}\right)\right]-\frac{1}{\breve{d}-\dot{c}}\int_{\dot{c}}^{\breve{d}} g(\hat{U})d\hat{U}\right| \le \frac{1}{64}(\breve{d}-\dot{c})(\Gamma-\gamma). \tag{7}$$

Corollary 3 By substituting ų$= \frac{\dot{c}+3\breve{d}}{4}$ in (3), we get

$$\left|\frac{1}{16}\left[g\left(\frac{29\dot{c}+3\breve{d}}{32}\right)+g\left(\frac{13\dot{c}+3\breve{d}}{16}\right)+2g\left(\frac{5\dot{c}+3\breve{d}}{8}\right)+4g\left(\frac{\dot{c}+3\breve{d}}{4}\right)+4g\left(\frac{3\dot{c}+\breve{d}}{4}\right)+2g\left(\frac{\dot{c}+\breve{d}}{4}\right)+g\left(\frac{3\dot{c}+13\breve{d}}{16}\right)+g\left(\frac{3\dot{c}+29\breve{d}}{32}\right)\right]-\frac{1}{\breve{d}-\dot{c}}\int_{\dot{c}}^{\breve{d}} g(\hat{U})d\hat{U}\right| \le \frac{1}{64}(\breve{d}-\dot{c})(\Gamma-\gamma). \tag{8}$$

Case: 2 For $\acute{g}' \in L^1[\dot{c},\breve{d}]$

Theorem 2 Let I: $\subset \mathbb{R} \to \mathbb{R}$ be a differentiable mapping on I^0, the interior of the interval I, and let $\dot{c},\breve{d} \in I$ with $\dot{c} < \breve{d}$. If $\acute{g}' \in L^1[\dot{c},\breve{d}]$,and $\gamma \le \acute{g}'(\hat{U}) \le \Gamma \forall$ ų$\in [\dot{c},\breve{d}]$, then the following inequality holds for all ų$\in \left[\dot{c},\frac{\dot{c}+\breve{d}}{2}\right]$, we have

$$\left|\frac{1}{16}\left[g\left(\frac{7\dot{c}+u}{8}\right)+g\left(\frac{3\dot{c}+u}{4}\right)+2g\left(\frac{\dot{c}+u}{2}\right)+4g(u)+4g(\dot{c}+\breve{d}-u)+2g\left(\frac{\dot{c}+2\breve{d}-2u}{2}\right)+g\left(\frac{\dot{c}+4\breve{d}-u}{4}\right)+g\left(\frac{\dot{c}+8\breve{d}-u}{8}\right)\right]-\frac{1}{\breve{d}-\dot{c}}\int_{\dot{c}}^{\breve{d}} g(\hat{U})d\hat{U}\right| \le \frac{1}{128(\breve{d}-\dot{c})}\left[(43\dot{c}+21\breve{d}-64u)(\dot{c}-u)\right](\Gamma-\gamma). \tag{9}$$

Proof. Let

$$c = \frac{\Gamma+\gamma}{2}$$

then

$$\frac{1}{\breve{d}-\dot{c}}\int_{\dot{c}}^{\breve{d}} P(u,\hat{U})g'(\hat{U})d\hat{U} - \frac{c}{\breve{d}-\dot{c}}\int_{\dot{c}}^{\breve{d}} P(u,\hat{U})d\hat{U} = \frac{1}{\breve{d}-\dot{c}}\int_{\dot{c}}^{\breve{d}} P(u,\hat{U})[g'(\hat{U})-c]d\hat{U}$$
$$= \frac{1}{16}\left[g\left(\frac{7\dot{c}+u}{8}\right)+g\left(\frac{3\dot{c}+u}{4}\right)+2g\left(\frac{\dot{c}+u}{2}\right)+4g(u)+4g(\dot{c}+\breve{d}-u)+2g\left(\frac{\dot{c}+2\breve{d}-2u}{2}\right)+g\left(\frac{\dot{c}+4\breve{d}-u}{4}\right)+g\left(\frac{\dot{c}+8\breve{d}-u}{8}\right)\right]-\frac{1}{\breve{d}-\dot{c}}\int_{\dot{c}}^{\breve{d}} g(\hat{U})d\hat{U},$$

where

$$\int_{\dot{c}}^{\breve{d}} P(u,\hat{U})d\hat{U} = 0.$$

On the other hand,

$$\left|\frac{1}{\check{d}-\dot{c}}\int_{\dot{c}}^{\check{d}} P(\mathrm{u},\widehat{U})[\mathrm{g}'(\widehat{U})-c]d\widehat{U}\right| \le \frac{1}{\check{d}-\dot{c}}\max_{\widehat{U}\in[\dot{c},\check{d}]}|\mathrm{g}'(\widehat{U})-c|\int_{\dot{c}}^{\check{d}}|P(\mathrm{u},\widehat{U})|d\widehat{U}. \tag{10}$$

Since

$$\max_{\widehat{U}\in[\dot{c},\check{d}]}|\mathrm{g}'(\widehat{U})-c| \le \frac{\Gamma+\gamma}{2} \tag{11}$$

and

$$\frac{1}{\check{d}-\dot{c}}\int_{\dot{c}}^{\check{d}}|P(\mathrm{u},\widehat{U})|d\widehat{U} = \frac{21}{64(\check{d}-\dot{c})}\left[(2\dot{c}+\check{d}-3\mathrm{u})(\dot{c}-\mathrm{u})+\frac{1}{64}(\dot{c}-\mathrm{u})^2\right]. \tag{12}$$

From $(10)-(12)$, we get (9).

Case. 3:

Theorem 3 Let ǵ: $[\dot{c},\check{d}]\to\mathbb{R}$ be differentiable mapping on $(\dot{c},\check{d})$. If ǵ′ $\in L^1[\dot{c},\check{d}]$ and $\gamma \le \acute{g}'(\widehat{U}) \le \Gamma$

$$\begin{aligned}&\left|\frac{1}{16}\left[\mathrm{g}\left(\frac{7\dot{c}+\mathrm{u}}{8}\right)+\mathrm{g}\left(\frac{3\dot{c}+\mathrm{u}}{4}\right)+2\mathrm{g}\left(\frac{\dot{c}+\mathrm{u}}{2}\right)+4\mathrm{g}(\mathrm{u})+4\mathrm{g}(\dot{c}+\check{d}-\mathrm{u})+2\mathrm{g}\left(\frac{\dot{c}+2\check{d}-2\mathrm{u}}{2}\right)\right.\right.\\&\left.\left.+\mathrm{g}\left(\frac{\dot{c}+4\check{d}-\mathrm{u}}{4}\right)+\mathrm{g}\left(\frac{\dot{c}+8\check{d}-\mathrm{u}}{8}\right)\right]-\frac{1}{\check{d}-\dot{c}}\int_{\dot{c}}^{\check{d}}\mathrm{g}(\widehat{U})d\widehat{U}\right| \le \Omega(S-\gamma)\end{aligned} \tag{13}$$

And

$$\begin{aligned}&\left|\frac{1}{16}\left[\mathrm{g}\left(\frac{7\dot{c}+\mathrm{u}}{8}\right)+\mathrm{g}\left(\frac{3\dot{c}+\mathrm{u}}{4}\right)+2\mathrm{g}\left(\frac{\dot{c}+\mathrm{u}}{2}\right)+4\mathrm{g}(\mathrm{u})+4\mathrm{g}(\dot{c}+\check{d}-\mathrm{u})+2\mathrm{g}\left(\frac{\dot{c}+2\check{d}-2\mathrm{u}}{2}\right)\right.\right.\\&\left.\left.+\mathrm{g}\left(\frac{\dot{c}+4\check{d}-\mathrm{u}}{4}\right)+\mathrm{g}\left(\frac{\dot{c}+8\check{d}-\mathrm{u}}{8}\right)\right]-\frac{1}{\check{d}-\dot{c}}\int_{\dot{c}}^{\check{d}}\mathrm{g}(\widehat{U})d\widehat{U}\right| \le \Omega(S-\Gamma)\end{aligned} \tag{14}$$

for all ų∈ $\left[\dot{c};\frac{\dot{c}+\check{d}}{2}\right]$, where

$$\Omega = \max_{\widehat{U}\in[\dot{c},\check{d}]}|P(\mathrm{u},\widehat{U})|,$$
$$S = \frac{\mathrm{g}(\check{d})-\mathrm{g}(\dot{c})}{\check{d}-\dot{c}},$$
$$\gamma = \inf_{\widehat{U}\in[\dot{c},\check{d}]}\mathrm{g}'(\widehat{U}),$$
$$\Gamma = \sup_{\widehat{U}\in[\dot{c},\check{d}]}\mathrm{g}'(\widehat{U}).$$

Proof. As we know

$$\begin{aligned}&\frac{1}{\check{d}-\dot{c}}\int_{\dot{c}}^{\check{d}}P(\mathrm{u},\widehat{U})\mathrm{g}'(\widehat{U})d\widehat{U}-\frac{1}{(\check{d}-\dot{c})^2}\int_{\dot{c}}^{\check{d}}P(\mathrm{u},\widehat{U})d\widehat{U}.\int_{\dot{c}}^{\check{d}}\mathrm{g}'(\widehat{U})d\widehat{U}=\frac{1}{16}\left[\mathrm{g}\left(\frac{7\dot{c}+\mathrm{u}}{8}\right)+\mathrm{g}\left(\frac{3\dot{c}+\mathrm{u}}{4}\right)+2\mathrm{g}\left(\frac{\dot{c}+\mathrm{u}}{2}\right)\right.\\&\left.+4\mathrm{g}(\mathrm{u})+4\mathrm{g}(\dot{c}+\check{d}-\mathrm{u})+2\mathrm{g}\left(\frac{\dot{c}+2\check{d}-2\mathrm{u}}{2}\right)+\mathrm{g}\left(\frac{\dot{c}+4\check{d}-\mathrm{u}}{4}\right)+\mathrm{g}\left(\frac{\dot{c}+8\check{d}-\mathrm{u}}{8}\right)\right]\end{aligned} \tag{15}$$

We denote

$$R_n(\mathrm{u}) = \frac{1}{\check{d}-\dot{c}}\int_{\dot{c}}^{\check{d}}P(\mathrm{u},\widehat{U})\mathrm{g}'(\widehat{U})d\widehat{U}-\frac{1}{(\check{d}-\dot{c})^2}\int_{\dot{c}}^{\check{d}}P(\mathrm{u},\widehat{U})d\widehat{U}.\int_{\dot{c}}^{\check{d}}\mathrm{g}'(\widehat{U})d\widehat{U}. \tag{16}$$

If $c \in R$ is an arbitrary constant

$$R_n(\mathrm{u}) = \frac{1}{\check{d}-\dot{c}}\int_{\dot{c}}^{\check{d}}(\mathrm{g}'(\widehat{U})-c)\left[P(\mathrm{u},\widehat{U})-\frac{1}{\check{d}-\dot{c}}\int_{\dot{c}}^{\check{d}}P(\mathrm{u},s)ds\right]d\widehat{U}. \tag{17}$$

Since

$$\int_{\dot{c}}^{\check{d}}\left[P(\mathrm{u},\widehat{U})-\frac{1}{\check{d}-\dot{c}}\int_{\dot{c}}^{\check{d}}P(\mathrm{u},s)ds\right]d\widehat{U}=0.$$

Further more, we have

$$|R_n(\mathrm{u})| \leq \frac{1}{\breve{d}-\dot{c}} \max_{\widehat{U}\in[\dot{c},\breve{d}]} \left|P(\mathrm{u},\widehat{U})-0\right| \int_{\dot{c}}^{\breve{d}} \left|\mathrm{g}'(\widehat{U})-c\right| d\widehat{U}$$

and

$$\max_{\widehat{U}\in[\dot{c},\breve{d}]} \left|P(\mathrm{u},\widehat{U})\right| = \Omega. \quad (18)$$

From [1]-[3], we get

$$\int_{\dot{c}}^{\breve{d}} \left|\mathrm{g}'(\widehat{U})-\gamma\right| d\widehat{U} = (S-\gamma)(\breve{d}-\dot{c}), \quad (19)$$

$$\int_{\dot{c}}^{\breve{d}} \left|\mathrm{g}'(\widehat{U})-\Gamma\right| d\widehat{U} = (\Gamma-S)(\breve{d}-\dot{c}). \quad (20)$$

By using $(5), (6), (15), (18)-(20)$, we get (13) and (14).

Case. 4: When $\acute{g}' \in L^2[\dot{c},\breve{d}]$

Theorem 4 Let $\acute{g}: [\dot{c},\breve{d}] \to \mathbb{R}$ be an absolutely continuous mapping in $(\dot{c},\breve{d})$. If $\acute{g}' \in \mathrm{L}^2[\dot{c},\breve{d}]$, then we have

$$\begin{aligned}&\left|\frac{1}{16}\left[\mathrm{g}\left(\frac{7\dot{c}+\mathrm{u}}{8}\right)+\mathrm{g}\left(\frac{3\dot{c}+\mathrm{u}}{4}\right)+2\mathrm{g}\left(\frac{\dot{c}+\mathrm{u}}{2}\right)+4\mathrm{g}(\mathrm{u})+4\mathrm{g}(\dot{c}+\breve{d}-\mathrm{u})+2\mathrm{g}\left(\frac{\dot{c}+2\breve{d}-2\mathrm{u}}{2}\right)\right.\right.\\&\left.\left.+\mathrm{g}\left(\frac{\dot{c}+4\breve{d}-\mathrm{u}}{4}\right)+\mathrm{g}\left(\frac{\dot{c}+8\breve{d}-\mathrm{u}}{8}\right)\right]-\frac{1}{\breve{d}-\dot{c}}\int_{\dot{c}}^{\breve{d}} \mathrm{g}(\widehat{U})d\widehat{U}\right|\\&\leq\sqrt{\frac{\sigma(\mathrm{g}')}{\breve{d}-\dot{c}}}\times\left[\frac{1}{3072}\left(697\dot{c}^2+805\dot{c}\breve{d}+256\breve{d}^2-2199\dot{c}\mathrm{u}-1317\breve{d}\mathrm{u}+1758\mathrm{u}^2\right)\right]^{\frac{1}{2}}\end{aligned} \quad (21)$$

for all ɥ$\in \left[\dot{c},\frac{\dot{c}+\breve{d}}{2}\right]$, where

$$\sigma(\mathrm{g}') = \|\mathrm{g}''\|_2^2 - \frac{\left(\mathrm{g}(\breve{d})-\mathrm{g}(\dot{c})\right)^2}{\breve{d}-\dot{c}} = \|\mathrm{g}''\|_2^2 - S^2(\breve{d}-\dot{c}).$$

Proof. Let $R_n(\mathrm{u})$ is defined as in (16) then from (15), we get

$$\begin{aligned}R_n(\mathrm{u}) = &\left|\frac{1}{16}\left[\mathrm{g}\left(\frac{7\dot{c}+\mathrm{u}}{8}\right)+\mathrm{g}\left(\frac{3\dot{c}+\mathrm{u}}{4}\right)+2\mathrm{g}\left(\frac{\dot{c}+\mathrm{u}}{2}\right)+4\mathrm{g}(\mathrm{u})+4\mathrm{g}(\dot{c}+\breve{d}-\mathrm{u})+2\mathrm{g}\left(\frac{\dot{c}+2\breve{d}-2\mathrm{u}}{2}\right)\right.\right.\\&\left.\left.+\mathrm{g}\left(\frac{\dot{c}+4\breve{d}-\mathrm{u}}{4}\right)+\mathrm{g}\left(\frac{\dot{c}+8\breve{d}-\mathrm{u}}{8}\right)\right]-\frac{1}{\breve{d}-\dot{c}}\int_{\dot{c}}^{\breve{d}} \mathrm{g}(\widehat{U})d\widehat{U}\right|.\end{aligned}$$

If we choose

$$c = \frac{1}{\breve{d}-\dot{c}}\int_{\dot{c}}^{\breve{d}} \mathrm{g}'(s)ds$$

in (17) and using the Cauchy's inequality;

$$\begin{aligned}|R_n(\mathrm{u})| &\leq \frac{1}{\breve{d}-\dot{c}}\int_{\dot{c}}^{\breve{d}} \left|\mathrm{g}'(\widehat{U})-\frac{1}{\breve{d}-\dot{c}}\int_{\dot{c}}^{\breve{d}} \mathrm{g}'(s)ds\right|\left|P(\mathrm{u},\widehat{U})-\frac{1}{\breve{d}-\dot{c}}\int_{\dot{c}}^{\breve{d}} P(\mathrm{u},s)ds\right| d\widehat{U}\\&\leq \frac{1}{\breve{d}-\dot{c}}\left[\int_{\dot{c}}^{\breve{d}}\left(\mathrm{g}'(\widehat{U})-\frac{1}{\breve{d}-\dot{c}}\int_{\dot{c}}^{\breve{d}} \mathrm{g}'(s)ds\right)^2 d\widehat{U}\right]^{\frac{1}{2}}\times\left[\int_{\dot{c}}^{\breve{d}}\left(P(\mathrm{u},\widehat{U})-\frac{1}{\breve{d}-\dot{c}}P(\mathrm{u},s)ds\right)^2 d\widehat{U}\right]^{\frac{1}{2}}\\&\leq \sqrt{\sigma(\mathrm{g}')}(\breve{d}-\dot{c})^{\frac{-1}{2}}\times\left[\frac{1}{3072}\left(697\dot{c}^2+805\dot{c}\breve{d}+256\breve{d}^2-2199\dot{c}\mathrm{u}-1317\breve{d}\mathrm{u}+1758\mathrm{u}^2\right)\right]^{\frac{1}{2}}.\end{aligned}$$

Corollary 4 If we substitute ɥ$= \frac{\dot{c}+\breve{d}}{2}$, in (21), we get

$$\left|\frac{1}{16}\left[\mathrm{g}\left(\frac{15\dot{c}+\breve{d}}{16}\right)+\mathrm{g}\left(\frac{7\dot{c}+\breve{d}}{8}\right)+2\mathrm{g}\left(\frac{3\dot{c}+\breve{d}}{4}\right)+8\mathrm{g}\left(\frac{\dot{c}+\breve{d}}{2}\right)+2\mathrm{g}\left(\frac{\breve{d}}{2}\right)+\mathrm{g}\left(\frac{\dot{c}+7\breve{d}}{8}\right)+\mathrm{g}\left(\frac{\dot{c}+15\breve{d}}{16}\right)\right]-\frac{1}{\breve{d}-\dot{c}}\int_{\dot{c}}^{\breve{d}} \mathrm{g}(\widehat{U})d\widehat{U}\right|$$

$$\leq \sqrt{\frac{\sigma(g')}{ğ-ċ}}\left[\frac{37}{3072}(ċ-ğ)^2\right]^{\frac{1}{2}}. \tag{22}$$

Now we state another case.

2.5 Case. 5: When ǵ'' ∈ $L^2[ċ, ğ]$

Theorem 5 Let ǵ: $[ċ, ğ] \to \mathbb{R}$ be a twice absolutely continuous differentiable mapping in $(ċ, ğ)$ with ǵ'' ∈ $L^2[ċ, ğ]$.

$$\left|\frac{1}{16}\left[g\left(\frac{7ċ+u}{8}\right)+g\left(\frac{3ċ+u}{4}\right)+2g\left(\frac{ċ+u}{2}\right)+4g(u)+4g(ċ+ğ-u)+2g\left(\frac{ċ+2ğ-2u}{2}\right)\right.\right.$$
$$\left.\left.+g\left(\frac{ċ+4ğ-u}{4}\right)+g\left(\frac{ċ+8ğ-u}{8}\right)\right]-\frac{1}{ğ-ċ}\int_{ċ}^{ğ} g(\widehat{U})d\widehat{U}\right|$$
$$\leq \left[\frac{1}{3072\pi}(697ċ^2+805ċğ+256ğ^2-2199ċu-1317ğu+1758u^2)\right]^{\frac{1}{2}}\times(ğ-ċ)^{\frac{3}{2}}\|g''\|_2 \tag{23}$$

for all ų∈ $\left[ċ, \frac{ċ+ğ}{2}\right]$.

Proof. Let $R_n(u)$ be defined by (16) from (15)

$$R_n(u)=\left|\frac{1}{16}\left[g\left(\frac{7ċ+u}{8}\right)+g\left(\frac{3ċ+u}{4}\right)+2g\left(\frac{ċ+u}{2}\right)\right.\right.$$
$$\left.\left.+4g(u)+4g(ċ+ğ-u)+2g\left(\frac{ċ+2ğ-2u}{2}\right)+g\left(\frac{ċ+4ğ-u}{4}\right)+g\left(\frac{ċ+8ğ-u}{8}\right)\right]-\frac{1}{ğ-ċ}\int_{ċ}^{ğ} g(\widehat{U})d\widehat{U}\right|.$$

If we choose $C = ǵ'\left(\frac{ċ+ğ}{2}\right)$ in (17) and use the Cauchy's Inequality, we get

$$|R_n(u)| \leq \frac{1}{ğ-ċ}\int_{ċ}^{ğ}\left|g'(\widehat{U})-g'\left(\frac{ċ+ğ}{2}\right)\right|\left|P(u,\widehat{U})-\frac{1}{ğ-ċ}\int_{ċ}^{ğ}P(u,s)ds\right|d\widehat{U}$$
$$\leq \frac{1}{ğ-ċ}\left[\int_{ċ}^{ğ}\left(g'(\widehat{U})-g'\left(\frac{ċ+ğ}{2}\right)\right)^2 d\widehat{U}\right]^{\frac{1}{2}}\times\left[\int_{ċ}^{ğ}\left(P(u,\widehat{U})-\frac{1}{ğ-ċ}P(u,s)ds\right)^2 d\widehat{U}\right]^{\frac{1}{2}}.$$

We may apply Diaz-Metcalf inequality[1] or [13], to obtain

$$\int_{ċ}^{ğ}\left(g'(\widehat{U})-g'\left(\frac{ċ+ğ}{2}\right)\right)^2 d\widehat{U} \leq \frac{(ğ-ċ)^2}{\pi^2}\|g''\|_2^2.$$

We also have

$$\int_{ċ}^{ğ}\left(P(u,\widehat{U})-\frac{1}{ğ-ċ}P(u,s)ds\right)^2 d\widehat{U}=\int_{ċ}^{ğ}\left(P(u,\widehat{U})\right)^2 d\widehat{U}$$
$$=\frac{1}{3072}(ğ-ċ)(697ċ^2+805ċğ+256ğ^2-2199ċu-1317ğu+1758u^2). \tag{24}$$

Corollary 5 If we substitute ų= $\frac{ċ+3ğ}{4}$, in (23) we get

$$\left|\frac{1}{16}\left[g\left(\frac{29ċ+3ğ}{32}\right)+g\left(\frac{13ċ+3ğ}{16}\right)+2g\left(\frac{5ċ+3ğ}{8}\right)+4g\left(\frac{ċ+3ğ}{4}\right)+4g\left(\frac{3ċ+ğ}{4}\right)+2g\left(\frac{ċ+ğ}{4}\right)\right.\right.$$
$$\left.\left.+g\left(\frac{3ċ+13ğ}{16}\right)+g\left(\frac{3ċ+29ğ}{32}\right)\right]-\frac{1}{ğ-ċ}\int_{ċ}^{ğ} g(\widehat{U})d\widehat{U}\right| \leq \left[\frac{1}{3072\pi}\left(\frac{2057}{8}(ċ-ğ)^2\right)\right]^{\frac{1}{2}}(ğ-ċ)^{\frac{3}{2}}\|g''\|_2.$$

An application to Composite Quadrature Rules

Let $I_n: \dot{c} = \mathrm{u}_0 < \mathrm{u}_1 < \ldots < \mathrm{u}_{n-1} < \mathrm{u}_n = \breve{d}$ be a division of the interval $[\dot{c}, \breve{d}]$, $\xi_i \in [\mathrm{u}_i, \mathrm{u}_{i+1}](i = 0,1,\ldots n-1)$; a sequence of intermediate points $h_i = \mathrm{u}_{i+1} - \mathrm{u}_i (i = 0,1,\ldots n-1)$. We have the following quadrature formula:

When $\acute{g}' \in \mathrm{L}^1[\dot{c}, \breve{d}]$

Theorem 6 Let $\acute{g}: \mathrm{I} \subset \mathbb{R} \to \mathbb{R}$ be a differentiable mapping on I^0, the interior of the interval I, and let $\dot{c}, \breve{d} \in \mathrm{I}$ with $\dot{c} < \breve{d}$. If $\acute{g}' \in \mathrm{L}^1[\dot{c}, \breve{d}]$ and $\gamma \le \acute{g}'(\widehat{\mathrm{U}}) \le \Gamma \forall \mathrm{u} \in \left[\dot{c}, \frac{\dot{c}+\breve{d}}{2}\right]$,

$$\int_{\dot{c}}^{\breve{d}} \mathrm{g}(\widehat{\mathrm{U}}) d\widehat{\mathrm{U}} = \dot{c}(\mathrm{g}, I_n) + R(\mathrm{g}, I_n), \tag{25}$$

where

$$\dot{c}(\mathrm{g}, I_n) = \frac{1}{16}\sum_{i=0}^{n-1} h_i \left[\mathrm{g}\left(\frac{29\mathrm{u}_i + 3\mathrm{u}_{i+1}}{32}\right) + \mathrm{g}\left(\frac{13\mathrm{u}_i + 3\mathrm{u}_{i+1}}{16}\right) + 2\mathrm{g}\left(\frac{5\mathrm{u}_i + 3\mathrm{u}_{i+1}}{8}\right) + 4\mathrm{g}\left(\frac{\mathrm{u}_i + 3\mathrm{u}_{i+1}}{4}\right) + 4\mathrm{g}\left(\frac{3\mathrm{u}_i + \mathrm{u}_{i+1}}{4}\right) + 2\mathrm{g}\left(\frac{\mathrm{u}_i + \mathrm{u}_{i+1}}{4}\right) + \mathrm{g}\left(\frac{3\mathrm{u}_i + 13\mathrm{u}_{i+1}}{16}\right) + \mathrm{g}\left(\frac{3\mathrm{u}_i + 29\mathrm{u}_{i+1}}{32}\right)\right] \tag{26}$$

and

$$|R(\mathrm{g}, I_n)| \le \frac{1}{64}(\Gamma - \gamma)\sum_{i=0}^{n-1} h_i \tag{27}$$

for all $\xi_i \in [\mathrm{u}_i, \mathrm{u}_{i+1}]$, where $h_i = \mathrm{u}_{i+1} - \mathrm{u}_i, (i = 0,1,\ldots n-1)$.

Proof. Apply (7) on the interval $[\mathrm{u}_i, \mathrm{u}_{i+1}], \xi_i \in [\mathrm{u}_i, \mathrm{u}_{i+1}]$ where $h_i = \mathrm{u}_{i+1} - \mathrm{u}_i, (i = 0,1,\ldots n-1)$,

$$R(\mathrm{g}, I_n) = \int_{\mathrm{u}_i}^{\mathrm{u}_{i+1}} \mathrm{g}(\widehat{U}) d\widehat{U} - \frac{1}{16}\sum_{i=0}^{n-1} h_i \left[\mathrm{g}\left(\frac{29\mathrm{u}_i + 3\mathrm{u}_{i+1}}{32}\right) + \mathrm{g}\left(\frac{13\mathrm{u}_i + 3\mathrm{u}_{i+1}}{16}\right) + 2\mathrm{g}\left(\frac{5\mathrm{u}_i + 3\mathrm{u}_{i+1}}{8}\right) + 4\mathrm{g}\left(\frac{\mathrm{u}_i + 3\mathrm{u}_{i+1}}{4}\right) + 4\mathrm{g}\left(\frac{3\mathrm{u}_i + \mathrm{u}_{i+1}}{4}\right) + 2\mathrm{g}\left(\frac{\mathrm{u}_i + \mathrm{u}_{i+1}}{4}\right) + \mathrm{g}\left(\frac{3\mathrm{u}_i + 13\mathrm{u}_{i+1}}{16}\right) + \mathrm{g}\left(\frac{3\mathrm{u}_i + 29\mathrm{u}_{i+1}}{32}\right)\right].$$

Adding over i from 0 to $n-1$,

$$R(\mathrm{g}, I_n) = \sum_{i=0}^{n-1} \int_{\mathrm{u}_i}^{\mathrm{u}_{i+1}} \mathrm{g}(\widehat{U}) d\widehat{U} - \frac{1}{16}\sum_{i=0}^{n-1} h_i \left[\mathrm{g}\left(\frac{29\mathrm{u}_i + 3\mathrm{u}_{i+1}}{32}\right) + \mathrm{g}\left(\frac{13\mathrm{u}_i + 3\mathrm{u}_{i+1}}{16}\right) + 2\mathrm{g}\left(\frac{5\mathrm{u}_i + 3\mathrm{u}_{i+1}}{8}\right) + 4\mathrm{g}\left(\frac{\mathrm{u}_i + 3\mathrm{u}_{i+1}}{4}\right) + 4\mathrm{g}\left(\frac{3\mathrm{u}_i + \mathrm{u}_{i+1}}{4}\right) + 2\mathrm{g}\left(\frac{\mathrm{u}_i + \mathrm{u}_{i+1}}{4}\right) + \mathrm{g}\left(\frac{3\mathrm{u}_i + 13\mathrm{u}_{i+1}}{16}\right) + \mathrm{g}\left(\frac{3\mathrm{u}_i + 29\mathrm{u}_{i+1}}{32}\right)\right]$$

$$R(\mathrm{g}, I_n) = \int_{\dot{c}}^{\breve{d}} \mathrm{g}(\widehat{U}) d\widehat{U} - \frac{1}{16}\sum_{i=0}^{n-1} h_i \left[\mathrm{g}\left(\frac{29\mathrm{u}_i + 3\mathrm{u}_{i+1}}{32}\right) + \mathrm{g}\left(\frac{13\mathrm{u}_i + 3\mathrm{u}_{i+1}}{16}\right) + 2\mathrm{g}\left(\frac{5\mathrm{u}_i + 3\mathrm{u}_{i+1}}{8}\right) + 4\mathrm{g}\left(\frac{\mathrm{u}_i + 3\mathrm{u}_{i+1}}{4}\right) + 4\mathrm{g}\left(\frac{3\mathrm{u}_i + \mathrm{u}_{i+1}}{4}\right) + 2\mathrm{g}\left(\frac{\mathrm{u}_i + \mathrm{u}_{i+1}}{4}\right) + \mathrm{g}\left(\frac{3\mathrm{u}_i + 13\mathrm{u}_{i+1}}{16}\right) + \mathrm{g}\left(\frac{3\mathrm{u}_i + 29\mathrm{u}_{i+1}}{32}\right)\right].$$

From (7),

$$|R(\mathrm{g}, I_n)| = \left|\int_{\dot{c}}^{\breve{d}} \mathrm{g}(\widehat{U}) d\widehat{U} - \frac{1}{16}\sum_{i=0}^{n-1} h_i \left[\mathrm{g}\left(\frac{29\mathrm{u}_i + 3\mathrm{u}_{i+1}}{32}\right) + \mathrm{g}\left(\frac{13\mathrm{u}_i + 3\mathrm{u}_{i+1}}{16}\right) + 2\mathrm{g}\left(\frac{5\mathrm{u}_i + 3\mathrm{u}_{i+1}}{8}\right) + 4\mathrm{g}\left(\frac{\mathrm{u}_i + 3\mathrm{u}_{i+1}}{4}\right) + 4\mathrm{g}\left(\frac{3\mathrm{u}_i + \mathrm{u}_{i+1}}{4}\right) + 2\mathrm{g}\left(\frac{\mathrm{u}_i + \mathrm{u}_{i+1}}{4}\right) + \mathrm{g}\left(\frac{3\mathrm{u}_i + 13\mathrm{u}_{i+1}}{16}\right) + \mathrm{g}\left(\frac{3\mathrm{u}_i + 29\mathrm{u}_{i+1}}{32}\right)\right]\right| \le \frac{1}{64} h_i (\Gamma - \gamma).$$

Hence proved.

When $\acute{g}' \in L^2[\dot{c}, \breve{d}]$

Theorem 7 Let $\mathrm{h_i} = \mathrm{u}_{i+1} - \mathrm{u}_i = \mathrm{h} = \frac{\breve{d} - \dot{c}}{\mathrm{n}} (\mathrm{i} = 0,1,\ldots,\mathrm{n}-1)$ and let $\acute{g}: [\dot{c}, \breve{d}] \to \mathbb{R}$ be an absolutely continuous mapping in $(\dot{c}, \breve{d})$ with $\acute{g}' \in \mathrm{L}^2[\dot{c}, \breve{d}]$.

$$\int_{\dot{c}}^{\breve{d}} \mathrm{g}(\mathrm{u})d\mathrm{u} = \dot{c}(\mathrm{g}, I_n) + R(\mathrm{g}, I_n),$$

and

$$|R(\mathrm{g}, I_n)| \leq \sqrt{\frac{37(\breve{d}-\dot{c})}{3072}\sigma(\mathrm{g}')}.$$

Proof. Applying (22) to the interval $[\mathrm{u}_i, \mathrm{u}_{i+1}]$, then

$$\left|\frac{h}{16}\left[\mathrm{g}\left(\frac{15\mathrm{u}_i+\mathrm{u}_{i+1}}{16}\right)+\mathrm{g}\left(\frac{7\mathrm{u}_i+\mathrm{u}_{i+1}}{8}\right)+2\mathrm{g}\left(\frac{3\mathrm{u}_i+\mathrm{u}_{i+1}}{4}\right)+8\mathrm{g}\left(\frac{\mathrm{u}_i+\mathrm{u}_{i+1}}{2}\right)+2\mathrm{g}\left(\frac{\mathrm{u}_{i+1}}{2}\right)+\mathrm{g}\left(\frac{\mathrm{u}_i+7\mathrm{u}_{i+1}}{8}\right)\right.\right.$$
$$\left.\left.+\mathrm{g}\left(\frac{\mathrm{u}_i+15\mathrm{u}_{i+1}}{16}\right)\right]-\int_{\mathrm{u}_i}^{\mathrm{u}_{i+1}}\mathrm{g}(\widehat{U})d\widehat{U}\right| \leq \sqrt{\frac{37h}{3072}}(\mathrm{u}_i-\mathrm{u}_{i+1})\left[\int_{\mathrm{u}_i}^{\mathrm{u}_{i+1}}\left(\mathrm{g}(\widehat{U})\right)^2 d\widehat{U}-\frac{(\mathrm{g}(\mathrm{u}_{i+1})-\mathrm{g}(\mathrm{u}_i))^2}{h}\right]^{\frac{1}{2}}$$

for $i = 0,1,\ldots,n-1$.
Now adding over i from 0 to $n-1$, using the triangle Inequality and Cauchy's inequality twice, we get

$$\left|\frac{h}{16}\sum_{i=0}^{n-1}\left[\mathrm{g}\left(\frac{15\mathrm{u}_i+\mathrm{u}_{i+1}}{16}\right)+\mathrm{g}\left(\frac{7\mathrm{u}_i+\mathrm{u}_{i+1}}{8}\right)+2\mathrm{g}\left(\frac{3\mathrm{u}_i+\mathrm{u}_{i+1}}{4}\right)+8\mathrm{g}\left(\frac{\mathrm{u}_i+\mathrm{u}_{i+1}}{2}\right)+2\mathrm{g}\left(\frac{\mathrm{u}_{i+1}}{2}\right)+\mathrm{g}\left(\frac{\mathrm{u}_i+7\mathrm{u}_{i+1}}{8}\right)\right.\right.$$
$$\left.\left.+\mathrm{g}\left(\frac{\mathrm{u}_i+15\mathrm{u}_{i+1}}{16}\right)\right]-\int_{\mathrm{u}_i}^{\mathrm{u}_{i+1}}\mathrm{g}(\widehat{U})d\widehat{U}\right| \leq \sqrt{\frac{37h}{3072}}\sum_{i=0}^{n-1}\left((\mathrm{u}_i-\mathrm{u}_{i+1})\left[\int_{\mathrm{u}_i}^{\mathrm{u}_{i+1}}\left(\mathrm{g}(\widehat{U})\right)^2 d\widehat{U}-\frac{\left(\mathrm{g}(\mathrm{u}_{i+1})-\mathrm{g}(\mathrm{u}_i)\right)^2}{h}\right]^{\frac{1}{2}}\right)$$
$$\leq \sqrt{\frac{37h}{3072}}\sqrt{n}\left[\|\mathrm{g}'\|_2^2-\frac{n}{\breve{d}-\dot{c}}\sum_{i=0}^{n-1}\left(\mathrm{g}(\mathrm{u}_{i+1})-\mathrm{g}(\mathrm{u}_i)\right)^2\right]^{\frac{1}{2}}$$
$$\leq \sqrt{\frac{37h}{3072}}\sqrt{n}\left[(\mathrm{u}_i-\mathrm{u}_{i+1})\left(\|\mathrm{g}'\|_2^2-\frac{\left(\mathrm{g}(\breve{d})-\mathrm{g}(\dot{c})\right)^2}{\breve{d}-\dot{c}}\right)\right]^{\frac{1}{2}}$$
$$= \sqrt{\frac{37(\breve{d}-\dot{c})}{3072}(\mathrm{u}_i-\mathrm{u}_{i+1})\sigma(\mathrm{g}')}.$$

When $\acute{\mathrm{g}}'' \in \boldsymbol{L^2[\dot{c}, \breve{d}]}$

Theorem 8 Let $\mathrm{h_i} = \mathrm{u_{i+1}} - \mathrm{u_i} = \mathrm{h} = \frac{\breve{\mathrm{d}}-\dot{\mathrm{c}}}{\mathrm{n}}(\mathrm{i} = 0,1,\ldots,\mathrm{n}-1)$ and let $\acute{\mathrm{g}}: [\dot{\mathrm{c}}, \breve{\mathrm{d}}] \to \mathbb{R}$ be a twice continuously differentiable mapping in $(\dot{\mathrm{c}}, \breve{\mathrm{d}})$ with $\acute{\mathrm{g}}'' \in \mathrm{L}^2[\dot{\mathrm{c}}, \breve{\mathrm{d}}]$. Then,

$$\int_{\dot{c}}^{\breve{d}} \mathrm{g}(\mathrm{u})d\mathrm{u} = \dot{c}(\mathrm{g}, I_n) + R(\mathrm{g}, I_n),$$

where

$$|R(\mathrm{g}, I_n)|$$
$$\leq \left[\frac{2057}{24576\pi}\right]^{\frac{1}{2}}\frac{(\breve{d}-\dot{c})^{\frac{5}{2}}}{n^{\frac{5}{2}}}(\dot{c}-\breve{d})\|\mathrm{g}''\|_2.$$

Proof. Applying (25) to the interval $[\mathrm{u}_i, \mathrm{u}_{i+1}]$, we get

$$\left|\frac{h}{16}\left[\mathrm{g}\left(\frac{29\mathrm{u}_i+3\mathrm{u}_{i+1}}{32}\right)+\mathrm{g}\left(\frac{13\mathrm{u}_i+3\mathrm{u}_{i+1}}{16}\right)+2\mathrm{g}\left(\frac{5\mathrm{u}_i+3\mathrm{u}_{i+1}}{8}\right)+4\mathrm{g}\left(\frac{\mathrm{u}_i+3\mathrm{u}_{i+1}}{4}\right)+4\mathrm{g}\left(\frac{3\mathrm{u}_i+\mathrm{u}_{i+1}}{4}\right)+2\mathrm{g}\left(\frac{\mathrm{u}_i+\mathrm{u}_{i+1}}{4}\right)\right.\right.$$
$$\left.\left.+\mathrm{g}\left(\frac{3\mathrm{u}_i+13\mathrm{u}_{i+1}}{16}\right)+\mathrm{g}\left(\frac{3\mathrm{u}_i+29\mathrm{u}_{i+1}}{32}\right)\right]-\int_{\mathrm{u}_i}^{\mathrm{u}_{i+1}}\mathrm{g}(\widehat{U})d\widehat{U}\right| \leq \left[\frac{2057}{24576\pi}\right]^{\frac{1}{2}}h^{\frac{5}{2}}(\mathrm{u}_i-\mathrm{u}_{i+1})\left[\int_{\mathrm{u}_i}^{\mathrm{u}_{i+1}}\mathrm{g}''(\widehat{U})d\widehat{U}\right]^{\frac{1}{2}}.$$

By adding over i from 0 to $n-1$, applying the triangle inequality and Cauchy's inequality, we have

$$\left|\frac{h}{16}\sum_{i=0}^{n-1}\left[g\left(\frac{29u_i+3u_{i+1}}{32}\right)+g\left(\frac{13u_i+3u_{i+1}}{16}\right)+2g\left(\frac{5u_i+3u_{i+1}}{8}\right)\right.\right.$$
$$\left.\left.+4g\left(\frac{u_i+3u_{i+1}}{4}\right)+4g\left(\frac{3u_i+u_{i+1}}{4}\right)+2g\left(\frac{u_i+u_{i+1}}{4}\right)+g\left(\frac{3u_i+13u_{i+1}}{16}\right)+g\left(\frac{3u_i+29u_{i+1}}{32}\right)\right]-\int_{u_i}^{u_{i+1}} g(\widehat{U})d\widehat{U}\right|$$
$$\leq\left[\frac{2057}{24576\pi}\right]^{\frac{1}{2}}h^{\frac{5}{2}}\sum_{i=0}^{n-1}\left((u_i-u_{i+1})\left[\int_{u_i}^{u_{i+1}}g''(\widehat{U})d\widehat{U}\right]^{\frac{1}{2}}\right)$$
$$\leq\left[\frac{2057n}{24576\pi}\right]^{\frac{1}{2}}h^{\frac{5}{2}}\sum_{i=0}^{n-1}(u_i-u_{i+1})\left[\sum_{i=0}^{n-1}\int_{u_i}^{u_{i+1}}g''(\widehat{U})d\widehat{U}\right]^{\frac{1}{2}}\left[\frac{2057}{24576\pi}\right]^{\frac{1}{2}}\frac{(\check{d}-\dot{c})^{\frac{5}{2}}}{n^{\frac{5}{2}}}(\dot{c}-\check{d})\|g''\|_2.$$

Conclusion

In this paper, we constructed a generalization of Ostrowski's type inequalities for different norms by using some famous inequalities. Some perturbed results are also discussed. In addition, we gave a new idea of peano kernel i.e. 9-step linear kernel. In the last section, we applied our obtained results to numerical integration.

Conflict of interests

There are no conflicts of interest in this work.

References

[1] D. S.Mitrinovic', J. E. Pečaric', A. M. Fink, Inequalities involving functions and their integrals and derivatives, Kluwer Acadamic Publishers, Dordrecht, (1991).

[2] D. S. Mitrinovic', J. Pečaric', A. M. Fink, Classical and New Inequalities in Analysis, Kluwer Academic Publishers, Dordrecht (1993).

[3] D. S. Mitrinovic' , J. E. Pečaric', A. M. Fink, Inequalities for Functions and their Integrals and Derivatives, Kluwer Academic Publishers, Dordrecht (1994).

[4] N. S. Barnett, P. Cerone, S. S. Dragomir, J. Roumeliotis, A survey on Ostrowski type inequalities for twice differentiable mappings and applications, *Inequality Theory and Applications*, 1 (2001) 33-86.

[5] A. Qayyum, S. Hussain, A generalized Ostrowski-Gruss type Inequality for bounded differentiable mappings and its applications, Journal of Inequalities and Applications, 1 (2013).

[6] Qayyum, M. Shoaib, A. E. Matouk, M. A. Latif , On New Generalized Ostrowski Type Integral Inequalities, *Abstract and Applied Analysis*, 1 (2014) 1-8.

[7] A. Qayyum, M. Shoaib, I. Faye , M. A. Latif , A generalized inequality of Ostrowski type for mappings whose second derivatives belong to L_1 (a,b) and applications, *International Journal of Pure and Applied Mathematics*, 98 (2) (2015)

[8] A. Qayyum, M. Shoaib, I. Faye , Some New Generalized Results on Ostrowski Type Integral Inequalities with Application, *Journal Of Computational Analysis and Applications*, 19(4) (2015).

[9] A. Qayyum, M. Shoaib, I. Faye, A companion of Ostrowski Type Integral Inequality using a 5-step kernel With Some Applications, *Filomat,* 30(13) (2016) 3601–3614

[10] A. Qayyum, M. Shoaib, I. Faye , Companion of Ostrowski-Type Inequality based on 5-step quadratic kernel and Applications, *Journal of Nonlinear Science & Applications*, 9 (2016) 537-552.

[11] A. Qayyum, M. Shoaib, I. Faye, Refinements of Some New Efficient Quadrature Rules, AIP conference proceedings 1787, 080003(2016).

[12] S. Erden, Companions Of Perturbed Type Inequalities For Higher-Order Differentiable Functions, *Cumhuriyet Sci. J.*, 40(4) (2019) 819-829.

[13] N. Ujevi´c, New bounds for the first Inequality of Ostrowski-Grüss type and applications, *Computer and Mathematics with Application*, 46 (2003) 421-427.

Cumhuriyet Sci. J., 44(3) (2023) 531-537
DOI: https://doi.org/10.17776/csj.1262453

Cumhuriyet Science Journal

| csj.cumhuriyet.edu.tr | Founded: 2002 ISSN: 2587-2680 e-ISSN: 2587-246X Publisher: Sivas Cumhuriyet University

Relations Among Minimal Elements of a Family of Sets with Respect to Various Set Order Relations

İlknur Atasever Güvenç[1,a,*]

[1] *Department of Mathematics, Faculty of Science, Eskişehir Technical University, Eskişehir, Türkiye*
**Corresponding author*

Research Article

History
Received: 09/03/2023
Accepted: 26/05/2023

ABSTRACT

In this article, some set order relations given for set-optimization criterion which is one of the solution concept of set-valued optimization problems are considered. Minimal elements of a family of sets with respect to these set order relations are compared in detail. For this comparison relations between set order relations mentioned in this article are used. Also, in cases where a family of minimal sets is not a subset of the other one, examples are given.

Keywords: Set-valued optimization, Set order relations, Minimal solution.

[a] *iatasever@eskisehir.edu.tr* *https://orcid.org/0000-0003-0952-1024*

Introduction

A set-valued optimization problem is a problem which has a set-valued objective map. The set optimization approach, which is based on the idea of comparing values of objective map, is one of the solution concepts to solve set-valued optimization problems. For set comparison Nishnianidze [1], Young [2], Kuroiwa [3], Jahn and Ha [4] and Karaman et. al. [5] defined set order relations. One can see [6-20] for further works based on these order relations, including existence theorems for minimal elements, scalarizations, derivatives and optimality conditions etc.

In this article, the set of minimal elements of a family of sets with respect to set order relations $\preccurlyeq_c, \preccurlyeq_{mc}, \preccurlyeq_{mn}, \preccurlyeq_m, \preccurlyeq_s, \preccurlyeq_l, \preccurlyeq_u, \preccurlyeq_{m_1}, \preccurlyeq_{m_2}$ are compared each other in detail. The cases when a set of minimal elements includes the other one is proved and counter examples are given for other cases. Some of the counter examples in this article also can be given by using relations given in Example 3.4 in [4]. Also, in [Example 2.2, 11], it is shown that an m_2 −minimal element may not be an l −minimal element and vice versa. But in this article, it is also aimed to present different examples to contribute to the literature. Finally, all the relations presented in this article are summarized in figures.

Known Set Order Relations

In this section, we recall the known set order relations defined by Nischnianidze [1], Young [2], Kuroiwa [3], Jahn and Ha [4], Karaman et.al. [5].

For a normed space $(Y,\|\cdot\|)$ the algebraic sum and Minkowski (Pontryagin) difference of A and B is defined by

$$A+B:=\{a+b \mid a\in A, b\in B\},$$
$$A\dot{-}B:=\{x\in Y \mid x+B\subset A\},$$

respectively.

A set $K\subset Y$ is called a cone if $\lambda y\in K$ for all $\lambda\geq 0$ and $y\in K$. In this work, $K\subset Y$ is a nonempty, convex, pointed $(K\cap(-K)=\{0_Y\})$, cone with nonempty interior. $\operatorname{conv} A$ and $\operatorname{int} A$ denotes the convex hull of A and the topological interior of A, respectively. Also, $B(x,\varepsilon)$ denotes the closed ball with center x and radius ε, and

$$\mathcal{P}(Y)=\{A\subset Y \mid A\neq\emptyset\}.$$

A partial order relation $\leq_K$ is defined on Y via cone K as the following way:

$$x\leq_K y :\Leftrightarrow y-x\in K.$$

By using this vector order relation, the set of minimal and maximal elements of a nonempty subset A of Y are given as follows:

$$\min A:=\{x\in A \mid A\cap(x-K)=\{x\}\}.$$
$$\max A:=\{x\in A \mid A\cap(x+K)=\{x\}\}.$$

The set less order relation $\preccurlyeq_s$ was defined by Nishnianidze [1] and Young [2], u-type less order relation $\preccurlyeq_u$ and l-type less order relation $\preccurlyeq_l$ were given by Kuroiwa [3] and useful characterizations of these relations was given by Jahn and Ha [4] as the following definition.

Definiton 2.1. Let $A, B \in \mathcal{P}(Y)$. Then,

i. $A \preccurlyeq_l B :\Leftrightarrow B \subset A + K$,
ii. $A \preccurlyeq_u B :\Leftrightarrow A \subset B - K$,
iii. $A \preccurlyeq_s B :\Leftrightarrow B \subset A + K \; and \; A \subset B - K$.

Proposition 2.2. [4] Let $A, B \in \mathcal{P}(Y)$. Then, the following assertion holds:

$$A \preccurlyeq_s B \text{ and } B \preccurlyeq_s A \Leftrightarrow B + K = A + K, B - K = A - K.$$

The certainly less order relation $\preccurlyeq_c$ is defined as follows:

Definition 2.3. [4] Let $A, B \in \mathcal{P}(Y)$. Then,
$A \preccurlyeq_c B :\Leftrightarrow (A = B)$ or $(A \neq B, \forall x \in A \; \forall y \in B: x \leq_K y)$.

The minmax less order relation ($\preccurlyeq_m$), the minmax certainly less order relation ($\preccurlyeq_{mc}$) and the minmax certainly nondominated order ($\preccurlyeq_{mn}$) relations are defined as:

Definition 2.4. [4] Let $A, B \in \mathcal{M}$.

i. $A \preccurlyeq_m B :\Leftrightarrow \min A \preccurlyeq_s \min B$ and $\max A \preccurlyeq_s \max B$,

ii. $A \preccurlyeq_{mc} B :\Leftrightarrow (A = B)$
or $(A \neq B, \min A \preccurlyeq_c \min B$ and $\max A \preccurlyeq_c \max B)$,

iii. $A \preccurlyeq_{mn} B :\Leftrightarrow (A = B)$ or $(A \neq B, \max A \preccurlyeq_s \min B)$,

where $\mathcal{M} =$
$\{A \in \mathcal{P}(Y) \mid \min A$ and $\max A$ are nonempty $\}$.

Definition 2.5. [4] Let $A \in \mathcal{M}$. If the following equivalent conditions are satisfied

i. $\min A + K = A + K$ and $\max A - K = A - K$,
ii. $A \subset \min A + K$ and $A \subset \max A - K$,

then A is said to have the quasi domination property.

We denote the family of sets which have quasi domination property as $\mathcal{M}_0$.

The following relations are satisfied for $\preccurlyeq_s, \preccurlyeq_l, \preccurlyeq_u$.

Proposition 2.6. [4] Let $A, B \in \mathcal{P}(Y)$. Then,

i. $A \preccurlyeq_s B \Longrightarrow A \preccurlyeq_l B$,
ii. $A \preccurlyeq_s B \Longrightarrow A \preccurlyeq_u B$,
iii. $A \preccurlyeq_l B$ doesn't always imply $A \preccurlyeq_u B$ and vice versa.

Proposition 2.7. [4] Let $A, B \in \mathcal{M}_0$ with $A \neq B$. Then,

i. $A \preccurlyeq_c B \Longrightarrow A \preccurlyeq_{mc} B \Longrightarrow A \preccurlyeq_m B \Longrightarrow A \preccurlyeq_s B$,
ii. $A \preccurlyeq_c B \Longrightarrow A \preccurlyeq_{mn} B \Longrightarrow A \preccurlyeq_m B$,
iii. $A \preccurlyeq_{mn} B$ doesn't always imply $A \preccurlyeq_{mc} B$ and vice versa.

Indeed, quasi domination property is not required for relations $A \preccurlyeq_c B \Longrightarrow A \preccurlyeq_{mc} B \Longrightarrow A \preccurlyeq_m B$ and
$A \preccurlyeq_c B \Longrightarrow A \preccurlyeq_{mn} B$ and $A \preccurlyeq_c B \Longrightarrow A \preccurlyeq_s B$.

Following set order relations $\preccurlyeq_{m_1}$ and $\preccurlyeq_{m_2}$ were introduced by Karaman et.al. [5]

Definition 2.8. Let $A, B \in \mathcal{P}(Y)$.

i. $A \preccurlyeq_{m_1} B :\Leftrightarrow (B \dot{-} A) \cap K \neq \emptyset$,
ii. $A \preccurlyeq_{m_2} B :\Leftrightarrow (A \dot{-} B) \cap (-K) \neq \emptyset$.

$\preccurlyeq_{m_1}$ and $\preccurlyeq_{m_2}$ are partial order relations on the family of nonempty and bounded subsets of Y.

Proposition2.9. [4]: Let $A, B \in \mathcal{M}$. Then, following statements hold:

i. $A \preccurlyeq_m B$ and $B \preccurlyeq_m A \Leftrightarrow$
$\min A + K = \min B + K, \max A - K = \max B - K,$
$\min A - K = \min B - K, \max A + K = \max B + K.$
ii. If K is pointed then,
$A \preccurlyeq_{mc} B$ and $B \preccurlyeq_{mc} A \Leftrightarrow \min A =$
$\min B$ and $\max A = \max B$.

iii. If K is pointed and $A, B \in \mathcal{M}_0$ then,

$$A \preccurlyeq_m B \text{ and } B \preccurlyeq_m A \Leftrightarrow \min A = \min B \text{ and } \max A = \max B.$$

Remark 2.10: Quasi domination property was not used in the proof of Proposition 2.9 (iii) [Proposition 3.4, 4]. Since, we assume the pointedness of K, the proposition can be restated as:

Proposition 2.11: Let $A, B \in \mathcal{M}$. Then, following statements are equivalent:

i. $A \preccurlyeq_m B$ and $B \preccurlyeq_m A$,
ii. $A \preccurlyeq_{mc} B$ and $B \preccurlyeq_{mc} A$,
iii. $\min A = \min B$ and $\max A = \max B$.

By using these set order relations, minimal element of a family of sets is defined as the following way.

Definition 2.12. [4,5,12] Let $\mathcal{S} \subset \mathcal{P}(Y)$ and $* \in \{u, l, s, m, c, mn, mc, m_1, m_2\}$. The set $A \in \mathcal{S}$ is called a $*$-minimal element of $\mathcal{S}$ if for any $B \in \mathcal{S}$ such that $B \preccurlyeq_* A$ implies $A \preccurlyeq_* B$. The family of $*$-minimal elements of $\mathcal{S}$ is denoted by $* - \min \mathcal{S}$.

Relations Between Minimal Sets with Respect to Set Order Relations

In this section, we compare the set of minimal elements of a family of sets with respect to set orders mentioned in the previous section.

Proposition 3.1: Let $\mathcal{S} \subset \mathcal{M}$. Then, we have $mn - \min \mathcal{S} \subset c - \min \mathcal{S}$.

Proof: Let $A \in mn - \min \mathcal{S}$ and there exist $B \in \mathcal{S}$ such that $B \preccurlyeq_c A$. Since $\preccurlyeq_c$ is a partial order it suffices to show $A = B$. As $B \preccurlyeq_c A$ from Proposition 2.7 we have $B \preccurlyeq_{mn} A$. Since A is an mn-minimal element of $\mathcal{S}$ we get $A \preccurlyeq_{mn} B$. So, from the definition of $\preccurlyeq_{mn}$ we have $\max A \preccurlyeq_s \min B$ which gives

$$\min B \subset \max A + K, \quad (3.1)$$
$$\max A \subset \min B - K. \quad (3.2)$$

Now, we show that $A = B$. Assume the contrary. Inequality $B \preccurlyeq_c A$ implies that

$$b \leq_K a \text{ for all } a \in A \text{ and } b \in B. \tag{3.3}$$

Let $b_{min} \in \min B$. From (3.1) there exists $a_{max} \in \max A$ and $k_1 \in K$ such that $b_{min} = a_{max} + k_1$. Hence, $a_{max} \leq_K b_{min}$. From (3.3), we have $b_{min} \leq_K a_{max}$. Pointedness of K gives that $b_{min} = a_{max}$. So, $b_{min} \in \max A$. Thus, $\min B \subset \max A$. Similarly, the converse implication can be proved by using (3.2). So, $\min B = \max A$. This equality implies that $A = B$. Indeed, let $b \in B$. For any $y \in \max A\,(= \min B)$, from (3.3), we have $b \leq_K y$. Since $y \in \min B$ and K is pointed we obtain $b = y \in \min B$ which means $B \subset \min B$. As $\min B \subset B$, we get $\min B = B$. The equality $A = \max A$ can be shown similarly. Therefore, we obtain $B = \min B = \max A = A$. This contradicts with assumption. So $A = B$ and hence $A \in c - \min \mathcal{S}$.

Note that a c-minimal element does not have to be an mn-minimal element.

Example 3.2: Let $Y = \mathbb{R}^2$, $K = \mathbb{R}^2_+$, $A = B\big((0,0),1\big), C = B\left(\left(2,\frac{3}{2}\right),1\right)$ and $\mathcal{S} = \{A, C\}$. Then, we have $(0,1) \in A, \left(2,\frac{1}{2}\right) \in C$ and $(0,1) \not\leq_K \left(2,\frac{1}{2}\right)$, $\left(2,\frac{1}{2}\right) \not\leq_K (0,1)$ which gives $A \not\preccurlyeq_c C$ and $C \not\preccurlyeq_c A$. Hence, $c - \min \mathcal{S} = \{A, C\}$. In addition,

$$\min A = \{\,(x,y) \mid x^2 + y^2 = 1, x, y \leq 0\,\},$$
$$\max A = \{\,(x,y) \mid x^2 + y^2 = 1, x, y \geq 0\,\},$$
$$\min C = \left\{(x,y) \;\middle|\; (x-2)^2 + \left(y - \frac{3}{2}\right)^2 = 1, x \leq 2, y \leq \frac{3}{2}\right\},$$
$$\max C = \left\{(x,y) \;\middle|\; (x-2)^2 + \left(y - \frac{3}{2}\right)^2 = 1, x \geq 2, y \geq \frac{3}{2}\right\}.$$

Since $\max A \subset \min C - K$ and $\min C \subset \max A + K$ we have $A \preccurlyeq_{mn} C$. It is obvious that $C \not\preccurlyeq_{mn} A$. So, $C \notin mn - \min \mathcal{S}$.

Proposition 3.3: Let $\mathcal{S} \subset \mathcal{M}$. Then, we have $mc - \min \mathcal{S} \subset c - \min \mathcal{S}$.

Proof: Let $A \in mc - \min \mathcal{S}$ and there exist $B \in \mathcal{S}$ such that $B \preccurlyeq_c A$. Suppose $B \neq A$. Since $B \preccurlyeq_c A$ from Proposition 2.7 we have $B \preccurlyeq_{mc} A$. From mc-minimality of A we have $A \preccurlyeq_{mc} B$. So, by Proposition 2.11, we obtain

$$\min A = \min B\,, \max A = \max B.$$

Since $B \neq A$ and $B \preccurlyeq_c A$, inequality (3.3) holds. Let $a \in A$. Then, from (3.3) $y \leq a$ for any $y \in \max B = \max A$. As $y \in \max A$ and K is pointed we get $a = y \in \max A$. Hence, $A \subset \max A = \max B \subset B$.

Let $b \in B$. Then, from (3.3), $b \leq_K a$ for all $a \in \min A = \min B$. Hence from minimality of a and pointedness of K we obtain $b = a \in \min B$. Thus, $B \subset \min B = \min A \subset A$. So, $A = B$ which contradicts with the assumption.

Proposition 3.4: Let $\mathcal{S} \subset \mathcal{M}$. Then, $m - \min \mathcal{S} \subset mc - \min \mathcal{S}$.

Proof: Let $A \in m - \min \mathcal{S}$ and $B \preccurlyeq_{mc} A$ for some $B \in \mathcal{S}$. Then, from Proposition 2.7 we have $B \preccurlyeq_m A$. As A is m-minimal element we get $A \preccurlyeq_m B$. From Proposition 2.11 we obtain $A \preccurlyeq_{mc} B$. Hence, $A \in mc - \min \mathcal{S}$.

The converse inclusion in Proposition 3.4 is not true in general. The following example shows this fact.

Example 3.5: Let $Y = \mathbb{R}^2$, $K = \mathbb{R}^2_+, A = B\big((0,0),1\big), B = A \cap \{\,(x,y) \mid y \geq -x\,\}$. Then,

$\min A = \{\,(x,y) \mid x^2 + y^2 = 1, x, y \leq 0\,\}$, $\min B = \operatorname{conv}\left\{\left(-\frac{1}{\sqrt{2}},\frac{1}{\sqrt{2}}\right),\left(\frac{1}{\sqrt{2}},-\frac{1}{\sqrt{2}}\right)\right\}$,

$\max A = \max B = \{\,(x,y) \mid x^2 + y^2 = 1, x, y \geq 0\,\}$.

Since $\min A \not\preccurlyeq_c \min B$ and $\min B \not\preccurlyeq_c \min A$ we have $A \not\preccurlyeq_{mc} B$ and $B \not\preccurlyeq_{mc} A$. So, $mc - \min \mathcal{S} = \{A, B\}$.

Furthermore, $\min A \subset \min B - K$, $\min B \subset \min A + K, \max A = \max B$. Then, we have $\min A \preccurlyeq_s \min B$ and $\max A \preccurlyeq_s \max B$, i.e. $A \preccurlyeq_m B$. As $\min B \not\subset \min A - K$ we get $B \not\preccurlyeq_m A$. Hence, $m - \min \mathcal{S} = \{A\}$.

This example also implies that $mc - \min \mathcal{S} \not\subset * - \min \mathcal{S}$ where $* \in \{s, l, m_1, m_2\}$. Now, we show this fact.

It is clear that $A \preccurlyeq_s B$, $B \not\preccurlyeq_s A, A \preccurlyeq_l B$, $B \not\preccurlyeq_l A$. So, $B \notin s - \min \mathcal{S}$ and $B \notin l - \min \mathcal{S}$.

Furthermore, $A \dot{-} B = \{(0,0)\}$ and $B \dot{-} A = \emptyset$. Thus, $A \preccurlyeq_{m_2} B$, $B \preccurlyeq_{m_1} A, B \not\preccurlyeq_{m_2} A$ and $A \not\preccurlyeq_{m_1} B$. Then it follows

$m_2 - \min \mathcal{S} = \{A\}$ and $m_1 - \min \mathcal{S} = \{B\}$.

Remark 3.6: Also note that an mc −minimal element does not have to be a u −minimal element. For example, if

$Y = \mathbb{R}^2$, $K = \mathbb{R}^2_+, A = B\big((0,0),1\big), B = A \cap \{\,(x,y) \mid y \leq -x\,\}$, then it can be shown that $mc - \min \mathcal{S} = \{A, B\}$ and

$u - \min \mathcal{S} = \{B\}$, similar with Example 3.5.

The following corollary is a direct consequence of Proposition 3.3 and Proposition 3.4.

Corollary 3.7: Let $\mathcal{S} \subset \mathcal{M}$. Then, $m - \min \mathcal{S} \subset c - \min \mathcal{S}$.

Proposition 3.8: Let $\mathcal{S} \subset \mathcal{P}(Y)$. Then $s - \min \mathcal{S} \subset c - \min \mathcal{S}$.

Proof: Let $A \in s - \min \mathcal{S}$. Suppose there exists $B \in \mathcal{S}$ such that $B \preccurlyeq_c A$ and $A \neq B$. $B \preccurlyeq_c A$ implies $B \preccurlyeq_s A$ from Proposition 2.7. Since A is an s-minimal element, we obtain $A \preccurlyeq_s B$. Therefore,

$$B \subset A + K, \tag{3.4}$$
$$A \subset B - K. \tag{3.5}$$

Let $b \in B$. Then, from (3.4), there exists $a \in A$ and $k_1 \in K$ such that $b = a + k$. So, $a \leq_K b$. Since $B \preccurlyeq_c A$ and $B \neq A$, we have inequality (3.3) and hence $b \leq_K a$. From pointedness of K we obtain $b = a \in A$ which gives $B \subset A$. Conversely, let $a \in A$. Then from (3.5), there exists $b \in B$ and $k_2 \in K$ such that $a = b - k_2$. Thus, we have $a \leq_K b$. The inequality (3.3) implies $b \leq_K a$. Pointedness of K gives $a = b \in B$. Since $a \in A$ is arbitrary we obtain $A \subset B$. Therefore, $A = B$ which contradicts with the assumption. So, $A = B$ and $A \in c - \min \mathcal{S}$.

As seen in the following example an l −minimal or an u −minimal element does not have to be a $*$ −minimal element where $*\in \{c, mc, mn, m, s, u, m_1, m_2\}$ or

$*\in \{c, mc, mn, m, s, l, m_1, m_2\}$, respectively.

Example 3.9: Let $Y = \mathbb{R}^2$, $K = \mathbb{R}^2_+, A = [0,1] \times [0,1], B = \{(1,1)\}$ and $\mathcal{S} = \{A, B\}$. Then, $A \preccurlyeq_u B$ and $B \preccurlyeq_u A$. Hence, $u - \min \mathcal{S} = \{A, B\}$. Since $x \leq_K (1,1)$ for all $x \in A$, $A \preccurlyeq_c B$. Also, the relation $B \preccurlyeq_l A$ is obvious. So, from Proposition 2.6 and Proposition 2.7 we have $A \preccurlyeq_* B$ and $B \preccurlyeq_* A$,and then it follows $* - \min \mathcal{S} = \{A\}$ where $*\in \{c, mc, mn, m, s, l\}$.

In addition, $(0,0) \in A \dot{-} B = \{(-1,-1)\} + A$ and $B \dot{-} A = \emptyset$. Hence, we get $B \preccurlyeq_{m_1} A, A \preccurlyeq_{m_2} B, A \preccurlyeq_{m_1} B$ and $B \preccurlyeq_{m_2} A$.Thus, $m_1 - \min \mathcal{S} = \{B\}$ and $m_2 - \min \mathcal{S} = \{A\}$.

If $A = \{(0,0)\}, B = [0,1] \times [0,1]$ and $\mathcal{S} = \{A, B\}$ one can easily see $l - \min \mathcal{S} = \{A, B\}$, $* - \min \mathcal{S} = \{A\}$ where

$*\in \{c, mc, mn, m, s, u, m_1\}$ and $m_2 - \min \mathcal{S} = \{B\}$.

Also note that an m_1 −minimal or an m_2 −minimal element does not have to be a $*$ −minimal element where

$*\in \{c, mc, mn, m, s, l, u, m_2\}$ and
$*\in \{c, mc, mn, m, s, l, u, m_1\}$, respectively.

Example 3.10: Let $Y = \mathbb{R}^2$, $K = \mathbb{R}^2_+$, $A = B\big((0,0), 1\big), C = B((4,4), 2)$ and $\mathcal{S} = \{A, C\}$. Then, $A \dot{-} C = \emptyset$ and

$C \dot{-} A = B((4,4), 1)\} \subset K$. So, we have $A \preccurlyeq_{m_2} C$ and $C \preccurlyeq_{m_2} A$, respectively. Hence, $m_2 - \min \mathcal{S} = \{A, C\}$. In addition,

$$\min A = \{(x,y) \mid x^2 + y^2 = 1, x, y \leq 0\},$$
$$\max A = \{(x,y) \mid x^2 + y^2 = 1, x, y \geq 0\},$$
$$\min C = \{(x,y) \mid (x-4)^2 + (y-4)^2 = 4, x, y \leq 4\},$$
$$\max C = \{(x,y) \mid (x-4)^2 + (y-4)^2 = 4, x, y \geq 4\}.$$

Since $(x,y) \leq_K (a,b)$ for all $(x,y) \in A$ and $(a,b) \in C$ it follows $A \preccurlyeq_c C$. Also, $C \not\subset A - K$ and $A \not\subset C + K$, i.e. $C \preccurlyeq_u A$ and $C \preccurlyeq_l A$, respectively. Hence, from Proposition 2.6 and Proposition 2.7 we have $A \preccurlyeq_* C$ and $C \preccurlyeq_* A$ where

$*\in \{c, mc, mn, m, s, l, u\}$. Thus, $C \notin * - \min \mathcal{S}$ for $*\in \{c, mc, mn, m, s, l, u\}$.

Furthermore, since $A \dot{-} C = \emptyset$ and $C \dot{-} A = B((4,4), 1)\} \subset K$, we have $C \preccurlyeq_{m_1} A$ and $A \preccurlyeq_{m_1} C$, respectively. Thus,

$C \notin m_1 - \min \mathcal{S}$.

If $A = B\big((0,0), 2\big), C = B((4,4), 1)$, then similarly we have, $m_1 - \min \mathcal{S} = \{A, C\}$ and $C \notin * - \min \mathcal{S}$ for

$*\in \{c, mc, mn, m, s, l, u, m_2\}$.

Following example shows that a c-minimal element does not have to be a $*$-minimal element where $*\in \{ mc, m, m_1, m_2, s, l, u \}$.

Example 3.11: Let $Y = \mathbb{R}^2$, $K = \mathbb{R}^2_+$, $A = B\big((1,1), 1\big), B = ([0,2] \times [0,2])\backslash\{(x,y) \mid (x-1)^2 + (y-1)^2 > 1, x, y \leq 1\}$ and $\mathcal{S} = \{A, B\}$. Since, $(1,0), (0,1) \in A \cap B$, $(1,0) \not\leq_K (0,1)$ and $(0,1) \not\leq_K (1,0)$, we have $A \preccurlyeq_c B$ and $B \preccurlyeq_c A$. Hence, $c - \min \mathcal{S} = \{A, B\}$.

Also, $\min A = \min B = \{(x,y) \mid (x-1)^2 + (y-1)^2 = 1, x, y \leq 1\}$,

$\max A = \{(x,y) \mid (x-1)^2 + (y-1)^2 = 1, x, y \geq 1\}$ and $\max B = \{(2,2)\}$.

Now, we show this fact for each order relation.

i. It is obvious that $(x,y) \leq_K (2,2)$ for all $(x,y) \in \max A$. So, $\min A \preccurlyeq_c \min B$, $\max A \preccurlyeq_c \max B$, i.e. $A \preccurlyeq_{mc} B$. Also, $B \preccurlyeq_{mc} A$ because $(2,2) \not\leq_K (x,y)$ for any $(x,y) \in \max A$. Therefore, $B \notin mc - \min \mathcal{S}$.
ii. Since $\min A = \min B$ and $\max A \preccurlyeq_s \max B$, we have $A \preccurlyeq_m B$. Also, $\max B \preccurlyeq_s \max A$ which implies $B \preccurlyeq_m A$. So, $B \notin m - \min \mathcal{S}$.
iii. $A \subset B - K$ and $B \not\subset A - K$ imply $A \preccurlyeq_u B$ and $B \preccurlyeq_u A$, respectively. Thus, $B \notin u - \min \mathcal{S}$.
iv. From (iii) and (iv), we have $A \preccurlyeq_s B$ and $B \preccurlyeq_s A$. So, $B \notin s - \min \mathcal{S}$.
v. Since $B \dot{-} A = \{(0,0)\}, A \dot{-} B = \emptyset$, we get $A \preccurlyeq_{m_1} B$, $B \preccurlyeq_{m_1} A$ and $B \preccurlyeq_{m_2} A$, $A \preccurlyeq_{m_2} B$. Hence, $B \notin m_1 - \min \mathcal{S}$ and $A \notin m_2 - \min \mathcal{S}$.

This example also shows that an mn −minimal element does not have to be a $*$-minimal element where $*\in \{ mc, m, m_1, m_2, s, u \}$. Indeed, $\max A \preccurlyeq_s \min B$ and $\max B \preccurlyeq_s \min A$. Hence, $mn - \min \mathcal{S} = \{A, B\}$.

If we consider $A = B\big((1,1), 1\big), B = ([0,2] \times [0,2])\backslash \{(x,y) \mid (x-1)^2 + (y-1)^2 > 1, x, y \geq 1\}$, it can easily be seen that $mn - \min \mathcal{S} = c - \min \mathcal{S} = \{A, B\}$ and $l - \min \mathcal{S} = \{B\}$.

Proposition 3.12: Let $\mathcal{S} \subset \mathcal{M}_0$. Then, following conditions are satisfied:

i. $m - \min \mathcal{S} \subset mn - \min \mathcal{S}$,
ii. $s - \min \mathcal{S} \subset m - \min \mathcal{S}$,
iii. $s - \min \mathcal{S} \subset mc - \min \mathcal{S}$,
iv. $s - \min \mathcal{S} \subset mn - \min \mathcal{S}$.

Proof:

i. Let $A \in m-\min \mathcal{S}$ and there exist $B \in \mathcal{S}$ such that $B \preccurlyeq_{mn} A$. If $A = B$ then, A is obviously an mn-minimal element. If $A \neq B$ then, $\max A \preccurlyeq_s \min B$. From Proposition 2.7, we have $B \preccurlyeq_m A$. Since $A \in m-\min \mathcal{S}$, we obtain $A \preccurlyeq_m B$. From Proposition 2.11, we get $\min A = \min B$ and $\max A = \max B$. Hence, we obtain $\max B = \max A \preccurlyeq_s \min B = \min A$ which implies $A \preccurlyeq_{mn} B$. So $A \in mn-\min \mathcal{S}$.

ii. Let $A \in s-\min \mathcal{S}$ and there exist $B \in \mathcal{S}$ such that $B \preccurlyeq_m A$. $B \preccurlyeq_m A$ implies $B \preccurlyeq_s A$ from Proposition 2.7. Since $A \in s-\min \mathcal{S}$, we have $A \preccurlyeq_s B$. Hence, we get $A + K = B + K$ and $A - K = B - K$ from Proposition 2.2. Also, quasi domination property of A and B implies $\min A + K = A + K = B + K = \min B + K$, $\max A - K = A - K = B - K = \max B - K$. Since, $B \preccurlyeq_m A$, we have $\min A = \min B$ and $\max A = \max B$. So, from Proposition 2.11, we obtain $A \preccurlyeq_m B$. Thus, $A \in m-\min \mathcal{S}$.

iii. Proof is obtained directly from (ii) and Proposition 3.4.

iv. It can be obtained directly from (i) and (ii).

If quasi domination property in Proposition 3.12 is omitted then, results may not be true as seen in the following examples.

Example 3.13: Let $K = \mathbb{R}^2_+$, $A = \{(x,y) \mid -x < y \leq 1-x\} \cup \{(x,y) \mid y = -x, x \leq 0\}$, $B = \{(x,y) \mid y = 2-x\}$ and $\mathcal{S} = \{A, B\}$. Then,

$$\begin{aligned} \min A &= \{(x,y) \mid y = -x, x \leq 0\}, \\ \max A &= \{(x,y) \mid y + x = 1\}, \\ \min B = \max B &= B, \end{aligned}$$

And $A \notin \mathcal{M}_0$. As $\min B \not\subset \min A + K$, we have $\min A \not\preccurlyeq_s \min B$. So, $A \not\preccurlyeq_m B$. Also, it is clear that $B \not\preccurlyeq_m A$. It follows $A, B \in m-\min \mathcal{S}$. Also, it is obvious that $\max A \preccurlyeq_s \min B$ and $\max B \not\preccurlyeq_s \min A$. Hence, $A \preccurlyeq_{mn} B$ and $B \not\preccurlyeq_{mn} A$, respectively. Then, we obtain $B \notin mn-\min \mathcal{S}$.

Example 3.14: Let $K = \mathbb{R}^2_+$, $A = \{(-1,1)\} \cup \operatorname{int} B\big((1,0),1\big)$, $B = \{(0,2)\}$ and $\mathcal{S} = \{A, B\}$. It can be easily seen that

$$\begin{aligned} \min A = \max A &= \{(-1,1)\}, \\ \min B = \max B &= B, \end{aligned}$$

and $A \notin \mathcal{M}_0$. Since $A \not\subset B - K$, we obtain $A \not\preccurlyeq_u B$ which implies $A \not\preccurlyeq_s B$. Also, as $A \not\subset B + K$ i. e. $B \not\preccurlyeq_l A$ and it follows $B \not\preccurlyeq_s A$. So, $A, B \in s-\min \mathcal{S}$.

However, we have $A \preccurlyeq_m B$ and $B \not\preccurlyeq_m A$ which imply $B \notin m-\min \mathcal{S}$.

Also, since $\max A \preccurlyeq_s \min B$ and $\max B \not\preccurlyeq_s \min A$ we obtain $A \preccurlyeq_{mn} B$ and $B \not\preccurlyeq_{mn} A$, respectively. Then, $B \notin mn-\min \mathcal{S}$.

Furthermore, since $(-1,1) \leq_K (0,2)$ and $(0,2) \not\leq_K (-1,1)$, we have $\min A \preccurlyeq_c \min B$, $\max A \preccurlyeq_c \max B$, $\min B \not\preccurlyeq_c \min A$ and $\max B \not\preccurlyeq_c \max A$. These relations imply $A \preccurlyeq_{mc} B$ and $B \not\preccurlyeq_{mc} A$. Hence, $B \notin mc-\min \mathcal{S}$.

An mc −minimal element does not have to be an mn −minimal element. To show this fact Example 3.4 in [4] by Jahn and Ha can be used as follows.

Example 3.15 [4] Let $K = \mathbb{R}^2_+$, $A = \operatorname{conv}\{(-2,0),(-3,-1),(0,-2)\}$, $B = \operatorname{conv}\{(4,2),(0,2),(4,-2)\}$ and $\mathcal{S} = \{A, B\}$. Then as proved in [4], we have $A \preccurlyeq_{mn} B$ and $A \not\preccurlyeq_{mc} B$. It is obvious that $B \not\preccurlyeq_{mn} A$. Hence, $B \in mc-\min \mathcal{S}$ and $B \notin mn-\min \mathcal{S}$.

Next example shows that $m-\min \mathcal{S} \not\subset * - \min \mathcal{S}$ and $s-\min \mathcal{S} \not\subset * - \min \mathcal{S}$ where $* \in \{u, l, m_1, m_2\}$.

Example 3.16: Let $K = \mathbb{R}^2_+$, $A = [-1,1] \times [-1,1]$, $B = \{(0,0)\}$ and $\mathcal{S} = \{A, B\}$. Then,

$$\begin{aligned} \min A &= \{(-1,-1)\}, \\ \max A &= \{(1,1)\}, \\ \min B = \max B &= \{(0,0)\}. \end{aligned}$$

Since $(0,0) \not\leq_K (-1,-1)$ and $(1,1) \not\leq_K (0,0)$, we have $\min B \not\preccurlyeq_s \min A$ and $\max A \not\preccurlyeq_s \max B$, respectively. Then, it follows $B \not\preccurlyeq_m A$ and $A \not\preccurlyeq_m B$ and $m-\min \mathcal{S} = \{A, B\}$. However, as $B = \{(0,0)\} \subset A - K$ and $A \not\subset \{(0,0)\} - K = -K$ we obtain $B \preccurlyeq_u A$ and $A \not\preccurlyeq_u B$, respectively. Thus, $A \notin u-\min \mathcal{S}$. Also, since $B = \{(0,0)\} \subset A + K$ and $A \not\subset B + K$ we get $A \preccurlyeq_l B$ and $B \not\preccurlyeq_l A$. Hence, $B \notin l-\min \mathcal{S}$. Furthermore, since $B \not\preccurlyeq_l A$ and $A \not\preccurlyeq_u B$, we have $B \not\preccurlyeq_s A$ and $A \not\preccurlyeq_s B$. So, $s-\min \mathcal{S} = \{A, B\}$. In addition, it can be easily seen that $A \dot{-} B = A$ and $B \dot{-} A = \emptyset$. Then, it follows $B \preccurlyeq_{m_1} A$, $A \preccurlyeq_{m_2} B$, $A \not\preccurlyeq_{m_1} B$ and $B \not\preccurlyeq_{m_2} A$. So, $A \notin m_1-\min \mathcal{S}$ and $B \notin m_2-\min \mathcal{S}$.

The following example implies that an m −minimal element does not have to be an s −minimal element.

Example 3.17: Let $K = \mathbb{R}^2_+$, $A = \operatorname{conv}\{(1,0),(0,1)\}$, $B = [1,2] \times [0,1]$ and $\mathcal{S} = \{A, B\}$. We have

$$\begin{aligned} \min B &= \{(1,0)\}, \\ \max B &= \{(2,1)\}, \\ \min A = \max A &= A. \end{aligned}$$

So, it follows $\min A \not\preccurlyeq_s \min B$ and $\min B \not\preccurlyeq_s \min A$. Hence, $A \not\preccurlyeq_m B$ and $B \not\preccurlyeq_m A$. Then, we obtain $m-\min \mathcal{S} = \{A, B\}$. Also, we get $A \preccurlyeq_l B, A \preccurlyeq_u B, B \not\preccurlyeq_l A$ and $B \not\preccurlyeq_u A$ which imply $A \preccurlyeq_s B, B \not\preccurlyeq_s A$. Thus, $B \notin s-\min \mathcal{S}$.

The results in this article are summarized in Figures 1-9 below.

We have

$m_1 - \min \rightleftarrows * - \min$ where $* \in \{c, mc, mn, m, s, l, u, m_2\}$,

$m_2 - \min \rightleftarrows * - \min$ where $* \in \{c, mc, mn, m, s, l, u, m_1\}$,

$l - \min \rightleftarrows * - \min$ where $* \in \{c, mc, mn, m, s, u, m_1, m_2\}$,

$u - \min \rightleftarrows * - \min$ where $* \in \{c, mc, mn, m, s, l, m_1, m_2\}$.

So, these relations will be omitted in the figures.

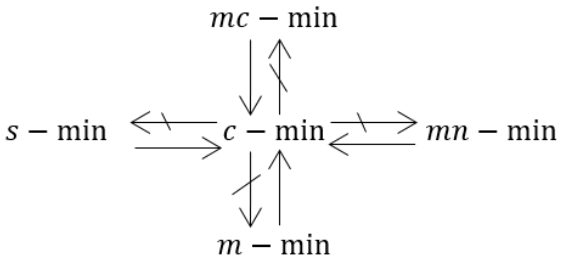

Figure 1. Comparison of c −minimal elements with others

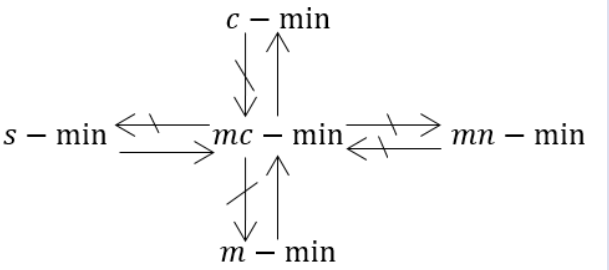

Figure 2. Comparison of mc −minimal elements with others under quasi domination assumption

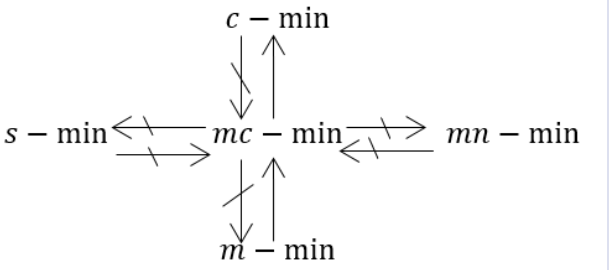

Figure 3. Comparison of mc −minimal elements with others without quasi domination assumption

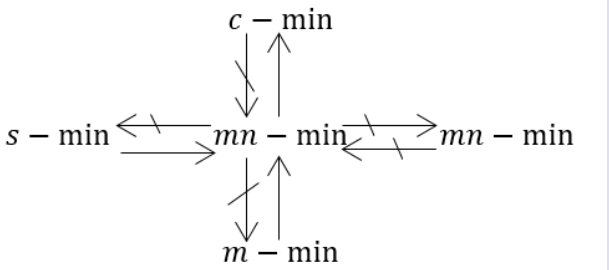

Figure 4. Comparison of mn −minimal elements with others under quasi domination assumption

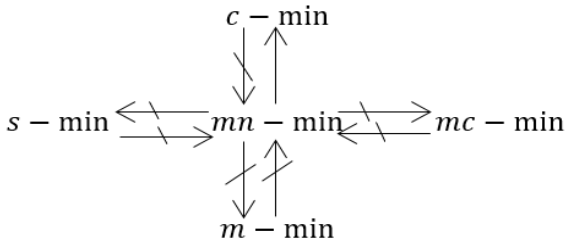

Figure 5. Comparison of mn −minimal elements with others without quasi domination assumption

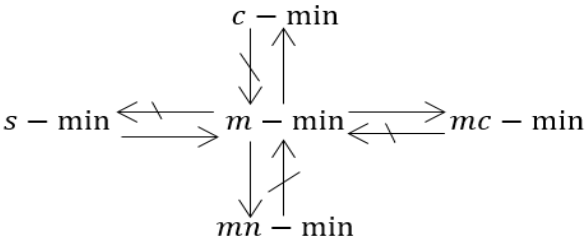

Figure 6. Comparison of m −minimal elements with others under quasi domination property assumption

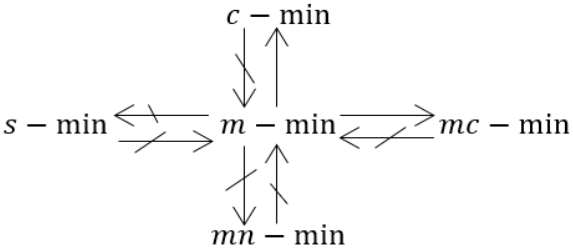

Figure 7. Comparison of m −minimal elements with others without quasi domination assumption

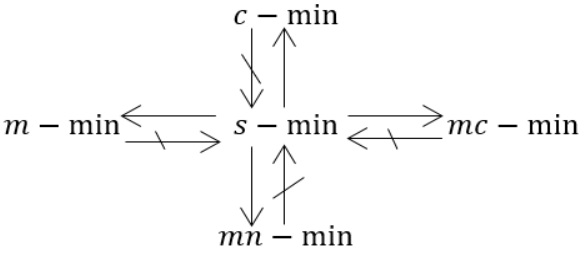

Figure 8. Comparison of s −minimal elements with others under quasi domination property assumption

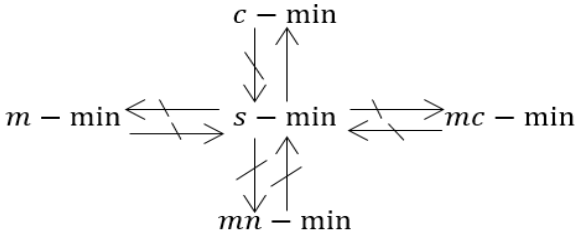

Figure 9: Comparison of s −minimal elements with others without quasi domination assumption

Conflicts of interest

There are no conflicts of interest in this work.

References

[1] Nishnianidze Z.G., Fixed Points Of Monotonic Multiple-Valued Operators, *Bull Georgian Acad Sci.,* 114 (1984) 489–491.

[2] Young R.C.,The Algebra Of Many-Valued Quantities, *Math Ann.*, 104 (1931) 260–290.

[3] Kuroiwa D., The Natural Criteria in Set-Valued Optimization. Research on Nonlinear Analysis and Convex Analysis, *Surikaisekikenkyusho Kokyuroku,* 1031 (1998) 85–90.

[4] Jahn J., Ha T.X.D., New Order Relations in Set Optimization, *J. Optimiz Theory App.*, 148 (2003) 209–236.

[5] Karaman E., Soyertem M., Atasever Güvenç İ., Tozkan D., Küçük M., Küçük Y., Partial Order Relations on Family of Sets and Scalarizations for Set Optimization, *Positivity*, 22 (2018) 783-802.

[6] Jahn J., Characterizations of the Set Less Order Relation in Nonconvex Set Optimization, *Journal of Optimization Theory and Applications* 193 (2022) 523–544.

[7] Kuroiwa D., Some Criteria in Set-Valued Optimization, Investigations on Nonlinear Analysis and Convex Analysis. *Surikaisekikenkyusho Kokyuroku*; 985 (1998) 171–176.

[8] Kuroiwa D., Existence Theorems of Set Optimization with Set-Valued Maps, *J. Inf. Optim*., 24 (2003) 73–84.

[9] Kuroiwa D. On Set-Valued Optimization, *Nonlinear Anal*., 47 (2001) 1395–1400.

[10] Kuroiwa D., Existence of Efficient Points of Set Optimization with Weighted Criteria, J. Nonlinear Convex A., 4 (2003) 117–123.

[11] Khushboo, Lalitha C.S., Scalarizations for a Set Optimization Problem Using Generalized Oriented Distance Function. *Positivity,* 23 (2019) 1195–121.

[12] Hernández E., Rodríguez-Marín L., Nonconvex Scalarization in Set Optimization with Set-Valued Maps, *J. Math. Anal. Appl.* 325 (2007) 1–18.

[13] Karaman E., Güvenç İ.A., Soyertem M., Optimality Conditions in Set-Valued Optimization Problems with Respect to a Partial Order Relation by Using Subdifferentials, *Optimization,* 70(3) (2021) 613-650.

[14] Karaman E., Soyertem M., Güvenç İ.A., Optimality Conditions in Set-Valued Optimization Problem with Respect to a Partial Order Relation via Directional Derivative, *Taiwan J. Math.* 24(3) (2020) 709-722.

[15] Karaman E., Nonsmooth Set Variational Inequality Problems and Optimality Criteria for Set Optimization, *Miskolc Math Notes,* 21(1) (2020) 229-240.

[16] Khan A.A., Tammer C., Zălinescu C., Set-Valued Optimization: An Introduction with Applications. Berlin, (2015).

[17] Küçük M., Soyertem M., Küçük Y., On the Scalarization of Set-Valued Optimization Problems with Respect to Total Ordering Cones. In: Hu, B., Morasch, K., Pickl, S., Siegle, M., (Eds). Operations research proceedings, Heidelberg: Springer (2011) 347–352..

[18] Küçük M., Soyertem M., Küçük Y., Atasever İ., Vectorization of Set-Valued Maps with Respect to Total Ordering Cones and its Applications to Set-Valued Optimization Problems, *J. Math. Anal.* 385 (2012) 285–292.

[19] Ha T.X.D., A Unified Scheme for Scalarization in Set Optimization, *Optimization*, 55 (2021) 3603-3616.

[20] Truong Xuan Duc Ha, A unified scheme for scalarization in set optimization, *Taylor & Francis Online,* (2023)

[21] Atasever Güvenç İ., On Weak Minimal Solutions of Set Valued Optimization Problems and Comparison of Some Set Order Relations, *Eskişehir Teknik Üniversitesi Bilim ve Teknoloji Dergisi B - Teorik Bilimler*, 11(1) (2023) 60-69.

Cumhuriyet Sci. J., 44(3) (2023) 538-546
DOI: https://doi.org/10.17776/csj.1258286

Cumhuriyet Science Journal

| csj.cumhuriyet.edu.tr | Founded: 2002 ISSN: 2587-2680 e-ISSN: 2587-246X Publisher: Sivas Cumhuriyet University

An Analytical Approach to Contaminant Transport with Spatially and Temporally Dependent Dispersion in a Heterogeneous Porous Medium

Raja Ram Yadav[1,a], Sujata Kushwaha[1,b,*], Lav Kush Kumar[2,c], Joy Roy[3,d]

[1] *Department of Mathematics and Astronomy, University of Lucknow, Lucknow-226007, U.P., India*
[2] *Department of Applied Science, BabuBanarasi Das Institute of Technology and Management, Lucknow-226028, U.P., India*
[3] *Department of Mathematics, Aryavart Institute of Higher Education, Lucknow-226005, U.P., India*
**Corresponding author*

Research Article

History
Received: 01/03/2023
Accepted: 30/08/2023

ABSTRACT

This study presents an analytical solution to the one-dimensional advection-dispersion equation (ADE) for a semi-infinite heterogeneous aquifer system with space and time-dependent groundwater velocity and dispersion coefficient. The dispersion coefficient is assumed to be proportional to the groundwater flow velocity. In addition, retardation factor, first-order decay and zero-order production terms are also considered. Contaminants and porous media are assumed to be chemically inert. Initially, it is assumed that some uniformly distributed solutes are already present in the aquifer domain. The input point source is considered uniformly continuous and increasing nature in a semi-infinite porous medium. The solutions are obtained analytically using the Laplace Integral Transform Technique (LITT). The nature of the concentration profile of the resulting solution for different parameters in different time domains is illustrated graphically.

Keywords: Groundwater, Pollutant, Advection, Dispersion, Retardation factor.

[a] *yadav_rr2@yahoo.co.in* *https://orcid.org/0000-0002-1311-5435*
[b] *sujatakushwaha14@gmail.com* *https://orcid.org/0000-0003-0467-3862*
[c] *lk.verma13@gmail.com* *https://orcid.org/0000-0001-9039-7205*
[d] *joyroy2904@gmail.com* *https://orcid.org/0000-0003-0403-3048*

Introduction

In recent years, excessive use of pesticides in agriculture, unplanned urbanization, illegal industrial activities, and seepage of chemicals into groundwater have contributed to the deterioration of water quality. Hazardous substances can sometimes cause serious health problems even at low concentrations, so treatment is often required to achieve sustainability. Several factors, including source geometry, solute shape and orientation, play an important role in influencing the concentration profile throughout transport process. The complex structure of the aquifer systems makes forecasting the degree of contamination and remedial measures extremely challenging. In order to deal with groundwater pollution, it is imperative to study solute transport in groundwater systems. To efficiently estimate and predict such problems, mathematical models are very useful. The advection-dispersion equation (ADE) mathematically describes the physical, chemical and biological processes that are primarily responsible for the movement of pollutants in porous media. Analytical or semi-analytical solutions of the advection-dispersion equation are often used for preliminary risk assessment of groundwater pollution and accurate prediction of pollution intensity in aquifer systems.

Many studies have been published in the literature to solve the advection-dispersion equation (ADE) assuming constant pore velocity and dispersion coefficient (Shi et al., 2016, [1] Guerrero et al., 2013 [2]). However, groundwater flow fluctuates both in temporally and spatially due to the different recharge rates of aquifer systems at different locations and time. Especially in summer and rainy season, the change of groundwater flow pattern is more obvious. The dispersion coefficient measured in the laboratory is quite different from the dispersion coefficient obtained in the field. Bear (1972) [3] and Mishra et al., (1991) [4] observed these discrepancies in dispersion as scale dependence of the dispersivity. Elder (1959) [5] derived an expression for the longitudinal dispersion coefficient for an infinitely wide open channel assuming a logarithmic velocity distribution using Taylor's theory. After establishing that the transverse velocity distribution is the dominant mechanism for longitudinal diffusion, Fischer (1967) [6] proposed an alternative formulation for the longitudinal diffusion coefficient. According to stochastic analysis, the dispersion transport is time dependent and rises until it reaches an asymptotic value (Gelhar et al., 1979) [7]. Valocchi (1989) [8] used spatial moment analysis to investigate how adsorption kinetics affects the spatial moments of depth-averaged pollution plumes. Shan and Javendel (1997) [9] developed an analytical solution for solute transport in a vertical section of a homogeneous aquifer with steady and uniform groundwater flow. In a semi-infinite homogeneous river, Wadi et al., (2014) [10] obtained an analytical solution to the one-dimensional solute transport problem using the Laplace transform technique. Kumar and Yadav (2014) [11] developed a 1D analytical solution for conservative solute transport in

heterogeneous porous media for uniform and varying pulse type input point sources. Natarajan (2016) [12] studied the effect of time- and distance-dependent dispersion coefficients on the transport of multi-species pollutants in porous media. Rubol et al., (2016) [13] simulated solute transport in the soil layer of plant roots using the advection-diffusion equation (ADE) with spatially variable coefficients. Kumar et al., (2019) [14] investigated the effect of the source/sink term on the transport of solutes in porous media. Younes et al., (2020) [15] studied the effect of travel distance on the dispersion value in porous media and found that the difference in travel distance is mainly determined by the transverse dispersion. Yadav et al., (2023) [16] studied analytical solutions for scale and time dependent solute transport in heterogeneous porous medium.

As this work could have a big impact on other research areas that uses forms of the ADE, such as the study of fish survival in rivers, radionuclide release from an area source, and radioactive substance dispersion released from nuclear power plants among others. For determining conditions and suitable locations for fish survival by using the solution of the two coupled pollution and aeration equations by Raafat, P. B., et.al (2023)[17]. A novel analytical approach for advection diffusion equation for radionuclide release from an area source by Esmail et. al (2020)[18].

In the current model, the Laplace Integral Transform approach is employed to get analytical solutions for the convection-diffusion equation to explain a conservative solute transport process in a heterogeneous porous formation. The variable coefficients of the ADE are reduced to constant coefficients by employing appropriate transformations that take into account the space and time-dependent expressions. Dispersion and velocity both depend on space and time and are considered separately for each time period. Such studies may be updated daily, monthly, fortnightly or annually based on information obtained from different positions and times within the contaminated area. This work may also apply to other physical conditions that are affected by an increase in source concentration. The developed model is very useful for understanding the concentration levels at any position and time and in the aquifer systems.

Mathematical Formulation and Analytical Solutions

Here, we focus on groundwater flow that transports a neutral and inert solute through a heterogeneous porous medium. The solute is conservative and the porous structure is heterogeneous, adsorbing and semi-infinitely long. The one-dimensional contaminant transport equation can be expressed in Cartesian form as follows (Bear, 1972) [3]:

$$R\frac{\partial c}{\partial t}=\frac{\partial}{\partial x}\left\{D(x,t)\frac{\partial c}{\partial x}-U(x,t)c\right\}-\gamma c+\mu \tag{1}$$

Where, $c[ML^{-3}]$ is the contaminant concentration at position $x[L]$ and time $t[T]$. $D(x,t)[L^2T^{-1}]$ and $U(x,t)\ [LT^{-1}]$ are longitudinal dispersion coefficient and groundwater velocity, respectively. $\gamma[T^{-1}]$ is the first order decay constant and $\mu[ML^{-3}T^{-1}]$ is the zero order production rate coefficient for solute which represents internal/external production of the solute in the medium. All solute transport through porous media is affected by a dimensionless quantity called the retardation factor (R). Adsorption causes a significant delay, which is considered as a retardation factor in the equation. The zero gradient boundary condition is enforced at the outlet, which can not only meet the mass balance requirements, but also ensure the consistency of the concentration at $x\to\infty$.

In the process of finding the analytical solution of the convection-diffusion equation by using the Laplace Integral Transformation, it is necessary to convert the variable coefficients into constant coefficients. The time- and position-dependent dispersion and groundwater velocity along the longitudinal direction is taken in degenerated form as follows:

$$\left.\begin{aligned}&U(x,t)=U_0(1+ax)F(t),\\&D=D_0(1+ax)^2F(t),\\&\gamma=\gamma_0F(t),\\&\mu=\mu_0F(t),\\&R=R_0\end{aligned}\right\} \tag{2}$$

where, D_0 and U_0 denote the initial dispersion coefficient and longitudinal groundwater velocity, respectively. γ_0, μ_0 and R_0 are the respective initial first-order decay constant, zero-order production coefficient and retardation factor, respectively.

where,

$$F(t)=\begin{cases}f_1\ (m_1t)\ ;0\le t<t_1\\ f_2\ (m_2t)\ ;t_1\le t<t_2\\ f_3\ (m_3t)\ ;t_2\le t<\infty\end{cases} \tag{3}$$

The expression $f_i(m_it);i=1,2,3$ is dimensionless. m_i are unsteady parameters having dimension, inverse of time variable. Here $f_1\ (m_1t)$ is chosen such that $f_1\ (m_1t)=1$ for $m_1=0$ or $t=0$. It is obvious that $F(t)$ is dimensionless function. a is the heterogeneity parameter having dimension, inverse of position variable.

Analytical Solution of the Problem for Uniform Input Point Source

The first condition Eq. (4) is an initial condition that says, at time $t=0$, there is some uniformly concentration c_i everywhere in the semi-infinite flow domain where, $x\ge 0$.The second condition Eq. (5) specifies continuous injection of a uniform input from the inlet boundary at $x=0$ (Yadav and Kumar, 2018)[16]. At other end as $x\to\infty$, it is assumed that a gradient of zero concentration exist forever Eq. (6).

So, the consideration of initial and boundary conditions for the above governing Eq. (1) are as follows:

Initial and Boundary Conditions

$$c(x,t) = c_i;\ t = 0, x \geq 0 \tag{4}$$

$$c(x,t) = c_0 G(t);\quad x = 0, t > 0 \tag{5}$$

$$\frac{\partial c(x,t)}{\partial x} = 0; x \to \infty, t \geq 0 \tag{6}$$

where, $G(t) = m^* \int_0^t F(t)dt$ (7)

where, m^* is unsteady parameters having dimension, inverse of time variable and $G(t)$ is also dimensionless function.

Incorporating of Eq.(2) into Eqs. (1) and (4-6) yields, we have as follows:

$$R_0 \frac{\partial c}{\partial t} = \frac{\partial}{\partial x}\left\{D_0(1+ax)^2 F(t)\frac{\partial c}{\partial x} - U_0(1+ax)F(t)c\right\} - \gamma_0 F(t)c + \mu_0 F(t) \tag{8}$$

The initial and boundary conditions are reduced as follows:

$$c(x,t) = c_i\ ; t = 0, x \geq 0 \tag{9}$$

$$c(x,t) = c_0 G(t)\ ; x = 0, t > 0 \tag{10}$$

$$\frac{\partial c(x,t)}{\partial x} = 0;\quad x \to \infty, t \geq 0 \tag{11}$$

Mathematical substitution can simplify the structure of the equation and provide greater degree of freedom for the solution. So, we introduce the following transformation Eq. (12) to keep the variable coefficient independence of space in Eq. (8) [19]:

$$X = \int_0^x \frac{1}{(1+ax)}dx \text{ or } X = \frac{1}{a}log(1+ax) \tag{12}$$

The value of the variable X is 0 for $x = 0$ and $X > 0$ for $x > 0$.

In order to determine the analytical solution to the convection-diffusion equation using the Laplace integral transform, the variable coefficients must be changed to constant coefficients. Incorporating Eq. (12) into Eqs. (8-11) yields:

$$\frac{R_0}{F(t)}\frac{\partial c}{\partial t} = D_0\frac{\partial^2 c}{\partial X^2} - U_1\frac{\partial c}{\partial X} - \gamma_1 c + \mu_0 \tag{13}$$

where,

$$U_1 = U_0 - D_0 a\ ,\quad \gamma_1 = \gamma_0 + U_0 a\ , \quad c(X,t) = c_i\ ; \qquad X \geq 0, t = 0 \tag{14}$$

$$c(X,t) = c_0 G(t);\quad X = 0, t > 0 \tag{15}$$

$$\frac{\partial c(X,t)}{\partial X} = 0; X \to \infty, t \geq 0 \tag{16}$$

We introduce the new time variable T with the help of the following transformation Eq.(17) as follows (Crank, 1975) [20]:

$$T = \int_0^t F(t)dt = \int_0^{t_1} f_1(m_1 t)dt + \int_{t_1}^{t_2} f_2(m_2 t)dt + \int_{t_2}^{t} f_3(m_3 t)dt \tag{17}$$

It is obvious that $T = 0$ for $t = 0$ and $T > 0$ for $t > 0$.

Use the transformation given in Eq. (17), Eqs. (13-16) simplifies to the following form:

$$R_0\frac{\partial c}{\partial T} = D_0\frac{\partial^2 c}{\partial X^2} - U_1\frac{\partial c}{\partial X} - \gamma_1 c + \mu_0 \tag{18}$$

$$c(X,T) = c_i\ ; T = 0, X \geq 0 \tag{19}$$

$$c(X,T) = c_0 m^* T;\quad X = 0, T > 0 \tag{20}$$

$$\frac{\partial c(X,T)}{\partial X} = 0; X \to \infty, T \geq 0 \tag{21}$$

We employ another transformation as follows to remove the convective term from the Eq. (18):

$$c(X,T) = k(X,T)\exp\left[\frac{U_1}{2D_0}X - \frac{1}{R_0}\left(\frac{U_1^2}{4D_0} + \gamma_1\right)T\right] + \frac{\mu_0}{\gamma_1} \tag{22}$$

Where, $k(X,T)$ is the dependent variable that depends on the position and time variables.

Eqs.(18-21) are converted to the following form by applying the transformation in Eq. (22), as :

$$R_0\frac{\partial k}{\partial T} = D_0\frac{\partial^2 k}{\partial X^2} \tag{23}$$

$$k(X,T) = \left(c_i - \frac{\mu_0}{\gamma_1}\right)exp(-\beta X);\ X \geq 0, T = 0 \tag{24}$$

$$k(X,T) = \left(c_0 m^* T - \frac{\mu_0}{\gamma_1}\right)exp(\eta^2 T)\ ;\ X = 0, T > 0 \tag{25}$$

$$\frac{\partial k(X,T)}{\partial X} + \beta k(X,T) = 0; X \to \infty, T > 0 \tag{26}$$

where, $\eta^2 = \frac{1}{R_0}\left(\frac{U_1^2}{4D_0} + \gamma_1\right)$, $\beta = \frac{U_1}{2D_0}$.

We solve this boundary value problem in the Laplace domain by applying the Laplace Integral Transformation Technique (LITT) to the Eqs. (23-26) as follows:

$$\bar{k}(X,p) = \frac{c_0 m^*}{(p-\eta^2)^2} exp\left(-X\sqrt{\frac{pR_0}{D_0}}\right) - \frac{\mu_0}{\gamma_1}\frac{1}{(p-\eta^2)} exp\left(-X\sqrt{\frac{pR_0}{D_0}}\right) - \left(c_i - \frac{\mu_0}{\gamma_1}\right)\frac{1}{(p-\rho^2)} exp\left(-X\sqrt{\frac{pR_0}{D_0}}\right) + \left(c_i - \frac{\mu_0}{\gamma_1}\right)\frac{exp(-\beta X)}{(p-\rho^2)} \quad (27)$$

Where

$$\rho = \frac{U_1}{2\sqrt{R_0 D_0}}.$$

The analytic solution to the advection dispersion equation, applying an Inverse Laplace Integral to the Eq. (27) and apply the transformation Eq. (22) in reverse order, we have:

$$c(X,T) = \left\{\begin{matrix} m^* c_0 J_1(X,T) - \frac{\mu_0}{\gamma_1} H_1(X,T) - \left(c_i - \frac{\mu_0}{\gamma_1}\right) I_1(X,T) + \left(c_i - \frac{\mu_0}{\gamma_1}\right) \\ exp(-\beta X + \rho^2 T) \end{matrix}\right\} exp\left\{\frac{U_1}{2D_0} - \frac{1}{R_0}\left(\frac{U_1^2}{4D_0} + \gamma_1\right)\right\} + \frac{\mu_0}{\gamma_1} \quad (28)$$

where,

$$J_1(X,T) = \frac{1}{4\eta}\left(2\eta T - \sqrt{\frac{R_0}{D_0}}X\right) exp\left(\eta^2 T - \eta\sqrt{\frac{R_0}{D_0}}X\right) erfc\left(\frac{\sqrt{R_0}}{2\sqrt{D_0 T}}X - \eta\sqrt{T}\right) + \frac{1}{4\eta}\left(2\eta T + \sqrt{\frac{R_0}{D_0}}X\right) exp\left(\eta^2 T + \eta\sqrt{\frac{R_0}{D_0}}X\right) erfc\left(\frac{\sqrt{R_0}}{2\sqrt{D_0 T}}X + \eta\sqrt{T}\right)$$

$$H_1(X,T) = \frac{1}{2}\left\{\begin{matrix} \exp\left(\eta^2 T - \eta\sqrt{\frac{R_0}{D_0}}X\right) erfc\left(\frac{\sqrt{R_0}}{2\sqrt{D_0 T}}X - \eta\sqrt{T}\right) + \\ \exp\left(\eta^2 T + \eta\sqrt{\frac{R_0}{D_0}}X\right) erfc\left(\frac{\sqrt{R_0}}{2\sqrt{D_0 T}}X + \eta\sqrt{T}\right) \end{matrix}\right\}$$

$I_1(X,T)$ is obtained by replacing η with ρ in $H_1(X,T)$.

Analytical solution of the problem for varying input point source

In this case, we also consider a one-dimensional transport problem with decay and source terms in a semi-infinite heterogeneous porous domain. The varying nature of the input point source is described by Eq. (29), applied along the flow to the analytical solution of the advection dispersion equation.

In the first scenario, the concentration of the input at the origin $(x = 0)$ of the medium always remains the same, which may not be possible in the real world. Illegal human activities on the surface of the earth may lead to an increase/decrease in pollution levels at the source. Such condition is mathematically expressed as mixed-type condition Eq. (29).

$$-D(x,t)\frac{\partial c(x,t)}{\partial x} + U(x,t)c = U(x,t)c_0 G(t)\ ; \quad x = 0, t > 0 \quad (29)$$

Substituting the expression of Eq. (2) into Eq. (29), we have:

$$-D_0\frac{\partial c(x,t)}{\partial x} + U_0\, c = U_0\, c_0 G(t); \qquad x = 0,\ \ t > 0 \quad (30)$$

Incorporating the transformation of Eq. (12), Eq. (30) reduced as follows:

$$-D_0\frac{\partial c(X,t)}{\partial X} + U_0\, c = U_0\, c_0 G(t); \qquad X = 0,\ \ t > 0 \quad (31)$$

Incorporating Eq. (17), Eq. (31) can be simplified as follows:

$$-D_0\frac{\partial c(X,T)}{\partial X} + U_0 c = U_0 c_0 m^* T\ ;\ X = 0, T > 0 \quad (32)$$

Using transformation given in Eq. (22), the Eq. (32) reduces into following form;

$$-D_0\frac{\partial k(X,T)}{\partial X} + \left(U_0 - \frac{U_1}{2}\right)k = U_0\left(c_0 m^* T - \frac{\mu_0}{\gamma_1}\right) exp(\eta^2 T)\ ;\ X = 0, T > 0 \quad (33)$$

where, $\eta^2 = \frac{1}{R_0}\left(\frac{U_1{}^2}{4D_0} + \gamma_1\right)$

Apply the Laplace Integral Transformation technique in Eq.(33) using Eqs.(23,24, 26) as in previous case, obtained following result:

$$\bar{k}(X,p) = \frac{U_0 c_0 m^*}{\sqrt{R_0 D_0}} \frac{1}{(p-\eta^2)^2(\sqrt{p}+\sigma)} exp\left(-X\sqrt{\frac{pR_0}{D_0}}\right) - \frac{U_0\mu_0}{\gamma_1\sqrt{R_0 D_0}} \frac{1}{(p-\eta^2)(\sqrt{p}+\sigma)} exp\left(-X\sqrt{\frac{pR_0}{D_0}}\right)$$
$$-\frac{U_0}{\sqrt{R_0 D_0}}\left(c_i - \frac{\mu_0}{\gamma_1}\right)\frac{1}{(p-\rho^2)(\sqrt{p}+\sigma)} exp\left(-X\sqrt{\frac{pR_0}{D_0}}\right) + \left(c_i - \frac{\mu_0}{\gamma_1}\right)\frac{exp(-\beta X)}{(p-\rho^2)} \quad (34)$$

where, $\rho = \frac{U_0 - aD_0}{2\sqrt{R_0 D_0}}, \sigma = \frac{U_0 + aD_0}{2\sqrt{R_0 D_0}}$.

Taking the Inverse Laplace Integral Transform into Eq. (34) and use the transformation Eq. (22), we obtain the desired solution of the advection-diffusion equation as follows:

$$C(x,T) = \left\{\begin{matrix}\frac{m^* c_0 U_0}{\sqrt{R_0 D_0}} I(X,T) + \frac{U_0\mu_0}{\gamma_1\sqrt{R_0 D_0}} J(X,T) - \frac{U_0}{\sqrt{R_0 D_0}}\left(c_i - \frac{\mu_0}{\gamma_1}\right) H(X,T) + \left(c_i - \frac{\mu_0}{\gamma_1}\right) \\ exp(\beta X - \rho^2 T)\end{matrix}\right\} \quad (35)$$
$$exp\left(\frac{U_1}{2D_0}X - \frac{1}{R_0}\left(\frac{U_1^2}{4D_0}\right)T\right) + \frac{\mu_0}{\gamma_1}$$

where

$$I(X,T) = c_1\left\{\frac{1}{\sqrt{\pi T}} exp\left(-\frac{R_0 X^2}{4D_0 T}\right) + \eta\, exp\left(\eta^2 T - \eta\sqrt{\frac{R_0}{D_0}}X\right) erfc\left(\frac{1}{2}\sqrt{\frac{R_0}{D_0}}X - \eta\sqrt{T}\right)\right\}$$
$$+ c_2\left\{\begin{matrix}\left(1 - \eta\sqrt{\frac{R_0}{D_0}}X + 2\eta^2 T\right) exp\left(\eta^2 T - \eta\sqrt{\frac{R_0}{D_0}}X\right) \\ erfc\left(\frac{1}{2}\sqrt{\frac{R_0}{D_0}}X - \eta\sqrt{T}\right) + 2\eta T\left\{\frac{1}{\sqrt{\pi T}} exp\left(-\frac{R_0 X^2}{4D_0 T}\right)\right\}\end{matrix}\right\}$$
$$+ c_3\left\{\frac{1}{\sqrt{\pi T}} exp\left(-\frac{R_0 X^2}{4D_0 T}\right) - \eta\, exp\left(\eta^2 T + \eta\sqrt{\frac{R_0}{D_0}}X\right) erfc\left(\frac{1}{2}\sqrt{\frac{R_0}{D_0}}X + \eta\sqrt{T}\right)\right\}$$

$$c_4\left\{\begin{matrix}\left(1 + \eta\sqrt{\frac{R_0}{D_0}}X + 2\eta^2 T\right) exp\left(\eta^2 T + \eta\sqrt{\frac{R_0}{D_0}}X\right) erfc\left(\frac{1}{2}\sqrt{\frac{R_0}{D_0}}X + \eta\sqrt{T}\right) \\ -2\eta T\left\{\frac{1}{\sqrt{\pi T}} exp\left(-\frac{R_0 X^2}{4D_0 T}\right)\right\}\end{matrix}\right\}$$
$$+ c_5\left\{\frac{1}{\sqrt{\pi T}} exp\left(-\frac{R_0 X^2}{4D_0 T}\right) - \rho\, exp\left(\rho^2 T + \rho\sqrt{\frac{R_0}{D_0}}X\right) erfc\left(\frac{1}{2}\sqrt{\frac{R_0}{D_0}}X + \rho\sqrt{T}\right)\right\}$$

$$J(X,T) = \frac{1}{2(\eta+\sigma)}\exp\left(\eta^2 T - \eta\sqrt{\frac{R_0}{D_0}}X\right) erfc\left(\frac{\sqrt{R_0}}{2\sqrt{D_0 T}}X - \eta\sqrt{T}\right) - \frac{1}{2(\eta-\sigma)}\exp\left(\eta^2 T + \eta\sqrt{\frac{R_0}{D_0}}X\right)$$
$$erfc\left(\frac{\sqrt{R_0}}{2\sqrt{D_0 T}}X + \eta\sqrt{T}\right) + \frac{\eta}{\eta^2 - \sigma^2}\exp\left(\sigma^2 T + \sigma\sqrt{\frac{R_0}{D_0}}X\right) \times erfc\left\{\frac{\sqrt{R_0}}{2\sqrt{D_0 T}}X + \sigma\sqrt{T}\right\},$$

$c_1 = \frac{2\eta+\sigma}{4\eta^3(\eta+\sigma)^2}, c_2 = \frac{1}{4\eta^2(\eta+\sigma)}$, $c_3 = -\frac{2\eta-\sigma}{4\eta^3(\eta-\sigma)^2}, c_4 = \frac{1}{4\eta^2(\sigma-\eta)}$,

$$c_5 = \frac{1}{(\sigma-\eta)^2(\sigma+\eta)^2},$$

$$X = \frac{1}{a}\log(1+ax), T = \int_0^t F(t)dt,$$

The value of $H(X,T)$ is obtained by replacing η with ρ in $J(X,T)$

Result and Discussion

Analytical solutions are developed for the advection-diffusion equation (ADE) under the hypothetical scenario of time-dependent groundwater flow in a 1D heterogeneous porous formulation. Point source is considered to enter the domain from the left end $x = 0$. Separate graphs are drawn to show the effect of each parameter on the variation in solute concentration. For a set of input hydrological data, the obtained analytical solutions Eq. (28) and Eq. (35) for uniform and varying input point sources are shown with various graphs. The values of the parameters and empirical constants involved in the boundary conditions and the governing equations are taken from published papers, e.g. (Kumar et al., 2010)[21]. The parameters affecting the concentration distribution are illustrated with the help of various graphs.Contaminant concentration values are evaluated for longitudinal porous domains $0 \le x(km) \le 25$. The values of common input parameters and constants are assumed as follows:

$c_0(\mathrm{kg/km^3}) = 1.0, c_i(\mathrm{kg/km^3}) = 0.1, U_0(\mathrm{km/year}) = 0.65,$ $\mu_0(\mathrm{kg/km^3} year^{-1}) = 0.11, \gamma_0(year^{-1}) = 0.11.$

The mathematical expression for a time-dependent function $F(t)$ that varies in each time domain is assumed to be as follows:

$$F(t) = \begin{cases} exp\ (m_1 t)\ ; 0 \le t < t_1 \\ s_1\, exp(m_2(t-t_1)) + s_2\ ; t_1 \le t < t_2 \\ s_3 \dfrac{m_3(t-t_2)}{m_3(t-t_2)+1} + s_4; t_2 \le t < \infty \end{cases}$$

The values of the unsteady parameters m^*, m_1, m_2 and m_3 are $0.4(year^{-1})$, $0.1(year^{-1})$,$0.3\ (year^{-1})$ and $0.4\ (year^{-1})$, respectively. The values of time t_1 and t_2 are taken $1(year)$and $5(year)$, respectively and the value of $s_1 = 0.36839, s_2 = 0.736781\ s_3 = 0.917324$and $s_4 = 1.9598795012568466$, respectively.

Uniform input solution

Figs. (1-4) demonstrate the concentration pattern of a uniform input point source for a heterogeneous porous medium described by the analytical solution Eq. (28).

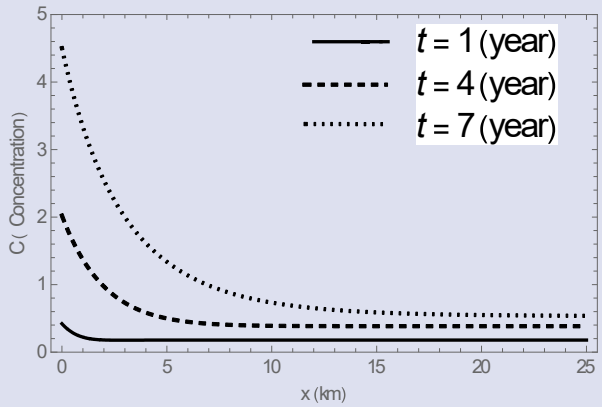

Figure 1. Contaminant concentration profile obtained in Eq. (28) for different time t(year)=1,4,7

Fig.(1) demonstrates dimensionless concentration distributions for different time $t(year) = 1,4,7$ and given groundwater velocity $U_0(kmyear^{-1}) = 0.65$, dispersion coefficients $D_0(km^2year^{-1}) = 0.67$ and retardation factor $R = 1.15$ while other parameters are fixed. It exemplifies the pattern of concentration dispersion caused by a constant uniform point source. Concentration levels were found to be higher for longer time, lower for shorter time, and then stabilize as moved away from the source boundary. The concentration value appears different at different times at the origin, decreases rapidly as the position increases, and tends to be stable at the other end.

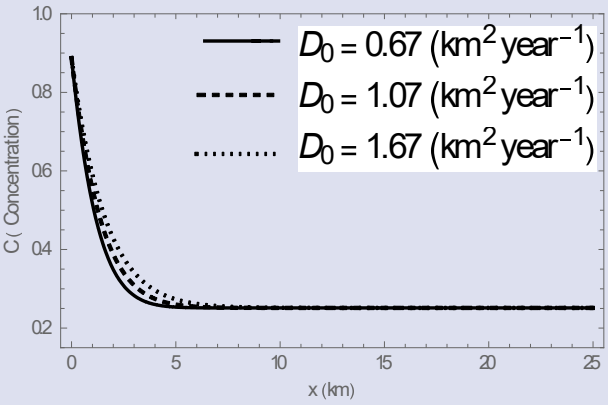

Figure 2. Contaminant concentration profile obtained in Eq. (28) for different dispersion $D_0(km^2year^{-1}) = 0.67,1.07,1.67$

Fig.(2) shows the effect of various dispersion coefficients $D_0(km^2year^{-1}) = 0.67,1.07,1.67$ on the concentration distribution for a specific period of time $t\,(year) = 2$ and retardation factor $R = 1.15$ while other parameters remain unchanged. It can be seen that the concentration pattern near the entry point becomes more pronounced as the dispersion coefficient increases. Although the concentration values for all dispersion coefficients at the entry point $(x = 0)$ are the same. The concentration level decreases with space from a starting point ($x = 0$) and becomes constant towards the outlet boundary.

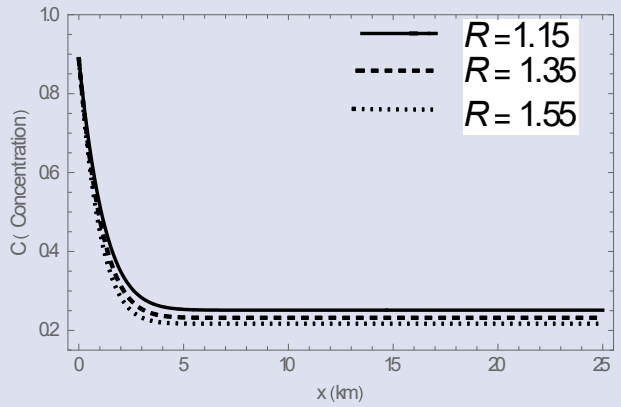

Figure 3. Contaminant concentration profile obtained in Eq. (28) for different retardation $R = 1.15,1.35,1.55$

Fig.(3) depicts the effect of several retardation factor $R = 1.15,1.35,1.55$for dispersion coefficient $D_0(km^2year^{-1}) = 0.67$, on pollutant concentrations at time $t(year) = 2$.For different retardation factors, the concentration values at the entry point are same, but fluctuations in the concentration distribution can be observed near the boundary point and towards the other boundary in the steady state.

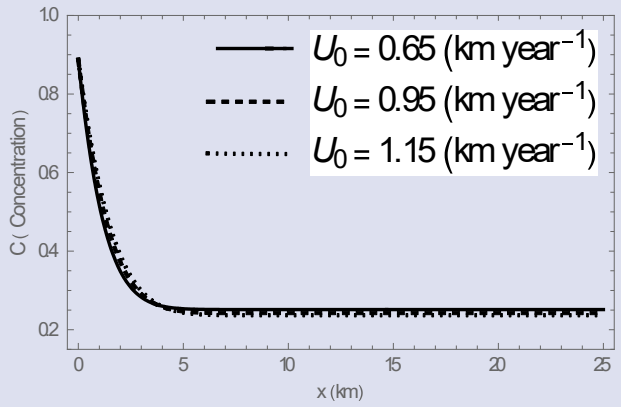

Figure 4. Contaminant concentration profile obtained in Eq. (28) for different velocity $U_0(kmyear^{-1}) = 0.65,0.95,1.15$

Fig. (4) shows the effect of variation of different ground water velocity $U_0(kmyear^{-1}) = 0.65,0.95,1.05$at common values of time $t(year) = 2$, retardation factor $R = 1.15$ and dispersion coefficient $D_0(km^2year^{-1}) = 0.67$, keeping the other parameters constant. It can be observed that the concentration pattern is higher for higher ground water velocity, the variation in the concentration distribution profile is quite significant the near inlet boundary. Near the middle position from $x = 1.5$ to $x = 2.4$, the greatest change can be seen.

Varying input solution

Figs. (5–8) display the solute concentration patterns for varying input point sources in the heterogeneous porous medium described by Eq. (35).

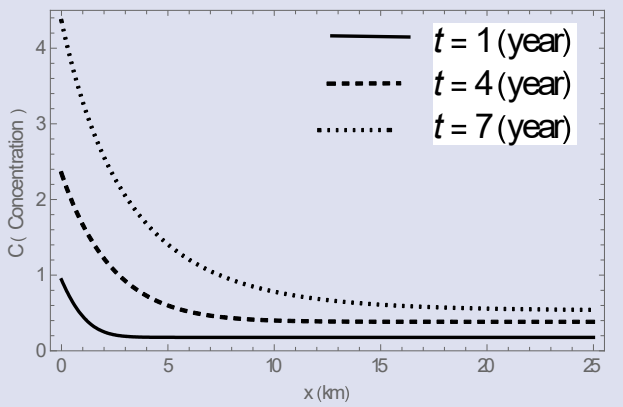

Figure 5. Contaminant concentration profile obtained in Eq. (35) for different time $t(year) = 1,4,7$

Fig.(5) illustrates the dimensionless concentration distribution for different time $t(year) = 1,4,7$and for fix retardation factor $R = 1.15$, ground water velocity $U_0(km\ year^{-1}) = 0.65$ and dispersion coefficient $D_0(km^2year^{-1}) = 0.67$. It reveals the concentration distribution pattern produced by a uniform continuous point source. Concentration levels near to the source boundary are observed to be higher for higher time and lower for lower time, and stabilize after a distance away from the origin.

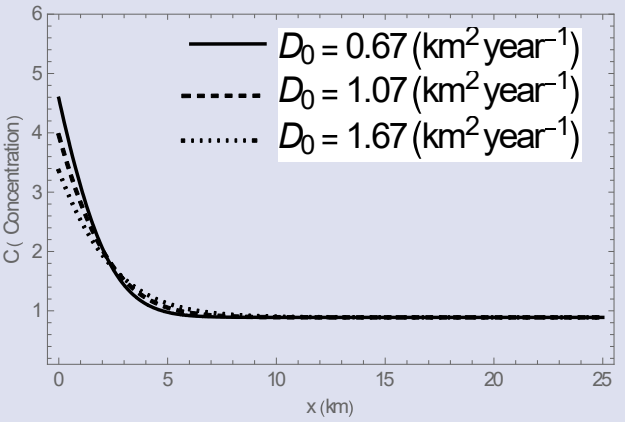

Figure 6. Contaminant concentration profile obtained in Eq. (35) for different dispersion $D_0(km^2year^{-1}) = 0.67,1.07,1.67$

Fig.6. shows the pollutant concentration with various dispersion coefficients$D_0(km^2year^{-1}) = 0.67,1.07,1.67$ at time $t(year) = 2$, retardation factor $R = 1.15$and ground water velocity $U_0(kmyear^{-1}) = 0.65$, keeping the other parameters fixed. The variation in solute concentration caused by various diffusion coefficients in both space and time are shown in this figure. It can be observed that at particular position the concentration level is higher for lower dispersion coefficient near the source boundary but after some distance traveled from the origin order gets reversed. This is due to the fact that dispersion phenomenon causes the spreading of the plume in the medium.

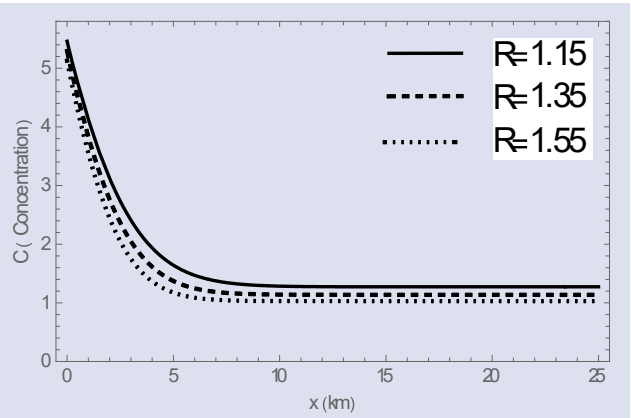

Figure 7. Contaminant concentration profile obtained in Eq. (35) for different retardation $R = 1.15,1.35,1.55$

Fig. (7) shows the pollutant concentration with various retardation factors $R = 1.15,1.35,1.55$ on the concentration distribution for dispersion coefficient at $D_0(km^2year^{-1}) = 0.67$, time $t(year) = 2$, ground water velocity $U_0(kmyear^{-1}) = 0.65$, and keeping all other parameters are fixed. For each location on a certain domain, the pollution concentration decreases as the retardation factor increases. The solute concentration is directly affected by the retardation factor (R) during solute transport. It is clear that as the retardation factor increases, the concentration level decreases, and near the inlet boundary, the concentration profile changes significantly. At particular point, the lower the retardation factor, the higher the concentration level.

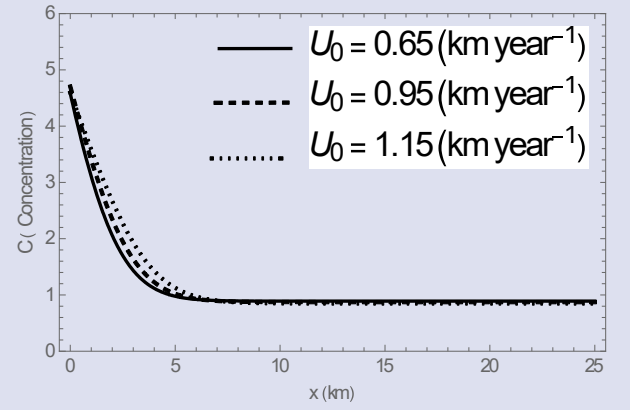

Figure 8. Contaminant concentration profile obtained in Eq. (35) for different velocity $U_0(kmyear^{-1}) = 0.65,0.95,1.15$

Fig.(8) shows the effect of groundwater flow velocity $U_0(year^{-1}) = 0.65,0.95,1.05$on the concentration profile for a fixed retardation factor$R = 1.15$ and dispersion coefficient$D_0(km^2year^{-1}) = 0.67$ at time $t(year) = 2$ and keeping all other parameters fixed. The concentration distribution fluctuates more near the inlet boundary, and it can also be observed that the higher the groundwater velocity, the steeper the concentration distribution.

Special Case I. If we take $c_i = 0, \gamma = 0, \mu = 0, R = 1, F(t) = 1, G(t) = 1$ in our model for uniform input point source then obtained analytical solution of the problem for uniform input point source is similar to one obtained by Kumar et al. (2010) [21]and given by;

$$c(X,t) = \begin{Bmatrix} c_0 Q_1(X,t) \\ exp(-\beta X + \rho^2 t) \end{Bmatrix} exp\left\{ \frac{U_1}{2D_0} X - \left(\frac{U_1^2}{4D_0} \right) t \right\} \quad (36)$$

where,

$$Q_1(X,t) = \frac{1}{2}\left\{ exp\left(\eta^2 t - \eta \sqrt{\frac{R_0}{D_0}} X \right) erfc\left(\frac{\sqrt{R_0}}{2\sqrt{D_0 T}} X - \eta\sqrt{t} \right) + exp\left(\eta^2 t + \eta \sqrt{\frac{R_0}{D_0}} X \right) erfc\left(\frac{\sqrt{R_0}}{2\sqrt{D_0 T}} X + \eta\sqrt{t} \right) \right\}$$

Special Case II. If we take $c_i = 0, \gamma = 0, \mu = 0, R = 1, F(t) = 1, G(t) = 1$ in our model for varying input point source then obtained analytical solution of the problem for varying input point source is similar to one obtained by Jaiswal et al. (2011) [22]and given by;

$$C(x,T) = \left\{ \frac{c_0 U_0}{\sqrt{D_0}} N(X,t) \right\} \exp\left(\frac{U_1}{2D_0} X - \left(\frac{U_1^2}{4D_0} \right) t \right) \quad (37)$$

where,

$$N(X,t) = \frac{1}{2(\eta+\sigma)} exp\left(\eta^2 t - \eta \sqrt{\frac{1}{D_0}} X \right) erfc\left(\frac{\sqrt{1}}{2\sqrt{D_0 T}} X - \eta\sqrt{t} \right) - \frac{1}{2(\eta-\sigma)} exp\left(\eta^2 t + \eta \sqrt{\frac{1}{D_0}} X \right) erfc\left(\frac{\sqrt{1}}{2\sqrt{D_0 t}} X + \eta\sqrt{t} \right) + \frac{\eta}{\eta^2 - \sigma^2} exp\left(\sigma^2 t + \sigma \sqrt{\frac{1}{D_0}} X \right) \times erfc\left\{ \frac{\sqrt{1}}{2\sqrt{D_0 t}} X + \sigma\sqrt{t} \right\},$$

Conclusions

With solute degrading at varying rate, an analytical solution of this kind vividly shows concentration details at various time domains. Such solutions are important for assessing contamination levels in a variety of downstream conditions away from the source of ingestion. From the obtained solution, we can estimate the variation of the concentration with time and space. The fact that the values of groundwater velocity and diffusivity vary over time intervals makes the results more realistic. The obtained results show that temporally

dependent input sources have a significant impact on pollutant transport. The two key parameters, diffusion coefficient and retardation factor, have a great influence on the change of solute concentration. Aquifers are generally heterogeneous in nature. Current mathematical models can predict the concentration of pollutants in the medium, which can help to take remedial measures. The developed mathematical model can be considered as an effective tool for understanding the transport behavior of pollutants in surface water and groundwater phenomena. Changes in dispersion and velocity have an impact on the levels of pollutant concentration in the aquifer system. From the obtained solution we can estimate the variation of the concentration with time and space. The results of this study can be used to enhance the planning and management of water pollution problems, as well as the many physical conditions defined by traffic phenomena.

Conflicts of interest

There are no conflicts of interest in this work.

References

[1] Shi X., Lei T., Yan Y., Zhang F., Determination and impact factor analysis of hydrodynamic dispersion coefficient within a gravel layer using an electrolyte tracer method, *International Soil and Water Conservation Research*, 4(2) (2016) 87–92.

[2] Guerrero J. S. P., Pontedeiro E. M. Van Genuchten M. T., Skaggs T. H., Analytical solutions of the one-dimensional advection– dispersion solute transport equation subject to time-dependent boundary conditions, *Chem. Eng. J.*, 221(2013) 487–491.

[3] Bear J., Dynamics of flow in porous media*. New York: American ElsevierPublishing Co,* (1972).

[4] Mishra S., Brigham W. E., Orr Jr. E. M., Tracer and pressure test analysis for characterization of areally heterogeneous reservoirs, *Soc. Pet. Engrs. J.,* 22(4) (1991) 479-489.

[5] Elder J. W., The dispersion of marked fluid in turbulent shear flow, *J. Fluid Mech.*, 5 (1959) 544-560.

[6] Fischer H. B., The mechanics of dispersion in natural streams, *J. Hydraul. Div*. *ASCE*, 93(6) (1967) 187-216.

[7] Gelhar L. W., Gross G. W., Duffy C. J., Stochastic methods of analysing groundwater recharge In: Hydrology of areas of low precipitation, *In Proc. of the Camberra Symp.,* (1979) 313-321.

[8] Valocchi A. J., Spatial moment analysis of the transport of kinetically adsorbing solutes through stratified aquifers, *Water Resources Research*, 25(2) (1989) 273-279.

[9] Shan C., Javandle I., Analytical solutions for solute transport in a vertical aquifer section, *Journal of Contaminant Hydrology*, 27(1-2) (1997) 63-82.

[10] Wadi A. S., Dimian M. F., Ibrahim F. N., Analytical solutions for one-dimensional advection–dispersion equation of the pollutant concentration, *Journal of Earth System Science*, 123(2014) 1317-1324.

[11] Kumar A., Yadav R. R., One-dimensional solute transport for uniform and varying pulse type input point source through heterogeneous medium, *Environmental Technology*, 36(4) (2014) 487-495.

[12] Natarajan N., Effect of distance-dependent and time-dependent dispersion on nonlinearly sorbed multispecies contaminants in porous media, *ISH Journal of Hydraulic Eng*., 22 (2016) 16-29.

[13] Rubol S., Battiato I, De Barros F. P., Vertical dispersion in vegetated shear flows, *Water Resources Research*, 52(10) (2016) 8066-8080.

[14] Kumar R., Chatterjee A., Singh M. K., Singh V. P., Study of solute dispersion with source/sink impact in semi-infinite porous medium, *Pollution ,* 6(1) (2019) 87-98.

[15] Younes A., Fahs M., Ataie-Ashtiani B., Simmons C. T., Effect of distance-dependent dispersivity on density-driven flow in porous media, *Journal of Hydrology.,* 589 (2020) 125204.

[16] Yadav R. R., Kushwaha S., Roy J, Kumar, L.K., Analytical Solutions for Scale and Time Dependent solute transport in heterogeneous sorous medium, *Journal of Water Resources and Ocean Science,* 12(1) (2023) (1-11).

[17] Raafat P.B., Ibrahim F.N., Saleh A., On determining conditions and suitable locations for fish survival by using the solution of the two coupled pollution and aeration equations, Sci. Rep., 13 6560 (2023).

[18] Esmail S., Agrawal P., Shaban A., A novel analytical approach for advection diffusion equation for radionuclide release from an area source, *Nuclear Engineering and Technology*, 52(4) (2020) 819-826

[19] Yadav R. R., Kumar L. K., Two-dimensional conservative solute transport with temporal and scale-dependent dispersion: Analytical solution, *International Journal of Advance in Mathematics*, 2 (2018) 90-111.

[20] Crank J., The Mathematics of Diffusion, Oxford Univ. Press, London, 2nd Ed., (1975).

[21] Kumar A., Jaiswal D. K., Kumar N., Analytical solutions to one-dimensional advection-diffusion equation with variable coefficients in semi-infinite media, *J. Hydrol*., 380(3-4) (2010) 330-337.

[22] Jaiswal D. K., Kumar A., Analytical solutions of advection-dispersion equation for varying pulse type input point source in one-dimension, *International Journal of Engineering, Science and Technology*, 3(1) (2011) 22-29.

Cumhuriyet Sci. J., 44(3) (2023) 547-560
DOI: https://doi.org/10.17776/csj.1293551

Cumhuriyet Science Journal

| csj.cumhuriyet.edu.tr | Founded: 2002 ISSN: 2587-2680 e-ISSN: 2587-246X Publisher: Sivas Cumhuriyet University

3D Stabilized FEM Solution of the MHD Equations in an External Medium and Around a Solid

Selçuk Han Aydın[1,a,*], Mahir Ceylan Erdoğan[1,b]

[1] *Department of Mathematics, Faculty of Science, Karadeniz Technical University, Trabzon, Türkiye*
**Corresponding author*

Research Article

History
Received: 06/05/2023
Accepted: 30/08/2023

ABSTRACT

In this study, we consider 3-D MagnetoHydroDynamic (MHD) flow problems with different configurations which are mathematically expressed by system of coupled partial differential equation with coupled boundary conditions. These equations are solved numerically using one of the most popular schemes named as the finite element method (FEM) with SUPG type stabilized version in order to obtain accurate and stable solutions especially for the high values of the problem parameters. Obtained numerical solutions are visualized in terms of figures by taking the 2-D slices of the 3-D data in order to emphasize the accuracy of the proposed formulation.

Keywords: 3D-FEM, Stabilization, MHD flow, Exterior medium, Conducting solid.

[a] *shaydin@ktu.edu.tr* *https://orcid.org/0000-0002-1419-9458* [b] *erdoganmahir@gmail.com* *https://orcid.org/0000-0001-9775-5271*

Introduction

Besides the recent developments in the numerical methods, the finite element method (FEM) is one of the oldest but still popular numerical scheme for the solution of the engineering and mathematical boundary value problems even defined in complex geometries. Therefore, many researchers are paid attention to generate the different version of FEM with the combination of other modern numerical schemes. As results of these attentions, thousands of papers and hundreds of books are produced in the academic literature. H-version, p-version, hp-adaptive version, scaled boundary finite element version, stabilized versions, discontinuous version, extended version and smoothed versions are the most known ones. In order to formulate the real life problems, 3D-FEM is well suited numerical scheme for the solutions of the problems that don't have the analytical result. Therefore addition to 2-D case, we will pay attention to 3-D FEM applications (see [1-16] and references therein).

Noticed that, after 20^{th} century many authors performed both analytical and numerical studies about MagnetoHydroDynamic (MHD) due to the it's applications in many different areas such as MHD ion propulsion, liquid-metal and cooling of nuclear reactors, power generation, etc. Derivation of the corresponding differential equations using the Navier-Stokes equations, Maxwell equations with the Lorentz force and the theory of the MHD can be found in [17-19].

It is known that the value of the Hartmann number that exist in the MHD flow equations is large for the case of strong magnetic applications in which case the corresponding equation becomes convection dominated. However, standard numerical methods have some numerical troubles in the sense of stability for these type of problems. The FEM has advantage that one can consider different stabilization techniques additional to the standard formulation. Streamline Upwind Petrov-Galerkin (SUPG) method [20] is one of the mostly preferred stabilization technique in which stable solutions are obtained by adding mesh-dependent terms to the standard Galerkin FEM formulation. Even there are many papers in different areas as applications of MHD and stabilized FEM, let's refer only a few of them on recent years [21-34] and references therein.

We first considered the solution of the 2-D version of the coupled MHD equation which is firstly introduced in [35] with magnetic induction of exterior region using the Boundary Element Method (BEM) in [36] and DRBEM [37]. Then FEM-BEM coupling approach with stabilization is applied to the extended version of the problem by considering an insulated solid inside the fluid case in [38]. As a further stage, we decided to consider the 3-D version of the same problem. Firstly, as a 3-D application of FEM-BEM coupling approach is applied by Han Aydın in [39]. After giving the details of the stabilization in 3-D FEM in [40], this study is prepared as the next step application of the most general case of the coupled MHD problem in 3-D domains. Another contribution of this study to the literature beside the 3-D stabilized FEM application is obtaining the accurate solutions of the huge sized sparse systems using open source libraries. Therefore, as our knowledge, this study will fill the gap

on literature in this research area and demonstrate FEM only solution of the MHD equations.

The rest of the paper is organized as follows: The following section describes the mathematical modeling and FEM formulation of the considered 3 different cases with the addition stabilized terms0. In Numerical Results and Discussion we will display the figures of the obtained numerical solutions with required explanations. Finally, some concluding remarks are provided in the last section.

Mathematical Modeling

Mathematical modeling of the considered MHD flow problem can be derived using Navier-Stokes equations and Maxwell equations from electromagnetic theory using also the Ohm's law. Before writing the corresponding coupled system of partial differential equations, let's define some notations. The subscripts s, f [or F] and e corresponds to solid, fluid and external medium, respectively. Then the solid domain is $\Omega_s \in IR^3$, the fluid domain is $\Omega_f \in IR^3$ and the domain of the external medium is $\Omega_e \in IR^3$. Similarly, the normal vectors are also defined as n_s, n_f, n_e. The parameters Re, Rh, Rm_s, Rm_f and Rm_e are the Reynolds number, magnetic pressure, magnetic Reynolds number of the solid, magnetic Reynolds number of the fluid and magnetic Reynolds number of the external medium, respectively.

We consider 3 different problem configurations in the context of this study as;

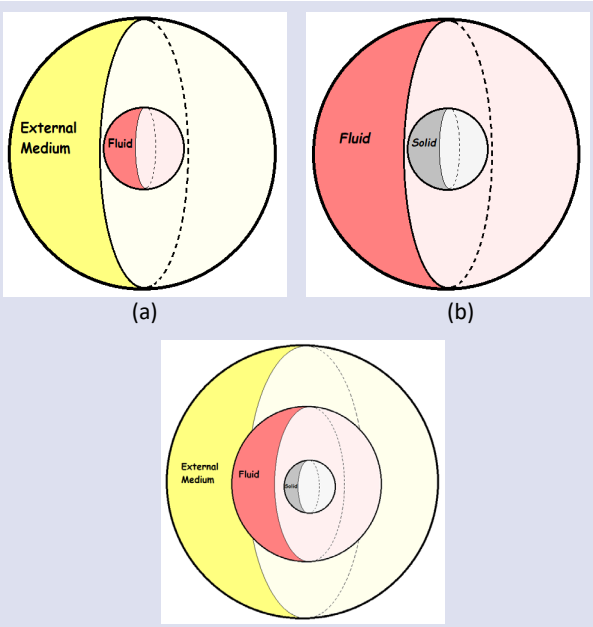

Figure 1. Problem configurations for different three cases

Case 1: Fluid inside an external medium

This is the first case of the considered MHD problem. We assume that the fluid is through the domain $\Omega_f$due to the constant pressure gradiend and the fluid is viscous, incompressible and electrically conducting. Also there is an externally applied magnetic field with an intensity $B_0$where it's direction through x axis with and angle β and through z axis with and angle α. The fluid domain is surrounded with an electrically conducting external domain Ω_e Figure 1(a). Then the system of coupled partial differential equations are defined as [39].

$$\left.\begin{aligned} \nabla^2 V^f + Re \cdot Rh \cdot (sin\,\alpha\, cos\,\beta \frac{\partial B^f}{\partial x} + sin\,\alpha\, sin\,\beta \frac{\partial B^f}{\partial y} + cos\,\alpha \frac{\partial B^f}{\partial z}) = -1 \\ \nabla^2 B^f + Rm_f \cdot (sin\,\alpha\, cos\,\beta \frac{\partial V^f}{\partial x} + sin\,\alpha\, sin\,\beta \frac{\partial V^f}{\partial y} + cos\,\alpha \frac{\partial V^f}{\partial z}) = 0 \end{aligned}\right\} \quad in\ \Omega_f \tag{1}$$

$$\nabla^2 B^e = 0 \quad in\ \Omega_e \tag{2}$$

with the boundary conditions

$$\left.\begin{aligned} V^f = 0 \\ B^e = B^f \\ \frac{1}{Rm_e}\frac{\partial B^e}{\partial n_e} = \frac{1}{Rm_f}\frac{\partial B^f}{\partial n_f} \end{aligned}\right\} \quad \in \partial\Omega_f \cap \partial\Omega_e = \Gamma_{fe}\,. \tag{3}$$

Noticed that even the external medium is unbounded, due to the FEM formulation, we need to define an artificial boundary on the outer side of the external domain Ω_e as $\Gamma_e$for the domain discretization where either $B^e = 0$ (known as the Drichlet type boundary condition) or $\frac{\partial B^e}{\partial n_e} = 0$ (Neumann type boundary condition) are specified on that boundary. The Drichlet type boundary condition is compatible with the behavior of the real potential solution of B^e such that it is assumed that $B^e \to 0$ as $[x^2 + y^2 + z^2] \to \infty$which is called as Saint-Venant principle [36]. Similarly, the Neumann type boundary condition corresponds to the free exit behavior of the induced magnetic field. However, if this type of boundary condition is specified, induced magnetic field solutions can be obtained up to a constant. Therefore, in order to obtain a unique solution, the obtained induced magnetic values should be normalized by using the identity

$$\iiint_\Omega B d\Omega = 0 \tag{4}$$

where $B = B^s \cup B^f \cup B^e$.

Case 2: Fluid around a solid

As a second case, we assume that there is an electrically conducting solid inside the fluid having the domain Ω_s (Figure 1(b)). The rest of the fluid conditions are all same as in the previous case. Then, the system of equations and the boundary conditions are written as;

$$\nabla^2 B^s = 0 \quad in\ \Omega_s \tag{5}$$

$$\left.\begin{aligned} \nabla^2 V^f + Re \cdot Rh \cdot (\sin\alpha\cos\beta\frac{\partial B^f}{\partial x} + \sin\alpha\sin\beta\frac{\partial B^f}{\partial y} + \cos\alpha\frac{\partial B^f}{\partial z}) = -1 \\ \nabla^2 B^f + Rm_f \cdot (\sin\alpha\cos\beta\frac{\partial V^f}{\partial x} + \sin\alpha\sin\beta\frac{\partial V^f}{\partial y} + \cos\alpha\frac{\partial V^f}{\partial z}) = 0 \end{aligned}\right\} \quad in\ \Omega_f \tag{6}$$

with the coupled boundary conditions on the intersection of the fluid and solid domains as

$$\left.\begin{aligned} V^f = 0 \\ B^f = B^s \\ \frac{1}{Rm_f}\frac{\partial B^f}{\partial n_f} = \frac{1}{Rm_s}\frac{\partial B^s}{\partial n_s} \end{aligned}\right\} \quad \in \partial\Omega_f \cap \partial\Omega_s = \Gamma_{sf} \tag{7}$$

and additionally we assume that the exterior side of the fluid domain is insulated so $B^f = 0$ on that boundary.

Case 3: Fluid around a solid and inside an external medium

Finally, in the third case which is the combination of the first two cases, we consider a fluid both inside an electrically conducting exterior medium and around a conducting medium Figure 1(c). Then the full system of equations are written as:

$$\nabla^2 B^s = 0 \quad in\ \Omega_s \tag{8}$$

$$\left.\begin{aligned} \nabla^2 V^f + Re \cdot Rh \cdot (\sin\alpha\cos\beta\frac{\partial B^f}{\partial x} + \sin\alpha\sin\beta\frac{\partial B^f}{\partial y} + \cos\alpha\frac{\partial B^f}{\partial z}) = -1 \\ \nabla^2 B^f + Rm_f \cdot (\sin\alpha\cos\beta\frac{\partial V^f}{\partial x} + \sin\alpha\sin\beta\frac{\partial V^f}{\partial y} + \cos\alpha\frac{\partial V^f}{\partial z}) = 0 \end{aligned}\right\} \quad in\ \Omega_f \tag{9}$$

$$\nabla^2 B^e = 0 \quad in\ \Omega_e \tag{10}$$

with the boundary conditions on the intersection of the fluid and solid domains as

$$\left.\begin{aligned} V^f = 0 \\ B^f = B^s \\ \frac{1}{Rm_f}\frac{\partial B^f}{\partial n_f} = \frac{1}{Rm_s}\frac{\partial B^s}{\partial n_s} \end{aligned}\right\} \quad \in \partial\Omega_f \cap \partial\Omega_s = \Gamma_{sf} \text{ and } \left.\begin{aligned} V^f = 0 \\ B^e = B^f \\ \frac{1}{Rm_e}\frac{\partial B^e}{\partial n_e} = \frac{1}{Rm_f}\frac{\partial B^f}{\partial n_f} \end{aligned}\right\} \quad \in \partial\Omega_f \cap \partial\Omega_e = \Gamma_{fe} \tag{11}$$

and similar to the first case, on Γ_e either $B^e = 0$or $\frac{\partial B^e}{\partial n_e} = 0$.

FEM Formulation

As a first step we will reformulate the given equation in the fluid domain by change of a new variable B^Fas $B^F = \frac{Re\cdot Rh\cdot B^f}{Ha}$ where $Ha = \sqrt{Re \cdot Rh \cdot Rm_f}$ is the Hartmann number of the fluid. Then the equations are written in the new form as [39]

$$\left.\begin{aligned} \nabla^2 V^f + \left[M_x\frac{\partial B^F}{\partial x} + M_y\frac{\partial B^F}{\partial y} + M_z\frac{\partial B^F}{\partial z}\right] = -1 \\ \nabla^2 B^F + \left[M_x\frac{\partial V^f}{\partial x} + M_y\frac{\partial V^f}{\partial y} + M_z\frac{\partial V^f}{\partial z}\right] = 0 \end{aligned}\right\} \ in\ \Omega_f \tag{12}$$

for $M_x = Ha\sin\alpha\cos\beta$, $M_y = Ha\sin\alpha\sin\beta$ and $M_z = Ha\cos\alpha$. Then as a second step, we will decouple these coupled equations using the following transformation by defining the new variables $U_1(x,y,z)$ and $U_2(x,y,z)$ as

$$\begin{aligned} U^1 &= V^f + B^F, \\ U^2 &= V^f - B^F, \end{aligned} \tag{13}$$

then equations become

$$\nabla^2 B^s = 0 \quad in\ \Omega_s \tag{14}$$

$$\left.\begin{aligned} \nabla^2 U^1 + M\cdot\nabla U^1 &= -1 \\ \nabla^2 U^2 - M\cdot\nabla U^2 &= -1 \end{aligned}\right\} in\ \Omega_f \tag{15}$$

$$\nabla^2 B^e = 0 \quad in\ \Omega_e \tag{16}$$

where $M = (M_x, M_y, M_z)$.

Before obtaining the finite element formulation of the given equations, let's define the required function spaces.

- $L^2(\Omega)$: the space of square integrable functions over the domain Ω,
- $H^1(\Omega)$: the Sobolev space of $L^2(\Omega)$ functions whose derivatives are square integrable functions in Ω,
- $H_0^1(\Omega)$: the Sobolev subspace of $H^1(\Omega)$ functions in Ω with zero value on the boundary $\partial\Omega$.

In order to construct the FEM formulation, the problem domain should be partitioned to the elements (linear tetrahedron elements in our computations) in a standard way (e.g. no overlapping, no vertex on the edge or side of a neighboring elements, etc). Then, we can obtain the standard Galerkin FEM weak formulation to the these decoupled system of equations by employing the linear function space $L = (H_0^1(\Omega))^2$ as: Find $\{B^s; U^1; U^2; B^e\} \in \{L\times L\times L\times L\}$ such that

$$\begin{aligned} &a(\nabla B^s, \nabla s) - \ell(\frac{\partial B^s}{\partial n_s}, s) + a(\nabla U^1, \nabla w^1) - b(M_x\frac{\partial U^1}{\partial x} + M_y\frac{\partial U^1}{\partial y} + M_z\frac{\partial U^1}{\partial z}, w^1) - \ell(\frac{\partial U^1}{\partial n_f}, w^1) \\ &\quad + a(\nabla U^2, \nabla w^2) + b(M_x\frac{\partial U^2}{\partial x} + M_y\frac{\partial U^2}{\partial y} + M_z\frac{\partial U^2}{\partial z}, w^2) - \ell(\frac{\partial U^2}{\partial n_f}, w^2) + a(\nabla B^e, \nabla e) \\ &\quad - \ell(\frac{\partial B^e}{\partial n_e}, e) = b(1, w^1) + b(1, w^2) \end{aligned} \tag{17}$$

$\forall\{s; w^1; w^2; e\} \in \{L\times L\times L\times L\}$ where $a(\nabla u, \nabla v)$, $b(u,v)$ and $\ell(u,v)$ are the usual bi-linear and linear forms for the domain and boundary integrals such that

$$a(\nabla u, \nabla v) = \iiint_\Omega \left(\frac{\partial u}{\partial x}\frac{\partial v}{\partial x} + \frac{\partial u}{\partial y}\frac{\partial v}{\partial y} + \frac{\partial u}{\partial z}\frac{\partial v}{\partial z}\right) d\Omega, \quad b(u,v) = \iiint_\Omega (uv)\, d\Omega$$

and $\ell(\frac{\partial u}{\partial n}, v) = \iint_\Gamma \left(\frac{\partial u}{\partial n} v\right) d\partial\Omega$

Then, the variational formulation is written by the choice of finite dimensional subspaces $L_h \subset L$, defined by discretization of the domain to the linear tetrahedron elements as [7]: Find $\{{B_h}^s; {U_h}^1; {U_h}^2; {B_h}^e\} \in \{L_h\times L_h\times L_h\times L_h\}$ such that

$$\begin{aligned} &a(\nabla {B_h}^s, \nabla s_h) - \ell(\frac{\partial {B_h}^s}{\partial n_s}, s_h) + a(\nabla {U_h}^1, \nabla {w_h}^1) - b(M_x\frac{\partial {U_h}^1}{\partial x} + M_y\frac{\partial {U_h}^1}{\partial y} + M_z\frac{\partial {U_h}^1}{\partial z}, {w_h}^1) - \ell(\frac{\partial {U_h}^1}{\partial n_f}, {w_h}^1) \\ &\quad + a(\nabla {U_h}^2, \nabla {w_h}^2) + b(M_x\frac{\partial {U_h}^2}{\partial x} + M_y\frac{\partial {U_h}^2}{\partial y} + M_z\frac{\partial {U_h}^2}{\partial z}, {w_h}^2) - \ell(\frac{\partial {U_h}^2}{\partial n_f}, {w_h}^2) \\ &\quad + a(\nabla {B_h}^e, \nabla e_h) - \ell(\frac{\partial {B_h}^e}{\partial n_e}, e_h) = b(1, {w_h}^1) + b(1, {w_h}^2) \end{aligned} \tag{18}$$

$\forall\{s_h; {w_h}^1; {w_h}^2; e_h\} \in \{L_h\times L_h\times L_h\times L_h\}$

$$a(\nabla {B_h}^s, \nabla s_h) - \ell(\frac{\partial {B_h}^s}{\partial n_s}, s_h) + a(\nabla {U_h}^1, \nabla {w_h}^1) - b(M_x \frac{\partial {U_h}^1}{\partial x} + M_y \frac{\partial {U_h}^1}{\partial y} + M_z \frac{\partial {U_h}^1}{\partial z}, {w_h}^1) - \ell(\frac{\partial {U_h}^1}{\partial n_f}, {w_h}^1)$$
$$+ \tau_K \cdot b(-M_x \frac{\partial {U_h}^1}{\partial x} - M_y \frac{\partial {U_h}^1}{\partial y} - M_z \frac{\partial {U_h}^1}{\partial z} - 1, -M_x \frac{\partial {w_h}^1}{\partial x} - M_y \frac{\partial {w_h}^1}{\partial y} - M_z \frac{\partial {w_h}^1}{\partial z})$$
$$+ a(\nabla {U_h}^2, \nabla {w_h}^2) + b(M_x \frac{\partial {U_h}^2}{\partial x} + M_y \frac{\partial {U_h}^2}{\partial y} + M_z \frac{\partial {U_h}^2}{\partial z}, {w_h}^2) - \ell(\frac{\partial {U_h}^2}{\partial n_f}, {w_h}^2) + \tau_K \quad (19)$$
$$\cdot b(M_x \frac{\partial {U_h}^2}{\partial x} + M_y \frac{\partial {U_h}^2}{\partial y} + M_z \frac{\partial {U_h}^2}{\partial z} - 1, M_x \frac{\partial {w_h}^2}{\partial x} + M_y \frac{\partial {w_h}^2}{\partial y} + M_z \frac{\partial {w_h}^2}{\partial z}) + a(\nabla {B_h}^e, \nabla e_h)$$
$$- \ell(\frac{\partial {B_h}^e}{\partial n_e}, e_h) = b(1, {w_h}^1) + b(1, {w_h}^2)$$

with the stabilization parameter

$$\tau_K = \begin{cases} \dfrac{h_K}{2Ha} \text{ if } Pe_k \geq 1 \\ \dfrac{h_K^2}{12} \text{ if } Pe_k < 1 \end{cases} \quad (20)$$

where h_K h_K is the diameter of the element Kwhich is calculated as the longest side of the corresponding tetrahedron element, $Pe_K = h_K \frac{Ha}{6}$ is the Peclet number.

Now, one can turn back to original unknowns with inverse transformations

$$V^f = \frac{U^1 + U^2}{2} \text{ and } B^F = \frac{U^1 - U^2}{2} \quad \rightarrow \quad B^f = \frac{Ha}{Re \cdot Rh} B^F \quad (21)$$

and since the coefficients $\frac{Rm_f}{Rm_e} \geq 1$ and $\frac{Rm_f}{Rm_s} \geq 1$, use the relations in the coupled boundary conditions as

$$\frac{\partial B^f}{\partial n_f} = \frac{Rm_f}{Rm_s} \frac{\partial B^s}{\partial n_s} \quad \text{and} \quad \frac{\partial B^f}{\partial n_f} = \frac{Rm_f}{Rm_e} \frac{\partial B^e}{\partial n_e} \quad (22)$$

Then one gets the final variational form of the equations as

$$a(\nabla {B_h}^s, \nabla s_h) - \ell(\frac{\partial {B_h}^s}{\partial n_s}, s_h) + a(\nabla {U_h}^1, \nabla {w_h}^1) - b(M_x \frac{\partial {U_h}^1}{\partial x} + M_y \frac{\partial {U_h}^1}{\partial y} + M_z \frac{\partial {U_h}^1}{\partial z}, {w_h}^1) - \ell(\frac{\partial {U_h}^1}{\partial n_f}, {w_h}^1) + \tau_K \cdot$$
$$b(-M_x \frac{\partial {U_h}^1}{\partial x} - M_y \frac{\partial {U_h}^1}{\partial y} - M_z \frac{\partial {U_h}^1}{\partial z} - 1, -M_x \frac{\partial {w_h}^1}{\partial x} - M_y \frac{\partial {w_h}^1}{\partial y} - M_z \frac{\partial {w_h}^1}{\partial z}) + a(\nabla {U_h}^2, \nabla {w_h}^2) + b(M_x \frac{\partial {U_h}^2}{\partial x} + \quad (23)$$
$$M_y \frac{\partial {U_h}^2}{\partial y} + M_z \frac{\partial {U_h}^2}{\partial z}, {w_h}^2) - \ell(\frac{\partial {U_h}^2}{\partial n_f}, {w_h}^2) + \tau_K \cdot b(M_x \frac{\partial {U_h}^2}{\partial x} + M_y \frac{\partial {U_h}^2}{\partial y} + M_z \frac{\partial {U_h}^2}{\partial z} - 1, M_x \frac{\partial {w_h}^2}{\partial x} + M_y \frac{\partial {w_h}^2}{\partial y} +$$
$$M_z \frac{\partial {w_h}^2}{\partial z}) + a(\nabla {B_h}^e, \nabla e_h) - \ell(\frac{\partial {B_h}^e}{\partial n_e}, e_h) = b(1, {w_h}^1) + b(1, {w_h}^2)$$

We will obtain the system of linear equations in matrix-vector forms

Case 1:
$$\begin{bmatrix} K+S & -Re \cdot Rh \cdot C & 0 \\ -Rm_f \cdot C & K+S & -\frac{Rm_f}{Rm_e} \cdot Q \\ 0 & 0 & K \end{bmatrix} \begin{Bmatrix} V^f \\ B^f \\ B^e \end{Bmatrix} = \begin{Bmatrix} R_1 \\ R_2 \\ 0 \end{Bmatrix} \quad (24)$$

Case 2:
$$\begin{bmatrix} K & 0 & 0 \\ 0 & K+S & -Re \cdot Rh \cdot C \\ -\frac{Rm_f}{Rm_s} \cdot Q & -Rm_f \cdot C & K+S \end{bmatrix} \begin{Bmatrix} B^s \\ V^f \\ B^f \end{Bmatrix} = \begin{Bmatrix} 0 \\ R_1 \\ R_2 \end{Bmatrix} \quad (25)$$

Case 3:
$$\begin{bmatrix} K & 0 & 0 & 0 \\ 0 & K+S & -Re \cdot Rh \cdot C & 0 \\ -\frac{Rm_f}{Rm_s} \cdot Q & -Rm_f \cdot C & K+S & -\frac{Rm_f}{Rm_e} \cdot Q \\ 0 & 0 & 0 & K \end{bmatrix} \begin{Bmatrix} B^s \\ V^f \\ B^f \\ B^e \end{Bmatrix} = \begin{Bmatrix} 0 \\ R_1 \\ R_2 \\ 0 \end{Bmatrix} \quad (26)$$

where K, C, S and Q are the matrices and R_1 and R_2 are the vectors with the entries

$$K_{ij} = \iiint_\Omega \left(\frac{\partial N_i}{\partial x} \frac{\partial N_j}{\partial x} + \frac{\partial N_i}{\partial y} \frac{\partial N_j}{\partial y} + \frac{\partial N_i}{\partial z} \frac{\partial N_j}{\partial z} \right) d\Omega,$$

$$C_{ij} = \iiint_{\Omega} \left(M_x \frac{\partial N_i}{\partial x} + M_y \frac{\partial N_i}{\partial y} + M_z \frac{\partial N_i}{\partial z} \right) N_j d\Omega, \quad Q_{ij} = \iint_{\Gamma} \frac{\partial N_i}{\partial n} N_j d\,\partial\Omega,$$

$$S_{ij} = \iiint_{\Omega} \tau_K \left(M_x \frac{\partial N_i}{\partial x} + M_y \frac{\partial N_i}{\partial y} + M_z \frac{\partial N_i}{\partial z} \right) \left(M_x \frac{\partial N_j}{\partial x} + M_y \frac{\partial N_j}{\partial y} + M_z \frac{\partial N_j}{\partial z} \right) d\Omega,$$

$$R_{1_i} = \iiint_{\Omega} N_i d\Omega, \quad R_{2_i} = \iiint_{\Omega} \tau_K \left(M_x \frac{\partial N_i}{\partial x} + M_y \frac{\partial N_i}{\partial y} + M_z \frac{\partial N_i}{\partial z} \right) d\Omega.$$

One can obtain the all unknown values from the solution of these system of linear equations. Noticed that, due to the structure of the FEM formulation, obtained linear system of equations are in sparse form. Therefore it is better to solve the system using an efficient sparse solver.

Highlights of the Algorithm

- Initialize the parameters and the problem domain.
- Calculate the element matrices and vectors using the stabilized formulation (if the element is on the fluid domain) and apply the global matrix contribution.
- Apply the boundary conditions
- Solve the obtained system using Umfpack sparse solver.

Numerical Results and Discussion

In this section, we will demonstrate the proposed numerical scheme over some test problems in terms of the contour line figures as 2-D slices of the 3-D domain solutions. The problem domains are selected as $\Omega_s = \{(x,y,z) \,|\, x^2 + y^2 + z^2 \le 1\}$, $\Omega_f = \{(x,y,z) \,|\, x^2 + y^2 + z^2 \le 1\}$ for Case1 and $\Omega_f = \{(x,y,z) \,|\, 1 \le x^2 + y^2 + z^2 \le 4\}$ for Cases 2 and 3 and $\Omega_e = \{(x,y,z) \,|\, 1 \le x^2 + y^2 + z^2 \le 4\}$ for Case 1 and $\Omega_e = \{(x,y,z) \,|\, 4 \le x^2 + y^2 + z^2 \le 9\}$ for Case 3. For the comparision, we have also tested the cubic domain for Case1 as $\Omega_f = \{(x,y,z) \,|\, -1 \le x,y,z \le 1\}$ and $\Omega_e = \{(x,y,z) \,|\, -2 \le x,y,z \le 2\} \setminus \Omega_f$. Additionally, all we know that the resulting coefficient matrix in FEM formulation is in sparse form and its size is too large for the 3-D domain problems especially for the Case 3. On the numerical implementation side, user modified version of an open source sparse solver UMFPACK with long integer data types for the large sized systems is used with OpenMP support in GNU Fortran compiler in order to reduce the storage size and the computational time. Finally, the domain integrals over the tetrahedron elements and and the boundary integrals over the triangular elements are calculated numerilcally using 5 points and 4 points numerical quadrature methods, respectively such that numerical values are equal to the analytical values of the integrals.

Effect of the stabilization:

Before giving the results for the considered cases, we want to display the effect of the stabilization. It is seen from Figure 2 that even over the rough mesh and high values of the problem parameters ($\mathrm{Re} = 10,\ Rh = 10,\ Rm_f = 100$), there are some instabilities and oscillations on the solution contours obtained from standard Galerkin FEM formulation (left sub-figures (a) and (c)), the stabilized formulation eliminates these numerical difficulties (right sub-figures (b) and (d)) especially on the velocity solutions.

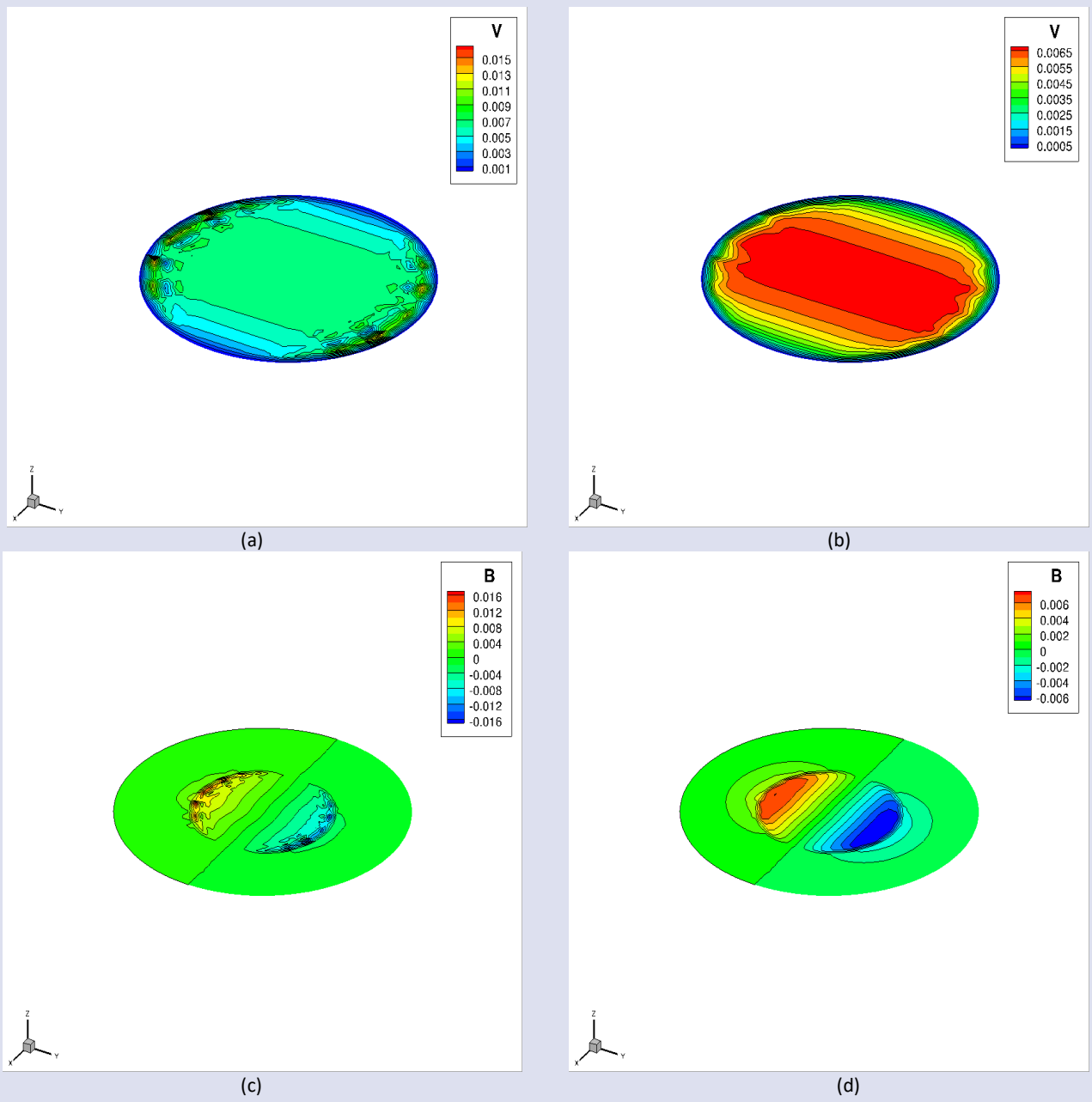

Figure 2. Velocity (a-b) and induced magnetic field (c-d) contour lines for different $x-y-z$ slices for $Re=10, Rh=10, Rm_f=100, Rm_e=1, \alpha=\pi/2, \beta=\pi/2$.

Case 1:

In this subsection, we displayed the effect of ratio of $\frac{Rm_f}{Rm_e}$ on the contour lines of the induced magnetic field solutions. It is seen from Figure 3 that even the continuity requirement is satified, there is a strong change on the intersection of the fluid and external domain boundary. Due to the Drichlet type boundary condition, contour lines close themselves on the exterior side of the external domain. Velocity contour lines are also compatible with the 2-D case of the considered MHD problem.

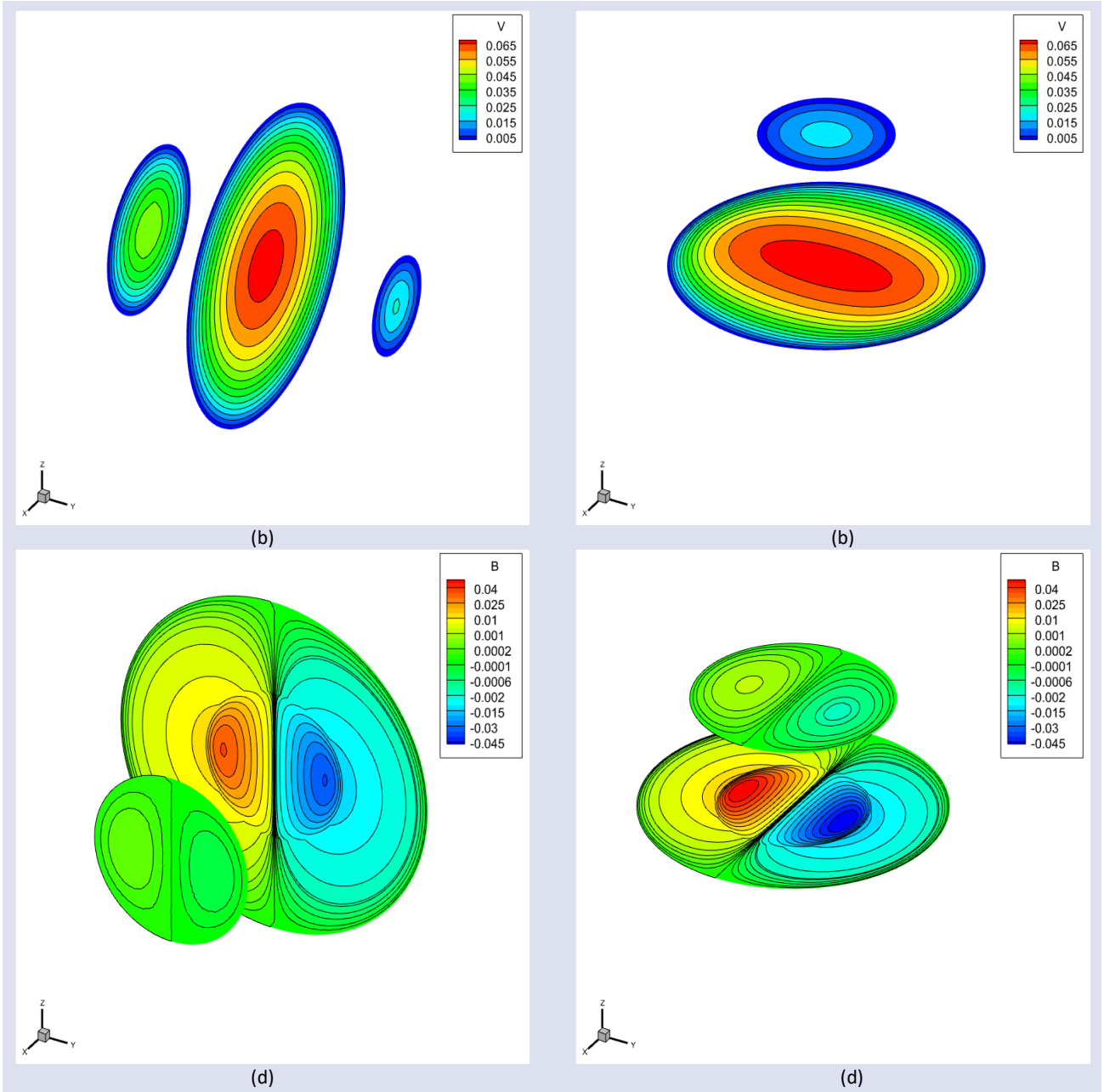

Figure 3. Velocity (a-b) and induced magnetic field (c-d) contour lines for different $x-y-z$ slices for $Re=10, Rh=1, Rm_f=10, Rm_e=1, \alpha=\pi/2, \beta=\pi/2$.

For the comparison, the same problem configuration is considered for the cubic domain in Figure 4 as defined above. Noticed that the behavior of the both spherical and cubic domains are similar to each other except the numerical difficulties at the corners on the induced magnetic field solution lying on the exterior region as predicted.

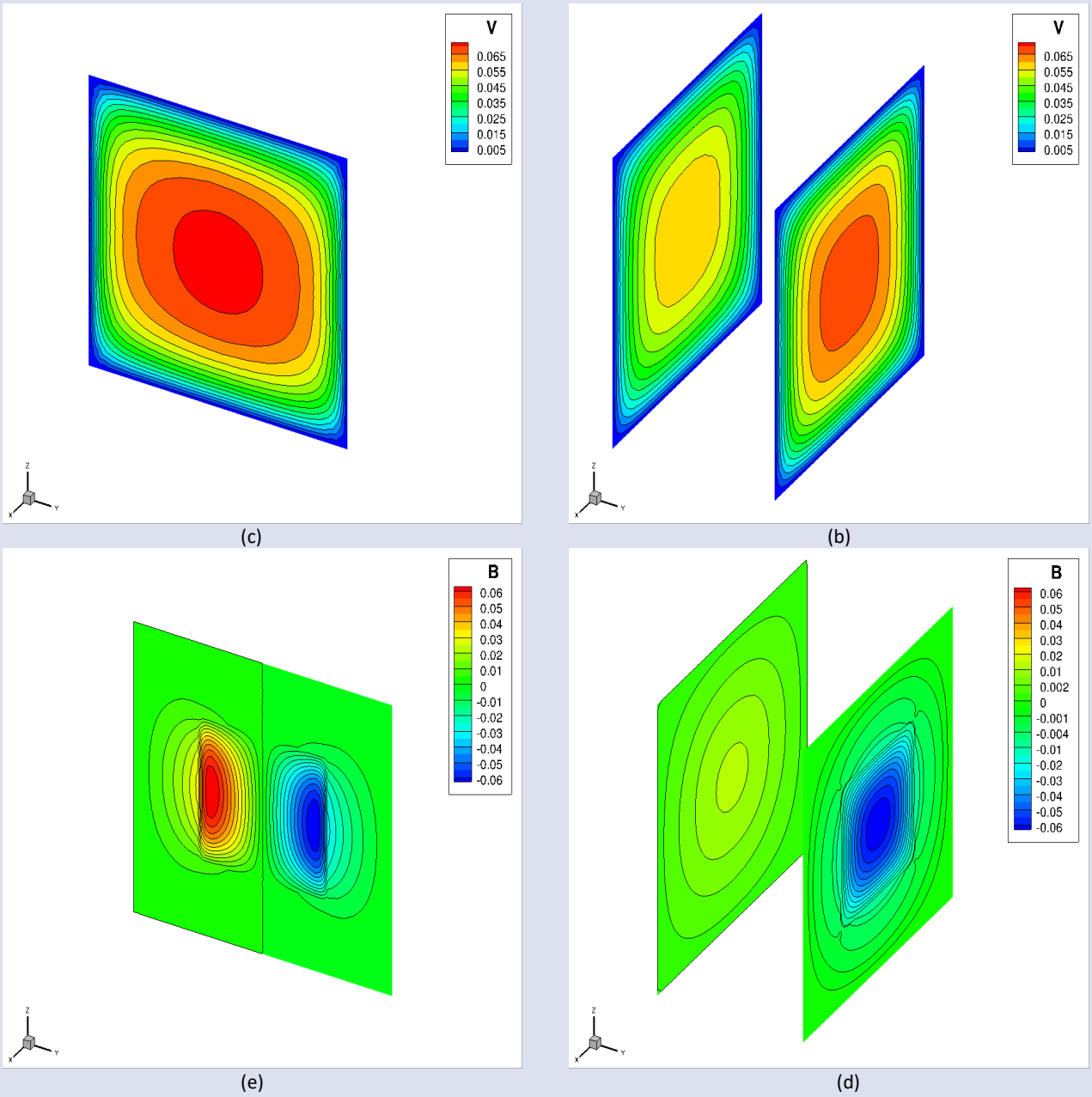

Figure 4. Velocity (a-b) and induced magnetic field (c-d) contour lines for different $x-y-z$ slices for $Re=10, Rh=1, Rm_f=10, Rm_e=1, \alpha=\pi/2, \beta=\pi/2$.

In Figure 5, we tested the effect of Neumann type boundary condition, effect of the high value of the Hartmann number and also the effect of direction of the applied external magnetic field ($\alpha=\pi/2$, $\beta=\pi/4$). It is seen that there is a boundary layer formation where it's position is changing depending on the selected slice due to the value of β and the flow becomes stagnant. One can see that the contour lines of the induced magnetic field are perpendicular to the exterior boundary due to the effect of the Neumann type boundary condition.

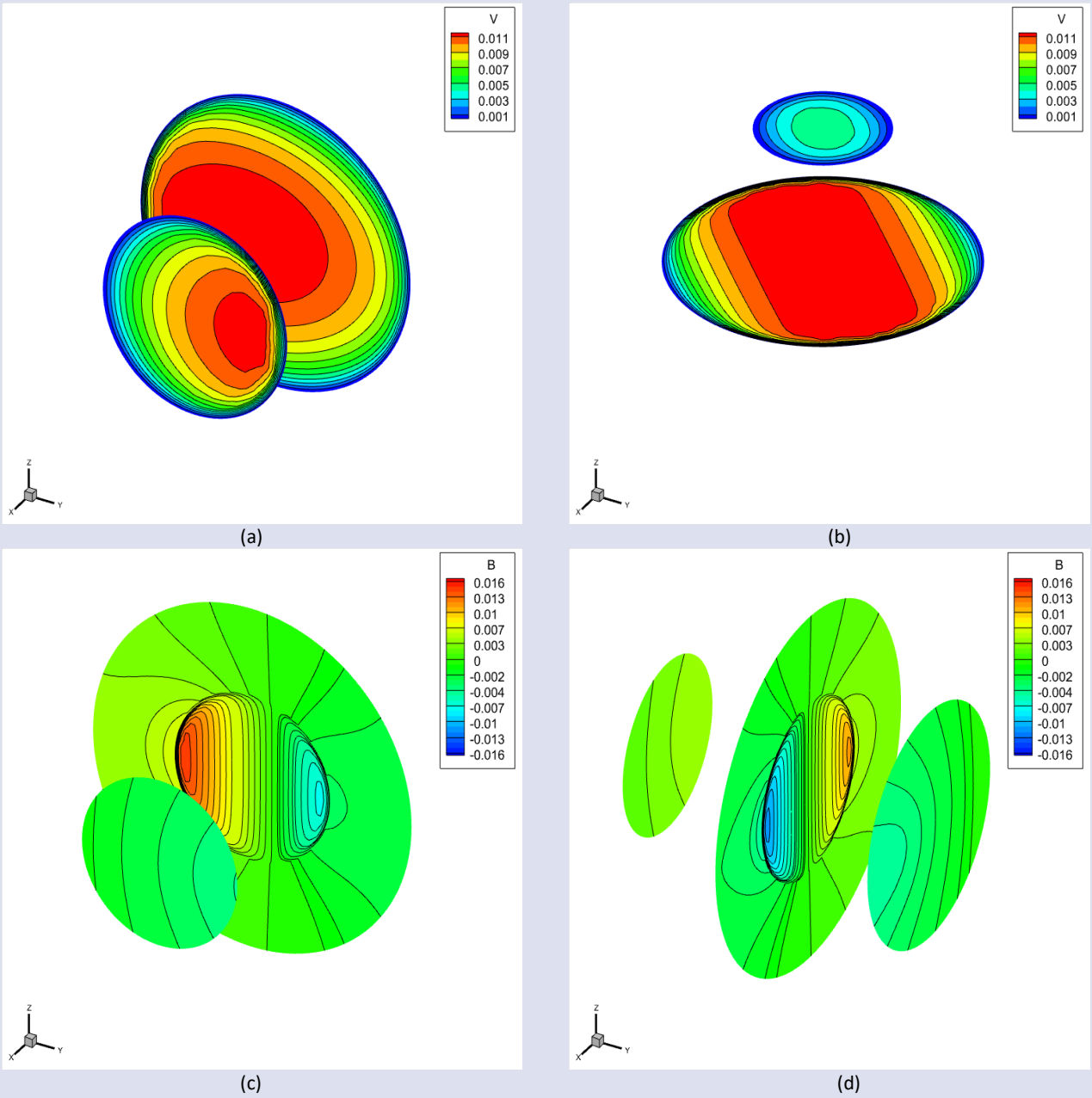

Figure 5. Velocity (a-b) and induced magnetic field (c-d) contour lines for different $x-y-z$ slices for $Re=10, Rh=5, Rm_f=50, Rm_e=1, \alpha=\pi/2, \beta=\pi/4$.

Case 2:

In order visualize the solid inside a fluid case, we selected the problem parameters as $Re=50, Rh=5, Rm_f=10, Rm_s=1, \alpha=\pi/2, \beta=0$. We want to display the effects of high values of problem parameters Re and Rh Rh on the flow behavior. It is seen that contour lines of both velocity and induced magnetic field are parallel with direction of the externally applied magnetic field due to the high value of the Hartmann number (see Figure 6).

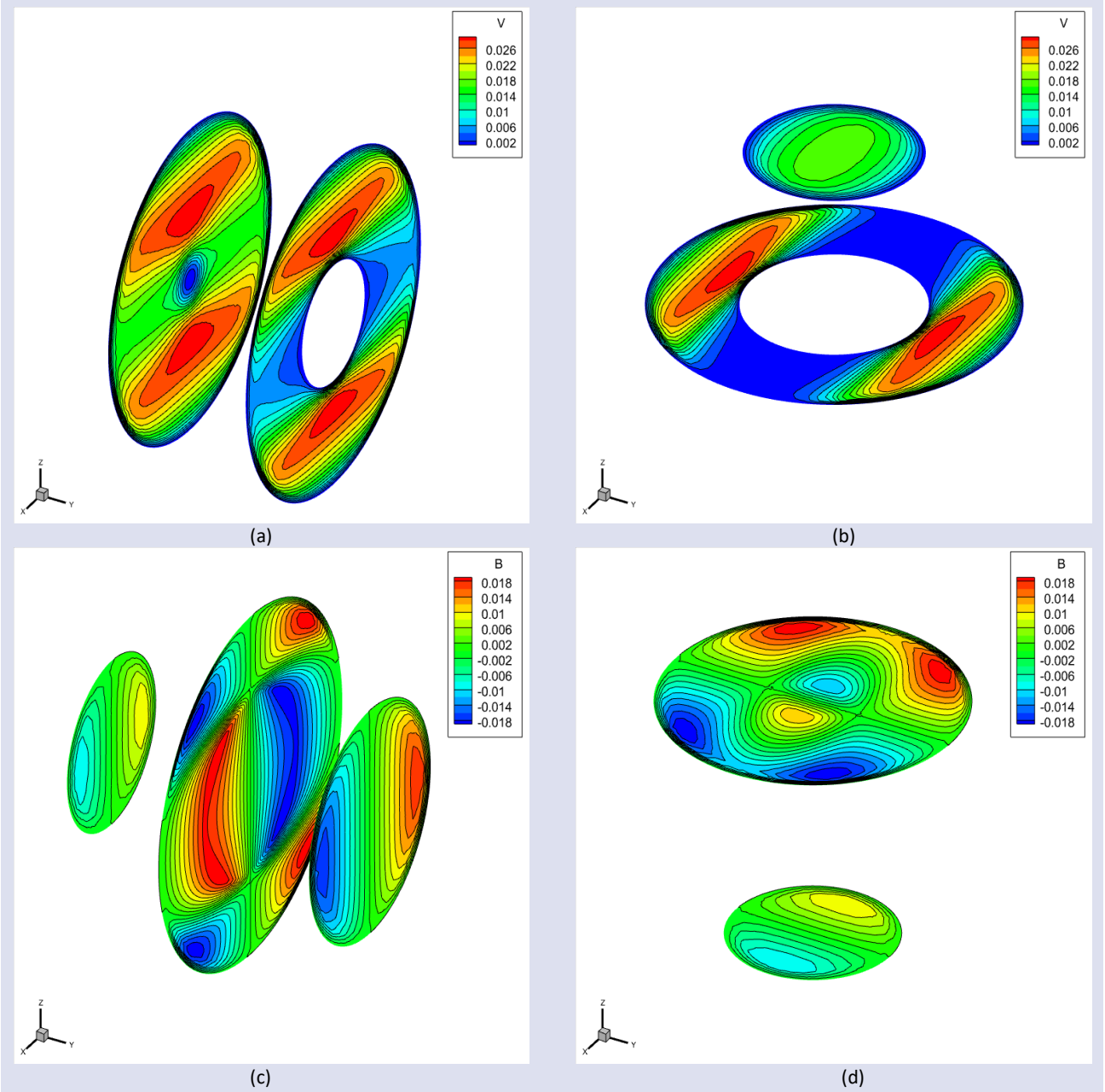

Figure 6. Velocity (a-b) and induced magnetic field (c-d) contour lines for different $y-z$ slices for $Re=50, Rh=5, Rm_f=10, Rm_s=1, \alpha=\pi/2, \beta=0$.

Case 3:

Finally, let's display the numerical solutions for the most general case. In Figure 7, we selected the problem parameters $Rm_s=1, Rm_f=1, Rm_e=1$ in order to display the smooth continuation of the contour lines of induced magnetic field solutions. It is also seen that the velocity takes it's maximum value at the center of the fluid domain as expected.

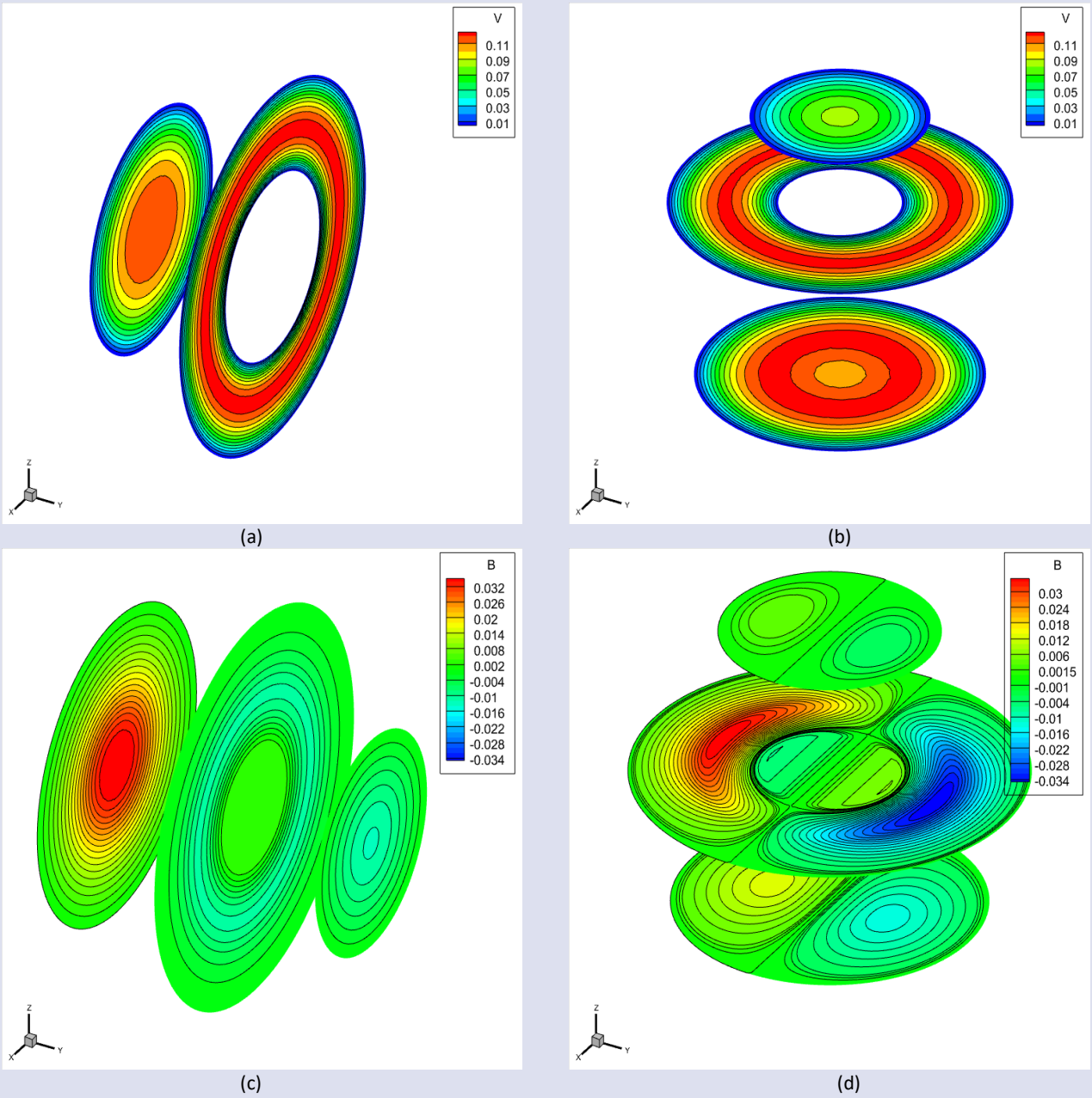

Figure 7. Velocity (a-b) and induced magnetic field (c-d) contour lines for different $y-z$ slices for $Re=1, Rh=1, Rm_s=1, Rm_f=1, Rm_e=1, \alpha=\pi/2, \beta=\pi/2$.

Additionally, in Figure 8, we have compared the induced magnetic field solutions for different problem parameters. One can see that contour lines are again parallel with the direction of B_0 and flow behavior is compatible with the literature results [36-39].

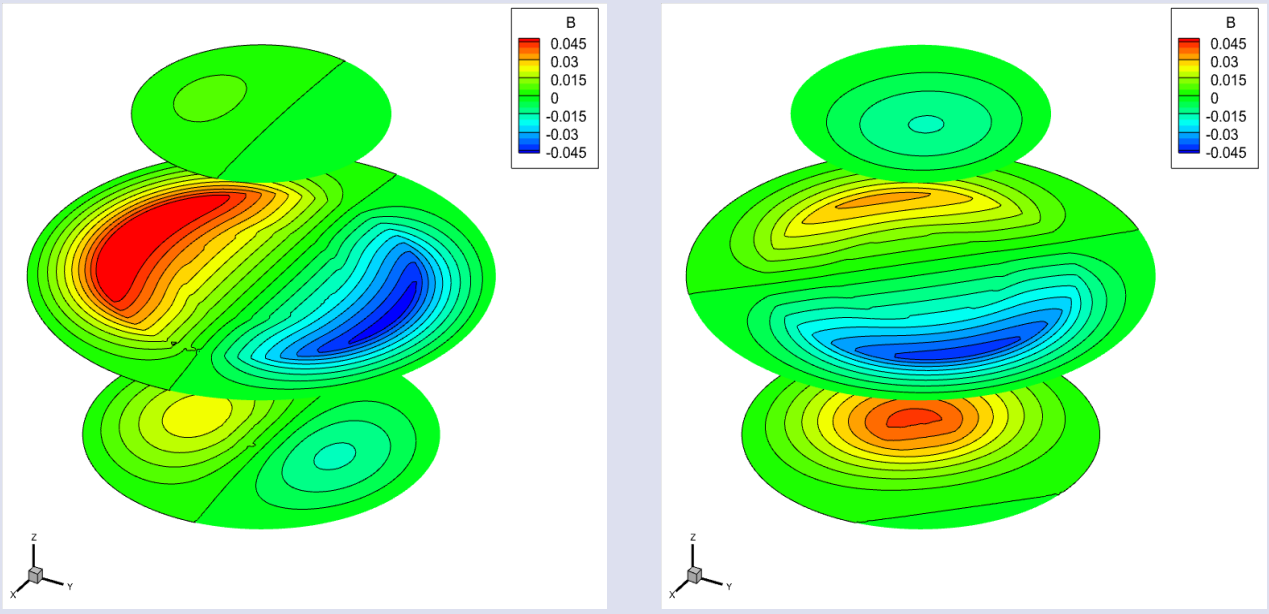

(a) (b)

Figure 8. Induced magnetic field contour lines for the y slice for $Re = 10, Rh = 1, Rm_s = 10, Rm_f = 100, Rm_e = 1, \alpha = \pi/2, \beta = \pi/2$ (a) and for $Re = 5, Rh = 5, Rm_s = 5, Rm_f = 50, Rm_e = 1, \alpha = \pi/4, \beta = \pi/4$ (b).

Conclusion

The SUPG typed stabilized FEM formulation of the 3-D MHD flow problem with three different problem configurations which have not been considered in the previous literature studies are provided in this study in a detail way. The proposed formulations are tested on some benchmark problems. Obtained solutions are displayed in terms of figures and one can see that the numerical solutions are stable and agree with the 2-D version of the similar problems.

Conflicts of interest

There are no conflicts of interest in this work.

Acknowledgments

The author wish to thank Prof. Dr. M. Tezer-Sezgin for her valuable support, comments and suggestions.

References

[1] Iwona A.W., Lucyna B., Lukasz D., Marek M., Stanislaw H.I., Modelling 3D dynamics of offshore lattice jib cranes by means of the rigid finite element method, *Journal of Ocean Engineering and Marine Energy,* 9 (2023) 495-513.

[2] Saimi A., Bensaid I., Fellah A., Effect of crack presence on the dynamic and buckling responses of bidirectional functionally graded beams based on quasi-3D beam model and differential quadrature finite element method, *Archive of Applied Mechanics,* 93 (2023) 3131–3151.

[3] Joshi K.K., Kar V.R., Elastoplastic Behaviour of Multidirectional Porous Functionally Graded Panels: A Nonlinear FEM Approach, *Iran J. Sci. Technol. Trans. Mech. Eng.,* (2023).

[4] Shao Z., Li X.S., Xiang P., A new computational scheme for structural static stochastic analysis based on Karhunen–Loève expansion and modified perturbation stochastic finite element method, *Computational Mechanics*, 71 (2023) 917-933.

[5] Gatica G.N., Nunez N., Ruiz-Baier R., Mixed-Primal Methods for Natural Convection Driven Phase Change with Navier–Stokes–Brinkman Equations, *Journal of Scientific Computing*, 95 (2023) 79.

[6] Vantyghem G., Ooms T., Corte W.D., FEM modelling techniques for simulation of 3D concrete printing, (2020).

[7] Liu W.K., Li S., Park H.S., Eighty Years of the Finite Element Method: Birth, Evolution, and Future, *Arch. Computat. Methods Eng.*, 29 (2022) 4431-4453.

[8] Xu H., Zou D., Kong X., Hu Z., Study on the effects of hydrodynamic pressure on the dynamic stresses in slabs of high CFRD based on the scaled boundary finite-element method, *Soil Dynamics and Earthquake Engineering*, 88 (2016) 223–236.

[9] Hell S., Becker W., The scaled boundary finite element method for the analysis of 3D crack interaction, *Journal of Computational Science*, 9(7) (2015) 76–81.

[10] Anjos, G.R., Borhani,N., Mangiavacchi, N., Thome J.R., A 3D moving mesh Finite Element Method for two-phase flows, *Journal of Computational Physics*, 270 (2014) 366–377.

[11] Schott B., Wall W.A., A new face-oriented stabilized XFEM approach for 2D and 3D incompressible Navier-Stokes equations, *Comput. Methods Appl. Mech. Engrg.*, 276 (2014) 233–265.

[12] Gravenkamp H., Man H., Song C., Prager J., The computation of dispersion relations for three-dimensional elastic waveguides using the Scaled Boundary Finite Element Method, *Journal of Sound and Vibration*, 332 (2013) 3756–3771.

[13] Stephan E.P., Maischak M., Leydecker F., An hp-adaptive finite element/boundary element coupling method for electromagnetic problems, *Comput. Mech.*, 39 (2007) 673–680.

[14] Geramy A., Sharafoddin F., Abfraction: 3D analysis by means of the finite element method, *Dental Research*, 34(7) (2003) 526–533.

[15] Rachowicz W., Demkowicz L., An hp-adaptive finite element method for electromagnetics: Part II. A 3D implementation, *Int. J. Numer. Meth. Engng.*, 53 (2002) 147–180.

[16] Chakraborty S., Bhattacharyya B., An efficient 3D stochastic finite element method, *International Journal of Solids and Structures*, 39 (2002) 2465–2475.

[17] Hartmann J., Theory of the laminar flow of an electrically conductive liquid in a homogeneous magnetic field, *K. Dan. Vidensk. Selsk. Mat. Fys. Medd.*, 15(6) (1937) 1-28.

[18] Shercliff J.A., Steady motion of conducting fluids in pipes under transverse magnetic fields, *Math. Proc. Cambridge*, 49 (1953) 136–144.

[19] Dragoş L., Magnetofluid Dynamics, *Abacus Pres*, 1975, 92-99.

[20] Brooks A.N., Hughes T.J.R., Streamline upwind/Petrov-Galerkin formulations for convection dominated flows with particular emphasis on the incompressible Navier-Stokes equations, *Comput. Methods Appl. Mech. Engrg.*, 32 (1982) 199-259.

[21] Rao S., A Numerical Study on Unsteady MHD Williamson Nanofluid Flow past a Permeable Moving Cylinder in the presence of Thermal Radiation and Chemical Reaction, *Biointerface Research in Applied Chemistry*, 13(5) (2023) 436.

[22] Zhao Y., Global well-posedness for the compressible non-resistive MHD equations in a 3D infinite slab, *Nonlinear Analysis*, 227 (2023) 113162.

[23] Patel A., Bhattacharyay R., 3D Thermo-fluid MHD simulation in a complex flow geometry, *Fusion Engineering and Design*, 191 (2023) 113558.

[24] Wang Z., Liu H., Global well-posedness for the 3-D generalized MHD equations, *Applied Mathematics Letters*, 140 (2023) 108585.

[25] Tezer-Sezgin M., Aydın S.H., Stabilized FEM solution of MHD duct flow with conducting cracks in the insulation, *Journal of Computational and Applied Mathematics*, 4230 (2023) 114936.

[26] Aggul M., Eroglu F.G., Kaya S., Artificial compression method for MHD system in Elsässer variables, *Applied Numerical Mathematics*, 185 (2023) 72-87.

[27] Chen Y., Peng Y., Shi X., A new blowup criterion for a generalized Hall-MHD system concerning the deformation tensor, *Applied Mathematics Letters*, 140 (2023) 108567.

[28] Fu L., An Efficient Low-Dissipation High-Order TENO Scheme for MHD Flows, *Journal of Scientific Computing*, 90(1) (2022) 1-24.

[29] Faizan, M., Ali, F., Loganathan, K. Zaib, A., Reddy, C.A., Abdelsalam, S.I., Entropy analysis of sutterby nanofluid flow over a riga sheet with gyrotactic microorganisms and Cattaneo-Christov double diffusion, *Mathematics*, 10(17) (2022) 3157.

[30] Luo Y., Fan X., Kim C.N., MHD flows in a U-channel under the influence of the spatially different channel-wall electric conductivity and of the magnetic field orientation, *Journal of Mechanical Science and Technology*, 35 (2021) 4477-4487.

[31] Wang H., Chen L., Zhang N.M., Ni M.J., Numerical simulations of MHD flows around a 180-degree sharp bend under a strong transverse magnetic field, *Nuclear Fusion*, 61(12) (2011) 126069.

[32] Aydin S.H., Nesliturk A.I., Tezer-Sezgin M., Two-level finite element method with a stabilizing subgrid for the incompressible MHD equations, *International Journal for Numerical Methods in Fluids*, 62(2) (2010) 188–210.

[33] Nesliturk A.I., Tezer-Sezgin M., Finite element method solution of electrically driven magnetohydrodynamic flow, *Journal of Computational and Applied Mathematics*, 192 (2006) 339–352.

[34] Codina R., Silva N.H., Stabilized finite element approximation of the stationary magneto-hydrodynamics equations, *Computational Mechanics*, 38 (2006) 344–355.

[35] Lungu E., Pohoata A., Finite element-boundary element approach of MHD pipe flow, *Proc. of Conf. on Fluid Mech. and Technical Appl.*, Bucharest, Romania, 2005, 79-88.

[36] Tezer-Sezgin M., Han Aydın S., BEM Solution of MHD Flow in a Pipe Coupled with Magnetic Induction of Exterior Region, *Computing* 95(1) (2013) 751–770.

[37] Han Aydın S., Tezer-Sezgin M., DRBEM Solution of MHD Pipe Flow in a Conducting Medium, *Journal of Computational and Applied Mathematics*, 259(B) (2014) 720–729.

[38] Han Aydın S., Selvitopi H., Stabilized FEM-BEM coupled solution of MHD pipe flow in an unbounded conducting medium, *Engineering Analysis with Boundary Elements*, 87(2) (2018) 122–132.

[39] Aydin, S.H., Stabilized solution of the 3-D MHD flow problem with FEM-BEM coupling approach, *Engineering Analysis with Boundary Elements*, 140 (2022) 519–530.

[40] Aydın S.H., Erdoğan M.C., Stabilization in 3-D FEM and solution of the MHD equations, *Mathematical Methods in the Applied Sciences,* (2023).

Cumhuriyet Sci. J., 44(3) (2023) 561-566
DOI: https://doi.org/10.17776/csj.1267158

Cumhuriyet Science Journal

| csj.cumhuriyet.edu.tr | Founded: 2002 ISSN: 2587-2680 e-ISSN: 2587-246X Publisher: Sivas Cumhuriyet University

Legendre Computational Algorithm for Linear Integro-Differential Equations

Taiye Oyedepo[1,a,*], Abayomi Ayotunde Ayoade[2,b], Ganiyu Ajileye[3,c], Nneoma Joyce Ikechukwu[4,d]

[1] *Department of Applied Sciences, Federal College of Dental Technology and Therapy, Enugu, Nigeria.*
[2] *Department of Mathematics, University of Lagos, Lagos, Nigeria.*
[3] *Department of Mathematics and Statistics, Federal University Wukari Taraba, Nigeria.*
[4] *Department of Applied Sciences, Federal College of Dental Technology and Therapy, Enugu, Nigeria.*
**Corresponding author*

Research Article

History
Received: 18/03/2023
Accepted: 07/09/2023

ABSTRACT

This work presents a collocation computational algorithm for solving linear Integro-Differential Equations (IDEs) of the Fredholm and Volterra types. The proposed method utilizes shifted Legendre polynomials and breaks down the problem into a series of linear algebraic equations. The matrix inversion technique is then employed to solve these equations. To validate the effectiveness of the suggested approach, the authors examined three numerical examples. The results obtained from the proposed method were compared with those reported in the existing literature. The findings demonstrate that the proposed algorithm is not only accurate but also efficient in solving linear IDEs. In order to present the results, the study employs tables and figures. These graphical representations aid in displaying the numerical outcomes obtained from the algorithm. All calculations were performed using Maple 18 software.

Keywords: Legendre polynomials, Fredholm and Volterra integro-differential equations, Approximate solution, Matrix inversion.

[a] *oyedepotaiye12@gmail.com* *https://orcid.org/0000-0001-9063-8806*
[b] *ayoayoade@unilag.edu.ng* *https://orcid.org/0000-0003-3470-0147*
[c] *ajileye@fuwukari.edu.ng* *https://orcid.org/0000-0002-4161-686X*
[d] *nnesco4god@gmail.com* *https://orcid.org/0000-0001-9049-3037*

Introduction

Integro-Differential Equations (IDEs) are types of mathematical equations that involve both derivatives and integrals. They arise in various fields of science and engineering, including physics, biology, economics, and finance, where systems exhibit memory or history-dependent behavior. Unlike Ordinary Differential Equations (ODEs) that involve only derivatives, integro-differential equations incorporate the influence of past values of the unknown function through the integration term. Integro-differential equations often appear in problems involving diffusion, propagation of waves, population dynamics, and control theory, among others. They provide a more realistic description of phenomena that exhibit memory effects or spatial interactions. Since most IDEs cannot be solved analytically, researchers have focused on developing numerical methods to obtain approximate solutions. Several authors have contributed to this area. For example, [1] employed the differential transform method, [2] used the Bernstein operational matrix approach, [3] applied the Chebyshev collocation method, [4] employed Lucas collocation method, and [5] introduced the reliable iterative method for Volterra-Fredholm IDEs. In [6], Euler polynomials with the least squares method are used to solve IDEs. In [7], the Adomian decomposition method was used to solve Boundary Value Problems (BVPs) associated with fourth-order IDEs. The Trapezoidal rule and the Variational Iteration Method (VIM) were investigated for linear IDEs in [8], and VIM was also employed in [9] to solve fourth-order IDEs. For Fredholm-Volterra IDEs, various methods were utilized. [10] employed the projection method based on a Bernstein collocation approach; [11] used the Bernstein collocation method; [12] applied a fixed-point iterative algorithm; [13] utilized the Chebyshev polynomial approach; and [14] employed a collocation method based on Bernstein polynomials. In [15], a new numerical method was developed specifically for solving systems of Volterra IDEs. In [16], the Lucas polynomial is employed to solve nonlinear differential equations with variable delays. The use of third-kind Chebyshev polynomials for solving IDEs was examined in [17] and [18]. In [19], Chebyshev Computational Approach is used to find the numerical solution Volterra-Fredholm integro-differential equations. Other methods mentioned in this study include the Hermite collocation method [20], the extended minimal residual method [21], the quadrature-difference method [22], and Adomian's decomposition approach [23], which were used to solve Fredholm IDEs. Based on the works mentioned above, this study propose a computational algorithm that utilizes shifted Legendre polynomials. This technique is inspired by previous research and aims to enhance the outcomes achieved by [18].

The general form of the class of problem considered in this work is given as:

$$\sum_{i=0}^{n} \rho_i(w)\xi^i(w) = f(w) + \int_0^w K(w,v)\xi(v)dv \qquad (1)$$

$$\sum_{i=0}^{n} \rho_i(w)\xi^i(w) = f(w) + \int_0^1 K(w,v)\xi(v)dv, \qquad (2)$$

with the initial conditions

$$\xi^r(0) = \xi_r \qquad r = 0,1,2,\cdots n-1.$$

Where r^{th} represent derivatives, K and $\rho_i(w)$, $i = 0,1,2,\cdots n$ with $\rho_i(w) \neq 0$ are known functions, $f(w)$ is a known function and $\xi^i(w)$ is the i^{th} derivatives of the unknown function $\xi(w)$ to be determined, and (1) and (2) are referred to as Volterra and Fredholm IDEs respectively.

Materials and Method

Definition 1: An integral equation is an equation that has an unknown function, $\xi(w)$, that appears under the integral sign. Standard integral equation has the following form:

$$\xi(w) = f(w) + \lambda \int_{g(w)}^{h(w)} K(w,t)\xi(t)dt \ ,$$

where K(w,t) is a function of two variables w and t known as the kernel or the nucleus of the integral equation, $g(w)$ and $h(w)$ are the limits of integration, λ is a constant parameter.

Definition 2: Legendre's polynomial of degree n is denoted and defined by

$$\tau_n(w) = \sum_{r=0}^{[\frac{n}{2}]} (-1)^r \frac{(2n-2r)!}{2^n.r!(n-r)!(n-2r)!} w^{n-2r} \ ,$$

where

$$\left[\frac{n}{2}\right] = \begin{cases} \frac{n}{2} & if\ \ n\ is\ even \\ \frac{n-1}{2}, & if\ n\ is\ odd. \end{cases}$$

$n\tau_n(w) = (2n-1)w\tau_{n-1}(w) - (n-1)\tau_{n-2}(x); n \geq 2$, starting with

$$\tau_0(w) = 1, \tau_1(w) = w$$

Hence, the first few of Legendre Polynomials on the interval [-1,1] is given below:

$$\left.\begin{aligned} \tau_0(w) &= 1 \\ \tau_1(w) &= w \\ \tau_2(w) &= \frac{1}{2}(3w^2 - 1) \\ \tau_3(w) &= \frac{1}{2}(5w^3 - 3w) \end{aligned}\right\} \qquad (3)$$

The shifted equivalent of (3) that valid in [0, 1] are given as

$$\left.\begin{aligned} \tau^*_0(w) &= 1 \\ \tau^*_1(x) &= 2w - 1 \\ \tau^*_2(w) &= 6w^2 - 6w + 1 \\ \tau^*_3(x) &= 20w^3 - 30w^2 + 20w - 1 \end{aligned}\right\} \qquad (4)$$

Definition 3: Absolute Error: We defined absolute error as follows in this study: Absolute Error=$|\boldsymbol{\tau}(w) - \tau(w)|;\ -1 \leq w \leq 1$, where $\boldsymbol{\tau}(w)$ is the exact solution and $\tau(w)$ is the approximate solution.

Proposed Method

In order to find the numerical approximation to the general class of problem considered in this study, we assumed an approximate solution by means of the shifted Legendre polynomials in the form:

$$(w) = \sum_{r=0}^{n} \tau^*_r(w)\, c_r, \qquad (5)$$

where, $c_r, r = 0(1)n$ are to be found. Thus, substituting Eq. (5) into Eq. (1) gives

$$\sum_{i=0}^{n} \rho_i(w) \sum_{r=0}^{n} \tau^{*i}_r(w)\, c_r = f(w) + \int_a^w k(w,v) \sum_{r=0}^{n} \tau^*_r(v)\, c_r dv \ , \qquad (6)$$

where $\tau^{*i}(w)$ is the i^{th} derivative of $\tau^*(w)$.

Let $p(w) = \sum_{i=0}^{n} \rho_i(w) \sum_{r=0}^{n} \tau^{*i}_r(w)\, c_r$ and $q(w) = \int_a^w k(w,v) \sum_{r=0}^{n} \tau^*_r(v)\, c_r dv$.

Thus, equation (6) becomes

$$p(w) - q(w) = f(w) \qquad (7)$$

The linear algebraic system of equations in $(n+1)$ unknown constants $e'_i s$ is obtained by collocating Eq. (7) at the evenly spaced point $w_i = a + \frac{(b-a)i}{n}$, $(i = 0(1)n)$.

Additional equations are obtained from initial conditions Eq. (3), which are represented in matrix form:

$$\begin{pmatrix} Z_{11} & Z_{12} & Z_{13} & Z_{14} & \cdots & Z_{1n} \\ Z_{21} & Z_{22} & Z_{23} & Z_{24} & \cdots & Z_{2n} \\ \vdots & \vdots & \vdots & \vdots & \cdots & \vdots \\ Z_{m1} & Z_{m2} & Z_{m3} & Z_{m4} & \cdots & Z_{mn} \\ Z_{11}^{\ 0} & Z_{12}^{\ 0} & Z_{13}^{\ 0} & Z_{14}^{\ 0} & \cdots & Z_{1n}^{\ 0} \\ Z_{21}^{\ 1} & Z_{22}^{\ 1} & Z_{23}^{\ 1} & Z_{24}^{\ 1} & \vdots & Z_{2n}^{\ 0} \\ \vdots & \vdots & \vdots & \vdots & \cdots & \vdots \\ Z_{m1}^{\ n-1} & Z_{m2}^{\ n-1} & Z_{m3}^{\ n-1} & Z_{m4}^{\ n-1} & & Z_{mn}^{\ n-1} \end{pmatrix} \begin{pmatrix} c_0 \\ c_1 \\ \vdots \\ \vdots \\ \vdots \\ \vdots \\ c_n \end{pmatrix} = \begin{pmatrix} E_{11} \\ E_{21} \\ \vdots \\ E_{mn} \\ E_{11}^{\ 0} \\ E_{22}^{\ 1} \\ \vdots \\ E_{mn}^{\ n-1} \end{pmatrix} \qquad (8)$$

where $Z_i{}'s$ and $Z_i^{*\prime}s$ are the coefficients of c_{is} and $E_i{}'s$ are values of $f(w_i)$. The matrix inversion approach is then used to solve the system of equations in order to obtain the unknown constants.

$$\begin{pmatrix} c_0 \\ c_1 \\ \vdots \\ \vdots \\ \vdots \\ c_n \end{pmatrix} = \begin{pmatrix} Z_{11} & Z_{12} & Z_{13} & Z_{14} & \cdots & Z_{1n} \\ Z_{21} & Z_{22} & Z_{23} & Z_{24} & \cdots & Z_{2n} \\ \vdots & \vdots & \vdots & \vdots & \cdots & \vdots \\ Z_{m1} & Z_{m2} & Z_{m3} & Z_{m4} & \cdots & Z_{mn} \\ {Z_{11}}^0 & {Z_{12}}^0 & {Z_{13}}^0 & {Z_{14}}^0 & \cdots & {Z_{1n}}^0 \\ {Z_{21}}^1 & {Z_{22}}^1 & {Z_{23}}^1 & {Z_{24}}^1 & \cdots & {Z_{2n}}^0 \\ \vdots & \vdots & \vdots & \vdots & \cdots & \vdots \\ {Z_{m1}}^{n-1} & {Z_{m2}}^{n-1} & {Z_{m3}}^{n-1} & {Z_{m4}}^{n-1} & \cdots & {Z_{mn}}^{n-1} \end{pmatrix}^{-1} \begin{pmatrix} E_{11} \\ E_{21} \\ \vdots \\ E_{mn} \\ {E_{11}}^0 \\ {E_{22}}^1 \\ \vdots \\ {E_{mn}}^{n-1} \end{pmatrix} \quad (9)$$

The required approximate solution is obtained by solving Eq. (9) and then substituting the unknown constant values into the assumed approximate solution.

Numerical Examples

Example 1 **[18]:** Consider the second-order Fredholm integro-differential equation

$$\xi^{(ii)}(w) = e^w - \frac{4}{3}w + \int_0^1 wv\xi(v)dv$$

Subject to the initial conditions

$$\xi(0) = 1, \xi'(0) = 2.$$

The exact solution is $\xi(w) = w + e^w$

By applying the aforementioned technique to example 1, which is solved at n = 9, we obtained the following constants and the necessary approximation:

$c_0 = 2.21828182923867$, $c_1 = 1.34515451545867$,
$c_2 = 0.139863996066064$, $c_3 = 0.0139312558593461$,
$c_4 = 0.000992587579099529$, $c_5 = 0.0000550476656947328$,
$c_6 = 0.00000249897543908013$, $c_7 = 9.59643311863878 \times 10^{-8}$,
$c_8 = 3.20747900718829 \times 10^{-9}$, $c_9 = 1.18693253142732 \times 10^{-10}$

$$\xi(w) = 0.9999999999 + 1.999999998w + 0.5000000002w^2 + 0.1666668768w^3 + 0.04166493183w^4 + 0.008339701772w^5 + 0.001376126408w^6 + 0.0002131111947w^7 + 0.00001531135797w^8 + 0.000005770865966w^9$$

Table 1. Shows comparison of the absolute errors for Example 1.

w_i	Absolute Error of our Method n=9	Absolute Error of our Method n=10	Absolute Error of our Method n=11	Absolute Error of our Method n=15	Absolute Error of our Method n=16	Absolute Error of our Method n=17	Absolute Error of [5] n=10
0.0	1.000E-10	9.000E-10	9.000E-10	1.000E-10	9.000E-10	1.000E-10	4.79E-06
0.2	0.000E+00	7.100E-10	7.200E-10	4.000 E+00	3.000E-10	1.000E-10	5.03E-06
0.4	1.000E-10	1.220E-09	1.230E-09	1.100E-09	2.900E-09	1.100E-09	6.74E-06
0.6	0.000E+00	3.000E-10	1.300E-09	1.000E-09	2.200E-09	3.100E-09	7.91E-06
0.8	0.000E+00	1.000E-10	1.200E-09	1.000E-09	1.800E-09	1.100E-09	7.58E-06
1.0	0.000E+00	1.000E-10	1.000E-09	1.100E-09	2.000E-10	2.100E-09	1.11E-05

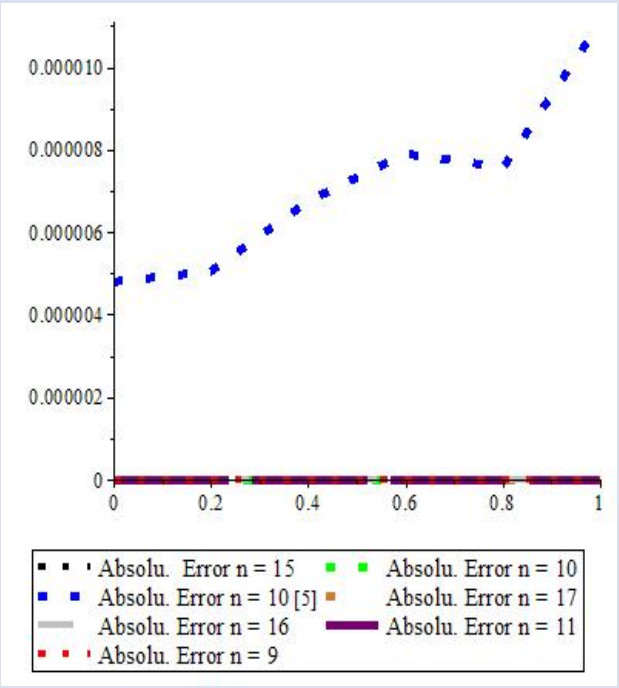

Figure 1. Shows the graphical representation of the exact and approximate solutions to the Example 1.

Example 2. [18]: Consider fourth-order Volterra integro- differential equation

$$\xi^{(iv)}(w) = -1 + \xi(w) + \int_0^w (w - v)\xi(v)dv$$

Subject to the initial conditions
$\xi(0) = -1, \xi'(0) = 1, \xi''(0) = 1, \xi'''(0) = -1.$

The exact solution is $\xi(w) = \sin w - \cos w$

By applying the aforementioned technique to example 2, which is solved at n = 9, we obtained the following constants and the necessary approximation:

$c_0 = -0.381773289713882$, $c_1 = 0.661692203358418$,
$c_2 = 0.0325913563567896$, $c_3 = -0.0111522290510834$,
$c_4 = -0.000234317964781481$, $c_5 = 0.0000444449128009975$,
$c_6 = 5.93499121704253 \times 10^{-7}$, $c_7 = -7.78764893501739 \times 10^{-8}$,
$c_8 = -7.57650814696993 \times 10^{-10}$ $c_9 = 7.61473616036433 \times 10^{-11}$

$$\xi(w) = -1.000000001 + w + 0.5w^2 - 0.166666666w^3 - 0.04166666964w^4 + 0.00833351048w^5 + 0.001388125394w^6 - 0.0001969077181w^7 - 0.00002641124722\tau^8 + 0.000003702284721w^9$$

Table 2. Shows comparison of the absolute errors for Example 2.

w_i	Absolute Error of our Method n=9	Absolute Error of our Method n=10	Absolute Error of our Method n=11	Absolute Error of our Method n=15	Absolute Error of our Method n=16	Absolute Error of our Method n=17	Absolute Error of [5] n=10
0.0	1.000E-09	0.000E+00	0.000E+00	0.000E+00	0.000E+00	0.000E+00	6.00E-09
0.2	1.030E-09	1.416E-10	2.000E-10	1.870E-10	0.000E+00	3.000E-10	2.10E-09
0.4	7.400E-10	4.070E-10	3.700E-10	3.018E-10	0.000E+00	0.000E+00	6.20E-09
0.6	2.000E-10	5.993E-10	6.000E-10	5.548E-10	1.000E-09	9.000E-10	6.80E-09
0.8	9.000E-10	9.746E-10	8.000E-10	7.561E-10	1.000E-09	2.000E-10	4.77E-09
1.0	3.100E-09	1.228E-09	1.200E-09	1.244E-09	1.000E-09	1.000E-09	9.55E-07

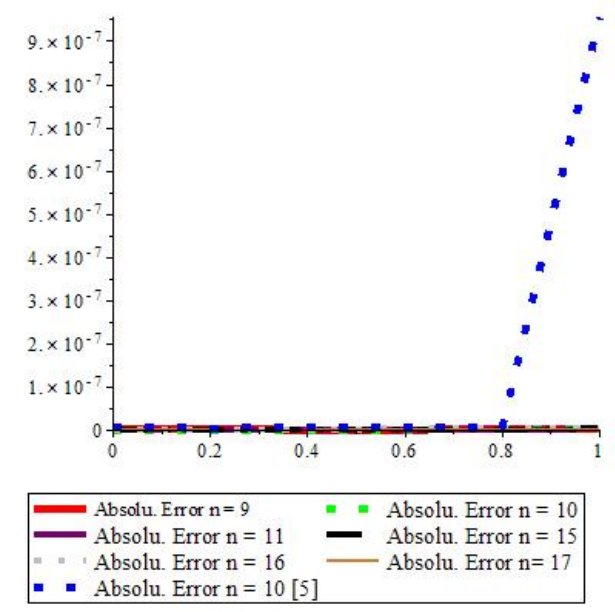

Figure 2. Shows the graphical representation of the exact and approximate solutions to the Example 2.

Example 3. [18]: Consider the following second-order Volterra integro- differential equation

$$\xi^{(ii)}(w) = 2 - 2w\sin w - \int_0^w (w-\upsilon)\xi(\upsilon)d\upsilon$$

Subject to the initial conditions

$$\xi(0) = 0, \xi'(0) = 0.$$

The exact solution is $\xi(w) = w\sin w$

By applying the aforementioned technique to example 3, which is solved at n = 9, we obtained following constants and the necessary approximation:

$c_0 = 0.301168679731766$, $c_1 = 0.435959616897170$,
$c_2 = 0.121472377673670$, $c_3 = -0.0153164866040020$,
$c_4 = -0.00191302106873919$, $c_5 = 0.000092580090134849 3$,
$c_6 = 0.0000746980787237939$, $c_7 = -2.17442225378117 \times 10^{-7}$
$c_8 = -1.28999931101810 \times 10^{-8}$

$$\xi(w) = -1.24991699 \times 10^{-11} - 9.910471 \times 10^{-11}w + w^2 + 3.37729139 \times 10^{-9}w^3 - 0.1666699038w^4 + 0.00001365628761w^5 + 0.008301749153w^6 + 0.0000428124374w^7 - 0.0002324198696w^8 + 0.00001475487962w^9$$

Table 3. Shows comparison of the absolute errors for Example 3.

w_i	Absolute Error of our Method n=9	Absolute Error of our Method n=10	Absolute Error of our Method n=11	Absolute Error of our Method n=15	Absolute Error of our Method n=16	Absolute Error of our Method n=17	Absolute Error of [5] n=10
0.0	1.250E-11	2.297E-11	4.294E-11	4.761E-11	4.803E-11	6.272E-11	1.13E-10
0.2	3.100E-10	2.000E-11	7.706E-12	3.309E-11	3.522E-11	9.268E-11	2.56E-07
0.4	7.000E-10	1.000E-10	2.571E-10	1.003E-10	1.944E-13	1.162E-10	2.22E-07
0.6	1.000E-09	4.000E-10	6.571E-10	0.000E+00	1.150E-10	2.513E-10	1.68E-07
0.8	1.300E-09	5.000E-10	6.571E-10	9.654E-11	1.533E-10	2.206E-10	5.38E-07
1.0	1.700E-09	6.000E-10	9.571E-10	2.143E-10	3.412E-10	1.952E-10	9.55E-07

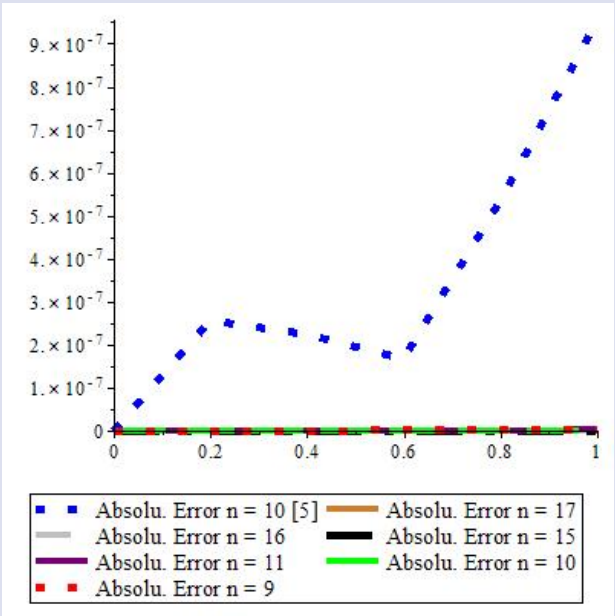

Figure 3: Shows the graphical representation of the exact and approximate solutions to the Example 3.

Conclusion

This work introduced a numerical approach for solving linear integro-differential equations by combining shifted Legendre polynomials with the collocation method. The method was applied to three specific numerical examples, and the results were compared to a previous study [18] that used the collocation method with Chebyshev third-kind polynomials at n = 10. The table of results clearly indicates that the proposed technique outperformed the method employed in [18] in terms of performance. The errors obtained using the suggested method were consistently smaller than those reported in [18]. This demonstrates the superiority of the recommended approach for solving IDEs. Based on these findings, we strongly recommend adopting the provided approach when dealing with linear integro-differential equations.

Conflicts of interest

There are no conflicts of interest in this work.

References

[1] Behiry S.H, Mohamed S.I., Solving high-order nonlinear Volterra-Fredholm integro-differential equations by differential transform method, *Natural Science,* 4(8)(2012), 581-587.

[2] Maleknejad K., Basirat B., E. Hashemizadeh E., A Bernstein operational matrix approach for solving a system of high order linear Volterra–Fredholm integro-differential equations, *Mathematical Computational Modell*, 55(3) (2012) 1363–1372.

[3] Mishra V.N., Marasi H.R., Shabanian H. Sahlan, M.N., Solution of Volterra –Fredholm integro-differential equations using Chebyshev collocation method, *Global Journal Technology and Optimization*, (1) (2017) 1-4.

[4] Deniz E., Nurcan B.S. Numerical solution of high-order linear Fredholm integro-differential equations by Lucas Collocation method. *International Journal of Informatics and Applied Mathematics & Statistics*, 5(2) (2022) 24–40.

[5] Deniz E., Nurcan B.S. Numerical solution of high-order linear Fredholm integro-differential equations by Lucas Collocation method. *International Journal of Informatics and Applied Mathematics, & Statistics*, 5(2) (2022) 24–40.

[6] Shoushan A.F. Al-Humedi H.O. The numerical solutions of integro-differential equations by Euler polynomials with least squares method. *Palarch's Journal Of Archaeology Of Egypt/Egyptology Journals*, 18(4) (2021) 1740–1753.

[7] Hashim I. Adomian decomposition method for solving BVPs for fourth-order integro-differential equations, *Journal of Computer and Applied Mathematics*, 193 (2006) 658-664.

[8] Saadati R., Raftari B., Adibi H. S.M., Vaezpour S.M., Shakeri S., A comparison between the Variational Iteration method and Trapezoidal rule for solving linear integro-differential equations, *World Applied Sciences Journal,* 4(3) (2008) 321–325.

[9] Sweilam N.H., Fourth order integro-differential equations using variational iteration method, *Computer Mathematics Applications*, 54 (2007) 1086-1091.

[10] Acar N.I., Daşcıoğlu A., Projection method for linear Fredholm–Volterra integro-differential equations, *Journal of Taibah University for Science*, 13(1) (2019) 644-650.

[11] Akyüz-DaGcJoLlu A., Acar N., Güler C., Bernstein collocation method for solving nonlinear Fredholm-Volterra integro differential equations in the most general form, *Journal of Applied Mathematics*, 134272 (2014) 1-8.

[12] Berenguer M.I., Gamez D., Opez Linares, A.J.L., Fixed-point iterative algorithm for the linear Fredholm-Volterra integro-differential equation, *Journal of Computational and Applied Mathematics*, 370894 (2012) 1-12.

[13] Yüksel G., Gülsu M. Sezer, M. A Chebyshev polynomial approach for high-order linear Fredholm-Volterra integro-differential equations, *Gazi University Journal of Science,* 25(2) (2012) 393-401.

[14] Yuzbası S. A collocation method based on Bernstein polynomials to solve nonlinear Fredholm–Volterra integro-differential equations, *Applied Mathematics Computation*, 273 (2016) 142–154.

[15] Loh R.J., Phang C., A new numerical scheme for solving system of Volterra integro-differential equation, *Alexandria Enginerring Journal*, 57(2) (2018) 1117-1124.

[16] Gumgum S., Savaşaneril N.B., Kurkcu O.K., Sezer M.S., Lucas polynomial solution of nonlinear differential equations with variable delays, *Hacettepe Journal of Mathematics & Statistics*, 49(2) (2020) 553–564.

[17] Sakran M.R.A., Numerical solutions of integral and integro -differential equations using Chebyshev polynomial of the third kind, *Applied Mathematics and Computation*, 5 (2019) 66 -82.

[18] Ayinde A.M, James A.A., Ishaq A.A. and Oyedepo T. A new numerical approach using Chebyshev third kind polynomial for solving integro-differential equations of

higher order, *Gazi University Journal of Science, Part A*, 9(3) (2022) 259-266.

[19] Oyedepo T., Ayoade A.A., Oluwayemi M.O.,Pandurangan R., Solution of Volterra-Fredholm integro- differential equations using the Chebyshev computational approach, *International Conference on Science, Engineering and Business for Sustainable Development Goals (SEB-SDG),Omu-Aran, Nigeria*, 1 (2023) 1-6.

[20] Akgonullu N., Şahin N., Sezer M., A Hermite collocation method for the approximation solutions of higher-order linear Fredholm integro-differential equations, *Numerical Methods for Partial Differential Equations*, 27(6) (2011) 1707-1721.

[21] Aruchunan E., Sulaiman J., Numerical solution of second order linear Fredholm integro-differential equations using generalized minimal residual method, *American, Journal of the Applied Sciences,* 7(6) (2010) 780–783.

[22] Jalius C., Abdul Z., Majid, Numerical solution of second-Order Fredholm integro-differential equations with boundary conditions by Quadrature-Difference method, *Hindawi Journal of Applied Mathematics,* 2645097 (2017) 1-5.

[23] Vahidi A.R., Babolian E., AsadiCordshooli G., Azimzadeh, Z., Numerical solution of Fredholm integro-differential equation by Adomian's decomposition method, *International Journal of Mathematical Analysis,* 3 (2009) 1769–1773.

[24] Bhrawy A., Tohidi E., Soleymani F., A new Bernoulli matrix method for solving high-order linear and nonlinear Fredholm integro-differential equations with piecewise intervals, *Appl. Math. Comput.*, 219(2) (2012) 482-497.

Cumhuriyet Sci. J., 44(3) (2023) 567-582
DOI: https://doi.org/10.17776/csj.1269391

Cumhuriyet Science Journal

| csj.cumhuriyet.edu.tr | Founded: 2002 ISSN: 2587-2680 e-ISSN: 2587-246X Publisher: Sivas Cumhuriyet University

Exploration of Seasonal Metal Pollution in Karacaören II Dam Lake Sediment Samples using X-ray Fluorescence Method

Gokhan Apaydin[1,a], Oguz Kagan Koksal[2,b*], Erhan Cengiz[3,c], Murat Sirin[4,d], Hasan Baltas[4,e], Engin Tirasoglu[1,f]

[1] *Department of Physics, Faculty of Science, Karadeniz Technical University, 61080, Trabzon, Türkiye*
[2] *Department of Electrical Electronics Engineering, Faculty of Engineering, Adiyaman University, 02040, Adiyaman, Türkiye*
[3] *Department of Fundamental Science, Faculty of Rafet Kayis Engineering, Alanya Alaaddin Keykubat University, 07425, Antalya, Türkiye*
[4] *Faculty of Arts and Science, Department of Physics, Rize Recep Tayyip Erdoğan University, 53100, Rize, Türkiye*
**Corresponding author*

Research Article

History
Received: 22/03/2023
Accepted: 07/07/2023

ABSTRACT

In this study, the seasonal metal pollution of sediment samples taken from twelve distinct notes of the Karacaören II Dam Lake was examined. The quantity of metal in soil samples was determined using energy dispersive X-ray fluorescence spectroscopy. The geoaccumulation index and enrichment factor expressions were created using the metal concentrations found in the sediments. Seasonal values at the local, state, and international levels were compared to the findings. The ratios of the elements copper, zinc, lead, arsenic, nickel, chromium, and mercury, measured in parts per million (ppm), were found to be 42-96, 53-78, 11-14, 4-7, 233-244, and 611-711, respectively. There is also discussion of the sediments' elemental composition and degree of pollution. In contrast, it was found that the Urbach energy increased from 0.246 eV to 0.630 eV with increasing levels of V2O5. These synthetic glasses' densities and molar volumes were also investigated and discussed.

Keywords: Karacaören II dam lake, Sediment, Heavy metal, Pollution, ED-XRF.

[a] *gapaydin@ktu.edu.tr* *https://orcid.org/0000-0002-4647-344X*
[b] *okoksal@adiyaman.edu.tr* *https://orcid.org/0000-0003-2671-6683*
[c] *erhan.cengiz@alanya.edu.tr* *https://orcid.org/0000-0002-4094-5784*
[d] *murat.sirin@erdogan.edu.tr* *https://orcid.org/0000-0001-6864-752X*
[e] *hasan.baltas@erdogan.edu.tr* *https://orcid.org/0000-0002-1939-8253*
[f] *engint@ktu.edu.tr* *https://orcid.org/0000-0001-7953-5638*

Introduction

Land use, chemical use, population growth, and distribution all have an impact on the environment. Sediments play a significant role in determining the level of contamination in aquatic systems [1]. They represent the history of pollution by acting as both toxin transporters and sinks, providing a record of watershed inputs into aquatic ecosystems [2, 3]. Metals are among the pollutants that have a substantial environmental impact. They accumulate in suspended particles and sediment instead of being eliminated from water by self-purification, which allows them to enter the food chain by being eaten by higher-level species [4, 5]. They are a constant in aquatic environments, moving only within different regions of them [6].

Using the energy dispersive X-ray fluorescence technique, sediment pollution in Lake Victoria has been linked to anthropogenic activity [7]. Additionally, to study heavy metal pollution, surface sediments from the Suez Gulf [5], Seyhan Dam [8], Egirdir Lake [9], and and Wadi Al Arab Dam [4] were statistically analyzed. Dam lakes are essential for irrigation and the supply of drinking water. Karacaören Dam Lake is one of Turkey's most important dam lakes. Numerous investigations have shown that heavy metal contamination, especially in aquatic environments, has been present on a global scale for more than ten years. What makes this dam notable is the lack of a scientific assessment of the level of pollution.

Marine habitat contamination is still a serious ecological issue on a global scale. The two primary sources of pollution are man-made and natural sources. The main causes of natural pollution are wave action, glacier erosion, ore-bearing rocks, metals released from sediments by chemical reactions, wind-blown dust, forest fires, chemical leaching of bedrock, water drainage basins, runoff from banks, and small amounts of vegetation. The primary sources of anthropogenic emissions include mining operations, industrial waste disposal, fossil fuel consumption in automobiles, and the smelting and refining of metals [10-14]. Anthropogenic sources, particularly those near coastal sediment, have a considerable impact on the metal's production [15]. As a result, sediments in marine environments can teach aquatic systems about heavy metal pollutants.

The pollution of heavy metals has a big impact on how contaminated aquatic systems are. It is generally known that sediments play a crucial role in the entry of heavy metals into the marine ecosystem [16, 17]. Sediment is therefore essential in determining the extent of heavy metal contamination in the marine environment [18, 19].

Using Karacaören-I Dam Lake as a case study, an investigation of a small-scale rainbow trout farm

(Oncorhynchus mykiss Walbaum, 1792) in Turkey's inland waters was done [20]. Trace metals in sediment and water, as well as their bioaccumulation, were studied in samples of carp (Cyprinus carpio L., 1758) obtained from the Karacaoren (I) Dam Lake in Turkey [21]. The fatty acid makeup of the muscle lipids of five fish species from Turkey's Işıklı and Karacaören Dam Lakes was examined [22]. Checking for the presence of heavy metals and metal levels in five distinct fish species from Işkl Dam Lake and Karacaören Dam Lake in Turkey [23]. For Turkey's Pikeperch (Sander lucioperca Linnaeus, 1758), changes in the population structure of Karacaoren-I Dam Lake were examined [24]. The mortality ratio and stock of the vimba (Vimba vimba tenella (Nordmann, 1840)) species in Karacaoren I Dam Lake were investigated (Burdur-Turkey) [25]. An analysis of the biological traits, chemical make-up, and meat yield of the Vimbra (Vimba vimba tenella (Nordmann, 1840)) population in the Karacaören I Dam Lake was conducted [26, 27]. The importance of the lake is increased by the desire to use it as a water source, but there is a lack of evidence that the lake is polluted, which has attracted attention. This investigation is important for revealing the pollution in sediments.

Recent years have seen a rise in the significance of technological research in preventing environmental contamination. Our concern for the environment has sparked the development of technologies like electric cars and renewable energy sources. Despite how important these developments are, there is still the problem of identifying and remediating environmental harm. This study is essential for determining the area's risk of environmental pollution and for providing information for further research.

Materials and Methods

Sample Locations

Despite the fact that the Karacaören II Dam Lake was initially built to meet the needs for irrigation and energy, it is thought to be used today for drinking water. When the area is geologically analyzed, it is known that it contains minerals like copper, lead, and zinc, according to statistics from the MTA agency. Along with these contaminants, cage fishing is reportedly practiced in a number of towns, parks, highways, and man-made structures. In order to evaluate the entire lake using the study's findings, twelve sampling stations were chosen. The road, the agricultural area, the residential area, etc. were all taken into account when choosing the points, as well as the fact that the intervals were almost equal. Coordinates are given based on the features. The coordinates and maps for these twelve locations are shown in the graphic below. Samples will be available for four seasons. The locations shown in Figure 1 were the sites where the sediment samples were collected in May, August, November, and February.

Figure 1. Sampling points of the study area by using google earth

Sediment Samples

At the locations shown in Table 1, sediment samples were taken from the fish farms in the lake in May, August, November, and February.

Table 1 Coordinates for the current sediment specimens

Sample Station	Latitude	Longitude
1	37°20'17.18"K	30°48'38.43"D
2	37°19'57.47"K	30°48'46.08"D
3	37°19'35.50"K	30°48'53.95"D
4	37°19'7.07"K	30°48'51.59"D
5	37°18'46.29"K	30°48'51.91"D
6	37°18'22.71"K	30°48'42.59"D
7	37°17'57.85"K	30°48'51.89"D
8	37°18'14.49"K	30°49'2.37"D
9	37°18'40.79"K	30°49'8.82"D
10	37°18'33.76"K	30°49'31.32"D
11	37°18'33.76"K	30°49'31.32"D
12	37°19'59.69"K	30°49'20.32"D

Samples will be collected during all four seasons. Using a "Van Ween grap," samples were taken from the

lake's bottom. The lengthy sampling process was caused by the old settlements (trees, ruins of homes, etc.) in the reservoir. On occasion, samples were taken by approaching the edges. For elemental and radioactivity analyses, enough sediment samples were gathered, placed in clean bags, and delivered to the lab.

Sample Preparation for Sediment

The sediment samples were dried for 96 hours at 105 Celsius in the oven after being put in plastic containers and brought to the laboratory environment (4 seasons x 12 stations) [28]. To reduce the effect of particle size that could result in measurement errors, these dry materials were ground in the grinding mill, powdered in agate, and then passed through a 37-mm sieve. It can be seen that by doing this, the EDXRF readings' margin of error is decreased. Powdered sediment samples were placed in plastic bags with a code that indicated their approximate weight of 20 g for EDXRF studies. 200 g of samples were placed into plastic-lidded containers, whose mouths were then tightly sealed in order to measure radioactivity. After that, the samples were given some time to balance. Samples were kept in a cold environment in the lab prior to the measurement process.

Energy Dispersive X-ray Fluorescence Measurement System

An energy dispersive X-ray fluorescence spectrometer (EDXRF) is typically used to evaluate distinct X-rays and scattering photons produced by photon-matter interaction quantitatively and qualitatively. The elements themselves are calculated by calculating the energy of the X-rays that were collected from the sample that was being studied, and the amount of the elements is calculated by counting the incoming rays. As a result of its quickness and sensitivity, simplicity of use, and lack of material damage, it is essential in technological and scientific research. In order to calculate the concentrations of heavy metals (in the Na-U element range), this method analyzes samples in all forms, including solid (mineral, metal, polymer), liquid (water, oil, petroleum products), thin film, and pressed powder. It allows us to analyze it.

Calculations

Restrictions on detection based on the effectiveness of the device as measured by net measurement time;

$$DL = \frac{3C}{N_p}\sqrt{\frac{N_b}{t}} \quad (1)$$

The acronyms in the equation stand for detection limit (DL), concentration (C), net peak count (NPC), background count rate (BCR), and time (t) in that order [28].Based on measurement time, Table 2 shows detection limits.

Table 2 Limits on detection dependent on time

Element	Aluminum	Sulphur	Chromium	Manganese	Iron	Nickel	Copper	Zinc	Arsenic	Mercury	Lead
Detection Limit (parts per million) (1500s)	2,36	1,10	0,93	0,39	0,43	0,47	0,52	0,20	0,34	0,98	1,37

The comparison with the sediment reference material (NRCMESS-3) used to assess the measurement accuracy of the EDXRF system is shown in Table 3.

Table 3 Results of a certified reference material sediment (NRCMESS-3) concentration

Element	NRCMESS-3 (parts per million)	Measured (parts per million)
Calcium	%1,47±0,06	%1,54
Chromium	105±4	108
Manganese	324±12	316
Iron	%4,34±0,11	%4,40
Nickel	46,9±2,2	45,1
Copper	33,9±1,6	35,4
Zinc	159±8	157
Arsenic	21,2±1,1	21,4
Strontium	129±11	130
Lead	21,1±0,7	19,2

Calculation of the geo-accumulation index (I Geo) of sediment samples

The geo-accumulation index (Igeo) will be used to assess the level of metal contamination in sediment samples. The formula for the geo-accumulation index is as follows:

$$I_{geo} = \log_2\left(\frac{C_n}{1.5 * B_n}\right) \quad (2)$$

The background matrix adjustment factor resulting from lithogenic effects is 1.5, where Cn = the concentration of n heavy metals in the residue, Bn = the mean geochemical background value of element n, and [29]. Table 4 presents the evaluation criteria in light of the collected data.

Table 4 Geo-accumulation Classification [30]

Geo-accumulation Index	Geo-accumulation classification	Description
≤0	0	No contamination.
0-1	1	No contamination to minimal contamination.
1-2	2	The contamination level is average.
2-3	3	There is a mild to severe level of contamination.
3-4	4	There is significant contamination.
4-5	5	There is moderately to extremely moderate contamination.
5<	6	There is too much contamination.

Enhancement factor

It is a method for evaluating metal pollution caused by pollutants in working environments as well as pollution caused by people. In particular, Al and Fe components are used in the normalizing operations. The enrichment factor can be calculated using the formula below [31];

$$\mathrm{EF} = \frac{\mathrm{X/Fe\ (Sediment)}}{\mathrm{X/Fe\ (Earth\ Crust)}} \quad (3)$$

The amount of metal in the sediment is represented by X. Fe (sediment) is the metal with the highest concentration in the investigated sediment. The earth's crust contains a lot of Fe [32]. The evaluation criteria are shown in Table 5 along with the EF results.

Table 5 Enhancement Factor [33]

Enhancement factor	Description
≤1	No enhancement.
3-5	Minimum enhancement.
5-10	Average enhancement.
10-25	From average to severe enhancement.
25-50	Severe enhancement.
>50	Very severe enhancement.

Statistical Calculation

The dry weight values were used to calculate the metal content of the sediment samples, and the results were given as parts per million. These grouped data were fed into the Statistical Package for the Social Sciences Environment. We examined the connections between the elements themselves as well as the connections between the position and the elements. All statistical analyses were performed in a computer environment using the Statistical Package for the Social Sciences application.

Results and Discussion

Metal Values in Sediment Samples

The results of the study showed that lead, aluminum, chromium, manganese, iron, nickel, copper, zinc, arsenic, and other elements were present in the sediment samples. The seasonal variations in the samples are shown in Tables 6–9.

Table 6: Metal concentrations (parts per million) of sediment samples for the period of May

Station No	Aluminum	Sulphur	Chromium	Manganese	Iron	Nickel	Copper	Zinc	Arsenic	Mercury	Lead
1	156430	1845	1334,6	702,28	32890	213,88	46,58	72,94	6,84	2,86	14,08
2	153293	1788	817,92	685,21	27437	134,19	45,15	55,46	6,98	Not detected	11,03
3	179057	1398	507,89	569,36	34563	221,92	45,11	45,24	4,06	1,01	10,04
4	154954	2324	527,61	641,52	29667	166,16	43,98	56,41	8,89	1,26	11,73
5	130850	3250	547,32	713,68	24770	110,39	42,85	67,57	13,7	1,51	13,42
6	182377	Not detected	449,74	711,80	36633	244,03	39,99	100,7	3,89	1,78	11,81
7	186940	Not detected	566,71	742,15	39663	285,72	42,35	76,36	4,52	2,38	11,40
8	191503	Not detected	683,67	772,50	42693	327,40	44,72	52,00	5,15	2,98	10,98
9	195070	Not detected	648,71	786,48	42023	325,30	49,00	57,78	5,24	Not detected	13,54
10	188220	Not detected	630,40	867,24	40553	273,72	38,00	51,33	7,08	Not detected	11,53
11	125866	10160	164,21	981,90	13700	Not detected	26,78	39,29	2,99	Not detected	9,471
12	186203	1298	537,30	841,16	38937	269,22	41,86	53,29	3,67	Not detected	13,52
Minimum	125866	1298	164,21	569,36	13700	110,39	26,78	39,29	2,99	1,01	9,47
Maximum	195070	10160	1334,60	981,90	42693	327,40	49,00	100,70	13,70	2,98	14,08
Average	169230	3152	618,01	751,27	33627	233,81	42,20	60,70	6,08	1,97	11,88

Table 7: Metal concentrations (parts per million) of sediment samples for the period of August

Station No	Aluminum	Sulphur	Chromium	Manganese	Iron	Nickel	Copper	Zinc	Arsenic	Mercury	Lead
1	152855	1906	593,91	620,36	32485	226,95	38,35	41,70	5,29	0,93	11,87
2	171600	ND	572,99	707,81	39360	292,94	95,56	55,62	3,73	Not detected	14,99
3	146415	1936	699,62	666,02	34175	247,61	45,41	44,62	6,37	0,85	12,02
4	128095	4385	598,37	981,81	33530	232,05	78,18	63,31	9,24	2,49	13,51
5	153950	5960	614,41	679,01	34750	228,54	48,51	60,30	3,17	Not detected	16,60
6	170960	4125	839,07	698,92	37360	268,74	47,86	56,29	3,62	Not detected	14,67
7	187970	2290	1063,7	718,82	39970	308,94	47,20	52,29	4,06	Not detected	12,75
8	167810	Not detected	672,94	680,98	34630	235,45	37,75	43,08	5,50	Not detected	12,02
9	145020	1683	969,87	836,21	33660	219,00	35,14	42,60	5,51	Not detected	11,60
10	153615	4960	808,65	681,40	32570	249,49	40,11	63,05	4,00	Not detected	13,83
11	141300	6895	1144,3	664,12	26530	162,70	32,33	52,66	5,19	Not detected	12,39
12	166590	5065	677,34	665,94	32250	244,19	45,67	64,70	3,94	Not detected	11,76
Minimum	128095	1683	572,99	620,36	26530	162,70	32,33	41,70	3,17	0,85	11,60
Maximum	187970	6895	1144,3	981,81	39970	308,94	95,56	64,70	9,24	2,49	16,60
Average	157182	3921	771,26	716,78	34273	243,05	49,34	53,35	4,97	1,42	13,17

Table 8: Metal concentrations (parts per million) of sediment samples for the period of November

Station No	Aluminum	Sulphur	Chromium	Manganese	Iron	Nickel	Copper	Zinc	Arsenic	Mercury	Lead
1	172255	2960	639,01	880,63	40665	340,40	51,93	78,04	8,07	Not detected	12,87
2	180655	Not detected	599,82	744,48	41600	292,12	45,94	55,16	5,67	1,44	13,27
3	167545	1585	687,03	668,42	32900	211,07	38,75	40,62	5,73	0,51	12,18
4	175165	1562	966,14	790,36	39695	246,11	48,34	71,08	9,05	0,73	17,58
5	151355	2485	478,91	797,07	38215	214,87	59,62	58,70	10,9	3,18	15,21
6	162615	1899	480,19	740,17	36350	202,89	51,50	53,97	9,64	Not detected	12,45
7	179405	2595	615,94	707,72	34085	218,47	42,89	75,06	5,16	Not detected	10,45
8	193630	Not detected	535,56	697,48	38560	272,59	42,13	51,27	4,35	1,73	12,28
9	195085	1552	597,33	711,69	42450	305,28	57,45	64,63	5,52	Not detected	16,83
10	180155	Not detected	653,37	694,72	33185	233,08	35,74	44,22	4,71	Not detected	10,50
11	169960	Not detected	555,49	852,37	37970	234,71	36,94	43,96	7,16	0,91	11,79
12	187065	Not detected	650,47	790,29	44315	350,99	53,74	57,56	3,50	Not detected	14,14
Minimum	151335	1552	478,91	668,42	32900	202,89	35,74	40,62	3,50	0,51	10,45
Maximum	195085	2960	966,14	880,63	44315	350,99	59,62	78,04	10,9	3,18	17,58
Average	176241	2091	621,61	756,82	38333	260,22	47,08	57,86	6,62	1,42	13,3

Table 9: Metal concentrations (parts per million) of sediment samples for the period of February

Station No	Aluminum	Sulphur	Chromium	Manganese	Iron	Nickel	Copper	Zinc	Arsenic	Mercury	Lead
1	192420	2830	528,89	587,37	35665	287,91	42,93	58,59	3,24	Not detected	13,19
2	196875	Not detected	539,73	636,98	39030	273,00	48,41	66,93	4,67	Not detected	12,28
3	215460	Not detected	480,33	635,14	39920	270,05	49,05	57,83	5,16	1,10	10,89
4	138420	Not detected	916,31	690,71	37265	234,86	49,75	55,25	5,95	Not detected	19,74
5	93690	4195	631,61	790,77	23495	164,27	44,67	36,76	10,1	Not detected	7,99
6	175375	Not detected	603,35	796,63	45165	308,35	46,67	55,03	11,3	1,62	14,54
7	192540	1649	542,87	724,94	39380	268,71	44,77	64,36	4,71	Not detected	11,13
8	197945	1072	463,07	650,38	41480	292,53	53,64	63,64	3,96	Not detected	11,45
9	188075	Not detected	510,90	684,50	40150	282,53	43,06	53,75	4,75	Not detected	12,02
10	170310	Not detected	769,30	710,55	33220	229,18	39,72	47,59	4,78	Not detected	10,69
11	194330	1566	869,26	1076,6	50230	337,19	72,41	81,30	5,94	Not detected	19,33
12	129720	1612	479,27	318,78	26840	105,6	25,57	43,78	4,33	Not detected	10,01
Minimum	93690	1072	463,07	318,78	23495	105,60	25,57	36,76	3,24	1,10	7,99
Maximum	215460	4195	916,31	1076,6	50230	337,19	72,41	57,06	11,3	1,62	19,74
Average	173763	2154	611,24	691,95	37653	254,52	46,72	77,90	5,74	1,36	12,77

The concentration of heavy metals in the sea and lake bottoms has risen over time as a result of the rocks going through processes like fragmentation, transit, sedimentation, and human activity. Metals in water-soluble forms precipitate and amass in the sediment, especially in wide areas where rivers meet lakes and seas. Heavy metal accumulation is more pronounced. The results of the study showed that lead, aluminum, chromium, manganese, iron, nickel, copper, zinc, arsenic, and other elements were present in the sediment samples. Based on the average values of the samples, the concentration changes of the element's chromium, nickel, copper, zinc, arsenic, and lead are depicted in figures 2–8. Chromium, nickel, copper, zinc, and other changes are depicted in figures 2 through 8. Based on the average values of the samples, the concentration changes of the element's chromium, nickel, copper, zinc, arsenic, and lead are depicted in figures 2–8. Based on the average values of the samples, Figures 2–8 depict changes in the concentrations of the element's chromium, nickel, copper, zinc, arsenic, and lead as well as changes in accordance with the global "freshwater sediment quality" standards (Table 10).

Table 10: Freshwater sediment quality criteria

		Concentration (parts per million)				
	Element	Rare effect level	Threshold effect level	Occasional effect level	Probable effect level	Frequent effect level
Metal	Arsenic	4,1	5,9	7,6	17	23
	Chrome	25	37	57	90	120
	Copper	22	36	63	200	700
	Lead	25	35	52	91	150
	Mercury	0,094	0,17	0,25	0,49	0,87
	Nickel	Not detected	Not detected	47	Not detected	Not detected
	Zinc	80	120	170	310	770

* Environment Canada and Ministère du Développement durable, de l'Environnement et des Parcs du Québec. 2007, "Criteria for the Asse ssment of Sediment Quality in Quebec and Application Frameworks: Prevention, Dredging and Remediation" 39 p

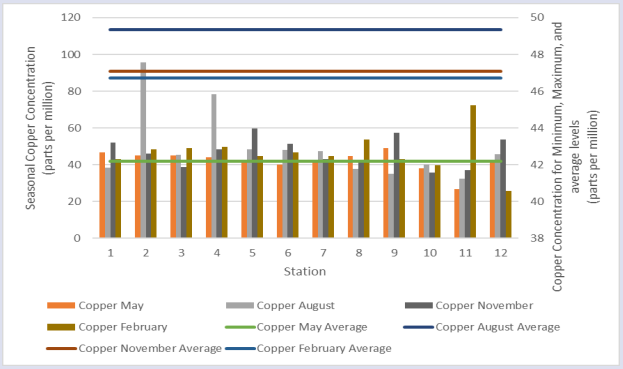

Figure 2. Seasonal variation of copper concentration versus sampling points of the study area

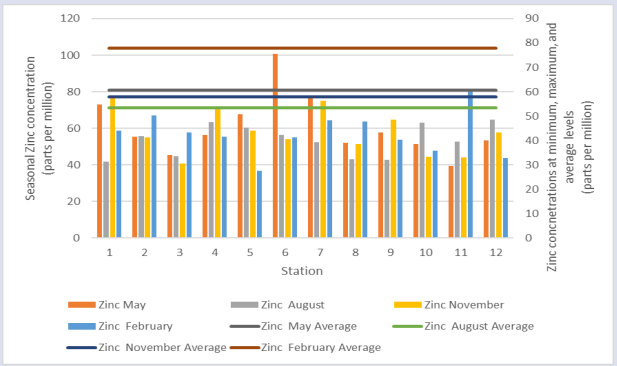

Figure 3. Seasonal variation of zinc concentration versus sampling points of the study area

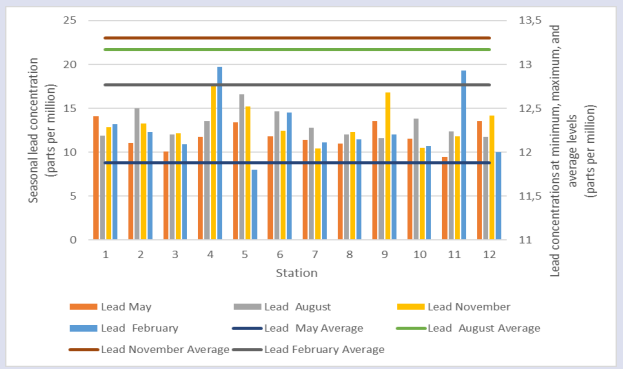

Figure 4. Seasonal variation of lead concentration versus sampling points of the study area

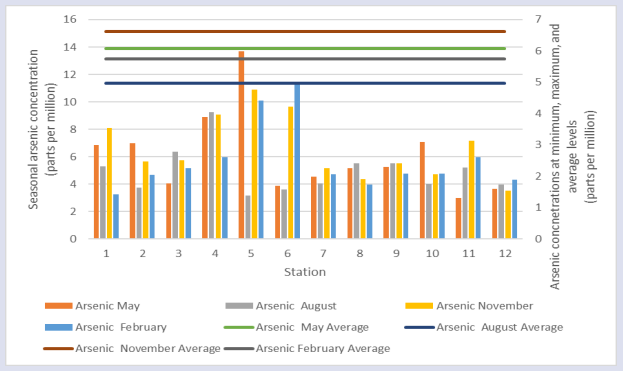

Figure 5. Seasonal variation of arsenic concentration versus sampling points of the study area

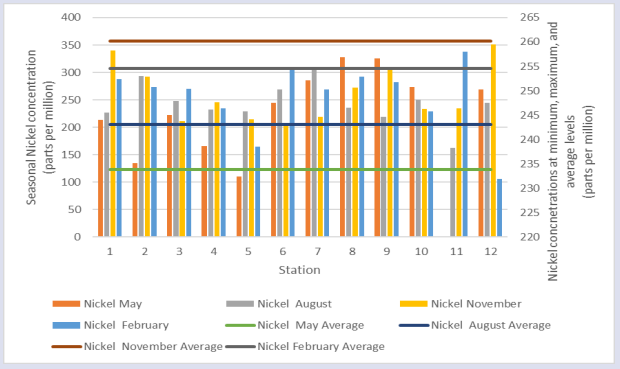

Figure 6. Seasonal variation of nickel concentration versus sampling points of the study area

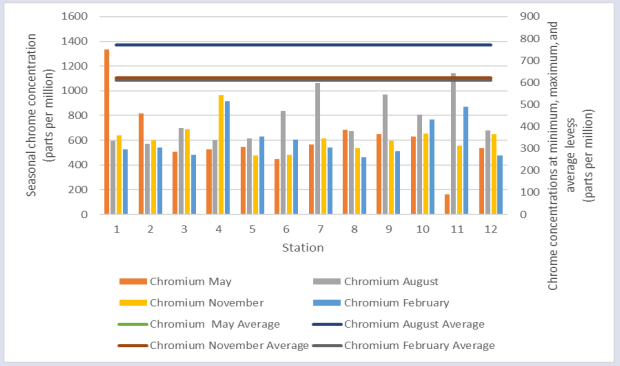

Figure 7. Seasonal variation of chrome concentration versus sampling points of the study area

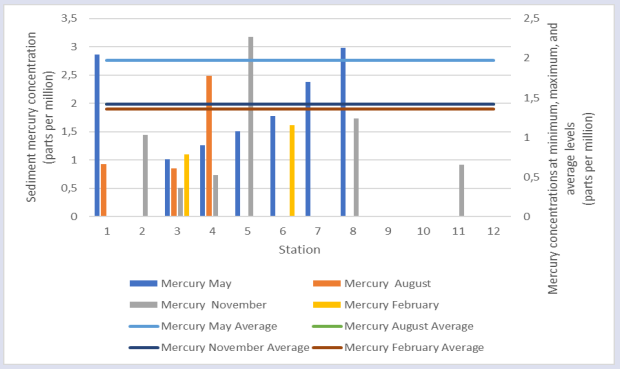

Figure 8. Seasonal variation of mercury concentration versus sampling points of the study area

Aluminum: During the month of February, the aluminum value was measured at 93690-215460 parts per million (minimum-maximum). At each station, the aluminum value was calculated as follows: 125866-195070 (minimum-maximum) parts per million in May, 128095 (minimum-maximum) parts per million in August, and 151335-195085 (minimum-maximum) parts per million in November. The average values of the eras were found to be high (80000 parts per million) when compared to the average abundance value of Karuskopf [33] in the earth's crust.

Sulphur: Sulphur values were detected in May at stations 6, 7, 8, 9, and 10 because they were below the detection thresholds. The min-max range during this time was measured to be 1298-10160 parts per million.

In August, it was undetectable at stations 2 and 8. The change range is between 1683 and 6895 parts per million. In November, it was undetectable at stations 2,8,10,11, and 12. The min-max range for this time period was 1552-2960 parts per million. At stations 2,3,4,6,9, and 10 in February, it was undetectable. The fluctuation range is 107-4195 parts per million. 2400 parts per million is the average abundance value in the crust of the planet.

Chromium: The element chromium has been detected at all times and locations. The change occurred between 164.21 and 1334.60 parts per million (minimum-maximum) when all time periods were considered. It has been noted that when the international standards for freshwater sediment quality are taken into account, the chromium element's effect level is above the diffuse effect threshold [33] defined the sediment range as 41-125 parts per million.

Iron: Taking into account all four seasons, iron concentrations ranged from 13700 to 50230 parts per million. Iron concentrations were also found in other lakes, according to studies (Table 21). In most instances, the concentration values are comparable. Our values on average were less abundant than the average abundance in the earth's crust, which was estimated by [32] to be 47200 parts per million.

Nickel: The nickel element's change range in our investigation is between 105.6 and 350.99 parts per million. When the international standards for the quality of freshwater sediment are taken into account, it has been noted that the nickel element's effect level is higher than the transient effect level.

Copper: Copper was discovered throughout the sampling's locations and times. Between 25.57 and 95.56 parts per million, there can be a change. The effect level of the copper element was found to be above the temporary effect level at stations 2 and 4 in the period of November and at station no. 11 in the period of February, while other values were below this, according to the international standards for freshwater sediment quality.

Zinc: The zinc element fluctuated between 36.76 and 100.70 parts per million at all times and locations. For the month of May, all concentrations' effect levels—with the exception of station 6—are below the level for uncommon effects.

Arsenic: The arsenic element in the investigation had a concentration range (minimum-maximum) of 2.99-13.70 parts per million. The influence level of the element Arsenic is transient while taking into account the periods of May, August, and November at station 4, May, November, and February periods at station 5, November, and February periods at station 6, and November at station 1. The other numbers, which are above the OEL, have been seen to be below this level.

Mercury: Mercury was discovered at stations 1, 3, 4, 8, 2, 3, and 5 in May, at stations 1, 3, 4, and 8 in August, and at stations 11 and 3.6 in November. The concentration range is 0.51 to 3.18 parts per million (minimum-maximum). For the month of November, all readings were found to be higher than the widespread effect level, with the exception of stations 3 and 4.

Lead: All epochs and points contained lead. The concentration range (min-max) in the study covered a range of 7.99 to 19.74 parts per million. The sediment range [34]'s investigation was determined to be 3 parts per million. The Pb element's rare-effect level has been found to be below the international standard for freshwater sediment quality.

Figure 9. illustrates the counter maps of the elements in the sediment samples according to latitude and longitude that were created by averaging the periods.

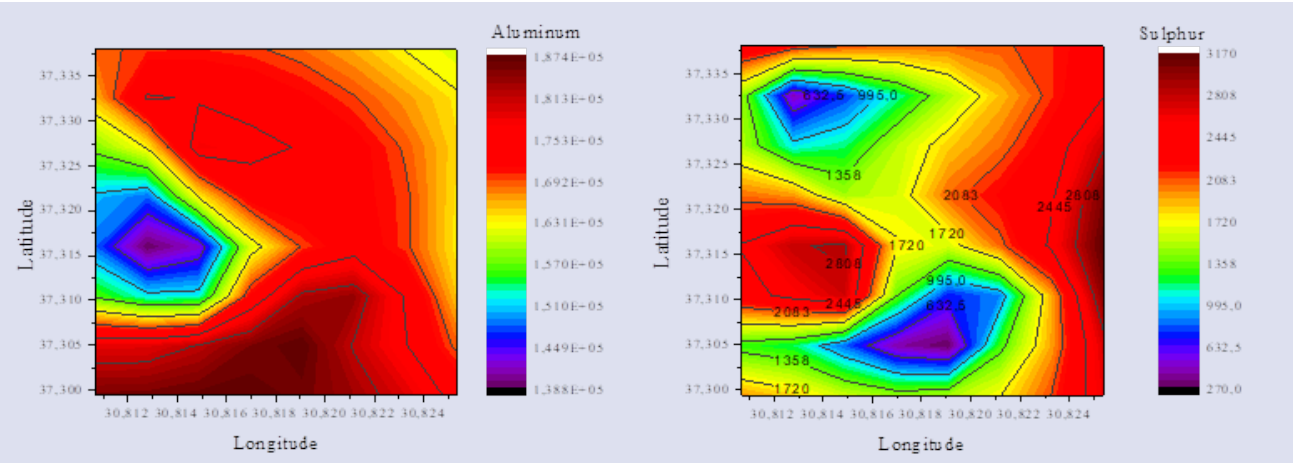

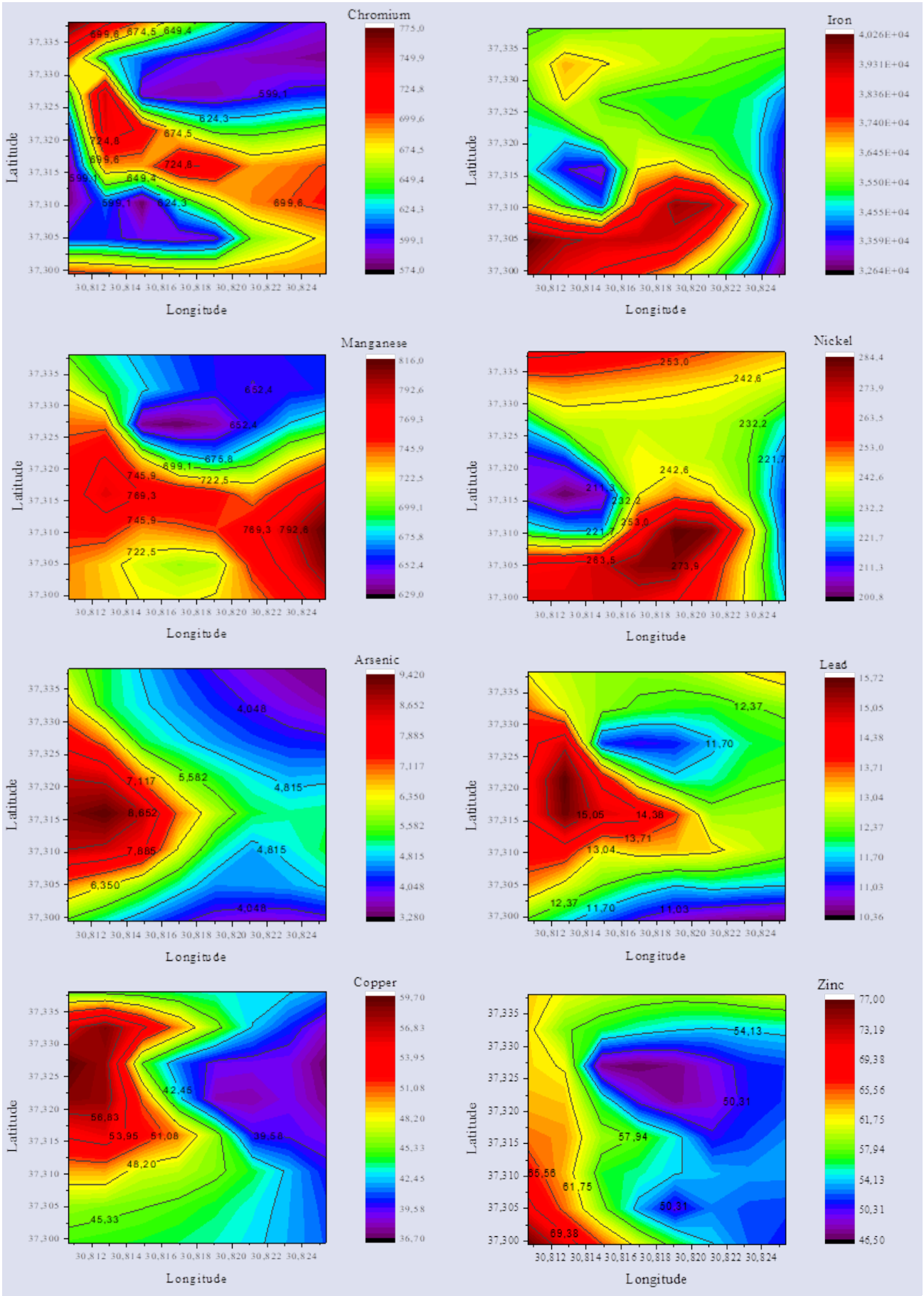

Figure 9. Spatial distribution of metal contents for sediment matrices

Table 11. lists studies that various researchers in our nation have conducted in dam lakes. When the papers are analyzed, it becomes clear that atomic absorption spectroscopy and inductively coupled plasma type spectroscopy procedures were used for the examinations. Regional geological variances have resulted in differences in elemental concentration. Sulphur, Nickel, Copper, Arsenic, and Mercury elements were also found in our analysis, which is also consistent with the findings of earlier sediment analyses in the study area. The elements were found to have varied concentrations as a consequence of the use of several spectroscopic techniques.

Table 11. Various studies on dam lakes in our country

	(Parts per million)										
	Aluminium	Sulphur	Chromium	Manganese	Iron	Nickel	Copper	Zinc	Arsenic	Mercury	Lead
Atatürk Dam[a]	-	-	-	73,6-514,07	12587-19265	43,69-139,69	14,57-22,7	59,14-60,79	-	-	-
Seyhan Dam[b]	-	-	118,95	803,63	39350	-	19,80	39,09	-	-	-
Karacaören II Dam[c]	3,314-1068	-	41-125	305-558	7430-14680	-	-	19-330	-	-	3
Avşar Dam[d]	-		14,48	-	25268	29,99	29,98	-	-	-	2.44
Enne Dam[e]	-	-	59,08	626,40	34030	136,82	27,84	272,00	-	-	88,96
Porsuk Dam[e]	-	-	78,40	642,80	36550	159,12	26,08	656,40	-	-	90,00
Gökçekaya Dam[f]			421		16918	153	165	312,56	42,98	-	121.24
In current work (minimum-maximum)	93690-215460	1072-10160	164,21-1334,60	318,78-1076,6	13700-50230	105,60-350,99	25,57-95,56	36,76-100,70	2,99-13,70	0,51-3,18	7,99-19,74

[a] [34], [b] [35], [c] [36], [d] [37], [e] [38], [f] [39]

Values for the sediment geo-accumulation index (I_{geo})

Tables 12–15 display the calculated and given values of the geo-accumulation index for all time periods, which is used to evaluate metal contamination in sediment samples.

Table 12. Sediment geoaccumulation index values for the period of May

Station No	Aluminium	Sulphur	Chromium	Manganese	Iron	Nickel	Copper	Zinc	Arsenic	Mercury	Lead
1	0,38	-0,96	3,31	-0,86	-1,11	1,07	-0,54	-0,97	-1,5	2,25	-1,09
2	0,35	-1,01	2,60	-0,90	-1,37	0,40	-0,58	-1,36	-1,48	-	-1,44
3	0,58	-1,36	1,91	-1,16	-1,03	1,12	-0,58	-1,66	-2,26	0,74	-1,58
4	0,37	-0,63	1,97	-0,99	-1,25	0,70	-0,62	-1,34	-1,13	1,07	-1,36
5	0,12	-0,15	2,02	-0,84	-1,52	0,11	-0,66	-1,08	-0,51	1,33	-1,16
6	0,60	-	1,74	-0,84	-0,95	1,26	-0,76	-0,50	-2,32	1,57	-1,34
7	0,64	-	2,07	-0,78	-0,84	1,49	-0,67	-0,90	-2,19	1,99	-1,40
8	0,67	-	2,34	-0,72	-0,73	1,68	-0,59	-1,45	-1,92	2,31	-1,45
9	0,70	-	2,26	-0,70	-0,75	1,67	-0,46	-1,30	-1,90	-	-1,15
10	0,65	-	2,22	-0,56	-0,80	1,42	-0,83	-1,47	-1,46	-	-1,38
11	0,07	1,50	0,28	-0,38	-2,37	-	-1,33	-1,86	-2,71	-	-1,66
12	0,63	-1,47	1,99	-0,60	-0,86	1,40	-0,69	-1,42	-2,41	-	-1,15

Table 13. Sediment geoaccumulation index values for the period of August

Station No	Aluminum	Sulphur	Chromium	Manganese	Iron	Nickel	Copper	Zinc	Arsenic	Mercury	Lead
1	0,35	-0,92	2,14	-1,04	-1,12	1,15	-0,82	-1,77	-1,88	0,63	-1,34
2	0,52	-	2,09	-0,85	-0,85	1,52	0,50	-1,36	-2,38	-	-1,00
3	0,29	-0,89	2,38	-0,94	-1,0	1,28	-0,57	-1,68	-1,61	0,51	-1,35
4	0,09	0,28	2,15	-0,38	-1,08	1,19	0,21	0,01	-1,08	2,05	-1,15
5	0,36	0,73	2,19	-0,91	-1,03	1,16	-0,48	-1,24	-2,62	-	-0,85
6	0,51	0,20	2,64	-0,87	-0,92	1,40	-0,50	-1,34	-2,43	-	-1,03
7	0,65	-0,65	2,98	-0,83	-0,82	1,60	-0,52	-1,45	-2,26	-	-1,23
8	0,48	-	2,32	-0,90	-1,03	1,21	-0,84	-1,73	-1,82	-	-1,32
9	0,27	-1,10	2,84	-0,61	-1,07	1,10	-0,94	-1,74	-1,82	-	-1,37
10	0,36	0,46	2,58	-0,90	-1,12	1,29	-0,75	-1,18	-2,28	-	-1,12
11	0,24	0,94	3,08	-0,94	-1,42	0,67	-1,06	-1,44	-1,91	-	-1,28
12	0,47	0,49	2,33	-0,94	-1,13	1,26	-0,56	-1,14	-2,31	-	-1,35

Table 14. Sediment geoaccumulation index values for the period of November

Station No	Aluminum	Sulphur	Chromium	Manganese	Iron	Nickel	Copper	Zinc	Arsenic	Mercury	Lead
1	0,52	-0,28	2,24	-0,53	-0,80	1,74	-0,38	-0,87	-1,27	-	-1,22
2	0,59	-	2,15	-0,78	-0,77	1,52	-0,56	-1,37	-1,78	1,26	-1,18
3	0,48	-1,18	2,35	-0,93	-1,11	1,05	-0,80	-1,81	-1,77	-0,23	-1,30
4	0,55	-1,20	2,84	-0,69	-0,83	1,27	-0,48	-1,00	-1,11	0,28	-0,77
5	0,33	-0,53	1,83	-0,68	-0,89	1,07	-0,18	-1,28	-0,84	2,41	-0,98
6	0,44	-0,92	1,83	-0,78	-0,96	0,99	-0,39	-1,40	-1,02	-	-1,27
7	0,58	-0,47	2,19	-0,85	-1,05	1,10	-0,65	-0,92	-1,92	-	-1,52
8	0,69	-	1,99	-0,87	-0,88	1,42	-0,68	-1,47	-2,16	1,53	-1,29
9	0,70	-1,21	2,15	-0,84	-0,74	1,58	-0,23	-1,14	-1,82	-	-0,83
10	0,59	-	2,27	-0,88	-1,09	1,19	-0,92	-1,69	-2,05	-	-1,51
11	0,50	-	2,04	-0,58	-0,90	1,20	-0,87	-1,70	-1,45	0,60	-1,35
12	0,64	-	2,27	-0,69	-0,68	1,78	-0,33	-1,31	-2,48	-	-1,09

Table 15. Sediment geoaccumulation index values for the period of February

Station No	Aluminum	Sulphur	Chromium	Manganese	Iron	Nickel	Copper	Zinc	Arsenic	Mercury	Lead
1	0,68	-0,35	1,97	-1,12	-0,99	1,50	-0,65	-1,28	-2,59	-	-1,19
2	0,71	-	2,00	-1,00	-0,86	1,42	-0,48	-1,09	-2,06	-	-1,29
3	0,84	-	1,83	-1,01	-0,83	1,40	-0,46	-1,30	-1,92	0,87	-1,46
4	0,21	-	2,76	-0,88	-0,93	1,20	-0,44	-1,37	-1,71	-	-0,60
5	0,36	0,22	2,23	-0,69	-1,59	0,69	-0,60	-1,95	-0,95	-	-1,91
6	0,55	-	2,16	-0,68	-0,65	1,60	-0,53	-1,37	-0,79	1,43	-1,04
7	0,68	-1,13	2,01	-0,81	-0,85	1,40	-0,59	-1,15	-2,05	-	-1,43
8	0,72	-1,75	1,78	-0,97	-0,77	1,52	-0,33	-1,16	-2,30	-	-1,39
9	0,65	-	1,92	-0,90	-0,82	1,47	-0,65	-1,41	-2,04	-	-1,32
10	0,51	-	2,51	-0,84	-1,09	1,17	-0,77	-1,58	-2,03	-	-1,49
11	0,70	-1,20	2,69	-0,24	-0,50	1,72	0,10	1,22	-1,71	-	-0,63
12	0,11	-1,16	1,83	-2,00	-1,40	0,05	-1,40	-1,70	-2,17	-	-1,58

When the standards listed in Table 6 are applied to the sediment sample geo-accumulation indices computed (Tables 12–15), The coordinates number 11 for the month of May show average pollution for the elements aluminum and nickel, no contamination for the element chromium, moderate pollution for the element chromium, and severe pollution for the element mercury. As can be seen from the data for the August timeframe, aluminum and sulfur pollution are between no pollution and normal pollution, whereas chromium pollution is between average-severe pollution and severe pollution. Nickel pollution falls between no pollution and average pollution, whereas mercury pollution falls between no pollution and moderate-severe pollution. When the standards listed in Table 6 are applied to the sediment sample geo-accumulation indices computed (Tables 12–15), The coordinates number 11 for the month of May show average pollution for the element's aluminum and nickel, no contamination for the element chromium, moderate pollution for the element chromium, and severe pollution for the element mercury. As can be seen from the data for the August timeframe, aluminum and sulfur pollution are between no pollution and normal pollution, whereas chromium pollution is between average-severe pollution and severe pollution. Nickel pollution falls between no pollution and average pollution, whereas mercury pollution falls between no pollution and moderate-severe pollution.

Values for the sediment enrichment factor

The values for the enrichment factors that will be used in the evaluation of metal pollution caused by contaminants in the lake as well as pollution brought on by human activity are shown in the tables below (Tables 16–19).

Table 16. Enrichment factor values for sediment samples from May

Station No	Aluminum	Sulphur	Chromium	Manganese	Iron	Nickel	Copper	Zinc	Arsenic	Mercury	Lead
1	2,78	0,42	3,45	0,38	0,36	1,75	0,45	0,23	0,21	1,22	0,31
2	2,57	-	2,97	0,39	0,39	2,01	0,99	0,27	0,13	-	0,35
3	2,53	0,44	4,25	0,43	0,40	1,99	0,55	0,26	0,27	1,17	0,33
4	2,25	1,14	4,15	0,72	0,44	2,13	1,09	0,94	0,44	3,89	0,42
5	2,61	1,29	3,55	0,42	0,38	1,75	0,56	0,33	0,13	-	0,43
6	2,70	0,80	4,36	0,38	0,37	1,85	0,50	0,28	0,13	-	0,34
7	2,77	0,41	5,03	0,36	0,36	1,93	0,45	0,23	0,13	-	0,27
8	2,86	-	3,56	0,38	0,35	1,65	0,40	0,22	0,20	-	0,29
9	2,54	0,39	5,94	0,54	0,39	1,78	0,43	0,25	0,23	-	0,32
10	2,78	1,08	4,68	0,42	0,36	1,91	0,46	0,35	0,16	-	0,36
11	3,14	1,63	7,20	0,44	0,32	1,35	0,41	0,31	0,23	-	0,35
12	3,05	1,01	3,61	0,38	0,33	1,72	0,49	0,33	0,15	-	0,28

Table 17. Enrichment factor values for sediment samples from November

Station No	Aluminum	Sulphur	Chromium	Manganese	Iron	Nickel	Copper	Zinc	Arsenic	Mercury	Lead
1	2,81	0,39	7,58	0,42	0,36	1,61	0,53	0,39	0,27	3,66	0,36
2	3,30	0,39	4,74	0,42	0,30	1,03	0,52	0,30	0,28	-	0,29
3	3,06	0,26	2,52	0,30	0,33	1,46	0,45	0,21	0,14	1,12	0,22
4	3,08	0,50	3,03	0,39	0,32	1,26	0,50	0,31	0,35	1,62	0,30
5	3,12	0,83	3,72	0,51	0,32	0,99	0,58	0,43	0,65	2,30	0,41
6	2,94	-	2,19	0,37	0,34	1,57	0,39	0,47	0,13	1,96	0,26
7	2,78	-	2,69	0,37	0,36	1,80	0,40	0,34	0,15	2,55	0,24
8	2,65	-	3,17	0,38	0,38	2,01	0,42	0,23	0,17	3,12	0,23
9	2,74	-	2,96	0,38	0,37	1,96	0,45	0,25	0,16	-	0,28
10	2,74	-	2,98	0,43	0,37	1,71	0,36	0,23	0,23	-	0,25
11	5,42	2,69	1,16	0,73	0,18	-	0,38	0,26	0,15	-	0,30
12	2,82	0,23	2,56	0,43	0,35	1,70	0,40	0,24	0,12	-	0,29

Table 18. Enrichment factor values for sediment samples from August

Station No	Aluminum	Sulphur	Chromium	Manganese	Iron	Nickel	Copper	Zinc	Arsenic	Mercury	Lead
1	3,18	0,49	2,44	0,29	0,31	1,76	0,40	0,26	0,10	-	0,27
2	2,98	-	2,44	0,30	0,34	1,63	0,44	0,29	0,15	-	0,25
3	3,18	-	1,98	0,28	0,31	1,47	0,40	0,23	0,15	1,02	0,20
4	2,19	-	5,88	0,47	0,46	2,00	0,64	0,34	0,26	-	0,57
5	2,35	1,49	5,99	0,79	0,43	2,06	0,85	0,33	0,66	-	0,34
6	2,29	-	3,06	0,43	0,44	2,07	0,47	0,26	0,40	1,85	0,33
7	2,88	0,29	2,51	0,35	0,35	1,64	0,41	0,28	0,15	-	0,23
8	2,82	0,18	2,08	0,31	0,36	1,74	0,48	0,27	0,12	-	0,23
9	2,76	-	2,41	0,34	0,36	1,77	0,41	0,24	0,16	-	0,26
10	3,02	-	4,02	0,39	0,33	1,58	0,41	0,24	0,17	-	0,25
11	2,28	0,27	3,98	0,52	0,44	2,04	0,66	1,44	0,19	-	0,40
12	2,85	0,41	3,28	0,23	0,35	0,96	0,35	0,28	0,21	-	0,31

Table 19: Enrichment factor values for sediment samples from February

Station No	Aluminum	Sulphur	Chromium	Manganese	Iron	Nickel	Copper	Zinc	Arsenic	Mercury	Lead
1	2,50	0,57	3,30	0,48	0,40	2,32	0,54	0,38	0,29	-	0,30
2	2,56	-	2,95	0,39	0,39	1,90	0,45	0,26	0,19	1,59	0,29
3	3,00	0,32	3,64	0,38	0,33	1,48	0,41	0,20	0,21	0,61	0,29
4	2,60	0,30	4,90	0,42	0,38	1,65	0,49	0,34	0,32	0,83	0,40
5	2,34	0,55	2,81	0,50	0,43	1,67	0,70	0,33	0,44	4,20	0,40
6	2,64	0,39	2,62	0,43	0,38	1,47	0,56	0,28	0,36	-	0,31
7	3,11	0,48	3,05	0,37	0,32	1,43	0,43	0,35	0,18	-	0,23
8	2,96	-	2,46	0,34	0,34	1,66	0,39	0,22	0,14	1,79	0,25
9	2,71	0,27	2,72	0,34	0,37	1,84	0,52	0,28	0,17	-	0,35
10	3,20	-	3,22	0,36	0,31	1,52	0,35	0,21	0,16	-	0,23
11	2,64	-	2,91	0,47	0,38	1,62	0,39	0,22	0,26	1,07	0,28
12	2,49	-	3,09	0,40	0,40	2,21	0,51	0,26	0,12	-	0,30

The calculated enrichment factor for the sediment sample is shown in Tables 16 through 19. The enrichment factor index was assessed using the criteria shown in Table 7. When the enrichment factor values for the May period are examined, the elements sulfur, manganese, iron, copper, zinc, arsenic, and lead exhibit no signs of human enrichment (with the exception of coordinate number 11). However, there are only very slight to moderate enrichments in the aluminum and chromium elements. Elements sulfur and nickel only show minor enrichments for coordinate no. 11, whereas mercury elements show modest to medium enrichments. August saw no enrichment of manganese, iron, copper, zinc, arsenic, or lead elements. There were also small and average enrichments for nickel, no enrichment for the element mercury, small and average-severe enrichments for chromium, small and average-severe enrichments for chromium, small and average enrichments for aluminum, and no enrichment for sulfur. The enrichment factor values for the November timeframe show no enrichment in the elements sulfur, manganese, iron, copper, zinc, arsenic, and lead. The elements aluminum and chromium showed small and average enrichments, medium enrichments in the element nickel, no enrichment in the element mercury, and minor enrichments in the other elements. There were also small and average enrichments for nickel, no enrichment for the element mercury, small and average-severe enrichments for chromium, small and average-severe enrichments for chromium, small and average enrichments for aluminum, and no enrichment for sulfur. The enrichment factor values for the November timeframe show no enrichment in the elements sulfur, manganese, iron, copper, zinc, arsenic, and lead. The elements aluminum and chromium showed small and average enrichments, medium enrichments in the element nickel, no enrichment in the element mercury, and minor enrichments in the other elements.

Statistics for the Sediment Sample

Tables 20-23 show the seasonal correlation coefficients between the position and water sample components.

Table 20: May period correlation coefficients between sediment sample's location and elements

	Location	Aluminum	Sulphur	Chromium	Manganese	Iron	Nickel	Copper	Zinc	Arsenic	Mercury	Lead
Location	1											
Aluminum	-,511	1										
Sulphur	,721	-,964*	1									
Chromium	-,859	-,002	-,264	1								
Manganese	,022	-,871	,709	,493	1							
Iron	-,772	,941	-,997**	,337	-,653	1						
Nickel	-,831	,903	-,985*	,429	-,575	,995**	1					
Copper	-,993**	,609	-,798	,792	-,141	,842	,891	1				
Zinc	-,236	-,715	,503	,701	,966*	-,436	-,344	,119	1			
Arsenic	,683	-,977*	,999**	-,212	,745	-,992**	-,974*	-,765	,548	1		
Mercury	-,733	-,211	-,057	,978*	,664	,133	,231	,647	,834	-,004	1	
Lead	-,205	-,737	,530	,678	,974*	-,464	-,373	,088	1,000**	,574	,816	1

Table 21. August period correlation coefficients between sediment samples location and elements

	Location	Aluminum	Sulphur	Chromium	Manganese	Iron	Nickel	Copper	Zinc	Arsenic	Mercury	Lead
Location	1											
Aluminum	-,511	1										
Sulphur	,721	-,964*	1									
Chromium	-,859	-,002	-,264	1								
Manganese	,022	-,871	,709	,493	1							
Iron	-,772	,941	-,997**	,337	-,653	1						
Nickel	-,831	,903	-,985*	,429	-,575	,995**	1					
Copper	-,993**	,609	-,798	,792	-,141	,842	,891	1				
Zinc	-,236	-,715	,503	,701	,966*	-,436	-,344	,119	1			
Arsenic	,683	-,977*	,999**	-,212	,745	-,992**	-,974*	-,765	,548	1		
Mercury	-,733	-,211	-,057	,978*	,664	,133	,231	,647	,834	-,004	1	
Lead	-,205	-,737	,530	,678	,974*	-,464	-,373	,088	1,000**	,574	,816	1

Table 22: November period correlation coefficients between sediment sample's location and elements

	Location	Aluminum	Sulphur	Chromium	Manganese	Iron	Nickel	Copper	Zinc	Arsenic	Mercury	Lead
Location	1											
Aluminum	-,666	1										
Sulphur	,855	-,956	1									
Chromium	-,426	,959	-,833	1								
Manganese	,888	-,249	,521	,038	1							
Iron	,744	,004	,289	,288	,968	1						
Nickel	,099	,677	-,432	,858	,545	,739	1					
Copper	,999*	-,700	,878	-,467	,866	,712	,052	1				
Zinc	,590	,210	,086	,479	,895	,979	,862	,552	1			
Arsenic	,987	-,536	,760	-,273	,951	,842	,259	,978	,713	1		
Mercury	,901	-,924	,995	-,776	,601	,380	-,343	,920	,181	,818	1	
Lead	,077	,693	-,451	,869	,527	,724	1,000**	,031	,850	,238	-,364	1

Table 23: February period correlation coefficients between sediment sample's location and elements

	Location	Aluminum	Sulphur	Chromium	Manganese	Iron	Nickel	Copper	Zinc	Arsenic	Mercury	Lead
Location	1											
Aluminum	-,160	1										
Sulphur	-,612	-,683	1									
Chromium	,149	-,276	,115	1								
Manganese	,073	,156	,094	,596*	1							
Iron	,034	,759**	-,647	,186	,581*	1						
Nickel	-,222	,786**	-,348	,120	,631*	,910**	1					
Copper	-,057	,404	-,191	,466	,850**	,744**	,749**	1				
Zinc	,350	,271	-,311	,493	,703*	,612*	,480	,793**	1			
Arsenic	-,053	-,472	,718	,235	,430	-,035	-,040	,114	-,022	1		
Mercury	-	-	-	-	-	-	-	-	-	-	-	
Lead	-,016	,179	-,425	,717**	,492	,647*	,510	,629*	,610*	,032	1,000**	1

To assist with seasonal reviews, tables were used. The Pearson correlation analysis for the month of May reveals a negative correlation between aluminum, chrome, iron, nickel, copper, zinc, mercury, and lead, but a positive correlation between sulfur, manganese, and arsenic. Only the correlation between the location and the copper element, however, is significant (p 0.05). When the relationships between the elements are examined, the element aluminum has a significant and adverse relationship with the elements sulfur and arsenic, while the element sulfur has an adverse relationship with the element's aluminum and iron and a significant and favorable relationship with the element arsenic. To assist with seasonal reviews, tables were used. The Pearson correlation analysis for the month of May reveals a negative correlation between aluminum, chrome, iron, nickel, copper, zinc, mercury, and lead, but a positive correlation between sulfur, manganese, and arsenic. Only the correlation between the location and the copper element, however, is significant (p 0.05). When the relationships between the elements are examined, the element aluminum has a significant and adverse relationship with the elements sulfur and arsenic, while the element sulfur has an adverse relationship with the element's aluminum and iron and a significant and favorable relationship with the element arsenic.

Looking at the correlation between position and elements in August, aluminum has a positive association with sulfur, chromium, and mercury, but a negative association with manganese, iron, nickel, copper, zinc, arsenic, and lead. However, only the chromium element exhibits a significant interaction (p 0.05). Significant positive correlations exist between aluminum and iron, nickel, and copper, while significant negative correlations exist with arsenic. The element sulfur only has a positive and significant association with mercury. No other element interacts with chromium in a significant way. The elements manganese and zinc have a positive and strong relationship. Nickel and aluminum both show a strong and positive association with iron. Looking at the correlation between position and elements in August, aluminum has a positive association with sulfur, chromium, and mercury, but a negative association with manganese, iron, nickel, copper, zinc, arsenic, and lead. However, only the chromium element exhibits a significant interaction (p 0.05). Significant positive correlations exist between aluminum and iron, nickel, and copper, while significant negative correlations exist with arsenic. The element sulfur only has a positive and significant association with mercury. No other element interacts with chromium in a significant way. The elements manganese and zinc have a positive and strong relationship. Nickel and aluminum both show a strong and positive association with iron.

Position and the Aluminum and Chromium elements exhibit a negative association when the data for the month of November are reviewed, whereas the other elements exhibit a positive relationship. Only the Copper element, though, has a discernible relationship with position. Only the elements Copper and lead displayed a positive and substantial connection when the relationships between the elements were studied.

According to the Pearson analysis for a year, there is a negative relationship between position and aluminum, sulfur, nickel, copper, arsenic, and lead, while a positive relationship exists between position and chromium, manganese, iron, zinc, and mercury. It only interacts with Mercury significantly. While the aluminum element has a positive and significant relationship with the elements iron and nickel, the sulfur element has no significant connections with any other elements. The elements manganese, mercury, and lead show a positive and strong association with the element chromium. There is a strong and positive correlation between mercury, iron, nickel, copper, zinc, and chromium. The elements iron and aluminum, manganese, nickel, copper, zinc, mercury, and lead all exhibit positive and significant correlations. While manganese, iron, copper, zinc, mercury, and lead are significantly and positively correlated with copper, aluminum, manganese, copper, and mercury are positively and significantly correlated with nickel. While

the zinc element exhibits positive and significant correlations with manganese, iron, copper, mercury, and lead, while the arsenic element only shows a positive and significant correlation with mercury, mercury shows positive and significant correlations with all of the other elements and a negative correlation with aluminum. The association of lead with chromium, iron, copper, and mercury is positive and significant.

Conclusion

Element analysis was performed on sediment samples collected seasonally from Karacaören II Dam Lake. The sediment sample metal analysis revealed the presence of the element's aluminum, sulfur, chromium, manganese, iron, nickel, copper, zinc, arsenic, mercury, and lead when the data were evaluated. It has been compared to research done in our country in various lakes using different spectroscopic techniques. According to the international "sediment quality assessment" criteria, Chromium and Mercury were found to be above the common effect level, Lead and Zinc were found to be below the rare effect level, Arsenic and Copper were found to be close to the temporary effect level, and Nickel was found to be above the temporary effect level. The enrichment factor and the geo-accumulation index were calculated for pollution indicator metrics in the sediments. Despite the absence of significant human enrichment in these elements, it has been discovered that aluminum, chromium, mercury, nickel, and zinc elements have a minor enrichment. The chromium element has contamination that ranges from average to severe compared to other elements. It is thought that communities and agricultural lands are the primary sources of pollution, particularly at the sites where the concentration of arsenic in the sediment samples is high. The density of chromium and nickel levels in the area is thought to be a result of the geological structure of the area, particularly mining activity. Overall, it is believed that the study's findings offer preliminary insight into how water is used for drinking in the province of Antalya. Before using any water, it is important to carefully consider the circumstances of the activities occurring in and around the lake. It's critical to assess the Isparta Stream's pollution levels before they enter the lake. After deciding to use the water, efforts should be made to raise awareness among locals in the villages close by to persuade them to keep all household waste and potential pollutants, particularly agricultural runoff, away from the lake. The condition of the farms operating in the lake should also be evaluated by the accredited institutions. All spectroscopic studies on water that use chemicals will be thoroughly cleaned before use.

Acknowledgements

This work has been made possible thanks to TUBITAK Project No. 115Y768 from the Turkish Council for Scientific and Technological Research

Conflicts of Interest

There are no conflicts of interest in this work.

References

[1] Casas J., Rosas H., Solé M., Lao C., Heavy metals and metalloids in sediments from the Llobregat basin, Spain, *Environmental Geology,* 44 (2003) 325-332.

[2] Singh K.P., Mohan D., Singh V.K., Malik A., Studies on distribution and fractionation of heavy metals in Gomti river sediments—a tributary of the Ganges, India, *Journal of Hydrology,* 312 (2005) 14-27.

[3] Mwamburi J., Variations in trace elements in bottom sediments of major rivers in Lake Victoria's basin, Kenya, *Lakes & Reservoirs: Research & Management*, 8 (2003) 5-13.

[4] Ghrefat H., Yusuf N., Assessing Mn, Fe, Cu, Zn, and Cd pollution in bottom sediments of Wadi Al-Arab Dam, Jordan, *Chemosphere,* 65 (2006) 2114-2121.

[5] Khaled A., El Nemr A., El Sikaily A., An assessment of heavy-metal contamination in surface sediments of the Suez Gulf using geoaccumulation indexes and statistical analysis, *Chemistry and Ecology,* 22 (2006) 239-252.

[6] Linnik P.M., Zubenko I.B., Role of bottom sediments in the secondary pollution of aquatic environments by heavy-metal compounds, *Lakes & Reservoirs: Research & Management*, 5 (2000) 11-21.

[7] Makundi I.N., A study of heavy metal pollution in Lake Victoria sediments by energy dispersive X-ray fluorescence, *Journal of Environmental Science and Health, Part A*, 36 (2001) 909-921.

[8] Çevik F., Göksu M.Z.L., Derici O.B., Fındık Ö., An assessment of metal pollution in surface sediments of Seyhan dam by using enrichment factor, geoaccumulation index and statistical analyses, *Environmental monitoring and assessment,* 152 (2009) 309-317.

[9] Şener Ş., Elitok Ö., Şener E., Davraz A., An investigation of Mn contents in water and bottom sediments from Eğirdir Lake, Turkey, *Mühendislik Bilimleri ve Tasarım Dergisi,* 1 (2011) 145-149.

[10] Bat L., Yesim Ozkan E., Oztekin H. Can, The contamination status of trace metals in Sinop coast of the Black Sea, Turkey, (2015).

[11] Bryan G., Some aspects of heavy metal tolerance in aquatic organisms, *Effects of pollutants on aquatic organisms,* 2 (1976) 7- 34.

[12] Fernandez-Leborans G., Herrero Y.O., Toxicity and bioaccumulation of lead and cadmium in marine protozoan communities, *Ecotoxicology and environmental safety,* 47 (2000) 266-276.

[13] Järup L., Hazards of heavy metal contamination, *British medical bulletin,* 68 (2003) 167-182.

[14] Turekian K.K., Marine geochemistry, Eos, *Transactions American Geophysical Union*, 52 (1971) IUGG237-IUGG244.

[15] Alkan A., Alkan N., Yanar B., Investigation of pollution levels originated from anthropogenic gadolinium in Ankara Stream, *Environmental Science and Pollution Research,* 27 (2020) 23677-23685.

[16] Chatterjee M., Silva Filho E., Sarkar S., Sella S., Bhattacharya A., Satpathy K., Prasad M., Chakraborty S., Bhattacharya B., Distribution and possible source of trace elements in the sediment cores of a tropical macrotidal

estuary and their ecotoxicological significance, *Environment International*, 33 (2007) 346-356.
[17] Idris A.M., Combining multivariate analysis and geochemical approaches for assessing heavy metal level in sediments from Sudanese harbors along the Red Sea coast, *Microchemical Journal,* 90 (2008) 159-163.
[18] Ozkan E.Y., Buyukisik B., Geochemical and statistical approach for assessing heavy metal accumulation in the southern Black Sea sediments, *Ekoloji,* 21 (2012) 11-24.
[19] Wardas M., Budek L., Rybicka E.H., Variability of heavy metals content in bottom sediments of the Wilga River, a tributary of the Vistula River (Krakow area, Poland), *Applied Geochemistry,* 11 (1996) 197-202.
[20] Diken G., Köknaroğlu H., Can İ., Cultural energy use and energy use efficiency of a small-scale rainbow trout (Oncorhynchus mykiss Walbaum, 1792) cage farm in the inland waters of Turkey: A case study from Karacaören-I Dam Lake, *Aquaculture Studies,* 21 (2020) 31-39.
[21] Kir I., Erdogan M., Engin M.S., Cay S., Trace metals in sediment, water and their bioaccumalation in Carp (Cyprinus Carpio L., 1758) samples, captured from the Karacaoren (I) Dam Lake, Turkey, *Fresenius Environmental Bulletin,* 25 (2016) 3557-3562.
[22] Citil O.B., Kalyoncu L., Kahraman O., Fatty acid composition of the muscle lipids of five fish species in Işıklı and Karacaören Dam Lake, Turkey, *Veterinary Medicine International*, (2014) 2014.
[23] Kalyoncu L., Kalyoncu H., Arslan G., Determination of heavy metals and metals levels in five fish species from Işıklı Dam Lake and Karacaören Dam Lake (Turkey), *Environmental monitoring and assessment,* 184 (2012) 2231-2235.
[24] Ozvarol Z., Karabacak G., Changes in the population structure of pikeperch (Sander lucioperca Linnaeus, 1758) Karacaoren-I Dam Lake, Turkey, *Journal of Animal and Veterinary Advances,* 10 (2011) 224-228.
[25] Ozvarol Z.A.B., Ramazan I., Mortality ratio and stock analysis of Vimba (Vimba vimba tenella (Nordmann, 1840)) population ın Karacaoren I Dam Lake (Burdur-Turkey), *Journal of Applied Biological Sciences*, 3 (2009) 143-147.
[26] Becer Z., İkiz R., Investigation of some biological characters of the Vimba (Vimba vimba tenella (Nordmann, 1840)) population in Karacaören I Dam Lake, *Turkish Journal of Veterinary & Animal Sciences,* 25 (2001) 111-117.
[27] Diler, A., Becer Z., Chemical composition and meat yield of vimba (Vimba vimba tenella (Nordmann, 1840)) in Karacaören I Dam Lake, *Turkish Journal of Veterinary & Animal Sciences,* 25 (2001) 87-92.
[28] Mahommed N., Makundi I., Optimization of EDXRF for the study of heavy metal pollution of Lake Victoria, *Tanzania Journal of Science,* 28 (2002) 7-24.
[29] Al-Haidarey M., Hassan F., Al-Kubaisey A., Douabul A., The geoaccumulation index of some heavy metals in Al-Hawizeh Marsh, Iraq, *E-Journal of Chemistry,* 7 (2010) S157-S162.
[30] Loska K., Cebula J., Pelczar J., Wiechuła D., KwapulińskiJ., Use of enrichment, and contamination factors together with geoaccumulation indexes to evaluate the content of Cd, Cu, and Ni in the Rybnik water reservoir in Poland, *Water, Air, and Soil Pollution,* 93 (1997) 347-365.
[31] Hasan A.B., Kabir S., Reza A.S., Zaman M.N., Ahsan A., Rashid M., Enrichment factor and geo-accumulation index of trace metals in sediments of the ship breaking area of Sitakund Upazilla (Bhatiary–Kumira), Chittagong, Bangladesh, *Journal of Geochemical Exploration*, 125 (2013) 130-137.
[32] Krauskoph K., Bird D., *Introduction to geochemistry* McGraw-Hill Inc, New York, (1995) 647.
[33] Krauskopf K.B., Bird D.K., *Introduction to geochemistry*, McGraw-Hill New York, 1967.
[34] Karadede H., Ünlü E., Concentrations of some heavy metals in water, sediment and fish species from the Atatürk Dam Lake (Euphrates), Turkey, *Chemosphere*, 41 (2000) 1371-1376.
[35] Çevik F., Göksu M.Z.L., Derici O.B., Fındık Ö., An assessment of metal pollution in surface sediments of Seyhan dam by using enrichment factor, geoaccumulation index and statistical analyses, *Environmental monitoring and assessment*, 152 (2009) 309-317.
[36] Kır I., Tumantozlu H., Investigation of some heavy metal accumulation in water, sediment and carp (Cyprinus carpio) samples of Karacaoren-II Dam Lake, *Ekoloji*, 21 (2012) 65-70.
[37] Öztürk M., Özözen G., Minareci O., Minareci E., Determination of heavy metals in fish, water and sediments of Avsar Dam Lake in Turkey, *Journal of Environmental Health Science & Engineering*, 6 (2009) 73-80.
[38] Uysal K., Özden Y., Çiçek A., Esengül K., Bioaccumulation ratios of sediment-bound heavy metals of Porsuk and Enne Dam Lakes (Kütahya/Turkey) to different tissues of common carp (Cyprinus carpio), *Aquatic Sciences and Engineering*, 25 (2010) 1-10.
[39] Akin B.S., Kırmızıgül O., Heavy metal contamination in surface sediments of Gökçekaya Dam Lake, Eskişehir, Turkey, *Environmental Earth Sciences*, 76 (2017) 1-11.

Cumhuriyet Sci. J., 44(3) (2023) 583-589
DOI: https://doi.org/10.17776/csj.1290957

Cumhuriyet Science Journal

| csj.cumhuriyet.edu.tr | Founded: 2002 ISSN: 2587-2680 e-ISSN: 2587-246X Publisher: Sivas Cumhuriyet University

Cross-Section Calculations of Medical Radioisotope ^{64}Cu via some Proton, Neutron and Deuteron Reactions

Tuğçe Gülümser [1,a,*], Abdullah Kaplan[1,b]

[1] *Department of Physics., Süleyman Demirel University, Isparta, Türkiye*
**Corresponding author*

Research Article

History
Received: 01/05/2023
Accepted: 11/07/2023

ABSTRACT

The Copper-64 radioisotope, whose academic research continues on diagnostic and therapeutic use, was examined in this study. ^{64}Cu radioisotope is unique among other Cu isotopes for medical usage due to its low positron energy, appropriate half-life, and short tissue penetration. In cases where experimental data are missing, cross-section calculations can be used, and the existence of the cross-section data may provide various advantages in managing time, cost, and efficiency. In this context, investigated detailed cross-section calculations of the ^{64}Cu isotope. To this end, cross-sections acquired from various calculation codes were compared with the literature, and alternative production routes were investigated. Using the nuclear reaction codes TALYS and EMPIRE, cross-section data of the ^{64}Cu isotope were obtained from the ^{64}Ni(p,n)^{64}Cu, ^{65}Cu(p,n+p)^{64}Cu, ^{68}Zn(p,n+α)^{64}Cu, ^{65}Cu(n,2n)^{64}Cu, ^{64}Ni(d,2n)^{64}Cu, and ^{63}Cu(d,p)^{64}Cu reactions with the equilibrium and pre-equilibrium models. The results were compared with the available literature data from the EXFOR database.

Keywords: Copper-64, Cross-section, EMPIRE 3.2, Medical Radioisotope, TALYS 1.95.

[a] *tugcegulumser87@gmail.com* *https://orcid.org/0000-0002-1168-4917* [b] *abdullahkaplan@sdu.edu.tr* *https://orcid.org/0000-0003-2990-0187*

Introduction

Radioisotopes are a fascinating and powerful aspect of modern science. These isotopes, which are unstable and emit radiation, have revolutionized industries ranging from medicine to agriculture. Their unique properties enable them to be used in various applications, such as cancer treatment and food preservation, making radioisotopes an essential part of our daily lives. One of the most significant applications of radioisotopes is in medical imaging and cancer treatment. Radioisotopes release radiation that can kill cancer cells, while imaging techniques use radioactive tracers to pinpoint the origin and extent of the disease. Today, the research and cost-effective production of medical radioisotopes are considerable in terms of easy access and the development of cancer treatments. For this purpose, the Copper-64 radioisotope, on which academic research continues for diagnostic and therapeutic purposes, was examined in this study [1, 2]. The element Copper (Cu) exists at 1.4–2.1 mg/kg in the human body, and it is significant because it is the third most abundant metal after Iron and Zinc [3]. Cu-64 is one of the Cu isotopes, with a half-life of 12.7 hours (β+(19%), β−(40%), EC (41%)), and gamma-ray energies of 511 (35%) and 1346 (0.6%) keV, respectively [1]. It is unique among Cu isotopes for medical use due to its low positron energy (650 keV endpoint), appropriate half-life, and short tissue penetration [4]. Thanks to these features and the absence of significant additional radioactive decay, it allows image acquisition from modern Positron Emission Tomography (PET) scanners with an accuracy of a few millimeters. ^{64}Cu is a cyclotron-produced radionuclide used for diagnosis and/or therapeutic (immuno-PET and hypoxia imaging) purposes [2]. At the same time, several articles were published in which ^{64}Cu was used as a radiotracer targeting neuroendocrine, prostate, and hypoxic tumors in cancer imaging [5-9]. It was emphasized that it was a new era-opening radioisotope in PET imaging [3]. In addition to the advantages mentioned, the only disadvantage is that, due to the low branching rate, it needs to be applied in more significant amounts than other commonly used ^{18}F and ^{11}C radioisotopes to obtain the same quality image in the same tissue. There are several methods for producing ^{64}Cu in the literature, but the ^{64}Ni(p,n) reaction is the most commonly used. In this production route, incoming proton energies of 11–14 MeV are hit against an enriched ^{64}Ni target, and the production cross-sections are highest at 11 MeV (max. 600 millibarns) [1]. This production process is also compatible with the low-energy cyclotrons commonly used to produce ^{18}F and ^{11}C. As mentioned earlier, radioisotopes are generally made this way, but the low natural abundance ^{64}Ni is a drawback, making the material expensive [2].

In cases where experimental data are missing, cross-section calculations can be used, which provides more advantages in terms of time and cost. Many studies contribute to the literature with cross-section calculations [10-12]. In this context, detailed cross-section calculations of the ^{64}Cu isotope, which has many uses in the medical field due to the advantages listed

above, were investigated. Therefore, different production routes were searched, and cross-sections derived from several calculation programs were compared with the experimental data of the reactions [13-16]. The production cross-section of the ^{64}Cu with the ^{64}Ni(p,n)^{64}Cu, ^{65}Cu(p,n+p)^{64}Cu, ^{68}Zn(p,n+α)^{64}Cu, ^{65}Cu(n,2n)^{64}Cu, ^{64}Ni(d,2n)^{64}Cu, and ^{63}Cu(d,p)^{64}Cu reactions were examined by using the equilibrium and pre-equilibrium models of nuclear reaction codes of TALYS 1.95 [17] and EMPIRE 3.2 [18]. In addition, calculation results and experimental data from the EXFOR [19] data library were compared. Calculations were done using the relative variance analysis method [20] to find the most compatible model with the experimental data. Finally, the results were compared with the most commonly used routes in IAEA (International Atomic Energy Agency) Radioisotopes and Radiopharmaceuticals Reports [1, 2].

Materials and Methods

The cross-section means the probability that a reaction occurs. It may not be possible to take measurements of some short half-lived nuclei. In such cases where the experimental data is insufficient or difficult to obtain, incomplete data can be completed using the results obtained by utilizing nuclear reaction codes. It is also advantageous in terms of time, effort, and cost. Many calculation programs are available to receive the cross-section data of various reactions; TALYS and EMPIRE, used in this study, are two of them. Various nuclear reaction programs are used in many studies in the literature, where more experimental data are needed to determine suitable calculation methods [21-30].

TALYS 1.95 is an open-source, free nuclear reaction analysis and prediction software. The TALYS nuclear reaction code has two related purposes. First, it is a nuclear physics tool to analyze nuclear reaction experiments. The second is to use it as a nuclear data tool by adjusting the reaction models and parameters when no measurements are available. In 2019, TALYS version 1.95 was released. It analyzes and estimates nuclear reactions with target's masses 12 and heavier neutron, proton, deuteron, triton, ^{3}He, and alpha-particle-induced within the 0.001–1000 MeV energy interval [17].

For this study, another program used to calculate the cross-section is EMPIRE 3.2. EMPIRE is a computer program comprising various nuclear models and nuclear reaction calculation codes designed to calculate the energies and particles over a wide range of energy. Deuterons, photons, nucleons, helions (^{3}He), tritons, alpha-particles, and light or heavy ions can be selected as projectiles. The possible energy range extends to several hundred MeV for the chosen particles [18].

A nuclear reaction mechanism depends on the energy of the incoming particle. Therefore, compound nuclear processes predominate in reactions in which incoming particles have energies below 10 MeV. The Hauser-Feshbach theory studies nuclear reactions resulting in the composite nucleus's decay into discrete and continuous states. In this study, equilibrium calculations have been acquired using the Hauser-Feshbach model. The following equation, which is the most basic version of the Hauser-Feshbach formula: denotes the cross-section of the compound nuclear reaction, where the input channel is represented by a, and the exit channel is β, with no spin and no angular momentum [31-32].

$$\sigma_{a\beta} = \pi \lambda_a^{2} (2\ell + 1)\, T_a T_\beta / \Sigma_i T_i \qquad (1)$$

Pre-equilibrium calculations were made using the Two-Component Exciton Model, which is highly effective at explaining the high-energy section of the energy spectrum in reactions involving protons, neutrons, and alpha particles with energies between 10 and 60 MeV. However, these models accurately anticipate the emitted particles' angular distributions. In the equation below, the pre-equilibrium cross-section of a particle k with emission energy E_k, the mean lifetime τ of the exciton state, the compound nuclear cross-section σ, and the emission rate W_k are shown [33-34].

$$\frac{d\sigma^{PY}}{dE_k} = \sigma^{CE} \sum_{p_\pi = p_\pi{}^0}^{p_\pi{}^{max}} \sum_{p_\nu = p_\nu{}^0}^{p_\nu{}^{max}} W_k(p_\pi, h_\pi, p_\nu, h_\nu, E_k)\, \tau(p_\pi, h_\pi, p_\nu, h_\nu)\, x\, P(p_\pi, h_\pi, p_\nu, h_\nu) \qquad (2)$$

The most similar model with the experimental data was determined using relative variance analysis. Equation 1 shows that the model with the slightest difference between the experimental data and the data obtained from the cross-section calculations is the best model that can be selected [20].

$$D = \frac{1}{N} \sum_{i=1}^{N} \left| S^{cal}{}_i - S^{exp}{}_i \right| / S^{exp}{}_i \qquad (3)$$

Results and Discussion

The production cross-sections of the ^{64}Ni(p,n)^{64}Cu, ^{65}Cu(p,n+p)^{64}Cu, ^{68}Zn(p,n+α)^{64}Cu, ^{65}Cu(n,2n)^{64}Cu, ^{64}Ni(d,2n)^{64}Cu and ^{63}Cu(d,p)^{64}Cu reactions were investigated up to 60 MeV using TALYS 1.95 and EMPIRE 3.2 nuclear reaction codes with equilibrium and pre-equilibrium models. Moreover, graphical representations of the results are shown in Figs. 1-6. The Two-

Component Exciton model represented the pre-equilibrium state of the TALYS 1.95 program and the equilibrium state by the Hauser-Feshbach model. Similarly, the EMPIRE 3.2 program employed the Hauser-Feshbach model for the equilibrium state and the Exciton Model for the pre-equilibrium state. The relative variance analysis method was utilized to identify the most appropriate reaction and model for producing the ^{64}Cu after comparing the calculated results with the experimental data from the EXFOR data library. Table 1 shows the results of the relative variance analysis. Furthermore, optimal production energy intervals are shown in Table 2.

The experimental data for the ^{64}Ni(p,n)^{64}Cu reaction and the graph of the data obtained from the calculations are shown in Figure 1; experimental data, which is indicated by dots, compared with the calculation results (lines) from the studies of Rebeles et al. [35], Avila-Rodriguez et al. [36], Tanaka et al. [37] and Guzhovskij et al. [38]. The pre-equilibrium models of the EMPIRE and TALYS programs for this reaction follow similar features to the experimental data. Still, the TALYS 1.95 Two-Component Exciton model fits better with the experimental data. In addition, according to the analysis results, as indicated in Table 1, the model most compatible with the experimental data is the TALYS Two-Component Exciton Model. The optimum production energy range of the reaction is shown in Table 2 and is 8→13 MeV.

Figure 2 depicts the data of the ^{65}Cu(p,n+p)^{64}Cu reaction with a two-channel output. Experimental data of the mentioned reaction were taken from the relevant study [39] from the EXFOR database [19]. The graph shows that after 20 MeV proton energy, the TALYS Two-Component Exciton model is in almost perfect agreement with the experimental data. As can be seen from Table 1, the TALYS Two-Component Exciton model is very close to the experimental data. The optimum production energy range of the reaction is 19→24 MeV, as shown in Table 2.

Figure 3 shows another two-output channel reaction through the ^{68}Zn(p,n+α)^{64}Cu. Experimental data was obtained from the study of Hilgers et al. [40]. Again, it is seen that no model could fit the experimental data up to 15 MeV of proton energy. However, after this energy value, it can be said that the Two-Component Exciton Model is more compatible with the experimental data than the other models, and the relative variance analysis also supports this result. This reaction's optimum production energy range is 21→26 MeV (Table 2).

Figure 4 shows the production cross-section of the ^{65}Cu(n,2n)^{64}Cu reaction, which is used to generate ^{64}Cu radioisotopes with the contributions of Mannhart's [41] and Paulsen's [42] studies. EMPIRE Hauser-Feshbach and the EMPIRE Exciton models are consistent with experimental data up to a 14 MeV neutron incident energy value. According to the results of the mathematical analysis, the EMPIRE Exciton model appeared to be the closest model to the experimental data. Therefore, this graph's optimum production energy range is 12→19 MeV.

The results of reaction ^{64}Ni(d,2n)^{64}Cu studied by Daraban et al. and Hermanne et al. [43, 44] were found in a similar feature to the theoretical model results. However, the pre-equilibrium models gave results closer to the experimental data. According to the calculation results in Table 1, the EMPIRE Exciton model gave the results most proximate to the experimental data. As mentioned above, the optimum production energy range of the reaction is 12→16 MeV.

The ^{63}Cu(d,p)^{64}Cu reaction is examined in Figure 6. The EMPIRE Exciton model in the graph perfectly agrees with the experimental data [45, 46]. The optimum generation energy range is 6→9 MeV. According to the calculation results, the EMPIRE Exciton model for the reaction in question gave the closest result to the experimental data.

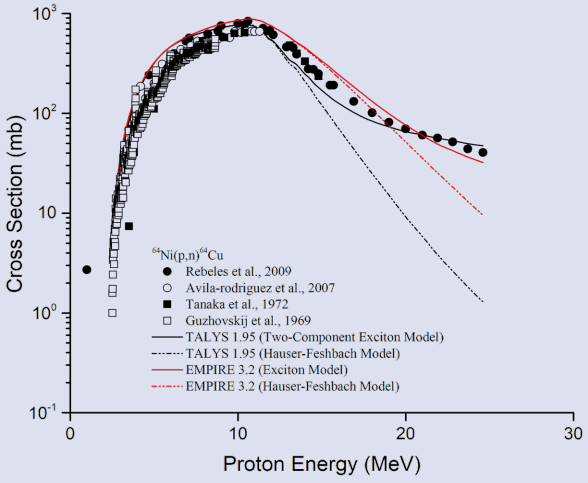

Figure 1. Cross-sections calculations of the ^{64}Ni(p,n)^{64}Cu reaction

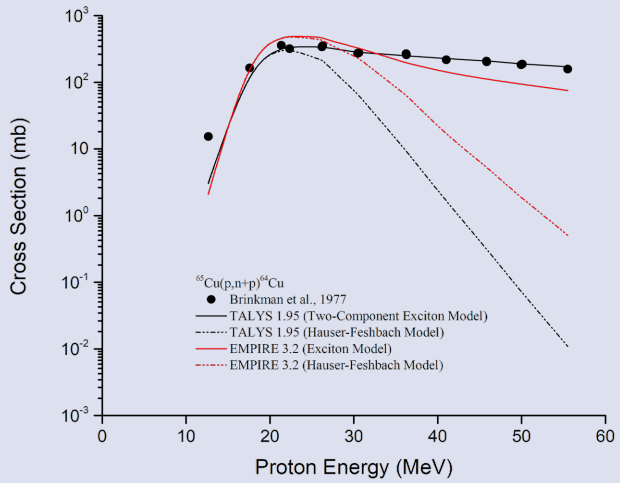

Figure 2. Cross-sections calculations of the ^{65}Cu(p,n+p)^{64}Cu reaction

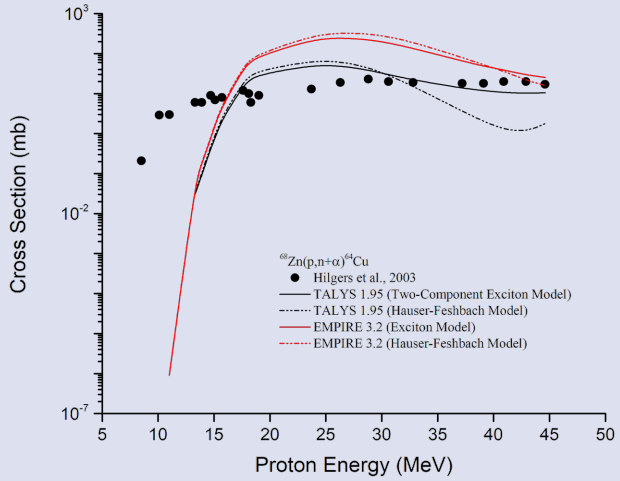

Figure 3. Cross-sections calculations of the ^{68}Zn(p,n+α)^{64}Cu reaction

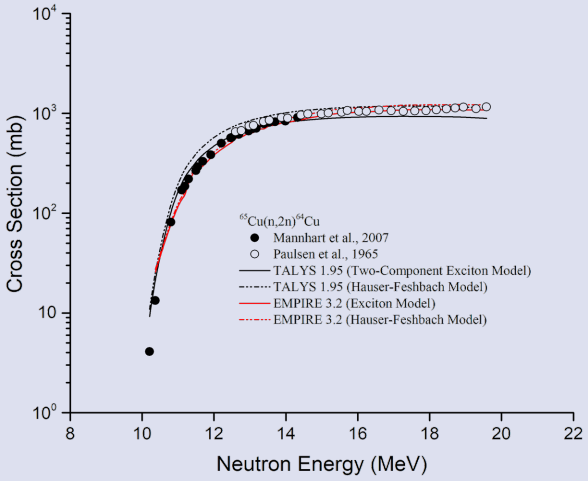

Figure 4. Cross-sections calculations of the ^{65}Cu(n,2n)^{64}Cu reaction

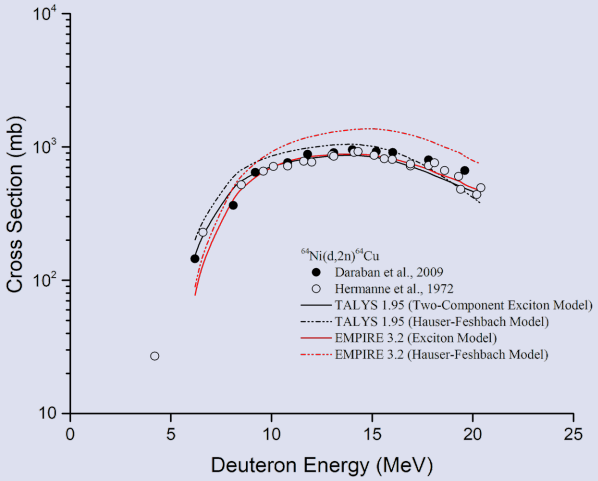

Figure 5. Cross-sections calculations of the ^{64}Ni(d,2n)^{64}Cu reaction

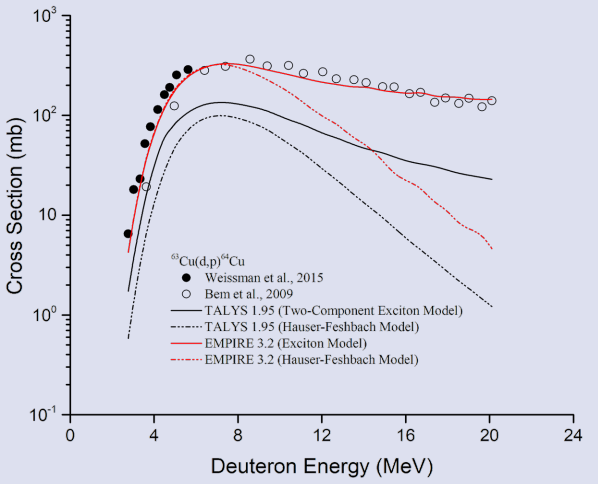

Figure 6. Cross-sections calculations of the ^{63}Cu(d,p)^{64}Cu reaction

Table 1. Relative variance analysis of ^{64}Cu production cross–section calculations

Reactions	TALYS Two-Component Exciton	TALYS Hauser-Feshbach	EMPIRE Exciton	EMPIRE Hauser-Feshbach
^{64}Ni(p,n)^{64}Cu	0.5982	0.6039	0.6173	0.6171
^{65}Cu(p,n+p)^{64}Cu	0.0527	0.6492	0.3759	0.5807
^{68}Zn(p,n+α)^{64}Cu	0.8430	1.2297	4.8293	6.3229
^{65}Cu(n,2n)^{64}Cu	0.1116	0.1441	0.0650	0.0664
^{64}Ni(d,2n)^{64}Cu	0.0772	0.1716	0.0677	0.4702
^{63}Cu(d,p)^{64}Cu	0.7788	0.8832	0.3760	0.7472

Table 2. Optimum energy of ^{64}Cu production

Radioisotope	Production Reaction	Optimum Energy Interval (MeV)
^{64}Cu	^{64}Ni(p,n)^{64}Cu	8→13
^{64}Cu	^{65}Cu(p,n+p)^{64}Cu	19→24
^{64}Cu	^{68}Zn(p,n+α)^{64}Cu	21→26
^{64}Cu	**^{65}Cu(n,2n)^{64}Cu**	12→19
^{64}Cu	^{64}Ni(d,2n)^{64}Cu	12→16
^{64}Cu	^{63}Cu(d,p)^{64}Cu	6→9

Conclusion

In this study, to contribute to the development of the ^{64}Cu radioisotope production routes, the production cross-sections of the ^{64}Ni(p,n)^{64}Cu, ^{65}Cu(p,n+p)^{64}Cu, ^{68}Zn(p,n+α)^{64}Cu, ^{65}Cu(n,2n)^{64}Cu, ^{64}Ni(d,2n)^{64}Cu and ^{63}Cu(d,p)^{64}Cu reactions have been examined up to 60 MeV via equilibrium and pre-equilibrium models with TALYS 1.95 and EMPIRE 3.2 nuclear reaction codes in where the graphical representations of the outcomes are given in Figs. 1-6. Two-Component Exciton Model was used in the TALYS 1.95 program for the pre-equilibrium state, while the Hauser-Feshbach model was used for the equilibrium state. Similarly, in EMPIRE 3.2 program, Exciton Model was used for the pre-equilibrium state, while the Hauser-Feshbach model was used for the equilibrium state. Calculated results have competed with experimental data taken from the EXFOR data library.

Considering the reactions examined in this study, the cross-section calculation results obtained with the pre-equilibrium models rather than the equilibrium models are compatible with the experimental data. On the other hand, the Hauser-Feshbach models describing the equilibrium state disagreed with the experimental results, except for Figures 4–5.

Conflicts of Interest

There are no conflicts of interest in this work.

References

[1] IAEA (International Atomic Energy Agency), IAEA Radioisotopes and Radiopharmaceuticals Reports No. 1; Cyclotron Produced Radionuclides: Emerging Positron Emitters for Medical Applications: ^{64}Cu and ^{124}I, https:// https://www.iaea.org/publications/10791/cyclotron-produced-radionuclides-emerging-positron-emitters-for-medical-applications-64cu-and-124i Retrieved April 4, 2022.

[2] IAEA (International Atomic Energy Agency), Cyclotron Produced Radionuclides: Principles and Practice, Technical Reports Series No. 465, https://www-pub.iaea.org/MTCD/publications/PDF/trs465_web.pdf. Retrieved March 21, 2022.

[3] Gutfilen B., Souza S. A., Valentini G., Copper-64: A Real Theranostic Agent, *Drug Des. Devel. Ther*., 12 (2018) 3235–3245.

[4] Boschi A., Martini P., Janevik-Ivanovska E., Duatti A., The Emerging Role of Copper-64 Radiopharmaceuticals as Cancer Theranostics, *Drug Disc. Today*, 23(8) (2018) 1489–1501.

[5] Capriotti G., Piccardo A., Giovannelli E., Signore A., Targeting Copper in Cancer Imaging and Therapy: A New Theragnostic Agent, *J Clin Med*, 12(1) (2022) 223.

[6] Peng F., Recent Advances in Cancer Imaging with ^{64}CuCl2 PET/CT, *Nucl Med Mol Imaging*, 56(2) (2022) 80-85.

[7] Jalilian AR., Osso JA Jr., Vera-Araujo J., et al., IAEA Contribution to the Development of ^{64}Cu Radiopharmaceuticals for Theranostic Applications, *Q. J. Nucl. Med. Mol. Imaging*, 64(4) (2020) 338-345.

[8] Follacchio GA., De Feo MS., De Vincentis G., Monteleone F., Liberatore M., Radiopharmaceuticals Labelled with Copper Radionuclides: Clinical Results in Human Beings, *Curr. Radiopharm*., 11(1) (2018) 22-33.

[9] Ahmedova A., Todorov B., Burdzhiev N., Goze C., Copper Radiopharmaceuticals for Theranostic Applications, *Eur. J. Med. Chem.*, 157 (2018) 1406-1425.

[10] Kaplan A., Şekerci M., Çapalı V., Photon Induced Reaction Cross-Section Calculations of Several Structural Fusion Materials, J Fusion Energ, 36 (2017) 213–217.

[11] Ozdogan H., ŞEKERCİ M., KAPLAN A, A new developed semi-empirical formula for the (alpha, p) reaction cross-section at 19 +/- 1 MeV, Modern Physics Letters A, 34 (2019) 6.

[12] Şekerci, M. Effects of theoretical models on the production cross-section calculations of some non-standard positron emitters., Eur. Phys. J. Plus 136 (2021) 1021.

[13] Krane, K.S., Nükleer Fizik II, Çev. Sarer B., Palme Yayıncılık, 479s (2001) Ankara.

[14] Özdoğan H., Şekerci M., Kaplan A., An Investigation on the Effects of Some Theoretical Models in the Cross-Section Calculations of ^{50,52,53,54}Cr(α,x) Reactions, *Phys. At. Nucl*., 83 (6) (2020) 820-827.

[15] Şekerci M., Özdoğan H., Kaplan A., An Investigation of Effects of Level Density Models and Gamma Ray Strength Functions on Cross-Section Calculations for the Production of ^{90}Y, ^{153}Sm, ^{169}Er, ^{177}Lu and ^{186}Re Therapeutic Radioisotopes via (n,g) Reactions, *Radiochim. Acta*, 108 (1) (2020) 11-17.

[16] Şekerci M., Theoretical Cross-Section Calculations for the (α,n) and (α,2n) Reactions on ^{46}Ti, ^{50}Cr, ^{54}Fe, and ^{93}Nb Isotopes, *Mosc. Univ. Phys. Bull*., 75 (2) (2020) 123-132.

[17] Koning A., Hilaire S., Goriely S., TALYS–1.95 A Nuclear Reaction Program, User Manual. 1st ed. NRG, The Netherlands (2019).

[18] Herman M., EMPIRE: Nuclear Reaction Model Code System for Data Evaluation, *Nuclear Data Sheets*, 108(12) (2007) 2655-2715.

[19] Zerkin V.V., Pritychenko B., The experimental nuclear reaction data (EXFOR): Extended Computer Database and Web Retrieval System, *Nucl. Instrum. Methods. Phys. Res. A*, 888 (2018) 31–43.

[20] Kurenkov, N.V., Lunev, V.P., Shubin, Y.N., Evaluation of Calculation Methods for Excitation Functions for Production of Radioisotopes of Iodine, Thallium and Other Elements, Applied Radiation and Isotopes, 50(3) (1999) 541-549.

[21] Gülümser T., Kaplan A., A Theoretical Study on the Production Cross–Section Calculations for ^{24}Na Medical Isotope, *Erzincan Üniversitesi Fen Bilimleri Enstitüsü Dergisi*, 14 (2) (2021) 802-813.

[22] Şekerci M., An Investigation of the Effects of Level Density Models and Alpha Optical Model Potentials on the Cross-Section Calculations for the Production of the Radionuclides ^{62}Cu, ^{67}Ga, ^{86}Y, and ^{89}Zr via Some Alpha Induced Reactions, *Radiochim. Acta*, 108 (6) (2019) 459-467.

[23] Şekerci M., Özdoğan H., Kaplan A., Investigation on the Different Production Routes of ^{67}Ga Radioisotope by Using Different Level Density Models*, Mosc. Univ. Phys. Bull*., 74 (2019) 277-281.

[24] Şekerci M., Özdoğan H., Kaplan A., Level Density Model Effects on the Production Cross-Section Calculations of

Some Medical Isotopes via (α,xn) Reactions where x=1–3, *Mod. Phys. Lett. A.*, 35 (2020) 24.

[25] Özdoğan H., Şekerci̇ M., Kaplan A., Photo-Neutron Cross-Section Calculations of ^{54,56}Fe, ^{90,91,92,94}Zr, ^{93}Nb and ^{107}Ag Isotopes with Newly Obtained Giant Dipole Resonance Parameters, *Appl. Radiat. Isot.*, 165 (2020).

[26] Özdoğan H., Estimation of (n,p) Reaction Cross Sections at 14.5±0.5 MeV Neutron Energy by Using Artificial Neural Network, *Appl. Radiat. Isot.*, (2021) 170.

[27] Kaplan A., Özdoğan H., Aydın A., Tel E., (γ,2n) Reaction Cross Section Calculations on Several Structural Fusion Materials, *Journal Fusion Energy*, 32 (2013) 431–436.

[28] Kaplan A., Özdoğan H., Aydın A., Tel E., Deuteron-Induced Cross Section Calculations of Some Structural Fusion Materials, *Journal of Fusion Energy*, 32 (2013) 97–102.

[29] Kaplan A., Tel E., Aydın A., The Equilibrium and Pre-equilibrium Neutron-Emission Spectra of Some Structural Fusion Materials for (n,xn) Reactions up to 16 MeV Energy, *Physics of Atomic Nuclei*, 72 (6) (2009) 903–910.

[30] Özdoğan H., Şekerci̇ M., Kaplan A., Investigation of Gamma Strength Functions and Level Density Models Effects on Photon Induced Reaction Cross–Section Calculations for the Fusion Structural Materials ^{46,50}Ti, ^{51}V, ^{58}Ni and ^{63}Cu, *Applied Radiation and Isotopes*, 143 (2019) 6-10.

[31] Carlson, B. V., 2001. A Brief Overview of Models of Nucleon-Induced Reactions, Workshop on Nuclear Data for Science & Technology: Accelerator Driven Waste Incineration, The Abdus Salam International Centre for Theoretical Physics, 10-21 September 2001, Miramare - Trieste, Italy, 185-239. Erişim Tarihi: 21.09.2021. http://www.iaea.org/inis/collection/NCLCollectionStore/_Public/38/071/38071998.pdf

[32] Griffin, J. J., 1966. Statistical model of intermediate structure, *Physical Review Letters*, 17, 478-481.

[33] Hauser, W., Feshbach, H., The Inelastic Scattering of Neutrons, *Physical Review*, 87(2) (1952) 366-373.

[34] Hodgson, P. E., Pre-Equilibrium Processes in Nuclear Reactions, Nature 292 (1981) 671-672.

[35] Rebeles, R. A., Van den Winkel, Hermanne, A. and Tárkányi, F., New measurement and evaluation of the excitation function of 64Ni(p,n) reaction for the production of 64Cu, *Nuclear Instruments and Methods in Physics Research*, 267 (2009) 457-461.

[36] Avila-Rodriguez, M.A., Nye, J.A., Nickles, R.J., Simultaneous production of high specific activity 64Cu and 61Co with 11.4 MeV protons on enriched 64Ni nuclei *Applied Radiation and Isotopes*., 65 (2007) 1115–1120.

[37] Tanaka, S., Furukawa, M., & Chiba, M., Nuclear reactions of nickel with protons up to 56 MeV, *Journal of Inorganic and Nuclear Chemistry*, 34 (1972) 2419-2426.

[38] Guzhovskii, B.Y., Borkin, I.M., Zvenigorodskii, A.G., Rudnev, V.S., Solodovnikov, A.P., Trusillo, S., Isospin mixing of isobar analog resonances observed for the 59,61,63,65Cu nuclei. *Izvestiya Rossiiskoi Akademii Nauk*., 33 (1969).

[39] Brinkman, G.A., Helmer, J., Lindner, L., *Rhys.Rev.Lett*., 28 (1977) 9.

[40] Hilgers, K., Stoll, T., Skakun, Y., Coenen, H., Qaim, S. M., Cross-section measurements of the nuclear reactions ^{nat}Zn(d,x)^{64}Cu, ^{66}Zn(d,α)^{64}Cu and ^{68}Zn(p,α+n)^{64}Cu for production of ^{64}Cu and technical developments for small-scale production of ^{67}Cu via the ^{70}Zn(p,α)^{67}Cu process., *Applied radiation and isotopes: including data, instrumentation and methods for use in agriculture, industry and medicine*, 59(5-6) (2003) 343–351.

[41] Mannhart, W., Schmidt, D., Measurement of Neutron Activation Cross Sections in the Energy Range from 8 MeV to 15 MeV, *Physikalisch-Technische Bundesanstalt Neutronenphysik Reports*, 53 (2007).

[42] Paulsen, A., Liskien, H., Cross Sections For The Reactions Mn^{55}(n,2n), Co^{59}(n,2n) Mg^{24}(n,p) and Al^{27}(n,α) in the 12.6-19.6 MeV Energy Region, *Journal of Nuclear Energy. Parts A/B. Reactor Science and Technology*, 19 (1965) 907.

[43] Daraban, L., Adam Rebeles, R., Hermanne, A., Tarkanyi, F., Takacs, S., Study of the excitation functions for ^{43K,} ^{43,44,44m}Sc and ^{44}Ti by proton irradiation on ^{45}Sc up to 37MeV, *Nuclear Instruments and Methods in Physics Research Section B: Beam Interactions with Materials and Atoms*, 267(5) (2009) 755–759.

[44] Hermanne, A., Tarkanyi, F., Takacs, S., Kovalev and F., Ignatyuk, Activation Cross Sections of the ^{64}Ni(d,2n)Reaction for the Production of the Medical Radionuclide ^{64}Cu, *Nucl. Instr. Meth. In Physics B*.,258 (2007).

[45] Weissman, L., Kreisel, A., Hirsh, T., Aviv, O., Berkovits, D., Girshevitz, O., Eisen, Y., Accurate measurements of the ^{63}Cu(d,p)^{64}Cu and ^{nat}Cu(d,x)^{65}Zn cross-sections in the 2.77–5.62 MeV energy range., *Nuclear Instruments and Methods in Physics Research Section B: Beam Interactions with Materials and Atoms*. 342 (2015) 7–12.

[46] Bém, P., Šimečková, E., Honusek, M., Fischer, U., Simakov, S.P., Forrest, R.A., Avrigeanu, M., Obreja, A., Román, F.L., Avrigeanu, V., Low and medium energy deuteron-induced reactions on {sup 27} al., *Physical Review C.*, 79 (2009) 044610.

Cumhuriyet Sci. J., 44(3) (2023) 590-594
DOI: https://doi.org/10.17776/csj.1061321

Cumhuriyet Science Journal

| csj.cumhuriyet.edu.tr | Founded: 2002 ISSN: 2587-2680 e-ISSN: 2587-246X Publisher: Sivas Cumhuriyet University

Comparison of Proton and Photon Radiotheraphy for Left-sided Breast Cancer via Dosimetric Calculations

Inci Yeşildere Özateş[1,a,*], Sinan Kuday[2,b]

[1] *Medical Physics, Institute of Graduate School of Sciences, İstanbul Aydin University, 34295, İstanbul, Türkiye*
[2] *Physics Department, Ankara University, Tandogan, 06100, Ankara, Türkiye*
**Corresponding author*

Research Article

History
Received: 21/01/2022
Accepted: 31/07/2023

ABSTRACT

Breast cancer is the most common type of cancer in women. Today, the radiotherapy method is widely preferred to treat cancer patients where proton therapy is a radiotherapy method used to destroy cancerous cells using proton beams with unique characteristics. Photon therapy, on the other hand, is a classical radiotherapy method that treats cancerous cells by targeting ionizing radiation. In our study, a tumor was placed in the left breast in a water phantom with the help of the Geant4 simulation program and geometry with critical organs was modeled. With this simulation, the doses received by the organs were interpreted and comparisons were made using the chi-square method as the two different source beams, proton and photon deployed. When the percentile values in the dose table are normalized for 1 Gy, the test statistic obtained as 0.467, and the H_0 hypothesis is rejected at the $\alpha = 0.975$ Statistically, we measured the significant differences between proton and photon dose values for tumors and other organs by Geant4 simulations.

Keywords: Breast cancer, Proton therapy, Photon therapy, GATE, Monte Carlo.

[a] *inci.yesildere@gmail.com* *https://orcid.org/0000-0002-7461-6719* [b] *kuday@cern.ch* *https://orcid.org/0000-0002-0116-5494*

Introduction

Recently, cancer has taken place on the top among health problems all around the world. It is seen that breast cancer is one of the cancer types that affect the health of women in many countries. The increase of cancer cases has led to a rise in the variety of diagnoses and treatments of cancer therefore radiotherapy is the most important factor for breast cancer. [1] Breast cancer radiotherapy aims to protect by giving a minimum dose to healthy tissues while creating a homogeneous dose distribution in the target volume [2] In photon radiotherapy, while the rays are moving through the living tissue, they are scattered by Compton scattering and when they reach the cancerous area, leaving most of their energy on the healthy tissue means that they have destroyed the healthy tissues. In proton radiotherapy, higher doses can be given to the cancerous area in a controlled manner and minimal damage to the healthy tissue can be achieved. Therefore, the use of protons in therapy has come to the fore. The large masses of the protons reduce the scattering in the tissue, so it focuses on the tumor without scattering too much and the healthy tissue is not damaged too much. Protons with energies in the range of 70-250 MeV are used in proton therapy. [3] Geant4-based GATE, a Monte-Carlo simulation software, is being developed by CERN, which has extensive physics resources and is a package program that can provide researchers with ease of analysis. It has been developed in many scientific fields such as modern physics, nuclear physics, radiation physics, nuclear physics. [4] It is important to make the necessary planning to leave the maximum of the radiation energy on the tumor and to give minimum damage to the surrounding healthy tissues, which is the most important factor in radiotherapy using the GATE program. [5]

The outline of the article is as follows: We will describe anthropomorphic phantom simulation in the next section using the GATE software. We will talk about algorithms and dose values obtained with GATE software. In the result part, the Pearson Chi-Square method has been used for analysis study of dozen data and tumor that has been obtained with a software of GATE. In the last part, we will explain the interpretation and result of our study.

Materials and Methods

Anthropomorphic Phantom Preparation with GATE v.9.8

The name Geant is formed by combining the words "Geometry and Tracking. It is a C++ program-based code library developed by CERN, which has an extensive physics library containing tools that can simulate the passage of all kinds of particles through matter and their interaction. [6] It is through macros that we can shape the simulation. In the GATE program, operations such as visualization, applying geometry, identification of physical variable, random number, simulation running hours , or number of participles are created by writing specific codes in Macro files. [7]

Geometry definition is the first step in defining simulation. World geometry, which we have determined as 2.1 m in X, Y, and Z coordinates, is created in the Cartesian coordinate system. Phantom data, created by Medical Internal Radiation Dose Committee, is utilized to simulate human body anatomy and determine the dose absorbed by animals. Whereas Human phantom, 1.70 m tall and 70 kg weight, indicates 20 or 30 years old adult, female phantom data has been utilized. [8] Using the phantom data created by MIRD, organs such as left and right breasts, tumor, heart, brachial plexus, skull, brain, thyroid, lungs, pancreas, stomach, and liver were defined. An adult woman with cancer of the left breast was created in our phantom. The tissues selection is defined as gate/…./setTissue according to the user. In GATE simulation, the physics list was designed as hadronic processes and was added to the physics list by defining it in the format /gate/physics/addPhysicList. Source designation can be defined in the format /gate/source/addSource. Proton and photon rays were determined as the source type. Afterward, the results of the information recorded by the actors which are added to the skin are filed.

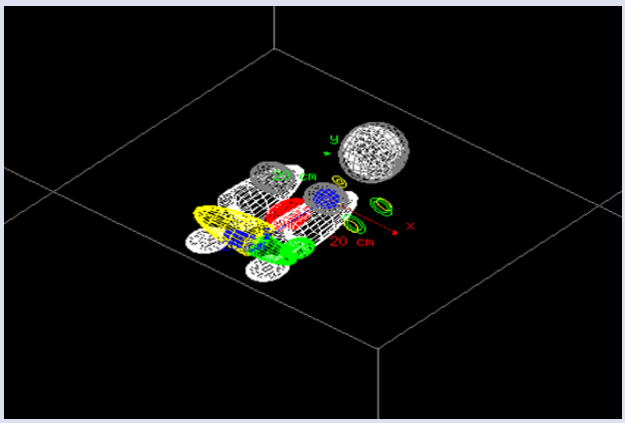

Figure 1. A view from the phantom we made in GATE

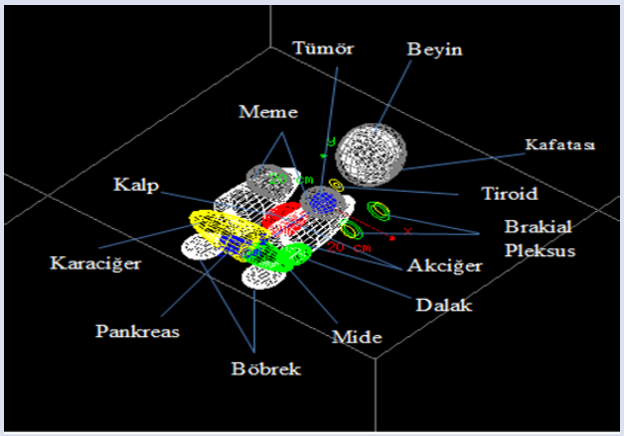

Figure 2. Representation of organs in the phantom prepared in GATE

Dispersed Dose Conversion Coefficient

In the simulation, the source was selected as a proton and photon particle with energy of 250 MeV and irradiation was performed by pencil beam scanning method (PBS). We examined the dose distribution of the tumor and non-target organs that we placed in the left breast as a result of the interactions in the GATE simulation, with the conversion coefficient values. The dose delivered to non-targeted normal organs or tissues is referred to as the “dispersed dose”.

The conversion coefficient was expressed in equation 1:

$$F = \frac{Dd}{Dt} \quad (1)$$

where F was the dispersed dose conversion coefficient, Dd and Dt were the doses delivered to non-targeted tissues and the targeted tissue, respectively. [12] Using table 2 data, the target dose value (Dt) was determined separately for the proton and as the non-target organ(s) dose value (Dd).

Table 1. Conversion coefficient values obtained for tumors and other organs

Proton (F)		Foton (F)	
Left Breast	0.220	Left Breast	0.163
Right Breast	0.008	Right Breast	8.486×10^{-4}
Tumor	1	Tumor	1
Brakial Pleksus	0.001	Brakial Pleksus	2.665×10^{-5}
Skull	2.676×10^{-9}	Skull	1.198×10^{-6}
Brain	1.298×10^{-9}	Brain	4.896×10^{-7}
Thyroid	1.567×10^{-9}	Thyroid	1.678×10^{-6}
Left Lung	7.210×10^{-8}	Left Lung	1.977×10^{-6}
Right Lung	4.459×10^{-9}	Right Lung	6.049×10^{-8}
Liver	4.994×10^{-8}	Liver	5.085×10^{-8}
Left kidney	1.669×10^{-9}	Left kidney	3.105×10^{-8}
Right Kidney	1.034×10^{-9}	Right Kidney	2.567×10^{-8}
Heart	2.189×10^{-7}	Heart	1.908×10^{-5}
Pancreas	8.484×10^{-10}	Pancreas	2.222×10^{-7}
Stomach	7.354×10^{-10}	Stomach	7.083×10^{-8}

Results and Discussion

The global tumor volume placed in the left breast is irradiated by a beam of protons and photons produced by a 300,000 accelerated beam of protons and photons with an energy of 250 MeV. Tumordose actor was called up from determined folder and counted by dose integral account. The pen beam scanning method was used for irradiation with protons and photons. In that study, the hydraulic process was identified in the Physics list, and proton and photon beams were used as a resource. Two separate irradiations were implemented for proton treatment and photon treatment methods. It was observed how many doses a tumor in the left breast received along with how many doses other critical organs were exposed and a comparison was made between the data. Clinically, it is planned to treat a breast tumor with approximately 2 Gy of absorbed radiation per day, 5 days a week, for a period of 5 or 6 weeks, depending on the tumor size. With this planning, it is aimed to irradiate approximately 50 Gy dose to the tumor at the end of the treatment. [7] In Table 1, 15 different organ structures and their stored dose values are given. Dose data in non-field organs remains very low.

Table 2. Dose values of Proton beam and Photon beam stored in organs for DoseActor algorithm of GATE for a single run at 250 MeV.

Proton DoseActor		Foton DoseActor	
Left Breast	2.13663 e-03 Gy	Left Breast	6.966450 e-06 Gy
Right Breast	8.32431 e-05 Gy	Right Breast	3.610050 e-08 Gy
Tumor	9.69002 e-03 Gy	Tumor	4.2541 e-05 Gy
Brakial Pleksus	1.32034 e-05 Gy	Brakial Pleksus	1.134 e-09 Gy
Skull	2.59312 e-11 Gy	Skull	5.09889 e-11 Gy
Brain	1.25811 e-11 Gy	Brain	2.08297 e-11 Gy
Thyroid	1.51849 e-11 Gy	Thyroid	7.138440 e-11 Gy
Left Lung	6.98735 e-10 Gy	Left Lung	8.41123 e-11 Gy
Right Lung	4.32123 e-10 Gy	Right Lung	2.57341 e-12 Gy
Liver	4.8393 e-10 Gy	Liver	2.16321 e-12 Gy
Left kidney	1.61762 e-11 Gy	Left kidney	1.32101 e-12 Gy
Right Kidney	1.00281 e-11 Gy	Right Kidney	1.09213 e-12 Gy
Heart	2.12195 e-09 Gy	Heart	8.12 e-10 Gy
Pancreas	8.2216 e-12 Gy	Pancreas	9.45320 e-12 Gy
Stomach	7.12691 e-12 Gy	Stomach	8.01321 e-12 Gy

Figure 3 and 4 show observed dose absorption values for proton (up) and photon (down) at 2D and 3D plots for left sided breast and tumor tissue respectively.

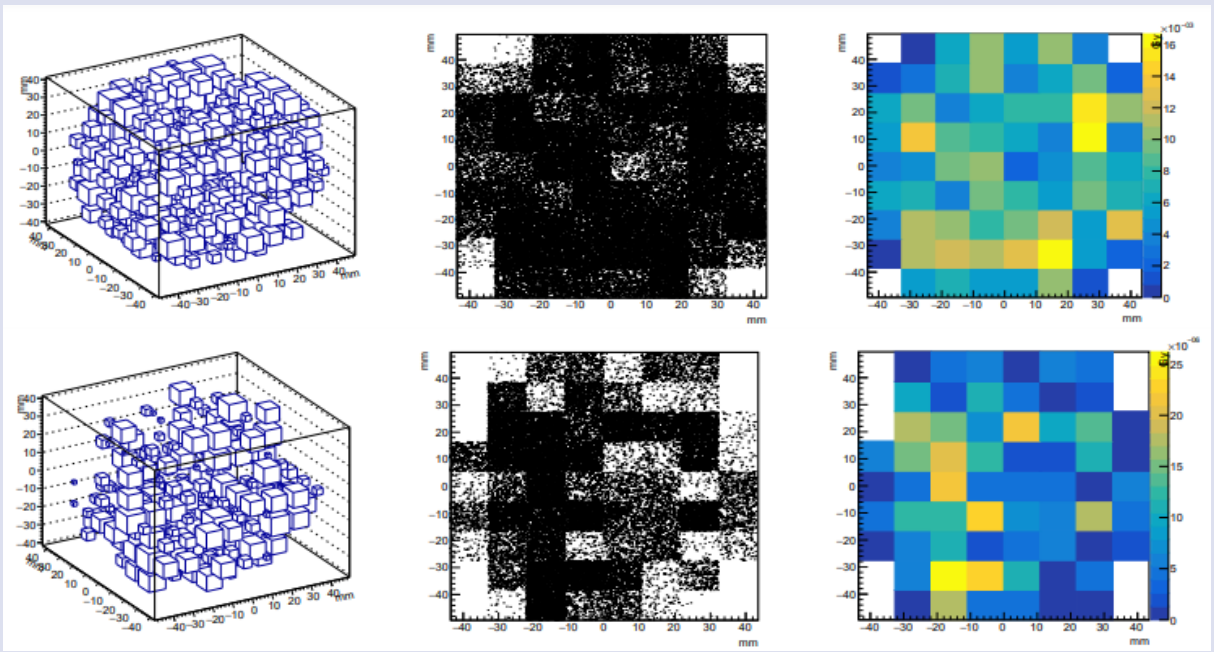

Figure 3. Evaluated via simulation in left breast tissue; first line for proton beams, 3B particle distribution (left), 2B particle distribution (middle) dose distribution (right), second line for photon beams, 3B particle distribution (left), 2B particle distribution (middle), dose distribution (right)

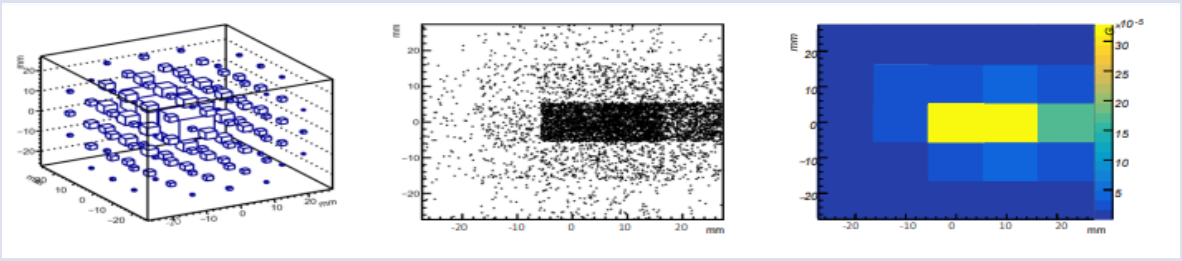

Figure 4. Evaluated via simulation in tumor tissue; first line for proton beams, 3B particle distribution (left), 2B particle distribution (middle) dose distribution (right), second line for photon beams, 3B particle distribution (left), 2B particle distribution (middle), dose distribution (right)

Analyses

The GATE software package was analyzed. The Chi-square method was used for the analysis of the data. In this test, it was examined whether the observed frequencies (Y) were suitable for the expected frequencies (Z) obtained according to a certain hypothesis. The expected values were chosen based on [9] for the proton and photon PTV dose delivery rates as 60% and OAR dose absorption rate as 40%.

The null hypothesis and alternative hypothesis for the chi-square method were established as follows:

H_0: There is no statistically significant difference between proton and photon dose values for tumors and other organs in respect of dose delivery rates.

H_1: There is a statistically significant difference between proton and photon dose values for tumors and other organs in respect of dose delivery rates.

The chi-square analyzes of the data we obtained are calculated over the total dose values, and the chi-square values are shown in Table 3. Calculating chi-square values, we have considered 1 Gy normalised dose values of Table-3 since the separation with proton and photon doses has become significant at the order of 1 Gy.

Table 3. Dose Delivery and Dose absorbtion rates where PTV (Primay Tumor Volume) and OAR (Organs At Risk)

Photon Total Dose	% Photon PTV Dose Delivery Rate	Photon Critical Organ (OAR) Total	% Photon OAR Dose Absorption Rate	% Photon Dose Conversion Coefficient (F) for Breast
4.95 e-05 Gy ProtonTotal Dose	85.86 % % Proton PTV Dose Delivery Rate	7.00 e-06 Gy Proton Critical Organ (OAR)Total Dose	14.14 % % Proton OAR Dose Absorption Rate	16.47 % % Proton Dose Conversion Coefficient (F) for Breast
1.19 e-02 Gy	81.27 %	2.23 e-03 Gy	18.73 %	23.05 %

Table 4. Chi-square dose chart

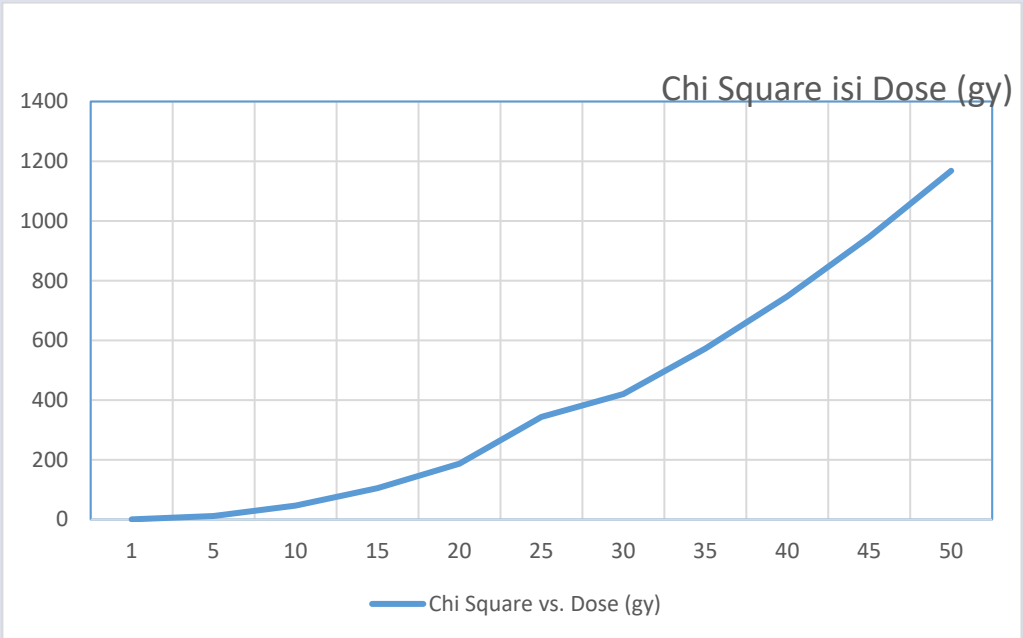

When the percentile values in the dose table are normalized for 1 GL, the test statistic obtained is 0.467, and the Ho hypothesis is rejected because it is greater than the Chi-square table value at the alpha = 0.975 significance level. Statistically significant differences were found between Proton and Photon dose values for tumors and other organs.

Conclusion

In conclusion, the importance of this study is to examine how many doses a tumor receives that we placed in the left breast along with other critical organs that we determined, using the proton radiation treatment and photon radiation treatment methods via the GATE simulation program. [7] There currently have been studies on experimental comparison between proton treatment and photon in the literatüre. [9-12]

The study [9] of Maroufkhani and his friends, MCNPX program Monte Carlo based has been simulated using proton beams. Given to the incoming proton beams in the appropriate energy range causes the Bragg peak to form in the breast tissue. However, due to second particles, the equivalent dose was evaluated for vital organs including the heart and lungs, including photons and neutrons. It has been reported that in breast cancer where proton therapy is compared with photon therapy, the doses formed in the heart and lungs are visible at low rates.

In the study of Lin and his friends [10] ten women patients, early diagnosis of left breast cancer was treated with the help of breast-conserving surgery and radiation. A study was planned by applying all breast proton and photon radiation for a real treatment. Doses given to heart, lad coronary artery, and lungs were made a comparison. Compared to the photon beam plane, proton beam radiation was associated with a 0.2 cm (3) dose to the left anterior descending artery, which is the critical structure for late radiation therapy effects.

In the study of Raptis et al. [11] they investigated the risk of second cancer of critical organs resulting from proton and photon therapy for breast cancer patients. Planning was done with protons and photons to deliver 50 Gy in 25 fractions to the left breast of 12 patients. Lungs, right breast, heart, and esophagus were evaluated as critical organs at risk of developing second cancer. As a result, they stated that protons have more advantages than photons in terms of cancer stimulation.

According to the data we obtained from this study when the percentile values in the dose table are normalized for 1 Gy, the test statistic is 0.467, and the H_0 hypothesis is rejected because it is greater than the Chi-square table value at the alpha = 0.975 significance level. Statistically significant differences were found between Proton and Photon dose values for tumors and other organs if the total dose injected is at the order of 1 Gy or higher. The use of a simulation program (GATE) in this study is promising for similar studies. In radiotherapy, it is important to irradiate the highest radiation energy to the cancerous area, to cause minimal damage to the dose to which other healthy tissues are exposed, and to determine and minimize the out-of-area doses that occur in people working with radiation.

Conflicts of interest

The authors declare that they have no conflict of interest.

References

[1] Yeşil S., The Dosimetric Comparison of the Tomotherapy Helical and Tomotherapy Direct Treatment Techniques in the Radiotherapy of Bilateral Breast Cancer, M.Sc., Istanbul Aydin University, Undergraduate Education Institute, (2019).

[2] Kumaş A., Radiation Physics and Medical Applications, 2nd ed. Ankara, (2006) 128-135.

[3] Martin J. E., Physics for Radiation Protection, 2nd ed.Berlin, (2011) 251-330.

[4] Karadeniz Yildirim A., Determination of Internal Dosimetry in Yttrium-90 Microsphere Treatment by Monte Carlo Method, Ph.D., Istanbul University, Institute of Science and Technology, (2019).

[5] Krane K.S., Nuclear Physics 1, 1st ed, United States of America, (2001) 192-201.

[6] Armutlu B., Proton Therapy with Gate Simulation in the Treatment of Non-Small Cell Lung Cancer, M.Sc., Istanbul Aydin University, Undergraduate Education Institute, (2020).

[7] Panagiotis P., Dosimetry Applications in GATE Monte Carlo Toolkit, *Physica Medica*, 41 (2017) 136-140.

[8] Shdeed T. A., Nahili M., Issa N. A., Bitar A., Study of absorbed dose in important organs during helical CT chest scan using MCNP code and MIRD phantom, *The Egyptian Journal Of Radiology And Nuclear Medicine*, 47(4) (2016) 1649-1663.

[9] Maroufkhani F., Abtahi S.M.M., Kakavand T., Assessment of secondary particles in breast proton therapy by Monte Carlo simulation code using MCNPX, *International Journal of Radiation Research,* 19(1) (2020) 23-29.

[10] Lilie L. L., Sabina V., Andreea D., Daniele Ravanelli K. S., Sonny B., Zelig T., Stefan B. & Gary F., Proton beam versus photon beam dose to the heart and left anterior descending artery for left-sided breast cancer, *Acta Oncologica,* 54(7) (2015) 1032-1039.

[11] Raptis A., Jakab Ö., Oscar A., Anno M.F., Iuliana T.D., Alexandru D., Cancer risk after breast proton therapy considering physiological and radiobiological uncertainties, *Physica Medica,* 76 (2020) 1-6.

[12] Mehrdad B., Dragana K., Dragoslav N., Kwan Y., A comparative study on dispersed doses during photon and proton radiation therapy in pediatric applications, *Plos One*, 16(3) (2021) 1-20.

Cumhuriyet Sci. J., 44(3) (2023) 595-601
DOI: https://doi.org/10.17776/csj.1239911

Cumhuriyet Science Journal

| csj.cumhuriyet.edu.tr | Founded: 2002 ISSN: 2587-2680 e-ISSN: 2587-246X Publisher: Sivas Cumhuriyet University

Synthesis and Characterization of Tb–Er Co–Doped Bi2O3 Solid Electrolyte Systems

Murat Balcı[1, a, *]

[1] *Department of Physics, Faculty of Science, Erciyes University, Kayseri, Türkiye*
**Corresponding author*

Research Article

History
Received: 21/01/2022
Accepted: 31/07/2023

ABSTRACT

In this study, solid state reactions were used to create Er–Tb co–doped Bi2O3 solid electrolyte systems. Four Point Tip Technique (FPPT), Thermo–gravimetric and Differential Thermal Analysis (TG & DTA), and X–Ray Diffraction (XRD) were used to characterize the generated samples' structural and thermal properties, and electrical conductivity. The samples 05Er05TbSB, 05Er10TbSB, and 15Er05TbSB stabilized with cubic δ–phase at room temperature, according to XRD data. Due to the smaller dopants ions compared to the host Bi3+ cation, the lattice constants estimated for these samples were lower than those of the pure cubic phase. The samples were thought to be thermally stable in the studied temperature range since the thermal curves did not show endothermic or exothermic peak development indicating a potential phase change. According to the Arrhenius equation, the temperature–dependent conductivity graphs displayed a linear change. The conductivity measurements clearly indicated that an increase in doping rate results in a sudden drop in electrical conductivity. The calculated activation energies increased with the doping ratio and varied from 0.64 eV to 1.12 eV. At 700 °C, it was determined to be 0.128 $S.cm^{-1}$ for the sample 05Er05TbSB, which had the greatest conductivity and lowest activation energy among all samples. The conductivity was discovered to decrease and activation energy to increase when the doping ratio was gradually raised.

Keywords: Phase Transition, X–Ray Diffraction, Electrical Activation Energy, Electrical conductivity, Solid–State Reaction.

[a] *muratbalci@erciyes.edu.tr* *https://orcid.org/0000–0003–1297–1691*

Introduction

Solid oxide fuel cells (SOFCs) are alternative energy sources that use electrochemistry to create electrical energy. Because it has a higher electrical efficiency output than other fuel cells, this system may be used as an extra source of electricity in standard power units such as hospitals, schools, and companies [1, 2]. However, the SOFC cell's high operating temperature creates several internal challenges. The most serious of them is temperature–related wear (corrosion) at the electrode–electrolyte interfaces, which lowers cell electrical efficiency and reduces battery life [3]. A typical SOFC cell is made up of three basic solid layers. These are the anode, where the fuel gas is oxidized, the cathode, where the oxygen gas is reduced, and the electrolyte layer, which allows the transport of O^{2-} ions from the cathode to the anode boundary [4, 5]. The corrosions cause the solid electrolyte layer to deteriorate, causing the cell to short circuit and the open circuit voltage to decrease dramatically.

Most researchers have also reported internal problems caused by high operating temperature in recent years, and studies have accelerated to lower the SOFC operating temperature to intermediate (500 °C – 750 °C) and low temperatures (300 °C – 500 °C) [6]. The literature commonly claims that at low operating temperatures, intracellular kinetic reactions slow down and the temperature–dependent electrical conductivity of the solid electrolyte decreases. Because of the poor ion conductive performance of the electrolyte, the great electrical efficiency attained at high temperatures is greater than at low temperatures. To compensate for this sudden loss in thermo–electrical efficiency, several researchers have moved to novel types of solid electrolyte synthesis research. Ytterbium–stable Zirconia (YSZ) type solid electrolytes are commonly used in today's SOFC units due to their structural and thermal resilience at high temperatures. [7, 8]. However, the electrical conductivity of YSZ decreases significantly at low operating temperatures. In contrast, Bismuth Oxide (Bi_2O_3)–based solid electrolyte systems, which are anticipated to be a good solid electrolyte option, exhibit greater electrical conductivity in the same temperature range as YSZ electrolytes [9, 10]. This situation has attracted the attention of many researchers who are studying on the synthesis and characterization of solid electrolyte materials. Many studies on Bi_2O_3 phases in the literature have found that the cubic δ–phase has the highest electrical conductivity of any solid electrolyte at comparable temperatures [11–15]. However, the stability of this phase in a relatively restricted temperature range (729 °C – 824 °C) throws doubt on these materials' solid electrolyte candidacy. Nevertheless, several successful studies have shown that this phase can be stabilized by doping rare earth oxides

(Ln_2O_3, Ln: Er, Eu, Dy, and so on) into the pure crystal. But, conductivity studies on this phase indicated that the stabilized phase's electrical conductivity was lower than that of the pure phase. This abrupt drop in conductivity is commonly attributed to the partial cation exchange associated with doping, which results in a loss in polarization power. Due to its $6s^2$ single electron chain, the host Bi^{3+} cation has a larger anion polarization power than the rare earth cations (Ln^{3+}) that replace itself [16]. In reality, a cation's polarizing power is related to its effective ion radius. As a result, using highly polarizable rare earth cations as dopants can help compensate for this dramatic drop in electrical conductivity [16, 17]. Many research on the stability of the cubic δ–phase, on the other hand, demonstrated that utilizing cations with lower radius for doping compared to the host Bi^{3+} (1.17 Å) cation yielded more successful results in stability studies. Otherwise, the rhombohedral crystal structure, which has lower electrical conductivity, is shown to become stable. In terms of doping strategy, studies using single, double, and triple doping methods yielded successful results in the literature, although the maximum electrical conductivity was obtained with the double doping method [18, 19].

The $(Bi_2O_3)_{1-x-y}$ $(Er_2O_3)_x(Tb_4O_7)_y$ ternary systems with doped two rare earth oxides were fabricated by solid state reactions at ambient temperature under air circumstances. The produced samples were structurally characterized using the X–Ray Diffraction (XRD) method, thermally characterized using the Thermo–gravimetry and Differential Thermal Analysis (TG&DTA) methodology, and electrically characterized using the Four Point End Technique (FPPT). Each characterization's results were compared to the others, and the data were interpreted individually in terms of the creation of the stable cubic δ–phase.

Materials and Methods

Sample Preparation

The high quality (> 99.0%) Bi_2O_3 ceramic powders and rare earth oxides (Er_2O_3, Tb_4O_7) were supplied from Sigma Aldrich Company. Under atmospheric circumstances, solid state reactions were used to create the desired $(Bi_2O_3)_{1-x-y}$ $(Er_2O_3)_x$ $(Tb_4O_7)_y$ ternary mixtures. The doping mole percentages were determined using a specific stoichiometry in order to investigate the effects of the doping ratio on the electrical conductivity and crystalline phase structure of the material. The additive mole percentages of $(Bi_2O_3)_{1-x-y}$ $(Er_2O_3)_x$ $(Tb_4O_7)_y$ triple solid mixtures are listed in Table 1. Powder chemicals were weighed using a precision digital scale before being crushed in an agate mortar with a pestle for about 25 minutes to obtain desirable dopant diffusion. The mixtures were then put in a programmed furnace utilizing heat–resistant alumina boats and annealed for 100 hours at 750 °C, which is temperature above the phase transition temperature (729 °C). This temperature was chosen to ensure that the cubic phase was the dominant phase all crystal structure for all temperatures and that the dopants diffused into the pure crystal more successfully. The annealed powder mixtures were then utilized to make disc–shaped pallet samples with a diameter of 13 mm and a thickness of 0.5 mm in order to conduct the XRD and conductivity tests. The pallet examples were created using a SPECAC type pressing machine, which can apply 10 tons of mechanical pressure along the vertical axis.

Table 1. Molar dopant ratios of $(Bi_2O_3)_{1-x-y}$ $(Er_2O_3)_x$ $(Tb_4O_7)_y$ ternary mixtures.

Samples	Molar dopant ratios of components		
	x : y (mol %)	Contents ratios (1: ↔ 5 %)	Total dopant concentration (mol %)
05Er05TbSB	05 : 05	1:1	10
05Er10TbSB	05 : 10	1:2	15
10Er05TbSB	10 : 05	2:1	15
15Er05TbSB	15 : 05	3:1	20
15Er10TbSB	15 : 10	3:2	25
20Er05TbSB	20 : 05	4:1	25
20Er10TbSB	20 : 10	4:2	30

Characterization Techniques

The samples' XRD patterns were created using a Panalytical Empyrean model X–ray diffractometer with a scanning step of 0.02°/s and a range of 10°< 2θ < 90°. To detect X–rays scattered from distinct atomic planes, a thallium (Ta)–activated sodium iodide detector (NaI) was employed. For scanning process, monochromatic X–rays with a wavelength of 1.54 Å generated by Cu–K_α radiation were utilized. The X–Powder and Win–Index software's were used to index diffraction patterns. All XRD patterns were superimposed in the scanned angle range to observe single phase stability. The Perkin Elmer Diamond model Thermogravimetric and Differential Thermal Analysis (TG & DTA) equipment was used to analyze the thermal behavior of the samples throughout a temperature range of 30 °C to 1000 °C with a constant heating rate of 10 °C/min. The obtained DTA curves were thoroughly examined to see whether a phase transition could occur during the uniform heating operation. Temperature dependent TGA curves, on the other hand, were considered to evaluate mass change. Finally, the FPPT was used to measure the temperature–dependent electrical conductivity of the samples. The conductivity measurements were carried out by heating the alumina kit system at a constant up from room temperature to about 950 °C in a controlled furnace. For measurements, four high–purity platinum wires with a diameter of 0.5 mm were used. Each of these platinum wires was touched on the pallet sample at 0.20 cm intervals, and the current and voltage values from two of the channels were measured. To properly determine the temperature, K–type thermal couples were placed quite close to the sample. Current and voltage data were measured using a Keithley 2400 DC power supply and a Keithley 2700 multimeter. The measurements' data were sent to the controlled computer environment using an electronic

interface card that followed the "General Purpose Interface Bus" (GPIB) standard.

Result and Discussions

X–Ray Diffraction Method

Fig. 1 depicts the superimposed XRD patterns generated at room temperature. On each diffraction pattern, the cubic δ–phase and monoclinic α–phase diffraction peaks are identified. As they only include cubic δ–phase peaks, samples 05Er05TbSB, 05Er10TbSB, and 15Er05TbSB were determined to be stable in a single phase, that is, homogeneous phase structure, according to the peak positions marked in Fig. 1. When the diffraction patterns of other samples are thoroughly examined, it is discovered that they include both α–phase and δ–phase peaks [20]. As a result, at room temperature, these samples have a mixed phase structure. Additionally, there is a relationship between the doping rate and the intensity of the α–phase peaks, which are mixed phase indicators. As a result, it can be said that number of α–phase peaks increase as the dopant ratio increases [21]. This reveals that the rare earth cations settled in the crystal lattice by the doping process not only do not replace the Bi^{3+} cation, but also settle at various ion centres, increasing the defect density. Based on this perspective, the crystal defect density of samples generated with a high doping ratio increases, and the scattering peaks on the diffraction pattern indicating the development of mixed phases may be increased. Also, according to the literature, when the doping ratio increases, the lattice stress increases and the crystal size decreases. This suggests that the doping level be kept as low as possible in order for stability studies to be successful [22, 23].

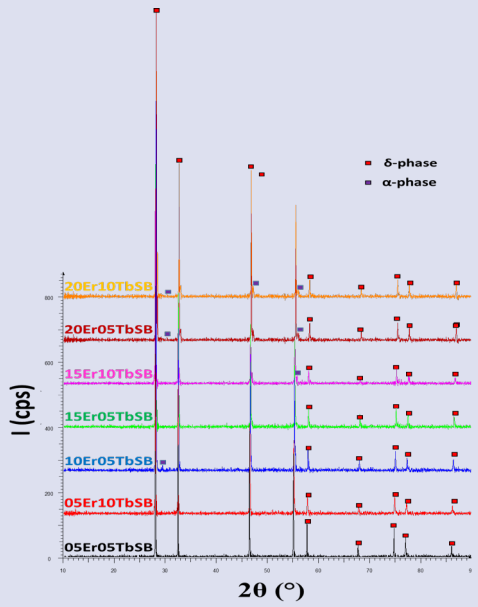

Figure 1. Superimposed XRD pattern of annealed samples at room temperature

Average crystal size and micro strain were determined using Eq. (1) and (2), respectively, for the lattice parameters.

$$D = \frac{k\lambda}{\beta cos\theta} \quad (1)$$

$$\epsilon = \frac{\beta}{4tan\theta} \quad (2)$$

The Scherrer formula is used to calculate crystal size in Eq. (1), where k is the shape factor, λ is the wavelength, β is the Fwhm value, and θ is the Bragg diffraction angle. The Stokes–Wilson formula is given in Eq. (2), where ε is the micro strain. Table 2 displays some of the estimated lattice parameters that have been related to the structural analysis results. Table 2 clearly shows the association between doping ratio and structural characteristics. The lattice constant of the samples stable with the cubic δ–phase is smaller than that of the pure cubic phase. The fundamental reason for this is because the rare earth cations that are doped into the lattice have a lower radius than the host Bi^{3+} cation. In the literature, this is referred to as lattice narrowing [24].

Table 2. Results of the structural analysis as well as the calculated lattice parameters.

Samples	Crystal structure parameters			
	Crystal size (nm)	Micro strain (%)	Crystal phase	Lattice constant
05Er05TbSB	78.2	0.0143	δ	5.512
05Er10TbSB	71.4	0.0167	δ	5.509
10Er05TbSB	73.2	0.0158	α, δ	Mixed
15Er05TbSB	65.1	0.0195	δ	5.493
15Er10TbSB	61.7	0.0221	α, δ	Mixed
20Er05TbSB	52.5	0.0216	α, δ	Mixed
20Er10TbSB	48.3	0.0326	α, δ	Mixed

Thermal Analysis

Fig. 2 shows temperature–dependent DTA and TGA curves for some manufactured samples. On the DTA curves, neither endothermic nor exothermic peak development was seen, indicating a probable phase transition, as shown in the figures. The temperature–dependent phase transition, in reality, begins with a change in crystal symmetry. According to the literature, the DTA curve for pure Bi_2O_3 powders reveals an endothermic peak at around 729 °C, suggesting the transition from the monoclinic α–phase to the cubic δ–phase.

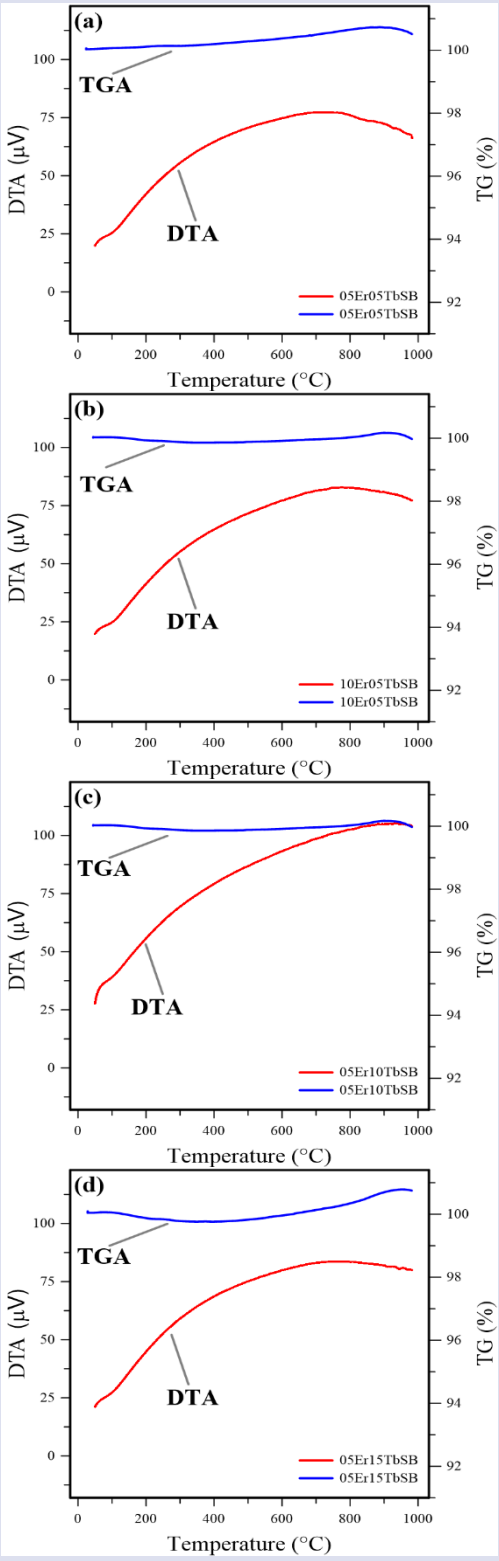

Figure 2. Temperature dependent DTA and TGA curves.

The lack of such a phase transition in our research for doped Bi_2O_3 powders can be ascribed to increasing lattice stress with doping. In other words, as a result of partial cation exchange, the dislocation density in the crystal lattice increases, preventing the lattice from transitioning to the lower symmetric crystal order [27]. Moreover, the DTA system's very fast heating rate might obscure a possible phase change. The heating rate used in this investigation was 10 °C/min, which may be insufficient for identifying phase transitions that produce minor temperature increases. The temperature–dependent TGA curves, on the other hand, reveal that mass losses are minimal. Mass losses in oxide–based ceramic systems, on the other hand, are commonly attributed to the removal of O_2 gas from the structure. Because the cation exchange caused by doping changes the polarization power. Besides, the Bi—O bonds are known to be stronger than Ln—O bonds, and this, together with doping, allows for the formation of additional oxygen anion vacancies in the lattice [28]. As a result of a chemical reaction, an O2– ion in the anion sublattice can be converted into the O_2 and therefore removed from the lattice. As a result, such reactions might be regarded as the principal cause of mass losses.

Conductivity Measurements

Fig. 3a shows the temperature–dependent conductivity graphs of the manufactured pallet samples. As seen in the graphs, increasing the doping rate results in a significant drop in conductivity. This is due to the partial cation exchange produced by the doping process between the host Bi^{3+} and Er^{3+} or Tb^{4+}.

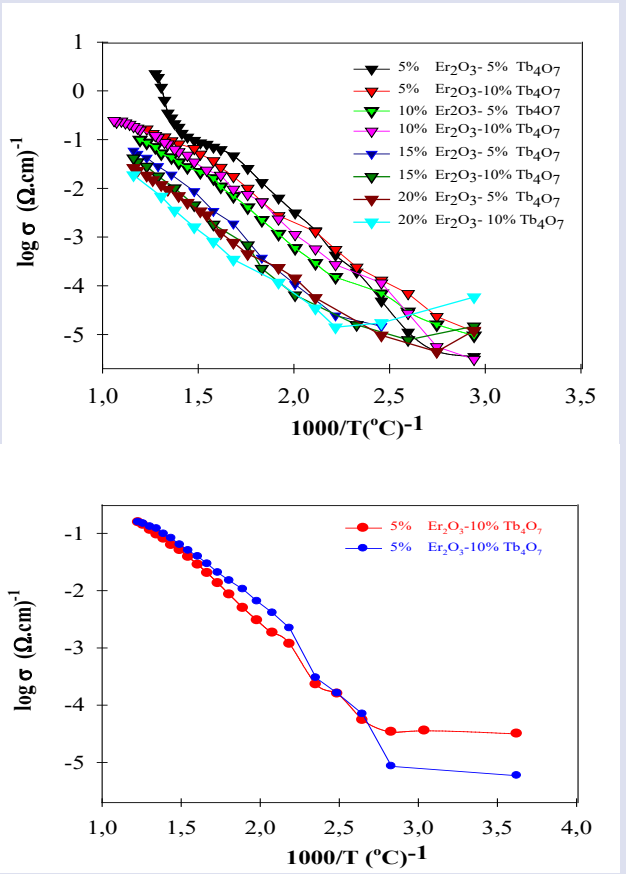

Figure 3. Arrhenius plots depending on temperature.

It is also well known that the Bi^{3+} cation has a strong polarization power, which is also described as the ability to disturb the anion sublattice. As a result, including rare earth cations into the lattice will result in a significant drop in polarization power. As a natural consequence, the conductivity curve of the 20Er05TSB sample generated with a high doping ratio is the lowest of all samples. In addition, as shown in the Fig.3a, the conductivity graph of sample 05Er05TbSB exhibits a sharp increase about 600 °C. This sudden increase in

conductivity is known as the order–disorder transition (ODT), which is a structural change in the oxygen sublattice of crystal system [29, 30]. With this ODT, some oxygen ions migrate from the regular 8c region to the octahedral regions known as 32f, which require less activation to jump to surrounding vacant ion centers. With this transition, the oxygen–ion mobility in the lattice accelerates, and the number of ions contributing to electrical conductivity increases significantly [31, 32]. On the other hand, the conductivity graph of sample 05Er10TbSB, whose heating (red) and cooling (blue) curves are shown in Fig. 3b. As seen in the graph, the change in conductivity with temperature follows the same trend. This demonstrates the chemical and structural stability of this sample when subjected to heat treatments. If you pay attention, the cooling conductivity curve has more conductivity than the heating conductivity curve. In fact, this is to be expected because the disorder–order transition becomes more difficult during cooling, and the consequences of high temperatures persist longer. The electrical activation energy were determined using the Arrhenius equation given by following equation.

$$\sigma_T = \sigma_0 \exp\left(-\frac{E_A}{k_B T}\right) \quad (3)$$

In equation (3), σ_T represents conductivity at any temperature, σ_0 represents conductivity at absolute temperature, E_A represents activation energy, and k_B represents the Boltzmann constant. Table 3 displays electrical activation energies derived from the conductivity graphs, as well as the conductivity values measured at 600 and 700 °C.

Table 3. Findings of conductivity measurements and electrical activation energies.

Samples	Conductivity measurement results		
	Conductivity at 600 °C $(\Omega.cm)^{-1}$	Conductivity at 700 °C $(\Omega.cm)^{-1}$	Activation Energy (eV)
05Er05TbSB	645E–4	128E–3	0.64
05Er10TbSB	269E–4	109E–3	0.73
10Er05TbSB	87.7E–4	36.2E–3	0.88
15Er05TbSB	27.1E–4	14.1E–3	0.92
15Er10TbSB	13.4E–4	65.6E–4	0.86
20Er05TbSB	8.51E–4	61.7E–4	1.02
20Er10TbSB	4.67E–4	28.6E–4	1.12

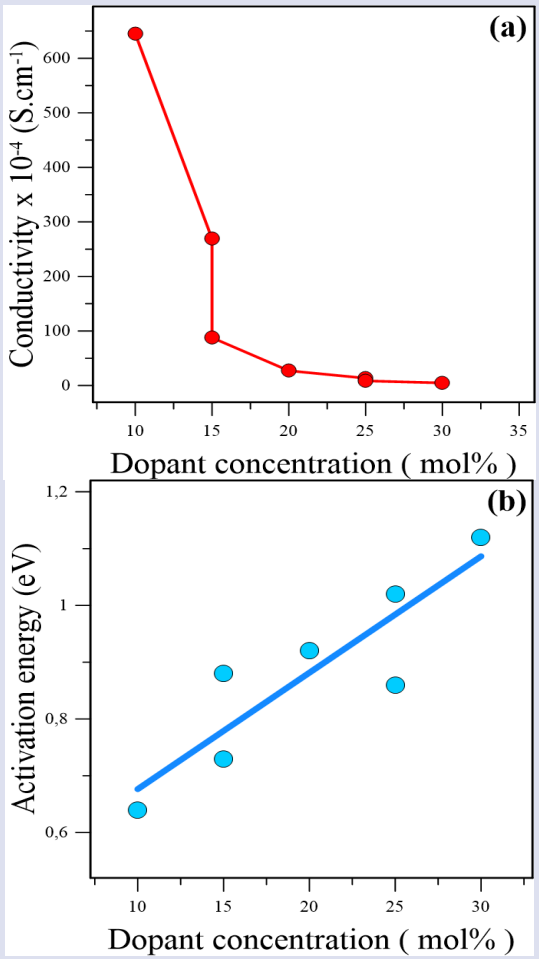

Figure 4. Activation energy and conductivity change according to doping concentration.

As seen in Table 3, as the doping ratio increases at the same temperature, the conductivity values drop while the activation energies increase. The activation energy is defined here as the lowest amount of energy necessary for an oxygen ion in the anion sublattice to hop to the unoccupied ion centers in the surrounding sublattice [33, 34]. As the doping ratio increases, so do the lattice dislocations, and rare earth cations introduced into the lattice can settle at lattice trap spots for oxygen ions [35]. The trapping of these O^{2-} ions, which are believed to contribute to ion conduction, increases the activation energy and, as a result, lowers conductivity.

Fig. 4a and b also depict how conductivity and activation energy change with doping ratio, respectively. The sample 05Er05TbSB created with the lowest doping ratio has the highest conductivity and the lowest activation energy, as seen in the figure. Low doping treatment can be regarded to be crucial in terms of reaching the maximum conductivity aim in stability investigations. In the case of heavy doping, on the other hand, the crystal lattice creates a large activation energy and so shows low electrical conductivity [36]. It has been underlined that the doping ratio should be kept as low as possible in order to produce stability and high electrical conductivity in research that employ the double doping technique and are also included in the literature. Jung et

al produced the binary operation $(Bi_2O_3)_{1-x-y}$ $(Dy_2O_3)_x$ $(WO_2)_y$ and attained the highest conductivity for a low doping of 12%. Furthermore, they proposed that by fixing this doping ratio, a 2:1 (Dy:W) dopant content ratio was efficient in reaching the greatest conductivity (0.57 $S.cm^{-1}$ at 700 °C) [37].

Conclusion

In this study, solid state reactions were used to create $(Bi_2O_3)_{1-x-y}$ $(Er_2O_3)_x$ $(Tb_4O_7)_y$ ternary systems, which were then characterized using XRD, TGA&DTA, and FPPT techniques. The effects of doping ratio on phase stability were clearly demonstrated by XRD data. Among all samples, the XRD diffraction pattern of 05Er05TbSB, 05Er10TbSB, and 15Er05TbSB indicated cubic δ–phase stability. Other samples, on the other hand, were discovered to exhibit mixed phase structure because their diffraction patterns showed monoclinic α–phase related peaks. Because the temperature dependent DTA curves did not show the creation of an endothermic or exothermic peak, which implies a phase transition, it was determined that the synthesized materials were thermally stable in the studied temperature range. The temperature–dependent conductivity graphs revealed that the doping ratio affected the electrical conductivity mechanism significantly. As a result, the sample with the lowest doping had the maximum conductivity at 700 °C, measuring 0.128 $S.cm^{-1}$. Furthermore, the activation energy determined on the conductivity curve of this sample was 0.64 eV, the lowest. These findings suggest that increasing lattice dislocation in samples produced with a high doping ratio shortens ion conduction channels and resulting in a substantial increase in activation energy. Because of the variation in polarizability of rare earth cations, it was assumed that the conductivity measurements acquired were lower than 0.57 S/cm^{-1}, the maximum conductivity value in the literature.

Conflicts of interest

There are no conflicts of interest in this work.

References

[1] Zakaria Z., Mat Z.A., Hassan S.H.A., Kar Y.B., A review of solid oxide fuel cell component fabrication methods toward lowering temperature, *Int. J. Energy Res.*, 44 (2020) 594–611.

[2] Azizi M.A., Brouwer J., Progress in solid oxide fuel cell–gas turbine hybrid power systems: System design and analysis, transient operation, controls and optimization, *Appl. Energy.*, 215 (2018) 237–289.

[3] Mahato N., Banerjee A., Gupta A., et al, Progress in material selection for solid oxide fuel cell technology: A review, *Prog. Mater. Sci.*, 72 (2015) 141–337.

[4] Singh M., Zappa D., Comini E., Solid oxide fuel cell: Decade of progress, future perspectives and challenges, *Int. J. Hydrog.*, 46 (2021) 27643–27674.

[5] Güldeste A., Aldoori M., Balci M., et al., Synthesis and characterization of Dy–Eu–Tm co–doped cubic phase stabilized bismuth oxide based electrolytes in terms of intermediate temperature–solid oxide fuel cells (IT–SOFCs), *J. Rare Earths.*, 41(3) 2023 406–412.

[6] Wachsman E. D., Lee K.T., Lowering the Temperature of Solid Oxide Fuel Cells, *Science,* 334 (2011) 935–939.

[7] Azad A.M., Larose S., Akbar S.A., Bismuth oxide–based solid electrolytes for fuel cells, *J. Mater. Sci.*, 29(1994) 4135–4151.

[8] Arı M., Balcı M., Polat Y., Synthesis and characterization of (Bi2O3)1−x−y−z(Gd2O3)x (Sm2O3)y(Eu2O3)z quaternary solid solutions for solid oxide fuel cell, *Chin. J. Phys.*, 56 (2018) 2958–2966.

[9] Ozlu H.T., Cakar S., Ersoy E., et al.,The bulk electrical conductivity properties of d–Bi2O3 solid electrolyte system doped with Yb2O3, *J. Therm. Anal. Calorim.*, 122 (2015) 525–536.

[10] Dilpuneet S., Aidhy J.C., Susan B.N., et al., Vacancy–Ordered Structure of Cubic Bismuth Oxide from Simulation and Crystallographic Analysis, *J. Am. Ceram. Soc.*, 91 (2008) 2349–2356.

[11] Jung D.W., Juan C.N., Duncan K.L., et al., Enhanced long–term stability of bismuth oxide–based electrolytes for operation at 500 °C, *Ionics*, 16 (2010) 97–103.

[12] Arasteha S., Maghsoudipour A., Alizadeh M., et al., Effect of Y2O3 and Er2O3 co–dopants on phase stabilization of bismuth oxide, *Ceram. Int.*, 37 (2011) 3451–3455.

[13] Bandyopadhyay S., Dutta A.A., Structural insight into the electrical properties of Dy–Ho co–doped phase stabilized Bismuth Oxide based electrolytes, *J. Electroanal. Chem.*, 817 (2018) 55–64.

[14] Cardenas P.S., Ayala M.T., Muñoz J., et al.,High ionic conductivity dysprosium and tantalum Co–doped bismuth oxide electrolyte for low–temperature SOFCs, *Ionics*, 26 (2020) 4579–4586.

[15] Tran T.B., Navrotsky A., Energetics of Dysprosia–Stabilized Bismuth Oxide Electrolytes, *Chem. Mater.*, 24 (2012) 4185–4191.

[16] Wachsman E. D., Boyapati S., Jiang N., Effect of dopant polarizability on oxygen sublattice order in phase–stabilized cubic bismuth oxides, *Ionics*, 7 (2001) 1–6.

[17] Jung D.W., Lee K.T., Wachsman E.D., Dysprosium and Gadolinium Double Doped Bismuth Oxide Electrolytes for Low Temperature Solid Oxide Fuel Cells, *J. Electrochem. Soc.*, 163 (2016) 411–415.

[18] Wachsman E.D., Boyapati S., Kaufman M.J., et al., Modeling of Ordered Structures of Phase–Stabilized Cubic Bismuth Oxides, *J. Am. Chem. Soc.*, 83 (2004) 1964–1968.

[19] Wang X., Zhou W., De Lisio J.B., et al., Doped δ–bismuth oxides to investigate oxygen ion transport as a metric for condensed phase thermite ignition, *Phys. Chem. Chem. Phys.*, 19 (2017) 12749–12758.

[20] Jaiswal N., Gupta B., Kumar D., et al., Effect of addition of erbium stabilized bismuth oxide on the conductivity of lanthanum doped ceria solid electrolyte for IT–SOFCs, *J. Alloys Compd.*, 633 (2015) 174–182.

[21] Trana T.B., Navrotsky A., Energetics of disordered and ordered rare earth oxide–stabilized bismuth oxide ionic conductors, *Phys. Chem. Chem. Phys.*, 16 (2014) 2331–2337.

[22] Kış M., Polat Y., Erdoğan B., et al., New fabricated electrolytes based on Dy3+–Tm3+ double–doped δ–Bi2O3–type cubic phase, *J. Aust. Ceram. Soc.*, 56 (2020) 987–993.

[23] Kuo Y.L., Liu L.D., Lin S.E., et al., Assessment of structurally stable cubic Bi12TiO20 as intermediate temperature solid oxide fuels electrolyte, *J. Eur. Ceram*., 31 (2011) 3119–3125.

[24] Rivera O.D., Martínez A., Rodil S.E., Interpretation of the Raman spectra of bismuth oxide thin films presenting different crystallographic phases, *J. Alloys Compd*., 853 (2021) 157245.

[25] Hou J., Bi L., Qian J., Zhu Z., et al., Study of the Crystal Structures of New Buffer Materials Bi 1−x Y x O 1.5. J. Supercond, *Nov. Magn.*, 23 (2010) 1011–1014.

[26] Yogamalar R., Srinivasan R., Vinu A., et al., X–ray peak broadening analysis in ZnO nanoparticles, Solid State Commun., 149 (2009) 1919–1923.

[27] Koçyiğit S., Gökmen Ö., Temel S., et al., Structural investigation of boron undoped and doped indium stabilized bismuth oxide nanoceramic powders, *Ceram. Int*., 39 (2013) 7767–7772.

[28] Bandyopadhyay S., Dutta A., Thermal, optical and dielectric properties of phase stabilized δ – Dy–Bi2O3 ionic conductors, *J. Phys. Chem. Solids*., 102 (2015) 12–20.

[29] Torun H.O., Çakar S., Thermal characterization of Er–doped and Er–Gd co–doped ceria–based electrolyte materials for SOFC, *J. Therm. Anal. Calorim*., 133 (2018) 1233–1239.

[30] Jung D.W., Duncan K.L., Wachsman E.D., Effect of total dopant concentration and dopant ratio on conductivity of (DyO1.5)x–(WO3)y–(BiO1.5)1−x−y, *Acta Mater*., 58 (2010) 355–363.

[31] Painter A.S., Huang Y.L., Wachsman E.D, Durability of (La0.8Sr0.2)0.95MnO3–δ–(Er0.2Bi0.8)2O3 composite cathodes for low temperature SOFCs, *J. Power Sources*., 360 (2017) 391–398.

[32] Jiang N., Wachsman E.D., Structural Stability and Conductivity of Phase–Stabilized Cubic Bismuth Oxides, *J. Am. Ceram. Soc*., 82 (1999) 3057–3064.

[33] Aytimur A., Koçyiğit S., Uslu İ., et al., Fabrication and characterization of bismuth oxide–holmia nanofibers and nanoceramics, *Curr. Appl. Phys*., 13 (2013) 581–58.

[34] Chou T., Liu L.D., Wei W.C.J., Phase stability and electric conductivity of Er2O3–Nb2O5 co–doped Bi2O3 electrolyte, *J. Eur. Ceram*., 31 (2011) 3087–3094.

[35] Panuh D., Ali S.A.M., Yulianto D., et al., Effect of yttrium–stabilized bismuth bilayer electrolyte thickness on the electrochemical performance of anode–supported solid oxide fuel cells, *Ceram. Int*., 47 (2021) 6310–6317.

[36] Wachsman E.D., Effect of oxygen sublattice order on conductivity in highly defective fluorite oxides, *J. Eur. Ceram. Soc*., 24 (2004) 1281–1285.

[37] Fruth V., Ianculescu A., Berger D., et al., Synthesis, structure and properties of doped Bi2O3, *J. Eur. Ceram. Soc*., 26 (2006) 3011–3016.

Cumhuriyet Sci. J., 44(3) (2023) 602-609
DOI: https://doi.org/10.17776/csj.1320712

Cumhuriyet Science Journal

| csj.cumhuriyet.edu.tr | Founded: 2002 ISSN: 2587-2680 e-ISSN: 2587-246X Publisher: Sivas Cumhuriyet University

Bayesian Analysis for the Modified Frechet–Exponential Distribution with Covid-19 Application

Neriman Akdam [1,a,*]

[1] *Department of Biostatistics, Faculty of Medicine, Selcuk University, Konya, Türkiye*
**Corresponding author*

Research Article

History
Received: 28/06/2023
Accepted: 12/09/2023

ABSTRACT

In this manuscript, the maximum likelihood estimators and Bayes estimators for the parameters of the modified Frechet–exponential distribution. Because the Bayes estimators cannot be obtained in closed forms, the approximate Bayes estimators are computed using the idea of Lindley's approximation method under squared-error loss function. Then, the approximate Bayes estimates are compared with the maximum likelihood estimates in terms of mean square error and bias values using Monte Carlo simulation. Finally, real data sets belonging to COVID-19 death cases in Europe and China to are used to demonstrate the emprical results belonging to the approximate Bayes estimates, the maximum likelihood estimates.

Keywords: Modified Frechet–Exponential distribution, Bayes estimator, Lindley's approximation, Monte Carlo simulation, Squared-error loss function.

[a] *nkaradayi@selcuk.edu.tr* *https://orcid.org/0000-0002-0204-6657*

Introduction

The exponential distribution is one of the popular lifetime distributions with wide application in reliability analysis, medical studies, and applied statistics. In addition, the Frechet distribution is one of the important distributions. Recently, some generalizations and extensions of the Frechet distribution are derived for modeling data: such as exponentiated Frechet distribution [1], gamma extended Frechet distribution [2], Marshall–Olkin Frechet distribution [3], weibull Frechet distribution [4], modified Frechet–Rayleigh distribution [5], novel Kumaraswamy power Frechet distribution [6], modified Frechet–exponential distribution [7].

The modified Frechet–exponential (MFE) distribution is introduced by Farhat et al. [7]. The MFE distributions with parameter (α, λ) is shown with $MFE(\alpha,\lambda)$ where $\alpha > 0$ and $\lambda > 0$. The probability density function (pdf), cumulative distribution function (cdf), hazard function and survival function of X random variable has the modified frechet-exponential distribution with α and λ parameters are as follows;

$$f(x;\alpha,\lambda) = \frac{\alpha\lambda\, exp(-\lambda x - (1 - exp(-\lambda x))^{\alpha})\,(1 - exp(-\lambda x))^{\alpha-1}}{1 - exp(-1)}, x > 0, \alpha > 0, \lambda > 0 \quad (1)$$

$$s(x;\alpha,\lambda) = \frac{\exp(-1) - \exp\left(-(1-\exp(-\lambda x))^{\alpha}\right)}{\exp(-1) - 1} \quad (2)$$

$$h(x;\alpha,\lambda) = \frac{\alpha\lambda\, exp(-\lambda x - (1 - exp(-\lambda x))^{\alpha})\,(1 - exp(-\lambda x))^{\alpha-1}}{exp(-(1 - exp(-\lambda x))^{\alpha}) - exp(-1)} \quad (3)$$

$$s(x;\alpha,\lambda) = \frac{\exp(-1) - \exp\left(-(1-\exp(-\lambda x))^{\alpha}\right)}{\exp(-1) - 1} \quad (4)$$

where x > 0, $\alpha > 0$ and $\lambda > 0$.

In this study, Bayesian estimators of the modified Frechet–exponential distribution is investigated. There are a lot of studies that refer to the bayes estimation of different distributions under the complete samples [8-17].

The main objective of this manuscript is to develop the approximate Bayes estimators under square error loss functions and compare them with maximum likelihood estimators (MLEs) in terms of MSE and bias values of estimates. The rest of the manuscript is organized as follows. In Section 2, the MLEs for parameters are derived. In section 3, the approximate Bayes estimators under squared error loss function are achieved by using Lindley's

approximation. Using Monte Carlo simulation, The approximate Bayes estimation are compared with the maximum likelihood estimation in terms of MSE and bias values. Then, results are tabulated in section 4. In section 5, real data sets belonging to COVID-19 death cases in Europe and China to are used to demonstrate the emprical results belonging to the approximate Bayes estimates, the maximum likelihood estimates. Finally, conclusions are given in Section *6*.

Maximum Likelihood Estimation

Let $(X_1, X_2, \dots, X_n)$ denote a random sample taken from$MFE(\alpha,\lambda)$ distribution with observed values $(x_1, x_2, \dots, x_n)$. Then, the likelihood function $\ell(\alpha,\lambda)$ and the log-likelihood function$(\alpha,\lambda) = log\,\ell\,(\alpha,\lambda)$ can be written as

$$\ell(\alpha,\lambda) = \frac{(\alpha\lambda)^n}{(1-exp(-1))^n} exp\left[-\sum_{i=1}^{n}\lambda x_i\right] exp\left[-\sum_{i=1}^{n}(1-exp(-\lambda x_i))^{\alpha}\right]\prod_{i=1}^{n}(1-exp(-\lambda x_i))^{\alpha-1} \quad (5)$$

and

$$L(\alpha,\lambda) = n\,log(\alpha\lambda) - n\,log(1-exp(-1)) - \sum_{i=1}^{n}\lambda x_i - \sum_{i=1}^{n}(1-exp(-\lambda x_i))^{\alpha} + (\alpha-1)\sum_{i=1}^{n} log(1-exp(-\lambda x_i))^{\alpha-1} \quad (6)$$

respectively. Taking the partial derivatives of $L(\alpha,\lambda)$ according to α and λ parameters and as a result of equalizing them to zero, the following equations are obtained;

$$L_1 = \frac{\partial L}{\partial \alpha} = \frac{n}{\alpha} - \sum_{i=1}^{n}(1-exp(-\lambda x_i))^{\alpha}\,log(1-exp(-\lambda x_i)) + \sum_{i=1}^{n} log(1-exp(-\lambda x_i)) = 0 \quad (7)$$

$$L_2 = \frac{\partial L}{\partial \lambda} = \frac{n}{\lambda} - \sum_{i=1}^{n} x_i - \alpha\sum_{i=1}^{n} x_i\,exp(-\lambda x_i)\,(1-exp(-\lambda x_i))^{\alpha-1} + (\alpha-1)\sum_{i=1}^{n}\frac{x_i\,exp(-\lambda x_i)}{(1-exp(-\lambda x_i))} = 0 \quad (8)$$

The nonlinear equations (7) and (8) can be solved by using Newton-Raphson method, which is one of the numerical methods in MATLAB program.

Bayes Estimation

Assuming that $(X_1, X_2, \dots, X_n)$ a sample having $MFE(\alpha,\lambda)$ distribution and α and λ parameters are independent random variables with prior Gamma distributions. Then the density functions for α and λ parameters are given by,

$$\pi_1(\alpha) = \frac{\alpha^{a_1-1}\,exp(-b_1\alpha)\,b_1^{a_1}}{\Gamma(a_1)} a_1, b_1, \alpha > 0 \quad (9)$$

$$\pi_2(\lambda) = \frac{\lambda^{a_2-1}\,exp(-b_2\lambda)\,b_2^{a_2}}{\Gamma(a_2)} a_2, b_2, \lambda > 0 \quad (10)$$

respectively. In this case, the joint prior and the log of joint prior density functions can be written as follows

$$\pi(\alpha,\beta) = \frac{\alpha^{a_1-1}b_1^{a_1}\lambda^{a_2-1}b_2^{a_2}}{\Gamma(a_1)\Gamma(a_2)} exp(-b_1\alpha)\,exp(-b_2\lambda) \quad (11)$$

And

$$\rho(\alpha,\lambda) = (a_1-1)\,log\,\alpha + (a_2-1)\,log\,\lambda - b_1\alpha - b_2\lambda + +a_1\,log(b_1) + a_2\,log(b_2) - log[\Gamma(a_1)] - log[\Gamma(a_2)] \quad (12)$$

respectively. Then, the joint posterior density function of α and λ parameters is obtained by

$$P(\alpha,\lambda|X) = \frac{k(\alpha,\lambda)\,exp[-\sum_{i=1}^{n}\lambda x_i]\,exp[-\sum_{i=1}^{n}(1-exp(-\lambda x_i))^{\alpha}]\prod_{i=1}^{n}(1-exp(-\lambda x_i))^{\alpha-1}}{\int_0^{\infty}\int_0^{\infty} k(\alpha,\lambda)\,exp[-\sum_{i=1}^{n}\lambda x_i]\,exp[-\sum_{i=1}^{n}(1-exp(-\lambda x_i))^{\alpha}]\prod_{i=1}^{n}(1-exp(-\lambda x_i))^{\alpha-1}\,d\alpha d\lambda} \quad (13)$$

where $k(\alpha,\lambda) = \alpha^{n+a_1-1}\lambda^{n+a_2-1}\,exp(-b_1\alpha)\,exp(-b_2\lambda)$. Thus, the Bayes estimate of $u(\alpha,\lambda)$ that is any function of α and λ under a squared error loss function can be written as follows,

$$\hat{u}_B(\alpha,\lambda) = E[u(\alpha,\lambda)] = \frac{\int_0^\infty \int_0^\infty u(\alpha,\lambda) e^{[L(\alpha,\lambda)+\rho(\alpha,\lambda)]} d\alpha d\lambda}{\int_0^\infty \int_0^\infty e^{[L(\alpha,\lambda)+\rho(\alpha,\lambda)]} d\alpha d\lambda} \tag{14}$$

Due to the fact that the equation given in (14), which consists of the ratio of two integrals, can not be obtained in closed-form, the Bayes Estimators of parameters using Lindley's approximation under the squared error loss (quadratic loss) function are computed.

Lindley's Approximation

Lindley's approximation which is an approximation of the Bayes estimate was suggested by Lindley [18]. Lindley's approximation used to approximate the ratio of two integrals such as (14) that can not be solved analytically. Lindley's approximation has been used by many authors (Ahmad et al. [19], Kundu et al. [20], Preda et al. [21], Singh et al. [22], Akdam et al. [23], Çiftci et al. [24], Akdam [25]) to compute the approximate Bayes estimators of different lifetime distributions. The formulas as regards Lindley's approximation are given by,

$$u_{BL}(\hat{\alpha},\hat{\lambda}) = E[u(\alpha,\lambda)/X] \approx\approx \left[u(\hat{\alpha},\hat{\lambda}) + \frac{1}{2}\sum_{i=1}^{2}\sum_{j=1}^{2}(u_{ij} + 2u_i\rho_j)\sigma_{ij} + \frac{1}{2}\sum_{i=1}^{2}\sum_{j=1}^{2}\sum_{k=1}^{2}\sum_{l=1}^{2} L_{ijk}\sigma_{ij}\sigma_{kl}u_l \right] \tag{15}$$

where $\hat{\alpha}$ and $\hat{\lambda}$are the MLE of α and λ , respectively, and

$u_i, i = 1,2$are the unary partial derivatives and $u_{ij}, i, j = 1,2$ are the binary partial derivatives of $u(\alpha,\lambda)$ with respect to α and λ parameters, respectively.$L_{ij}, i, j = 1,2$ are the binary partial derivatives andL_{ijk}, i, j, k $= 1,2$ are the trinary partial derivatives of log-likelihood function $L(\alpha,\lambda)$ with respect to α and λ parameters, respectively, and

$\left[-L_{ij}\right]^{-1} = \left[\sigma_{ij}\right]$, $i, j = 1,2$. σ_{ij} is the (*i*, *j*)-th element of the matrix$\left[\sigma_{ij}\right]$. From(12), we get

$$\rho_1 = \frac{\partial\rho(\alpha,\lambda)}{\partial\alpha} = \frac{a_1-1}{\alpha} - b_1 \,, \quad \rho_2 = \frac{\partial\rho(\alpha,\lambda)}{\partial\lambda} = \frac{a_2-1}{\lambda} - b_2$$

and then, we have the following values of L_{ij} for *i*, *j* = 1,2 and L_{ijk} for *i*, *j*,*k* = 1,2

$$L_{11} = -\frac{n}{\alpha^2} - \sum_{i=1}^{n}\left(1-\exp\left(-\lambda x_i\right)\right)^{\alpha}\log\left(1-\exp\left(-\lambda x_i\right)\right)^2$$

$$L_{12} = -\sum_{i=1}^{n}\frac{\left(1-\exp\left(-\lambda x_i\right)\right)^{\alpha}\alpha x_i\exp\left(-\lambda x_i\right)\log\left(1-\exp\left(-\lambda x_i\right)\right)^2}{\left(1-\exp\left(-\lambda x_i\right)\right)}$$

$$+\frac{\left(1-\exp\left(-\lambda x_i\right)\right)^{\alpha} x_i\exp\left(-\lambda x_i\right)}{\left(1-\exp\left(-\lambda x_i\right)\right)} + \sum_{i=1}^{n}\frac{x_i\exp\left(-\lambda x_i\right)}{\left(1-\exp\left(-\lambda x_i\right)\right)} = L_{21}$$

$$L_{22} = -\frac{n}{\alpha^2} - \left[\sum_{i=1}^{n}\frac{\left(1-\exp\left(-\lambda x_i\right)\right)^{\alpha}\alpha^2 x_i^2\left(\exp\left(-\lambda x_i\right)\right)^2}{\left(1-\exp\left(-\lambda x_i\right)\right)^2} - \frac{\left(1-\exp\left(-\lambda x_i\right)\right)^{\alpha}\alpha x_i^2\exp\left(-\lambda x_i\right)}{\left(1-\exp\left(-\lambda x_i\right)\right)}\right.$$

$$\left. - \frac{\left(1-\exp\left(-\lambda x_i\right)\right)^{\alpha}\alpha x_i^2\left(\exp\left(-\lambda x_i\right)\right)^2}{\left(1-\exp\left(-\lambda x_i\right)\right)^2}\right] + (\alpha-1)\sum_{i=1}^{n}\left[-\frac{x_i^2\exp\left(-\lambda x_i\right)}{\left(1-\exp\left(-\lambda x_i\right)\right)} - \frac{x_i^2\left(\exp\left(-\lambda x_i\right)\right)^2}{\left(1-\exp\left(-\lambda x_i\right)\right)^2}\right]$$

$$L_{111} = -\frac{2n}{\alpha^3} - \sum_{i=1}^{n}\left(1-\exp\left(-\lambda x_i\right)\right)^{\alpha}\log\left(1-\exp\left(-\lambda x_i\right)\right)^3$$

$$L_{112}=-\left[\sum_{i=1}^{n}\frac{\left(1-\exp\left(-\lambda x_i\right)\right)^{\alpha}\alpha x_i\left(\exp\left(-\lambda x_i\right)\right)\log\left(1-\exp\left(-\lambda x_i\right)\right)^{2}}{\left(1-\exp\left(-\lambda x_i\right)\right)}+\frac{2\left(1-\exp\left(-\lambda x_i\right)\right)^{\alpha}\log\left(1-\exp\left(-\lambda x_i\right)\right)x_i\exp\left(-\lambda x_i\right)}{\left(1-\exp\left(-\lambda x_i\right)\right)}\right]$$

$$L_{112}=L_{121}=L_{211}$$

$$L_{122}=-\left[\sum_{i=1}^{n}\frac{\left(1-\exp\left(-\lambda x_i\right)\right)^{\alpha}\alpha^{2}x_i^{2}\left(\exp\left(-\lambda x_i\right)\right)^{2}\log\left(1-\exp\left(-\lambda x_i\right)\right)}{\left(1-\exp\left(-\lambda x_i\right)\right)^{2}}-\frac{\left(1-\exp\left(-\lambda x_i\right)\right)^{\alpha}\alpha x_i^{2}\left(\exp\left(-\lambda x_i\right)\right)\log\left(1-\exp\left(-\lambda x_i\right)\right)}{\left(1-\exp\left(-\lambda x_i\right)\right)}-\frac{\left(1-\exp\left(-\lambda x_i\right)\right)^{\alpha}\alpha x_i^{2}\left(\exp\left(-\lambda x_i\right)\right)^{2}\log\left(1-\exp\left(-\lambda x_i\right)\right)}{\left(1-\exp\left(-\lambda x_i\right)\right)^{2}}+\frac{2\left(1-\exp\left(-\lambda x_i\right)\right)^{\alpha}\alpha x_i^{2}\left(\exp\left(-\lambda x_i\right)\right)^{2}}{\left(1-\exp\left(-\lambda x_i\right)\right)^{2}}-\frac{\left(1-\exp\left(-\lambda x_i\right)\right)^{\alpha}x_i^{2}\left(\exp\left(-\lambda x_i\right)\right)}{\left(1-\exp\left(-\lambda x_i\right)\right)}-\frac{\left(1-\exp\left(-\lambda x_i\right)\right)^{\alpha}x_i^{2}\left(\exp\left(-\lambda x_i\right)\right)^{2}}{\left(1-\exp\left(-\lambda x_i\right)\right)^{2}}\right]+\sum_{i=1}^{n}\left(\frac{x_i^{2}\left(\exp\left(-\lambda x_i\right)\right)}{\left(1-\exp\left(-\lambda x_i\right)\right)}-\frac{x_i^{2}\left(\exp\left(-\lambda x_i\right)\right)^{2}}{\left(1-\exp\left(-\lambda x_i\right)\right)^{2}}\right)$$

$$L_{122}=L_{221}=L_{212}$$

$$L_{222}=\frac{2n}{\alpha^{3}}-\left[\sum_{i=1}^{n}\frac{\left(1-\exp\left(-\lambda x_i\right)\right)^{\alpha}\alpha^{3}x_i^{3}\left(\exp\left(-\lambda x_i\right)\right)^{3}}{\left(1-\exp\left(-\lambda x_i\right)\right)^{3}}-\frac{3\left(1-\exp\left(-\lambda x_i\right)\right)^{\alpha}\alpha^{2}x_i^{3}\left(\exp\left(-\lambda x_i\right)\right)^{2}}{\left(1-\exp\left(-\lambda x_i\right)\right)^{2}}-\frac{3\left(1-\exp\left(-\lambda x_i\right)\right)^{\alpha}\alpha^{2}x_i^{3}\left(\exp\left(-\lambda x_i\right)\right)^{3}}{\left(1-\exp\left(-\lambda x_i\right)\right)^{3}}+\frac{\left(1-\exp\left(-\lambda x_i\right)\right)^{\alpha}\alpha x_i^{3}\left(\exp\left(-\lambda x_i\right)\right)}{\left(1-\exp\left(-\lambda x_i\right)\right)}+\frac{3\left(1-\exp\left(-\lambda x_i\right)\right)^{\alpha}\alpha x_i^{3}\left(\exp\left(-\lambda x_i\right)\right)^{2}}{\left(1-\exp\left(-\lambda x_i\right)\right)^{2}}+\frac{2\left(1-\exp\left(-\lambda x_i\right)\right)^{\alpha}\alpha x_i^{3}\left(\exp\left(-\lambda x_i\right)\right)^{3}}{\left(1-\exp\left(-\lambda x_i\right)\right)^{3}}\right]+(\alpha-1)\sum_{i=1}^{n}\left(\frac{x_i^{3}\left(\exp\left(-\lambda x_i\right)\right)}{\left(1-\exp\left(-\lambda x_i\right)\right)}+\frac{3x_i^{3}\left(\exp\left(-\lambda x_i\right)\right)^{2}}{\left(1-\exp\left(-\lambda x_i\right)\right)^{2}}+\frac{2x_i^{3}\left(\exp\left(-\lambda x_i\right)\right)^{3}}{\left(1-\exp\left(-\lambda x_i\right)\right)^{3}}\right)$$

Finally, the approximate Bayes estimators for α and λ parameter of $MFE(\alpha,\lambda)$distribution under the squared error loss function are obtained as follows;

$$\hat{\alpha}_{LINDLEY}=\hat{\alpha}_{MLE}+\frac{1}{2}\sum_{i=1}^{2}\sum_{j=1}^{2}\left(u_{ij}+2u_i\rho_j\right)\sigma_{ij}+\frac{1}{2}\sum_{i=1}^{2}\sum_{j=1}^{2}\sum_{k=1}^{2}\sum_{l=1}^{2}L_{ijk}\sigma_{ij}\sigma_{kl}u_l\,,$$

$$\hat{\lambda}_{LINDLEY}=\hat{\lambda}_{MLE}+\frac{1}{2}\sum_{i=1}^{2}\sum_{j=1}^{2}\left(u_{ij}+2u_i\rho_j\right)\sigma_{ij}+\frac{1}{2}\sum_{i=1}^{2}\sum_{j=1}^{2}\sum_{k=1}^{2}\sum_{l=1}^{2}L_{ijk}\sigma_{ij}\sigma_{kl}u_l\,,$$

respectively.

Simulation Study

In this section, By means of Monte Carlo simulation study for different sample sizes (*n*) in terms of the MSE and bias values the performances of the approximate Bayes estimates (computed with Lindley under the squared error loss function) for α and λ parameters of $MFE(\alpha,\lambda)$ are compared with those of the MLE. Informative priors for $a_1=1, b_1=2, a_2=2, b_2=1$ are used while computing the approximate Bayes estimates. MSE for the estimate of α and λ parameters can be computed with $MSE=\frac{1}{10000}\sum_{i=1}^{10000}\left(\left(\hat{\alpha}_i,\hat{\lambda}_i\right)-(\alpha,\lambda)\right)^2$, where $\left(\hat{\alpha},\hat{\lambda}\right)$ is MLE or approximate Bayes estimation. α and λ is generated from Gamma distribution with parameter (a_1,b_1) and (a_2,b_2) respectively. All the computations are based on 10.000 replications in MATLAB program. Finally, the MSE and bias values are tabulated in Table 1-4.

Table 1. ML and approximate Bayes estimates, MSE and bias values, for $(\alpha=2,\lambda=2)$

n	MLE			$BAYES_{LINDLEY}$			MLE			$BAYES_{LINDLEY}$		
	$\hat{\alpha}$	bias	MSE	$\hat{\alpha}$	bias	MSE	$\hat{\lambda}$	bias	MSE	$\hat{\lambda}$	bias	MSE
20	2.3033	0.5851	0.6629	1.5434	0.4581	0.2718	2.2027	0.4794	0.4025	1.5084	0.4916	0.2789
30	2.2317	0.4754	0.4652	1.7874	0.2866	0.1224	2.1540	0.3971	0.2737	1.7261	0.3225	0.1485
40	2.1681	0.3950	0.3055	1.8763	0.2756	0.1112	2.1097	0.3338	0.1903	1.8103	0.2825	0.1159
50	2.1275	0.3471	0.2217	1.9122	0.2669	0.1072	2.0876	0.2930	0.1444	1.8570	0.2548	0.0960
70	2.0921	0.2808	0.1394	1.9503	0.2331	0.0854	2.0641	0.2468	0.1006	1.9058	0.2216	0.0742
100	2.0586	0.2277	0.0876	1.9659	0.2029	0.0644	2.0432	0.2016	0.0660	1.9361	0.1867	0.0537
150	2.0406	0.1820	0.0548	1.9814	0.1685	0.0447	2.0283	0.1622	0.0422	1.9586	0.1545	0.0369
200	2.0300	0.1605	0.0419	1.9865	0.1519	0.0362	2.0220	0.1437	0.0328	1.9703	0.1386	0.0295
350	2.0186	0.1187	0.0224	1.9944	0.1148	0.0206	2.0139	0.1060	0.0179	1.9847	0.1036	0.0168
500	2.0111	0.0981	0.0153	1.9945	0.0960	0.0145	2.0081	0.0886	0.0124	1.9879	0.0874	0.0119

Table 2. ML and approximate Bayes estimates, MSE and bias values, for $(\alpha=3,\lambda=2)$

n	MLE			$BAYES_{LINDLEY}$			MLE			$BAYES_{LINDLEY}$		
	$\hat{\alpha}$	bias	MSE	$\hat{\alpha}$	bias	MSE	$\hat{\lambda}$	bias	MSE	$\hat{\lambda}$	bias	MSE
20	3.3136	0.7989	1.0526	1.7531	1.2469	1.7122	2.1111	0.3876	0.2398	1.4005	0.5995	0.3823
30	3.3510	0.7637	1.1211	2.2675	0.7325	0.6274	2.1153	0.3506	0.2041	1.6376	0.3676	0.1727
40	3.2821	0.6571	0.8499	2.5387	0.4745	0.3239	2.0954	0.3030	0.1563	1.7532	0.2823	0.1122
50	3.2330	0.5795	0.6417	2.6802	0.4146	0.2493	2.0785	0.2706	0.1221	1.8145	0.2454	0.0876
70	3.1592	0.4714	0.3999	2.8027	0.3744	0.2065	2.0566	0.2254	0.0830	1.8768	0.2070	0.0638
100	3.1123	0.3820	0.2545	2.8795	0.3280	0.1629	2.0386	0.1842	0.0548	1.9173	0.1733	0.0454
150	3.0746	0.3109	0.1596	2.9272	02806	0.1203	2.0270	0.1505	0.0363	1.9478	0.1442	0.0317
200	3.0513	0.2624	0.1120	2.9441	0.2436	0.0918	2.0194	0.1300	0.0269	1.9611	0.1256	0.0244
350	3.0310	0.1975	0.0623	2.9716	0.1886	0.0556	2.0108	0.0971	0.0149	1.9780	0.0951	0.0141
500	3.0192	0.1624	0.0421	2.9783	0.0805	0.0391	2.0059	0.0814	0.0104	1.9832	0.0805	0.0101

Table 3. ML and approximate Bayes estimates, MSE and bias values, for $(\alpha=0.6,\lambda=0.8)$

n	MLE			$BAYES_{LINDLEY}$			MLE			$BAYES_{LINDLEY}$		
	$\hat{\alpha}$	bias	MSE	$\hat{\alpha}$	bias	MSE	$\hat{\lambda}$	bias	MSE	$\hat{\lambda}$	bias	MSE
20	0.6727	0.1403	0.0397	0.6733	0.1279	0.0307	0.9823	0.3234	0.2266	0.8447	0.2874	0.0557
30	0.6424	0.1043	0.0201	0.6485	0.1000	0.0182	0.9110	0.2406	0.1115	0.8488	0.1807	0.0554
40	0.6307	0.0880	0.0137	0.6370	0.0860	0.0130	0.8793	0.1969	0.0715	0.8415	0.1621	0.0450
50	0.6262	0.0105	0.0782	0.6317	0.0769	0.0102	0.8664	0.1782	0.0578	0.8390	0.1538	0.0407
70	0.6159	0.0637	0.0068	0.6204	0.0630	0.0067	0.8435	0.1441	0.0360	0.8271	0.1305	0.0286
100	0.6128	0.0523	0.0045	0.6161	0.0520	0.0045	0.8319	0.1185	0.0239	0.8216	0.1108	0.0205
150	0.6083	0.0436	0.0031	0.6106	0.0434	0.0031	0.8219	0.0973	0.0155	0.8157	0.0932	0.0141
200	0.6058	0.0372	0.0022	0.6076	0.0371	0.0022	0.8160	0.0825	0.0112	0.8116	0.0800	0.0104
350	0.6038	0.0278	0.0012	0.6048	0.0277	0.0012	0.8102	0.0611	0.0060	0.8078	0.0600	0.0058
500	0.6019	0.0232	0.0009	0.6026	0.0232	0.0009	0.8053	0.0508	0.0041	0.8037	0.0502	0.0040

Table 4 . ML and approximate Bayes estimates, MSE and bias values, for $(\alpha = 1.6, \lambda = 0.8)$

n	MLE			$BAYES_{LINDLEY}$			MLE			$BAYES_{LINDLEY}$		
	$\hat{\alpha}$	bias	MSE	$\hat{\alpha}$	bias	MSE	$\hat{\lambda}$	bias	MSE	$\hat{\lambda}$	bias	MSE
20	1.8675	0.4801	0.5056	1.6782	0.2930	0.1320	0.8993	0.2146	0.0855	0.8129	0.1441	0.0327
30	1.7571	0.3534	0.2532	1.6800	0.2788	0.1316	0.8637	0.1669	0.0495	0.8193	0.1333	0.0291
40	1.7185	0.2968	0.1655	1.6733	0.2529	0.1099	0.8474	0.1425	0.0349	0.8180	0.1220	0.0244
50	1.6921	0.2557	0.1192	1.6616	0.2270	0.0890	0.8389	0.1242	0.0262	0.8173	0.1102	0.0199
70	1.6651	0.2100	0.0765	1.6473	0.1940	0.0636	0.8268	0.1036	0.0177	0.8128	0.0955	0.0147
100	1.6483	0.1744	0.0514	1.6375	0.1654	0.0456	0.8193	0.0854	0.1190	0.8101	0.0807	0.0105
150	1.6299	0.1394	0.0324	1.6236	0.1348	0.0300	0.8125	0.0690	0.0077	0.8068	0.0666	0.0071
200	1.6203	0.1201	0.0233	1.6160	0.1172	0.0221	0.8088	0.0598	0.0057	0.8047	0.0583	0.0054
350	1.6119	0.0894	0.0127	1.6096	0.0882	0.0124	0.8056	0.0447	0.0032	0.8033	0.0440	0.0031
500	1.6092	0.0752	0.0090	1.6076	0.0745	0.0089	0.8041	0.0377	0.0022	0.8025	0.0373	0.0022

As shown in Tables 1-4, MSE and the bias values of all estimates are given for different n values. The performances of the Lindley approximate Bayes estimates outdo those of the ML estimates. For ML and Bayes estimator methods, it is observed that when the n values increase, the bias, MSEs of the estimates decrease to zero.

Data Analysis

In this section, the analysis of real data set is presented for illustrative purposes.

Real Data-1: The real data-1 set represent daily deaths due to COVID-19 in Europe from 1st March to 30 March (https://covid19.who.int/) [26].

Real Data-1, n=31:

6	18	29	28	47	55	40	150	129	184	263	237	336	219	612	434	
648	706	838	1129	1421	118	116	1393	1540	1941	2175	2278	2824	2803	2667		

First, it is checked whether MFE distribution can be used or not to analyze these data set. The Kolmogorov-Smirnov (KS) Z have been used to check the goodness-of-fit via MATLAB program. ML estimates, KS-Z and p- values based on above data is shown in Table 5.

Table 5 . Kolmogorov-Smirnov Z and the corresponding p-values for ML estimates

Methods	Estimates	Kolmogorov-Smirnov Z	p-values
MLE	$\hat{\alpha}$=0.7057$\hat{\lambda}$=0.00073	0.1076	0.8654

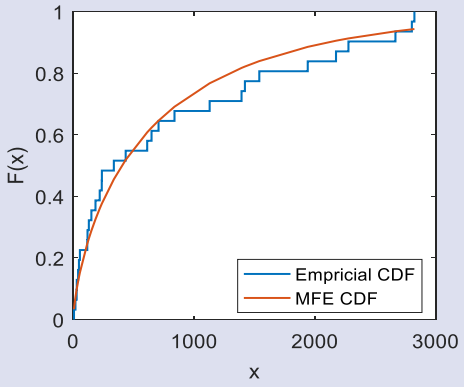

Figure 1: Plot Empricial CDF and MFE CDF for data-1

In this case, ML and approximate Bayes estimates for α and λ parameters are as follows.

	MLE		*BAYES*$_{Lindley}$	
n	$\hat{\alpha}$	$\hat{\lambda}$	$\hat{\alpha}$	$\hat{\lambda}$
31	0.7057	0.00073	0.7540	0.00081

Real Data-2: The real data-2 set represent Daily deaths due to COVID-19 in China from 23 January to 28 March(https://www.worldometers. info/coronavirus/country/china/)[19].

Real Data-2, n=66:

8	16	15	24	26	26	38	43	46	45	57	64	65	73	73	86	
89	97	108	97	146	121	143	142	105	98	136	114	118	109	97	150	
71	52	29	44	47	35	42	31	38	31	30	28	27	22	17	22	
11	7	13	10	14	13	11	8	3	7	6	9	7	4	6	5	
3	5															

First, it is checked whether MFE distribution can be used or not to analyze these data set. The Kolmogorov-Smirnov Z have been used to check the goodness-of-fit via MATLAB program. ML estimates, KS-Z and p- values based on above data is shown in Table 6.

Table 6 . Kolmogorov-Smirnov Z and the corresponding p-values for ML estimates

Methods	Estimates	Kolmogorov- Smirnov Z	p-values
MLE	$\hat{\alpha}$=1.2666 $\hat{\lambda}$=0.0184	0.0928	0.6208

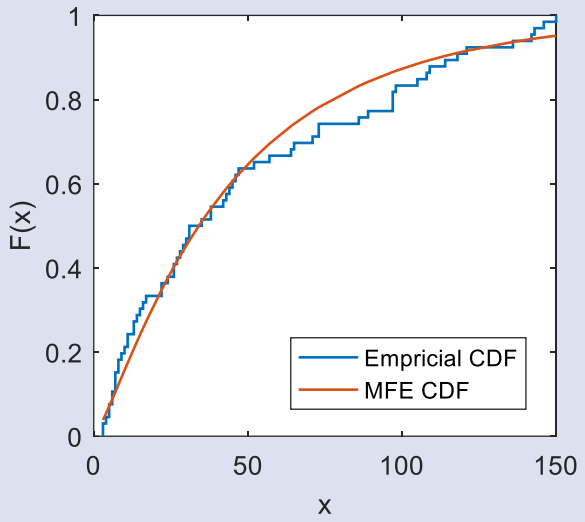

Figure 2: Plot Empricial CDF and MFE CDF for data-2

In this case, ML and approximate Bayes estimates for α and λ parameters are as follows.

	MLE		***BAYES*** $_{Lindley}$	
n	$\hat{\alpha}$	$\hat{\lambda}$	$\hat{\alpha}$	$\hat{\lambda}$
66	1.2666	0.0184	1.3009	0.0190

Conclusions

In this article, I have considered the MLE and approximate Bayes estimators for parameters of MFE distribution based on complete sample. It has been observed that the maximum likelihood estimators of the parameters can be obtained by using Newton-Raphson method. Because the Bayes estimators of the parameters cannot be obtained in explicit forms, we have obtained the approximate Bayes estimators using Lindley approximation method under squared-error loss function. I have compared the performance of the approximate Bayes estimates with the ML estimates by means of Monte Carlo simulations, and it has been observed that the performances of approximate Bayes estimates are better than those of ML estimates. Further, MSE values of the estimates of α and λ parameters obtained by using Lindley's approximation method are lower than those obtained by using MLE.

Concluding Remarks

The MFE distribution introduced by [7] is studied in this work with relation to MLE and Bayes estimation methods. For different parameter values and different sample sizes, simulations are performed. When the sample size is increased, the MSE and bias values are observed to decrease and approach zero. In addition, the estimations and KS outcomes for MLE and Bayes estimators are examined for two real datasets. The simulation results show that Bayesian estimators perform well on the bias and MSE criteria, and that the MLE and Bayesian estimators are close to each other in a large sample.

Conflicts of interest

All authors declare that they have no conflict of interest.

References

[1] Nadarajah S., Kotz S., The Exponentiated Frechet Distribution, *Interstat Electronic Journal*, 14 (2003) 01-07.

[2] da Silva R. V., de Andrade T. A., Maciel D. B., Campos R. P., Cordeiro G. M., A New Lifetime Model: The Gamma Extended Frechet Distribution, *Journal of Statistical Theory and Applications,* 12(1) (2013) 39-54.

[3] Krishna E., Jose K. K., Alice T., Ristic M. M., The Marshall-Olkin Frechet Distribution, *Communications in Statistics-Theory and Methods*, 42(22) (2013) 4091-4107.

[4] Afify Z., Yousof H. M., Cordeiro G. M., Ortega E. M. M., Nofal Z. M., The Weibull Frechet Distribution and Its Applications, *Journal of Applied Statistics*, 43(14) (2016) 2608- 2626.

[5] Ali M., Khalil A., Mashwani W. K., Alrajhi S., Al-Marzouki S., Shah K., A Novel Fréchet-Type Probability Distribution: its properties and applications, *Mathematical Problems in Engineering*, (2022) 1-14.

[6] Alsadat N., Ahmad A., Jallal M., Gemeay A. M., Meraou M. A., Hussam E., Hossain M. M., The Novel Kumaraswamy Power Frechet Distribution with Data Analysis Related to Diverse Scientific Areas, *Alexandria Engineering Journal*, 70 (2023) 651-664.

[7] Farhat A. T., Ramadan D. A., El-Desouky B.S., Statistical Inference of Modified Frechet–Exponential Distribution with Applications to Real-Life Data, *Appl. Math. Inf. Sci.*, 17(1) (2023) 109-124.

[8] Touw A. E., Bayesian Estimation of Mixed Weibull Distributions, *Reliability Engineering & System Safety*, 94(2) (2009) 463-47.

[9] Dey S., Bayesian Estimation of the Parameter and Reliability Function of an Inverse Rayleigh Distribution, *Malaysian Journal of Mathematical Sci.*, 6(1) (2012) 113-124.

[10] Abbas K., Yincai T., Comparison of Estimation Methods for Frechet Distribution with Known Shape, *Caspian Journal of Applied Sciences Research*, 1(10) (2012) 58-64.

[11] Kundu D., Gupta A.K., Bayes Estimation for the Marshall–Olkin Bivariate Weibull Distribution, *Computational Statistics and Data Analysis*, 57(2013) 271–281.

[12] Dey S., Dey. T., Kundu D., Two-Parameter Rayleigh Distribution: Different Methods of Estimation, *American*

Journal of Mathematical and Management Sci., 33(1) (2014) 55-74.

[13] Abbas K., Abbasi N. Y., Ali A., Khan S. A., Manzoor S., Khalil A., Khalil U., Khan M. D., Hussain Z., Altaf M., Bayesian Analysis of Three-Parameter Frechet Distribution with Medical Applications, *Hindawi Computational and Mathematical Methods in Medicine*, 9089856 (2019) 8.

[14] Ramos P. L., Louzada F., Ramos E., The Fréchet Distribution: Estimation and Application - An Overview, *Journal of Statistics & Management Systems*, 23(3) (2020) 549–578.

[15] Ahmad H. A. H., Almetwally E. M., Marshall-Olkin Generalized Pareto Distribution: Bayesian and Non Bayesian Estimation, *Pak. J. Stat. Oper. Res.*, 16 (1) (2020) 21-33.

[16] Almongy H. M., Almetwally E.M., Aljohani H.M., Alghamdi A. S., Hafez E. H., A New Extended Rayleigh Distribution with Applications of COVID-19 Data, *Results in Physics*, 23 (2021) 104012.

[17] EL-Sagheer R. M., Shokr E. M., Mahmoud M. A. W., El-Desouky B.,Inferences for Weibull Fréchet Distribution Using a Bayesian and Non-Bayesian Methods on Gastric Cancer Survival Times, *Hindawi Computational and Mathematical Methods in Medicine*, 9965856 (2021) 12.

[18] Lindley D.V., Approximate Bayesian Methods, *Trabajos de Estadistica*, 31 (1980) 223-237.

[19] Ahmad K.E., Jaheen Z.F., Approximate Bayes Estimators Applied to the Inverse Gaussian Lifetime Model, *Computers Math. Applic.*, 12 (1995) 39-47.

[20] Kundu D., Gupta R.D., Generalized Exponential Distribution: Bayesian Estimations, *Computational Statistics & Data Analysis*, 52 (2008) 1873-1883.

[21] Preda V., Panaitescu E., Constantinescu A., Bayes Estimators of Modified-Weibull Distribution Parameters using Lindley's Approximation, *Wseas Transactions on Mathematics*, 7 (2010) 539-549.

[22] Singh S.K., Singh U., Yadav A.S., Bayesian Estimation of Marshall–Olkin Extended Exponential Parameters under Various Approximation Techniques, *Hacettepe Journal of Mathematics and Statistics*, 43(2) (2014) 347 – 360.

[23] Akdam N., Kınacı İ., Saraçoğlu B., Statistical Inference of Stress-Strength Reliability for the Exponential Power (EP) Distribution based on Progressive Type-II Censored Samples, *Hacettepe Journal of Mathematics and Statistics*, 46 (2017) 239-253.

[24] Çiftci F., Saraçoğlu B., Akdam N., Akdoğan Y., Estimation of Stress-Strength Reliability for Generalized Gompertz Distribution under Progressive Type-II Censoring, *Hacettepe Journal of Mathematics and Statistics*, (2023).

[25] Akdam N., Bayes Estimation for the Rayleigh–Weibull Distribution Based on Progressive Type-II Censored Samples for Cancer Data in Medicine, *Symmetry,* 15(9) (2023) 1754.

[26] Sindhu T. S., Shafiq A., Al-Mdallal Q.M, Exponentiated Transformation of Gumbel Type-II Distribution for Modeling COVID-19 Data, *Alexandria Engineering Journal*, 60(1) (2021) 671-689.

Cumhuriyet Sci. J., 44(3) (2023) 610-616
DOI: https://doi.org/10.17776/csj.1180040

Cumhuriyet Science Journal

| csj.cumhuriyet.edu.tr | Founded: 2002 ISSN: 2587-2680 e-ISSN: 2587-246X Publisher: Sivas Cumhuriyet University

Estimation of the Density and Cumulative Distribution Functions of the Topp-Leone Distribution

Lazhar Benkhelifa [1,a,*]

[1] *Department of Mathematics and Informatics, Larbi Ben M'Hidi University, Oum El Bouaghi, 04000, Algeria*
**Corresponding author*

Research Article

History
Received: 25/09/2022
Accepted: 05/09/2023

ABSTRACT

In this paper, we estimate the probability density function and the cumulative distribution function of the Topp-Leone distribution. We use the maximum likelihood estimation, uniformly minimum variance unbiased estimation, least squares estimation, weighted least squares estimation, Cramér-von Mises estimation, Anderson-Darling estimation and method of percentile estimation. The consistency of these methods is illustrated in a simulation study. Finally, a real data set is given to assess the performance of proposed methods.

Keywords: Topp-Leone distribution, Maximum likelihood least squares estimation, Weighted least squares estimation, Cramér-von Mises estimation, Anderson-Darling estimation.

[a] *l.benkhelifa@yahoo.fr* *https://orcid.org/0000-0002-7271-418X*

Introduction

We say that the continuous random variable *X* has the Topp-Leone distribution if its probability density function (PDF) is given by $for\ 0 < x < 1$,

$$f(x) = \alpha(2-2x)(2x-x^2)^{\alpha-1}, \qquad \alpha > 0. \quad (1)$$

The corresponding cumulative distribution function (CDF) is

$$F(x) = (2x-x^2)^{\alpha}. \quad (2)$$

The Topp-Leone distribution was developed in 1955 by Topp and Leone [22]. In the last two decades, this distribution has a great attention by several authors. For exemple, the structural properties of this distribution are obtained in [18]. Many reliability measures of the Topp-Leone distribution are studied by Ghitany et al. [10]. Vicari et al. [23] proposed a two-sided generalized version of this distribution. Genç [8] derived the moments of order statistics from this distribution. Genç [9] estimated the probability *P(X>Y)* for this distribution. Bayoud [5] derived the admissible minimax estimates for the shape of this distribution. Akgül [1] estimated system reliability of multicomponent stress-strength model for Topp-Leone distribution. More recently, Long [15] obtained the estimation and prediction for this distribution based on the double Type-I hybrid censored data. Using progressively censored samples from this distribution, the inference of multicomponent stress-strength reliability are derived by Saini et al. [20]. Benkhelifa [6] proposed a new distribution called the alpha power Topp-Leone Weibull distribution.

In many research fields, it is necessary to estimate the PDF and/or CDF. For example, to estimate the Kullback-Leibler divergence, Rényi entropy and Fisher information we estimate the PDF whereas we use the CDF for estimating the quantile function, Bonferroni and Lorenz curves. To estimate the hazard rate function, the probability weighted moments and the mean deviation about mean; we use the PDF and CDF together.

There are several studies on the estimation of PDF and CDF for some distributions. We mention: Pareto distribution by Dixit and Jabbari [7], generalized exponential-Poisson distribution by Bagheri et al. [3], exponentiated Weibull distribution by Alizadeh et al. [2], Weibull extension model by Bagheri et al. [4], Lindley distribution by Maity and Mukherjee [16], inverse Rayleigh distribution by Maleki Jebely et al. [27] and exponentiated Burr XII distribution by Hassan et al. [12].

In this paper, we estimate the PDF and CDF of the Topp-Leone distribution by the following methods: maximum likelihood (ML), uniformly minimum variance unbiased (UMVU), least squares (LS), weighted least squares (WLS), Cramér-von Mises (CvM), Anderson-Darling (AD) and percentile (PC) methods of estimation.

Maximum Likelihood Estimators

Suppose $X_1, X_2, \ldots, X_n$ is a random sample from the Topp-Leone distribution. It easy to show that the ML estimator of α, denoted by $\hat{\alpha}_{ML}$ is given by

$$\hat{\alpha}_{ML} = \frac{-n}{\sum_{i=1}^{n} ln\left(2X_i - {X_i}^2\right)}.$$

So, we use the invariance property of ML method to obtain the ML estimators of the PDF (1) and the CDF (2) which are,

$$\hat{f}(x) = \hat{\alpha}_{ML}(2-2x)(2x-x^2)^{\hat{\alpha}_{ML}-1},$$

and

$$\hat{F}(x) = (2x-x^2)^{\hat{\alpha}_{ML}},$$

respectively for $0 < x < 1$.

It is obliged to find the PDF of random variable $\hat{\alpha}_{\mathrm{ML}}$ to compute $E([\hat{f}(x)]^r)$ and $E([\hat{F}(x)]^r)$.

Let $Z_i = -ln\left(2X_i - {X_i}^2\right), i = 1, \dots, n$ *and* $T = \sum_{i=1}^{n} Z_i$. So, it easy to show that Z_i has an exponential distribution with PDF given by

$$f_{Z_1}(z) = \alpha e^{-\alpha z}, \qquad \text{for } z > 0,$$

and then T has a gamma distribution with the following PDF:

$$F_T(t) = \frac{\alpha^n \ t^{n-1}}{\Gamma(n)} e^{-\alpha t}, \qquad \text{for } t > 0.$$

So we can obtain the PDF of $\hat{\alpha}_{ML} = \mathrm{S} = \mathrm{n/T}$ which is

$$f_S(s) = \frac{n^n \ \alpha^n}{\Gamma(n) s^{n+1}} e^{-\frac{\alpha n}{s}}, \qquad \text{for } s > 0. \tag{3}$$

In the following Theorem, we give $E([\hat{f}(x)]^r)$ and $E([\hat{F}(x)]^r)$.

Theorem 2.1. We have $E([\hat{f}(x)]^r) = \frac{2(\alpha n)^{\frac{n+r}{2}}(2-2x)^r}{\Gamma(n)(2x-x^2)^r}\left(\frac{-1}{rln(2x-x^2)}\right)^{\frac{r-n}{2}} K_{r-n}\left(2\sqrt{-n\alpha rln(2x-x^2)}\right)$ and

$$E([\hat{F}(x)]^r) = \frac{2(\alpha n)^{\frac{n}{2}}}{\Gamma(n)}\left(\frac{-1}{rln(2x-x^2)}\right)^{\frac{-n}{2}} K_{-n}\left(2\sqrt{-n\alpha rln(2x-x^2)}\right),$$

where K_v is the modified Bessel function of the second kind of order v.

Proof. From Equation (3), we can write

$$\begin{aligned} E([\hat{f}(x)]^r) &= \int_0^{+\infty} [s(2-2x)(2x-x^2)^{s-1}]^r \, e^{-\frac{\alpha n}{s}} ds \\ &= \frac{n^n \ \alpha^n \ (2-2x)^r}{\Gamma(n)(2x-x^2)^r} \int_0^{+\infty} s^{r-n-1}(2x-x^2)^{rs} e^{-\frac{\alpha n}{s}} ds \\ &= \frac{n^n \ \alpha^n \ (2-2x)^r}{\Gamma(n)(2x-x^2)^r} \int_0^{+\infty} s^{r-n-1} e^{rsln(2x-x^2)} e^{-\frac{\alpha n}{s}} ds. \end{aligned}$$

Using the formula (3.471.9) in [11], we get

$$\int_0^{+\infty} s^{r-n-1} e^{rsln(2x-x^2)} e^{-\frac{\alpha n}{s}} ds = 2\left(\frac{-\alpha n}{rln(2x-x^2)}\right)^{\frac{r-n}{2}} K_{r-n}\left(2\sqrt{-n\alpha rln(2x-x^2)}\right).$$

So

$$E([\hat{f}(x)]^r) = \frac{2(\alpha n)^{\frac{n+r}{2}}(2-2x)^r}{\Gamma(n)(2x-x^2)^r}\left(\frac{-1}{rln(2x-x^2)}\right)^{\frac{r-n}{2}} K_{r-n}\left(2\sqrt{-n\alpha rln(2x-x^2)}\right).$$

We can get $E([\hat{F}(x)]^r)$ in a similar manner, and then the proof of Theorem 2.1 is finished.

Remark. When *r=1*, we observe that the estimators $\hat{f}(x)$ and $\hat{F}(x)$ are biased for *f(x)* and *F(x)*, respectively.

In the following Theorem, we give the MSEs of $\hat{f}(x)$ and $\hat{F}(x)$.

Theorem 2.2. The MSE of $\hat{f}(x)$ is given by

$$\begin{aligned} \mathrm{MSE}\left(\hat{f}(x)\right) = &\frac{2(\alpha n)^{\frac{n+2}{2}}(2-2x)^2}{\Gamma(n)(2x-x^2)^2}\left(\frac{-1}{2ln(2x-x^2)}\right)^{\frac{2-n}{2}} K_{2-n}\left(2\sqrt{-2n\alpha ln(2x-x^2)}\right) \\ &- \frac{8(\alpha n)^{\frac{n+1}{2}}(1-x)f(x)}{\Gamma(n)(2x-x^2)}\left(\frac{-1}{ln(2x-x^2)}\right)^{\frac{1-n}{2}} K_{1-n}\left(2\sqrt{-n\alpha ln(2x-x^2)}\right) + f^2(x), \end{aligned}$$

while the MSEs of $\hat{F}(x)$ is

$$\mathrm{MSE}\big(\hat{F}(x)\big) = \frac{2(\alpha n)^{\frac{n}{2}}}{\Gamma(n)}\left(\frac{-1}{2ln(2x-x^2)}\right)^{\frac{-n}{2}} K_{-n}\left(2\sqrt{-2n\alpha ln(2x-x^2)}\right)$$
$$-\frac{4(\alpha n)^{\frac{n}{2}}F(x)}{\Gamma(n)}\left(\frac{-1}{ln(2x-x^2)}\right)^{\frac{-n}{2}} K_{-n}\left(2\sqrt{-n\alpha ln(2x-x^2)}\right) + F^2(x).$$

Proof. We know that

$$\mathrm{MSE}\big(\hat{f}(x)\big) = E([\hat{f}(x)]^2) - 2f(x)\mathrm{E}\big(\hat{f}(x)\big) + f^2(x),$$

then, we obtain $\mathrm{MSE}\big(\hat{F}(x)\big)$) by setting *r=1* and $E([\hat{f}(x)]^2)$ by *r=2* in Theorem 2.1. Similarly, we can get $\mathrm{MSE}\big(\hat{F}(x)\big)$.

UMVU Estimators

Here, we derive the UMVU estimators of the PDF and the CDF of the Topp-Leone distribution. Also, we give the MSEs of these estimators.

If $X_1, X_2, \dots, X_n$ is a random sample from the Topp-Leone distribution, then $T = -\sum_{i=1}^{n} ln\big(2X_i - {X_i}^2\big)$ is a complete sufficient statistic for α. Let $f^*(x)$ be the UMVU estimator of *f(x)*. Then using Lehmann-Scheffé theorem, we have

$$\mathrm{E}(f^*(x)\,) = \int f_{X_1|\mathrm{T}}(x_1|t) f_{\mathrm{T}}(t)dt = \int f_{X_1,\mathrm{T}}(x_1,t)dt = f_{X_1}(x_1),$$

where $f_{X_1|\mathrm{T}}(x_1|t) = f^*(x)$ is the conditional PDF of X_1 given *T* and $f_{X_1,\mathrm{T}}(x_1,t)$ is the joint PDF of X_1 and *T*. To find $f_{X_1|\mathrm{T}}(x_1|t)$, we need the following Lemma.

Lemma 3.1. The conditional PDF of X_1 given *T=t* is

$$f_{X_1|\mathrm{T}}(x|t) = \frac{(n-1)(2-2x)\big(t+ln(2x-x^2)\big)^{n-2}}{(2x-x^2)t^{n-1}}, \qquad for\ -ln(2x-x^2) < t < \infty.$$

Proof. We know that $T = \sum_{i=1}^{n} Z_i$ is a random variable has the PDF given by (3). So, after some elementary algebra, the conditional PDF of Z_1 given *T* is

$$h_{Z_1|\mathrm{T}}(z|t) = \frac{(n-1)(t-z)^{n-2}}{t^{n-1}}, \qquad \text{for } 0 < z < t.$$

Then

$$f_{X_1|\mathrm{T}}(x|t) = \frac{2-2x}{2x-x^2} h_{Z_1|\mathrm{T}}(-ln(2x-x^2)|t), \qquad for\ -ln(2x-x^2) < t < \infty,$$

and the proof of Lemma is finished.

Theorem 3.1. The UMVU estimators of *f(x)* and *F(x)* are given by

$$\tilde{f}(x) = \frac{(n-1)(2-2x)\big(t+ln(2x-x^2)\big)^{n-2}}{(2x-x^2)t^{n-1}},$$

and

$$\tilde{F}(x) = \left(\frac{t+ln(2x-x^2)}{t}\right)^{n-1},$$

respectively for $-ln(2x-x^2) < t < \infty$.

Proof. From Lemma 3.1, we observe immediately that $\tilde{f}(x)$ is the UMVU estimator of *f(x)*. By integrating $\tilde{f}(x)$, we obtain $\tilde{F}(x)$.

The following Theorem gives the MSEs of $\tilde{f}(x)$ and $\tilde{F}(x)$.

Theorem 3.2. Let *T=t* be given. The MSEs of $\tilde{f}(x)$ and $\tilde{F}(x)$ are respectively given by

$$\mathrm{MSE}\left(\tilde{f}(x)\right) = \frac{A^2}{\Gamma(n)}\sum_{i=1}^{2n-4}\binom{2n-4}{i} b^i a^{i+3}\Gamma(n-i-2,-ab) - f^2(x),$$

and

$$\mathrm{MSE}\left(\tilde{F}(x)\right)=\frac{1}{\Gamma(n)}\sum_{i=1}^{2n-2}\binom{2n-2}{i}b^i a^{i+1}\Gamma(n-i,-ab)-F^2(x),$$

where $A=\frac{(n-1)(2-2x)}{2x-x^2}$, $b=ln(2x-x^2)$ and $\Gamma(s,x)=\int_x^{\infty}t^{s-1}\,e^{-t}dt$ is the complementary incomplete gamma function.

Proof. We have

$$\tilde{f}(x)=\frac{A(t+b)^{n-2}}{t^{n-1}}$$

and

$$\mathrm{MSE}\left(\tilde{f}(x)\right)=E([\hat{f}(x)]^2)-f^2(x).$$

From Equation (3),

$$\begin{aligned}E([\hat{f}(x)]^2)&=\frac{A^2\alpha^n}{\Gamma(n)}\int_{-b}^{+\infty}\left[\frac{(t+b)^{n-2}}{t^{n-1}}\right]^2 t^{n-1}e^{-\alpha t}dt=\frac{A^2\alpha^n}{\Gamma(n)}\int_{-b}^{+\infty}\frac{(t+b)^{2n-4}}{t^{2n-2}}t^{n-1}e^{-\alpha t}dt\\&=\frac{A^2\alpha^n}{\Gamma(n)}\int_{-b}^{+\infty}\frac{(t+b)^{2n-4}}{t^{2n-4}}t^{n-3}e^{-\alpha t}dt=\frac{A^2\alpha^n}{\Gamma(n)}\int_{-b}^{+\infty}\left(\frac{t+b}{t}\right)^{2n-4}t^{n-3}e^{-\alpha t}dt\\&=\frac{A^2\alpha^n}{\Gamma(n)}\int_{-b}^{+\infty}\left(1+\frac{b}{t}\right)^{2n-4}t^{n-3}e^{-\alpha t}dt.\end{aligned}$$

We have

$$\left(1+\frac{b}{t}\right)^{2n-4}=\sum_{i=1}^{2n-4}\binom{2n-4}{i}\left(\frac{b}{t}\right)^i.$$

So

$$E([\hat{f}(x)]^2)=\frac{A^2\alpha^n}{\Gamma(n)}\int_{-b}^{+\infty}\left[\sum_{i=1}^{2n-4}\binom{2n-4}{i}\left(\frac{b}{t}\right)^i\right]t^{n-3}e^{-\alpha t}dt=\frac{A^2\alpha^n}{\Gamma(n)}\sum_{i=1}^{2n-4}\binom{2n-4}{i}b^i\int_{-b}^{+\infty}t^{n-i-3}e^{-\alpha t}dt.$$

The change of variables $u=\alpha t$, yields

$$E([\hat{f}(x)]^2)=\frac{A^2\alpha^n}{\Gamma(n)}\sum_{i=1}^{2n-4}\binom{2n-4}{i}\frac{b^i}{\alpha^{n-i-3}}\int_{-\alpha b}^{+\infty}u^{n-i-3}e^{-u}du=\frac{A^2}{\Gamma(n)}\sum_{i=1}^{2n-4}\binom{2n-4}{i}b^i\alpha^{i+3}\,\Gamma(n-i-2,-ab).$$

In a similar manner, we can find $\mathrm{MSE}\left(\tilde{F}(x)\right)$.

Least Squares and Weighted Least Squares Estimators

Swain et al. [21] proposed the LS and WLS methods. In this section, we use these methods to estimate α. Let $x_{(1)},\dots,x_{(n)}$ be the order observations of the random variables following the Topp-Leone distribution with size n. The LS estimator of α, denoted by $\tilde{\alpha}_{LS}$, is obtained by minimizing the function

$$\sum_{i=1}^{n}\left(\left(2x_{(i)}-x_{(i)}^2\right)^{\alpha}-\frac{i}{n+1}\right)^2,$$

while the WLS estimator of α, denoted by $\tilde{\alpha}_{WLS}$, is obtained by minimizing the function

$$\sum_{i=1}^{n}\frac{(n+2)(n+1)^2}{i(n-i+1)}\left(\left(2x_{(i)}-x_{(i)}^2\right)^{\alpha}-\frac{i}{n+1}\right)^2.$$

So, the LS and WLS estimators of the PDF and the CDF of the Topp-Leone distribution given, for $0<x<1$, by

$$\tilde{f}(x)=\tilde{\alpha}(2-2x)(2x-x^2)^{\tilde{\alpha}-1},$$

and

$$\tilde{F}(x)=(2x-x^2)^{\tilde{\alpha}},$$

where $\tilde{f}=\tilde{f}_{LS}$, $\tilde{F}=\tilde{F}_{LS}$ and $\tilde{\alpha}=\tilde{\alpha}_{LS}$ when we use the LS method and $\tilde{f}=\tilde{f}_{WLS}$, $\tilde{F}=\tilde{F}_{WLS}$ and $\tilde{\alpha}=\tilde{\alpha}_{WLS}$ for WLS method. Since it's difficult to find the MSEs of these estimators analytically, we shall calculate them by simulation.

Cramér-von Mises and Anderson Darling estimators

Let $x_{(1)},\dots,x_{(n)}$ be the order observations of the random variables following the Topp-Leone distribution with size n. The CvM estimator of the parameter α, denoted by $\tilde{\alpha}_{\mathrm{CvM}}$, of the Topp-Leone distribution is obtained by minimizing the function

$$\frac{1}{12n}+\sum_{i=1}^{n}\left(\left(2x_{(i)}-x_{(i)}^2\right)^{\alpha}-\frac{2i-1}{2n}\right)^2,$$

whereas the AD estimator of α, denoted by $\tilde{\alpha}_{\mathrm{AD}}$, is obtained by minimizing

$$-n+\sum_{i=1}^{n}(2i-1)\left(\alpha ln\left(2x_{(i)}-x_{(i)}^2\right)+ln\left(1-\left(2x_{(i)}-x_{(i)}^2\right)^{\alpha}\right)\right)^2.$$

So, the CvM and AD estimators of the PDF and the CDF of the Topp-Leone distribution given, for 0 < x < 1, by

$\tilde{f}(x)=\tilde{\alpha}(2-2x)(2x-x^2)^{\tilde{\alpha}-1}$,
and
$\tilde{F}(x)=(2x-x^2)^{\tilde{\alpha}}$,

where $\tilde{f}=\tilde{f}_{\mathrm{CvM}}$, $\tilde{F}=\tilde{F}_{\mathrm{CvM}}$ and $\tilde{\alpha}=\tilde{\alpha}_{\mathrm{CvM}}$ when we use the CvM method and $\tilde{f}=\tilde{f}_{\mathrm{AD}}$, $\tilde{F}=\tilde{F}_{\mathrm{AD}}$ and $\tilde{\alpha}=\tilde{\alpha}_{\mathrm{AD}}$ for AD method. Since it's difficult to find the MSEs of these estimators analytically, we shall calculate them by simulation.

Estimators Based on Percentiles

The PC method proposed by Kao [13-14]. In this section, the PC estimators of the PDF and the CDF of the Topp-Leone distribution are derived. Let $x_{(1)},\dots,x_{(n)}$ be the order observations of the random variables following the Topp-Leone distribution with size *n*. The PC estimator of α, denoted by $\tilde{\alpha}_{\mathrm{PC}}$, is obtained by minimizing

$$\sum_{i=1}^{n}\left(ln(p_i)-\alpha ln\left(2x_{(i)}-x_{(i)}^2\right)\right)^2$$

where $p_i=\frac{i}{n+1}$. It easy to show that

$$\tilde{\alpha}_{\mathrm{PC}}=\frac{\sum_{i=1}^{n}ln\left(2x_{(i)}-x_{(i)}^2\right)ln(p_i)}{\sum_{i=1}^{n}ln^2\left(2x_{(i)}-x_{(i)}^2\right)}.$$

So, the PC estimators of the PDF and the CDF are given by

$\tilde{f}(x)=\tilde{\alpha}_{\mathrm{PC}}(2-2x)(2x-x^2)^{\tilde{\alpha}_{\mathrm{PC}}-1}$,
and
$\tilde{F}(x)=(2x-x^2)^{\tilde{\alpha}_{\mathrm{PC}}}$,
respectively. Since it's difficult to find the MSEs of these estimators analytically, we shall compute them by simulation.

Simulation study

In this section, we carry out a simulation study to compare ML, UMVU, LS, WLS, PC, CvM and AD estimators of the PDF and the CDF for the Topp-Leone distribution. The random samples are generated from the Topp-Leone distribution for a given parameter *α*=1, 2 and 3 by using the inversion method: $X=\sqrt{1-U^{1/\alpha}}$, where *U* is a standard uniform random variable. The sample sizes of generated random samples are *n*=10, 20, 50 and 100, where the simulation is repeated 1000 times.

Table 1 gives the results of the simulation. We observe that the values of MSE converge to zero when *n* increases for all methods. So we can say that the estimators are consistent. Also, we see that the ML estimates of the PDF and the CDF have the lowest value of MSEs. This means that the ML estimators perform better than the others estimators.

Table 1. MSEs of the PDF and the CDF estimators.

		α=1		α=2		α=3	
n	**Methods**	**PDF**	**CDF**	**PDF**	**CDF**	**PDF**	**CDF**
10	ML	0.0837	0.0112	0.0238	0.1021	0.0511	0.0464
	UMVU	0.1021	0.0920	0.0436	0.1355	0.0518	0.0678
	PC	0.1313	0.1047	0.0982	0.1513	0.1099	0.0897
	LS	0.1967	0.2001	0.1869	0.1901	0.2010	0.1649
	WLS	0.1741	0.1699	0.1107	0.1812	0.1334	0.1121
	CvM	0.1450	0.1218	0.1005	0.1697	0.1101	0.1026
	AD	0.1601	0.1497	0.1087	0.1801	0.1254	0.1059
20	ML	0.0716	0.0053	0.0200	0.0921	0.0341	0.0344
	UMVU	0.0921	0.1152	0.0398	0.1040	0.0403	0.0516
	PC	0.1296	0.1007	0.0772	0.1106	0.0885	0.0662
	LS	0.1941	0.2158	0.1552	0.1681	0.1819	0.1398
	WLS	0.1601	0.1841	0.1079	0.1282	0.1223	0.0997
	CvM	0.1309	0.1181	0.0905	0.1609	0.1004	0.0992
	AD	0.1575	0.1367	0.0992	0.1788	0.1187	0.1003
50	ML	0.0102	0.0026	0.0010	0.0352	0.0028	0.0039
	UMVU	0.0467	0.0788	0.0035	0.0502	0.0177	0.0207
	PC	0.0816	0.0985	0.0225	0.0651	0.0412	0.0388
	LS	0.1511	0.1772	0.1398	0.1436	0.1196	0.1006
	WLS	0.1153	0.1380	0.0996	0.1041	0.0757	0.0967
	CvM	0.1098	0.1101	0.0702	0.1410	0.0866	0.0756
	AD	0.1271	0.1167	0.0803	0.1575	0.0982	0.0811
100	ML	0.0005	0.0016	0.00016	0.0017	0.00018	0.00047
	UMVU	0.0050	0.0042	0.00077	0.0123	0.0092	0.0084
	PC	0.0071	0.0056	0.0087	0.0209	0.0104	0.0196
	LS	0.0930	0.1004	0.0799	0.0874	0.0889	0.0917
	WLS	0.0931	0.1086	0.0599	0.0676	0.0727	0.0729
	CvM	0.0801	0.0998	0.0404	0.0590	0.0363	0.0606
	AD	0.1053	0.1060	0.0503	0.0602	0.0542	0.0699

Application to Real Data

To compare between ML, LS, WLS, CvM, AD and PC estimators for the PDF and the CDF, we use the following data set: 0.2160, 0.0150, 0.4082, 0.0746, 0.0358, 0.0199, 0.0402, 0.0101, 0.0605, 0.0954, 0.1359, 0.0273, 0.0491, 0.3465, 0.0070, 0.6560, 0.1060, 0.0062, 0.4992, 0.0614, 0.5320, 0.0347 and 0.1921. We took this data set from [19]. It represents the times between failures of secondary reactor pumps. In order to obtain data between 0 and 1, a normalization operation is done by dividing the original data set by 10.

To assess the behavior of ML, PC, LS and WLS estimators, we use the following criteria:

- Maximum likelihood criterion, which is given by $\mathrm{MLC} = -2\mathrm{lnL}$,
- Akaike information criterion, that is defined as $\mathrm{AIC} = -2\mathrm{lnL} + 2\mathrm{k}$,
- Bayes information criterion that is defined as by $BIC = -2lnL + kln(n)$,
- Akaike information criterion corrected, which is defined by $AICc = AIC + ((2k(k+1))/(n-k-1))$,
- Hannan-Quinn criterion, that is defined as $HQC = -2lnL + 2kln(ln(n))$,

where lnL is the estimated value of the maximum log-likelihood, k is the number of parameters and n is the number of observations.

The model which has lowest values of MLC, AIC, BIC, $AICc$ and HQC is selected as the best model to fit the data. The values of the estimates of the parameter and the model selection criteria for the different estimation methods are given in Table 2. It is clear from Tables 2 that the ML estimate has the smallest value for all the model selection criteria. This indicates that the ML estimator is superior than the LS, WLS, CvM, AD and PC estimators.

Plots the fitted PDFs versus the histogram are given in Figure 1(a) while the fitted CDFs plots versus the empirical CDF are given in Figure 1(b). It is easy to see from these plots that the ML method provides the good fit compared to the other methods.

Table 2. Estimations of the parameter and the model selection criteria for the data set.

Methods	Estimate of α	MLC	AIC	BIC	AICc	HQC
ML	0.4891	-37.5653	-35.5653	-34.4298	-35.3749	-35.2798
LS	0.3988	-36.6694	-34.6694	-33.5339	-34.4789	-34.3838
WLS	0.4375	-37.2901	-35.2901	-34.1546	-35.0996	-35.0045
CvM	0.4023	-36.7424	-34.7424	-33.6069	-34.5520	-34.4569
AD	0.4156	-36.9867	-34.9867	-33.8512	-34.7962	-34.7011
PC	0.4979	-37.5580	-35.5580	-34.4226	-35.3676	-35.2725

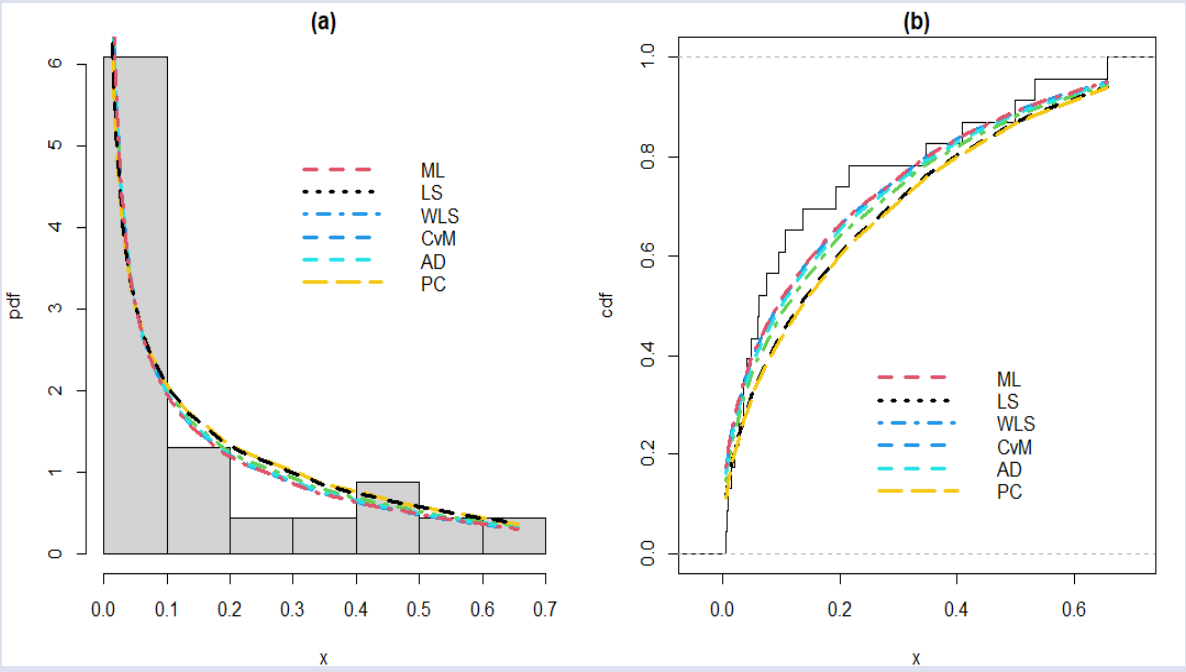

Figure 1. Fitted (a) PDFs versus the histogram and (b) CDFs versus the empirical CDF for the various estimation methods.

Conclusion

In this paper, we have considered seven methods of estimation: ML, UMVU, LS, WLS, CvM, AD and PC method for the PDF and the CDF of the Topp-Leone distribution. We have compared these estimators by a simulation study and a real data application. A simulation study shows that all estimators are consistent and the ML estimator performs better than the other estimators. Also, an application to real data set proves that the ML method provides the good fit than the other methods of estimation.

Conflicts of interest

There are no conflicts of interest in this work.

Acknowledgments

I thank the editor and the referees for their valuable comments and suggestions.

References

[1] Akgül F. G., Reliability estimation in multicomponent stress-strength model for Topp-Leone distribution*, J. Stat. Comput. Simul,* 89 (2019) 2914-2929.

[2] Alizadeh M., Bagheri S.F., Baloui Jamkhaneh E., Nadarajah, S., Estimates of the PDF and the CDF of the exponentiated Weibull distribution, *Braz. J. Probab. Stat*., 29 (2015) 695-716.

[3] Bagheri S.F., Alizadeh M., Baloui Jamkhaneh E., Nadarajah S., Evaluation and comparison of estimations in the generalized exponential-Poisson distribution, *J. Stat. Comput. Simul.*, 84 (2014) 2345-2360.

[4] Bagheri S. F., Alizadeh M., Nadarajah S., Deiri E., Efficient estimation of the PDF and the CDF of the weibull extension model, *Commun. Stat. Simul. Comput.*, 45 (2016) 2191-2207.

[5] Bayoud H.A., Admissible minimax estimators for the shape parameter of Topp-Leone distribution, *Comm. Statist. Theory Methods*, 45 (2016) 71-82.

[6] Benkhelifa L., Alpha power Topp-Leone Weibull distribution: Properties, Characterizations, Regression modeling and applications, *J. Stat. Manag. Systs.*, 25 (2022) 1945-1970.

[7] Dixit U.J., Jabbari Nooghabi M., Efficient estimation in the Pareto distribution, *Stat. Methodol.*, 7 (2010) 687-691.

[8] Genç A.İ., Moments of order statistics of Topp-Leone distribution, *Statist. Papers*, 53 (2012) 117-131.

[9] Genç A.İ., Estimation of P(X>Y) with Topp-Leone distribution, *J. Stat. Comput. Simul.*, 83 (2012) 326-339.

[10] Ghitany M.E., Kotz S., Xie M., On some reliability measures and their stochastic orderings for the Topp-Leone distribution*, J. Appl. Stat.*, 32 (2005) 715-722.

[11] Gradshteyn I.S., Ryzhik I.M., Table of Integrals, Series, and Products. Sixth ed. Academic Press, San Diego, (2000).

[12] Hassan A. S., Assar S. M., Ali K. A., Nagy H. F., Estimation of the density and cumulative distribution functions of the exponentiated Burr XII distribution, *Stat. Transit*, 22 (2021) 171-189.

[13] Kao J.H.K., Computer methods for estimating Weibull parameters in reliability studies, *Trans. IRE-Reliab. Qual. Control*., 13 (1958) 15-22.

[14] Kao J.H.K., A graphical estimation of mixed Weibull parameters in life testing electron tubes, *Technometrics*, 1 (1959) 389-407.

[15] Long B., Estimation and prediction for Topp--Leone distribution using double Type-I hybrid censored data, *J. Stat. Comput. Simul.*, 92 (2022) 2999-3019.

[16] Maiti S. S., Mukherjee I., On estimation of the PDF and CDF of the Lindley distribution, *Commun. Stat. Simul. Comput.,* 47 (2018) 1370-1381.

[17] Maleki Jebely F., Zare K., Deiri E., Efficient estimation of the PDF and the CDF of the inverse Rayleigh distribution, *J. Stat. Comput. Simul.*, 88 (2018) 75-88.

[18] Nadarajah S., Kotz S., Moments of some J-shaped distributions, *J. Appl. Stat*., 30 (2003) 311-317.

[19] Suprawhardana M.S., Prayoto S., Total time on test plot analysis for mechanical components of the RSG-GAS reactor, *Atom Indones,* 25 (1999) 81-90.

[20] Saini S., Tomer S., Garg R., Inference of multicomponent stress-strength reliability following Topp-Leone distribution using progressively censored data, *J. Appl. Statist*., (2022)

[21] Swain J., Venkatraman S., Wilson J., Least squares estimation of distribution functions in Johnson's translation system, *J. Stat. Comput. Simul.,* 29 (1988) 271-297.

[22] Topp C.W., Leone F.C., A family of J-shaped frequency functions, *J. Amer. Statist. Assoc*., 50 (1955) 209-219.

[23] Vicari D., Van Dorp J.R., Kotz S., Two-sided generalized Topp and Leone (TS-GTL) distributions, *J. Appl. Statist.*, 35 (2008) 1115-1129.

AUTHOR GUIDELINES

Thank you for choosing to submit your paper to Cumhuriyet Science Journal. The following instructions will ensure we have everything required so your paper can move through pre-evaluating, peer review, production and publication smoothly. Please take the time to read and follow them as closely as possible, as doing so will ensure your paper matches the journal's requirements.

Submission

Cumhuriyet Science Journal is an international, peer-reviewed, free of charge journal covering the full scope of both natural and engineering sciences. Manuscripts should be submitted by one of the authors of the manuscript as online submission after registration to the Cumhuriyet Sciences Journal. Microsoft Word (.doc, .docx, .rtf), files can be submitted. There is no page limit. If there is a problem while uploading the files of manuscript, please try to reduce their file size, especially manuscripts including embedded figures. Submissions by anyone other than one of the authors will not be accepted. The submitting author takes responsibility for the paper during submission and peer review. If for some technical reason submission through the online submission systme is not possible, the author can contact csj@cumhuriyet.edu.tr for support.

Submission or processing charges

Cumhuriyet Science Journal does not charge any article submission, processing charges, and printing charge from the authors.

Terms of Submission

Papers must be submitted on the understanding that they have not been published elsewhere (except in the form of an abstract or as part of a published lecture, review, or thesis) and are not currently under consideration by another journal. The submitting author is responsible for ensuring that the article's publication has been approved by all the other coauthors. It is also the authors' responsibility to ensure that the articles emanating from a particular institution are submitted with the approval of the necessary institution. Only an acknowledgment from the editorial office officially establishes the date of receipt. Further correspondence and proofs will be sent to the author(s) before publication unless otherwise indicated. It is a condition of submission of a paper that the corresponding author permit editing of the paper for readability. All enquiries concerning the publication of accepted papers should be addressed to csj@cumhuriyet.edu.tr. Please note that Cumhuriyet Science Journal uses iThenticate software to screen papers for unoriginal material. By submitting your paper to Cumhuriyet Science Journal are agreeing to any necessary originality checks your paper may have to undergo during the peer review and production processes. Upon receiving a new manuscript, the Editorial office conducts initial pre-refereeing checks to ensure the article is legible, complete, correctly formatted, original, within the scope of the journal in question, in the style of a scientific article and written in clear English. Any article that has problems with any of the journal criteria may be rejected at this stage.

Peer Review

This journal operates a single blind review process. All contributions will be initially assessed by the editor for suitability for the journal. Papers deemed suitable are then typically sent to a minimum of two independent expert reviewer to assess the scientific quality of the paper. The author is required to upload the revised article to the system within 15 days by making the corrections suggested by the referee. The article will be rejected if there are no fixes in it. The Editor is responsible for the final decision regarding acceptance or rejection of articles. The Editor's decision is final

Title and Authorship Information

The following information should be included

Paper title

Full author names

Full institutional mailing addresses

Corresponding address

Email address

Abstract

The manuscript should contain an abstract. The researchers who are native speakers of Turkish have to add Turkish title and abstract as well. The abstract should be self-contained and citation-free and should be 250-300 words.

Keywords

Keywords of the scientific articles should be selected from the web address of www.bilimadresleri.com

Introduction

This section should be succinct, with no subheadings.

Materials and Methods

This part should contain sufficient detail so that all procedures can be repeated. It can be divided into subsections if required.

Conflicts of interest

Sample sentence if there is no conflict of interest: The authors stated that did not have conflict of interests.

Acknowledgements

Sample sentences for acknowledgements: The work was supported by grants from CUBAP (T-11111). We would like to acknowledge Prof. Mehmet Sözer, MD, for his precious technical and editorial assistance. We would like to thank

References

References to cited literature should be identified by number in the text in square brackets and grouped at the end of the paper in numerical order of appearance. Each reference must be cited in the text. Always give inclusive page numbers for references to journal articles and a page range or chapter number for books. References should be styled and punctuated according to the following examples

[1] Karaca E., Ulusoy S., Morgül Ü., Ulusoy H.I., Development of Analytical Method for Sensitive Determination of Streptozotocin based on Solid Phase Extraction, Cumhuriyet Sci. J., 41 (4) (2020) 826-831. (sample reference for journals)

[2] Keskin B., Ozkan A.S., Inverse Spectral Problems for Dirac Operator with Eigenvalue Dependent Boundary and Jump Conditions, Acta Math. Hungar., 130 (2011) 150-159(sample reference for journals)

[3] Mazur M.T., Kurman R.J., Dysfunctional Uterine Bleeding. In: Mazur M.T., Kurman R.J., (Eds). Diagnosis of endometrial biopsies and curettings, A practical approach. 2nd ed. Berlin: Springer, (2005) 100-120. (sample reference for book chapters)

[4] Mazur M.T., Kurman R.J.,Diagnosis of endometrial biopsies and curettings, A practical approach. 2nd ed. Berlin, (2005) 100-120. (sample reference for book)

[5] National Cancer Institute, Surveillance Epidemiology and End Results. Cancer of the Corpus and Uterus, NOS. Available at: http://seer.cancer.gov/statfacts/html/corp.html?statfacts_page=corp. Retrieved March 2, 2008. (sample reference for websites)

[6] Surname N., Title of thesis, PD or master thesis, Name of university, name of institue, year. (sample reference for thesis)

[7] Surname N., Title of fulltext conference paper, name of conference, city, year, pages. (sample reference for Abstratcs in conferences are not accepted as a valid reference except full text)

Preparation of Figures

Each figure can be integrated in the paper body or separately uploaded and should be cited in a consecutive order. Figure widths can be 4-6 inch as 300 dpi. The labels of the figures should be clear and informative. The name and the subtitles of the figures must be 9-point font.

Preparation of Tables

Tables should be cited consecutively in the text. Every table must have a descriptive title and if numerical measurements are given, the units should be included in the column heading. Tables should be simple with simple borders and text written as left text. The name and the subtitle of the tables must be 9-point font

Proofs

Corrected proofs must be returned to the publisher within 2 weeks of receipt. The publisher will do everything possible to ensure prompt publication. It will therefore be appreciated if the manuscripts and figures conform from the outset to the style of the journal.

Copyright

Ethical Guidelines

New methods and ethically relevant aspects must be described in detail, bearing in mind the following:

Human Experiments. All work must be conducted in accordance with the Declaration of Helsinki (1964). Papers describing experimental work on human subjects who carry a risk of harm must include:

A statement that the experiment was conducted with the understanding and the consent of the human subject.

A statement that the responsible Ethical Committee has approved the experiments.

Animal Experiments. Papers describing experiments on living animals should provide:

A full description of any anaesthetic and surgical procedure used.

Evidence that all possible steps were taken to avoid animal suffering at each stage of the experiment. Papers describing experiments on isolated tissues must indicate precisely how the donor tissues were obtained.

Submission Preparation Checklist

As part of the submission process, authors are required to check off their submission's compliance with all of the following items, and submissions may be rejected that do not adhere to these guidelines.

The submission has not been previously published, nor is it before another journal for consideration (or an explanation has been provided in Comments to the Editor).

The submission file is in Microsoft Word document file (Times New Roman) format.

Where available, URLs for the references have been provided.

The text is single-spaced; uses a 11-point font; employs italics, rather than underlining (except with URL addresses); and all illustrations, figures, and tables are placed within the text at the appropriate points, rather than at the end.

The text adheres to the stylistic and bibliographic requirements outlined in the Author Guidelines, which is found in About the Journal.

If submitting to a peer-reviewed section of the journal, the instructions in Ensuring a Double-Blind Review have been followed.